Is your personality written in a ratio of finger lengths? *p. 923*

Summer books roundup *p. 926*

A paleo-Antarctic legacy in Asian rainforests *p. 972*

Science

$15
7 JUNE 2019
SPECIAL ISSUE
sciencemag.org

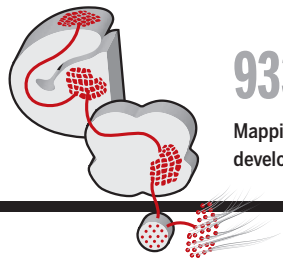
AAAS



ORGANOIDS

CONTENTS

7 JUNE 2019 • VOLUME 364 • ISSUE 6444



933 & 987
Mapping whiskers in the developing mouse brain



CREDITS: (FROM TOP) BASED ON A. TIRIAC BY A. KITTERMAN/*SCIENCE*; STEPHAN SCHMITZ/FOLIO ART

NEWS

IN BRIEF

912 News at a glance

IN DEPTH

915 RAT ERADICATION LAUNCHED ON POPULATED ISLAND
"Landmark" Lord Howe Island project alarms some residents but will likely save local fauna *By J. Pickrell*

916 NATIONAL ACADEMY TO ALLOW EXPULSION OF HARASSERS
Gray-haired, mostly male members vote in bylaw change *By M. Wadman*

917 NEW PENTAQUARKS HINT AT ZOO OF EXOTIC MATTER
Short-lived particles made of five quarks may resemble molecules in their structure *By A. Cho*

918 PEROVSKITE LEDS BEGIN TO SHINE
Solar cell wonder materials could also revolutionize lighting and displays *By R. F. Service*
▸ *SCIENCE ADVANCES* RESEARCH ARTICLE BY N. ZHOU *ET AL*. 10.1126/sciadv.aav8141; PODCAST

919 RADICAL OPEN-ACCESS PLAN IS DELAYED A YEAR
In response to criticisms, Plan S also lifts cap on article fees *By T. Rabesandratana*

920 DNA BARCODES JUMP-START SEARCH FOR NEW SPECIES
$180 million project aims to identify 2 million species *By E. Pennisi*

921 WOMEN OF COLOR FACE DOUBLE DOSE OF BIAS
Postdoc application study reveals gender and racial preferences *By K. Langin*

922 BIPARTISAN BILL PROPOSES FORUM ON U.S. ACADEMIC ESPIONAGE
Congress asked to set up National Academies roundtable *By J. Mervis*

FEATURES

923 THE MISMEASURE OF HANDS?
Some researchers say a simple ratio of finger lengths can predict personality and health. Others say that's wishful thinking *By M. Leslie*

INSIGHTS

BOOKS *ET AL.*

926 THE SCIENTIST'S SUMMER READING LIST

PERSPECTIVES

932 RISING METHANE: A NEW CLIMATE CHALLENGE
The amount of the greenhouse gas methane in Earth's atmosphere is rising rapidly *By S. E. Mikaloff Fletcher and H. Schaefer*

933 EMBRYONIC NEURAL ACTIVITY WIRES THE BRAIN
Disruption of spontaneous activity prevents formation of cortical whisker maps *By A. Tiriac and M. B. Feller*
▸ REPORT P. 987

935 IMAGING MAGNETIC 2D CRYSTALS WITH QUANTUM SENSORS
Odd- and even-layer variations in magnetization occur in two-dimensional chromium triiodide *By J. Fernández-Rossier*
▸ REPORT P. 973

936 HOW FAST WILL THE ANTARCTIC ICE SHEET RETREAT?
Feedbacks between glacier retreat and the solid Earth may slow ice loss from Antarctica *By E. J. Steig*
▸ RESEARCH ARTICLE P. 969

937 CELL FATE DECISIONS DURING DEVELOPMENT
Cell differentiation involves activation of mutually exclusive genetic programs *By R. Mayor*
▸ RESEARCH ARTICLE P. 971

938 MUTATED CLONES ARE THE NEW NORMAL
Measuring and understanding the dynamics of clonal cell populations is key for cancer prevention *By C. Tomasetti*
▸ RESEARCH ARTICLE P. 970

940 DAVID A. HAMBURG (1925–2019)
Renowned physician-psychiatrist and humanitarian *By H. V. Fineberg*

Published by AAAS



POLICY FORUM

941 ETHICS OF INCLUSION: CULTIVATE TRUST IN PRECISION MEDICINE
We must explore how studies enhance diversity, inclusion *By S. S.-J. Lee* et al.

LETTERS

943 CHINA'S DAMS THREATEN GREEN PEAFOWL
By W. Tang et al.

943 SCIENCE-BASED WILDLIFE DISEASE RESPONSE
By J. Vicente et al.

944 SPECIAL EDUCATIONAL NEEDS AND FIELDWORK
By D. Chiarella

945 TECHNICAL COMMENT ABSTRACTS

RESEARCH

IN BRIEF

966 From *Science* and other journals

RESEARCH ARTICLES

969 ICE SHEETS
Slowdown in Antarctic mass loss from solid Earth and sea-level feedbacks *E. Larour* et al.
RESEARCH ARTICLE SUMMARY; FOR FULL TEXT: dx.doi.org/10.1126/science.aav7908
▸ PERSPECTIVE P. 936

970 HUMAN GENETICS
RNA sequence analysis reveals macroscopic somatic clonal expansion across normal tissues *K. Yizhak* et al.
RESEARCH ARTICLE SUMMARY; FOR FULL TEXT: dx.doi.org/10.1126/science.aaw0726
▸ PERSPECTIVE P. 938

971 NEURODEVELOPMENT
Spatiotemporal structure of cell fate decisions in murine neural crest *R. Soldatov* et al.
RESEARCH ARTICLE SUMMARY; FOR FULL TEXT: dx.doi.org/10.1126/science.aas9536
▸ PERSPECTIVE P. 937

972 PALEOBOTANY
Eocene Fagaceae from Patagonia and Gondwanan legacy in Asian rainforests *P. Wilf* et al.
RESEARCH ARTICLE SUMMARY; FOR FULL TEXT: dx.doi.org/10.1126/science.aaw5139

REPORTS

973 MAGNETISM
Probing magnetism in 2D materials at the nanoscale with single-spin microscopy *L. Thiel* et al.
▸ PERSPECTIVE P. 935

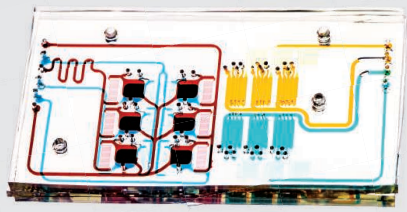
976 SUPERCONDUCTIVITY
Magnetic field–induced pair density wave state in the cuprate vortex halo *S. D. Edkins* et al.

981 RADIO ASTRONOMY
A radio ridge connecting two galaxy clusters in a filament of the cosmic web *F. Govoni* et al.

984 PHYSICS
Stable Casimir equilibria and quantum trapping *R. Zhao* et al.

987 NEURODEVELOPMENT
Prenatal activity from thalamic neurons governs the emergence of functional cortical maps in mice *N. Antón-Bolaños* et al.
▸ PERSPECTIVE P. 933

991 NEUROSCIENCE
Social transmission of food safety depends on synaptic plasticity in the prefrontal cortex *M. Loureiro* et al.



SPECIAL SECTION
ORGANOIDS

INTRODUCTION
946 Approximating organs

REVIEWS
948 Self-organization of stem cells into embryos: A window on early mammalian development *M. N. Shahbazi* et al.

952 Cancer modeling meets human organoid technology *D. Tuveson and H. Clevers*

956 Organoids by design *T. Takebe and J. M. Wells*

960 Organoids-on-a-chip *S. E. Park* et al.

ON THE COVER



Reconstruction of a human airway organoid by 3D confocal microscopy (DNA, blue; CD24, red). Organoids generated in culture and on platforms provide excellent model systems for the study of normal organ development and disease. This special issue highlights several features of current organoid research. See page 946.
Image: Anne Rios, Princess Máxima Center, Utrecht, Netherlands

DEPARTMENTS

911 EDITORIAL
A new narrative for the ocean
By Jane Lubchenco and Steven D. Gaines

1002 WORKING LIFE
Time to branch out
By Kara Mosovsky

New Products 996
Science Careers 997

SCIENCE (ISSN 0036-8075) is published weekly on Friday, except last week in December, by the American Association for the Advancement of Science, 1200 New York Avenue, NW, Washington, DC 20005. Periodicals mail postage (publication No. 484460) paid at Washington, DC, and additional mailing offices. Copyright © 2019 by the American Association for the Advancement of Science. The title SCIENCE is a registered trademark of the AAAS. Domestic individual membership, including subscription (12 months): $165 ($74 allocated to subscription). Domestic institutional subscription (51 issues): $1971; Foreign postage extra: Mexico, Caribbean (surface mail) $55; other countries (air assist delivery): $98. First class, airmail, student, and emeritus rates on request. Canadian rates with GST available upon request, GST #125488122. Publications Mail Agreement Number 1069624. **Printed in the U.S.A.**
Change of address: Allow 4 weeks, giving old and new addresses and 8-digit account number. **Postmaster:** Send change of address to AAAS, P.O. Box 96178, Washington, DC 20090–6178. **Single-copy sales:** $15 each plus shipping and handling; bulk rate on request. **Authorization to reproduce** material for internal or personal use under circumstances not falling within the fair use provisions of the Copyright Act can be obtained through the Copyright Clearance Center (CCC), www.copyright.com. The identification code for *Science* is 0036-8075. *Science* is indexed in the *Reader's Guide to Periodical Literature* and in several specialized indexes.

CREDITS: (FROM LEFT) TOUCH MAPPER; THE BIOLINES LABORATORY DIRECTED BY D. HUH AT THE UNIVERSITY OF PENNSYLVANIA

Published by AAAS

EDITORIAL

A new narrative for the ocean

Narratives help frame our thinking and action. On the eve of World Oceans Day and in anticipation of the United Nations Decade of Ocean Science for Sustainable Development (2021–2030), a new narrative for the ocean is warranted—one that reflects current scientific knowledge and inspires new science and effective action.

For most of human history, people considered the ocean so immense, bountiful, and resilient that it was impossible to deplete or disrupt it. The overarching narrative was, "The ocean is so vast, it is simply too big to fail." This mindset persists today, bringing even more intense, unsustainable uses of the ocean that reflect ignorance; the allure of new economic opportunity; or the need for food, resources, and development. However, the folly of this too-big-to-fail narrative has become glaringly obvious through overpowering scientific evidence of depletion, disruption, and pollution. Climate change, ocean acidification, habitat destruction, overfishing, and nutrient, plastic, and toxic pollution are insidious. These changes threaten the most vulnerable people; the economic prosperity, quality of life, and opportunities for everyone; and the well-being of the ocean's amazing life forms. Problems appear too complex, vested interests too powerful, and system inertia too great, especially as demands on the ocean escalate. A new narrative has arisen: "The ocean is massively and fatally depleted and disrupted. The ocean is simply too big to fix." The result? Depression and lack of engagement and motivation.



"In healing the ocean, we can heal ourselves."

Yet despite the undeniable challenges, hints of a new ocean mindset are emerging. Many powerful solutions already exist and could be scaled up. Opportunities abound to develop new solutions that are based on efficiency, incentives, technology, biotechnology, and regenerative and holistic approaches. Moreover, because the ocean is central to the functioning of the planet and human well-being, many ocean solutions could bring substantial co-benefits to address poverty, hunger, economic development, inequity, peace, security, coastal resilience, and climate mitigation and adaptation. For example, reforming fisheries to "fish smarter, not harder" can help restore ocean ecosystems; reduce impacts of climate change; and enhance food security, job creation, and poverty alleviation. Combining remote sensing, artificial intelligence, big data, machine learning, transparency, and new policies can minimize illegal fishing. Enabling sustainable aquaculture—especially of low trophic species—could contribute substantially to food security, with a much smaller environmental footprint than that of terrestrial animal production. Creating fully and highly protected, well-designed marine protected areas will safeguard biodiversity, replenish the ocean, and help mitigate and adapt to climate change and ocean acidification. Incorporating ocean actions into the climate agenda is essential to reducing greenhouse gas emissions and adapting to climate disruption. Expanding the range of effective solutions and scaling them globally requires scientists to engage actively with communities, fishers, businesses, nongovernmental organizations, managers, and policy-makers so that solutions are complementary, integrated, effective, and rapid.

A new narrative does not automatically change the status quo but, if widely adopted, can reset expectations and liberate ingenuity. Yes, the challenges are fierce, and the future is unpredictable. But here is an opportunity to replicate, accelerate, and escalate existing successes while driving innovative and transformative changes. Key players in the policy and business communities are open to innovation. Now is the moment for more scientists to pivot from simply documenting the tragedy underway to also creating scalable solutions.

It is time for a new ocean narrative that says, "The ocean is so central to our future. It's too important to neglect." In creating a new solution space for the ocean, we can also address broader global problems. In healing the ocean, we can heal ourselves. The ocean sustains and feeds us. It connects us. It is our past and our future. The ocean is not too big to fail, nor is it too big to fix. It is too big to ignore.

– Jane Lubchenco and Steven D. Gaines

Jane Lubchenco *is the distinguished university professor at Oregon State University, former administrator of the U.S. National Oceanic and Atmospheric Administration (2009–2013), and the first U.S. Science Envoy for the Ocean (2014–2016). lubchenco@oregonstate.edu Twitter: @JaneLubchenco*

Steven D. Gaines *is dean and distinguished professor at the Bren School of Environmental Science and Management at the University of California, Santa Barbara. gaines@ucsb.edu*

10.1126/science.aay2241

PHOTO: ALTANAKA/SHUTTERSTOCK.COM

Published by AAAS



Lord Howe Island has reefs, forests, and endemic species threatened by invasive rodents.

BIODIVERSITY

Rat eradication launched on populated island

"Landmark" Lord Howe Island project alarms some residents but will likely save local fauna

By **John Pickrell**

A beguiling, 11-kilometer-long speck of land in the Pacific Ocean 780 kilometers northeast of Sydney, Australia, Lord Howe Island hosts some of the world's southernmost tropical coral reefs as well as throngs of endemic birds and insects. But invasive species have laid siege to its unique biodiversity, the worst of them the black rats that first scurried ashore in 1918 after the steamship *SS Makambo* grounded on the reef. Now, a unique effort to eradicate the invaders is unfolding—against a background of controversy among the island's roughly 380 human inhabitants.

To protect or restore native species, introduced rodents have been extirpated on more than 700 islands worldwide, many around New Zealand, with its rich but threatened endemic fauna. But the Lord Howe project, years in the making, "will be the largest rodent eradication undertaken on a permanently inhabited island anywhere in the world," says Andrew Walsh of the Lord Howe Island Rodent Eradication Project, who is overseeing the effort to spread 42 tons of poisoned cereal pellets across the island. Some 28,000 bait stations were filled across farmed and residential areas starting 22 May, and helicopters will scatter baits over more forested and mountainous parts of the island as soon as weather permits.

Walsh and his colleagues hope to undo some of the damage from the voracious rodents, which have wiped out five endemic birds, two plants, and 13 insects, including the 15-centimeter-long, black, waxy-looking Lord Howe Island stick insect, also called the phasmid or tree lobster (*Dryococelus australis*). Some lost species, including the phasmid, have subsequently been rediscovered on surrounding islets. Eliminating the estimated 360,000 rodents—including house mice, which arrived in the 1860s—could allow the native animals to return to the main island, and will also protect another 70 or more threatened species, such as the little shearwater, masked booby, and several endemic palms that grow in the island's cloud forest.

"It's going to be a landmark project throughout the history of eradications," says Ian Hutton, naturalist and curator of the Lord Howe Island Museum, who has led research and conservation on the island since the 1980s. But the fact that Lord Howe Island—a UNESCO World Heritage Site that is officially part of the Australian state of New South Wales—is a tourist destination with an established human population created a unique challenge. Many residents feared the baits might harm children, pets, cattle, and other wildlife or damage the lucrative tourist trade.

The island's governing body decided in 2017 to go ahead with the AU$10.5 million eradication, after 15 years of research and planning and a referendum that saw 52% of islanders vote in favor. But others remained bitterly opposed. "This whole thing will be a disaster. We might as well kiss our World Heritage listing goodbye," islander Rodney Thompson told Sydney's *The Daily Telegraph* newspaper in April.

"We have families that have been here six generations, and some have a sense of ownership of the island," says Hutton, a longtime advocate for the eradication.

Originally scheduled for 2018, the effort was postponed for a year because of a snag in government pesticide permits, organizers say. The delay gave them time to rethink how baits would be distributed in occupied areas, which brought many remaining detractors on board.



Rodents wiped out the cigar-size Lord Howe Island stick insect on the main island, but it clung to life on a nearby islet.

PHOTOS: IAN HUTTON

Published by AAAS

People weren't the only complication. Research in 2007 had revealed that the poison, a rodenticide called brodifacoum, might endanger two endemic birds, the Lord Howe Island woodhen and the Lord Howe Island currawong. Since April, a team from Sydney's Taronga Zoo has been involved in rounding them up, housing the roughly 200 woodhens and 125 currawongs captured so far—more than half the wild populations—in aviaries and pens. The birds have "settled in beautifully," says Leanne Elliott, wildlife conservation officer at the zoo. Once the poison has broken down, they'll be released into the wild again, likely in stages toward the end of the year.

By then the rats should be gone, and biodiversity should start to rebound, says Melanie Massaro, an ornithologist at Charles Sturt University in Albury, Australia, who has been studying the currawong. Providing the eradication is successful, she says, "Some smaller seabirds that have been previously lost will likely start breeding on the island again; some populations of currently threatened species will increase in numbers; and there's also the potential of reintroducing species."

One early returnee might be the Lord Howe stick insect, long thought extinct. In 2001, a few individuals were found clinging to life atop windswept Ball's Pyramid, a 551-meter-tall rocky sea stack 23 kilometers to the southwest. The insects have since been bred at Australia's Melbourne Zoo, and in 2017 researchers confirmed that their DNA matches that of museum specimens collected from the main island more than a century ago. The first step in the species return will come in 2021 with a trial release of captive-bred phasmids onto an islet in Lord Howe's lagoon that is now being revegetated.

"It's all going to be done very carefully," Hutton says. "In 100 years, there have been a lot of changes and the phasmid was part of an ecosystem that has altered," he says, arguing that some of the missing birds may once have kept it in check. Without native predators, the stick insect population could surge.

Then again, some of those birds may return as well. Norfolk Island, about 900 kilometers to the north, hosts related subspecies of parrots, owls, and several other birds that once made their home on Lord Howe. They are contenders for reintroductions. Others, such as the Kermadec petrel and white-bellied storm petrel, found on surrounding islets, may return on their own—providing this summer's campaign can end the centurylong reign of the rats. ■

John Pickrell is a science journalist in Sydney, Australia.



Members of the National Academy of Sciences may be ousted for offenses including sexual harassment.

PHOTO: MAXWELL MACKENZIE/NATIONAL ACADEMY OF SCIENCES

SCIENTIFIC COMMUNITY

National academy to allow expulsion of harassers

Gray-haired, mostly male members vote in bylaw change

By **Meredith Wadman**

The prestigious U.S. National Academy of Sciences (NAS) in Washington, D.C., has voted to allow expulsion of members for breaches of its Code of Conduct, including sexual harassment. Until now, election to the 156-year-old academy, a pinnacle of scientific achievement, has been a lifetime honor.

In voting that concluded on 31 May with results announced this week, 84% of those who cast ballots approved an amendment to the organization's bylaws allowing expulsion of a member by a two-thirds vote of NAS's 17-member Council. Sixteen percent voted against the change. The average age of NAS members is 72; 83% are men. Although 2242 NAS members were eligible to vote, the academy did not disclose how many participated.

"All women who have had a tough road–even those who have made it—I'm sure like me are happy to see this day where they can finally say: 'The climate is gonna change,'" says Marcia McNutt, president of NAS, who has spent the past year laying the groundwork for the vote by holding meetings with members around the country. "No longer will a climate be tolerated that doesn't allow women to have the same chance as their male colleagues."

In June 2018, the National Academies of Sciences, Engineering, and Medicine (NASEM), of which NAS is a part, issued a landmark report documenting pervasive sexual harassment in those disciplines. "We know from research that one of the most potent predictors of sexual harassment is [an] organization's tolerance of it," says Lilia Cortina of the University of Michigan in Ann Arbor, an expert on sexual harassment who helped write the report. "This vote … sends a strong message that this institution will not tolerate gender-based abuse or harbor known abusers."

Under a process developed by NAS's Council, any person can bring a complaint about an NAS member for any breach of the organization's Code of Conduct, which spans behaviors including bullying, discrimination, sexual harassment, and scientific misconduct—the last defined as fabrication, falsification, or plagiarism. NAS would not investigate such claims. Rather, the complainant must document wrongdoing by presenting official findings by outside funding agencies, journals, or institutions.

McNutt says she expects requests to expel existing members "very soon," adding, "I think some will be more straightforward than others." NAS members whose universities have concluded they sexually harassed women include astronomer Geoff Marcy, formerly of the University of California (UC), Berkeley, and evolutionary biologist Francisco Ayala, formerly of UC Irvine.

A year ago, BethAnn McLaughlin, a neuroscientist at Vanderbilt University in Nashville, founded the nonprofit #MeTooSTEM and launched a petition since signed by 5889 people urging NAS to expel harassers. "I'm thrilled," she says of the vote. "Belonging to a scientific society is an honor, not a right. I hope other science societies do the same immediately." ■

Published by AAAS

PARTICLE PHYSICS

New pentaquarks hint at zoo of exotic matter

Short-lived particles made of five quarks may resemble molecules in their structure

By **Adrian Cho**

Four years ago, when experimenters spotted pentaquarks—exotic, short-lived particles made of five quarks—some physicists thought they had glimpsed the strong nuclear force, which binds the atomic nucleus, engaging in a bizarre new trick. New observations have now expanded the zoo of pentaquarks, but suggest a tamer explanation for their structure. The findings, from the Large Hadron Collider beauty experiment (LHCb), a particle detector fed by the LHC at CERN, the European particle physics laboratory near Geneva, Switzerland, suggest pentaquarks are not bags of five quarks binding in a new way, but are more like conventional atomic nuclei.

"I'm really excited that the new data send such a clear message," says Tomasz Skwarnicki, an LHCb physicist at Syracuse University in New York who led the study. But, he notes, "It may not be the message some people had hoped for."

Pentaquarks are heavier cousins of protons and neutrons, which are also made of quarks. In ordinary matter, quarks come in two types, up and down. Atom smashers can blast four heavier types of quarks into brief existence: charm, strange, top, and bottom. Quarks cling to one another through the strong force so mightily they cannot be isolated. Instead, they are almost always found in groups of three in particles known as baryons—including the proton and neutron—or in pairs called mesons, which consist of a quark and an antimatter quark.

But for decades, some theorists have hypothesized the existence of larger bundles of quarks. In recent years, experimenters have found evidence for four-quark particles, or tetraquarks. Then, in 2015, LHCb reported signs of two pentaquarks (*Science*, 15 January 2016, p. 217).

Some theorists argue that the new particles are bags of four and five quarks, bound together through the exchange of quantum particles called gluons, adding a new wrinkle to the often intractable theory of the strong force. Others argue they're more like an atomic nucleus. In this "molecular" picture a pentaquark is a three-quark baryon stuck to a two-quark meson the same way that protons and neutrons bind in a nucleus—by exchanging short-lived pi mesons.

LHCb's new pentaquarks, reported this week in *Physical Review Letters* (*PRL*), bolster the molecular picture. In 2015, LHCb researchers reported a pentaquark with a mass of 4450 megaelectron volts (MeV), 4.74 times the mass of the proton. With nine times more data, they now find in that mass range two nearly overlapping but separate pentaquarks with masses of 4440 MeV and 4457 MeV. They also find a lighter pentaquark at 4312 MeV. Each contains the same set of quarks: charm, anticharm, two ups, and a down. (Previous hints of a pentaquark at 4380 MeV have faded away.)

The lightest pentaquark has a mass just below the sum of a particular baryon and meson that together contain the correct quark ingredients. The heavier pentaquarks have masses just below the sum of the same baryon and a related meson with extra internal energy. That suggests each pentaquark is just a baryon bound to a meson, with a tiny bit of mass taken up in binding energy. "This is a no-brainer explanation," says Marek Karliner, a theorist at Tel Aviv University in Israel.

The molecular picture also helps explain why the pentaquarks, although fleeting, appear to be more stable than expected, Karliner says. That's because packaging the charm quark in the baryon and anticharm quark in the meson separates them, keeping them from annihilating each other.

Other theorists rushed to a similar conclusion when LHCb researchers discussed their results at a conference in La Thuile, Italy, in March. For example, within a day, Li-Sheng Geng, a theorist at Beihang University in Beijing, and colleagues posted a paper, in press at *PRL*, that uses the molecular picture to predict the existence of four more pentaquarks that should be within LHCb's reach.

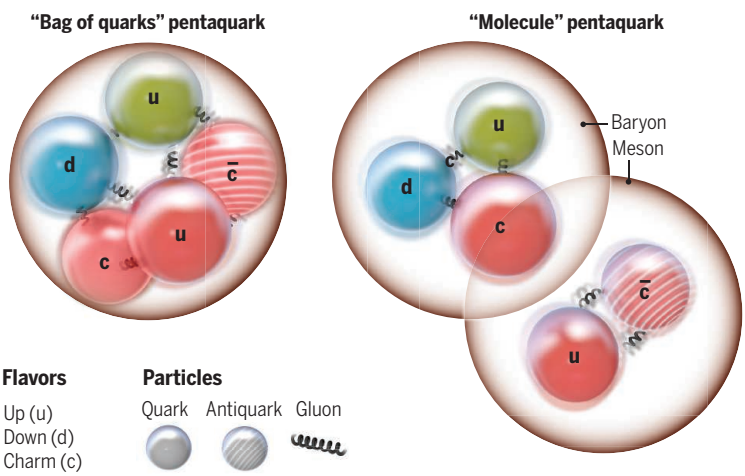
But the bag-of-quarks picture is not dead. Pentaquarks should occasionally form when protons are bombarded with gamma ray photons, as physicists at Thomas Jefferson National Accelerator Facility in Newport News, Virginia, are trying to do. But they have yet to spot any pentaquarks. That undermines the molecular picture because it predicts higher rates for such photoproduction than the bag-of-quarks model does, says Ahmed Ali, a theorist at DESY, the German accelerator laboratory in Hamburg. "They are already almost excluding the molecular interpretation," he says. Others say it's too early to draw such conclusions.

The structure of pentaquarks isn't necessarily an either/or proposition, notes Feng-Kun Guo, a theorist at the Chinese Academy of Sciences in Beijing. Quantum mechanics allows a tiny object to be both a particle and a wave, or to be in two places at once. Similarly, a pentaquark could have both structures simultaneously. "It's just a question of which one is dominant," Guo says.

Regardless of the binding mechanism, the new pentaquarks are exciting because they suggest the existence of a whole new family of such particles, Karliner says. "It's like a whole new periodic table." ■

Pack your bags

Quarks, usually found in trios or pairs, come in six flavors and three colors, akin to electric charge. New pentaquarks may resemble molecules rather than bags of individual quarks.



GRAPHIC: V. ALTOUNIAN/*SCIENCE*

Published by AAAS

MATERIALS SCIENCE

Perovskite LEDs begin to shine

Solar cell wonder materials could also revolutionize lighting and displays

By **Robert F. Service**

In solar cells, the cheap, easy to make materials called perovskites are adept at turning photons into electricity. Now, perovskites are turning the tables, converting electrons into light with an efficiency on par with that of the commercial organic light-emitting diodes (LEDs) found in cellphones and flat screen TVs. And in a glimpse of how they might one day be harnessed, researchers reported last week in *Science Advances* that they've used a 3D printer to pattern perovskites for use in full-color displays.

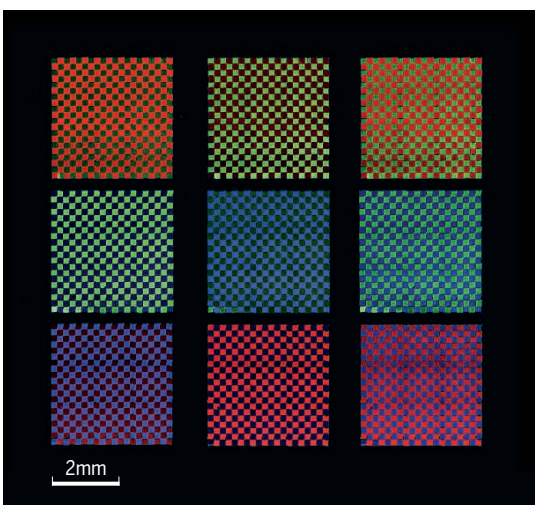
"It's a fantastic result, and quite inspirational," says Richard Friend, a physicist at the University of Cambridge in the United Kingdom whose team created the first perovskite LED in 2014. The result raises hopes that the computer screens and giant displays of the future will consist of these cheap crystalline substances, made from common ingredients. Friend cautions, however, that the new perovskite displays aren't yet commercially viable.

The materials in current semiconductor LEDs, including the organic versions, require processing at high temperatures in vacuum chambers to ensure the resulting semiconductors are pristine. By contrast, perovskites can be prepared simply by mixing their chemical components in solution at room temperature. Only a brief heat treatment is needed to crystallize them. And even though the perovskite crystals end up with imperfections, these defects typically don't destroy the materials' ability to emit light.

In most perovskite LEDs, electrodes sandwiching the light-emitting material deliver charges—negatively charged electrons and positively charged electron vacancies. When the charges meet at the center of the sandwich, electrons fill the vacancies and give up a bit of their energy as a photon of light.

The color of the photon depends on the perovskite's chemical constituents, enabling researchers to tune the color by changing the perovskite's recipe. The Cambridge group's first perovskite LEDs glowed near-infrared, red, or green, depending on their makeup. Since then, the team and other groups have made a full spectrum of colors.

The earliest perovskite LEDs converted only 0.76% of electrons into photons. That's because electrical charges moving through the material got stuck at the boundaries between the myriad crystallites making up the material. But numerous teams have overcome that hurdle. Late last year in *Nature Photonics*, for example, Friend's group reported that by adding a light-emitting polymer layer that helps steer charges around the surface defects, it had made red perovskite LEDs with an efficiency of 20.1%.



When combined with polarizing filters, 3D-printed perovskite nanowires produce adjustable multicolor displays.

A team led by chemist Edward Sargent at the University of Toronto in Canada took a different approach last year, spiking its perovskite recipe with an additive that formed crystalline shells around the perovskite crystallites. The shells blocked the defects from trapping charges, resulting in a green perovskite LED with 20.3% efficiency, the team reported in *Nature*. That remains well below the efficiency of many inorganic LEDs, but is probably good enough for some applications.

Researchers led by Feng Gao, a physicist at Linköping University in Sweden, reported online on 25 March in *Nature Photonics* that they developed yet another way to tackle the defect problem. They targeted the tendency of lead ions at the edges of perovskite crystallites to trap passing electrons. With an additive that bound to the lead, they reduced the ions' hunger for electrons and created a near-infrared LED that had 21.6% efficiency.

The pace of improvements in the past 5 years has been "quite exceptional," Friend says. Still, none of the perovskite devices survives more than about 50 hours, well below the estimated 10,000 hours needed for commercial use. Just why the perovskite crystals fall apart after a few dozen hours isn't clear, Gao says. But short lifetimes also plagued early organic LEDs, he notes. And perovskite solar cell–makers have largely solved similar longevity issues by protecting their devices from air and humidity. "I'm optimistic this area can also develop quickly, and perovskite LEDs can improve," Gao says.

If they do, the latest work from researchers led by Jennifer Lewis, a materials scientist at Harvard University, could point to new strategies for constructing displays. Lewis and her colleagues used a 3D printer to arrange tiny, wire-shaped perovskite structures in multicolor displays. As the "ink" carrying the nanowires passed through the printer nozzle, shear forces aligned them, Lewis says. The common orientation of the nanowires gave light from each LED a single preferred oscillation, or polarization.

For their prototype displays, Lewis's team didn't wire each LED to electrodes; instead, the researchers exposed the entire display to ultraviolet (UV) light. Like an applied electric voltage, the UV light kicks electrons out of their normal state, allowing them to move. Then, they can recombine with vacancies and emit visible light. But because the emitted light was polarized, Lewis and her colleagues could use polarizing filters to control it.

In one example, the researchers used three different perovskite formulations to create displays in which each pixel contained a red, green, and blue spot side by side, with the orientation of the nanowires in each spot offset by 60°. By rotating a polarizing filter, the researchers could mix colors or isolate a single color.

Plenty of hurdles remain for perovskite LEDs, Sargent says. But, he adds, "This work jumps ahead 10 years in the future and shows what cool things we can do." ■

IMAGE: N. ZHOU *ET AL.*, *SCI. ADV.* 5, EAAV8141 (2019)

Published by AAAS



ILLUSTRATION: DAVIDE BONAZZI/SALZMAN ART

PUBLISHING

Radical open-access plan is delayed a year

In response to criticisms, Plan S also lifts cap on article fees

By **Tania Rabesandratana**

Plan S, the program to crack down on scientific journals' paywalls led by European funders, last week fleshed out and relaxed some of the rules researchers will have to abide by. The update addresses concerns raised by researchers, librarians, and scientific publishers after initial guidelines came out in November 2018. It allows more time before researchers will have to publish their papers with full, immediate open access (OA) and drops, for now, the proposed cap on publishing fees that funders pay to OA journals.

The architects of Plan S "have engaged in a good quality dialogue" with the people who will deal with the plan's consequences, says Lidia Borrell-Damián, director for research and innovation at the European University Association in Brussels. As a result, the revised guidelines seem "much more nuanced and more realistic" than the initial set, says astrophysicist Luke Drury, former president of the Royal Irish Academy in Dublin.

Still unclear is whether the changes will convince other funders to join the movement (*Science*, 4 January, p. 11). And they have not mollified the plan's fiercest detractors, who maintain it restricts their freedom to publish. "The changes are cosmetic and trivial. They more or less ignored the critique," says Lynn Kamerlin, a structural biologist at Uppsala University in Sweden who co-authored an open letter against Plan S in November 2018 that now has about 1800 signatories.

Launched in September 2018, Plan S will require immediate OA for scientific papers stemming from research funded by the members of cOAlition S, a group that now has 19 public and private funders. One of the main changes in the update is a 1-year extension: Plan S rules will apply at the latest to research proposals solicited by funders starting in 2021, instead of 2020. That means the mandate will apply to papers published starting in 2022 or 2023, John-Arne Røttingen, chief executive of the Research Council of Norway in Oslo and a Plan S leader, said last week.

In another big change that several critics had called for, Plan S has shelved the idea of capping the amount funders will pay for article-processing charges (APCs), which some journals charge to publish OA articles. Instead, the funders will require a breakdown of what's behind APCs so that researchers can compare publishing venues before choosing one. (The funders may later introduce a cap "if unreasonable price levels are observed.")

"It is significant that cOAlition S listened to feedback that different approaches to peer review, as part of publishing, require different APCs," said Bill Moran, publisher of *Science* in Washington, D.C. (*Science*'s News section is editorially independent.)

Many publishers are happy to provide transparency about their fees, says Niamh O'Connor, chair-elect of the Association of Learned and Professional Society Publishers in London. "It's not uncommon for authors or referees to wonder about them."

Plan S funders hope more transparency will help authors make efficient, evidence-based decisions about where to publish, rather than relying on journals' perceived quality. That would support a secondary goal for cOAlition S—to shake up research assessment. Plan S now includes a pledge to base funding decisions on the intrinsic merit of researchers' work—not the names or impact factors of journals where they published previously.

The revised guidelines also spell out Plan S funders' support for the Open Access 2020 Initiative, which encourages national consortia of institutions to negotiate "read-and-publish" deals with publishers. The agreements allow researchers at those institutions to read paywalled content and publish OA papers for a single fee. But because the often-lengthy contract negotiations can be burdensome for publishers, cOAlition S now says it will develop model contracts to help smaller publishers enter these so-called "transformative agreements." It also now offers a "transformative journal" option, in which Plan S funders pay OA fees for authors to publish in subscription journals, providing those publications reduce subscription fees to offset their income from APCs and commit to 100% OA within an agreed time frame.

The updated guidance also clarifies Plan S's stance on hybrid journals—publications that charge subscription fees as well as APCs for authors who choose to publish OA—that lack the "transformative" commitment to full OA. The cOAlition S funders won't pay hybrid journals' APCs, but researchers can pay with other funds and remain Plan S compliant.

Finally, Plan S's revamped rules give more prominence to its version of "green" OA, in which scientists post peer-reviewed papers in OA repositories (*Science*, 17 May, p. 620) as soon as they are published in a paywalled journal. The new guidelines also relax the technical requirements for such repositories.

Overall, cOAlition S "really seem[s] to have listened to the research community. There are no major sticking points anymore," says Gareth O'Neill, a linguist at Leiden University in the Netherlands and past president of the European Council of Doctoral Candidates and Junior Researchers. "Now, we'll watch them, see what works and what doesn't, and hold them accountable." ■

Published by AAAS



On Borneo for a 2018 expedition to find new species, evolutionary biologist Marta Paterno of the University of Verona in Italy prepares samples for a portable DNA sequencer (center, by laptop).

BIODIVERSITY

DNA barcodes jump-start search for new species

$180 million project aims to identify 2 million species

By **Elizabeth Pennisi**

For centuries biologists have identified new species at a painstakingly slow pace, describing specimens' physical features and other defining traits, and often trying to fit a species into the tree of life before naming and publishing it. Now, they have begun to determine whether a specimen is likely a novel species in hours—and will soon do so at a cost of pennies. It's a revolution driven by short stretches of DNA—dubbed barcodes in a nod to the familiar product identifiers—that vary just enough to provide species-distinguishing markers, combined with fast, cheap DNA sequencers.

"Biodiversity science is entering a very golden era," says Paul Hebert of the University of Guelph in Canada. On 16 June, a team he leads will launch a $180 million global effort to identify more than 2 million new species of multicellular creatures. Other teams are also adopting the approach to comb samples for new species in their labs—or even directly in the field. With the world losing species faster than they are discovered, biologists are welcoming the technology.

"For many years I dreamed of changing the rules by being able to bring a portable genomic lab [to] where the samples are," says Massimo Delledonne, a genomicist at the University of Verona in Italy who recently performed barcoding studies in a forest on the island of Borneo that quickly revealed a new species of snail. "Field barcoding is now ready for prime time."

Biodiversity experts estimate that Earth has between 8.7 million and 20 million kinds of plants, animals, and fungi, but to date only 1.8 million of them have received formal descriptions. Insects, in particular, are a vast realm of undiscovered species. "Yet collectively, they may contribute more biomass in terrestrial habitats than all wild vertebrates combined," says Rudolf Meier, a biologist from the National University of Singapore who has been developing barcoding approaches with a small DNA sequencer.

In 2003, Hebert proposed the DNA barcode concept: that animal species could be distinguished by sequencing less than 1000 bases of mitochondrial DNA from a specimen. It took a while for the idea to catch on, but Hebert and other enthusiasts began to compile barcodes from known species. In 2010, for example, he spearheaded a consortium called the International Barcode of Life (iBOL), an $80 million effort centered at Guelph that began to build a reference library of known species with their identifying sequences. It now tops 7.3 million barcodes—each species can have more than one—and has proved to be a resource not only for identifying known organisms, but also for documenting their interactions with other species—including who eats whom—based on the different barcodes in a particular sample.

Now, with additional support in money and in-kind services from its 30 international partners, iBOL is about to start a 7-year follow-up effort. Called BIOSCAN, it will gather specimens and study species interactions at 2500 sites around the world, aiming to expand its reference library by 15 million barcode records, 90% of them coming from undescribed species. The data will set the stage for monitoring the effects of pollution, land-use changes, and global warming on biodiversity, Hebert says. Ultimately, "We will be able to track life on the planet the way we track the weather."

And, in a departure from iBOL's previous focus on deriving barcodes for known species, "One of the primary goals will be species discovery," Hebert says. If software fails to match a sample's barcode sequence to an existing species, it will immediately flag the specimen for closer genetic and visual scrutiny and possible identification as a new species. In the past, it might have taken years or even decades to confirm some organisms as new species—for example, certain flies in which species differ visibly only in the shape of the male genitalia.

Customized bioinformatics and sequencers that can read enough bases in one shot to get a full barcode will keep the cost low, Hebert predicts—about $1 per specimen including collection, preservation, DNA extraction, sequencing, and follow-up analysis. He expects the sequencing component of the overall costs will eventually drop to about $0.02 per specimen.

For now, all the specimens gathered for BIOSCAN's barcoding will be shipped to the University of Guelph. But Meier has been developing a barcoding approach that he hopes will be accessible to many labs doing species surveys. He got interested in more efficient ways of identifying species in 2012, when Singapore officials asked him to study tiny flies emerging from two local reservoirs. "It was a nightmare" to pin down the midge species responsible, he recalls. As a result, he, too, turned to barcoding.

Now, he's cataloging all of Singapore's biodiversity, particularly its "silent ma-

PHOTO: PIERRE ESCOUBAS/TAXON EXPEDITIONS 2018

Published by AAAS

jority," as he calls small insects. For this work, Meier says, "We abandoned the over-engineered and expensive techniques that are traditionally used for barcoding." Instead, he has turned to a recently developed sequencer called the MinION that is the size of a cellphone and costs less than $1000. Designed to identify DNA's four bases by how they change an electrical current when they pass through a nanometer pore, it sequences thousands of bases in one stretch, more than enough for a barcode.

Working with undergraduates and volunteers in Singapore who both collect and sequence specimens, Meier's team has already generated 200,000 insect barcodes. These represent 10,000 species, more than 70% of them new to science, he and his colleagues reported last year. Meier envisions many countries setting up such lab-based efforts to independently catalog their biodiversity.

His group recently demonstrated the power of the approach with a study of the insects an entomologist had caught in a single net trap in Kibale National Park in Uganda. Meier and his colleagues focused on a very large, diverse group of flies called Phoridae, which are hard to tell apart visually. Barcoding just one-third of the trap's haul of insects—about 8700 in all—yielded 650 Phoridae species new to science, the team reported in a 30 April preprint on bioRxiv. That's more than all the known Phoridae in tropical Africa. Emily Hartop from Stockholm University, an expert in fly identification, confirmed that the barcodes correctly separated species 90% of the time, Meier's group reports.



PHOTO: LYDIA GREENE

A miniaturized DNA sequencer taken to Madagascar identified mouse lemur species in a forest.

The numbers show "there's a lot of diversity out there that we have not named and don't know about," says John Kress, a botanist at the Smithsonian Institution's National Museum of Natural History in Washington, D.C.

Delledonne and his colleagues have been working out ways to do at remote field sites what Meier does in his Singapore lab. They, too, use a MinION sequencer, which is typically run by a laptop computer. The laptop normally requires an internet connection, but the sequencer's manufacturer, Oxford Nanopore Technologies, made it possible for the system to work in remote locations with no such access. Everything needed for barcoding fits into a carry-on suitcase.

On a 2018 Borneo expedition, the team joined with citizen scientists and barcoded about a dozen animals, among them a new snail they named *Microparmarion exquadratus* and described last year in the *Journal of Molluscan Studies*. In a 6 May bioRxiv preprint, the group detailed their protocols, so others can follow their footsteps. Anyone with a few days' training can now get set up to do barcoding in the field for less than $7000, Delledonne suggests. "We see how smartphones have changed our lives. We have shown that sequencing may follow the same trend."

Indeed, a team from Duke University in Durham, North Carolina, has just reported a similar field study with a MinION in the Madagascar dry forest, obtaining barcodes to identify mouse lemurs. A few decades ago, only a few species of these secretive, nocturnal primates were known. The tally is now up to 24, but finding new species is still slow. "It could sometimes take years," says Duke primatologist Marina Blanco. In a 26 May bioRxiv preprint, she, Duke ecologist Lydia Greene, and colleagues described using a MinION-based barcoding system to take a DNA sample from a live-trapped lemur, barcode it, and decide on the spot whether it was a new species.

The Duke work, says Delledonne, is a "good example of what is going to be the impact of mobile genomic labs on ecological and evolutionary studies."

For Meier, such field studies, along with his own lab's work, bode well for the democratization of barcoding: "It all points to the bright future of decentralized biodiversity science that yields rapid results." But Kress thinks industrial-scale efforts like BIOSCAN will be important as well if there's any hope to catalog all species on the planet. "It has to be both approaches in parallel," he says. "We will never get it done if we do it in individual labs." ■

WORKFORCE

Women of color face double dose of bias

Postdoc application study reveals gender and racial preferences

By **Katie Langin**

Bradley Miller is more likely to be hired than José Rodriguez. Zhang Wei (David) is more competent than Jamal Banks. And both Miller and Wei are more competent and hirable than Maria Rodriguez or Shanice Banks.

These postdoc job candidates are fictional. But the differences in how they're viewed based on name alone—despite identical CVs—by a sample of professors are real. That's according to a recent study that unearths evidence of racial bias in biology and a combination of gender and racial bias in physics, highlighting both the pervasive nature of various biases in science as well as important disciplinary differences.

"This is a really, really important study," says Corinne Moss-Racusin, a psychologist at Skidmore College in Saratoga Springs, New York. In 2012, Moss-Racusin published a similar study, which found that biology, chemistry, and physics faculty members who reviewed applications for a lab manager position favored applicants named John over otherwise identical applicants named Jennifer. The new study, published this week in the journal *Sex Roles*, is an important advance because it manipulates race as well as gender, she says. "It certainly supports a lot of anecdotal findings, self reports, correlational data—but to really have some hard experimental numbers … is really important."

Asia Eaton, a social psychologist at Florida International University in Miami and lead author of the study, says she and her colleagues decided to focus on the postdoc period because it is "a critical part of the pipeline," and also "a part of the pipeline where there are almost no checks and balances" to prevent bias. Principal investigators typically review postdoc applications in isolation—unlike graduate admission or

Published by AAAS

faculty hiring decisions, which are usually made by a committee and, in some cases, include practices to combat bias.

Eaton and her colleagues asked 251 physics and biology faculty members at eight U.S. research universities to evaluate a CV, telling them it represented a hypothetical applicant for a postdoc position. The name was manipulated to indicate the candidate's gender as well as their race and ethnicity—Asian, black, Latino, or white—based on common names for each group according to U.S. Census Bureau data. Accurately detecting bias in these types of experiments requires that participants don't know what they're being tested for, so the researchers told the faculty members that they were trying to figure out what kind of CV formatting is best.

Faculty members in biology viewed male and female applicants to be similarly competent and likely to be hired—a result Eaton "was happily surprised to see." But in physics, it was a different story: Faculty members preferred male applicants, rating them one point higher on competence—on a nine-point scale—and two points higher on hirability.

Faculty members in both disciplines exhibited racial bias. In physics, Asian and white applicants were given higher competence and hirability ratings than black and Latino applicants. In biology, Asian and white applicants were viewed as more competent than black applicants. Asian applicants were also viewed as more hirable than black and Latino applicants. (Ratings for Latino competence and white hirability didn't statistically differ from other groups.)

In physics, black and Latina women were doubly disadvantaged, rated three points lower in hirability than white and Asian men. "That's a really striking finding," Moss-Racusin says. "It's a hit for their gender and also for their race"—evidence of a "double jeopardy effect" that the scientific community needs to grapple with, she says.

"It's papers like these that are really important" for opening scientists' eyes to the reality of bias, says physicist Ramón Barthelemy of the University of Utah in Salt Lake City, who has studied challenges that women and LGBT people face in his discipline. In physics, the number of women has "stayed stubbornly low" despite a surge of female scientists in other disciplines, and a lack of awareness of bias may be one factor, he says. "I think that physicists do see themselves as being so objective that they couldn't possibly be doing these things." But presenting evidence of bias to "empirically thinking physicists" can change their perspective, he says. ■

NATIONAL SECURITY

Bipartisan bill proposes forum on U.S. academic espionage

Congress asked to set up National Academies roundtable

By **Jeffrey Mervis**

The free flow of people and ideas has helped make U.S. research universities the envy of the world. But those institutions have become a target amid growing concern from policymakers that international scientific collaborations may be undermining U.S. economic and military security by giving foreign governments, especially China, unfair access to new technology.

> ***"... we're proposing a unified approach to protect research without creating overlapping ... federal requirements."***
>
> **Representative Mikie Sherrill** (D–NJ)

Last week, a bipartisan group of legislators in the U.S. House of Representatives rallied to the aid of the research community by introducing a bill that would create two high-level forums for discussing the thorny issue. Its authors hope to insert the language into pending legislation governing programs at the Department of Defense, which is one of the few bills likely to pass Congress this year.

The foreign threat is real, says the bill's lead sponsor, Representative Mikie Sherrill (D–NJ). "There are serious and legitimate concerns about academic espionage at our universities," says Sherrill, a former federal prosecutor and Navy pilot. "That's why we're proposing a unified approach to protect research without creating overlapping or contradictory federal requirements." Representative Jim Langevin (D–RI), another chief co-sponsor, says the bill "will give schools the tools to defend themselves while also protecting the important academic and cultural contributions that international students bring to our country."

The Securing American Science and Technology Act of 2019 (H.R. 3038) would create a roundtable on science and national security at the U.S. National Academies of Sciences, Engineering, and Medicine (NASEM), giving senior research managers from industry and academia a chance to meet regularly with federal officials. The bill would also set up an interagency working group on the same topic within the White House.

Backers hope the two forums will address the thicket of regulations and policies governing the foreign research activities of faculty members. The discussions could include what types of research may require extra safeguards and whether some international interactions should be proscribed.

Recent U.S. government efforts to curb foreign influences on research have created anxiety among scientists. Acting in response to letters from the National Institutes of Health, for example, MD Anderson Cancer Center in Houston, Texas, and Emory University in Atlanta ousted five biomedical researchers who officials said had failed to properly disclose ties to Chinese institutions or committed other violations. All are Asian.

Similar public-private forums have been used successfully in the past to hash out thorny issues such as how to commercialize publicly funded research and how to regulate new technologies with both commercial and military uses. On 10 May, NASEM hosted what could be seen as a rehearsal for the proposed forums, using money from a private charity to bring together government and university officials.

One attendee was Kelvin Droegemeier, director of the White House Office of Science and Technology Policy. Last month, he added a new committee on research security to the interagency National Science and Technology Council (NSTC), which oversees federal research activities, drawing from two existing panels. However, the joint committee is also chewing on three other meaty issues: burdensome regulations on federally funded research, scientific misconduct, and sexual harassment and other factors creating a hostile work environment in science. The sponsors of the new bill think that's probably too much and believe it would be better to have an NSTC panel focused solely on security.

If the bill becomes law, university officials expect it will give them an entrée into a political debate from which they have been largely excluded. Mary Sue Coleman, head of the 62-member Association of American Universities in Washington, D.C., lauded lawmakers for "this important legislation to help protect our nation's scientific research enterprise." ■

Published by AAAS



THE MISMEASURE OF HANDS?

Some researchers say a simple ratio of finger lengths can predict personality and health. Others say that's wishful thinking *By* **Mitch Leslie**

If papers published in the past 6 months are right, a single number is enough to show whether people are likely to suffer a premature heart attack, land first authorship on published papers, become dependent on alcohol, or put on fat around the middle. That magic number is the ratio between the lengths of the second and fourth fingers, known as the 2D:4D ratio. It tends to be lower in men—meaning their fourth fingers tend to be longer than their second—than in women. Researchers who believe in its predictive power say it reflects a fetus's exposure to testosterone and other hormones that guide development, including that of the brain.

The idea that the lengths of human fingers reveal so much stems from the work of evolutionary biologist John Manning, now at Swansea University in the United Kingdom. But the field he inspired has ballooned beyond what he could have imagined. More than 1400 papers in just over 20 years have linked the finger ratio to attributes such as personality, cognitive abilities, and sexual orientation as well as to risk of illnesses such as cardiovascular disease, cancer, and amyotrophic lateral sclerosis. Researchers have even tried to use ratios gleaned from stenciled handprints on cave walls to determine whether the artists behind ancient paintings were men or women.

But the notion has also riled plenty of critics, who argue that researchers who rely on the 2D:4D comparison have been seduced by a simplistic, faulty measure.

ILLUSTRATION: STEPHAN SCHMITZ/FOLIO ART

Published by AAAS

Some doubters contend that the difference in ratios between the sexes is an illusion resulting from men's larger hands or that the measure itself is statistically problematic. "I'm skeptical about every single finding involving that ratio," says physiologist and biostatistician Douglas Curran-Everett of National Jewish Health in Denver.

Other detractors argue the field is rife with irreproducible findings. It's "like a house of cards built on an unknown and uncertain base," says psychologist Martin Voracek of the University of Vienna, who compares the work on finger ratios to phrenology or physiognomy, the discredited ideas that people's head shape or facial features, respectively, reveal their personalities, character, and intelligence.

Yet as a simple, easy-to-measure quantity that promises insight into a hidden time of life—early fetal development—the finger ratio has enticed an entire generation of researchers while dismaying many others. To behavioral neuroendocrinologist Kim Wallen of Emory University in Atlanta, a skeptic, the debate over the ratio and its significance "raises some fundamental issues about what we consider evidence."

A GERMAN ANATOMIST first reported in the 1870s that finger proportions typically differ between the sexes, but the observation remained a curiosity until Manning hauled the ratio into the spotlight in 1998. He was collaborating with colleagues at a fertility clinic in Liverpool, U.K., studying symmetry in the body, which some researchers suspected was connected to hormone levels. "I had a vague recollection that I'd heard about that sex difference" in finger ratios, Manning says. The disparity suggested a role for certain sex-related hormones. When he and colleagues measured finger ratios for patients at the clinic, lower ratios in men's right hands correlated with higher testosterone levels.

By studying children and young adults from the Liverpool area, the scientists also discovered that the finger ratio discrepancy between the sexes held for kids as young as 2 years. That finding led the researchers to postulate that the difference arose before birth and reflected hormone levels in the womb. The finger ratio, Manning explains, indicates the relative levels of testosterone and estrogen during early development.

Manning, who has written two books and more than 60 papers on the ratio, didn't expect that his findings would have such an impact. But the measure caught on. The idea that one number reveals so much about us is irresistible, notes statistical geneticist David Evans of the University of Queensland in Brisbane, Australia, who has studied the genetic basis of finger ratios. "Whenever you give a talk on the 2D:4D ratio, as soon as you mention it, everyone starts looking at their hands."

Researchers have used scanners, photocopiers, calipers, rulers, and even x-ray machines to assess finger length; in some studies the subjects measured themselves. Scientists can swiftly and cheaply amass large amounts of data. One BBC-sponsored online survey on sex differences gleaned self-reported finger ratios for more than 240,000 people. "I don't know a more accurate biomarker for prenatal androgen that can be readily measured in adults," says neuroscientist Marc Breedlove of Michigan State University in East Lansing.

Finger ratios also appeared to meet a scientific need. In the late 1950s, researchers proposed a then-radical idea—that testosterone and related sex hormones in the womb steer the brain's development and thereby shape adult behavior. Since then, scientists have sought links between prenatal hormone exposure and characteristics such as aggressiveness, sexual orientation, and spatial ability—along with the risk of conditions such as autism and addiction. But sampling hormones in an early fetus can endanger a pregnancy. No wonder researchers turned to the finger ratio as a simple readout of an otherwise inaccessible environment.

The studies build on subtle differences. Although the finger ratio is usually smaller in men, the gap between the sexes is small. In the BBC internet study, average right-hand values for men and women were 0.984 and 0.994, respectively. Moreover, the distributions for the two sexes overlap (see graphic, below), and the average ratios vary widely depending on subjects' geographical origins and ethnic backgrounds.

Nonetheless, many scientists are convinced that the 2D:4D ratio is a reliable indicator. "I think there is no longer any doubt that these ratios in humans reflect prenatal androgen exposure," Breedlove says. Biological anthropologist Bernhard Fink of the University of Göttingen in Germany, another champion of the ratio, adds that hundreds of studies have shown that it correlates with a variety of behaviors and abilities that can plausibly be connected to prenatal androgens. However, he acknowledges that the ratio typically explains just a "small to moderate" amount of the variation in any particular trait.

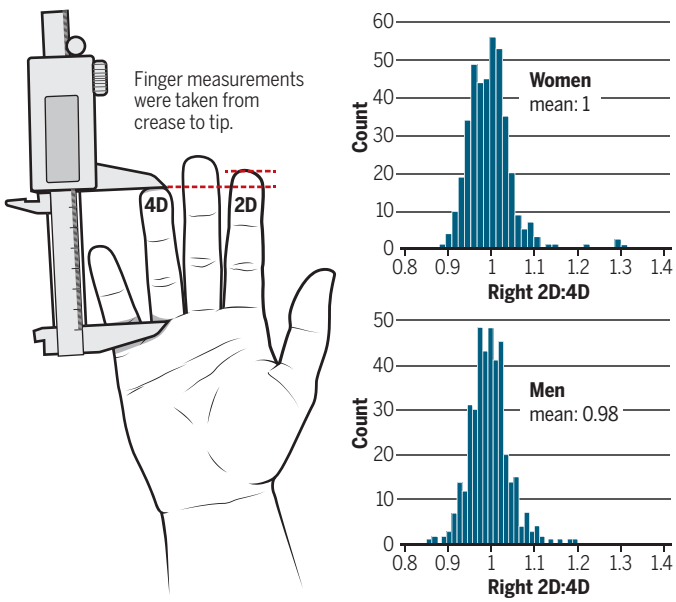
One high-profile use of the finger ratio has been to examine sexual orientation in women. Researchers have suggested that hormone levels early in development influence which sex people find attractive and that higher levels of testosterone and other androgens circulating through a female fetus might increase the odds of her being a lesbian. The hypothesis has been contentious and hard to test. Breedlove and colleagues thought finger ratios might yield new evidence, so in the early 2000s at street fairs in the San Francisco Bay Area in California, they "began asking people questions and Xeroxing their hands."

Although a difference in digit proportions was not evident between gay and straight men, the researchers determined that women who described themselves as lesbians had lower, more "masculine" finger ratios than did straight women. The unmistakable conclusion from that study and follow-ups, Breedlove says, is that "Testosterone does have an influence on human sexual orientation before birth."

Even among proponents of the finger ratio, however, those results didn't settle the controversy about prenatal hormones and sexual orientation. Manning, for instance,

The long and short of it

John Manning and colleagues' 1998 study comparing the lengths of index (2D) and ring (4D) fingers found a subtle difference between the sexes, which they and others attributed to hormones affecting early fetal development.



CREDITS: (GRAPHS) J. T. MANNING *ET AL*., *HUMAN REPRODUCTION*, VOL. 13, 3000, 1998; (ILLUSTRATION) V. ALTOUNIAN/*SCIENCE*

Published by AAAS

argues that the BBC study shows the opposite relationship—that early testosterone exposure is important for sexual orientation in men but not women.

Manning says the ratio also gives a glimpse of a person's future. For example, he says, finger ratios might forecast the effectiveness of prostate cancer treatments that block testosterone and of breast cancer treatments that block estrogen. "It's early days for this kind of thing," Manning says, but "we won't know until we do the studies."

The ratio's prognostic power is even stronger for sports, he says. Studies have uncovered associations between lower 2D:4D ratios and better performance in an array of athletic events, including soccer, long-distance running, rugby, skiing, rowing, and basketball. The effect is large enough, Manning contends, that teams should use finger ratio as a criterion for selecting players, "if we can get sports scientists to agree."

YET THE RATIO has met with continuing skepticism from scientists. Unable to safely sample blood from early fetuses, researchers haven't confirmed the ratio's fundamental assumption: that variation in lengths of the key digits correlates with differences in hormone levels in the fetus's blood during the first trimester of pregnancy, when fingers begin to form. Instead, scientists have turned to indirect evidence. The strongest support, Manning says, comes from animal studies that involved tweaking the hormone environment during pregnancy.

In one study, developmental biologist Martin Cohn of the University of Florida in Gainesville and his then-postdoc, Zhengui "Patrick" Zheng, altered the activity of the receptors that respond to the hormones. For example, the pair stimulated the androgen receptor by dosing pregnant female mice with dihydrotestosterone (DHT), the most common form of testosterone in the body, or gave them estrogen to prod its receptor. Three weeks after the females gave birth, the researchers measured the effects of their manipulations on the hind paws of the pups.

In female pups, they reported in a 2011 paper in the *Proceedings of the National Academy of Sciences*, boosting the activity of the androgen receptor in the mother increased the growth of the fourth digit and produced a lower 2D:4D ratio. Nudging the estrogen receptor, in contrast, curbed elongation of the fourth digit and yielded a higher 2D:4D ratio in male offspring.

"The sex hormones can tap into the genetic circuit that controls skeletal growth," Cohn concludes. And because "the mechanisms that control limb development in all vertebrates are very, very conserved," he says, the hormones probably act similarly in people.

But the results of another animal study contradict those findings. When neurobiologist Sabine Huber, now at the University of Münster in Germany, and colleagues tried to replicate Zheng and Cohn's study, they got the opposite results. Boosting DHT levels in pregnant mice induced higher, more feminine digit ratios in the hind paws of male pups, whereas blocking the androgen receptor led to lower, more masculine ratios in female pups. Huber says she's not sure why those results, reported in *PLOS ONE* in 2017, don't match those of the other study, but she says differences between the strains of mice she and Cohn's team used may have contributed.

Inconclusive results from two large studies that scanned the genome for gene variants linked to finger length also raise doubts about the 2D:4D ratio, critics say. Evans and his colleague Sarah Medland, a statistical geneticist at QIMR Berghofer Medical Research Institute in Brisbane, analyzed data on thousands of people, looking for a relationship between the ratio and variants in the molecular pathways that control testosterone levels or responsiveness to the hormone. They came up empty. In two studies, "We didn't find any strong evidence of testosterone involvement," Medland says.

"I just don't think that finger ratios are a scientifically reliable measure of the early hormone environment."
Melissa Hines, University of Cambridge

Skeptics suggest the 2D:4D ratio may be statistically meaningless. Ratios are intrinsically problematic, some statisticians say, because they can muddle the relationship between two variables. "A conclusion based on a ratio is likely to be off-target and misleading," says Gary Packard, a professor emeritus of biology from Colorado State University in Fort Collins, who has written extensively about pitfalls of statistics.

Before researchers use a ratio, Curran-Everett says, they should check that it meets certain mathematical criteria: A plot of its two variables should yield a line that passes through the origin, which indicates that the ratio's variables have a consistent relationship. But when evolutionary biologist Jaroslav Flegr of Charles University in Prague and colleagues performed that test in two studies of hundreds of finger length measurements, the 2D:4D ratio did not fulfill the criteria.

More sophisticated mathematical approaches to the data suggested the apparent difference in 2D:4D ratios between the sexes is merely a function of men's larger hands. Men may have longer fourth fingers because, as the hands get bigger, the fingers don't grow by the same amount—the fourth finger lengthens more than the second. In a 2017 study, Flegr and colleagues worked with researchers from Teesside University in Middlesbrough, U.K., to factor out the difference in hand sizes in their data. The male-female difference in digit ratios flipped—men now had higher values. That inversion suggests the widely reported sex difference in 2D:4D ratios is "not an effect of testosterone, it's an effect of the size of the hands," Flegr says.

That finding may help explain another problem that critics cite with 2D:4D studies: The results often can't be replicated. Melissa Hines, a psychologist and neuroscientist who studies human gender development at the University of Cambridge in the United Kingdom, once accepted the validity of the ratio. But she changed her mind when she asked some undergraduates to repeat published studies for their final-year projects. Even though students appeared to duplicate procedures from the studies, they couldn't obtain the same results.

"I'm not saying androgen is not at all important for human behavior. It is," she says. "I just don't think that finger ratios are a scientifically reliable measure of the early hormone environment." Wallen says the case that digit ratios are a proxy for hormone levels is so weak that when he became editor of the journal *Hormones and Behavior* 7 years ago, he decided to stop accepting papers that use them in that way.

Voracek, who like Hines once believed in the finger comparison, now says research on the 2D:4D ratio exemplifies the reproducibility crisis that has emerged in multiple fields of science over the past few years. Intriguing findings that appear in small studies disappear when scientists scrutinize larger groups or perform meta-analyses, he says.

Implementing some of the practices recommended for improving research credibility could help solidify the science and possibly bridge the gap between 2D:4D supporters and detractors, Voracek adds. Those measures include preregistered studies, in which investigators spell out their aims and methods before performing the work, and adversarial collaborations, in which scientists with clashing ideas team up.

But for now, skeptics and advocates of 2D:4D ratios seem to be talking past one another. Researchers who rely on the ratio aren't publishing their studies in *Hormones and Behavior*, but they are publishing. More than 20 papers using the digit ratio have already come out this year. ■

Published by AAAS



SUMMER BOOKS

The scientist's summer reading list

How will we eat in a warming world? What makes money real? Are we being good ancestors? From a graphic celebration of the semicentennial of the Apollo 11 mission to a dystopian foray into the digital afterlife, this year's summer reading picks—reviewed by an enthusiastic group of early-career scholars—aim to unpack where we came from and where we're headed. Focus on the big picture with an engaging exploration of space archaeology, dig into the details with a thought-provoking ode to algae, or sit back and LOL at an entertaining introduction to internet linguistics. –**Valerie Thompson**

Underland

Reviewed by **Ryan J. Haupt**[1]

Written as a travelogue, *Underland* documents Robert Macfarlane's excursions to some of the most remote and extreme subterranean places on Earth. Structured much like a trip to the underworld itself, the book begins with Macfarlane's descent below, where he reflects on humanity's complicated relationship with the world beneath our feet, and then ascends "sadder but wiser," just like the archetypal hero returning from the abyss.

During his travels, Macfarlane is often with a guide because the places he visits would be foolhardy to traverse alone. Some are scientists whose work beneath Earth's surface takes on a sense of holy purpose. These include a physicist in a slowly collapsing halite tunnel trying to detect the fleeting subatomic particles of creation and an ecologist listening in on the chemical conversations between trees. Many are not scientists but are experts nonetheless, deftly explaining the deadly mechanics of underground rivers, the societal dangers and cultural costs of mineral extraction, and the increasing pace of glacial retreat.

Macfarlane's exquisite prose vividly draws the reader into spaces that many may tremble to enter. There are times when the sensation evoked is one of such peril that it takes a few harried breaths and a frantic page turn to remember that he must have survived. He writes, while hunting for molin (meltwater holes) in the Knud Rasmussen glacier on Greenland, for example, "Your aim is to dislodge nothing, not even a grain of quartz. You move tenderly. .... You *never* put your full foot-weight on a boulder without testing it first. You *never* move

ILLUSTRATION: BENEDETTO CRISTOFANI/SALZMAN ART

Published by AAAS



when someone is directly below you on the fall-line. You *never* put your foot or your arm into a gap between rocks, in case the one above drops down. Shins and forearms break easily in stone jaws."

Much of humanity's relationship with the underground has to do with those who came before: The first to leave their marks on the cave wall or entomb a loved one with the hope that the underland would provide safe refuge in an afterlife. Macfarlane embraces that idea but also flips it with a refrain oft-repeated throughout the book: "Are we being good ancestors?"—a forward-thinking riff on philosopher T. M. Scanlon's question of "What We Owe to Each Other."

It is through this lens that Macfarlane deftly considers the strange economics of mining and the seemingly organic underground systems built beneath our cities to transport us, our supplies, and our waste. Countercultures thrive in such spaces among the dead of generations long passed.

We put important things underground, both to safeguard the past and to protect the future. Macfarlane's coda considers the long-term ramifications of storing nuclear waste, which will persist long after humanity is gone. How can we impress on future intelligent beings the absolute danger of something we have locked away as though it were something of incredible value?

Although there is empirically much to learn from *Underland*, there is perhaps more value in what is simply felt as one quietly contemplates Macfarlane's journey into our pockmarked planet.

Underland: A Deep Time Journey, *Robert Macfarlane,* Norton, 2019. 496 pp.

Archaeology from Space

Reviewed by **Dominique Langis-Barsetti**[2]

Ten years after the publication of her first scholarly tome dedicated to the relatively new field of "space archaeology" (*1*), Sarah Parcak leaves behind the matter-of-fact tone of textbooks to offer readers a more personal view on satellite remote sensing and how it has come to take its place in the archaeologist's toolbelt. Her new book takes readers across the globe as she seeks to understand the distant past with the help of modern satellites. Her writing is full of evocative anecdotes and personal insights gleaned from years of experience in dusty trenches as well as behind the computer screen, poring over satellite images.

The book divides itself between the trenches and the sky because results obtained through satellite imagery must always be verified on the ground. She introduces readers to the field of aerial remote sensing through numerous case studies, turning complex research into something much more approachable. In one such case, Parcak takes readers to the Skagafjörður Church and Settlement Survey, in northern Iceland, where ground-based survey methods yielded promising results, and the addition of satellite images allowed researchers to identify new Viking walls strewn across the landscape.

Despite her faith in the promises of space archaeology, Parcak's book is not exclusively about success stories. She very candidly includes the occasional failure, reminding us, and herself, that setbacks and disappoint-

Published by AAAS

ing results are part of scientific exploration. She recounts, for example, an exploration in eastern Canada, where she and her team had been prompted to look for elusive Viking settlements and other ancient native sites. Despite a promising start, excavations eventually revealed that the "structures" identified on satellite imagery were simply unusual geological features.

Parcak also addresses the challenges faced today by archaeology, including looting and antiquities trafficking, and makes a plea for improving diversity within the field, arguing that archaeology has much to gain from incorporating the interpretations and perspectives of people of different origins and backgrounds. True to this philosophy, she ends by introducing readers to GlobalXplorer, a crowdsourcing platform she developed to empower stakeholders around the world by giving them a chance to remotely participate in archaeology. Beyond its academic goals, the project seeks to raise awareness about the threats faced by cultural heritage sites worldwide, in the hope that concrete measures against looting and other destructive practices will gain widespread support.

Throughout the book, Parcak's love for her work and the people she studies is evident, and her enthusiasm is contagious. From Vikings in Iceland and Canada to amphitheaters in Italy and back to her first love, pharaonic Egypt, she brings both the present and the past to life.

REFERENCES AND NOTES

1. S. Parcak, *Satellite Remote Sensing for Archaeology* (Routledge, 2009)

Archaeology from Space: How the Future Shapes Our Past, *Sarah Parcak,* Henry Holt, 2019. 288 pp.

Digital Cash

Reviewed by **Rachel O'Dwyer**[3]

Things change so fast with digital money that by the time an academic monograph emerges on the subject, some of its ideas may have already lost currency. Rather than try and predict the future, Finn Brunton's *Digital Cash* is a "history of the present," presenting contemporary innovations in electronic money and cryptocurrency through an archaeology of digital cash—in particular, those put forward by the cypherpunk and Extropian communities.

It might seem that Bitcoin emerged fully fledged with Satoshi Nakamoto's 2008 White Paper. But where do the key innovations—building chains of anonymous trust and the ability to control the reproduction and circulation of digital tokens—come from? Brunton traces the technical roots of the cryptocurrency to innovations such as blind signatures and asymmetric key cryptography, developments in Adam Back's Hashcash and Hal Finney's reusable proof of work (RPOW), and innovations described on the cypherpunk listserv, which brought together privacy and security activists beginning in the late 1980s. The latter include David Chaum's Digi-Cash, Wei Dai's b-money, and Nick Szabo's bit gold, parts of which would later converge in Bitcoin.

Brunton also draws connections between digital cash and the Extropian community, a transhumanist movement that emerged in the early 1990s that believed wholeheartedly in both cryogenic freezing and Hayekian economics. He explores the ideological motivations driving these technical innovations, including privacy, libertarian anarchy, and imagined future utopias.

The book also delves deeper into the past, detailing the fascinating history of American money, from 19th-century "wildcat banking"—a system of state-chartered financial institutions backed by questionable security—through to the early-20th-century "scrip"—de facto currencies that took the form of railway bonds, crates of eggs, pounds of honey, cigars, sacks of potatoes, and personal IOUs.



Finn Brunton explores the origins of cryptocurrencies in *Digital Cash*.

In addition to a history of currency, *Digital Cash* is a book about time, because money is, as Brunton shows, a way of banking on the future. Often this money is a "time out of joint," embodied in Technocratic energy certificates or Extropian "idea futures" that never come to pass. The book also explores money as a technology of memory, an object that carries traces of its history and circulation from sediment and bacteria through to effigies of forgotten sovereigns, chains of signatures, and, more recently, transactional data.

Beautifully written and meticulously researched, *Digital Cash* manages to connect these multiple pasts to key contemporary questions of digital value, ownership, and politics. All of which begs the question: What imaginary utopias, dystopias, and possible futures are we carrying in our wallets at this very moment?

Digital Cash: The Unknown History of the Anarchists, Utopians, and Technologists Who Created Cryptocurrency, *Finn Brunton,* Princeton University Press, 2019. 266 pp.

Slime

Reviewed by **Maren Preuss**[4]

Ruth Kassinger's *Slime* illustrates the important role algae have played in the world over time and begins with the story of cyanobacteria, describing how these prokaryotic organisms shaped early life on Earth by producing an oxygenated atmosphere. To the present day, cyanobacteria symbiotically living in the aquatic fern *Azolla* still play important roles for organic rice cultivation methods in Japan.

Kassinger recounts stories from her travels around the world, from an excursion to a nori farm and processing plant in South Korea to a coral restoration project in Bonaire. Algae, she reveals, are extremely versatile and can be used not only as a human and animal food source but also to produce glass, explosives, fertilizer, shoes, and "designer" oils.

The production of algal-based bioplastics, Kassinger argues, might be the solution to our plastic pollution problem. *Slime* explores ongoing research on different algal usages, such as bioplastic production, including the work of Daniel Ducat, Taylor Weiss, and Eric C. Young at Michigan State University's Plant Research Laboratory. Because bacteria-producing plastics require sugar to synthesize polymers, most bioplastics are too expensive to compete with petroleum-based plastics. The Michigan State team has genetically modified cyanobacteria to constantly leak sugars produced by photosynthesis. Adding these algae to the same containers as plastic-producing bacteria provides all the sugars needed to produce plastic polymers.

Kassinger also discusses ocean warming because of climate change and increasing nutrient pollution as a result of agricultural fertilizer and sewage. Both ocean warming and water pollution destroy coral reefs and increase algal blooms, which can have devastating effects on local communities and ecosystem functions. "People focus on the

PHOTO: DAMIEN LOVERSO/ALAMY STOCK PHOTO

Published by AAAS



More than 25 million tons of macroalgae are harvested each year.

PHOTO: CAVAN/ALAMY STOCK PHOTO

gross algal blooms and blame the algae," she writes, "but the cause is entirely human."

Kassinger mentions throughout *Slime* the importance of brown algae and the associated kelp forests. Brown algae have high biomass, are major contributors to oxygen production, and provide habitat for many marine organisms. She misses an opportunity, however, to highlight how ocean warming and water pollution are threatening these highly productive kelp forests. Kelp forests on Tasmania's east coast have declined by more than 95%, for example, and were listed as the first threatened marine community by the Australian government in 2012.

Overall, *Slime* gives a distinct view into these underappreciated organisms and demonstrates our intertwined history with algae. Hopefully, it will help readers see algae in a different light.

Slime: How Algae Created Us, Plague Us, and Just Might Save Us, *Ruth Kassinger,* Houghton Mifflin Harcourt, 2019. 318 pp.

Because Internet

Reviewed by **Martine van Driel**[5]

In her new book, *Because Internet*, Gretchen McCulloch divides inhabitants of the internet into five groups, arguing that "[y]our experience of the internet and the language therein is shaped by who you were and who else was around at the time you joined."

"Old Internet People" came online when the internet first started and tend to use a lot of programmer jargon. "Full Internet People" joined the internet in the late 1990s or early 2000s as a social web, a place to continue with and expand on their existing, offline relationships. Most of their internet slang came from peers, who used abbreviations and emoticons to connote tone of voice. "Semi Internet People" joined around the same period and initially used the internet for work purposes but continued to live their social lives offline. To Semi Internet People, "All meaning is face value meaning." "Pre Internet People," the oldest group, are late adopters who only sporadically use the internet out of necessity. According to McCulloch, "Internet slang like acronyms and emoticons is not just unfamiliar to them, it signals membership in a group that they have no desire to be a part of." "Post Internet People," the youngest group, have grown up with access to the online world and tend to infer emotional meaning from subtle cues.

Although the title suggests that this book takes a prescriptive approach to language, discussing the "rules" for online communication, the content shows quite the opposite. McCulloch describes a variety of uses of the internet such as listservs, texting, social media, and memes and explains how language—primarily English, with some examples from other languages—has adapted to each function without judgment. She considers how emojis have developed from emoticons and discusses how gesture research can help us understand how emojis function in the world of texting and online chat. Explaining that both gestures and emojis fulfill a similar role in offline and online settings, she reveals how emojis make up for the lack of paralinguistic features in online communication. This section will be particularly interesting to nonacademics as well as junior researchers because she explicitly discusses the process she used in researching these features.

McCulloch resists exploring internet language as a new phenomenon. Instead, she builds her investigations on older research into sociolinguistic features, discussing key experiments such as William Labov's 1962 "fourth floor" study, which identified the presence of linguistic differences between social classes. These studies are woven into a compelling narrative rich with examples from her own online activities, a healthy dose of humor, and plenty of cat memes. Although it probably will not provide any novel insights for new media linguists, the breadth of topics covered—from conversation analysis to meme culture to the development of texting as we now know it—makes this book useful, engaging, and enjoyable.

Because Internet: Understanding the New Rules of Language, *Gretchen McCulloch,* Riverhead Books, 2019. 336 pp.

Moonbound

Reviewed by **Emily A. Margolis**[6]

As you bury your feet in the sand this summer, imagine tucking your toes into something a little more exciting: lunar regolith. This July marks the 50th anniversary of

Published by AAAS

the first human Moon landing, an event recently feted at box offices and on bookshelves. Jonathan Fetter-Vorm's nonfiction graphic novel *Moonbound: Apollo 11 and the Dream of Spaceflight* is the latest contribution to this commemorative craze.

In Fetter-Vorm's retelling, the familiar mission unfolds in parallel with historic events that made this moment possible. Beginning with the cosmic collision in which Earth's satellite formed, the graphic novel brings readers into the notebooks of astronomer Johannes Kepler, the imagination of author Jules Verne, the subterranean Nazi factory where concentration camp laborers assembled guided ballistic missiles, and the Soviet design bureau responsible for the first satellite. Deftly avoiding the trap of teleology, Fetter-Vorm alternates these historical vignettes—visually distinct in their monochromatic representation—with vibrantly colored scenes from inside Apollo 11 and on the lunar surface.

Wherever possible, Fetter-Vorm excerpts dialogue from mission transcripts and renders scenes from original photographs and films. His commitment to accuracy and detail are at their best inside the Apollo 11 command module, Columbia. In one panel, pilot Michael Collins is shown tracking the mission on a hand-drawn wall calendar. This and other markings (the walls functioned as a notepad of sorts) were largely unknown until 2016, when the Smithsonian National Air and Space Museum undertook a 3D scan and photometry of the spacecraft.

Through deep engagement with the latest historical scholarship, Fetter-Vorm commemorates the mission without simplifying it. He introduces readers to a cast of characters whose contributions to the space program were circumscribed by sexism and racism. His work acknowledges that the space age and civil rights struggle were not only contemporaneous but connected.

The book's epilogue reveals Fetter-Vorm's purpose: to inspire the next generation of space enthusiasts. It opens on a moment of discovery in 2012, as a submersible approaches remnants of a Saturn V rocket, Apollo's launch vehicle, on the ocean floor. The next page is dominated by the face of a young boy—eyes wide and mouth agape in wonder—as he encounters the recovered engine part at a museum. This sense of adventure and accomplishment, Fetter-Vorm suggests, can be recaptured through hard work, ingenuity, and national purpose.

Space scientists, engineers, and policymakers of the future—working for the public or private sector—must be prepared to address public relations challenges as well as scientific and technical ones. Almost as an afterthought, Fetter-Vorm gestures toward contemporary critiques of the Moon landing program. Fifty years on, it is easy to forget that the American public was generally ambivalent about this multibillion-dollar endeavor—a fact that dogged NASA from the early 1960s and that had a material impact on the way it conducted and presented Project Apollo.

Accessible to young adults but enjoyable for readers of all ages, *Moonbound* educates while it entertains.

Moonbound: Apollo 11 and the Dream of Spaceflight, *Jonathan Fetter-Vorm*, Hill and Wang, 2019. 256 pp.

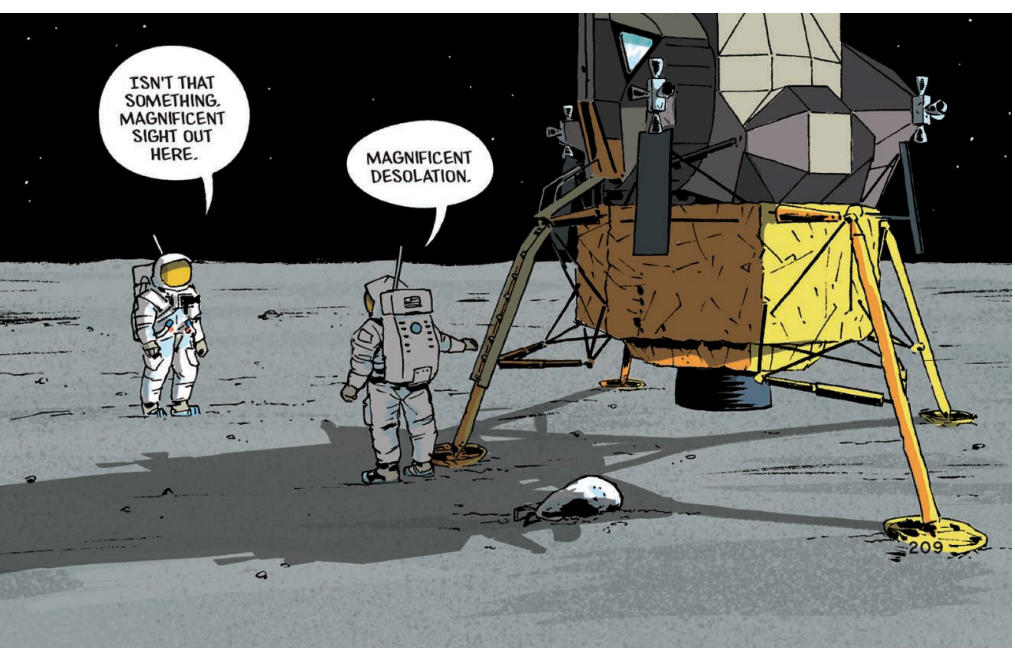


IMAGE: COURTESY OF JONATHAN FETTER-VORM AND HILL AND WANG

The Fate of Food

Reviewed by **Meha Jain**[7]

Imagine you have just eaten the best burger of your life, covered with creamy avocado, crisp lettuce, and a ripe tomato and nestled between a hearty bun. Now, what if that burger did not come from a cow but was cultivated from stem cells? What if the avocado spread was crafted by a 3D printer, and the lettuce and tomato were grown in a warehouse with no natural sunlight or soil? What if you learned that the bun was made by using an ancient ancestor of wheat that is more resilient to drought and was weeded and harvested by robots? Although this may sound like science fiction, according to journalist Amanda Little, it is all possible today.

Over the coming decades, food demand will increase as the world's population surpasses 9 billion people and diets change to include more land-intensive dairy and meat. At the same time, agricultural systems will likely face more uncertainty because of climate change and the degradation of natural resources on which they depend, such as fresh water and healthy soils. The United Nations estimates that food production may have to increase by up to 70% by mid-century to ensure global food security. In *The Fate of Food*, Little explores how we may be able to meet this growing demand and, answers the question: if we aren't able to, "how screwed *are* we exactly?"

Little interviews innovators at the forefront of a new wave of food production that is more automated, environmentally sustainable, and resilient. Her research takes her from smallholder farming systems in Ethiopia to large-scale organic farming operations in China and across more than a dozen U.S. states. During her travels, she meets with entrepreneurs who are blending technological innovation with tried-and-true agroecological practices and with individuals who are entirely upending traditional food production systems.

There are many potential solutions to sustainably increase food production, she reveals. These include using robots equipped with artificial intelligence (AI) to differentiate between crops and weeds (reducing the amount of herbicide applied to crops) and disseminating seeds that are more drought-tolerant to communities that have been ravaged by a lack of rain.

Little takes a balanced approach when describing each new technology or potential solution. She acknowledges, for example, that AI-enabled robots are only realistic for large-scale, relatively rich farmers. Similarly, she concedes that promoting new drought-resistant seed varieties can lead to

Published by AAAS



Drones may soon allow farmers to spot pests, weeds, and irrigation issues without setting foot in their fields.

problems if farmers become dependent on store-bought seeds and their prices rise.

Little's main point is an important one: In order to solve the world's impending food production challenges, we cannot take a one-size-fits-all approach of either "reinventing" the food system with technological innovations or "deinventing" it with a return to preindustrial organic farming. Instead, she proposes a third option, one that blends the use of new technologies and ways of farming with more traditional, sustainable agricultural approaches. If we adopt such a strategy, she is optimistic that we will meet growing food demand in a way that is simultaneously more sustainable, nutritious, and resilient.

The Fate of Food: What We'll Eat in a Bigger, Hotter, Smarter World, *Amanda Little,* Harmony, 2019. 350 pp.

Fall

Reviewed by **Bianca Jones Marlin**[8]

In his latest novel, *Fall*, Neal Stephenson tells the story of Richard Forthrast, better known as "Dodge," a video game magnate who has willed his brain to research in the hopes of being reanimated. Heeding the call of the "Eutropians," Dodge and seven others lead the charge for digital immortality, foretelling the emergence of new technology that will upload the brain of the financial elite to a virtual cloud. But what happens when a human-generated simulation begins to replicate the chaos by which life arose?

After his untimely death, Dodge's cryopreserved connectome is scanned and activated by using a vast network of computers, each processor dedicated to simulating the thousands of synaptic connections of an individual neuron. Emerging into the nascent "Bitworld," he experiences awareness amid a cacophony of static and light. Being the firstborn of the digital afterlife, Dodge is given free rein to design the world according to the pattern of his memory. But he is not alone for long. As other patrons are uploaded from the corporeal "Meatspace," Dodge assumes the role of king of the digital genesis, making subjects of the pantheon of bit-souls.

But Dodge's quest to create a more perfect life after death is challenged by the arrival of competing tech guru Elmo Shepherd, who seeks to impose his own version of eternity on the afterlife. Shepherd enters Bitworld with superior programming algorithms, acquired and refined after Dodge's death. He trades Dodge's lifelike renderings of uploaded souls for winged avatars, enslaved by his new algorithm. Dodge and his host of early Bitworld settlers retreat to an alternate plane described as the "lake of fire," waiting for an opportunity to reestablish their rule.

Eventually, Stevenson introduces the birth of new souls that are native to Bitworld, evoking a central question: Whence comes life and afterlife? Meatspace clientele struggle against the children of Bitworld for dwindling virtual resources. The children are faced with a moral conundrum, facing the prospect that their reality is filtered by the elite ruling class Shepherd has installed.

Fall invokes contemporary issues in neuroscience, focusing on the interplay between the hard-wired brain connectome and dynamics of synaptic learning. In doing so, Stephenson offers a sobering conclusion to the epistemology of the internet age that includes both subtle advice—reminding us, for example, that pride comes before the fall—and, ultimately, an outward rebuke of the quest for apotheosis.

In this great undertaking, however, Stephenson's cast of Meatspace characters is often lacking in dimensionality. They are described as unique individuals, but their contributions to dialogue could easily be interchanged with little repercussion. In addition, the book's generous narrative often strays toward the tangential without offering a clear contribution to the overall story arc. But perhaps it is Stephenson's intention that readers accompany Bitworld souls through aeons of incremental evolution, rediscovering the mundane as well as the sublime. Such an ambition would be admirable, but it fuels impatience in the reader, who may find herself wishing to return to the exciting central characters.

Fall offers an important allegory of mankind's struggle to understand our place in the universe, surrounded as we are by natural laws, myth, purpose-seeking, joy, and suffering. The reader is left with a sense that achieving perpetuity may ultimately be a pyrrhic victory.

ACKNOWLEDGMENTS

The author thanks J. Jones Marlin for helpful feedback and suggestions.

Fall; or, Dodge in Hell, *Neal Stephenson,* William Morrow, 2019. 890 pp.

10.1126/science.aax9532

[1]*Department of Geology and Geophysics, University of Wyoming, Laramie, WY 82071, USA. Email: rhaupt@uwyo.edu* [2]*Near and Middle Eastern Civilizations Department, University of Toronto, Toronto, ON M5S 1C1, Canada. Email: dominique.langis.barsetti@mail.utoronto.ca* [3]*CONNECT, Trinity College Dublin, College Green, Dublin 2, Ireland. Email: rachel.odwyer@gmail.com* [4]*School of Biological Sciences, Victoria University of Wellington, Wellington 6012, New Zealand. Email: maren.preuss@vuw.ac.nz* [5]*Department of English Language and Linguistics, University of Birmingham, Birmingham B15 2TT, UK. Email: m.a.vandriel.1@bham.ac.uk* [6]*Department of History of Science and Technology, Johns Hopkins University, Baltimore, MD 21218, USA. Email: emargol2@jhu.edu* [7]*School for Environment and Sustainability, University of Michigan, Ann Arbor, MI 48109, USA. Email: mehajain@umich.edu* [8]*Zuckerman Mind Brain Behavior Institute, Columbia University, New York, NY 10027, USA. Email: bjm2174@columbia.edu*

PHOTO: L. BRIAN STAUFFER, UNIVERSITY OF ILLINOIS AT URBANA-CHAMPAIGN

Published by AAAS

PERSPECTIVES

CLIMATE CHANGE

Rising methane: A new climate challenge

The amount of the greenhouse gas methane in Earth's atmosphere is rising rapidly

By **Sara E. Mikaloff Fletcher** *and* **Hinrich Schaefer**

In 2007, the amount of methane in the atmosphere (CH_4) began to rise after a 7-year period of near-zero growth (*1*). Recent research shows that a second step change occurred in 2014 (*2*). From 2014 to at least the end of 2018, the amount of CH_4 in the atmosphere increased at nearly double the rate observed since 2007 (see the figure). Because CH_4 is a potent greenhouse gas, rising atmospheric CH_4 presents a major challenge to achieving the goals set out in the Paris Agreement, an international consensus to limit temperature increase to 2°C or, if possible, to 1.5°C above preindustrial levels.

The causes for the recent rise in atmospheric CH_4 remain a subject of scientific debate, even for the initial period of increase from 2007 to 2014 (*1*–*8*). Process-based estimates of CH_4 emissions from inventory data, wetland models, and other information offer conflicting explanations, but measurements of the distribution of CH_4 in the atmosphere and its $^{13}C/^{12}C$ isotopic ratio at a global network of stations hold clues.

Although CH_4 has been rising across the globe, this growth has been largest in the midlatitudes and tropics of the Northern Hemisphere (*2*, *3*). Further, the proportion of ^{13}C in atmospheric CH_4 has declined as atmospheric CH_4 has risen (see the figure) (*1*, *2*). The $^{13}C/^{12}C$ ratio in CH_4 depends on the sources of the CH_4 emissions. Release from biogenic sources (such as wetlands and agriculture) reduces the proportion of ^{13}C in atmospheric CH_4, whereas fossil emissions slightly increase this proportion and biomass burning emissions increase it strongly (*1*, *2*). On the basis of selected CH_4 and $^{13}C/^{12}C$ time series from four latitudinal bands, a multibox atmospheric model, and a running-budget analysis, Nisbet *et al.* (*2*) identified three potential pathways consistent with both the CH_4 and isotope data: a surge in biogenic emissions, a decrease in the amount of CH_4 destroyed in the atmosphere through CH_4 oxidation, and an increase in fossil fuel emissions if balanced by a decrease in biomass burning.

Recent studies have identified source and sink processes that can explain part of the rise, but no single process can simultaneously account for the sudden onset of the rise and the steadiness of the increase, while remaining consistent with other available data. The most likely scenario is a combination of processes.

Biogenic emissions mainly come from wetlands and agriculture, particularly ruminant livestock. Multimodel wetland studies do not confirm an emission increase since 2007 (*3*, *9*). However, livestock inventories show that ruminant emissions began to rise steeply around 2002 and can account for about half of the CH_4 increase since 2007 (*4*).

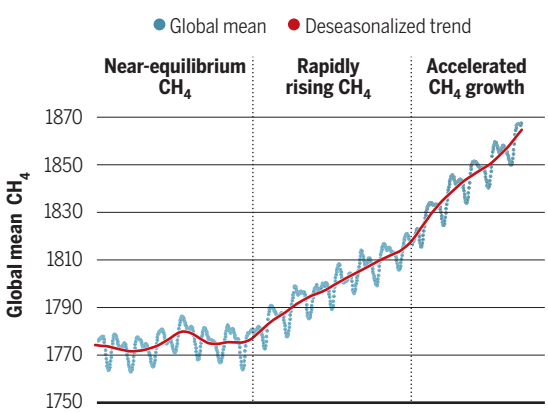
CH_4 is destroyed in the atmosphere by reaction with hydroxyl radicals (OH) and other atmospheric constituents. Reduced chemical destruction of CH_4 could both increase atmospheric CH_4 and decrease its proportion of ^{13}C. Actual OH changes over the past years are controversial (*5*, *6*), as is the role of sinks in global inversion studies (*7*, *8*). Only extreme changes in all major sinks can cause the observed CH_4 rise and still do not explain observed short-term variability (*2*), limiting the contribution that sinks are likely to make.

Increasing fossil emissions could explain the change, but a simultaneous reduction in ^{13}C-rich emissions from biomass burning is required to balance the $^{13}C/^{12}C$ trends. Fire reconstructions using satellite observations support such a decline with an emissions drop around 2006 (*10*). The resulting $^{13}C/^{12}C$ balance restricts fossil fuels to half of total additional emissions since 2007. Coal mining in East Asia is universally recognized to contribute to the CH_4 increase (*2*, *7*, *8*), whereas fossil CH_4 emissions from North America remained flat despite a nearly 50% increase in natural gas production (*11*).

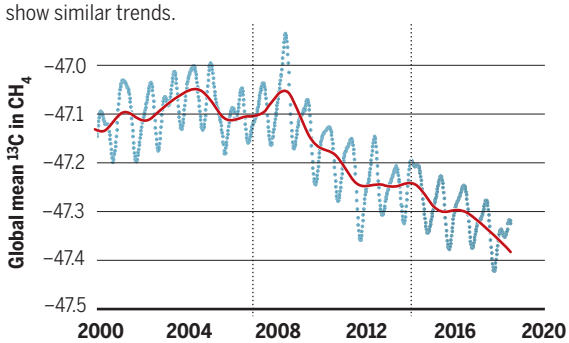
Coincident with the 2014 acceleration, Nisbet *et al.* find a source shift to the southern tropics, where wetlands are concentrated (*2*). They hypothesize that record high temperatures in 2014 and the following years spiked wetland CH_4 production. Such a wetland climate feedback challenges the commonly held view that wetland area rather than temperature is the main control of wetland CH_4 emissions (although some wetland CH_4 models are more temperature driven) (*10*). If natural wetlands, or changes in atmospheric chemistry, indeed accelerated the CH_4 rise, it may be a climate feedback that humans have

Methane trends

Data from U.S. National Oceanic and Atmospheric Administration observing stations show that global mean atmospheric CH_4 started to rise in 2007, with a sharper increase beginning in 2014 (*2*).



At the same time, the proportion of ^{13}C in CH_4 has been falling, providing insight into possible sources for the additional CH_4. Measurements from other observing station networks show similar trends.



GRAPHIC: N. CARY/*SCIENCE*; (DATA) HTTPS://WWW.ESRL.NOAA.GOV/GMD/DV/DATA

National Institute of Water and Atmospheric Research (NIWA), Greta Point, Wellington, New Zealand. Email: sara.mikaloff-fletcher@niwa.co.nz

Published by AAAS



Agriculture is thought to be responsible for over half of all anthropogenic CH_4 emissions and may have contributed to the rise in CH_4 since 2007.

PHOTO: SERGIO AZENHA/ALAMY STOCK PHOTO

little hope of slowing. Although studies have demonstrated the potential for substantial CH_4-climate feedbacks, they were expected to occur gradually, not reaching the magnitude observed by Nisbet *et al.* for decades (*12*).

While the scientific community continues to debate the causes of the CH_4 surge, the consequences are clear. The latest Intergovernmental Panel on Climate Change (IPCC) emission scenarios that limit warming to 1.5°C assume that the amount of CH_4 in the atmosphere will decrease by 35% between 2010 and 2050 (*13*). Yet, between 2007 and 2014, the amount has risen by an average of 5.7 parts per billion (ppb) per year, and by an average of 9.7 ppb per year since 2014. If this rise continues unabated, cuts to carbon dioxide and other greenhouse gases will need to be even steeper to achieve the Paris goal.

Atmospheric greenhouse gas measurements remain the fastest way to assess progress toward slowing climate change. More atmospheric observations are essential to understand the sources of rising CH_4, particularly in the tropics, which appear to be the engines of this change. Atmospheric models informed by CH_4 data will incorrectly attribute emission changes to regions poorly constrained by data, like equatorial ones (*3*).

Together with satellite observations and time series of additional tracers (*14*), a comprehensive global measurements network will be crucial to understand changes in CH_4. Ascension Island in the South Atlantic is currently the only tropical site with observations of CH_4, its $^{13}C/^{12}C$ ratio, and column CH_4 measurements, which are indispensable for validating satellite observations. Yet, this site is in danger of being discontinued. Ongoing support for vitally important sites like Ascension Island, and establishing similar ones in other parts of the tropics, will be crucial for studies of CH_4 trends.

Close integration between atmospheric observations, process-based studies, and policy is urgently needed to provide meaningful answers about the real emission reductions needed to meet the climate goals of the Paris Agreement. The World Meteorological Organization established the Integrated Global Greenhouse Gas Information System (IG^3IS) to address this issue. IG^3IS provides a bridge between the atmospheric greenhouse gas community and decision-makers. Timely dialogue between these groups has never been more essential, as the window for achieving the goals of the Paris Agreement is rapidly closing. ■

REFERENCES AND NOTES

1. H. Schaefer *et al.*, *Science* **352**, 80 (2016).
2. E. G. Nisbet *et al.*, *Global Biogeochem. Cycles* **33**, 318 (2019).
3. M. Saunois *et al.*, *Atmos. Chem. Phys.* **17**, 11135 (2017).
4. J. Wolf, G. R. Asrar, T. O. West, *Carbon Balance Manag.* **12**, 16 (2017).
5. M. Rigby *et al.*, *Proc. Natl. Acad. Sci. U.S.A.* **114**, 5373 (2017).
6. S. Naus *et al.*, *Atmos. Chem. Phys.* **19**, 407 (2019).
7. J. McNorton *et al.*, *Atmos. Chem. Phys.* **18**, 18149 (2018).
8. R. L. Thompson *et al.*, *Geophys. Res. Lett.* **45**, 11499 (2018).
9. B. Poulter *et al.*, *Environ. Res. Lett.* **12**, 094013 (2017).
10. J. R. Worden *et al.*, *Nat. Commun.* **8**, 2227 (2017).
11. X. Lan *et al.*, *Geophys. Res. Lett.* **46**, 4991 (2019).
12. J. F. Dean *et al.*, *Rev. Geophys.* **56**, 207 (2018).
13. V. Masson-Delmotte *et al.*, Eds., "Global Warming of 1.5°C. An IPCC special report on the impacts of global warming of 1.5°C above pre-industrial amounts and related global greenhouse gas emission pathways, in the context of strengthening the global response to the threat of climate change, sustainable development, and efforts to eradicate poverty" (World Meteorological Organization, 2018).
14. A. J. Turner, C. Frankenberg, E. A. Kort, *Proc. Natl. Acad. Sci. U.S.A.* **116**, 2805 (2019).

ACKNOWLEDGMENTS

This work was funded by the New Zealand Ministry of Business, Innovation, and Employment through contract C01X1817 and by NIWA through the Greenhouse Gases, Emissions and Carbon Cycle Science Programme. S.M.F. serves on the Scientific Steering Committee for the IG^3IS. We thank E. Dlugokencky (NOAA) for post-2017 CH4 data and S. Michel and B. Vaughn (CU/INSTAAR) for post-2017 isotope data.

10.1126/science.aax1828

NEUROSCIENCE

Embryonic neural activity wires the brain

Disruption of spontaneous activity prevents formation of cortical whisker maps

By **Alexandre Tiriac** *and* **Marla B. Feller**

The development of many sensory systems commonly involves patterned spontaneous activity of neurons, in which nearby neurons fire synchronously, forming waves of activity that propagate throughout a neural circuit. In concert with sensory experience and molecular factors, patterned spontaneous activity is critical for the formation of sensory maps, which are spatial representations in the brain of the sensory features they encode. The initial establishment of sensory maps is thought to be driven by molecular cues and later refined by neural activity, initially through patterned spontaneous activity and later by sensory-evoked activity. On page 987 of this issue, Antón-Bolaños *et al.* (*1*) use the mouse whisker system to show that at the earliest stages of innervation to the cortex during brain development, patterned spontaneous activity is required for the formation of functional sensory maps.

The whisker system of rodents is highly organized. In each brain area along the whisker sensory pathway, stimulation of a single whisker activates a distinct cluster of neurons that are spatially organized so that they match the layout of the whiskers on the snout (see the figure). In the primary somatosensory cortex, these arrays of clustered neurons are called barrels. The development of barrels has been described primarily by using anatomical techniques—staining methods that reveal clusters of somas, dendrites, and axon terminals—that match the functional maps, which are determined with physiological recordings. These sensory maps emerge in a developmental sequence, first appearing embryonically at the periphery and moving

Department of Molecular and Cell Biology and Helen Wills Neuroscience Institute, University of California, Berkeley, Berkeley, CA, USA. Email: mfeller@berkeley.edu

Published by AAAS

centrally, with the final stages of somatosensory map development consisting of the wiring of thalamocortical axons. This connects sensory thalamic nuclei to primary sensory cortices (*2*, *3*).

The whisker system has proven to be a powerful model for understanding the role of genes and activity in the maturation of sensory circuits. The organization of barrels at the thalamocortical synapse in layer 4 of the primary somatosensory cortex is highly stereotyped across animals. There are two stages that lead to the formation of barrels, which occurs by postnatal day 4 in mice (*4*). Thalamocortical axons representing the same whisker first form clusters upon innervation of the cortex by embryonic day 18. Cortical neurons then cluster around the organized thalamocortical axons. Neural activity is known to be important for cortical neuron clustering (*5*), but whether it matters for the first phase (thalamocortical axon clustering) remained unclear. However, it was recently discovered that the thalamus of embryonic mice exhibits patterned spontaneous activity weeks before barrel formation (*6*). This could be a powerful source of correlated activity during thalamic axon innervation of the cortex that could provide the activity necessary for barrel formation.

To test whether patterned spontaneous activity plays a role in barrel formation, Antón-Bolaños *et al.* used a transgenic approach in mice to alter patterned spontaneous thalamic activity by abolishing highly synchronized propagating waves while retaining asynchronous activity. This resulted in a substantial increase of the horizontal spread of activity across the somatosensory cortex elicited by focal thalamic stimulation and prevented the anatomical organization of barrels from forming. Moreover, barrels were absent in adults, indicating that sensory activity in the more mature transgenic mice could not compensate for the disruption of spontaneous activity during embryonic development.

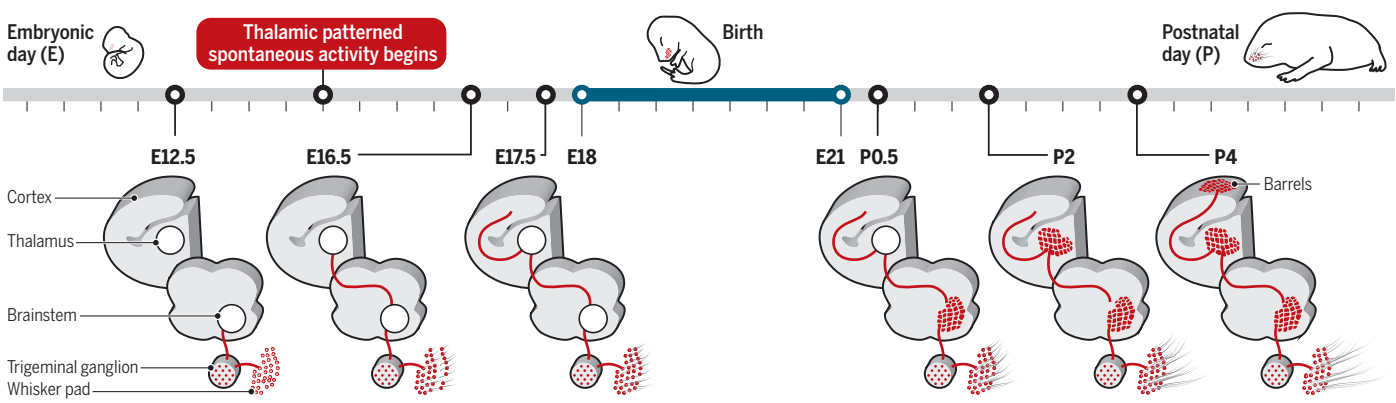
Antón-Bolaños *et al.* show that these phenotypes are due to both an expansion of thalamocortical axons that project to a larger area of the cortex and a local increase in cortical excitability. The expansion of thalamocortical axons parallels observations in the visual, auditory, and olfactory systems, in which disruption of patterned spontaneous activity disrupts the formation of retinotopic (visual) (*7*), tonotopic (sound) (*8*), and olfactory (smell) maps (*9*). The increase in cortical excitability was due in large part to an increase in the expression of metabotropic glutamate receptors. This is consistent with a previous study of mice lacking these receptors that did not form barrels, whereas thalamocortical axons still exhibited clustering (*10*). Antón-Bolaños *et al.* therefore elucidate a newly identified neural mechanism, one in which patterned spontaneous activity regulates the excitability of a neural network, which is necessary for the formation and maintenance of functional sensory maps (see the figure).

A remaining question pertains to the origin of the embryonic spontaneous thalamic waves. Because thalamic waves are observed as early as embryonic day 14.5 (*6*), which is before innervation of the thalamus by the brainstem, they are likely to be initially generated locally in the thalamus. However, at older ages, these thalamic waves may originate in or be modulated by brain regions presynaptic to the thalamus, such as the brainstem or trigeminal nerve ganglion. Antón-Bolaños *et al.* demonstrated that mechanical stimulation of whiskers at embryonic day 18.5 evoked responses in the somatosensory cortex, indicating that the functional pathway from whiskers to the thalamus is already present, which is consistent with studies demonstrating that fetal rats at embryonic day 16.5 are responsive to whisker stimulations (*11*). Active whisking in mice does not start until 14 days after birth, but spontaneous whisker movements, which are capable of driving thalamic activity, occur as early as postnatal day 4 (*12*, *13*). At this age, pharmacologically silencing the trigeminal nerve (which carries whisker information into the brain) completely abolishes patterned spontaneous activity in the cortex (*14*).

Patterned spontaneous activity in the somatosensory thalamus is analogous to patterned spontaneous activity in the retina, called retinal waves. During the first postnatal week, retinal waves are initiated by cells in the inner retina. However, as soon as photoreceptors make synaptic contact with the rest of the retina during the second postnatal week, visual stimulation increases the frequency of retinal waves (*15*). Whether the periphery or the barrel-like structures in the brainstem, which innervate the thalamus by embryonic day 16.5 (*3*), play a role in driving embryonic thalamic patterned spontaneous activity in vivo remains to be tested. ■

Development of the mouse whisker somatosensory system

Whisker somatosensory maps form in the mouse brain during early development. Map formation in the cortex depends on patterned spontaneous activity.



GRAPHIC: BASED ON A. TIRIAC BY A. KITTERMAN/*SCIENCE*

REFERENCES AND NOTES

1. N. Antón-Bolaños *et al.*, *Science* **364**, 987 (2019).
2. R. S. Erzurumlu, P. Gaspar, *Eur. J. Neurosci.* **35**, 1540 (2012).
3. G. Pouchelon, L. Frangeul, F. M. Rijli, D. Jabaudon, *Eur. J. Neurosci.* **35**, 1533 (2012).
4. M. Inan, M. C. Crair, *Neurosci.* **13**, 49 (2007).
5. T. Iwasato *et al.*, *Nature* **406**, 726 (2000).
6. V. Moreno-Juan *et al.*, *Nat. Commun.* **8**, 14172 (2017).
7. A. Thompson, A. Gribizis, C. Chen, M. C. Crair, *Curr. Opin. Neurobiol.* **42**, 136 (2017).
8. A. Clause *et al.*, *Neuron* **82**, 822 (2014).
9. C. R. Yu *et al.*, *Neuron* **42**, 553 (2004).
10. A. J. Hannan *et al.*, *Nat. Neurosci.* **4**, 282 (2001).
11. C. H. Narayanan, V. Hamburger, M. W. Fox, *Behaviour* **40**, 100 (1971).
12. A. Tiriac, B. D. Uitermarkt, A. S. Fanning, G. Sokoloff, M. S. Blumberg, *Curr. Biol.* **22**, 2075 (2012).
13. D. Akhmetshina, A. Nasretdinov, A. Zakharov, G. Valeeva, R. Khazipov, *J. Neurosci.* **36**, 9922 (2016).
14. H. Mizuno *et al.*, *Cell Rep.* **22**, 123 (2018).
15. A. Tiriac, B. E. Smith, M. B. Feller, *Neuron* **100**, 1059 (2018).

10.1126/science.aax8048

Published by AAAS

MAGNETISM

Imaging magnetic 2D crystals with quantum sensors

Odd- and even-layer variations in magnetization occur in two-dimensional chromium triiodide

By **Joaquin Fernández-Rossier**

The discovery of ferromagnetic order in monolayers of two different materials, CrI_3 (*1*) and $Cr_2Ge_2Te_6$ (*2*), has added ferromagnetism to the electronic properties displayed by two-dimensional (2D) crystals. Characterization of magnetic 2D crystals has relied on magneto-optical methods (*1*, *3*) such as the Kerr effect or magnetic circular dichroism that can interrogate small sample volumes. However, these probes do not provide an absolute measurement of the magnetic moment density and have very limited spatial resolution. On page 973 of this issue, Thiel *et al.* (*4*) use sensors based on nitrogen vacancy (NV)–center scanning magnetometry (*5*) to map the absolute magnetic moments of 2D crystals of CrI_3 with a resolution of a few tens of nanometers and show how the anomalous interlayer spin interactions vary with number of layers.

Bulk CrI_3 is a ferromagnetic insulator with a layered crystal structure (*6*). The Cr atoms have spin $S = 3/2$, and exchange coupling interactions both within and between layers lead to ferromagnetic ordering at temperatures at or below 61 K (*6*). Experiments in few-layer samples of CrI_3 that used magneto-optical effects (*2*) or tunneling electrons (*7*–*9*) found that interlayer exchange becomes antiferromagnetic, unlike bulk CrI_3. In few-layer CrI_3, a small magnetic field can offset the antiferromagnetic interlayer coupling and align the layers, providing a simple way to control magnetism in these systems.

The higher-resolution magnetic imaging performed by Thiel *et al.* uses the naturally occurring NV centers in diamond that consist of carbon atom vacancies (V) that lie next to nitrogen atom (N) substitutional impurities. The $S = 1$ NV centers have spin projections S_z of +1, 0, or –1. The NV centers readily emit single photons, with a photon yield that depends on S_z. In an optically detected magnetic resonance experiment (*5*), a static external magnetic field produces a Zeeman shift of the NV-center energy levels. The NV center is pumped both optically and with microwaves. The magnetic field of the microwave excites transitions between the spin levels of the NV center. When the microwave frequency matches the transition frequency of the spin levels that depend on the external magnetic field, a large variation of the occupation of the emissive states occurs, leading to a variation in the photon count. This optical readout of the resonance (and hence the magnetic field) has very high precision because of the long spin coherence time.

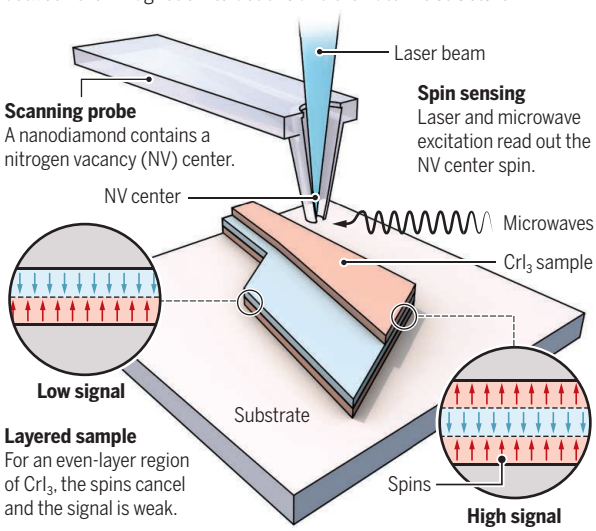
Attaching a nanodiamond to the tip of a scanning probe (*5*) enabled imaging of the magnetic field across the CrI_3 sample. At any given location, the magnetic field probed by the NV center is the sum of the external field, which is known, and the so-called stray field, which is created by the magnetization gradients that occur mainly at the boundaries and at domain walls of the CrI_3 sample (see the figure). Thiel *et al.* determined the magnetization field at the sample surface, given the measurement of the stray fields, by solving the inverse magnetostatics problem (finding the source distribution that generates the observed magnetic field), which is not straightforward and required some noise filtering. They then determined the average magnetization density for samples with different numbers of layers. Monolayers have average magnetization densities consistent with complete spin polarization of the Cr atoms. Thiel *et al.* found that samples with an even number of layers have a vanishing total magnetization, whereas samples with an odd number of layers have a magnetization similar to that of a single monolayer. These findings are consistent with the antiferromagnetic alignment between monolayers observed with other methods (*2*, *7*–*9*).

Lateral mapping revealed changes in magnetization resulting from changes in layer thickness as well as transitions between magnetic domains. Raman structural transitions of the CrI_3 thin film provided a strong indication that interlayer exchange is related to the stacking structure, as suggested in previous work (*6*, *9*, *10*). Also, in one experiment, accidental contact of the scanning tip with the sample punctured the nonmagnetic capping layer of a nine-layer sample, which restored the ferromagnetic interlayer exchange of the bulk and led to a factor of 9.7 increase in magnetization.

The success of the approach of Thiel *et al.*, together with the outstanding capabilities of NV-center scanning magnetometry (*5*, *11*), pave the way toward the widespread use of this technique. It could be used to explore the properties of magnetic 2D crystals, such as their spin waves, or the emergence of skyrmions. ■

Odds and evens

Thiel *et al.* used a high-resolution scanning method to measure quantitatively the magnetization of thin layers of CrI_3, finding a link between their magnetic interactions and their atomic structure.



GRAPHIC: C. BICKEL/*SCIENCE*

QuantaLab, International Iberian Nanotechnology Laboratory, 4715-330 Braga, Portugal. Email: jfrossier@gmail.com

REFERENCES AND NOTES

1. C. Gong *et al.*, *Nature* **546**, 265 (2017).
2. B. Huang *et al.*, *Nature* **546**, 270 (2017).
3. K. S. Novoselov, A. Mishchenko, A. Carvalho, A. H. Castro Neto, *Science* **353**, aac9439 (2016).
4. L. Thiel *et al.*, *Science* **364**, 973 (2019).
5. G. Balasubramanian *et al.*, *Nature* **455**, 648 (2008).
6. M. A. McGuire, H. Dixit, V. R. Cooper, B. C. Sales, *Chem. Mater.* **27**, 612 (2015).
7. D. R. Klein *et al.*, *Science* **360**, 1218 (2018).
8. T. Song *et al.*, *Science* **360**, 1214 (2018).
9. Z. Wang *et al.*, *Nat. Commun.* **9**, 2516 (2018).
10. D. Soriano, C. Cardoso, J. Fernández-Rossier, arXiv:1807.00357 (2018).
11. F. Casola, T. van der Sar, A. Yacoby, *Nat. Rev. Mater.* **3**, 17088 (2018).

ACKNOWLEDGMENTS

Supported by Fundação para a Ciência e a Tecnologia grants P2020-PTDC/FIS-NAN/3668/2014 and UTAPEXPL/NTec/0046/2017.

10.1126/science.aax6598

Published by AAAS

CLIMATE CHANGE

How fast will the Antarctic ice sheet retreat?

Feedbacks between glacier retreat and the solid Earth may slow ice loss from Antarctica

By **Eric J. Steig**

There is no longer any serious scientific doubt that the retreat of glaciers in Antarctica will eventually cause several meters of sea level rise, unless the emission of anthropogenic greenhouse gas is reduced substantially. By one estimate, each kilogram of carbon emitted as CO_2 will ultimately result in the melting of more than two metric tons of Antarctic ice (*1*). But how quickly this will happen remains highly uncertain, with the implications for society ranging from relatively moderate (*2*) to possibly catastrophic (*3*). Larour *et al.* (*4*) provide evidence in favor of a somewhat more moderate outlook: They show that the interaction of the ice sheet with the solid Earth—an important aspect of the problem not adequately captured by previous work—may slow down retreat.

Antarctica is losing ice mainly through the thinning, calving, and retreat of ice streams, the fast-flowing glaciers that drain the larger, slower-moving ice sheet into the ocean. A handful of ice streams in the Amundsen Sea region of West Antarctica (see the figure) contribute nearly 10% of the current global sea level rise of 3.4 mm/year. The ice discharge from Thwaites Glacier (see the photo), the largest glacier in this region, has more than doubled in recent years (*5*). The ongoing retreat of Amundsen Sea glaciers was initiated by the flow of warm, deep water onto the continental shelf (*6*), probably driven by anomalous wind conditions in the mid-20th century (*7*). Warm ocean water melts the glaciers from below, causing acceleration and grounding line retreat (the grounding line is the point where the glacier goes afloat to become an ice shelf).

The flow of glaciers depends critically on conditions at the glacier bed. The bed of Thwaites Glacier, like that of most other marine-terminating glaciers in Antarctica, slopes downward upstream of the grounding line. This geometry makes the glacier intrinsically unstable: The farther the glacier retreats, the deeper the water in which it terminates, and the more readily it melts and calves. Once retreat is initiated, atmosphere and ocean conditions become less important and the nonlinear dynamics of the glacier dominates its behavior (*8*). This makes the future behavior of such glaciers inherently difficult to predict. The presence of topographic highs on the bed, which act as pinning points, can stabilize these glaciers for a time, but the relatively smooth bed behind the current Thwaites grounding line suggests that continued retreat there may be inevitable (*9*), unless some other mechanism exists that could slow the retreat.

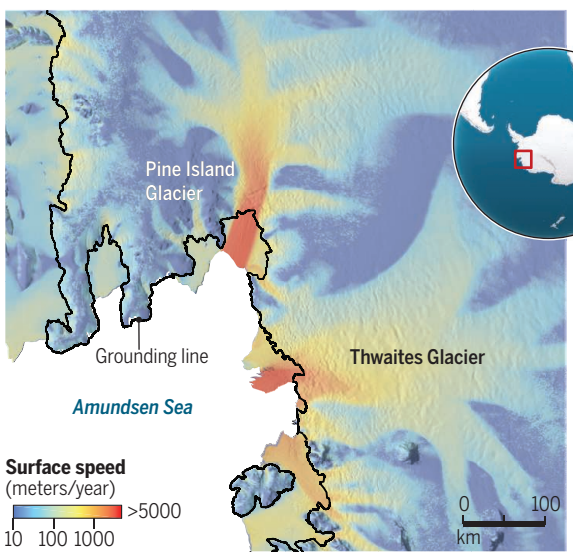
Larour *et al.* show that there is indeed a mechanism that may slow retreat, even if it is unlikely to stop it. As a glacier becomes smaller, it exerts less force on the underlying rock, which gradually rebounds and changes the bed geometry. This is known as glacial isostatic adjustment. Additionally, the redistribution of mass from the glacier to the ocean changes the local gravitational field. Both processes produce a local drop in sea level relative to the glacier bed (even while global sea level may be rising). This drop in sea level brings any potential pinning points closer to the bottom of the floating portion of the glacier. As a result, that portion of the glacier may ground, slowing the glacier's flow and reducing its retreat.

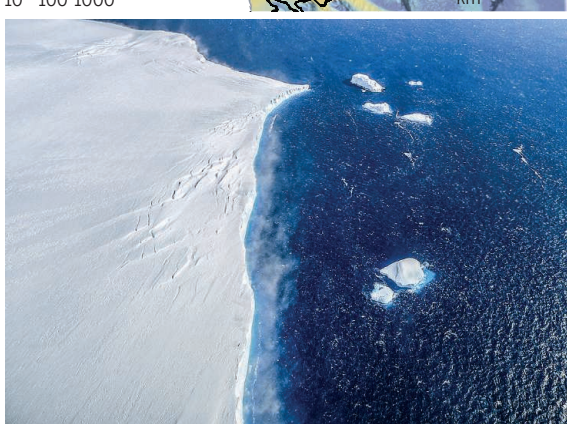
Both isostatic adjustment and gravitational effects tend to reduce rates of retreat because of the way in which the bed geometry evolves in relation to the position of the grounding line (*10, 11*). But most numerical model simulations have assessed such processes at relatively large spatial scales. Larour *et al.* show that their importance has thereby been underestimated. They have performed model simulations at the fine spatial resolution required for systems like the Thwaites Glacier, which is ~50 km wide, and the adjacent Pine Island Glacier, which is about half that width. Furthermore, their calculation accounts for the coupling between the solid-Earth and ice-flow processes at fine spatial scales and over time scales of weeks, rather than years or centuries.

Glacial isostatic adjustment involves both an initial elastic response and a slower viscous response. In glacier systems that are retreating very quickly, capturing the elastic component is critical for realistically modeling how the system will evolve. For example, retreat of the Thwaites Glacier and Pine Island Glacier grounding lines is extremely rapid at nearly 1 km/year (*5*). Larour *et al.* show that the elastic uplift component is greatly

Ice loss in West Antarctica

The two largest outlet glaciers in the Amundsen Sea region, Pine Island Glacier and Thwaites Glacier (photo), are retreating rapidly, contributing to sea level rise. The map shows surface speeds for the period of roughly 2016 to 2017 (*12*).





Department of Earth and Space Sciences, University of Washington, Seattle, WA 98105, USA.
Email: steig@uw.edu

CREDITS: (PHOTO) PETER NEFF; (GRAPHIC) BASED ON N. HOLSCHUH/UNIV. OF WASHINGTON BY N. DESAI/*SCIENCE*

Published by AAAS

underestimated if the model grid resolution is coarser than the 1-km spacing that they use in their simulations.

Larour *et al.*'s fine-scale treatment of the feedbacks between glacier retreat and solid-Earth processes shows that if projections of sea level rise ignore these feedbacks, they will be systematically too high. However, their results also show that these feedbacks are not likely to be very important over the coming century, but only on a time scale of a few centuries. This is because a very substantial mass loss must occur before the quantitative differences in model behavior become meaningful. In a sensitivity experiment, the authors find that by the year 2100, solid-Earth feedbacks would reduce mass loss from the Thwaites Glacier by only about 1%. By the year 2350, these feedbacks would reduce grounding line retreat by about 40% and would reduce Thwaites Glacier's contribution to sea level rise by more than 25%. Recently revised estimates of the mantle viscosity under the West Antarctic Ice Sheet (*11*), not accounted for by Larour *et al.*, imply that these numbers are conservative, probably by about a factor of 2.

For those concerned about potentially catastrophic sea level rise, the results of Larour *et al.* might be taken as welcome news. But it is important to recognize that Larour *et al.* do not make a specific prediction. There are too many unknowns about the topography of the glacier bed at the finest spatial scales, the process of glacier calving, and how winds and ocean currents will change. Rather, the results should serve as a guide to the magnitude and sign of the uncertainty in existing predictions, and as a road map for future research. Accounting for solid-Earth feedbacks suggests that although the greatest effects may be delayed by a few decades, Antarctic ice sheet retreat remains virtually certain. ■

REFERENCES AND NOTES

1. R. Winkelmann, A. Levermann, A. Ridgwell, K. Caldeira, *Sci. Adv.* **1**, e1500589 (2015).
2. T. L. Edwards *et al.*, *Nature* **566**, 58 (2019).
3. R. M. DeConto, D. Pollard, *Nature* **531**, 591 (2016).
4. E. Larour *et al.*, *Science* **364**, eaav7908 (2019).
5. P. Milillo *et al.*, *Sci. Adv.* **5**, eaau3433 (2019).
6. A. Jenkins *et al.*, *Nat. Geosci.* **3**, 468 (2010).
7. E. J. Steig, Q. Ding, D. S. Battisti, A. Jenkins, *Ann. Glaciol.* **53**, 19 (2012).
8. K. Christianson *et al.*, *Geophys. Res. Lett.* **43**, 10817 (2016).
9. I. Joughin, B. E. Smith, B. Medley, *Science* **344**, 735 (2014).
10. H. Konrad, I. Sasgen, D. Pollard, V. Klemann, *Earth Planet. Sci. Lett.* **432**, 254 (2015).
11. C. C. Hay *et al.*, *J. Clim.* **30**, 1881 (2017).
12. J. Mouginot, B. Scheuchl, E. Rignot, *Remote Sens.* **4**, 2753 (2012).

ACKNOWLEDGMENTS

Supported by NSF grant 1602435.

Published online 25 April 2019
10.1126/science aax2626

DEVELOPMENT

Cell fate decisions during development

Cell differentiation involves activation of mutually exclusive genetic programs

***By* Roberto Mayor**

The shape of our nose, the color of our skin, the movement of our gut, all depend on an extraordinary cell type called neural crest cells, which originate during embryogenesis. Since their discovery in 1868 (*1*), neural crest cells, which are present in all vertebrates, have fascinated developmental biologists (*2*). One of the amazing features of neural crest cells is their extraordinary multipotency: They form cartilage, muscle, neurons, glia, pigment cells, adrenal cells, and so on. (*3*). No other embryonic cell type can differentiate into so many different kinds of cells. However, how this multipotency is achieved is not understood. On page 971 of this issue, Soldatov *et al.* (*4*) clarify some of the mechanisms that explain how the multiplicity of cell types is generated by neural crest cells.

The neural crest is an embryonic stem cell population that is initially formed in an embryonic tissue layer called the ectoderm. The ectoderm will also form the neural tube, which later becomes the central nervous system. The neural crest is formed adjacent to the neural tube, in a region called the neural plate border, from where cells delaminate, migrate to colonize different tissues, and then differentiate (*3*, *5*). It has been shown using genetic labeling that neural crest cells are multipotent when they leave the neural tube and that their fate is decided after delamination (*6*–*8*), but how this multipotency is controlled has remained elusive.

Once neural crest cells are formed in the ectoderm, one of the first steps in their development is to delaminate and undergo an epithelial-to-mesenchymal transition (EMT), which is required for their migration (*9*). The classical view of neural crest EMT is that this is an abrupt process that results from the activation of a gene regulatory network (*10*). Soldatov *et al.* show that this is not the case, as they are able to resolve a sequence of stages around delamination, demonstrating that pre-EMT neural crest cells express genes associated with neural plate border and neural tube identity. More advanced neural crest cells down-regulate the expression of neural tube markers and increase the expression of neural crest cell–specific genes. This indicates that the transition from premigratory to migratory neural crest cells is more gradual and complex than initially thought.

This view is consistent with recent reports showing that EMT in cancer cells is not an all-or-nothing process, but rather a complex event with many steps controlled by different genes: Different cells undergoing EMT activate different aspects of the gene expression program at different times (*11*). Although the idea that EMT in the neural crest is not an abrupt process has been previously suggested (*12*), Soldatov *et al.* provide molecular evidence from single-cell RNA-sequencing data combined with spatial transcriptomics and lineage tracing in mouse neural crest differentiation. This allowed the identification of substages of EMT during delamination, characterized by specific marker expression.

One of the most intriguing conclusions from Soldatov *et al.* is the identification of specific steps involved in neural crest differentiation, in which progenitor cells undergo binary choices between possible fates as a result of their cellular history. This history is defined by the internal and external events that the cell has experienced, such as the autonomous activation of genes as well as signals from neighboring cells. Progenitor cells initially coactivate gene expression programs that lead to competing cellular fates (see the figure). These mutually exclusive cell fate programs then compete with each other. This competition is determined by differences in gene expression caused by historical changes that affect the transcriptome. Cells then up-regulate one program and down-regulate the other after a decision point (bifurcation). Thus, by inducing competing gene expression programs, the cell fate commitment process starts to look like a sequence of biasing factors that pull the cells in different directions, depending on their own history. It is likely that an interplay between these intrinsically developing biases interacts with extrinsic cues to shift the bias into a particular cell fate. This model challenges the cur-

Department of Cell and Developmental Biology, University College London, Gower Street, London WC1E 6BT, UK. Email: r.mayor@ucl.ac.uk

Published by AAAS

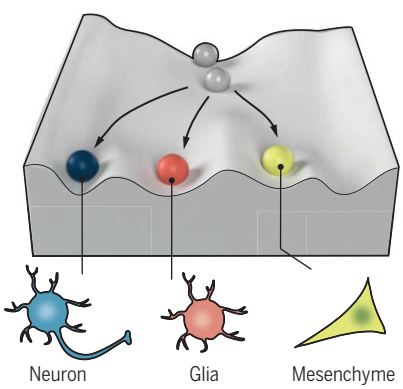
rent view in which neural crest cells abruptly activate only one of many alternative cell fate programs, leading to cell differentiation.

This revised vision for neural crest cell differentiation is consistent with what has been proposed for the differentiation of other cell types, such as those of the hematopoietic lineage (*13*). The first stable bifurcation identified in neural crest differentiation separates progenitors of the sensory lineage from those of autonomic and mesenchymal fates. This is followed by additional binary decisions that separate autonomic neuronal fate from mesenchymal differentiation. This contrasts with the current view in which a single precursor differentiates directly into specific cell types. In addition, Soldatov *et al.* show that many transcription factors considered as "master regulators" for specific lineages are not expressed at the time of the bifurcation to differentiate into these three lineages. This suggests that the activation of specific gene expression programs around the bifurcation point is triggered not by these master regulators, but by environmental conditions, such as chemical or mechanical cues (*3*, *14*).

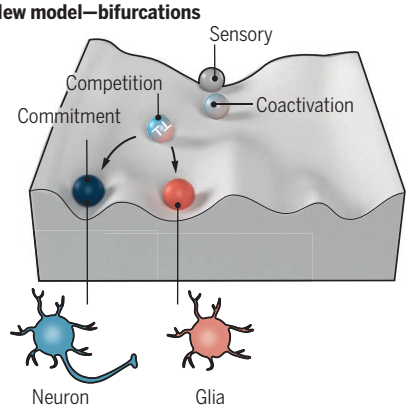
Models of cell differentiation

The classical versus new model of neural crest differentiation is depicted on a Waddington's landscape. Marbles represent cells differentiating down different paths as they roll down the hill.

Classical model



New model—bifurcations



Soldatov *et al.* also compare cell differentiation between neural crest formed in the head (cephalic) or the trunk of the embryo; showing that after delamination, the transcriptional signature that distinguishes the neural crest along the anterior-posterior axis of the embryo is erased, activating cell fate–specific gene expression programs. A mesenchymal program is activated in the cephalic neural crest, whereas a neuronal program is activated in the trunk.

The study of Soldatov *et al.* represents a supreme example of the use of single-cell analysis combined with spatial transcriptomics to address the question of cell differentiation in a heterogeneous cell population. The possibilities of applying similar approaches related to different aspects of neural crest development are enormous. For example, it has been proposed that neural crest behavior is different among different species (*15*). Comparing neural crest differentiation across different species could not only provide valuable insights into this conundrum but also reveal how neural crest originated during evolution. A comparison between normal neural crest and neural crest taken from embryos in which extracellular signals have been modified will provide valuable information about the role of external cues in neural crest differentiation. In addition, comparing neural crest between normal individuals and patients with neurocristopathies (pathologies associated with defective neural crest development) could clarify the origin of these diseases. The door is open to unraveling many of the mysteries that have surrounded the neural crest for more than 150 years. ■

REFERENCES AND NOTES

1. M. Bronner, *Dev. Biol.* **444** (suppl. 1), S1 (2018).
2. M. J. F. Barressi, S. F. Gilbert, in *Developmental Biology* (Oxford Univ Press, ed. 11, 2016), p. 463.
3. E. Dupin, G. W. Calloni, J. M. Coelho-Aguiar, N. M. Le Douarin, *Dev. Biol.* **444** (suppl. 1), S47 (2018).
4. R. Soldatov *et al.*, *Science* **364**, eaas9536 (2019).
5. J. A. Weston, S. L. Butler, *Dev. Biol.* **14**, 246 (1966).
6. S. Krispin, E. Nitzan, Y. Kassem, C. Kalcheim, *Development* **137**, 585 (2010).
7. M. C. McKinney *et al.*, *Development* **140**, 820 (2013).
8. A. Baggiolini *et al.*, *Cell Stem Cell* **16**, 314 (2015).
9. A. Szabó, R. Mayor, *Annu. Rev. Genet.* **52**, 43 (2018).
10. P. Betancur, M. Bronner-Fraser, T. Sauka-Spengler, *Annu. Rev. Cell Dev. Biol.* **26**, 581 (2010).
11. M. A. Nieto, R. Y.-J. Huang, R. A. Jackson, J. P. Thiery, *Cell* **166**, 21 (2016).
12. J. D. Ahlstrom, C. A. Erickson, *Development* **136**, 1801 (2009).
13. M. Hu *et al.*, *Genes Dev.* **11**, 774 (1997).
14. E. H. Barriga, K. Franze, G. Charras, R. Mayor, *Nature* **554**, 523 (2018).
15. E. H. Barriga, P. A. Trainor, M. Bronner, R. Mayor, *Development* **142**, 1555 (2015).

ACKNOWLEDGMENTS

R.M. thanks A. Shellard for comments. R.M. is supported by grants from BBSRC, MRC, and Wellcome Trust.

10.1126/science.aax7917

CANCER

Mutated clones are the new normal

Measuring and understanding the dynamics of clonal cell populations is key for cancer prevention

By **Cristian Tomasetti**

Cancers are formed by the expansion of harmful "mutational clones," which are cell populations carrying the same DNA mutations. How harmful they are depends on which mutated genes they contain. On page 970 of this issue, Yizhak *et al.* (*1*) add to the evidence that normal tissues are not so normal after all. Examining a substantial number of healthy tissues from almost 500 individuals, they found a large number of acquired (somatic) DNA mutations—some of which are typically associated with cancer—and mutational clones of macroscopic size, in the absence of cancer pathology. The presence in normal tissues of clonal cell populations, with mutations in cancer-associated genes, is informative about how a tumor evolves from the first mutation to a benign growth and, finally, to cancer.

Initial evidence that suggested the presence of several mutations in healthy cells came from mathematical modeling and statistical analyses of cancer DNA sequencing data to compare the mutational load in human cells before and after tumorigenesis (*2*). Independently of the specific estimates, the analysis provided indirect evidence that a substantial fraction of the somatic mutations found in cancers would have been present in those cells even in the absence of cancer (*2*). Subsequently, targeted DNA sequencing studies of normal tissues provided direct evidence for the presence of large numbers of somatic mutations and large numbers of microscopic mutational clones in the small sets of cancer-associated genes that were analyzed in

Division of Biostatistics and Bioinformatics, Department of Oncology, Sidney Kimmel Comprehensive Cancer Center, Johns Hopkins University School of Medicine, and Department of Biostatistics, Johns Hopkins Bloomberg School of Public Health, Baltimore, MD 21205, USA. Email: ctomasetti@jhu.edu

GRAPHIC: N. DESAI/*SCIENCE*

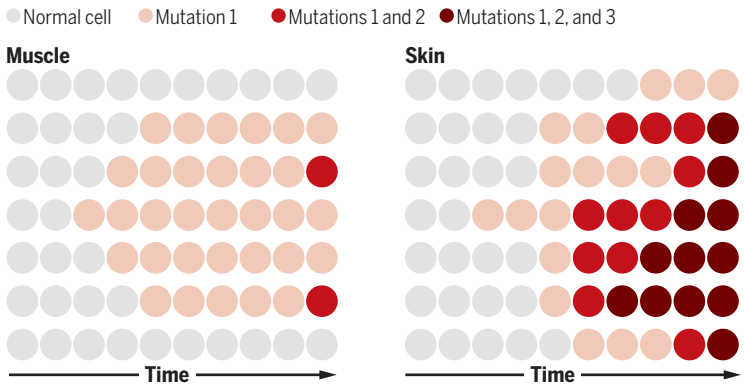
Published by AAAS

blood (*3*, *4*), skin (*5*), and esophagus (*6*, *7*).

The findings of Yizhak *et al.* were obtained by using a new method that analyzes RNA (instead of DNA) sequences from tissue samples. DNA mutations are subsequently detected from RNA sequences even when their frequency is very low, if they occur in highly expressed genes. In principle, their approach allowed the detection of mutational clones in normal tissues for every expressed gene, whereas previous analyses of normal tissues focused only on small sets of genes.

The accumulation of mutational clones with age

Cells in the body accumulate genetic mutations over time, with some of these mutations giving rise to large mutational clones. The rate of accumulation of these mutations and their clones depends on the tissue in which the cells reside; for example, it is much faster in skin than in muscle cells.



Yizhak *et al.* demonstrate the extent to which mutational clones are present in 29 different tissue types, with a focus on clones of larger (macroscopic) size. Large clonal populations are more likely to become cancer because of the larger number of cells at risk (*8*), making them the most critical to track. On average, the mutations that form these clonal populations were present in 5% of the estimated 30,000 to 730,000 cells analyzed in each sample (depending on the tissue type); therefore, these are relatively large populations. Clonal cell populations were found in tissues from almost all (95%) of the 488 individuals included in the study. Additionally, ~40% of the samples from the 29 human tissues studied contained at least one large mutational clonal population, with a small percentage (5%) of the samples having five or more of these mutational clones. A few of these clones were potentially pathological, with 33% of the individuals having a mutation in a gene that is implicated in cancer and with evidence suggesting a proliferative advantage for some of those mutations. These may be early transformed cells that occur during the initial phases of tumor evolution.

It is important to note that the approach only allowed the detection of relatively large clonal populations. Therefore, these results, together with evolutionary theory that larger clonal populations are less likely to be present than smaller ones (*8*), suggest that the numbers of smaller mutational clones would be exponentially larger than the numbers found when studying larger, macroscopic clones. Therefore, normal tissues may be more mutated than previously thought.

Yizhak *et al.* also found that the amount of somatic mutations increased with age. That normal cell populations forming tissues become huge mutational mosaics as humans age raises the question, what causes these mutations? Yizhak *et al.* found that the endogenous cell proliferation rate of a tissue increased the number of mutations (see the figure), with skin and esophagus having more mutations than those of brain and muscle cells, which proliferate less. This observation has been shown to have important consequences on the risk of cancer in different tissues (*9*). Similar to empirical evidence in cancer tissues (*10*), Yizhak *et al.* also found the largest presence of mutations in normal skin and lung, which are tissues largely affected by environmental (exogenous) factors such as sun exposure and smoking. Therefore, endogenous and exogenous processes, and their combination, are likely to be behind the mutational mosaicism, as previously suggested (*2*, *10*–*13*).

> ***"The presence in normal tissues of clonal cell populations, with mutations in cancer-associated genes, is informative about how a tumor evolves..."***

The findings of Yizhak *et al.* highlight the need for further understanding of the temporal dynamics of mutational mosaicism and clonal expansions in normal tissues. They also emphasize the need for assessing the relative contribution to cancer of endogenous mutational processes compared with those of unhealthy lifestyles and environmental exposures (*12*–*14*). These tasks are essential in order to properly stratify individuals and predict their age-dependent risk of cancer. Even the promise offered by cancer early-detection methodologies—such as sequencing circulating cell-free DNA from blood to find early signs of the presence of a cancer somewhere in the body—critically depends on understanding what is normal and what is not (*15*). For example, clonal hematopoiesis (*3*, *4*), the presence of mutational clones in blood cells, must be distinguished from the mutations found in cell-free DNA shed by a cancer.

It is not yet possible to properly assess probabilistically how far a tissue is from developing cancer. But methods and findings such as those in Yizhak *et al.* are an important step forward, especially when combined with clinical information and when individuals are followed in time. Overall, a more integrated approach to cancer prevention—to include both primary prevention methods, such as smoking cessation, and secondary prevention methods, such as early detection—is urgently needed to decrease cancer mortality (*16*). This approach should also account for the dynamics of mutational clones by properly assessing normal endogenous mutational processes, the microenvironment of a tissue (*17*), exogenous exposures that are potentially avoidable, and inheritance. ■

GRAPHIC: V. ALTOUNIAN/*SCIENCE*

REFERENCES AND NOTES

1. K. Yizhak *et al.*, *Science* **364**, eaaw0726 (2019).
2. C. Tomasetti, B. Vogelstein, G. Parmigiani, *Proc. Natl. Acad. Sci. U.S.A.* **110**, 1999 (2013).
3. G. Genovese *et al.*, *N. Engl. J. Med.* **371**, 2477 (2014).
4. S. Jaiswal *et al.*, *N. Engl. J. Med.* **371**, 2488 (2014).
5. I. Martincorena *et al.*, *Science* **348**, 880 (2015).
6. I. Martincorena *et al.*, *Science* **362**, 911 (2018).
7. A. Yokoyama *et al.*, *Nature* **565**, 312 (2019).
8. R. Durrett, S. Moseley, *Theor. Popul. Biol.* **77**, 42 (2010).
9. C. Tomasetti, B. Vogelstein, *Science* **347**, 78 (2015).
10. M. S. Lawrence *et al.*, *Nature* **499**, 214 (2013).
11. J. S. Welch *et al.*, *Cell* **150**, 264 (2012).
12. L. B. Alexandrov *et al.*, *Nature* **500**, 415 (2013).
13. C. Tomasetti, L. Li, B. Vogelstein, *Science* **355**, 1330 (2017).
14. J. D. Campbell *et al.*, *Cancer Prev. Res. (Phila.)* **9**, 119 (2016).
15. J. D. Cohen *et al.*, *Science* **359**, 926 (2018).
16. M. Song, B. Vogelstein, E. L. Giovannucci, W. C. Willett, C. Tomasetti, *Science* **361**, 1317 (2018).
17. S. Maman, I. P. Witz, *Nat. Rev. Cancer* **18**, 359 (2018).

ACKNOWLEDGMENTS

C.T. is supported by the John Templeton Foundation, the Maryland Cigarette Restitution Fund, the Marcus Foundation, the Lustgarten Foundation, and NCI P30CA006973.

10.1126/science.aax5525

Published by AAAS

RETROSPECTIVE

David A. Hamburg (1925–2019)

Renowned physician-psychiatrist and humanitarian

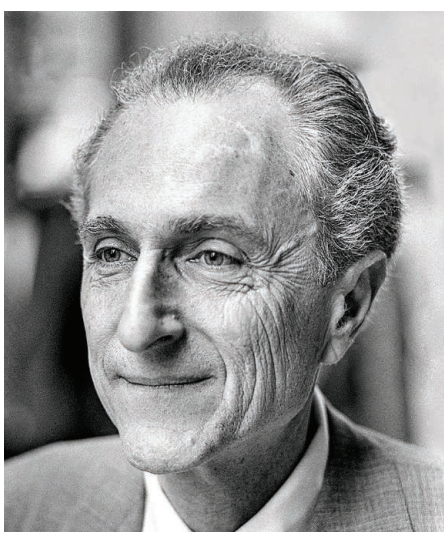
By **Harvey V. Fineberg**

David Allen Hamburg, who dedicated his life to relieving suffering and reducing the risk of global conflict, died on 21 April 2019 at age 93. His research on human development, stress, and behavior recast understanding of important sources of mental illness. Throughout his career, he shaped institutions and sought ways to bring people together for the causes of health, science, and world peace.

Born on 1 October 1925, David was raised in Evansville, Indiana. His grandfather, a pushcart peddler who had fled pogroms in Latvia, helped many relatives escape anti-Semitism in Eastern Europe. Foreshadowing his future work on prevention of genocide, David observed, "I grew up in the shadow of the Holocaust." David earned a Bachelor of Arts degree from Indiana University, Bloomington, in 1944 and an M.D. degree from the Indiana University School of Medicine in 1947. He trained in medicine and psychiatry at Michael J. Reese Hospital in Chicago and at Yale University, where he embarked on research on the effect of stress on the brain. There, David met his wife, Beatrix, the first African American woman to graduate from the Yale School of Medicine. After research stints at the Walter Reed Army Institute of Research in Washington, D.C., and back at Michael Reese Hospital, David served as chief of the adult psychiatry branch at the National Institute of Mental Health from 1958 to 1961. While investigating the biological basis of stress and behavior, David was also immersed in the experiential depths of psychiatry as a graduate of the Chicago Psychoanalytic Institute—an exceptional range in psychiatry.

In 1961, David accepted an appointment as chair of psychiatry at Stanford University School of Medicine. He established a new department of psychiatry and behavioral sciences, reflecting an inclusive approach to understanding mental illness, and he played a key role in the design and introduction of a new, interdisciplinary human biology program. During this period, David established a relationship with Jane Goodall's Gombe Stream Research Center in Tanzania, where students could undertake field studies of primate behavior. In May 1975, rebels from Zaire's People's Revolutionary Party raided the Gombe reserve and kidnapped three Stanford students and a young researcher from the Netherlands. David immediately traveled to Tanzania and joined the international team negotiating for release of the students. After 10 weeks of tense negotiations, all the students returned unharmed. This searing experience in the midst of stark poverty, deprivation, and conflict marked an inflection point in David's career, where the future and well-being of populations and of humanity as a whole began to take center stage.

That same year, David was appointed president of the Institute of Medicine (IOM)—as the health policy arm of the National Academy of Sciences in Washington, D.C., was then known. The fledgling institute had been founded in 1970 and remained unorganized. David established the core structure of program divisions that has persisted and evolved ever since. He stressed the value of interdisciplinary approaches to complex health issues, and he emphasized the importance of both excellence and relevance in the work of the institute. It was during this period that I served on my first IOM study committee and had an opportunity to witness David in action. He had a remarkable ability to absorb a group's discussion, distill it to the essence, and express emergent ideas in a way that elevated and reformulated the key concepts.



In 1980, David was appointed the inaugural director of Harvard University's interfaculty division on health policy research and education. Spanning Harvard's Kennedy School, Medical School, and School of Public Health, the division played into David's predisposition to seek multidisciplinary solutions to complex problems. As a rising professor of health policy at Harvard, I had an opportunity to interact regularly with David. Never one to indulge in small talk and never fully removed from his psychiatric roots, David was always ready to listen and advise on any personal or policy conundrum. He may have just gotten off the phone with a senator or cabinet secretary, but when he turned to you, you felt immediately the benefit of his full attention.

In 1982, the Carnegie Corporation of New York, a storied philanthropy, called on David to become its president. Here, for 15 years, David found the platform, resources, and latitude to give full voice to his convictions about the threat of global violence, while simultaneously strengthening the foundation's programs in health, education, and science. David established and, with former secretary of state Cyrus Vance, co-chaired the Carnegie Commission on Preventing Deadly Conflict. Through grants, he supported the Prevention of Proliferation Task Force at the Brookings Institution, which in turn inspired the Nunn-Lugar amendment that helped diminish nuclear arsenals as part of the Soviet Nuclear Threat Reduction Act of 1991. The strategy of prevention became a central tenet of David's approach, and he later titled his 2015 autobiography *A Model of Prevention: Life Lessons*.

Many accolades were showered on David, including the Presidential Medal of Freedom, the nation's highest civilian honor, in 1996, and the Public Welfare Medal of the National Academy of Sciences, its highest recognition for public service, in 1998. David relished the achievements of his family, coauthoring with his wife a book on preventing hatred and violence in childhood and adolescent development, and with his son, Eric, a book that stressed positive achievements toward world peace. David was especially proud of his daughter, Margaret, a renowned physician leader in her own right, who served as commissioner of the Food and Drug Administration and served as her father did as president of the American Association for the Advancement of Science (the publisher of *Science*).

David lived his life and made his mark in an unbroken continuum spanning discovery at the bench, the health of an individual, the well-being of populations, and global survival. In a world beset with conflict, when the capacity to destroy millions of lives has become ever more widely accessible, we will miss David's clear-eyed guidance on preventing the worst expressions of human aggression. ■

10.1126/science.aay0501

PHOTO: NEAL BOENZI/THE NEW YORK TIMES/REDUX

Gordon and Betty Moore Foundation, Palo Alto, CA, USA.
Email: harvey.fineberg@moore.org

Published by AAAS



POLICY FORUM

Transparency about the conduct and limits of precision medicine research is key to meaningful inclusion.

PHOTO: ISTOCK.COM/STEVE DEBENPORT

ETHICS AND DIVERSITY

Ethics of inclusion: Cultivate trust in precision medicine

We must explore how studies enhance diversity, inclusion

By **Sandra Soo-Jin Lee[1], Stephanie M. Fullerton[2], Aliya Saperstein[3], Janet K. Shim[4]**

Precision medicine is at a crossroads. Progress toward its central goal, to address persistent health inequities, will depend on enrolling populations in research that have been historically underrepresented, thus eliminating longstanding exclusions from such research (*1*). Yet the history of ethical violations related to protocols for inclusion in biomedical research, as well as the continued misuse of research results (such as white nationalists looking to genetic ancestry to support claims of racial superiority), continue to engender mistrust among these populations (*2*). For precision medicine research (PMR) to achieve its goal, all people must believe that there is value in providing information about themselves and their families, and that their participation will translate into equitable distribution of benefits. This requires an ethics of inclusion that considers what constitutes inclusive practices in PMR, what goals and values are being furthered through efforts to enhance diversity, and who participates in adjudicating these questions. The early stages of PMR offer a critical window in which to intervene before research practices and their consequences become locked in (*3*).

Initiatives such as the All of Us program have set out to collect and analyze health information and biological samples from millions of people (*1*). At the same time, questions of trust in biomedical research persist. For example, although the recent assertions of white nationalists were eventually denounced by the American Society of Human Genetics (*4*), the misuse of ancestry testing may have already undermined public trust in genetic research.

There are also infamous failures in research that included historically underrepresented groups, including practices of deceit, as in the Tuskegee Syphilis Study, or the misuse of samples, as with the Havasupai tribe (*5*). Many people who are being asked to give their data and samples for PMR must not only reconcile such past research abuses, but also weigh future risks of potential misuse of their data.

To help assuage these concerns, ongoing PMR studies should open themselves up to research, conducted by social scientists and ethicists, that examines how their approaches enhance diversity and inclusion. Empirical studies are needed to account for how diversity is conceptualized and how goals of inclusion are operationalized throughout the life course of PMR studies. This is not limited to selection and recruitment of populations but extends to efforts to engage participants and communities, through data collection and measurement, and interpretations and applications of study findings. A commitment to transparency is an important step toward cultivating public trust in PMR's mission and practices.

FROM INCLUSION TO INCLUSIVE

The lack of diverse representation in precision medicine and other biomedical research is a well-known problem. For example, rare genetic variants may be overlooked—or their association with common, complex diseases can be misinterpreted—as a result of sampling bias in genetics research (*6*). Concentrating research efforts on samples with largely European ancestry has limited the ability of scientists to make generalizable inferences about the relationships among genes, lifestyle, environmental exposures, and disease risks, and thereby threatens the equitable translation of PMR for broad public health benefit (*7*).

However, recruiting for diverse research participation alone is not enough. As with any push for "diversity," related questions arise about how to describe, define, measure, compare, and explain inferred similarities and differences among individuals and groups (*8*). In the face of ambivalence about how to represent population variation, there is ample evidence that researchers resort to using definitions of diversity that are heterogeneous, inconsistent, and sometimes competing (*9*). Varying approaches are not inherently problematic; depending on the scientific question, some measures may be more theoretically justified than others and, in many cases, a combination of measures can be leveraged to offer greater insight (*10*). For example, studies have shown that American adults who do not self-identify as white report better mental and physical health if they think others perceive them as white (*11*, *12*).

The benefit of using multiple measures of race and ancestry also extends to genetic studies. In a study of hypertension in Puerto Rico, not only did classifications based on skin color and socioeconomic status better predict blood pressure than genetic ancestry, the inclusion of these sociocultural measures also revealed an association between a genetic polymorphism and hypertension that was otherwise hidden (*13*). Thus, practices that allow for a diversity of measurement approaches, when accompanied by a commitment to

[1]*Division of Ethics, Department of Medical Humanities and Ethics, Columbia University, New York, NY, USA.* [2]*Department of Bioethics and Humanities, University of Washington, Seattle, WA, USA.* [3]*Department of Sociology, Stanford University, Stanford, CA, USA.* [4]*Department of Social and Behavioral Sciences, University of California, San Francisco, CA, USA. Email: sandra.lee@columbia.edu*

Published by AAAS

transparency about the rationales for chosen approaches, are likely to benefit PMR research more than striving for a single gold standard that would apply across all studies. These definitional and measurement issues are not merely semantic. They also are socially consequential to broader perceptions of PMR research and the potential to achieve its goals of inclusion.

STUDY PRACTICES, IMPROVE OUTCOMES

Given the uncertainty and complexities of the current, early phase of PMR, the time is ripe for empirical studies that enable assessment and modulation of research practices and scientific priorities in light of their social and ethical implications. Studying ongoing scientific practices in real time can help to anticipate unintended consequences that would limit researchers' ability to meet diversity recruitment goals, address both social and biological causes of health disparities, and distribute the benefits of PMR equitably. We suggest at least two areas for empirical attention and potential intervention.

First, we need to understand how "upstream" decisions about how to characterize study populations and exposures influence "downstream" research findings of what are deemed causal factors. For example, when precision medicine researchers rely on self-identification with U.S. Census categories to characterize race and ethnicity, this tends to circumscribe their investigation of potential gene-environment interactions that may affect health. The convenience and routine nature of Census categories seemed to lead scientists to infer that the reasons for differences among groups were self-evident and required no additional exploration (*9*). The ripple effects of initial study design decisions go beyond issues of recruitment to shape other facets of research across the life course of a project, from community engagement and the return of results to the interpretation of study findings for human health.

Second, PMR studies are situated within an ecosystem of funding agencies, regulatory bodies, disciplines, and other scholars. This partly explains the use of varied terminology, different conceptual understandings and interpretations of research questions, and heterogeneous goals for inclusion. It also makes it important to explore how expectations related to funding and regulation influence research definitions of diversity and benchmarks for inclusion.

For example, who defines a diverse study population, and how might those definitions vary across different institutional actors? Who determines the metrics that constitute successful inclusion, and why? Within a research consortium, how are expectations for data sharing and harmonization reconciled with individual studies' goals for recruitment and analysis? In complex research fields that include multiple investigators, organizations, and agendas, how are heterogeneous, perhaps even competing, priorities negotiated? To date, no studies have addressed these questions or investigated how decisions facilitate, or compromise, goals of diversity and inclusion.

The life course of individual studies and the ecosystems in which they reside cannot be easily separated and therefore must be studied in parallel to understand how meanings of diversity are shaped and how goals of inclusion are pursued. Empirically "studying the studies" will also be instrumental in creating mechanisms for transparency about how PMR is conducted and how trade-offs among competing goals are resolved. Establishing open lines of inquiry that study upstream practices may allow researchers to anticipate and address downstream decisions about how results can be interpreted and should be communicated, with a particular eye toward the consequences for communities recruited to augment diversity. Understanding how scientists negotiate the challenges and barriers to achieving diversity that go beyond fulfilling recruitment numbers is a critical step toward promoting meaningful inclusion in PMR.

TRANSPARENT REFLECTION, CULTIVATION OF TRUST

Emerging research on public perceptions of PMR suggests that although there is general support, questions of trust loom large. What we learn from studies that examine on-the-ground approaches aimed at enhancing diversity and inclusion, and how the research community reflects and responds with improvements in practices as needed, will play a key role in building a culture of openness that is critical for cultivating public trust.

Cultivating long-term, trusting relationships with participants underrepresented in biomedical research has been linked to a broad range of research practices. Some of these include the willingness of researchers to (i) address the effect of history and experience on marginalized groups' trust in researchers and clinicians; (ii) engage concerns about potential group harms and risks of stigmatization and discrimination; (iii) develop relationships with participants and communities that are characterized by transparency, clear communication, and mutual commitment; and (iv) integrate participants' values and expectations of responsible oversight beyond initial informed consent (*14*). These findings underscore the importance of multidisciplinary teams that include social scientists, ethicists, and policy-makers, who can identify and help to implement practices that respect the histories and concerns of diverse publics.

A commitment to an ethics of inclusion begins with a recognition that risks from the misuse of genetic and biomedical research are unevenly distributed. History makes plain that a multitude of research practices ranging from unnecessarily limited study populations and taken-for-granted data collection procedures to analytic and interpretive missteps can unintentionally bolster claims of racial superiority or inferiority and provoke group harm (*15*). Sustained commitment to transparency about the goals, limits, and potential uses of research is key to further cultivating trust and building long-term research relationships with populations underrepresented in biomedical studies.

As calls for increasing diversity and inclusion in PMR grow, funding and organizational pathways must be developed that integrate empirical studies of scientific practices and their rationales to determine how goals of inclusion and equity are being addressed and to identify where reform is required. In-depth, multidisciplinary empirical investigations of how diversity is defined, operationalized, and implemented can provide important insights and lessons learned for guiding emerging science, and in so doing, meet our ethical obligations to ensure transparency and meaningful inclusion. ■

REFERENCES AND NOTES

1. L. A. Hindorff, V. L. Bonham, L. Ohno-Machado, *Per. Med.* **15**, 403 (2018).
2. A. Harmon, "Why White Supremacists Are Chugging Milk (and Why Geneticists Are Alarmed)." *New York Times*, 17 October 2018.
3. D. MacKenzie, J. Wajcman, *The Social Shaping of Technology* (Open University Press, 1999).
4. "ASHG Denounces Attempts to Link Genetics and Racial Supremacy." *Am. J. Hum. Genet.* **103**, 636 (2018).
5. S. M. Reverby, *Examining Tuskegee: The Infamous Syphilis Study and Its Legacy* (Univ. of North Carolina Press, 2009).
6. S. M. Fullerton, *The Input-Output Problem: Whose DNA Do We Study, and Why Does It Matter* (Oxford Univ. Press, 2011).
7. A. B. Popejoy, S. M. Fullerton, *Nature* **538**, 161 (2016).
8. S. S. Lee, D. A. Bolnick, T. Duster, P. Ossorio, K. Tallbear, *Science* **325**, 38 (2009).
9. J. K. Shim, S. L. Ackerman, K. W. Darling, R. A. Hiatt, S. S.-J. Lee, *J. Health Soc. Behav.* **55**, 504 (2014).
10. A. Saperstein, J. M. Kizer, A. M. Penner, *Am. Behav. Sci.* **60**, 519 (2016).
11. I. Stepanikova, *Adv. Group Process.* **27**, 159 (2010).
12. C. P. Jones *et al.*, *Ethn. Dis.* **18**, 496 (2008).
13. C. C. Gravlee, A. L. Non, C. J. Mulligan, *PLOS ONE* **4**, e6821 (2009).
14. S. A. Kraft *et al.*, *Am. J. Bioeth.* **18**, 3 (2018).
15. A. E. Shields *et al.*, *Am. Psychol.* **60**, 77 (2005).

ACKNOWLEDGMENTS

Supported by NIH grant 1R01HG010330-01. The views and conclusions contained herein are those of the authors and should not be interpreted as representing official policies or endorsements, either expressed or implied, of NIH or the U.S. government.

10.1126/science.aaw8299

Published by AAAS



PHOTO: GREG C. GRACE/ALAMY STOCK PHOTO

Edited by **Jennifer Sills**

China's dams threaten green peafowl

The green peafowl (*Pavo muticus*)—the only native peafowl in China—is classified as Endangered on the International Union for Conservation of Nature (IUCN) Red List (*1*) and categorized as Critically Endangered on China's Biodiversity Red List (*2*). Over the past three decades, due to excessive hunting, habitat loss, resource competition, pesticide poisoning, deforestation, and inbreeding, green peafowls have sharply declined from between 800 and 1100 to fewer than 500 individuals in China (*1*, *2*). China's rush to build dams in Yunnan Province puts its remaining green peafowl populations in grave danger (*2*–*4*).

The Red River upstream district, China's last green peafowl habitat, is abundant in water resources and well suited to the construction of hydropower stations (*2*, *5*). Accordingly, the Jiasajiang Level 1 Hydropower Station was listed as a key project by the Yunnan provincial government in 2015 and scheduled to begin operation in 2021 (*4*). An environmental impact assessment failed to comprehensively describe the station's impact on biodiversity (*6*), and therefore the project began on schedule. Noise generated by the construction of the hydropower station disturbed the green peafowl and forced them to migrate to resource-limited areas (*2*). Once the station is complete, the dam will flood the last remaining habitat for green peafowl (*4*). As a result, the species will likely go extinct in China.

In addition to playing an important cultural role (*7*), green peafowls are a valuable genetic resource and an important component of China's biodiversity (*1*, *8*, *9*). The Chinese government has set up a provincial nature reserve to protect green peafowls (*5*), but the species will need additional conservation efforts. The Ministry of Ecology and Environment should be informed of the risks, and the authorities should conduct an immediate reevaluation of the ecological impact of this project, especially concerning the habitat of the green peafowls. Work on the Jiasajiang Level 1 Hydropower Station should stop until the assessment is complete. In the meantime, China should also increase the designated nature reserves, invest more to improve the green peafowl habitat, and increase patrols to control illegal hunting within protected areas.

Wangwang Tang*, Xiangxi Wang, Ming Yan, Guangming Zeng, Jie Liang*
College of Environmental Science and Engineering, Hunan University, Changsha 410082, China; Key Laboratory of Environmental Biology and Pollution Control (Hunan University), Ministry of Education, Changsha 410082, China.
*Corresponding author. E-mail: wtang@hnu.edu.cn (W.T.); liangjie@hnu.edu.cn (J.L.)

Dam construction could put China's native green peafowl (*Pavo muticus*) at risk of extinction.

REFERENCES AND NOTES

1. BirdLife International, *Pavo muticus* (IUCN Red list of Threatened Species, 2018); www.iucnredlist.org/species/22679440/131749282.
2. D. Kong *et al.*, *Avian Res.* **9**, 18 (2018).
3. W. Rong, "Dam-building threatens endangered green peacock" (2017); www.thethirdpole.net/en/2017/04/27/dam-building-threatens-endangered-green-peacock/.
4. H. Jingjing, "NGOs call for work to stop on Yunnan dam that may wipe out China's last green peafowl habitat," *Global Times* (2017); www.globaltimes.cn/content/1045006.shtml.
5. Y. Liu *et al.*, *Int. J. Galliform. Conserv.* **1**, 32 (2009).
6. "Environmental impact assessment report of the Jiasajiang Level 1 Hydropower Station in Yunnan province," (2014); www.doc88.com/p-0992324394228.html [in Chinese].
7. K. Kang, *J. Symb. Sandplay Therapy* **4**, 35 (2013).
8. N. Sukumal *et al.*, *Glob. Ecol. Conserv.* **3**, 11 (2015).
9. N. Sukumal *et al.*, *Bird Conserv. Int.* **27**, 414 (2017).

10.1126/science.aax4779

Science-based wildlife disease response

In 2007, the current outbreak of African swine fever (ASF), which severely affects wild boar populations and pigs, reached the Caucasus region. Since then, the virus has spread into eastern Europe and some places in central and western Europe (such as Belgium) through wild boar, domestic pigs, and human activities. The virus has raised serious concerns in countries with large pork industries, which may suffer economic losses due to trade restrictions (*1*). To control the outbreak, national authorities have taken drastic but likely ineffective measures that disregard the science of wildlife management.

Poland, for example, has massively increased culling of wild boar to minimize ASF spread and the risk of transmission to domestic pigs, despite opposition by experts (*2*, *3*). The policy does not include population monitoring that could evaluate its effectiveness (*4*). It also does not limit wild boar access to agricultural crops and

Published by AAAS

game feed, which is a key driver of population growth (*5*). Meanwhile, Denmark is building a 70-km border fence to exclude cross-border migration of wild boar (*6*). The fence will disrupt wildlife habitats (*6*), but it will not stop the virus from spreading through the transportation of live pigs, wild boar, or pig- and wild boar–derived tissues and products or through the movement of other objects carrying the virus, such as human clothing (*1*). Factors that govern wild boar abundance and virus spread are not bound by national borders. Instead of haphazard policies, we urge governments to agree on a coordinated response that adheres to the principles of modern wildlife management (*7*).

Adaptive wildlife management strategies consider the human dimension and prevent unsound reactive management. Improved wildlife population monitoring (*4*) and analysis are the best ways to determine which approaches to wildlife management are successful ecologically, economically, and socially. Sustainable management will depend on local circumstances and national wildlife management regulations, but science-based strategies can be implemented at the continental scale. Legislators across Europe should consult scientists and wildlife and animal health agencies before making decisions about wildlife policy. European countries should coordinate population monitoring and management. Shared responsibility for wildlife management among countries will enable funding for research that can critically evaluate its success. The ASF crisis can serve as a chance to develop a science-based wildlife policy for Europe.

Joaquín Vicente[1,2]*, Marco Apollonio[3], Jose A. Blanco-Aguiar[1], Tomasz Borowik[4], Francesca Brivio[5], Jim Casaer[5], Simon Croft[6], Göran Ericsson[7], Ezio Ferroglio[8], Dolores Gavier-Widen[9], Christian Gortázar[1], Patrick A. Jansen[10, 11], Oliver Keuling[12], Rafał Kowalczyk[4], Karolina Petrovic[4], Radim Plhal[13], Tomasz Podgórski[4,14], Marie Sange[12], Massimo Scandura[3], Krzysztof Schmidt[3], Graham C. Smith[6], Ramon Soriguer[2], Hans-Hermann Thulke[15], Stefania Zanet[8], Pelayo Acevedo[1,2]

[1]National Institute on Wildlife Research (IREC), University of Castilla-La Mancha and Consejo Superior de Investigaciones Científicas, Ciudad Real, Spain. [2]E.T.S. Ingenieros Agrónomos Ciudad Real, University of Castilla-La Mancha, Ciudad Real, Spain. [3]Department of Veterinary Medicine, University of Sassari, Sassari, Italy. [4]Mammal Research Institute, Polish Academy of Sciences, Białowieża, Poland. [5]Research Institute for Nature and Forest, Brussels, Belgium. [6]National Wildlife Management Centre, Animal and Plant Health Agency, Sand Hutton, York, UK. [7]Department of Wildlife, Fish, and Environmental Studies, Swedish University of Agricultural Sciences, Umea, Sweden. [8]University of Torino, Torino, Italy. [9]National Veterinary Institute, Uppsala, Sweden. [10]Wageningen University & Research, Wageningen, Netherlands. [11]Center for Tropical Forest Science, Smithsonian Tropical Research Institute, Balboa, Ancon, Panama. [12]Institute for Terrestrial and Aquatic Wildlife Research, University of Veterinary Medicine Hannover, Hannover, Germany. [13]Faculty of Forestry and Wood Technology, Mendel University in Brno, Brno, Czech Republic. [14]Czech University of Life Sciences, Prague, Czech Republic. [15]Helmholtz Centre for Environmental Research GmbH, UFZ, Leipzig, Germany.
*Corresponding author.
Email: joaquin.vicente@uclm.es

REFERENCES AND NOTES

1. EFSA Panel on Animal Health and Welfare (AHAW) *et al*., *EFSA J.* **16**, 5344 (2018).
2. K. Schmidt, R. Kowalczyk, H. Okarma, T. Podgórski, P. Chylarecki, "Experts against the proposal to depopulate wild boar in Poland," ENETWILD (2019); https://naukadlaprzyrody.pl/2019/01/09/list-otwarty-srodowiska-naukowego-w-sprawie-redukcji-populacji-dzikow/.
3. S. Walker, "Planned wild boar cull in Poland angers conservationists," *The Guardian* (2019); https://www.theguardian.com/environment/2019/jan/11/planned-wild-boar-cull-in-poland-angers-conservationists.
4. ENETWILD Consortium *et al*., *EFSA Supporting Publication* **15**, EN-1523 (2018).
5. G. Massei *et al*., *Pest Manag. Sci.* **71**, 492 (2015).
6. A. Mysterud, C. M. Rolandsen, *J. Appl. Ecol.* **56**, 519 (2019).
7. M. Apollonio *et al*., *Mammal Res.* **62**, 209 (2017).

10.1126/science.aax4310

Special educational needs and fieldwork

Special educational needs and disabilities can limit students interested in fields traditionally characterized by a large fieldwork component due to real or perceived physical barriers (*1*). Although much effort has been made to reduce the barriers and accommodate different types of disabilities and special educational needs (*2*), inclusivity is still challenging when it comes to fieldwork (*3*). Because many fieldwork experiences cannot be recreated in the lab, it is important to provide fieldwork opportunities that do not rely on the assumption of able-bodiedness among students (*4*). This should not be considered a limiting factor, because redesigning a field course to increase its inclusivity can result in an improved learning experience for all students and instructors. Academic departments should actively participate in discussions about program accessibility, rather than leaving affected students and the university's disability resources to find a solution (*5*).

The development of new techniques and the implementation of simple actions can represent a step forward in enhancing inclusion and equal opportunities in relation to fieldwork. Increasing the awareness of accessibility by all staff and students, as well as focusing on students'

PHOTO: TOUCH MAPPER

Published by AAAS



Tactile maps can help students overcome obstacles to fieldwork.

abilities rather than on their challenges, can make a real difference to the field experience and encourage more students to view disciplines that require fieldwork as viable career options (*3*). For instance, eliminating inaccessible locations, redesigning the field stops, and rearranging the schedule to reduce frequent transfers in and out of the bus will reduce the mental and physical stress on students. A sign-language interpreter can support field activities to help students with limited hearing. The use of audio field guides describing the field stops can improve the field experience for students who are blind, partially sighted, or who have specific learning disabilities. Tactile maps can represent a valid alternative to 2D maps to help students to perceive topography and geological structures. In addition, the use of real-time telepresence allows mobility-impaired students in a safer area to see and interact with the rest of the group even if they are located at some distance from the site. Finally, virtual technology can support field activities by simulating the experience of being in the field.

It is not always possible to overcome all potential barriers, and in some cases lab-based alternatives may have to suffice. However, these actions can help to reduce the experience gap for students with special educational needs and disabilities.

Domenico Chiarella
Clastic Sedimentology Investigation, Department of Earth Sciences, Royal Holloway University of London, Egham TW20 0EX, UK.
Email: domenico.chiarella@rhul.ac.uk

REFERENCES AND NOTES

1. H. S. Poussu-Olli, *Disability Soc.* **14**, 103 (1999).
2. J. Seale, *E-Learning and Disability in Higher Education: Accessibility Research and Practice* (Taylor and Francis, New York, 2014).
3. B. Gilley, C. Atchinson, A. Feig, A. Stokes, *Nat. Geosci.* **8**, 579 (2015).
4. T. Hall, M. Healey, M. Harrison, *Trans. Inst. Brit. Geogr.* **27**, 213 (2002).
5. M. Hayley, C. Roberts, A. Jenkins, J. Leach, *Planet* **6**, 24 (2002).

10.1126/science.aax7041

TECHNICAL COMMENT ABSTRACTS

Comment on "Designing river flows to improve food security futures in the Lower Mekong Basin"

John G. Williams, Peter B. Moyle, Ashley S. Halls

Sabo *et al.* (Research Articles, 8 December 2017, p. 1270) used statistical relationships between flow and catch in a major Lower Mekong Basin fishery to propose a flow regime that they claim would increase catch, if implemented by proposed dams. However, their catch data were not adjusted for known variation in monitoring effort, invalidating their analysis.

Full text: dx.doi.org/10.1126/science.aav8755

Response to Comment on "Designing river flows to improve food security futures in the Lower Mekong Basin"

John L. Sabo, Gordon W. Holtgrieve, Albert Ruhi, Mauricio E. Arias, Peng Bun Ngor, Vittoria Elliott, Timo Räsänen, So Nam

Williams *et al.* claim that the data used in Sabo *et al.* were improperly scaled to account for fishing effort, thereby invalidating the analysis. Here, we reanalyze the data rescaled per Williams *et al.* and following the methods in Sabo *et al*. Our original conclusions are robust to rescaling, thereby invalidating the assertion that our original analysis is invalid.

Full text: dx.doi.org/10.1126/science.aav9887

Published by AAAS

REVIEWS

Self-organization of stem cells into embryos: A window on early mammalian development *p. 948*

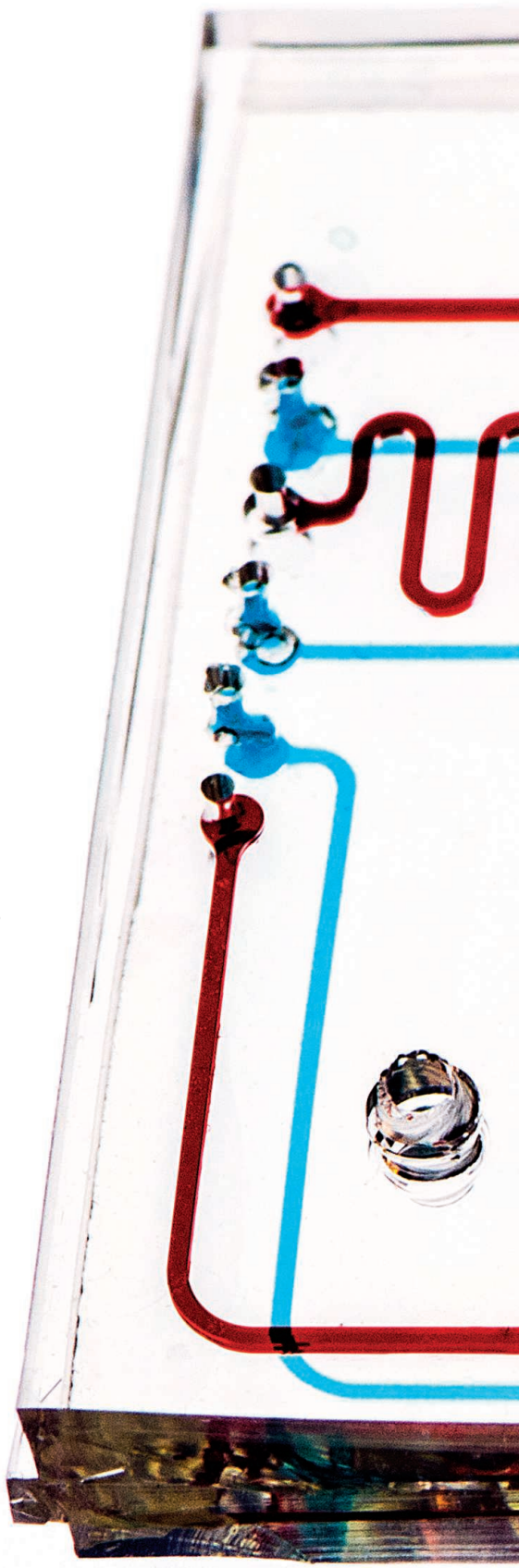
Cancer modeling meets human organoid technology *p. 952*

Organoids by design *p. 956*

Organoids-on-a-chip *p. 960*

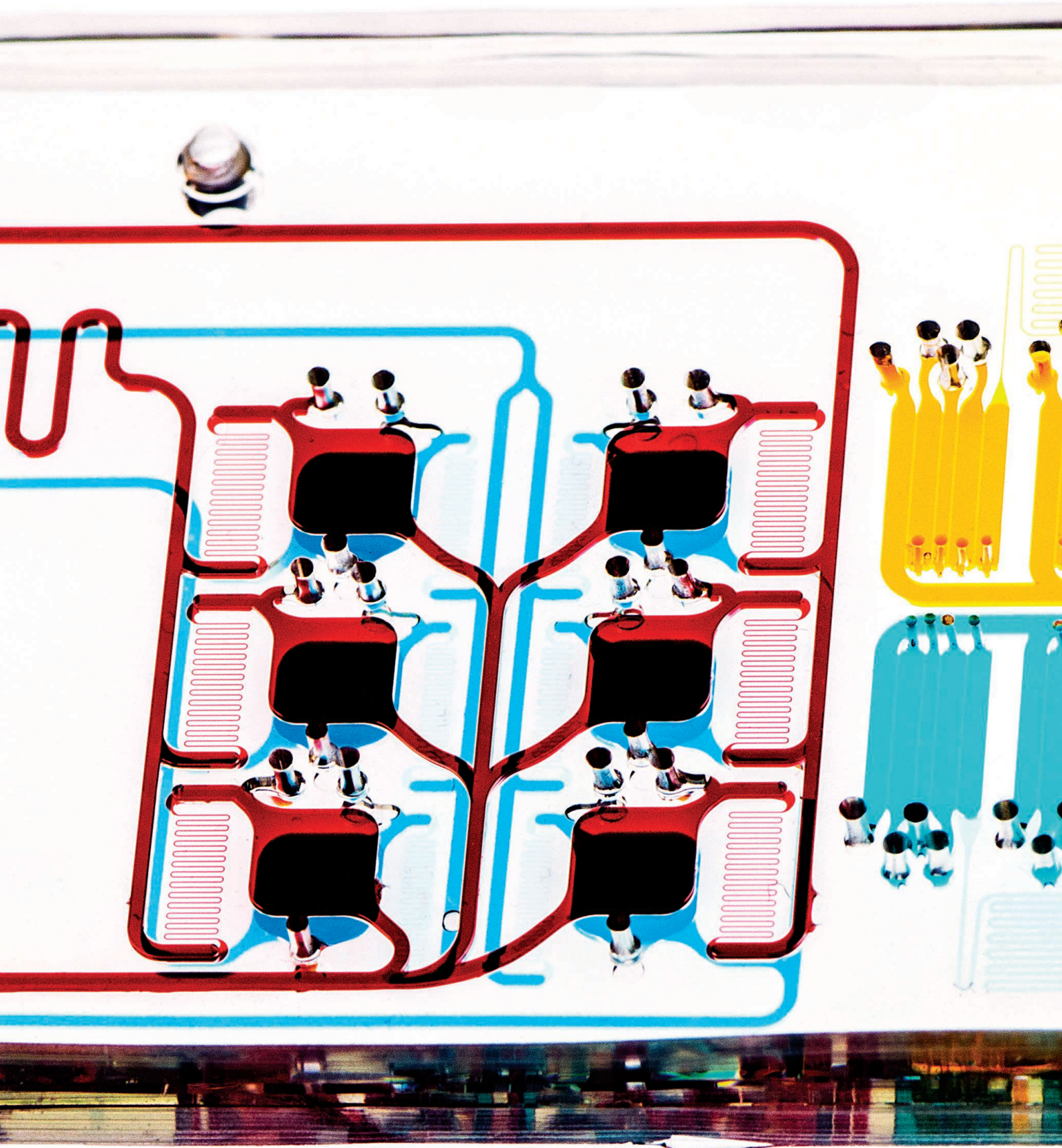
APPROXIMATING ORGANS

By **Beverly A. Purnell** *and* **Marc Lavine**



Less complex than a whole organ but more representative than clusters of cells in culture, organoids are composed of specific cell types that self-organize and recapitulate various aspects of organogenesis. As such, these 3D models enable studies of early organ development and tissue interactions. Furthermore, when constructed from patient-derived cells, they help us understand what happens in the disease state, including cancer. However, organs in a dish only approximate the real thing. They lack elements of the natural environment that are critical for influencing cell dynamics and morphogenesis. In addition, multiple cell lineages may contribute to a single organ, or physical features may be key. Hence, researchers are tasked with identifying and reconstructing these elements and interactions—whether they involve coculture with other cells to generate vasculature and provide innervation, or simulation of fluid flow as with organoids-on-a-chip. These engineered biological constructs can then more closely approximate nature's form and function. Continued tweaking of methods will yield exciting advances and solve classical embryology questions surrounding the generation of the three germ layers, breaking of symmetry, and axis formation, and may eventually lead to the replacement of faulty body parts though transplantation of organoid-generated tissues and organs.

Published by AAAS



Lung-on-a-chip. The red and blue chambers are where airway cells are cultured to model human small airways. The device has six chambers for the generation of six biological replicates. PHOTO: THE BIOLINES LABORATORY DIRECTED BY D. HUH AT THE UNIVERSITY OF PENNSYLVANIA

Published by AAAS

REVIEW

Self-organization of stem cells into embryos: A window on early mammalian development

Marta N. Shahbazi[1]*†, Eric D. Siggia[2]*†, Magdalena Zernicka-Goetz[1]*†

Embryonic development is orchestrated by robust and complex regulatory mechanisms acting at different scales of organization. In vivo studies are particularly challenging for mammals after implantation, owing to the small size and inaccessibility of the embryo. The generation of stem cell models of the embryo represents a powerful system with which to dissect this complexity. Control of geometry, modulation of the physical environment, and priming with chemical signals reveal the intrinsic capacity of embryonic stem cells to make patterns. Adding the stem cells for the extraembryonic lineages generates three-dimensional models that are more autonomous from the environment and recapitulate many features of the pre- and postimplantation mouse embryo, including gastrulation. Here, we review the principles of self-organization and how they set cells in motion to create an embryo.

Vertebrate development deploys orthologous sets of genes that first create the body axes—anterior-posterior (AP), dorsal-ventral (DV), and left-right (LR)—as well as the germ layers—endoderm, mesoderm, and ectoderm—and ultimately refines these patterns to the diverse adult forms we know. How are these spectacular feats of self-organization possible?

Although we have an inventory of genes that confer cell identity, we are far from understanding how their products communicate to generate embryonic patterns.

Multiple levels of regulation add robustness to embryonic development, but this redundancy makes the regulatory network difficult to decipher. Using stem cells as a model system to study embryology, we are now able to start peeling back these layers of regulation to reveal the dynamic organization of the embryo. Technical advances that created stem cell embryology were reviewed in (*1*). Here we focus on the principles of how cell communication at the molecular level enables embryonic self-organization in mouse and human embryos.

Mammalian embryo development

Preimplantation development is fairly conserved among mammalian species (*2*). Fertilization leads to a stepwise process of cell fate specification that culminates with the blastocyst comprising three cell types: the embryonic epiblast and the extraembryonic primitive endoderm and trophectoderm (*3*–*6*). Blastocyst implantation initiates a dialogue between the uterus and the embryo, which leads to the reorganization of both the embryo and the maternal tissues. Across diverse mammalian species, the basic relation between tissues is conserved, but postimplantation conceptuses present distinct embryonic architectures, from the cylinder-like shape of mouse embryos to the bilaminar disc of human embryos (*2*) (Fig. 1). How these different shapes evolved remains unknown.

Interactions between embryonic and extraembryonic tissues are critical to reshaping the developing embryo. In the mouse, the polar trophectoderm proliferates in response to fibroblast growth factor 4 (FGF4) secreted by the epiblast to form the extraembryonic ectoderm (*7*), which will form the placenta. Concomitantly, the epiblast and extraembryonic ectoderm undergo a process of lumenogenesis in response to extracellular matrix (ECM) secreted by the primitive endoderm–derived visceral endoderm (*8*, *9*). The fusion of the extraembryonic ectoderm and epiblast cavities leads to the formation of the proamniotic cavity (*10*), fundamental for the establishment of the body plan. This coincides with a symmetry-breaking event to form the anterior signaling center in the visceral endoderm (AVE) that defines the AP axis and the site of gastrulation (*11*–*13*).

In human embryos, the epiblast undergoes lumenogenesis in a similar way to that of the mouse, with one important difference: Epiblast in contact with the trophoblast forms the amniotic epithelium, whereas epiblast in contact with the hypoblast (visceral endoderm-equivalent) forms the epiblast disc (*1*, *2*, *14*). The mechanisms of symmetry breaking leading to AP axis formation in human embryos remain unknown, but mechanical and chemical cues are clearly involved. In cynomolgus monkey embryos, a

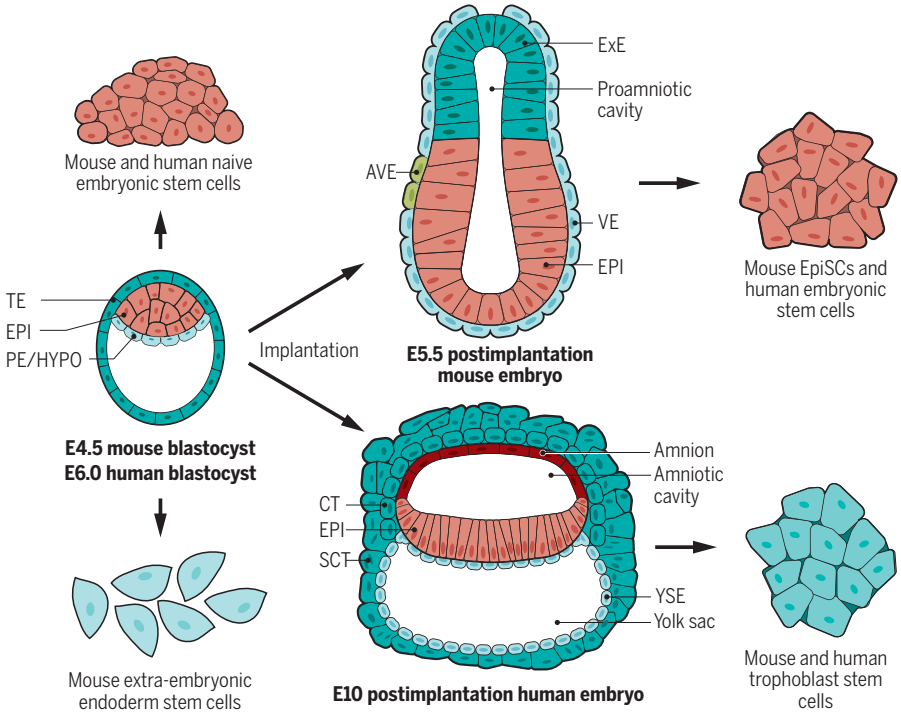


Fig. 1. Schematic representation of mouse and human pre- and postimplantation embryos and the stem cell lines that can be derived from them. Extraembryonic tissues are shown in different shades of teal, and epiblast derivatives in different shades of red. EPI, epiblast; TE, trophectoderm; PE, primitive endoderm (mouse), HYPO, hypoblast (human); ExE, extraembryonic ectoderm; VE, visceral endoderm; AVE, anterior visceral endoderm; CT, cytotrophoblast; SCT, syncytiotrophoblast; YSE, yolk sac endoderm.

[1]Mammalian Embryo and Stem Cell Group, Department of Physiology, Development and Neuroscience, University of Cambridge, Downing Street, Cambridge CB2 3DY, UK. [2]Center for Studies in Physics and Biology, The Rockefeller University, New York, NY 10065, USA.
*These authors contributed equally to this work.
†Corresponding author. Email: ms2261@cam.ac.uk (M.N.S.); siggiae@rockefeller.edu (E.D.S.); mz205@cam.ac.uk (M.Z.-G.)

population of hypoblast cells that expresses Wnt and Nodal inhibitors (DKK1 and CER1), characteristic of the mouse AVE, has been identified (*15*).

Is a dialogue between mother and embryo required for this morphogenesis? Comparative embryology provides a preliminary answer. In mammalian embryos such as pig, rabbit, and cow, embryonic morphogenesis and gastrulation take place before implantation (*16*, *17*). Mouse and human embryos can undergo early post-implantation morphogenesis without maternal input (*8*, *18*–*21*). Even if the uterine environment could help to modulate these events (*22*, *23*), the self-organizing capabilities of mammalian embryos (and stem cells) are becoming increasingly apparent.

Modes of self-organization

Although a system composed of invariant parts might be induced to self-assemble, here we focus mainly on self-organization that encompasses both patterning (fate change) by exchange of signals, as well as cell rearrangements. To further refine terminology, consider a supersaturated vapor that is spatially homogeneous until droplets nucleate and grow. The immediate trigger for a drop may be a speck of dust, but its subsequent expansion is reproducible. This is an example of spontaneous symmetry breaking, because the initially homogeneous vapor (the symmetric state) becomes an inhomogeneous mist of droplets. Analogous, self-organization occurs in systems of chemical reactions with diffusion where Turing showed that inhomogeneities with a characteristic spatial scale result from a random trigger to a uniform but unstable system (*24*). Embryology generally avoids spontaneous symmetry breaking because the outcome is too fragile; rather, it proceeds by progressive refinement of prior asymmetries, still suggestive of Turing's ideas.

The requirements for Turing instability are intuitively transparent: An activator induces the production of its own inhibitor, but the inhibitor diffuses more rapidly than the activator and confines the activator in space. This has the seemingly paradoxical consequence that the peak expression of both the activator and inhibitor are in the same place, rather than being opposed. Both modes of regulation are seen in the mouse embryo (*25*).

Because signaling pathways often involve secreted inhibitors, Turing phenomena are frequently posited. However, there are many confounding influences as exemplified by studies of digits and feather follicles in the skin (*26*–*28*). Reaction-diffusion systems can also account for the "community effect," articulated by John Gurdon, whereby a tissue forces the majority fate on cells within it (*29*–*31*).

In quantitative analogy to the surface tension–driven separation of oil and water, cells of different types can sort by differential adhesion (*32*). Chemotaxis can also contribute to pattern formation as in sporulation in *Dictyostelium*, and signaling pathways themselves can provide chemotactic signals (*33*).

Self-organization in embryonic stem cells

The disc shape of the human epiblast suggests the possibility of a two-dimensional (2D) model. Embryonic stem cells (ESCs) naturally supply the epiblast. The extraembryonic hypoblast and spatial confinement are modeled by micropatterns: Slides with arrays of disks where ECM proteins bind and control where cells adhere. The extraembryonic trophoblast is modeled by addition of BMP4 to the media to provide the morphogen trigger (*34*). As envisioned by Tam (*35*), the cells pattern with concentric rings of endoderm and mesoderm and a central disk of anterior epiblast (Figs. 2 and 3). The mesendoderm cells express the same markers and require the same signals (Wnt and Activin/Nodal induced downstream of BMP4) as does the mouse primitive streak, and the same secreted inhibitors are required to spatially confine the streak and shield the central epiblast from morphogens. Thus, a homogeneous layer of human ESCs (hESCs) can self-pattern on a scale of ~2000 cells, without contribution from extraembryonic lineages. Similarly, micropattern culture guides self-organization of ectodermal derivatives (*36*).

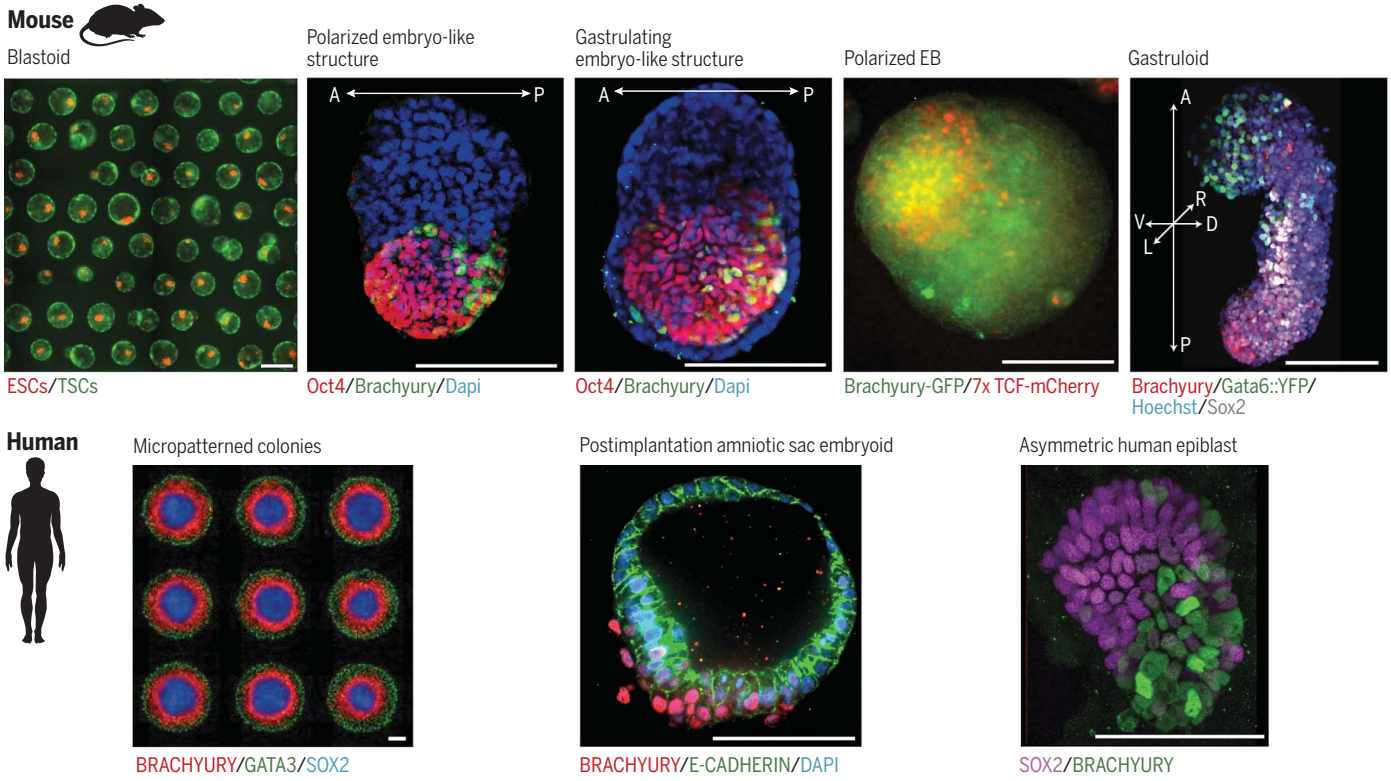


Fig. 2. Images of stem cell embryo models. Oct4 labels pluripotent epiblast cells; Brachyury marks mesoderm; Gata6 marks endoderm; Gata3 marks extraembryonic cells; Sox2 labels both ectoderm and pluripotent cells; 7xTCF-mCherry is a reporter of Wnt signaling activity; E-Cadherin labels cell-cell adhesion sites; and Dapi and Hoechst label nuclei. ESCs, embryonic stem cells; TSCs, trophoblast stem cells. Scale bars, 100 μm. These models are described in (*34*, *50*, *52*, *53*, *56*–*59*, *61*).

The micropattern system facilitates deciphering how cell fates are defined by distance from the colony boundary (*37*–*40*). hESCs are apicobasally polarized, and the BMP, Activin, and Nodal receptors are basolateral and not accessible to apical ligands except at the colony boundary. The secreted BMP inhibitor NOGGIN also restricts signaling to the colony boundary and is active from the apical side, suggesting complex signal transmission in polarized epithelia (*41*).

Receptor localization in the micropattern system, when folded into a cup-shape as in the mouse, helps explain why the proamniotic cavity (facing the apical side of the epiblast) does not short-circuit the proximal-distal patterning and why the initial BMP response is proximal only (*41*). This conjecture was confirmed by mistargeting the BMP receptors in the embryo (*42*).

Micropattern culture has been extended to the mouse (*43*). When mouse ESCs (mESCs) are differentiated to a postimplantation-like state (*44*) and transferred to micropatterns, they display properties similar to those of the pregastrulation epiblast. Differentiation with Wnt, Activin and BMP gives fates indicative of distal versus proximal streak derivatives.

Embryonic and extraembryonic stem cells have been shown to self-organize in 3D culture (*45*–*49*). When ESCs are cultured in a 3D gel supplemented with ECM, they form an apicalbasal polarized shell that eliminates the boundaries of micropattern culture, allowing control of substrate mechanics and chemistry. Human pluripotent cells cultured in such a system respond to BMP by polarizing and breaking symmetry into anterior epiblast and posterior primitive streak in a Wnt-dependent manner (*50*).

A synthesis of signals and mechanics can be achieved by placing hESCs on a 3D soft gel and doping the media above with a low concentration of ECM components (*51*, *52*). This treatment induces the patches to fold into closed polarized shells, which, depending on the initial cell density, can generate squamous, asymmetric, or columnar cysts. Squamous cysts represent an amnion-like tissue based on gene expression, cell shape, and BMP signaling activity (*51*), also active in the amnion of cynomolgous monkeys (*15*). Columnar cysts represent the epiblast, and asymmetric cysts undergo a symmetry-breaking event to form an amnion-like hemisphere and an epithelia-like disc (Figs. 2 and 3). The morphogenesis of the resulting amniotic sac plausibly requires BMP that induces Brachyury expression and EMT in the putative epiblast, but the mechanisms of symmetry breaking remain unknown. With the ability to define a gel surface in 3D, future studies will shed light on how morphology influences cell-cell signaling.

Embryoid bodies offer an alternative approach for eliciting the self-organizing potential of stem cells (*53*, *54*). When a clump of mESCs is given a pulse of Wnt agonist, it elongates into a tube showing markers for AP, DV, and LR axes (*55*, *56*) (Fig. 2). These so-called gastruloids recapitulate the spatiotemporal patterns of gene expression of embryos after gastrulation, such as homeobox (*HOX*) genes, in the correct temporal order and in nested telescoping domains (*57*).

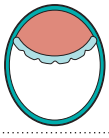
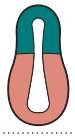
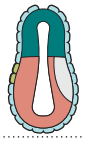
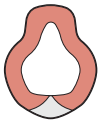
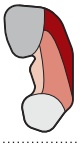
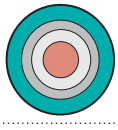
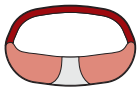
EMBRYO-LIKE STRUCTURE	STARTING COMPONENTS	SPECIES	EMBRYONIC STAGE	ADVANTAGES	DISADVANTAGES
Blastoid 	ESCs + TSCs	Mouse	Blastocyst	Self-assembly and self-organization between 2 cell types Morphogenesis + cell fate	Cellular interactions by chance (decreased efficiency) Limited developmental potential
Polarized embryo-like structure 	ESCs + TSCs	Mouse	Early post-implantation	Self-assembly and self-organization between 2 cell types Symmetry breaking in the absence of AVE	Cellular interactions by chance (decreased efficiency) Lack of EMT and gastrulation
Gastrulating embryo-like structure 	ESCs + TSCs + XEN cells	Mouse	Gastrulation	Self-assembly and self-organization between 3 cell types Morphogenesis + cell fate	Cellular interactions by chance (decreased efficiency) Limited epiblast patterning
Embryoid body 	ESCs	Mouse	Post-gastrulation	Self-organization of ESCs Symmetry breaking in the absence of exogenous cues	Limited patterning Lack of proper tissue organization
Gastruloid 	ESCs	Mouse	Post-gastrulation	Self-organization of ESCs Cell fate specification and tissue patterning	Limited morphogenesis Lack of proper tissue organization
Micropatterned colonies 	ESCs	Human	Post-gastrulation	Self-organization of ESCs Quantitative cell fate specification and tissue patterning	Limited morphogenesis 2D platform
PASE 	ESCs	Human	Gastrulation	Self-organization of ESCs Spontaneous amnion-epiblast fate split	Lack of precise control (decreased efficiency) Limited epiblast patterning
Asymmetric human epiblast 	ESCs	Human	Early post-implantation	Self-organization of ESCs Spontaneous symmetry breaking	Limited morphogenesis Lack of morphological in vivo equivalent

Fig. 3. Summary of stem cell models of the mouse and human embryo. For each model, the starting cell types, the corresponding embryonic stage, and the main advantages and disadvantages are shown. AVE, anterior visceral endoderm; EMT, epithelial-to-mesenchymal transition; PASE, postimplantation amniotic sac embryoid; ESCs, embryonic stem cells; TSCs, trophoblast stem cells; XEN cells, extraembryonic endoderm stem cells.

Self-organization of embryonic and extraembryonic stem cells

These ESC-only based models are informative in revealing how homogeneous populations of cells can give rise to different cellular fates through the process of self-organization. However, these models differ from those of natural embryos in their lack of extraembryonic tissues, which are critical for development and provide spatial context for signaling interactions. For this reason, new stem cell embryo models have been

developed that incorporate interactions of ESCs with extraembryonic cells (*58*–*61*) (Figs. 2 and 3).

Combining mESCs and trophoblast stem cells (TSCs) (Fig. 1) in ECM (*58*) to substitute for the basal membrane produced by the primitive endoderm leads to the generation of postimplantation embryo-like structures. In this model, cells polarize and form lumens in the ESC-derived embryonic and TSC-derived extraembryonic compartments that then join, in response to Nodal signaling (*58*, *60*). A domain of asymmetric Brachyury expression develops at the boundary between the ESC and TSC compartments. These polarized embryo-like structures induce mesoderm formation but do not proceed through gastrulation (Figs. 2 and 3). This event has been observed after substituting the ECM with the third stem cell type, extraembryonic endoderm (XEN) stem cells (Fig. 1), which provide the natural basement membrane (*59*, *60*). As a result, the formed structures look markedly similar to early postimplantation embryos in morphology, gene expression, and signaling communication. They break symmetry at the embryonic and extraembryonic boundary with the induction of AP patterning and EMT, leading to mesoderm and definitive endoderm formation (*59*). This self-organization occurs in response to BMP and Wnt signaling active during the cavity fusion process (*58*, *59*). Finally, the markers of primordial germ cells become expressed in a spatial-temporal manner characteristic of development. These structures induce decidualization upon their transfer to mouse foster mothers but do not develop further.

The self-assembly and subsequent self-organization into so-called gastrulating embryo-like structures are possible because the different stem cell types not only establish signaling among themselves but also provide the building blocks for spatial morphogenesis. The migration of ESCs to form the mesoderm layer, sandwiched between ESC-derived epiblast and XEN-derived visceral endoderm, and replacement of the XEN-layer with definitive endoderm are the hallmarks of early-to-mid gastrulation (*59*). This points to the essential requirement for the correct choreography of cells from embryonic and the two extraembryonic tissues to achieve correct form.

Will stem cell models ever pass the ultimate test of function, which is development following implantation? Combining mESCs and TSCs in a nonadherent platform leads to the generation of preimplantation embryo-like structures markedly similar to blastocysts, both in terms of shape, gene expression, and intercellular communication (*61*) (Fig. 2). These so-called blastoids can also induce decidualization, but then their development stops (Fig. 3). The derivation of extraembryonic stem cells that better match the expression signatures of real embryos should improve the morphology of these embryo-like structures (*62*, *63*). Similarly, the recent generation of expanded potential stem cells, which have the ability to form both embryonic and extraembryonic tissues, represents a promising tool for future research (*64*, *65*)

Conclusions and perspectives

Stem cell models of embryogenesis allow independent control of shape, mechanics, and means to juxtapose embryonic and extraembryonic tissues. Therefore, they represent powerful systems with which to address classic questions of embryology. For example, does gastrulation proceed in embryo-like structures of anomalous size, or does size have to be regulated first? Which combination of chemical and mechanical signals suffices to trigger primitive streak formation? To what extent can we induce gastrulation without AVE? Do the genetic barriers to chimerism operate through the same pathways as intraspecies cell competition? Stem cell systems will thus illuminate the genetic determinates of size and timing control.

Stem cell–derived embryos are models of development, and therefore they cannot fully recreate all the complexity of developing organisms. The field of stem cell embryology is in its infancy and will expand by tuning chemical and physical parameters, and using stem cell lines with broader developmental potential (*64*, *65*). Particularly interesting would be the combination of hESCs with human TSCs (*66*), and potentially human hypoblast stem cells, to recapitulate the human conceptus.

However, in devising these studies, it is important to consider when stem cell models of embryos acquire the protections attached to human embryos. Is a collection of cells that mimics gastrulation any more human than a brain organoid that might one day be endowed with sensory primordia (*67*)? It is clearly unethical to implant a stem cell–derived embryo into a human, yet many pregnancies fail or are impaired by placentation. Can stem cell models help to address this problem?

The promise for basic science is clear. Building embryos from stem cells, like the in vitro reconstitution of biochemical systems from purified components, is the test of whether we can understand the whole from the parts.

REFERENCES AND NOTES

1. M. N. Shahbazi, M. Zernicka-Goetz, *Nat. Cell Biol.* **20**, 878–887 (2018).
2. J. Rossant, P. P. L. Tam, *Cell Stem Cell* **20**, 18–28 (2017).
3. I. Bedzhov, S. J. Graham, C. Y. Leung, M. Zernicka-Goetz, *Philos. Trans. R. Soc. Lond. B Biol. Sci.* **369**, 20130538 (2014).
4. J. Rossant, P. P. Tam, *Development* **136**, 701–713 (2009).
5. K. Takaoka, H. Hamada, *Development* **139**, 3–14 (2012).
6. S. Nowotschin, A. K. Hadjantonakis, *Curr. Opin. Genet. Dev.* **20**, 420–427 (2010).
7. B. Feldman, W. Poueymirou, V. E. Papaioannou, T. M. DeChiara, M. Goldfarb, *Science* **267**, 246–249 (1995).
8. I. Bedzhov, M. Zernicka-Goetz, *Cell* **156**, 1032–1044 (2014).
9. S. Li, D. Edgar, R. Fässler, W. Wadsworth, P. D. Yurchenco, *Dev. Cell* **4**, 613–624 (2003).
10. N. Christodoulou *et al.*, *Nat. Cell Biol.* **20**, 1278–1289 (2018).
11. M. J. Stower, S. Srinivas, *Philos. Trans. R. Soc. Lond. B Biol. Sci.* **369**, 20130546 (2014).
12. T. A. Rodriguez, S. Srinivas, M. P. Clements, J. C. Smith, R. S. Beddington, *Development* **132**, 2513–2520 (2005).
13. P. P. Tam, R. R. Behringer, *Mech. Dev.* **68**, 3–25 (1997).
14. A. T. Hertig, J. Rock, E. C. Adams, *Am. J. Anat.* **98**, 435–493 (1956).
15. K. Sasaki *et al.*, *Dev. Cell* **39**, 169–185 (2016).
16. I. Hue, J. P. Renard, C. Viebahn, *Dev. Genes Evol.* **211**, 157–159 (2001).
17. J. E. Fléchon, J. Degrouard, B. Fléchon, *Genesis* **38**, 13–25 (2004).
18. M. N. Shahbazi *et al.*, *Nat. Cell Biol.* **18**, 700–708 (2016).
19. A. Deglincerti *et al.*, *Nature* **533**, 251–254 (2016).
20. Y. C. Hsu, *Nature* **239**, 200–202 (1972).
21. E. J. Jenkinson, I. B. Wilson, *Nature* **228**, 776–778 (1970).
22. I. Bedzhov *et al.*, *Cell Res.* **25**, 1368–1371 (2015).
23. R. Hiramatsu *et al.*, *Dev. Cell* **27**, 131–144 (2013).
24. H. Meinhardt, *Models of biological pattern formation: from elementary steps to the organization of embryonic axes*. (Academi Press, London, 1982).
25. G. Peng *et al.*, *Dev. Cell* **36**, 681–697 (2016).
26. T. W. Hiscock, P. Tschopp, C. J. Tabin, *Dev. Cell* **41**, 459–465 (2017).
27. A. E. Shyer *et al.*, *Science* **357**, 811–815 (2017).
28. J. Raspopovic, L. Marcon, L. Russo, J. Sharpe, *Science* **345**, 566–570 (2014).
29. J. B. Gurdon, *Nature* **336**, 772–774 (1988).
30. H. Bolouri, E. H. Davidson, *Dev. Biol.* **340**, 170–178 (2010).
31. A. Nemashkalo, A. Ruzo, I. Heemskerk, A. Warmflash, *Development* **144**, 3042–3053 (2017).
32. L. Canty, E. Zarour, L. Kashkooli, P. François, F. Fagotto, *Nat. Commun.* **8**, 157 (2017).
33. C. Kimura-Yoshida *et al.*, *Dev. Cell* **9**, 639–650 (2005).
34. A. Warmflash, B. Sorre, F. Etoc, E. D. Siggia, A. H. Brivanlou, *Nat. Methods* **11**, 847–854 (2014).
35. R. R. Behringer, M. Wakamiya, T. E. Tsang, P. P. Tam, *Genesis* **28**, 23–30 (2000).
36. G. Britton, I. Heemskerk, R. Hodge, A. A. Qutub, A. Warmflash, *bioRxiv* 518803 [Preprint] (2019); .
37. A. Yoney *et al.*, *eLife* **7**, e38279 (2018).
38. I. Heemskerk *et al.*, *eLife* **8**, e40526 (2019).
39. J. Massey *et al.*, *Proc. Natl. Acad. Sci. U.S.A.* **116**, 4989–4998 (2019).
40. I. Martyn, A. H. Brivanlou, E. D. Siggia, *Development* **146**, dev172791 (2019).
41. F. Etoc *et al.*, *Dev. Cell* **39**, 302–315 (2016).
42. Z. Zhang, S. Z. Zwick, E. Loew, J. S. Grimley, S. Ramanathan, *bioRxiv* 491290 [Preprint] (2018); .
43. S. M. Morgani, J. J. Metzger, J. Nichols, E. D. Siggia, A. K. Hadjantonakis, *eLife* **7**, e32839 (2018).
44. K. Hayashi, H. Ohta, K. Kurimoto, S. Aramaki, M. Saitou, *Cell* **146**, 519–532 (2011).
45. M. N. Shahbazi *et al.*, *Nature* **552**, 239–243 (2017).
46. Y. C. Poh *et al.*, *Nat. Commun.* **5**, 4000 (2014).
47. M. Y. Turco *et al.*, *Nature* **564**, 263–267 (2018).
48. A. Ranga *et al.*, *Proc. Natl. Acad. Sci. U.S.A.* **113**, E6831–E6839 (2016).
49. S. Haider *et al.*, *Stem Cell Reports* **11**, 537–551 (2018).
50. M. Simunovic *et al.*, *bioRxiv* 330704 (2018); .
51. Y. Shao *et al.*, *Nat. Mater.* **16**, 419–425 (2017).
52. Y. Shao *et al.*, *Nat. Commun.* **8**, 208 (2017).
53. D. ten Berge *et al.*, *Cell Stem Cell* **3**, 508–518 (2008).
54. J. M. Brickman, P. Serup, *Wiley Interdiscip. Rev. Dev. Biol.* **6**, e259 (2017).
55. D. A. Turner *et al.*, *Development* **144**, 3894–3906 (2017).
56. S. C. van den Brink *et al.*, *Development* **141**, 4231–4242 (2014).
57. L. Beccari *et al.*, *Nature* **562**, 272–276 (2018).
58. S. E. Harrison, B. Sozen, N. Christodoulou, C. Kyprianou, M. Zernicka-Goetz, *Science* **356**, eaal1810 (2017).
59. B. Sozen *et al.*, *Nat. Cell Biol.* **20**, 978–989 (2018).
60. S. Zhang *et al.*, *Nat. Commun.* **10**, 496 (2019).
61. N. C. Rivron *et al.*, *Nature* **557**, 106–111 (2018).
62. E. J. Vrij *et al.*, *bioRxiv* (2019).
63. J. Frias-Aldeguer *et al.*, *bioRxiv* 510362 (2019); https://doi.org/10.1101/510362.
64. Y. Yang *et al.*, *Cell* **169**, 243–257.e25 (2017).
65. J. Yang *et al.*, *Nature* **550**, 393–397 (2017).
66. H. Okae *et al.*, *Cell Stem Cell* **22**, 50–63.e6 (2018).
67. N. Rivron *et al.*, *Nature* **564**, 183–185 (2018).

ACKNOWLEDGMENTS

We are grateful to N. Rivron, B. Sozen, D. Turner, A. Martinez-Arias, J. Fu, M. Simunovic, A. Yoney, R. Nusse, D. ten Berge, and W. Koole for providing images for Fig. 2. **Funding:** M.N.S received funding from an Early Career Leverhulme Trust fellowship and an Advanced EMBO fellowship. Work in the laboratory of M.Z-G. is funded by the Wellcome Trust (207415/Z/17/Z) and the European Research Council (ERC grant 669198). Work of E.D.S. is funded by NIH grant GM101653. **Author contributions:** M.N.S., E.D.S., and M.Z.-G. conceptualized, wrote, and edited the manuscript. **Competing interests:** E.D.S. is a cofounder of Rumi Scientific.

10.1126/science.aax0164

REVIEW

Cancer modeling meets human organoid technology

David Tuveson[1,2]* and Hans Clevers[3,4]*

Organoids are microscopic self-organizing, three-dimensional structures that are grown from stem cells in vitro. They recapitulate many structural and functional aspects of their in vivo counterpart organs. This versatile technology has led to the development of many novel human cancer models. It is now possible to create indefinitely expanding organoids starting from tumor tissue of individuals suffering from a range of carcinomas. Alternatively, CRISPR-based gene modification allows the engineering of organoid models of cancer through the introduction of any combination of cancer gene alterations to normal organoids. When combined with immune cells and fibroblasts, tumor organoids become models for the cancer microenvironment enabling immune-oncology applications. Emerging evidence indicates that organoids can be used to accurately predict drug responses in a personalized treatment setting. Here, we review the current state and future prospects of the rapidly evolving tumor organoid field.

Techniques for culturing functional human breast epithelium in three-dimensional (3D) matrices have been championed for more than 30 years by Mina Bissell (*1*, *2*). Additionally, around a decade ago, Sasai and colleagues pioneered pluripotent stem cell (PSC)–based technology to create organoids that mirror specific parts of the central nervous system (CNS) (*3*, *4*). Lancaster and colleagues modified this technology and provided particularly notable examples of "mini-brain" structures (*5*). Although PSCs can be used to model everything ranging from tissues to organismal development, adult stem cells (ASCs) can also be isolated to generate organoid models of the primary tissues in which they reside. Specific growth factor cocktails allow long-term expansion of ASC organoids by mimicking the organ stem cell niche, as first established for mouse (*6*) and human (*7*) intestine and airway epithelium (*8*) [reviewed in (*9*)]. The organoid structures generated from PSCs and ASCs reflect crucial tissue features in terms of overall architecture, the collection of differentiated cell types, and tissue-specific function. Organoids thus represent a model system that can be compared to traditional genetically engineered mouse models (GEMMs), cell lines, and patient-derived xenografts (PDXs) (Table 1).

Besides being used to examine normal development, organoids have also been used to study tumorigenesis. In most organoid studies in the cancer field, primary carcinoma samples have been generated under ASC-organoid conditions. However, CRISPR mutagenesis technology has been applied to PSC-based organoids to generate cancer-causing mutations, for example, to model human brain tumors (*10*). In addition, Fine and colleagues have explored PSC-derived mini-brains as an environment for growing patient-derived glioblastoma cells (*11*).

The combination of R-spondin-1 (a Wnt amplifier acting through Lgr5), epidermal growth factor (EGF), and the bone morphogenetic protein (BMP) inhibitor noggin in a serum-free 3D matrix (Matrigel) supports the seemingly indefinite expansion of $Lgr5^+$ mouse crypt stem cells as 3D intestinal epithelial structures (*6*). Human gut organoids require additional components: Wnt, the transforming growth factor–β (TGFβ) inhibitor A83-01, and the p38 inhibitor SB202190. This growth factor cocktail also supports the propagation of patient-derived tumor organoids representing colorectal cancers (CRCs) (*7*). Small modifications allowed expansion of other epithelial tissues, such as pancreas and prostate (*12*, *13*), and carcinomas derived thereof (*14*–*16*), enabling the creation of "living biobanks" (*17*, *18*), where organoid cultures representative of disease diversity in terms of pathological subtypes and mutated-gene frequencies can be stored and disseminated to other investigators.

Two approaches to determine drug sensitivity in patient-derived samples have been widely exploited, namely the short-term culture of tumor sections (*19*) and xenotransplantation of the tumor into immunodeficient mice (i.e., PDXs) (*20*). Short-term culture allows for rapid in vitro screening at a reasonably large scale but is constrained by the limited proliferative capacity of the cultures. Xenotransplantation allows for in vivo screening but is slow and resource-intensive. Tumor organoid technology may bridge these two approaches. Initial studies have demonstrated the feasibility of medium-throughput drug screening on patient-derived organoids (PDOs) (*16*, *17*). Confirmation of in vitro observations on PDOs can be obtained in the PDX setting, as tumor organoids are readily transplantable into immunodeficient mice (*14*, *16*).

R-spondin–based culture conditions to propagate various other human carcinomas are now established, for example, for hepatocellular carcinoma and cholangiocarcinoma (*21*) and gastric (*22*, *23*), breast (*24*), bladder (*25*, *26*), esophageal (*27*), ovarian (*28*, *29*), lung (*30*), and pediatric

[1]Cold Spring Harbor Laboratory, Cold Spring Harbor, NY 11724, USA. [2]Lustgarten Foundation Pancreatic Cancer Research Laboratory, Cold Spring Harbor, NY 11724, USA. [3]Oncode Institute and Hubrecht Institute, Royal Netherlands Academy of Arts and Sciences, 3584 Utrecht, Netherlands. [4]University Medical Centre Utrecht, 3584 Utrecht, Netherlands.
*Corresponding author. Email: dtuveson@cshl.edu (D.T.); h.clevers@hubrecht.eu (H.C.)

Table 1. Properties of cancer model systems.
GEMM, genetically engineered mouse model; MDO, murine-derived organoid; MDOX, murine-derived organoid transplantation; CLs, cell lines; PDX, patient-derived xenograft; iPS, inducible pluripotential stem cell; PDO, patient-derived organoid; PDOX, patient-derived organoid transplantation.

	GEMM	MDO	MDOX	CLs	PDX	iPS	PDO	PDOX
Wild-type cell culture	+	+	+	–	–	+	+	–
Preinvasive cancer models	+	+	+	–	–	+	+	+
Invasive cancer models	+	+	+	+	+	+	+	+
Metastatic cancer models	+	+	+	+	+	+	+	+
Cost	$$$$	$$	$$$	$	$$	$$	$$	$$$
Time	++++	+	++	+	++++	+++	++	+++
Success rate	high	med	med	med	med	low	med	med
Throughput therapies	low	med	low	high	low	high	med	low

+ denotes 1 month or less; ++, 1–2 months; +++, 1–6 months; ++++, oftentimes more than several months.

ILLUSTRATIONS: KELLIE HOLOSKI/*SCIENCE*

kidney (*31*) cancers. Organoid cultures have enabled several observations: (i) Interpatient variation is captured and maintained. (ii) Organoids can typically be derived from patient material with high efficiency and can be xenotransplanted. (iii) Tumor organoids can faithfully report the drug response of the corresponding patient. (iv) Drug sensitivities of PDOs can be recapitulated in PDX settings.

Creating tumor organoid biobanks

The large majority of samples analyzed by cancer consortiums, such as the International Cancer Genome Consortium and The Cancer Genome Atlas, represent surgical specimens of primary tumors, whereas metastases typically represent the lethal stage of cancer. Theoretically, PDOs allow expansion of small tumor samples, enabling the analysis of cancer at any stage. Indeed, several studies have reported that organoids can be established from needle biopsies taken from, for example, liver cancer (*32*), pancreatic cancer (*33*, *34*), or from liver metastases of CRC (*35*). Gao *et al.* (*16*) have demonstrated the feasibility of growing organoids from circulating tumor cells in a prostate cancer patient. Studies have also reported the generation of healthy organoids from cells in urine (*31*) and from bronchial lavage material (*30*). It remains to be established whether these approaches will allow the outgrowth of tumor organoids as well. Thus, PDO biobanks greatly expand the types of patient samples that can be propagated and studied in the laboratory.

Most biobanking studies have confirmed that PDOs reflect the characteristics of the primary tumor, at least at the level of bulk tumor DNA sequence (*35*). However, it is less clear whether intratumoral heterogeneity is captured in organoid cultures. Another unaddressed variable is the clonal drift of "bulk" organoids over prolonged culture times. At least for a few studied CRC and ovarian cancer PDOs, this clonal drift appears to be relatively small (*18*, *29*).

PDOs established from single cells obtained from CRCs and from adjacent normal crypts (*36*) have allowed molecular and functional analyses that are not possible at the single-cell level. Such analyses revealed that CRC cells exhibit extensive mutational diversification and carry several times more somatic mutations than normal stem cells. Most mutations result from de novo mutational processes. The diversification of DNA methylation and transcriptome states in each tumor is stable and follows the phylogenetic tree of DNA mutations in that tumor. However, anticancer drug responses are markedly different between even closely related cells of the same tumor, indicating that pharmacological heterogeneity likely reflects epigenetic changes that alter gene expression among single cells in a tumor.

Several initiatives aim to make well-characterized PDO biobanks available to academia and industry. In addition to the technical challenges of banking living material, the ethics and informed consent–issues surrounding such biobanks are complex (*37*). The nonprofit HUB (www.hub4organoids.eu) establishes, characterizes, and distributes organoid biobanks. The Human Cancer Models Initiative (HCMI, https://ocg.cancer.gov/programs/HCMI) is a collaborative international consortium generating tumor-derived culture models annotated with genomic and clinical data. HCMI aims to make the developed models and related data available as a community resource.

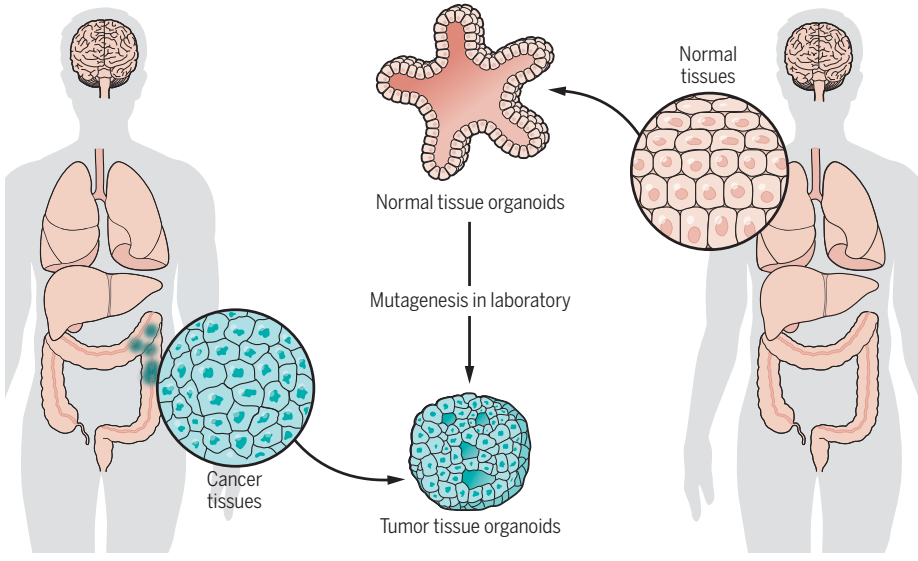


Fig. 1. Methods to generate a human cancer organoid biobank. A biobank of human cancer organoids can be generated directly from neoplastic tissues (left) or by genetic modification of organoids developed from normal tissues (right).

Organoids allow modeling of human carcinogenesis in a dish

Since Fearon and Vogelstein proposed the adenoma-to-carcinoma progression to be the result of an ordered series of specific oncogenic mutations, CRC has become the showcase example of cancer progression (*38*). Organoids can routinely be derived from normal human epithelia, allowing the in vitro mutational modeling of all stages of malignancy (Fig. 1). Sato and colleagues demonstrated the feasibility of growing various types of premalignant colon neoplasia in vitro. Whereas organoids at all stages were independent of Wnt/R-spondin because of activating Wnt pathway mutations, dependency on other niche growth factors was lost specifically at the adenoma-carcinoma transition (*18*). Two independent studies used CRISPR technology for the stepwise recreation of the adenoma-carcinoma progression starting from healthy, wild-type human colon organoids (*39*, *40*). CRCs carry recurrent mutations in members of the WNT, TGFβ, TP53, and phosphatidylinositol 3-kinase/mitogen-activated protein kinase (PI3K/MAPK) pathways. Organoids with mutated genes could be selected by removing individual growth factors: loss of the adenomatous polyposis coli (*APC*) gene led to Wnt/R-spondin independence; mutating *KRAS* led to EGF independence; mutating *SMAD4* led to noggin independence; and mutating TP53 led to nutlin-3 resistance. Quadruple mutants grow independently of all stem cell niche factors. Upon xenotransplantation into mice, quadruple mutants grow as invasive CRCs. A follow-up study demonstrated that these sequential oncogenic mutations facilitate efficient tumor growth, migration, and metastatic colonization, implying that the ability to metastasize is the direct consequence of the loss of dependency on specific niche signals (*41*).

> ***"...PDO biobanks greatly expand the types of patient samples that can be propagated and studied..."***

Meltzer and colleagues derived organoids from Barrett's esophagus patient biopsies (*42*). To document the role of APC in the malignant transformation of Barrett's esophagus, *APC* knock-out (APC^{KO}) organoids were created by CRISPR genome editing. APC^{KO} organoids displayed histologic atypia as well as higher proliferative and replicative activity, recapitulating the critical role of aberrant Wnt/β-catenin signaling activation in neoplastic transformation of Barrett's (*42*).

A more recent study used sequential CRISPR-mediated editing to create an organoid model for serrated CRC, a subtype associated with activating mutations in *BRAF*. After introduction of the activating mutation $Braf^{V600E}$ into normal colon organoids, inactivating mutations were introduced sequentially in *Tgfβr2*, the Wnt-inhibiting *Rnf43*, *Znrf3* ubiquitin ligases, and *P16/Ink4A*. Orthotopic transplantation of the compound mutant organoid lines, but not

ILLUSTRATION: KELLIE HOLOSKI/*SCIENCE*

Braf^{V600E} alone, generated adenocarcinoma with serrated features (*43*). In a similar approach, cancer progression was studied in wild-type human pancreas organoids by the sequential mutation of *KRAS* (K), *CDKN2A* (C), *TP53* (T), and/or *SMAD4* (S). Xenotransplantation into the subcutaneous space of immunodeficient mice showed that KC organoids failed to engraft, whereas KT organoids formed subcutaneous tumors resembling pancreatic intraepithelial neoplasia, yet only when co-transplanted with cancer-associated fibroblasts. KCTS organoids engrafted without cancer-associated fibroblasts (CAFs) and yielded pancreatic ductal adenocarcinomas (*15*).

Gut organoids can be subcloned after CRISPR modification, which allows the detailed study of cancer gene function. When key DNA repair genes are deleted by CRISPR and the resulting mutant organoid clones are subcloned after a period, specific mutational signatures appear that result from defective DNA repair. These signatures can be compared to known cancer-associated signatures. Indeed, mutation accumulation in organoids deficient in the mismatch repair gene *MLH1* correctly modeled mutation profiles of mismatch repair–deficient CRCs. Mutation of the cancer predisposition gene *NTHL1*, encoding a base excision repair protein, revealed a mutational signature previously observed in one breast cancer patient, who was then found to carry a germline *NTHL1* mutation (*44*). In another example, an activating *KRAS* mutation was introduced in a CRC organoid line that did not harbor Ras pathway mutations. Direct comparison of this isogenic pair of organoids revealed a marked effect of the *KRAS* mutation on drug response (*45*).

A major advance in mouse stem cell studies has been the creation of knock-in alleles of stem cell marker genes to allow the visualization, selective killing, and lineage tracing of the marker^{+} cells. Following similar strategies, Sato and colleagues have created Lgr5 knock-in alleles through CRISPR-driven modification in human colon cancer organoids, followed by xenotransplantation. Lineage-tracing experiments with a tamoxifen-inducible Cre knock-in allele also revealed the self-renewal and differentiation capacity of human LGR5^{+} cells in the xenografted CRC organoid–derived tumors. Selective ablation of LGR5^{+} tumor cells using an LGR5-iCaspase9 knock-in allele led to transient tumor regression. A KRT20 knock-in reporter marked differentiated cancer cells with only a limited life span and these cells reverted to LGR5^{+} self-renewing tumor cells upon LGR5^{+} CSC ablation, implying that human CRC growth is fueled by LGR5^{+} cancer stem cells as well as dedifferentiated tumor cells that can facultatively replace the cancer stem cells pool (*46*). De Sauvage and colleagues performed similar experiments using mouse organoids, and they specifically noted that Lgr5 cell ablation leads to primary tumor stasis whereas Lgr5^{+} cells were essential for liver metastasis (*47*).

Current ASC-based organoid technology does not support growth of normal CNS tissues, but PSC-derived cerebral organoids fill this gap. PSC-derived CNS organoids recapitulated brain tumorigenesis by introducing clinically relevant oncogenic mutations, helping to define the specific mutation combinations that result in glioblastoma-like tumors and primitive neuroectodermal tumor–like tumors. These transformed organoids were xenotransplantable and amenable to drug screening (*10*).

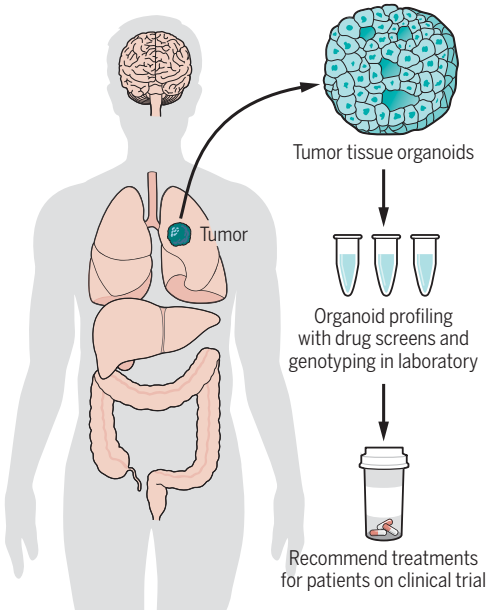


Fig. 2. Personalized medicine using human cancer organoids. Human cancer organoids can be used to rapidly determine drug sensitivities and molecular aberrations, and in clinical trials this information can be evaluated for its predictive potential.

Therefore, the combination of CRISPR and human organoid technology yields a versatile toolbox with which to build human cancer models in a stepwise fashion, generating isogenic sets of progressively more malignant organoids. In their design, they resemble GEMMs, and organoid engineering can expedite the generation of additional GEMMs as well as human cancer transplantation models.

Organoid cocultures identify tumor microenvironment characteristics and immune therapies

The tumor microenvironment (TME) modifies tumor progression and therapeutic response, yet it is challenging to characterize because it is challenging to maintain viably in tissue culture and manipulate ex vivo. Tumor organoid models generally lack an intact microenvironment. However, recent findings show that organoid cocultures with TME cells provide a new method to characterize some aspects of the TME. For example, the coculture of pancreatic stellate cells, a resident mesenchymal cell population, with pancreatic cancer PDOs produced the desmoplastic stroma typical of pancreatic carcinomas and directly led to the discovery of pancreatic CAF subtypes, including one that secreted interleukin-6 to support organoid proliferation (*48*). Additional investigations with PDO-CAF cocultures identified biochemical pathways responsible for the different CAF subtypes and thereby revealed methods to alter CAF composition in tumors (*49*). Nonetheless, these coculture systems are still being developed and a current unmet goal is to determine whether such PDO-CAF cocultures impart resistance to traditional and investigational drugs and whether they can be used to optimize therapeutic response ex vivo.

Immune cells are another common TME cell type, and PDO cocultures have shown early promise in evaluating this feature of human cancer. For example, a modification of traditional ASC organoid approaches introduced by Kuo and colleagues is to use air-liquid interface (ALI) cultures that include the typical Wnt-dependent media used in classical PDOs (*50*). Using such approaches, PDOs with immune and fibroblastic components can be propagated from primary tumor fragments for several weeks, and these ALI cultures display T cell clonal diversity that mirrors the T cell diversity in the patient's peripheral blood. ALI cultures have been applied to the analysis of immune checkpoint therapies in several human tumors that have variable clinical responses, including melanoma, lung cancer, and renal cell carcinoma, and these preliminary assessments have shown that a similar response rate occurs ex vivo (*50*). In addition, cocultures of PDOs generated from tumors with high mutational burden, such as microsatellite unstable CRC and tobacco-related non–small cell lung cancer, can be cultured with peripheral blood lymphocytes from that patient to generate CD8^{+} T cell clones that proliferate owing to the presence of putative neoantigens (*51*). In principle, such cocultures could be used to optimize the response of effector T cells against that patient's neoplastic cells or to generate a large number of effector T cells targeting the neoplastic cells for adoptive cell transplantation.

Organoid cultures for personalized medicine approaches

An important goal for organoid research is to determine whether they may represent, by analogy to infectious diseases, a "bacteriology test" for an individual's cancer, and the U.S. Blue Ribbon Panel for the Cancer Moonshot has proposed this as an objective (www.cancer.gov/research/key-initiatives/moonshot-cancer-initiative). To date, organoids derived from a variety of human tumors have shown a spectrum of responses to conventional and investigational drugs (Fig. 2). In limited cohorts of patients that were retrospectively analyzed, the response of PDOs to

ILLUSTRATION: KELLIE HOLOSKI/*SCIENCE*

therapies has largely mimicked the initial response of those patients to the same agents (*25*, *28*, *34*, *52*, *53*). These early studies have revealed multiple examples of exceptional responders to targeted drugs, where expected genetic alterations representing driver oncogenes or synthetic lethal pathways were logically matched to that therapy. The PDOs also provide models to develop drugs that circumvent innate or acquired resistance, and this has been shown to be particularly pertinent in the assessment of DNA repair pathways and replication fork stability in ovarian cancer PDOs (*28*). Importantly, the relative sensitivity of PDOs to cytotoxic drugs, which have a narrow therapeutic index in vivo compared with many targeted agents, may also reflect the clinical response of patients to those drugs (*34*, *52*, *53*).

Beyond the empiric potential of PDOs to help choose therapies for individual patients, large panels of PDOs representing one type of cancer have been used to develop biomarkers predictive of drug response for substantial numbers of patients. A recent study that used 66 pancreatic cancer PDOs compared standard cytotoxic drug responses to the gene expression of those PDOs and thereby derived a transcriptional signature of common responders to different chemotherapies (*34*). Although it is unknown whether the gene-expression signature reflects differences in drug pharmacology or drug response, when applied to an independent set of patient samples, this signature correctly identified a large group of patients with an improved response to that therapy (*34*).

To develop PDOs as a clinical test that can guide prospective cancer patient management, initial clinical studies should be designed that can measure the sensitivity and specificity of empiric PDO responses to a large number of the same patients treated with identical drugs. In parallel, other potential predictive biomarkers of therapeutic response, such as chemotherapy sensitivity gene expression signatures, can be assessed in a similar fashion. If the PDO empiric testing reflects patient responses in a large number of patients, PDOs should be further developed as a laboratory test and evaluated appropriately in a clinical trial. Currently, PDOs can be used to choose second-line or adjuvant therapies, because the time required to generate and test the PDO is on the order of 4 to 6 weeks. To shorten PDO development and drug testing to 1 week will require innovation but will also enable PDOs to be evaluated as a prospective test for cancer patients.

Current challenges in organoid research

Several challenges need to be addressed to improve organoid models, including the generation of cancer models that are currently not represented (for example, see Fig. 3), increasing the efficiency and decreasing the time for organoid outgrowth in current models, lowering the costs of organoid generation, and developing methods to perform high-throughput drug and immunotherapy screens (Table 1). Including TME elements besides immune cells and fibroblasts, for example, vascular and neural populations, will open additional research directions for organoid models. As these organoid models increase in sophistication, the genomic and epigenomic heterogeneity inherent in neoplastic cells will become important to consider as these are properties of cancer in humans that establish the behavior of the tumor and the response to therapies.

Outlook

By generating organoids and mimicking the TME, all phases of human cancer progression, including normal cells, preinvasive carcinomas, and invasive and metastatic cells, can be studied in the laboratory and stored in biobanks for worldwide dissemination. These cellular constructs can be interrogated for cancer biology and will undoubtedly continue to be a source of basic discoveries. For example, in certain early-stage human cancers, PDOs can be used to identify molecular aberrations that may serve as biomarkers and prevention targets. Additionally, PDOs are showing early promise in drug development, and clinical trials involving organoids should be designed to determine whether organoids are accurate mimics of a patient's cancer that may empirically predict their response to therapies. Organoids serve as a complement to other traditional cancer models, and the merits and deficits of each model system should be weighed when considering which one to use in cancer biology and medicine (Table 1). Organoid modeling is rapidly evolving, and although current challenges need to be addressed, the prospect that this approach will have a positive impact for basic cancer research and clinical advance is palpable.

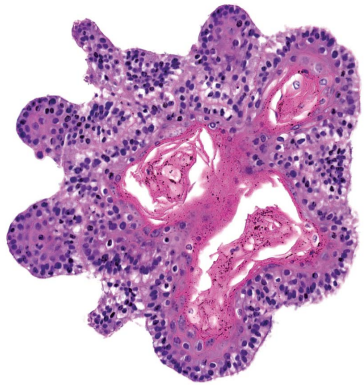


Fig. 3. An example of a new organoid model. Hematoxylin and eosin–stained section of an organoid grown from a squamous cell carcinoma of oral mucosa.

IMAGE: ELSE DRIEHUIS

REFERENCES AND NOTES

1. G. Y. Lee, P. A. Kenny, E. H. Lee, M. J. Bissell, *Nat. Methods* **4**, 359–365 (2007).
2. M. Simian, M. J. Bissell, *J. Cell Biol.* **216**, 31–40 (2017).
3. K. Muguruma, Y. Sasai, *Dev. Growth Differ.* **54**, 349–357 (2012).
4. M. Eiraku *et al.*, *Cell Stem Cell* **3**, 519–532 (2008).
5. M. A. Lancaster *et al.*, *Nature* **501**, 373–379 (2013).
6. T. Sato *et al.*, *Nature* **459**, 262–265 (2009).
7. T. Sato *et al.*, *Gastroenterology* **141**, 1762–1772 (2011).
8. J. R. Rock *et al.*, *Proc. Natl. Acad. Sci. U.S.A.* **106**, 12771–12775 (2009).
9. C. E. Barkauskas *et al.*, *Development* **144**, 986–997 (2017).
10. S. Bian *et al.*, *Nat. Methods* **15**, 631–639 (2018).
11. A. Linkous *et al.*, *Cell Rep.* **26**, 3203–3211.e5 (2019).
12. M. Huch *et al.*, *EMBO J.* **32**, 2708–2721 (2013).
13. W. R. Karthaus *et al.*, *Cell* **159**, 163–175 (2014).
14. S. F. Boj *et al.*, *Cell* **160**, 324–338 (2015).
15. T. Seino *et al.*, *Cell Stem Cell* **22**, 454–467.e6 (2018).
16. D. Gao *et al.*, *Cell* **159**, 176–187 (2014).
17. M. van de Wetering *et al.*, *Cell* **161**, 933–945 (2015).
18. M. Fujii *et al.*, *Cell Stem Cell* **18**, 827–838 (2016).
19. M. M. Centenera, G. V. Raj, K. E. Knudsen, W. D. Tilley, L. M. Butler, *Nat. Rev. Urol.* **10**, 483–487 (2013).
20. J. J. Tentler *et al.*, *Nat. Rev. Clin. Oncol.* **9**, 338–350 (2012).
21. L. Broutier *et al.*, *Nat. Med.* **23**, 1424–1435 (2017).
22. K. Nanki *et al.*, *Cell* **174**, 856–869.e17 (2018).
23. H. H. N. Yan *et al.*, *Cell Stem Cell* **23**, 882–897.e11 (2018).
24. N. Sachs *et al.*, *Cell* **172**, 373–386.e10 (2018).
25. S. H. Lee *et al.*, *Cell* **173**, 515–528.e17 (2018).
26. J. Mullenders *et al.*, *Proc. Natl. Acad. Sci. U.S.A.* **116**, 4567–4574 (2019).
27. X. Li *et al.*, *Nat. Commun.* **9**, 2983 (2018).
28. S. J. Hill *et al.*, *Cancer Discov.* **8**, 1404–1421 (2018).
29. O. Kopper *et al.*, *Nat. Med.* **25**, 838–849 (2019).
30. N. Sachs *et al.*, *EMBO J.* **38**, e100300 (2019).
31. F. Schutgens *et al.*, *Nat. Biotechnol.* **37**, 303–313 (2019).
32. S. Nuciforo *et al.*, *Cell Rep.* **24**, 1363–1376 (2018).
33. H. Tiriac *et al.*, *Gastrointest. Endosc.* **87**, 1474–1480 (2018).
34. H. Tiriac *et al.*, *Cancer Discov.* **8**, 1112–1129 (2018).
35. F. Weeber *et al.*, *Proc. Natl. Acad. Sci. U.S.A.* **112**, 13308–13311 (2015).
36. S. F. Roerink *et al.*, *Nature* **556**, 457–462 (2018).
37. A. L. Bredenoord, H. Clevers, J. A. Knoblich, *Science* **355**, eaaf9414 (2017).
38. E. R. Fearon, B. Vogelstein, *Cell* **61**, 759–767 (1990).
39. M. Matano *et al.*, *Nat. Med.* **21**, 256–262 (2015).
40. J. Drost *et al.*, *Nature* **521**, 43–47 (2015).
41. A. Fumagalli *et al.*, *Proc. Natl. Acad. Sci. U.S.A.* **114**, E2357–E2364 (2017).
42. X. Liu *et al.*, *Cancer Lett.* **436**, 109–118 (2018).
43. T. R. M. Lannagan *et al.*, *Gut* **68**, 684–692 (2019).
44. J. Drost *et al.*, *Science* **358**, 234–238 (2017).
45. C. S. Verissimo *et al.*, *eLife* **5**, e18489 (2016).
46. M. Shimokawa *et al.*, *Nature* **545**, 187–192 (2017).
47. F. de Sousa e Melo *et al.*, *Nature* **543**, 676–680 (2017).
48. D. Öhlund *et al.*, *J. Exp. Med.* **214**, 579–596 (2017).
49. G. Biffi *et al.*, *Cancer Discov.* **9**, 282–301 (2019).
50. J. T. Neal *et al.*, *Cell* **175**, 1972–1988.e16 (2018).
51. K. K. Dijkstra *et al.*, *Cell* **174**, 1586–1598.e12 (2018).
52. G. Vlachogiannis *et al.*, *Science* **359**, 920–926 (2018).
53. C. Pauli *et al.*, *Cancer Discov.* **7**, 462–477 (2017).

ACKNOWLEDGMENTS

We thank L. Baker for careful editing and assistance with manuscript production and M. Kheir Gouda and E. Driehuis for figure preparation. **Funding:** H.C. is supported by EU-ERC-670133 Organoid. This work was supported by the Lustgarten Foundation. D.T. is also supported by the Cold Spring Harbor Laboratory Association, the Cold Spring Harbor Laboratory and Northwell Health Affiliation, and the National Institutes of Health (NIH 5P30CA45508-29, 5P50CA101955-07, P20CA192996-03, 1U10CA180944-04, U01CA210240-01A1, 1R01CA188134-01, and 1R01CA190092-04). **Competing interests:** H.C. is inventor on several patents related to organoid technology. For full disclosure, see www.uu.nl/staff/JCClevers/. D.T. serves on the scientific advisory boards of Leap Therapeutics, Surface Oncology, and Bethyl Laboratories, which is not related to the subject matter of this manuscript. D.T. also serves on the board of scientific advisors for the NCI, the scientific advisory board of AACR, the scientific advisory council of Stand Up to Cancer, and the scientific advisory committee of the Georg-Speyer-Haus Institute for Tumor Biology and Experimental Therapy. D.T. is a distinguished scholar of the Lustgarten Foundation and director of the Lustgarten Foundation–designated Laboratory of Pancreatic Cancer Research.

10.1126/science.aaw6985

REVIEW

Organoids by design

Takanori Takebe[1,2,3,4]* and James M. Wells[1,3,5]*

Organoids are multicellular structures that can be derived from adult organs or pluripotent stem cells. Early versions of organoids range from simple epithelial structures to complex, disorganized tissues with large cellular diversity. The current challenge is to engineer cellular complexity into organoids in a controlled manner that results in organized assembly and acquisition of tissue function. These efforts have relied on studies of organ assembly during embryonic development and have resulted in the development of organoids with multilayer tissue complexity and higher-order functions. We discuss how the next generation of organoids can be designed by means of an engineering-based narrative design to control patterning, assembly, morphogenesis, growth, and function.

Organoids are three-dimensional (3D) structures with multicellular complexity and some level of tissue structure and function. For decades, organoids were derived through the deconstruction of adult organs and grown as complex but poorly defined tissues in vitro (*1*). However, they are also generated from embryonic or adult stem cells. Because organoids are both highly tractable and expandable and can be genetically manipulated, they are well suited to study organ development and pathophysiology in vitro (*2*). Human organoids have facilitated studies of human birth defects, human-specific pathogens, and screening of experimental drugs for efficacy before testing in patients (*3*).

Efforts in adult stem cell research have focused on stem cell identification, isolation, expansion in culture using niche factors (*4*), and differentiation to specific fates. For the past decade, scientists have sought to harness and control the potential of stem cells to generate organoids with specific tissue-level or organ-level complexity. Unlike adult stem cells, embryonic or induced pluripotent stem cells (PSCs) can form all tissues of the body and will spontaneously differentiate in vivo into a disorganized mass of differentiated tissues called a teratoma (Fig. 1). By manipulating factors that control embryonic organogenesis, methods have been developed to guide the stepwise differentiation of PSCs into embryonic germ layer–restricted organoids, organ-specific organoids, and even specific cell types such as hepatocytes, neurons, and cardiomyocytes (Fig. 1).

A major goal of organoid research is to use in vitro–derived constructs to replace diseased or aging organs. However, cellular complexity, tissue geometry, growth, and function present challenges in moving toward clinical applications. In addition, methods must be developed to generate organoids in a controlled and stereotypic manner to reduce heterogeneity. Below, we explore how the processes of normal organogenesis have been used to improve efforts to generate organoids ("organoidgenesis") and how engineering-based approaches may help to overcome obstacles and lead to better control over organoid assembly, growth, shape, and function.

[1]Center for Stem Cell and Organoid Medicine (CuSTOM), Cincinnati Children's Hospital Medical Center, Cincinnati, OH 45229, USA. [2]Division of Gastroenterology, Hepatology and Nutrition, Cincinnati Children's Hospital Medical Center, Cincinnati, OH 45229, USA. [3]Division of Developmental Biology, Cincinnati Children's Hospital Medical Center, Cincinnati, OH 45229, USA. [4]Institute of Research, Tokyo Medical and Dental University (TMDU), 1-5-45 Yushima, Bunkyo-ku, Tokyo 113-8510, Japan. [5]Division of Endocrinology, Cincinnati Children's Hospital Medical Center, Cincinnati, OH 45229, USA.
***Corresponding author. Email: james.wells@cchmc.org (J.M.W.); takanori.takebe@cchmc.org (T.T.)**

Organogenesis-inspired principles to direct organoidgenesis

Organoidgenesis efforts have focused on principles learned from studies of organogenesis, the process by which organs form in the developing embryo. Organogenesis can be loosely subdivided into stages (Fig. 2) (*5*). The first is formation of the three embryonic germ layers during gastrulation: ectoderm, mesoderm, and endoderm. The second stage subdivides (patterns) the germ layers into regional subdomains along the anterior-posterior (A-P) and dorsal-ventral (D-V) axis. The third stage involves a series of morphogenetic processes that drive the formation of 3D organ primordia at precise locations along the A-P and D-V axes. Once organ primordia are established, each organ becomes vascularized and innervated by endothelial precursors and neural crest cells, respectively. Vascularization brings oxygen, nutrients, and circulating factors, as well as hematopoietic cells (including macrophages) that can participate in organ development and persist postnatally.

From the onset of gastrulation, within 4 to 5 days in mice and 20 to 30 days in humans, organ primordia contain most of the necessary cellular components that will contribute to the fully functional organ. Much of the remaining development involves reciprocal paracrine interactions between cells and systemic cues delivered by the circulation; these interactions drive tissue growth, morphogenesis, and differentiation. In many respects, these early stages of organ development can be considered "self-assembly," a process used to describe how organoids form through assembly of a population of tissue progenitors. Therefore, controlling these early stages of organogenesis has been essential in directing organoidgenesis.

Providing direction to chaotic differentiation

Early efforts to control the stochastic differentiation of PSCs focused on guiding their differentiation

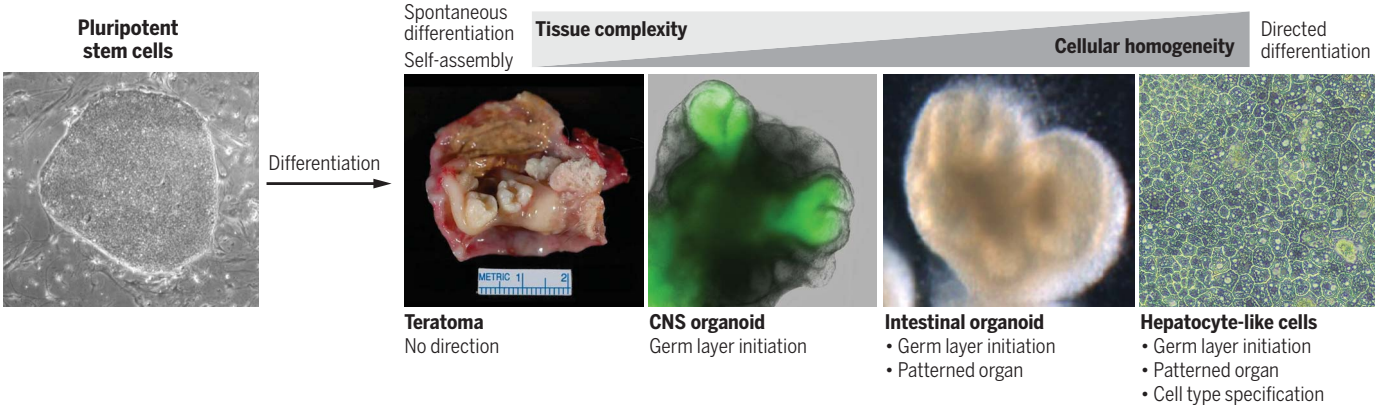


Fig. 1. Controlling the chaotic differentiation of pluripotent stem cells. Pluripotent stem cells (PSCs) stochastically differentiate in vivo into a disordered mix of tissues called teratomas [teratoma image by permission from Sanjay Mukhopadhyay, Cleveland Clinic]. PSC differentiation can be directed in a stepwise manner by controlling the initiation of germ layer formation [CNS organoid with an optic cup shown from (*29*) by permission from *Nature*, copyright 2011], organ patterning (intestinal organoids shown), and specification of individual cell types (hepatocytes shown).

into one of the three primary germ layers. The first example of this came from experiments with mouse and human PSCs that were differentiated into neural ectoderm aggregates that formed organoids containing a mix of forebrain derivatives such as cerebellum and optical tissues (*6*). Although ectoderm organoids start as symmetrical structures, uncontrolled symmetry-breaking events result in random pockets of differentiation, resulting in heterogeneous organoids containing a mix of diverse neural tissues. However, by manipulating signaling pathways to uniformly direct the regional pattern of organoids, PSCs can be directed to form specific organoid types representing the midbrain, hypothalamus, cerebellum, retina, cardiac, kidney, lung, esophagus, pancreas, liver, stomach (both fundus and antrum), small intestine, colon, etc. (*2*). Some of these first-generation organoid systems have remarkable cellular diversity. For example, intestinal organoids contain nearly all of the intestinal epithelial cell types, as well as intestinal mesenchyme that forms fibroblasts, smooth muscle fibers, and interstitial cells of Cajal.

Increasing organoid complexity

The next generation of organoidgenesis focused on incorporating critical cell types that are shared across organs, such as blood vessels, lymphatic vessels, nerves, stromal cells, and immune cells (Fig. 2). During organogenesis, many of these cell types arise in another region of the embryo and are delivered to the developing organ by migration or embryonic morphogenesis. In the case of organoidgenesis, vascular and neuronal cell types can be generated separately and introduced into forming organoids at a time that approximates their normal arrival during embryonic organogenesis. This approach was used to incorporate vascularity into brain and liver organoids (*7*, *8*), interneurons and microglia into brain organoids (*9*–*12*), and a functional enteric neuroglial plexus capable of controlling peristalsis in intestinal organoids (*13*).

A common feature of these studies is the remarkable ability of vascular and neuronal progenitor cells to incorporate into the developing organoid and self-organize into neural and vascular plexi. This supports the notion that stage-matched populations of progenitor cells that are placed together have the intrinsic ability to self-organize (*14*). As in the self-organization processes that occur during organogenesis in vivo, where different populations of progenitor cells communicate via paracrine factors to coordinate the formation of tissue structure, organoids form tissue structures when cells communicate and coordinate with each other in the microenvironment of the forming organoid.

Promoting organoid function and tissue maturity

Organoid systems have demonstrated a broad array of functionality, including muscle contractility, epithelial barrier function, neuronal activity, hepatocyte detoxification, gastric acid secretion, and secretion of insulin by beta cells. However, PSC-derived tissues tend to be more

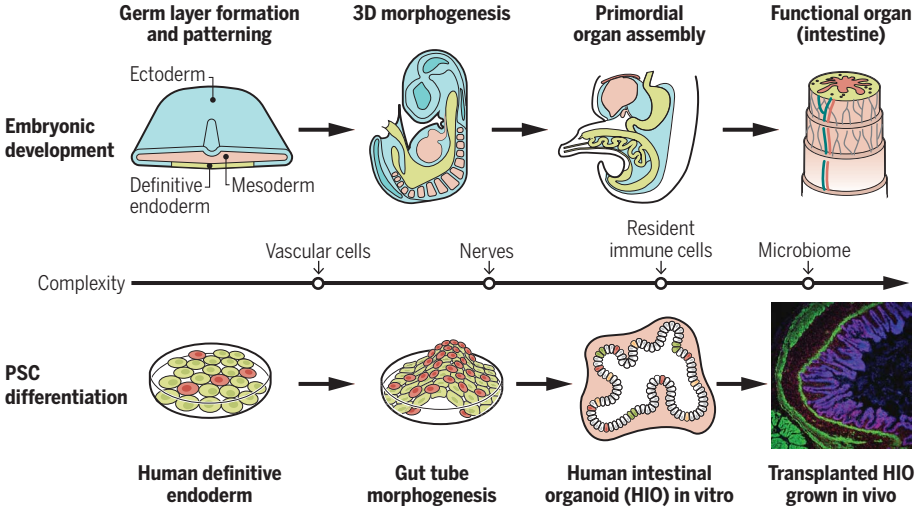


Fig. 2. Using principles of organogenesis to generate cellular complexity during organoidgenesis. The upper panel shows some of the main stages that drive assembly of organ primordia. The middle line indicates additional cell types that get incorporated into developing organs (vascular cells, nerves, immune cells) and how these cell types have been experimentally incorporated into developing organoids (lower panel). After transplantation, organoids can become vascularized by the host and continue to grow in size and undergo tissue morphogenesis.

fetal in nature and do not have the structure and full functionality of their adult counterparts. In humans, organs are able to support the life of premature infants born as early as 24 weeks of gestation (where full term = 40 weeks). Consistent with this, extending time in culture has improved maturation of brain, intestinal, and kidney organoids in the absence of any other manipulation (*15*–*17*). However, organoids in culture do not grow beyond a few millimeters in size because of limitations of passive diffusion of oxygen, nutrients, and the other humoral factors. This can be overcome by engrafting organoids onto a vascular bed in animals, where they become vascularized by the host and can continue to grow and mature (*8*, *13*, *18*, *19*). Human intestinal organoids continue to grow into centimeter-sized tissues with villi containing mature brush borders, circular and longitudinal muscle layers, and interstitial cells of Cajal. As an alternative to in vivo engraftment, engineered vascular systems could be designed to interface with organoids to promote their continued growth and function in vitro (*20*).

Tissue development, complexity, function, and maturity are interlinked. As organs develop and acquire early organ function, subsequent development processes can be triggered. For example, in the gut, the epithelium promotes smooth muscle differentiation; in turn, smooth muscle development and contraction can in turn promote epithelial villus formation (*21*). In the lungs, fetal breathing in the second and third trimester helps the maturation of human lung structure and function (*22*). Organoids can be used to investigate linkages among elapsed time, cellular complexity, and function, as well as the ways in which each may affect maturation. For example, intestinal organoids have been used to show that innervation, colonization by the microbiome, and mechanical stretch can improve tissue functions including intestinal barrier integrity and peristaltic contractions (*23*–*25*).

Organogenesis-inspired approaches have been a valuable driver of organoidgenesis. Organoid platforms can benefit from engineering design principles, synthetic biology (*25*), and systems biology to improve organoid function, maturation, reproducibility, scale-up, and integration into macrofluidic and microfluidic platforms (*26*).

Engineering principles to control organoidgenesis: Narrative engineering

"Stigmergy," a concept first introduced in insect biology to explain eusocial behaviors, is a form of indirect communication: a contextual, environmental, and interdependent coordination between individuals that is indirectly affected by their past actions (*27*). Dynamic multicellular self-organization in organoids requires the translation of such stigmergic elements (i.e., temporal and self-evolving biological events) into engineering-driven efforts that are not the common goal of the canonical tissue engineering concept (*28*). Sasai (*14*) elegantly translated this concept into biological systems of self-organization that tend to be strongly tied to history or memory, whereby the morphogenetic behavior of the group of cells is influenced not only by current conditions but also by preceding events. In other words, biological self-organization arises from progressive local interactions between cells of an initially disorganized system by environmental fluctuations, amplified by positive feedback. Thus, controlling biological history (or "narrative") in a biological system benefits from an integral design strategy that is founded on multiple evolving engineering-driven principles: tissue engineering, synthetic biology, biofabrication, biomaterials, manufacturing, and computational modeling, to name a few.

The new term narrative engineering applies to the interface between principles of biology and engineering for the controlled development of self-organizing systems (Box 1). Three general design strategies, modeled on how organs are assembled during embryonic development, have been adopted for the robust creation of organoid systems. These strategies comprise spatial, biological, and synthetic considerations (Fig. 3).

Space design

Homogeneous aggregate

Default shape and size information is a critical determinant to induce assembly (sorting) and pattern in self-developing systems. Indeed, the aggregation of homogeneous PSCs is most widely used to initiate tissue self-organization for derivation of eye cup (*29*), brain (*6*), and blood vessel (*30*) organoids. This self-organizing process is an aggregate size-sensitive phenomenon. For example, retinal cell differentiation occurs from a small aggregate of 300 mouse embryonic stem cells, and optic cups form from aggregates of 1000 to 2000 cells (*14*). Precise cell number dependence for asymmetric pattern emergence in part relates to a signaling threshold that will lead to local gradients via reaction-diffusion mechanisms and bistable signaling interaction (*14*). Therefore, aggregation size controls tissue patterning, which in turn alters subsequent self-organization programs.

Box 1. Narrative engineering.

A new field applies the interface principles of biology and engineering for the controlled development of self-organizing systems. Narrative engineering implements rationalized design to maximize the biological history (stigmergy) dependency that leads to the robust tissue self-organization of cell collectives in both time and space, including patterning, assembly, morphogenesis, and growth processes.

The following are key design considerations of narrative engineering:

1. Space design: Tissue designed as a spatial default for preparedness toward self-organization.

2. Biological environmental control: The selection of biology-inspired environmental modulators, which rationally recapitulate the full in vivo complexity of organogenesis, homeostasis, and regeneration.

3. Synthetic environmental control: The design of synthetic environmental modulators that are studied in multiple cutting-edge, engineer-driven disciplines: tissue engineering, synthetic biology, biofabrication, biomaterials, manufacturing, and computational modeling.

Note that these three elements are not necessarily independent but are interrelated processes during organoidgenesis.

Heterogeneous aggregate

Another major approach uses heterogeneous aggregates by coculturing multiple distinct progenitor types. A classical example is the sea sponge self-organization experiment, which uses a heterogeneous aggregate reconstituted from cells from dissociated embryos (*31*). At early embryonic stages of organogenesis, local intercellular interactions drive a self-assembly program of different regions of developing organs. Recent studies, for example, have cocultured endodermal cells with accessory cell types to reconstitute heterogeneous aggregates from multiple cell types including endothelial (*8*), neuronal (*13*), and mesenchymal cells (*32*). These aggregates self-assemble over time to develop, for instance, primitive vascular networks that augment post-transplant vascular perfusion and engraftment of organoids. Such heterogeneous progenitor interactions aid the integration of accessory structure into 3D organoids to achieve higher-order function.

Tissue boundary

Tissue-tissue interactions have been successfully modeled for the development of complex and interconnected tissues, particularly in the mixed culture of preformed 3D tissues. For example, teeth develop by conjugation of 3D reaggregates of oral ectoderm and tooth mesenchyme cultured in collagen gel to generate a tooth-germ structure, which can grow into a tooth after transplantation into the host (*33*). Recent experimental approaches have used two distinct stem cell–derived spheroids to model complex tissue-tissue interactions during early embryogenesis (*34*, *35*) and brain development (*11*, *12*). More precise spatial pre-patterning (Fig. 3) to introduce complex boundaries may benefit from evolving bioengineering approaches such as 3D bioprinting and scaffolding methods.

Biological environmental control

Design choice in 3D culture, such as the incorporation of soluble factors or extracellular matrix (ECM), can assist in recapitulating the mechanisms of organogenesis, homeostasis, and regeneration (Fig. 3).

Soluble factors

One of the first examples to incorporate soluble factors was in the derivation of intestinal organoids from adult stem cells [reviewed in (*36*)]. More recently, timely use of dosed soluble factors has been used to build complex patterning that occurs at the tissue boundary, for example, to model the interface of oral ectoderm and the overlying hypothalamic neuroectoderm to generate adenohypophysis tissues by hedgehog (*37*), or to balance ureteric epithelium and metanephric mesenchyme fates for kidney organoids by Wnt and fibroblast growth factor (FGF) (*17*). This provides a time- and dose-specific fluctuation of signaling pathways to trigger pattern formation that is subsequently stabilized by programmed intercellular interactions.

Extracellular matrix

The ECM has important signaling roles and is one of the most commonly manipulated parameters in tissue engineering (*1*). Matrigel-embedded cultures enabled the study of branching morphogenesis. In addition, a collagen I matrix was shown to change epithelial cell behavior, reducing the kinetics of cell polarization. Manipulating matrix composition is being leveraged to drive interconnected, fused intestinal organoid structure formation (*38*). Stiffness of the ECM, involving cell adhesion and contraction, is also an important modifier of biological properties. Larger (millimeter-scale) aggregates, termed condensates, can be stimulated by modulation of the mesenchyme-driven actomyosin pathway (*32*). Mesenchyme-driven condensation coupled with collagenous ECM has recently been used to design various tissue folding (*39*). Future advancements in spatiotemporal ECM manipulation, such as photodegradable or photoactivatable materials, are pivotal for engineering more complex context in vitro to achieve higher-order functions (*40*).

Synthetic environmental control

Historically, biologists have attempted to understand how mammalian organs can be cultured ex vivo. Organoid cultures based on such culture techniques include air-liquid interface, on-gel surface, gel-embedding, and roller ball cultures (*41*). These experimental systems feature the modulation of variables such as cell-intrinsic properties, perfusion, and mechanical properties (Fig. 3).

Cell-intrinsic properties

Recent synthetic biology–inspired processes such as chemical and genetic programming of tissue assembly represent powerful means to control symmetry breaking and facilitate programmed sorting (*40*). For example, hybridization of complementary DNA sequences coated on a cellular surface enabled the assembly of multicellular structures with defined cell-cell contacts (*42*). More recently, engineering cadherin-based adhesion in multicellular systems through the synthetic Notch system was shown to promote collective assembly from a random pattern (*43*). Thus, generation of pattern and shape can be triggered by a synthetic program.

Perfusion

Engineering approaches enable the precise control of the geometry input and output flow conditions, nutrient supply, and shear stress stimulation, as well as the local mechanical properties of the growing 3D tissues (*44*). Indeed, several fluidic culture systems containing a perfusible vascular system have been developed, one of which was proven to drive the maturation of PSC-derived kidney organoids (*45*). Designing vascularized systems to control in vitro growth, morphogenesis, and maturity of organoids will be an essential component of any narrative engineering approach.

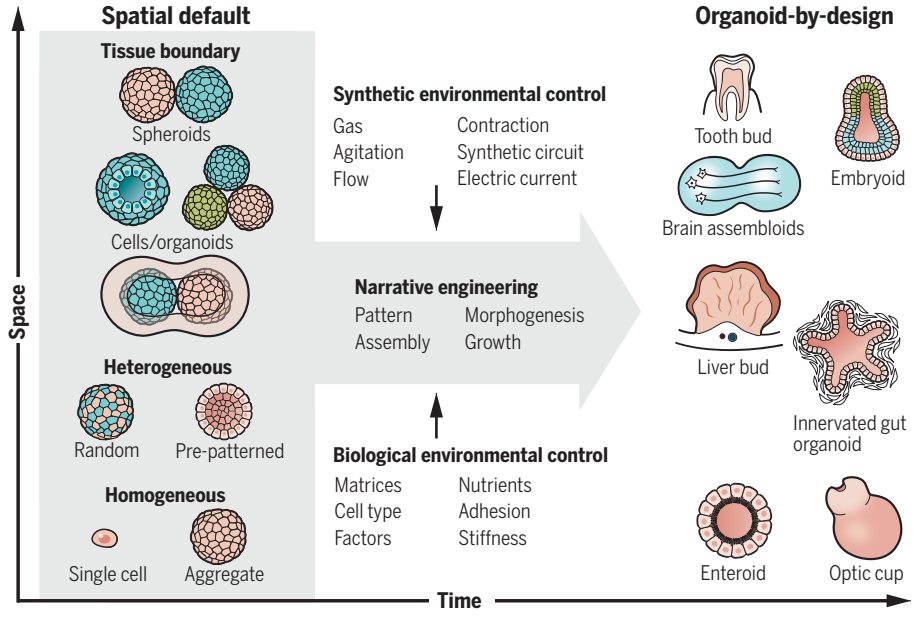


Fig. 3. Concept of narrative engineering. Starting from the initial default structures, the timed manipulation of environmental factors will facilitate complex and stereotyped organoid formation from stem cells. The right panel explains some examples of terminal products: Enteroids (gut epithelial organoids) or optic cup organoids develop from single or homogeneous stem cell aggregates, whereas vascularized liver bud or innervated gut organoids self-organize by coculturing heterogeneous progenitors. Recent examples of brain organoids and embryoids were self-assembled from the two distinct, preformed tissue aggregates. These self-organization processes are optimized by temporal modulation of biological and/or synthetic parameters.

Other mechanical and electrical stimuli

Mechanical forces (for example, fluid shear stress, contraction, hydrostatic pressure, and tissue distortion) can have a substantial impact on self-driven behaviors, including mechanochemical coupling and force sensing through the YAP/TAZ pathway (*46*), durotaxic collective migration (*47*), tissue-specific control of stiffness and mechanical anisotropy (*48*), and apoptosis-related force (*49*). Thus, mechanical force directs another signaling dimension in the regulation of tissue self-organization. Evolving organ-on-a-chip–based approaches, coupled with PSC tissue–based approaches, enable advanced mechanical modeling in organoids to stimulate maturation, for example, by mini-scale agitation in brain organoids (*50*), turbulence in megakaryocytes (*51*), and contraction in cardiac tissues (*52*). Cell behaviors can be electrochemically controlled using optogenetics, as in the control of neuronal activity in brain organoids (*7*, *8*). In biological self-organization, interaction rules of elements are not constant but generally evolve in time and space; therefore, timely strategic integration of engineering principles will complement the limitations of biological approaches to devise a superior, synergistic strategy to construct elaborate organoid architecture.

Conclusion

By applying the principles of organogenesis and narrative engineering, it should be possible to design organoids that are simple but highly defined, or highly complex and functional organoids. This approach acts as an interface between biology and engineering to drive robust, reliable, and effective organoidgenesis. New organoid systems can be designed to interrogate complex organogenesis that is otherwise inaccessible. For example, optic cup organoids coupled with 4D measurements, theoretical modeling, and experimental perturbation resolved a controversy associated with eye cup organogenesis (*29*). Emerging tools such as gene editing, single-cell analysis, optogenetics, chemogenetics, and superresolution/macroresolution imaging can be combined with in silico tools [e.g., agent-based (*53*) and force-based (*14*) modeling] to supervise better organoidgenesis using the three key design elements of narrative engineering. A more holistic approach may prove essential for improving the robustness of organoidgenesis to drive the growth and maturation that is required for better organ modeling and eventual transplantation-based therapies.

REFERENCES AND NOTES

1. M. Simian, M. J. Bissell, *J. Cell Biol.* **216**, 31–40 (2017).
2. H. A. McCauley, J. M. Wells, *Development* **144**, 958–962 (2017).
3. J. F. Dekkers *et al.*, *Sci. Transl. Med.* **8**, 344ra84 (2016).
4. J. M. Wells, F. M. Watt, *Nature* **557**, 322–328 (2018).
5. A. M. Zorn, J. M. Wells, *Annu. Rev. Cell Dev. Biol.* **25**, 221–251 (2009).
6. M. Eiraku *et al.*, *Cell Stem Cell* **3**, 519–532 (2008).
7. A. A. Mansour *et al.*, *Nat. Biotechnol.* **36**, 432–441 (2018).
8. T. Takebe *et al.*, *Nature* **499**, 481–484 (2013).
9. P. R. Ormel *et al.*, *Nat. Commun.* **9**, 4167 (2018).
10. C. M. Abreu *et al.*, *Front. Microbiol.* **9**, 2766 (2018).
11. Y. Xiang *et al.*, *Cell Stem Cell* **21**, 383–398.e7 (2017).
12. J. A. Bagley, D. Reumann, S. Bian, J. Lévi-Strauss, J. A. Knoblich, *Nat. Methods* **14**, 743–751 (2017).
13. M. J. Workman *et al.*, *Nat. Med.* **23**, 49–59 (2017).
14. Y. Sasai, *Nature* **493**, 318–326 (2013).
15. S. A. Sloan *et al.*, *Neuron* **95**, 779–790.e6 (2017).
16. J. R. Spence *et al.*, *Nature* **470**, 105–109 (2011).
17. M. Takasato *et al.*, *Nature* **526**, 564–568 (2015).
18. N. Daviaud, R. H. Friedel, H. Zou, *eNeuro* **5**, ENEURO.0219-18.2018 (2018).
19. C. L. Watson *et al.*, *Nat. Med.* **20**, 1310–1314 (2014).
20. K. Haase, R. D. Kamm, *Regen. Med.* **12**, 285–302 (2017).
21. K. D. Walton, D. Mishkind, M. R. Riddle, C. J. Tabin, D. L. Gumucio, *Wiley Interdiscip. Rev. Dev. Biol.* **7**, e317 (2018).
22. D. Warburton, *Neonatology* **111**, 398–401 (2017).
23. D. R. Hill *et al.*, *eLife* **6**, e29132 (2017).
24. H. M. Poling *et al.*, *Nat. Biomed. Eng.* **2**, 429–442 (2018).
25. T. Kitada, B. DiAndreth, B. Teague, R. Weiss, *Science* **359**, eaad1067 (2018).
26. S. E. Park, A. Georgescu, D. Huh, *Science* **364**, 960–965 (2019).
27. G. Theraulaz, E. Bonabeau, *Artif. Life* **5**, 97–116 (1999).
28. R. Langer, J. P. Vacanti, *Science* **260**, 920–926 (1993).
29. M. Eiraku *et al.*, *Nature* **472**, 51–56 (2011).
30. R. A. Wimmer *et al.*, *Nature* **565**, 505–510 (2019).
31. M. Takeichi, *Dev. Cell* **21**, 24–26 (2011).
32. T. Takebe *et al.*, *Cell Stem Cell* **16**, 556–565 (2015).
33. K. Nakao *et al.*, *Nat. Methods* **4**, 227–230 (2007).
34. S. E. Harrison, B. Sozen, N. Christodoulou, C. Kyprianou, M. Zernicka-Goetz, *Science* **356**, eaal1810 (2017).
35. N. C. Rivron *et al.*, *Nature* **557**, 106–111 (2018).
36. T. Sato, H. Clevers, *Science* **340**, 1190–1194 (2013).
37. H. Suga *et al.*, *Nature* **480**, 57–62 (2011).
38. N. Sachs, Y. Tsukamoto, P. Kujala, P. J. Peters, H. Clevers, *Development* **144**, 1107–1112 (2017).
39. A. J. Hughes *et al.*, *Dev. Cell* **44**, 165–178.e6 (2018).
40. L. M. Murrow, R. J. Weber, Z. J. Gartner, *Development* **144**, 998–1007 (2017).
41. E. R. Shamir, A. J. Ewald, *Nat. Rev. Mol. Cell Biol.* **15**, 647–664 (2014).
42. Z. J. Gartner, C. R. Bertozzi, *Proc. Natl. Acad. Sci. U.S.A.* **106**, 4606–4610 (2009).
43. S. Toda, L. R. Blauch, S. K. Y. Tang, L. Morsut, W. A. Lim, *Science* **361**, 156–162 (2018).
44. A. Sontheimer-Phelps, B. A. Hassell, D. E. Ingber, *Nat. Rev. Cancer* **19**, 65–81 (2019).
45. K. A. Homan *et al.*, *Nat. Methods* **16**, 255–262 (2019).
46. S. Dupont *et al.*, *Nature* **474**, 179–183 (2011).
47. R. Sunyer *et al.*, *Science* **353**, 1157–1161 (2016).
48. N. L. Nerurkar, C. Lee, L. Mahadevan, C. J. Tabin, *Nature* **565**, 480–484 (2019).
49. Y. Toyama, X. G. Peralta, A. R. Wells, D. P. Kiehart, G. S. Edwards, *Science* **321**, 1683–1686 (2008).
50. X. Qian *et al.*, *Cell* **165**, 1238–1254 (2016).
51. Y. Ito *et al.*, *Cell* **174**, 636–648.e18 (2018).
52. K. Ronaldson-Bouchard *et al.*, *Nature* **556**, 239–243 (2018).
53. H. Kaul, Y. Ventikos, *Brief. Bioinform.* **16**, 137–152 (2015).

ACKNOWLEDGMENTS

There are many excellent recent studies in organoid engineering that cannot be introduced because of space constraints. We apologize to those authors whose work we did not reference. **Funding:** Supported by NIH grants R01DK092456, U19 AI116491, P01 HD093363-01, and UG3 DK119982 (J.M.W.) and by NIH grant UG3 DK119982, PHS grant P30 DK078392 of the Digestive Disease Research Core Center in Cincinnati, the NY Stem Cell Foundation, JSPS, Takeda Science Foundation, and AMED grants JP18fk0210037h0001 and JP18bm0704025h0001 (T.T.). **Author contributions:** J.M.W. and T.T. jointly conceived of and wrote this review. **Competing interests:** J.M.W. is an inventor on the following patent/patent applications: 9,719,068, 10,174,289, 16/084,599, 15/515,840, PCT/US2018/054635, PCT/US2018/029083, and PCT/US2017/064600 that were held/submitted by Cincinnati Children's Hospital Medical Center and cover Organoid Based Technologies. T.T. serves on the scientific advisory board of Healios and granted licenses to Healios through Yokohama City University over their inventions that relate to the subject of this manuscript.

10.1126/science.aaw7567

REVIEW

Organoids-on-a-chip

Sunghee Estelle Park[1], Andrei Georgescu[1], Dongeun Huh[1,2,3]*

Recent studies have demonstrated an array of stem cell–derived, self-organizing miniature organs, termed organoids, that replicate the key structural and functional characteristics of their in vivo counterparts. As organoid technology opens up new frontiers of research in biomedicine, there is an emerging need for innovative engineering approaches for the production, control, and analysis of organoids and their microenvironment. In this Review, we explore organ-on-a-chip technology as a platform to fulfill this need and examine how this technology may be leveraged to address major technical challenges in organoid research. We also discuss emerging opportunities and future obstacles for the development and application of organoid-on-a-chip technology.

Decades of study in developmental biology and stem cell research have advanced our ability to recapitulate the key aspects of organogenesis in vitro. Recent years have seen considerable progress toward exploiting the self-organizing properties of pluripotent or adult stem cells to generate organotypic multicellular constructs known as organoids (*1*, *2*). Thanks to their ability to emulate microarchitecture and functional characteristics of native organs, organoids are emerging as a promising approach for the modeling of development, homeostasis, and disease of various human organs (*1*–*3*).

The conventional methods of forming organoids rely on three-dimensional (3D) culture of mammalian stem cells with sequential addition of growth factors. Although this approach has been widely used because of its simplicity, there is growing recognition that the current organoid culture techniques have the potential for substantial improvement. In particular, the random configuration of traditional 3D culture makes it difficult to precisely control organoids and their local environment. Existing culture systems also have limited capacity to reproduce the complex and dynamic microenvironment of a developing organ that provides instructive cues for organogenesis (*4*, *5*). The lack of these environmental signals poses challenges to achieving more complete, in vivo–like organoid development in a reproducible manner (*3*, *6*).

To address the limitations of conventional culture techniques, researchers in stem cell and developmental biology are forming alliances with engineers and physical scientists to develop advanced in vitro technologies for organoid research. At the forefront of this undertaking is the integration of organoids with organ-on-a-chip technology.

What are organs-on-a-chip?

Organs-on-a-chip can be broadly defined as microfabricated cell culture devices designed to model the functional units of human organs in vitro (*7*–*12*). In general, the construction of any organ-on-a-chip system is guided by design principles based on a reductionist analysis of its target organ (Fig. 1). The first step is to understand the anatomy of the target organ and reduce it to the basic elements essential for physiological function. These functional units are then examined to identify key features such as different cell types, structural organization, and organ-specific biochemical and physical microenvironments. For example, the alveolar–capillary unit of the lung consists of alveolar epithelial cells (cell type 1) and pulmonary microvascular endothelial cells (cell type 2) that are closely apposed to each other and separated by a thin interstitium (structural organization) (Fig. 1A). The epithelial and endothelial layers are subjected to air and blood flow, respectively, and the multilayered interface experiences breathing-induced cyclic mechanical stretch (organ-specific microenvironment).

Next, a cell culture device is designed to replicate the identified features. The device often contains multiple, individually addressable flow-through microchambers to grow multiple cell types while controlling the culture environment in a cell type–dependent manner. If necessary, additional components are incorporated that can be actuated mechanically, chemically, electromagnetically, or optically to emulate the biochemical and mechanical environment of the target organ. Finally, the designed device is produced using microfabrication techniques such as soft lithography (*13*).

The design strategy outlined here has been successfully implemented to create an organ-on-a-chip model of the alveolar–capillary unit of the lung (*14*). This system consists of two overlapping microchannels separated by a thin, flexible, microporous membrane (Fig. 1B, left). The compartmentalized design enables coculture of alveolar epithelial cells and lung microvascular endothelial cells on either side of the membrane while the cells are exposed to their respective tissue-specific environment (i.e., air on the alveolar side and fluid flow on the vascular side) (Fig. 1B, right). To mimic the deformation of the alveolar–capillary interface during breathing, the device is also equipped with two hollow microchambers alongside the culture channels, in which cyclic vacuum application induces stretching of the cell-lined intervening membrane (Fig. 1C).

By integrating living human cells with synthetically generated yet physiologically relevant microenvironments, organs-on-a-chip can mimic integrated organ-level functions necessary for physiological homeostasis, as well as complex disease processes (*15*, *16*). Furthermore, different organ-chip models can be fluidically linked to construct "body-on-a-chip" systems capable of simulating multiorgan interactions and physiological responses at the systemic level (*17*, *18*). Although these advanced model systems are still far from achieving the functionality of real human organs, their ability to capture key aspects of human physiology and pathophysiology makes them a promising approach for complementing and reducing animal studies for preclinical assessment of drugs, medical devices, and biomaterials (*7*, *9*, *19*). Organ-on-a-chip technology also provides an attractive in vitro platform for screening adverse health effects of chemicals, environmental materials, and consumer products (*10*, *20*).

What can organs-on-a-chip do for organoids?

The key to answering this question is to understand that organs-on-a-chip and organoids represent two fundamentally different yet complementary approaches toward the same goal of recapitulating the complexity of human organs in vitro. Organ-on-a-chip technology relies on our knowledge of human organs to engineer man-made constructs in which cells and their microenvironment are precisely controlled. In contrast, organoids follow intrinsic developmental programs and develop from self-organizing stem cells to reproduce the key structural and functional properties of their in vivo counterparts. Researchers are now exploring the possibility of synergistically combining the best features of each approach (*21*) to develop a more powerful in vitro technology. Here, we review recent studies inspired by this idea and examine how organ-on-a-chip technology can contribute to addressing major technical challenges in organoid research.

Challenge one: Microenvironmental control of organoids

A common strategy for constructing organoid models is to culture pluripotent or adult stem cells in a 3D environment. Although conventional 3D culture techniques provide a simple and effective means to produce organoids in a routine laboratory setting, their simplicity and ease of use often come at the expense of precise control. In this section, we elaborate on this problem and introduce emerging solutions provided by organ-on-a-chip technology.

Control of the biochemical microenvironment

Organoid development requires properly timed activation of morphogenetic signaling pathways to induce cell-fate specification and the physical

[1]Department of Bioengineering, University of Pennsylvania, Philadelphia, PA 19104, USA. [2]Institute for Regenerative Medicine, Perelman School of Medicine, University of Pennsylvania, Philadelphia, PA 19104, USA. [3]NSF Science and Technology Center for Engineering Mechanobiology, University of Pennsylvania, Philadelphia, PA 19104, USA.
*Corresponding author. Email: huhd@seas.upenn.edu

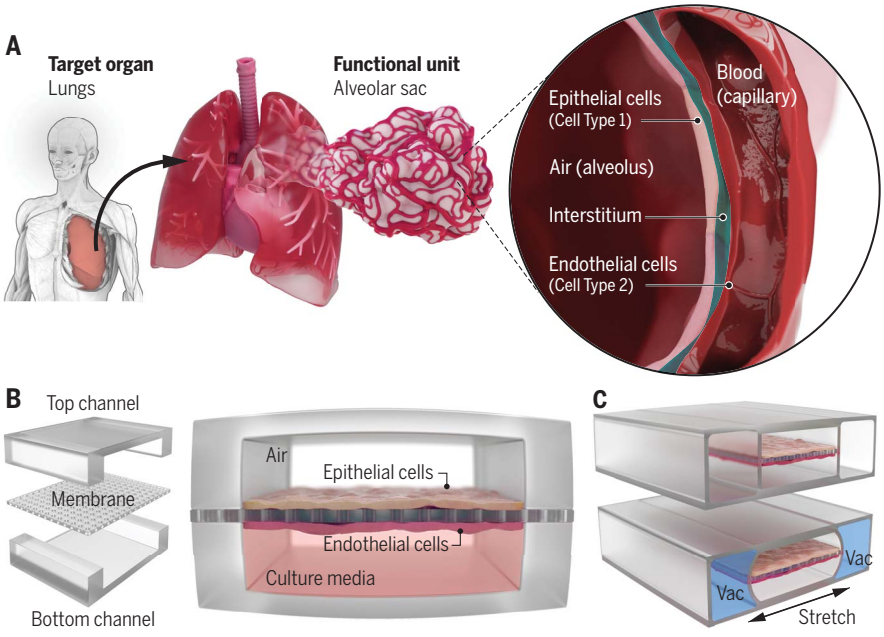


Fig. 1. Organ-on-a-chip design principles. (**A**) Reductionist analysis of a target organ (lung) identifies alveoli as the functional unit composed of epithelial and endothelial cells separated by a thin interstitium. (**B**) An analogous model is constructed from three layers to bring these two cell types into physiological proximity. (**C**) To mimic breathing-induced mechanical activity, the cells are cyclically stretched by applying vacuum (vac) to the side chambers. [Illustration: BIOLines Lab]

segregation of different cell types that together guide the process of self-organization (*22*). In conventional organoid culture, this is accomplished by applying exogenous morphogens at defined time points. During culture, diffusion of morphogens and cell-secreted soluble factors in organoids produces biochemical gradients in the local microenvironment of stem cells. These gradients, however, are not readily controllable owing to their spontaneous nature and often fail to simulate graded morphogen distributions critical for tissue patterning during organogenesis in vivo (*23*).

Researchers are beginning to harness the power of microengineering techniques to address this problem. A representative example can be found in a microfluidic system developed for in vitro modeling of neural tube development (*24*). This device contains a pair of microchannels that serve as the source and sink of soluble factors to generate stable morphogen gradients via diffusion across embryonic stem cell (ESC)–laden hydrogel constructs in a central culture chamber (Fig. 2A). The microengineered platform was used to mimic opposing gradients of sonic hedgehog (Shh) signaling molecules and bone morphogenetic protein (BMP) along the dorsoventral axis of neural tube, which induce neural tube patterning during spinal cord development. This study demonstrated spatially directed self-organization and differentiation of ESCs into motor neurons to generate in vivo–like tissue patterns. Microfluidic control of morphogen gradients also made it possible to examine the key determinants and temporal dynamics of Shh-induced ESC differentiation, revealing the existence of optimal morphogen concentrations for motor neuron differentiation. A similar method of generating gradients was employed in the development of a human brain organoid-on-a-chip to investigate adverse effects of nicotine on cortical development (*25*).

Recent studies have also demonstrated the combination of the source–sink approach with micropatterned culture scaffolds to generate physiological biochemical gradients in stem cell and organoid cultures. This strategy has been described in an intestine-on-a-chip system created by culturing self-renewing epithelial cells isolated from human enteroids on a microfabricated array of collagen pillars and microwells in a modified Transwell insert that mimicked the intestinal villi and crypts (Fig. 2B) (*26*). This device was used to recapitulate opposing gradients of Wnt and BMP signaling in the native biochemical niche of the intestinal epithelium. Notably, the morphogen gradients induced in vivo–like tissue compartmentalization in which stem cells and differentiated epithelial cells were confined to the crypts and the villi, respectively. This platform was modified in a separate study to model colonic crypts and reveal suppressed stem cell activity due to physiological gradients of proinflammatory cytokines and bacterial metabolites along the crypt–villus axis (*27*).

Control of nutrient supply

Organoids in 3D culture rely solely on passive diffusion to receive nutrients and oxygen and to remove waste products. As organoids grow larger, however, diffusive transport becomes insufficient to meet their increasing metabolic needs, eventually failing to support their growth and maturation (*28*). This problem in turn raises the question of how embryos in the body cope with the high metabolic demands of developing organs. Research in developmental biology has established that embryogenesis is tightly coupled with vascular development and that functional vasculature capable of delivering adequate blood supply is a requirement for later stages of organogenesis (*29*). On the basis of this observation, vascularization of organoids is emerging as a promising strategy to address the problem of limited nutrient supply and life span in traditional organoid models.

The ability of organs-on-a-chip to mimic perfusable blood vessels (*30*–*34*) may play an instrumental role in this effort, as illustrated by a tumor organoid-on-a-chip developed by Shirure *et al.* (*35*). The model was created in a microfluidic device consisting of three interconnected chambers that supported vasculogenic self-assembly of endothelial cells into a 3D network of perfusable blood vessels and their angiogenic growth toward organoid-like constructs derived from breast cancer patients (Fig. 2C). Although this process differs from blood vessel formation during embryogenesis, the microfluidic platform permitted vascularization of tumoroids and their perfusion under physiological flow conditions that recapitulated transport characteristics of the tumor microenvironment in vivo. The ability of this microdevice to support long-term culture was demonstrated by the maintenance of vascularized tumoroids for 22 days. By showing significantly reduced tumor growth after vascular perfusion with paclitaxel, this study also suggested the potential use of the model for preclinical screening of patient-specific responses to chemotherapy.

Although this study shows the feasibility of vascularizing and perfusing 3D multicellular constructs in microdevices, the same approach has not been demonstrated in the culture of pluripotent stem cell (PSC)–derived organoids. Vascularizing these types of organoids is potentially problematic, as specialized media required for stem cell differentiation may interfere with vascular self-assembly and remodeling. As an alternative strategy, it is possible to create miniaturized bioreactors that exploit forced convection and mixing of media to enhance nutrient supply for production and prolonged maintenance of organoids. This approach has been leveraged in brain and pancreatic organoid models (*36*–*38*).

Control of the biophysical microenvironment

A developing embryo experiences various types of mechanical forces, ranging from single-cell–generated traction forces to fluid shear stress and solid mechanical forces that arise from coordinated mechanical activity of large groups of cells (e.g., heart contraction, fetal breathing movement) (*39*). These forces act in concert with soluble morphogens and extracellular matrix (ECM) signals to regulate organ development and maturation

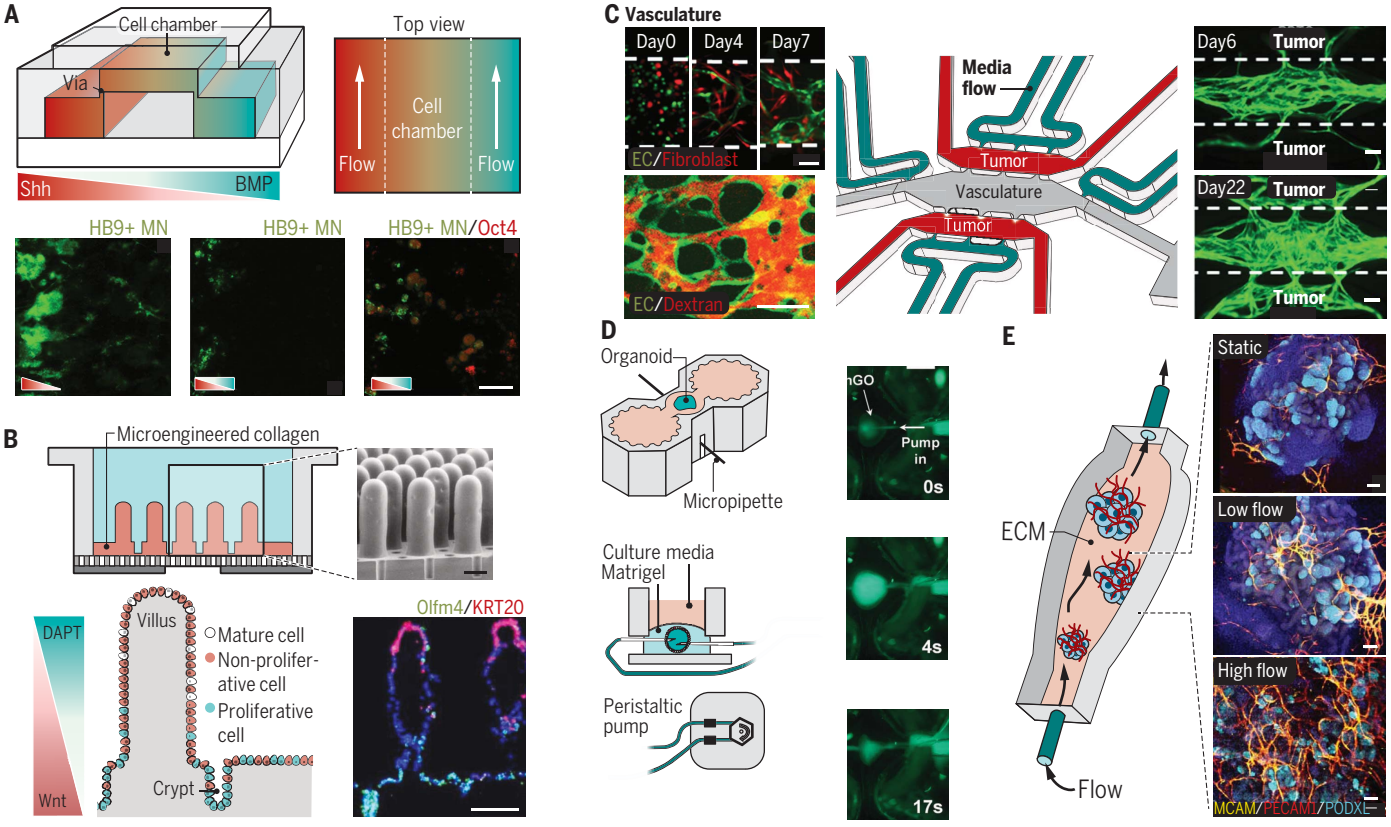


Fig. 2. Controlling the microenvironment of organoids-on-a-chip. (**A**) Physiological morphogen gradients are generated by diffusion between the source and sink microchannels. Purmorphamine (PM; an Shh agonist) gradients promote self-organization and differentiation of *HB9::GFP* transgenic reporter ESCs in the culture chamber into motor neurons (MN; green). Opposing gradients of PM and BMP induce spatial localization of motor neurons and pluripotent ESCs (Oct4; red). Scale bar, 200 μm. [Adapted from (*24*) with permission] (**B**) An intestine-on-a-chip can generate opposing gradients of Wnt and a γ-secretase inhibitor (DAPT) along the crypt–villus axis, which induces compartmentalization of proliferative (Olfm4) and nonproliferative (KRT20) cells. Scale bar, 100 μm. [Adapted from (*26*) with permission from Elsevier] (**C**) In a tumor organoid-on-a-chip, blood vessels are formed in the central chamber by coculturing endothelial cells (ECs) with fibroblasts in a hydrogel. Vascular perfusability is demonstrated by the flow of fluorescent dextran. The vessels in the central chamber grow into the tumor chambers to vascularize tumoroids. Scale bars, 100 μm. [Adapted from (*35*) with permission of Royal Society of Chemistry] (**D**) Luminal flow in the stomach is simulated in a stomach organoid-on-a-chip by cannulating human gastric organoids (hGO) in Matrigel to deliver fluid. The flow also induces cyclic deformation of the organoids, mimicking gastric motility. Scale bars, 2 mm. [Adapted from (*41*) with permission of Royal Society of Chemistry] (**E**) Kidney organoids are cultured under flow in a 3D printed device. Fluid shear stress enhances vascularization and maturation of kidney organoids, as demonstrated by increased vascular density and robust expression of vascular markers (PECAM1 and MCAM) and PODXL$^+$ cells. Scale bars, 100 μm. [Adapted from (*42*) with permission from Springer Nature]

(*40*). The lack of this biomechanical control is increasingly recognized as a limitation to developing fully mature organoids in culture and constructing physiologically relevant organoid models.

To address this problem, recent studies have demonstrated mechanically actuatable microengineered platforms that can generate and apply in vivo–like mechanical forces to organoids. For example, Lee *et al.* developed a stomach-on-a-chip model in which stomach organoids prepared from human PSCs were cultured in Matrigel and cannulated with a pair of micropipettes for fluidic access to the inner compartment (Fig. 2D) (*41*). With the use of a peristaltic pump connected to the pipettes, this platform generated fluid flow through the organoids to mimic luminal flow and rhythmic contraction of the stomach in vivo.

These types of mechanically active culture systems can also be used to generate physiological biomechanical cues that promote structural and functional maturation of developing organoids. The proof-of-concept of this approach was demonstrated by the recent report of human kidney organoids-on-a-chip, which were engineered in a 3D printed millimeter-scale chamber to examine the effect of fluid flow on vascularization and maturation of human PSC–derived kidney organoids (Fig. 2E) (*42*). During nephrogenesis, application of continuous flow resulted in the expansion of endothelial progenitors within the organoids and the formation of perfusable blood vessels in a shear stress–dependent manner. Notably, this response was accompanied by the production of more-mature tubular structures. Shear stress also induced prominent vascularization of glomerular compartments and increased formation and maturation of podocyte foot processes, revealing that flow-generated microenvironmental cues contribute to structural and functional development of kidney organoids in vitro. The beneficial effects of physiological fluid flow on the maturation of organoids have also been described in microengineered organoid models of the pancreas (*43*) and the intestine (*44*). These studies exemplify how organoids and organs-on-a-chip can be synergistically combined to achieve a level of cellular maturity not attainable when either technology is used alone.

Challenge two: Modeling tissue–tissue and multiorgan interactions

From a systems perspective, the complexity of the human body originates from dynamic interactions between its components within and across different levels of organization. The ability to emulate these interactions is essential for mimicking the integrated behavior of complex physiological systems in vitro. Organoids have the inherent ability to approximate the repertoire of cell types that

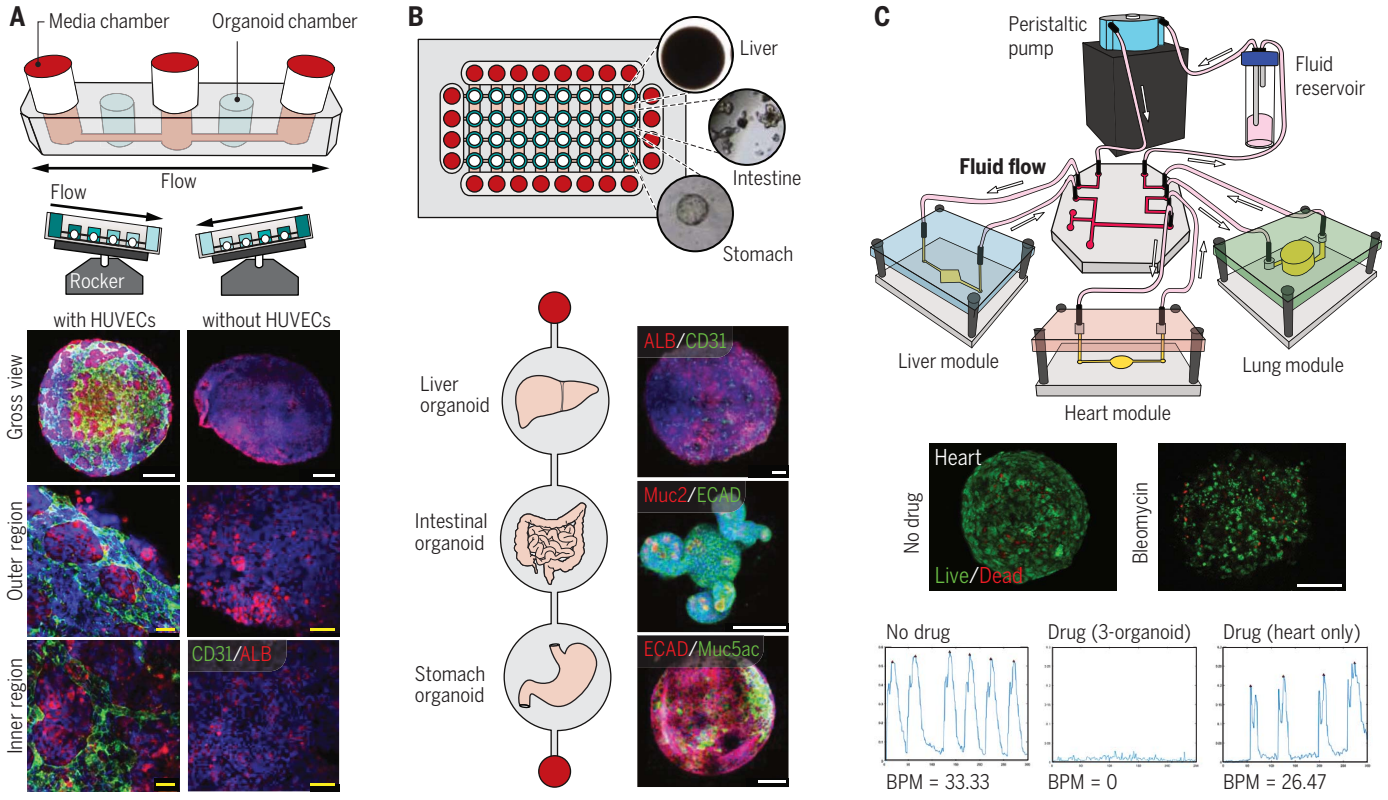


Fig. 3. Modeling tissue–tissue and organ–organ interactions in organoids-on-a-chip. (**A**) A vascularized liver organoid model is established in a rocker-actuated device containing serially connected media and culture chambers. Liver organoids grown with human umbilical vein endothelial cells (HUVECs) show increased albumin expression (ALB; red). Scale bars, 500 μm (white), 50 μm (yellow). [Adapted from (*45*) with permission from John Wiley and Sons] (**B**) A microfluidic array is used to demonstrate a multiorganoid model. Scale bars, 200 μm. [Adapted from (*45*) with permission from John Wiley and Sons] (**C**) A microengineered heart-lung-liver model is created by fluidically linking three culture modules for drug testing. Bleomycin treatment results in a loss of beating in heart organoids in the three-organ model (middle graph), but this response is absent in the heart-only model (right graph). Scale bar, 100 μm. BPM, beats per minute. [Adapted from (*46*) (CC BY 4.0)]

constitute the native organs and to recapitulate complex cellular cross-talk. Modeling biological interactions at higher levels of organization, however, remains a major challenge in current organoid models. This section will examine how organoid-on-a-chip technology may provide solutions to this problem.

Modeling tissue–tissue interactions

In virtually every organ, the interactions between different tissue types play a fundamental role in organ development, homeostasis, and disease. Efforts to advance organoid technology now aim to generate additional tissue types absent in traditional organoid cultures to more closely recapitulate the collection of specialized tissues in native organs and their dynamic interactions. This has been suggested as a promising approach to promote the maturation of organoids and improve their capacity to model complex physiological responses (*28*).

To this end, organs-on-a-chip provide a platform to engineer more-controllable and more-conducive environments for coculture of different cell and tissue types in organoid systems. Such capabilities have recently been demonstrated by a vascularized liver organoid-on-a-chip (*45*). In this work, a multicompartment microdevice was created to grow embryonic fibroblast-derived induced hepatic cells with human endothelial cells in an ECM hydrogel (Fig. 3A). The 3D constructs were also continuously perfused with media by using a laboratory rocker to mimic blood circulation in vivo. Coculture under this flow condition for 21 days produced vascularized liver organoids with robust staining for albumin, which was not observed in static culture. Notably, this study revealed that the interaction of hepatic tissues with the vasculature within the organoids increased the expression of hepatocyte-specific markers and improved hepatic functions. The enhanced maturity of coculture organoids also permitted more-sensitive detection of drug-induced liver toxicities.

Modeling multiorgan interactions

Efforts to establish a holistic understanding of human physiology have been challenged by the difficulty of modeling the human body as a system of interconnected and interdependent organs. Although organoids provide a powerful platform for modeling individual organs, their capabilities for recapitulating physiological interactions between different organs have yet to be investigated. Building upon advances in body-on-a-chip technology (*17*), researchers are beginning to microengineer in vitro platforms for coculture of different types of organoids to simulate multiorgan interactions.

Jin *et al.* developed a multiorgan model using a microfluidic array to coculture stem cell–derived liver, intestinal, and stomach organoids (Fig. 3B) (*45*). The organoids were maintained in different compartments but were allowed to communicate via rocker-induced media flow between culture chambers. The key demonstration of this study was to simulate bile acid homeostasis regulated by the interaction between the liver and the intestine in vivo. In response to exogenously applied bile acids, the model showed reduced expression of a bile acid synthesis enzyme (CYP7A1) in the liver organoids due to paracrine factors produced by the intestinal organoid, demonstrating the physiological interorgan cross-talk.

These types of multiorgan systems are believed to play an instrumental role in developing predictive preclinical models for biopharmaceutical applications. Skardal *et al.* explored this emerging opportunity in their microengineered heart-lung-liver model (*46*). This system was constructed

by combining 3D printed liver and heart organoids with microengineered lung tissues in a modular fashion and perfusing them with a common media in a closed loop (Fig. 3C). Notably, this model revealed previously unknown cardiotoxicity of a chemotherapeutic drug (bleomycin) due to the cytokine-mediated cross-talk between the lung and the heart tissues. Although further validation is necessary, this study illustrates the potential of microengineered multiorganoid systems as an advanced in vitro platform for preclinical drug screening.

Challenge three: Reducing variability

In contrast to the highly reproducible process of organogenesis in vivo, organoids develop with substantial variability in size, structural organization, functional capacity, and gene expression. This interorganoid variability has been identified as a major issue that limits the potential of organoid technology, especially for applications in disease modeling, drug screening, and transplantation (*6*, *28*). As discussed above, microengineered organoid systems can recapitulate the native niche of stem cells in developing embryos, providing a means to generate in vivo–like instructive cues and reproduce the tightly regulated programs of organogenesis to reduce stochasticity and variability. Recent advances in organ-on-a-chip technology also suggest other approaches to tackling this problem that rely on advanced instrumentation of microengineered culture devices.

Automated control of organoid culture

The precision and repeatability of mechanical automation provide an avenue to decrease the variability caused by inconsistent manual manipulation during tedious laboratory procedures such as organoid culture. The fragility, small size, and dynamic culture requirements of organoids, however, impose difficulties on our ability to directly leverage bulky laboratory instruments for automated culture. Microengineered systems are uniquely suited to address this problem by enabling precise and dynamic handling of fluids and tissues at the biological length scales of organoids while providing a platform amenable to automation.

For example, an entirely automated digital microfluidic platform demonstrated electrowetting-based control of hepatic organoids in a microdevice patterned with an array of electrodes (*47*) (Fig. 4A). By activating the electrodes in a defined sequence, this system allowed fluid droplets to move, merge, and split in a programmed manner. Using this platform, a study was conducted to demonstrate automated culture of organoid-like 3D hepatic constructs in media droplets and monitoring of their liver-specific function. The programmed actuation of the system also enabled the analysis of acetaminophen-induced hepatotoxicity without manual intervention. This type of integrated automation is key to achieving reproducibility in procedures that require precisely timed or continuous accurate manipulation over extended periods.

High-throughput manipulation and analysis of organoids

Another benefit of using microengineered systems for organoid culture is the opportunity to substantially increase the density at which organoids can be cultured and analyzed. This capability is potentially advantageous for reducing variability, as it offers the promise of enabling selection, manipulation, and screening of organoids in a high-throughput manner. A microfluidic platform created by Jin *et al.* provides an early demonstration of this approach (*48*). This system contained a high-density array of microfabricated pillars to immobilize many intestinal organoids and conduct optical measurement of their swelling as a result of osmotic changes and cholera toxin (Fig. 4B). Notably, the mechanical traps provided a means to physically screen out enteroids with improper size and capture the ones appropriate for analysis. Because the size of the trapping pillars is readily adjustable during microfabrication, this approach is tunable for size-based selection and also compatible with integration into more complex systems to enrich the homogeneity of organoid populations. Similar strategies have been demonstrated in microengineered culture of brain and liver organoids for drug testing applications (*49*, *50*).

Integration of biosensing

Efforts to address variability may be greatly facilitated by incorporating biosensing elements into culture platforms to permit continuous screening of organoids. A good example can be found in a multiorgan-on-a-chip device integrated with label-free biosensors for long-term monitoring of cardiac and liver organoids and primary hepatic spheroids (*51*). This system featured a universal electrochemical immunobiosensing platform capable of detecting up to eight different targets with high sensitivity and wide dynamic ranges (Fig. 4C). The multiplexed sensing capability was demonstrated by continuous and simultaneous triplet analysis of albumin, glutathione *S*-transferase α, and creatine kinase MB during drug treatment. Although the system was leveraged to measure drug-induced toxicities in this study, its capacity to perform continuous biosensing of secreted products from organoids would be highly valuable for screening-based

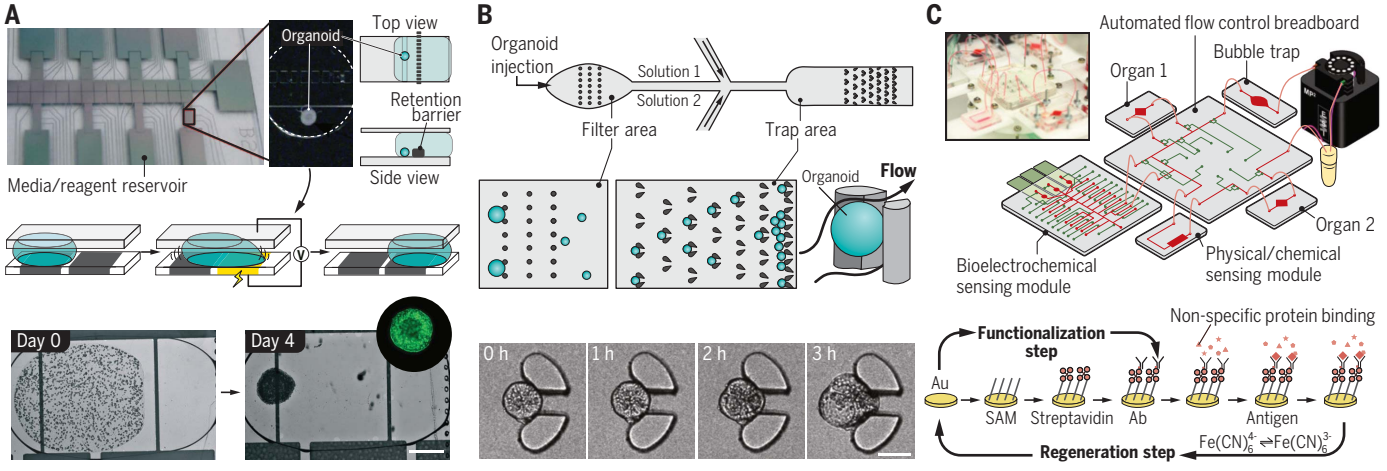


Fig. 4. Advanced organoid culture systems toward reduced variability. (**A**) In an electrowetting device, externally applied electric field renders the surface over the energized electrode (yellow) hydrophilic, inducing the motion of a liquid droplet toward the energized electrode. This principle is used to automate culture of liver organoids. Organoids grown in droplets are retained by microfabricated structures and undergo contraction over time. Scale bar, 100 μm. [Adapted from (*47*) with permission of Royal Society of Chemistry] (**B**) A microfluidic high-density pillar array allows for size-based filtering (upstream) and capturing of organoids (downstream) for analysis of swelling due to cholera toxin. Scale bar, 100 μm. [Adapted from (*48*) with permission of AIP Publishing] (**C**) A sensor-integrated multiorgan platform enables in situ monitoring of organoids. Gold microelectrodes act as immunobiosensors to detect specific antigens that use changes in interfacial electron-transfer kinetics of the probe, owing to their binding to surface-bound antibodies (Ab). SAM, self-assembled monolayer. [Adapted from (*51*)]

optimization of organoid culture conditions to minimize variability.

Outlook

Despite our best efforts, there is still a large gap between the current state-of-the-art of organoid technology and the reality of how organs develop and function in the body. Through the cross-fertilization of organoids with organs-on-a-chip, researchers are now seeking to fill this gap, with the ultimate goal of mirroring the complex inner workings of human organs in easily accessible and controllable model systems. Looking into the future of this very young field, we identify an array of opportunities.

Among the most promising applications of organoids-on-a-chip is drug discovery. Organoids or organs-on-a-chip alone have limited capacity to meet the broad range of needs that arise in the drug discovery process. The similarities of organoids to actual organs make them more attractive for target identification and validation early in the pipeline, whereas organs-on-a-chip as more-reproducible and more-controllable engineered constructs are better suited for efficacy and safety screening (*9*). By combining the strength of the two technologies, organoids-on-a-chip may serve as more versatile and predictive preclinical models that are broadly applicable to conventional and emerging drug discovery processes.

Organoids-on-a-chip may also play an instrumental role in creating patient- and population-specific disease models for personalized medicine. Microengineered devices provide a means to generate disease-specific culture environment that reconstitutes altered properties and biological interactions of diseased tissues (*7*, *8*, *10*, *15*). Such capabilities can be leveraged for maturation of patient-derived organoids to enhance the expression of in vivo–like disease phenotypes, which remains a major hurdle in the application of organoids for personalized medicine (*28*). Organoids-on-a-chip may also enable the development of personalized disease models using patient-derived tissue specimens as organoids. As evidenced by tumor organoids grown directly from patient biopsies, these types of organoids often display unpredictable growth patterns and substantial heterogeneity (*52*), which are difficult to handle using traditional in vitro techniques. The advantages of microengineered organoid systems may contribute to resolving some of these issues.

Regenerative medicine is another important area of opportunity. Based on the potential of organoids as unlimited source of tissue with regenerative capacity, studies have shown the feasibility of transplanting in vitro expanded organoids into animals to repair damaged organs (*53*). Clinical translation of this approach, however, remains a distant goal, owing to the low efficiency and safety concerns of transplantation (*28*). Organoids-on-a-chip may help address this problem by providing a platform for both high-content and high-throughput analysis to identify optimal conditions for in vitro expansion of organoids. Another exciting possibility is to engineer advanced anatomical and physiological features (e.g., vasculature, nerves) into organoids during in vitro expansion, with the goal of enhancing their engraftment and sustained function in vivo. Using microfabricated devices to produce such organoids on a clinically relevant scale is certainly a challenge, but with increasing efforts to develop high-throughput culture systems, this idea may open up a new frontier of regenerative medicine.

Although many opportunities lie ahead, organoids-on-a-chip as a nascent technology also face challenges. Typically, organoid-on-a-chip models are designed and constructed in a predetermined manner and thus have limited ability to recapitulate dynamic structural, environmental, and functional changes that occur during organogenesis. Addressing this limitation will require efforts to understand the spatiotemporal dynamics of organ development and to devise advanced engineering techniques to reproduce the evolution of developing organs in microengineered culture of organoids. The formation of organoids often requires hydrogels composed of Matrigel or similar basement membrane extracts that provide 3D structural support and enable proper morphogenesis (*54*, *55*). These materials, however, suffer from poorly defined compositions and batch-to-batch variability, which may be problematic for achieving a high degree of environmental controllability. Ongoing efforts to engineer new types of biomaterials with well-defined and tunable properties for organoid culture may hold the key to addressing this problem (*3*, *56*, *57*).

On a related note, the dominance of polydimethylsiloxane, which is known to absorb small molecules (*58*), in the fabrication of microdevices is a major concern for pharmaceutical applications. To tackle this issue, studies are under way to develop alternative materials and surface engineering techniques (*59*). For integrated multiorgan models, further investigations are needed to identify optimal culture conditions and media compositions for coculture of various cell types. Finally, three dimensionality and structural complexity of engineered organoid constructs will likely present distinctive challenges to imaging and analysis. As demonstrated by the recent report of brain organoids (*60*), this problem may be addressed by implementing device designs that enable precise positioning and confinement of organoids to make them more amenable for microscopic imaging. Tissue-clearing methods (*61*) and advanced 3D imaging techniques (*62*) may also be potential solutions.

The question of what organs-on-a-chip can do for organoids is shaping a new field of inquiry and a wave of innovation that will continue to evolve with inputs from a wide range of disciplines in science and engineering. Combining the strongest qualities of today's two most advanced in vitro technologies will require a vigorous exchange of ideas, perspectives, expertise, and resources between physical and biological sciences. With these efforts under way, the best of organoids is yet to come!

REFERENCES AND NOTES

1. H. Clevers, *Cell* **165**, 1586–1597 (2016).
2. M. A. Lancaster *et al.*, *Science* **345**, 1247125 (2014).
3. G. Rossi *et al.*, *Nat. Rev. Genet.* **19**, 671–687 (2018).
4. Y. Sasai, *Cell Stem Cell* **12**, 520–530 (2013).
5. H. A. McCauley *et al.*, *Development* **144**, 958–962 (2017).
6. X. Yin *et al.*, *Cell Stem Cell* **18**, 25–38 (2016).
7. D. Huh *et al.*, *Trends Cell Biol.* **21**, 745–754 (2011).
8. S. N. Bhatia *et al.*, *Nat. Biotechnol.* **32**, 760–772 (2014).
9. E. W. Esch *et al.*, *Nat. Rev. Drug Discov.* **14**, 248–260 (2015).
10. B. Zhang *et al.*, *Nat. Rev. Mater.* **3**, 257–278 (2018).
11. W. J. Polacheck *et al.*, *Lab Chip* **13**, 2252–2267 (2013).
12. K. Yum *et al.*, *Biotechnol. J.* **9**, 16–27 (2014).
13. G. M. Whitesides *et al.*, *Annu. Rev. Biomed. Eng.* **3**, 335–373 (2001).
14. D. Huh *et al.*, *Science* **328**, 1662–1668 (2010).
15. M. R. Ebrahimkhani *et al.*, *Drug Discov. Today* **19**, 754–762 (2014).
16. K. H. Benam *et al.*, *Annu. Rev. Pathol.* **10**, 195–262 (2015).
17. Y. I. Wang *et al.*, *Adv. Healthc. Mater.* **7**, 1701000 (2018).
18. J. H. Sung *et al.*, *Anal. Chem.* **91**, 330–351 (2019).
19. A. Polini *et al.*, *Expert Opin. Drug Discov.* **9**, 335–352 (2014).
20. S. Cho *et al.*, *Curr. Opin. Biotechnol.* **45**, 34–42 (2017).
21. T. Takebe *et al.*, *Cell Stem Cell* **21**, 297–300 (2017).
22. K. Kretzschmar *et al.*, *Dev. Cell* **38**, 590–600 (2016).
23. K. W. Rogers *et al.*, *Annu. Rev. Cell Dev. Biol.* **27**, 377–407 (2011).
24. C. J. Demers *et al.*, *Development* **143**, 1884–1892 (2016).
25. Y. Wang *et al.*, *Lab Chip* **18**, 851–860 (2018).
26. Y. Wang *et al.*, *Biomaterials* **128**, 44–55 (2017).
27. Y. Wang *et al.*, *Cell. Mol. Gastroenterol. Hepatol.* **5**, 113–130 (2017).
28. H. Clevers *et al.*, *Cell Stem Cell* **20**, 759–762 (2017).
29. B. M. Weinstein, *Dev. Dyn.* **215**, 2–11 (1999).
30. S. Kim *et al.*, *Lab Chip* **13**, 1489–1500 (2013).
31. A. Hasan *et al.*, *Biomed. Microdevices* **17**, 88 (2015).
32. D. B. Kolesky *et al.*, *Proc. Natl. Acad. Sci. U.S.A.* **113**, 3179–3184 (2016).
33. X. Wang *et al.*, *Lab Chip* **16**, 282–290 (2016).
34. M. B. Chen *et al.*, *Nat. Protoc.* **12**, 865–880 (2017).
35. V. S. Shirure *et al.*, *Lab Chip* **18**, 3687–3702 (2018).
36. S. H. Lee *et al.*, *Adv. Healthc. Mater.* **7**, 1701111 (2018).
37. E. Berger *et al.*, *Lab Chip* **18**, 3172–3183 (2018).
38. X. Qian *et al.*, *Cell* **165**, 1238–1254 (2016).
39. K. H. Vining *et al.*, *Nat. Rev. Mol. Cell Biol.* **18**, 728–742 (2017).
40. T. Mammoto *et al.*, *Development* **137**, 1407–1420 (2010).
41. K. K. Lee *et al.*, *Lab Chip* **18**, 3079–3085 (2018).
42. K. A. Homan *et al.*, *Nat. Methods* **16**, 255–262 (2019).
43. T. Tao *et al.*, *Lab Chip* **19**, 948–958 (2019).
44. M. J. Workman *et al.*, *Cell. Mol. Gastroenterol. Hepatol.* **5**, 669–677.e2 (2018).
45. Y. Jin *et al.*, *Adv. Funct. Mater.* **28**, 1801954 (2018).
46. A. Skardal *et al.*, *Sci. Rep.* **7**, 8837 (2017).
47. S. H. Au *et al.*, *Lab Chip* **14**, 3290–3299 (2014).
48. B. J. Jin *et al.*, *Biomicrofluidics* **8**, 024106 (2014).
49. Y. Zhu *et al.*, *Lab Chip* **17**, 2941–2950 (2017).
50. Y. Wang *et al.*, *Lab Chip* **18**, 3606–3616 (2018).
51. Y. S. Zhang *et al.*, *Proc. Natl. Acad. Sci. U.S.A.* **114**, E2293–E2302 (2017).
52. F. Weeber *et al.*, *Proc. Natl. Acad. Sci. U.S.A.* **112**, 13308–13311 (2015).
53. T. Nakamura *et al.*, *Cell. Mol. Gastroenterol. Hepatol.* **5**, 51–60 (2018).
54. M. A. Lancaster *et al.*, *Nature* **501**, 373–379 (2013).
55. M. A. Lancaster *et al.*, *Nat. Biotechnol.* **35**, 659–666 (2017).
56. Y. R. Lou *et al.*, *Biotechnol. Adv.* **36**, 132–149 (2018).
57. R. Cruz-Acuña *et al.*, *Matrix Biol.* **57-58**, 324–333 (2017).
58. E. Berthier *et al.*, *Lab Chip* **12**, 1224–1237 (2012).
59. K. Ren *et al.*, *Anal. Chem.* **82**, 5965–5971 (2010).
60. E. Karzbrun *et al.*, *Nat. Phys.* **14**, 515–522 (2018).
61. Y. Y. Chen *et al.*, *Proc. Natl. Acad. Sci. U.S.A.* **113**, 14915–14920 (2016).
62. R. Galland *et al.*, *Nat. Methods* **12**, 641–644 (2015).

ACKNOWLEDGMENTS

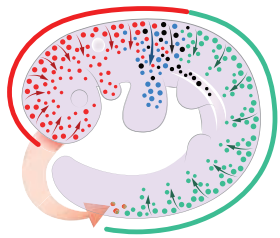
We thank G. Al, G. S. Worthen, and A. Paris for their input. **Funding:** This work was supported by the National Institutes of Health (NIH) (1DP2HL127720-01, 1UG3TR002198-01, and 1UC4DK104196-01), the National Science Foundation (CMMI:15-48571), the Paul G. Allen Family Foundation, the Alternatives Research and Development Foundation, and the University of Pennsylvania. D.H. is a recipient of the NIH Director's New Innovator Award and the Cancer Research Institute Technology Impact Award. **Competing interests:** D.H. holds equity in Emulate Inc. and consults for the company.

10.1126/science.aaw7894

RESEARCH

Fate choice in neural crest cells

Soldatov et al., *p. 971*



IN *SCIENCE* JOURNALS

Edited by **Stella Hurtley**



The mineralocorticoid receptor in the elephant shark (*Callorhinchus milii*) responds to progesterone.

STEROID HORMONES

An evolutionary change in ligand

Aldosterone binds to mammalian mineralocorticoid receptors to regulate electrolyte homeostasis. However, the mineralocorticoid receptor first arose in cartilaginous fish, which do not have aldosterone. Katsu *et al*. found that the mineralocorticoid receptor of the elephant shark, a cartilaginous fish found in the oldest group of jawed vertebrates, was activated by progesterone, which is an antagonist of the human mineralocorticoid receptor. These findings suggest that mineralocorticoid receptors may play an unappreciated role in reproductive physiology. —JFF

Sci. Signal. **12**, eaar2668 (2019).

PHYSICS

Something repulsive in the Casimir effect

Two uncharged objects (metal plates for instance) will experience an attractive force between them, the magnitude of which increases as they are brought closer together. This force, or Casimir effect, is caused by vacuum fluctuations of the electromagnetic field. Effectively, more modes outside than between the objects results in the objects being pushed together. Zhao *et al.* show that the extent of the electromagnetic fluctuations can be controlled by coating one of the objects with a dielectric (Teflon), which changes the Casimir effect to a repulsive force at small distances. This then cancels out the force between plates and produces a point of stable equilibrium. —ISO

Science, this issue p. 984

SUPERCONDUCTIVITY

Decoding the halo pattern

Magnetic fields can cause the formation of vortices in a superconductor. In cuprate superconductors, the vortex cores are surrounded by "halos," where the density of electronic states exhibits a checkerboard pattern. Edkins *et al.* used scanning tunneling spectroscopy to take a closer look into the halos. The results revealed that the patterns correspond to an exotic state called the pair density wave, in which the density of finite momentum Cooper pairs is spatially modulated. —JS

Science, this issue p. 976

RADIO ASTRONOMY

A radio ridge between two galaxy clusters

Galaxy clusters contain dozens or hundreds of galaxies, vast quantities of hot gas, and large amounts of dark matter. The gas can emit at radio wavelengths if it contains electrons at relativistic speeds, which can be injected by active galaxies or accelerated during a merger between two clusters. Govoni *et al.* used the Low-Frequency Array (LOFAR) radio telescope to observe a ridge of radio-emitting plasma extending between two galaxy clusters that are approaching a merger. The results imply that intergalactic magnetic fields connect the two clusters and challenge theories of particle acceleration in the intergalactic medium. —KTS

Science, this issue p. 981

PALEOBOTANY

Fossil Fagaceae from Patagonia

The oak family Fagaceae is thought to have its evolutionary origins in northern temperate forests and Southeast Asia. Wilf *et al.* now report 52-million-year-old fossils from the Southern Hemisphere

CREDITS: (PHOTO) MARINETHEMES.COM/KELVIN AITKIN; (GRAPHIC) SOLDATOV *ET AL.*

Published by AAAS

belonging to the still-living genus *Castanopsis*. Hypotheses of Fagaceae origins have focused only on the Northern Hemisphere. Ancestral *Castanopsis* may represent one of numerous paleo-Antarctic plant genera that are found with *Castanopsis* today in Southeast Asian rainforests. —AMS

Science, this issue p. 972

MALARIA

Targeting malaria transmission

To effectively block transmission of *Plasmodium falciparum*, vaccines must target appropriate antigens. To identify candidate antigens, Dantzler *et al.* studied immune responses from large cohorts of people who had been infected with *P. falciparum*. Multiple complementary assays revealed how antibodies recognize gametocytes, the sexual stage that allows transmission from human blood into mosquitoes. Interesting antigens were present in immature gametocytes, with a subset conserved among *P. falciparum* strains. Natural immunity to these antigens indicates that an appropriately designed vaccine could potentially interfere with malaria transmission. —LP

Sci. Transl. Med. **11**, eaav3963 (2019).

GLOBAL WARMING

Keep cool and carry on

The current trajectory of global warming is predicted to lead to an increase in global mean temperatures greater than preindustrial levels of 2.6° to 3.1°C by 2100. The Paris Agreement aims to keep that number below 2°C, with recent efforts pushing signatories to ratchet up those ambitions and stay below 1.5°C. Lo *et al.* assessed data on both climate and heat-related mortality from 15 major U.S. cities. They found that the current Paris Agreement limit should result in substantial reductions in mortality in all of these cities except for Atlanta, with Philadelphia seeing the greatest drop in heat-related deaths at 3.1%. Achieving the more ambitious 1.5°C target would translate into an estimated reduction in annual deaths of between 110 and 2720 per city. —AC and KJP

Sci. Adv. 10.1126/sciadv.aau4373 (2019).

NEURODEVELOPMENT

Brain map of touch sensation

The brain's somatosensory cortex contains a topographical map that reflects touch sensation inputs. During embryonic development, axons from the midbrain thalamus build columnar connections to the cortex in the absence of sensory input. Working in mice, Antón-Bolaños *et al.* found that these thalamocortical connections are responsible for organizing the somatosensory cortex (see the Perspective by Tiriac and Feller). Organization of the map in the cortex depends on spontaneous calcium waves in the embryonic thalamus. Thus, the somatosensory map is sketched out before actual sensory input begins to refine the details. —PJH

Science, this issue p. 987; see also p. 933

NEUROSCIENCE

This is safe, you can eat it

Social transmission of food preference is a model for studying nonspatial memory. In mice, a signal that food is safe to eat is transmitted by its smell along with molecules in the breath of a conspecific. How the odor itself is encoded and assigned valence is poorly understood. Loureiro *et al.* found a monosynaptic pathway between two brain areas, the piriform cortex and the medial prefrontal cortex, that plays a central role in this process. This connection strengthens during social interaction, thereby allowing a mouse to provide a food safety message to its companion. —PRS

Science, this issue p. 991

IN OTHER JOURNALS

Edited by **Caroline Ash** *and* **Jesse Smith**



The toxic pollen of teasel flowers does not deter bumblebees from gathering nectar.

POLLINATION

Pollen trade wars

For bees, pollen is an important source of protein and fats and is thus a strong motivation for visiting flowers. For plants, pollen is essential, and they do not want it lost to reproduction by greedy or inefficient pollinators. To circumvent this conflict, some plants have developed toxic pollen to deter consumption by pollinators. Wang *et al.* discovered that the flowers of teasel (*Dipsacus* spp.) contain a distasteful saponin in their pollen. After visiting a flower, bumblebees typically groom their hairy bodies to harvest adhering pollen grains—but not after visiting teasel flowers. The reason why some bumblebees still avidly visit this plant is because the nectar reward is generous and not tainted by the bitter saponin. Meanwhile, as bumblebees circulate among the plants to gather nectar, the ungroomed teasel pollen grains sticking to their hair ensures efficient pollination. —CA

Curr. Biol. **29**, 1401 (2019).

HIV VACCINES

It's all about delivery

Human immunodeficiency virus (HIV) has proved to be a notoriously difficult virus to vaccinate against. Most immunization studies focus on altering components of the vaccine to improve immune responses. Cirelli *et al.* instead asked what would happen if they changed the delivery method rather than vaccine composition. Slow vaccine delivery—in small amounts over several days—was found to enhance HIV neutralizing antibodies when compared with standard methods where the vaccine is injected all at once. Rhesus monkeys developed more potent T follicular helper cell responses, and germinal center B cells showed improved

PHOTO: RM FLORAL/ALAMY STOCK PHOTO

Published by AAAS

DIET EVOLUTION

A carnivore in herbivore's clothing

It is widely known that pandas eat bamboo. The conundrum is that these members of the order Carnivora show herbivore traits in their jaw and teeth but carnivore traits in their gut and digestive enzymes. Nie *et al.* used niche models, tracking, and nutrient analysis to better characterize the details of the bamboo diet and its absorption, and they find that pandas' motley traits may not be incongruous after all. Although their diet is vegetarian, pandas prefer to eat bamboo at stages in the plant's growth when it has the highest protein content. The macronutrient energy ratios that pandas obtain from bamboo by being picky are similar to those obtained by hypercarnivores that secure more than 70% of their diet from animal sources. Herbivory works well in bamboo forests with abundant resources. —SNV

Curr. Biol. **29**, 1677 (2019).



For pandas, bamboo can be as nutritious as meat.

engagement to viral envelope antigens. Slow-release vaccination strategies may open new avenues to tackle currently intractable pathogens. —PNK

Cell **177**, 1153 (2019).

STEM CELLS

Hormones control adrenal stem cells

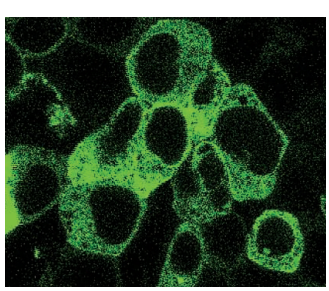
The adrenal cortex produces steroid hormones involved in stress responses. This part of the adrenal gland is sexually dimorphic. The cortex is larger in females, in whom it displays variable susceptibility to disease, including cancers. Grabek *et al.* examined the cellular basis of this sex bias. Females have much higher cell turnover, which means that the steroidogenic tissue is effectively replaced every 3 months. By contrast, male hormones suppress proliferation and stem cell recruitment. Females not only show increased proliferation but also recruitment of mesenchymal cells from the capsule. These responses depend on the hormonal environment rather than sex chromosomes. So, if androgens are removed, the stem cell compartment becomes activated, whereas adding androgens inhibits capsular stem cell activity. These sex-specific activities may be of relevance to disease susceptibility. —BAP

Cell Stem Cell 10.1016/j.stem.2019.04.012 (2019).

TARGETED DEGRADATION

Pathogen-sourced enzyme redirected

Cells of all types have the means to degrade specific proteins. These pathways can be hijacked by some bacteria to diminish host immune responses. The enzymes involved can in turn be used in the lab to modulate the proteome of eukaryotic cells. Ludwicki *et al.* attached a bacterial ubiquitin ligase to a protein that binds green fluorescent protein (GFP), thus redirecting it to add ubiquitin to GFP and GFP fusion proteins, which causes their degradation. The authors used polyamines and mRNA-binding proteins to stabilize and deliver mRNAs encoding an engineered ubiquitin ligase to cells. The mRNA nanoplexes enabled proteome editing both in vitro and in mice. —MAF



Confocal microscopy image of fluorescent protein targets expressed in HEK293T cells

ACS Cent. Sci. **5**, 852 (2019).

DIVERSITY

No more excuses for all-male panels

Biases, both implicit and explicit, impede the participation of women in STEM. Recent studies show that men are invited to speak on scientific panels at twice the rate that women are. McCullagh *et al.* describe the success of the "Request a Woman Scientist" database, part of the 500 Women Scientists organization, which works to build an inclusive scientific community. The database is composed of more than 7500 women from multiple disciplines and countries and provides anyone looking for scientific expertise with an extensive and multidisciplinary network of vetted women in science. To date, 11% of women scientists included in the database have been contacted to participate in media engagements, peer review, panel participation, educational outreach, and professional and research connections, further promoting the profile and participation of women in STEM. —MMc

PLOS Biol. **17**, e3000212 (2019).

ORGANIC CHEMISTRY

Outside help for a carbene catalyst

Metal catalysis is sometimes enhanced by secondary interactions with components that are not directly coordinated to the metal. Dhayalan *et al.* have explored this concept with metal-free organocatalysis. Specifically, they found that dynamically tethering a boronic acid to the periphery of an N-heterocyclic carbene catalyst raised enantioselectivity of a benzoin condensation. Furthermore, by applying a decision tree analysis correlating selectivity with parameters such as dipole moment and torsion angle, they efficiently optimized the boronic acid structure for gram-scale reactions. —JSY

Nat. Chem. **11**, 543 (2019).

PHOTOS: (TOP TO BOTTOM) STEVE BLOOM IMAGES/ALAMY STOCK PHOTO; M. B. LUDWICKI *ET AL.*, *ACS CENT. SCI.* **5**, 852 (2019)

Published by AAAS

ALSO IN *SCIENCE* JOURNALS

Edited by **Stella Hurtley**

HUMAN GENETICS

Somatic mosaicism in normal tissues

Somatic cells can accumulate mutations over the course of an individual's lifetime. This generates cells that differ genetically at specific loci within the genome. To explore how this genetic diversity in individuals contributes to disease, Yizhak *et al.* developed a method to detect mutations from RNA sequencing data (see the Perspective by Tomasetti). Applying this method to Cancer Genome Atlas samples and normal samples from the Genotype-Tissue Expression (GTEx) project generated a tissue-specific study of mutation accumulation. Somatic mutations were detected in nearly all individuals and across many normal human tissues in genomic regions called cancer hotspots and in genes that play a role in cancer. Interestingly, the skin, lung, and esophagus exhibited the most mutations, suggesting that the environment generates many human mutations. —LMZ

Science, this issue p. 970; see also p. 938

NEURODEVELOPMENT

Binary decisions refine fate decisions

Neural crest cells develop into tissues ranging from craniofacial bones to peripheral neurons. Combining single-cell RNA sequencing with spatial transcriptomics, Soldatov *et al.* analyzed how neural crest cells in mouse embryos decide among the various fates available to them (see the Perspective by Mayor). These multipotent cells become biased toward a given fate early on and step through a progression of binary decisions as their fate is refined. Competing fate programs coexist until increased synchronization favors one and repression disfavors the other. —PJH

Science, this issue p. 971; see also p. 937

ICE SHEETS

An uplifting effect

The rise in sea level that is occurring from the melting of Antarctica is only going to accelerate as climate warms. However, Larour *et al.* report that crustal uplift in the Amundsen Sea sector is helping to reduce grounding line retreat, thereby stabilizing the ice sheet and slowing its rate of mass loss (see the Perspective by Steig). This effect will not stop or reverse ice sheet loss, but it could delay the progress of dynamic mass loss of Thwaites Glacier by approximately 20 years. —HJS

Science, this issue p. 969; see also p. 936

MAGNETISM

A detailed look into 2D magnetism

The van der Waals material chromium triiodide (CrI_3) is a ferromagnet in the bulk but appears to become antiferromagnetic when thinned to a few atomic layers. Thiel *et al.* used a local magnetometry technique based on diamond nitrogen-vacancy centers to study the magnetism of these thin films at the nanoscale (see the Perspective by Fernández-Rossier). In agreement with previous results, films with odd numbers of layers had magnetization values consistent with that of a single layer, indicating antiferromagnetic coupling. But when the researchers' probe caused an accidental puncture, the magnetization of a nine-layer film increased approximately ninefold to a value expected in a ferromagnetic material. Further characterization suggested that the puncture had caused a structural transition, linking the structural and magnetic properties of this enigmatic system. —JS

Science, this issue p. 973; see also p. 935

CLIMATE

Why is methane rising?

Methane is a powerful greenhouse gas that is emitted through both natural and human-driven processes. In a Perspective, Mikaloff Fletcher and Schaefer highlight recent evidence for a rapid rise in the amount of methane emitted to Earth's atmosphere. This rise began in 2007 and accelerated in 2014. Isotope measurements suggest that the likely culprits include rising emissions from livestock and from burning fossil fuels. If the rise in methane continues, then even larger reductions in other greenhouse gas emissions will be required to limit climate warming to 1.5° or 2°C, as required under the 2015 Paris Agreement. —JFU

Science, this issue p. 932

IMMUNOTHERAPY

Tempering dendritic cell activation

Checkpoint blockade targeting cytotoxic T lymphocyte associated protein 4 (CTLA-4) and programed cell death 1 (PD-1) have changed the landscape of cancer therapeutics. However, much remains to be learned about the biology of these molecules. CTLA-4 expressed on T cells captures costimulatory molecules CD80 and CD86 from antigen-presenting cells by transendocytosis to inhibit CD28-mediated costimulation of T cell activation. Ovcinnikovs *et al.* report that regulatory T cells (T_{regs}) outperform conventional T cells in their ability to transendocytose CD80 and CD86 and that migratory dendritic cells are the main population targeted by T_{reg}-expressed CTLA-4 in vivo. These findings elucidate why CTLA-4 expressed on T_{regs} is so central in maintaining immune homeostasis. —AB

Sci. Immunol. **4**, eaaw0902 (2019).

Published by AAAS

RESEARCH ARTICLE SUMMARY

ICE SHEETS

Slowdown in Antarctic mass loss from solid Earth and sea-level feedbacks

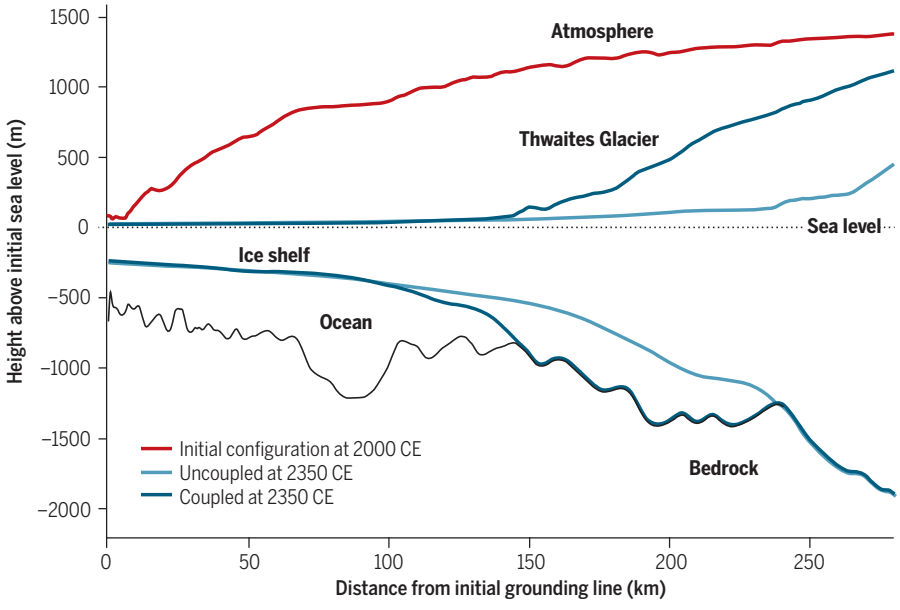
E. Larour*, H. Seroussi, S. Adhikari, E. Ivins, L. Caron, M. Morlighem, N. Schlegel

INTRODUCTION: Geodetic investigations of crustal motions in the Amundsen Sea sector of West Antarctica and models of ice-sheet evolution in the past 10,000 years have recently highlighted the stabilizing role of solid-Earth uplift on polar ice sheets. One critical aspect, however, that has not been assessed is the impact of short-wavelength uplift generated by the solid-Earth response to unloading over short time scales close to ice-sheet grounding lines (areas where the ice becomes afloat). Here, we present a new global simulation of Antarctic evolution at high spatiotemporal resolution that captures solid-Earth processes stabilizing and destabilizing ice sheets. These include interactions with global eustatic sea-level rise (SLR), self-attraction and loading (SAL) of the oceans, Earth's rotational feedback to SAL, and elastic uplift of the solid Earth.

RATIONALE: In Antarctica, dynamic thinning and retreat of ice streams has been the main driver of mass loss over the past decades, largely controlled by how grounding lines migrate and interact with bedrock pinning points. Studies have shown that the physical representation of grounding-line dynamics (GLD) can only be captured through simulations with a horizontal resolution higher than 1 km. Current models of SLR that incorporate solid-Earth processes with viscoelastic response tend to involve GLD that is resolved at much coarser resolutions (25 to 100 km) and involve time steps on the order of decades. Such resolution bounds are incompatible with capturing the complex bed topography of the ice streams of West Antarctica that are vulnerable to rapid retreat. In addition, a resolution of 25 to 100 km is inherently too coarse to capture short-wavelength elastic uplift generated by fast GLD. Elastic uplift generated by a 2-km grounding-line retreat, modeled as loss of 100-m-thick ice from a disk of 2-km radius, can reach 52 mm near the grounding line (centroid of the equivalent disk). At coarser resolutions (say, 16 km), the same model generates uplift one order of magnitude lower. This implies that uplift generated in simulations at coarse resolutions might underestimate how much uplift is generated during ungrounding of active areas of Antarctica such as Thwaites Glacier (TG), where highly complex grounding-line geometries and associated retreat are observed over short time scales on the order of years. Our goal was therefore to carry out a sensitivity study of sea level– and ice flow–related processes that incorporate kilometer-scale resolutions and global processes involving solid-Earth dynamics.

ON OUR WEBSITE

Read the full article at http://dx.doi.org/10.1126/science.aav7908



Sensitivity study of TG, Antarctica, 350 years into the future. Red, present-day surface of TG; dark blue, TG at 2350 CE without SLR or solid-Earth processes included in the simulation; light blue, configuration for a simulation that includes coupled SLR and solid-Earth processes; dotted black and solid black, present-day sea-level and bedrock position, respectively.

RESULTS: Our sensitivity study spans 500 years and demonstrates how in Antarctica, TG is particularly prone to negative feedback from SAL and elastic uplift. At year 2350, including these feedbacks leads to a ~20-year delay in dynamic mass loss of TG, corresponding to a 26.8% reduction in sea-level contribution, along with a reduction in grounding-line retreat of 38% and elastic uplift rates reaching ~0.25 m/year. At year 2100, though, this negative feedback is considerably lower, with a 1.34% reduction in sea-level contribution only. Not including a kilometer-scale resolution representation of such processes will lead to projections of SLR that will significantly overestimate Antarctic Ice Sheet contribution over several centuries.

CONCLUSION: For 21st-century projections, the effects we have modeled here remain negligible. However, for the period starting 2250 and after, SLR projections that would not account for such dynamic geodetic effects run the risk of consistently overestimating (by 20 to 40%) relative sea-level estimates. Our approach shows that significant stabilization in grounding-line migration occurs when uplift rates start approaching 10 cm/year. This has strong implications for late Quaternary reconstructions of SLR, for example, in which the inclusion of these solid-Earth processes will allow SLR modelers to gain a better grasp of the time scales involved in reaching maximum coastal inundation levels during extended warm periods. ■

The list of author affiliations is available in the full article online.
*Corresponding author. Email: eric.larour@jpl.nasa.gov
Cite this article as E. Larour *et al.*, *Science* **364**, eaav7908 (2019). DOI: 10.1126/science.aav7908

RESEARCH ARTICLE

ICE SHEETS

Slowdown in Antarctic mass loss from solid Earth and sea-level feedbacks

E. Larour[1,2]*, H. Seroussi[1], S. Adhikari[1], E. Ivins[1], L. Caron[1], M. Morlighem[3], N. Schlegel[1]

Geodetic investigations of crustal motions in the Amundsen Sea sector of West Antarctica and models of ice-sheet evolution in the past 10,000 years have recently highlighted the stabilizing role of solid-Earth uplift on polar ice sheets. One critical aspect, however, that has not been assessed is the impact of short-wavelength uplift generated by the solid-Earth response to unloading over short time scales close to ice-sheet grounding lines (areas where the ice becomes afloat). Here, we present a new global simulation of Antarctic evolution at high spatiotemporal resolution that captures all solid Earth processes that affect ice sheets and show a projected negative feedback in grounding line migration of 38% for Thwaites Glacier 350 years in the future, or 26.8% reduction in corresponding sea-level contribution.

Geodetic investigations of crustal uplift in the Amundsen Sea sector (ASS) of West Antarctica (*1*) and models of grounding-line retreat followed by readvance in the Ross Sea sector during the past 10,000 years (*2*) have recently highlighted the stabilizing role of solid-Earth uplift on polar ice sheets. The specific processes involved in this negative feedback have previously been extensively investigated, such as self-attraction and loading (SAL) (*3*), rotational feedback (*4*), and redistribution of mass in the Earth due to glacial isostatic adjustment (GIA) (*5*, *6*). Some of these processes, SAL and GIA in particular, have been shown to stabilize grounding-line retreat of ice sheets resting on retrograde slope (*7*–*9*).

Our focus is on how short-wavelength uplift generated by the unloading of Earth's crust over short time scales in the immediate vicinity of grounding lines further affects the dynamics of ice sheets' grounding-line migration, which has not previously been investigated. Grounding lines in Antarctica are geographically refined features that need to be spatially resolved at resolutions less than 1 km (*10*) and that migrate over short time scales (weeks to months) (*11*), which triggers the question of how to avoid underestimating the resulting uplift upon migration. Our global simulation of Antarctic evolution presented here is carried out at the necessary high temporal resolution (14 days and 365 days for the ice and solid Earth, respectively) and spatial resolution (1 to 50 km) required to capture the processes that stabilize and destabilize ice sheets. These include interactions that involve global eustatic sea-level rise (SLR), SAL, elastic rebound of the solid Earth, and rotational feedback.

In Antarctica, dynamic retreat of ice streams has been the main driver of mass loss (*12*). These ice streams are largely controlled by how their grounding lines migrate (*13*) and interact with pinning points (*14*). Recent research efforts have focused on the complex interactions between intrusion of warm circumpolar water near the grounding line (*11*), ungrounding of pinning points (*14*, *15*), and reduction in buttressing through loss of friction (*16*). A key aspect of understanding grounding-line dynamics (GLD) is to understand the relationship between the evolving sea level and the exact position of pinning points. As shown through NASA's Operation IceBridge topographic mapping as well as decades-long efforts to map grounding-line migration, highly resolved pinning points are present in critical areas of the West Antarctic Ice Sheet (WAIS) that can only be captured at kilometer-scale resolutions (*17*, *18*). In parallel, studies have shown that the physical representation of grounding-line migration can only be modeled through meshes that attain 1-km resolution (*19*). There has been recent interest in developing future projections of SLR that incorporate solid-Earth processes with Maxwellian viscoelastic response (*7*–*9*) and SAL (*7*, *20*). However, these tend to involve GLD that is resolved at much coarser resolutions (25 to 100 km) and involve time steps on the order of years or even decades. Such resolution bounds are incompatible with capturing the complex geometry of WAIS ice streams that are vulnerable to rapid retreat. For example, Pine Island Glacier (PIG) is 20 to 30 km wide at the grounding line, with complex grounding-line geometry that can only be resolved spatially at the 1- to 2-km level (*10*).

In addition, a resolution of 25 to 100 km is inherently too coarse to capture short-wavelength elastic uplift generated by fast grounding-line retreat and associated mass loss. As shown in Fig. 1, elastic uplift generated by a 2-km grounding-line retreat, modeled as loss of 100-m-thick ice from a disk of 2-km radius, can reach 52 mm near the grounding line (centroid of the equivalent disk). At coarser resolutions (say, 16 km), the same model generates uplift one order of magnitude lower. This implies that uplift generated in simulations such as (*7*–*9*) might underestimate how much uplift is generated during ungrounding of active areas of Antarctica such as Thwaites Glacier (TG) or PIG, where highly complex grounding-line geometries and associated retreat are observed over short time scales on the order of years. Some models, such as (*21*), have attained resolutions down to 6 km; however, in such cases GLD has not been considered interactively but prescribed offline, which precluded extensive negative feedback from manifesting themselves during the simulations. Our goal was to carry out a sensitivity study of sea level– and ice flow–related processes by incorporating kilometer-scale resolutions and global processes that involve solid-Earth dynamics. The ice-flow model robustly captures GLD at high resolution (1 km) and over very short time scales (2 weeks).

To understand the impact of solid-Earth dynamics, we needed to independently assess the role of each process. Our strategy was to incrementally introduce the following processes: (i) eustatic sea level; (ii) SAL of the ocean; (iii) elastic response of the solid Earth; (iv) elastic rotational feedback; and (v) background GIA (BGIA), considered here as an offline component and not an interactive model. Each of these processes includes the previous ones. To evaluate all of these processes, we relied on a control run capturing the traditional approach of ice-sheet models, in which ice-sheet evolution is independent of relative sea level (RSL) and other solid-Earth processes. We define this model as UNC (or uncoupled) (Fig. 2A and Table 1). RSL trends are recovered from UNC and similar types of models (*22*) by an a posteriori transfer of total mass loss to the ocean, leading to a global and uniform increase in sea level.

To account for the effects of eustatic sea level on ice dynamics, we relied on a model we term EUS (Fig. 2B and Table 1), where an update to RSL at the ice front is computed, thus modifying the pressure exerted by the ocean on ice-calving fronts as well as ice shelves' hydrostatic equilibrium. The eustatic increase in RSL originates in mass loss from all major glaciated areas of the world (ice sheets and glaciers). Essentially, as captured by the EUS model, an increase in RSL

[1]Jet Propulsion Laboratory, California Institute of Technology, Pasadena, CA, USA. [2]Joint Institute for Regional Earth System Science and Engineering, University of California, Los Angeles, Los Angeles, CA, USA. [3]Department of Earth System Science, University of California, Irvine, Croul Hall, Irvine, CA, USA.
*Corresponding author. Email: eric.larour@jpl.nasa.gov

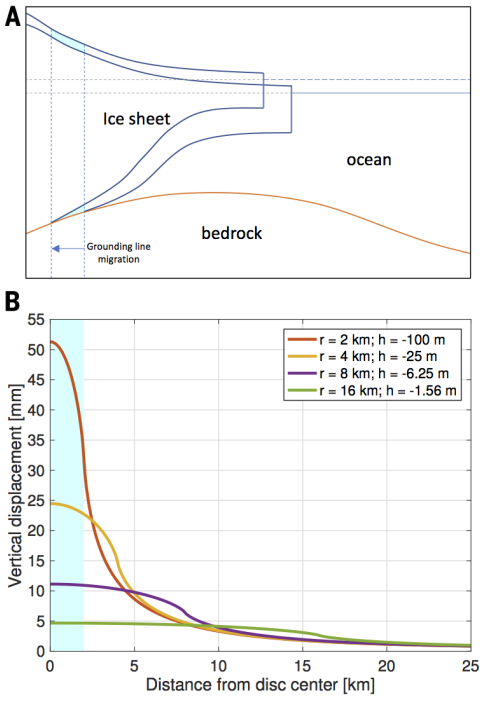


Fig. 1. GLD, unloading, and spatial resolution effects on solid-Earth deformation. (**A**) A sketch of dynamic evolution of an ice sheet/ice shelf system in which ice thinning at the grounding line results in migration and unloading of the underlying bedrock. The equivalent amount of ice (if thinning is neglected) that is removed from the bedrock is shaded in light blue. (**B**) Vertical displacement from unloading of this ice, modeled as a cylindrical load of ice [radius (r) = 2 km by height (h) = 100 m] that melts away. Effects of spatial resolution are explored by mapping the same volume of ice melt on to coarser disks having r = 16, 8, and 4 km, respectively. A 2-km resolution model can realistically capture the concentrated load and predicts substantial uplift, whereas a coarse-resolution model generates vertical displacement in the near field up to one order of magnitude lower. All of these simulations were performed for the Preliminary reference Earth model (PREM), having a continental crust (surface layer) with Lame parameters μ = 26.624 GPa (1 GPa = 10^9 Pa) and λ = 34.216 GPa.

lifts an ice shelf upward, resulting in grounding-line retreat, which leads to a positive feedback (*23*). However, as ice mass is lost, the local gravity attraction drops, resulting in reduced hydrostatic pressure at calving fronts. To account for this gravity of the ocean mass, we relied on the model we term SAL (Fig. 2C and Table 1), where the computation of RSL results in a negative feedback (*7*). The SAL model accounts for a rigid Earth in order to fully isolate its effects from the vertical motions of a compressible and seismologically constrained realistic Earth. To account for the effects of the elastic response of the solid Earth, we relied on a model that we define as ELA (Fig. 2D and Table 1), where we remove the hypothesis of a rigid Earth (*1*) and introduce elastic uplift of the bedrock in response to the ice mass loss unloading the Earth crust and associated sea-surface height. On marine sectors of the ice sheet, uplift tends to yield decreased grounding-line retreat (*8*). To account for effects owing to rotational feedback, we relied on the ROT model (Fig. 2E and Table 1), where we add rotational feedback effects attributable to global-scale mass redistribution associated with SAL and elastic deformation. The resulting computation of RSL (*3*, *24*, *25*) tends to lower the RSL in the vicinity of mass loss and feature long wavelengths, thus potentially introducing a slight negative feedback in grounding-line migration. Last, for BGIA effects, we did not model GIA interactively but rather relied on a precomputed offline background GIA time series that is superimposed on all other processes (Fig. 2F and Table 1, model run we term NSM for net sum model of all processes referred to above). This BGIA time series comes from a recent Bayesian global study by (*26*) that used Maxwellian viscoelasticity and that took into account variations in RSL on a compressible self-gravitating, rotating Earth owing to the response of the solid Earth to past ice and ocean mass changes. This response occurs over longer time scales (century and longer scales) and also tends to reduce grounding-line migration through uplift of the bedrock (*1*, *2*, *7*–*9*). Although rotational feedback occurs both on the BGIA and elastic time scales independently, we investigated and isolated the elastic rotational feedback contribution. We do include the rotational feedback contribution from BGIA in the computational scheme, but only as an a posteriori offline process. What is distinct about our subsequent investigation is the role played by the elastic response because this has seemingly been overlooked in all past studies owing to resolution limitations imposed by attempting to deal with Maxwellian viscoelasticity. Our goal was, therefore, to thoroughly quantify the impact of elasticity before attempting more complex interactions with Maxwellian or more advanced transient solid-Earth rheologies.

Model and setup

In order to solve for all the aforementioned processes, we were compelled to solve for both RSL and ice flow at high spatial resolution. For ice sheets, grounding-line migration needs to be captured at the 1-km-resolution level [Marine Ice Sheet Model Intercomparison Project for planview models 3D (MISMIP3d)] (*19*). This resolution is necessary to capture feedbacks between ice-flow dynamics and the bedrock topography. For RSL, knowledge of bedrock uplift and absolute sea level (ASL) is the prerequisite for application of the hydrostatic equilibrium criterion, which modulates the pace of grounding-line migration. This implies that SAL, ELA, and ROT models need to be solved at kilometer-scale resolutions near grounding lines or at least need to be investigated for their sensitivity to spatial resolutions (Fig. 1). Our working assumption is that by exploring the impact of kilometer-scale resolution in model representation of grounding-line retreat, the one-order-of-magnitude increase in uplift as isolated in our single cap unloading (Fig. 1) will generate significant negative feedback in the SAL, ELA, and, potentially, ROT models. The Ice Sheet System Model (ISSM) is an ice-flow modeling software (*27*) that is based on anisotropic unstructured meshes using the finite element method. It is therefore capable of meeting these requirements to capture GLD at 1-km-scale resolution (*11*), using anisotropic mesh refinement and higher-order thermomechanical representation of ice-flow dynamics (*11*). Recently, a global sea-level model that can capture SAL effects, elastic vertical uplift, and elastic rotational feedback down to kilometer-scale resolutions was formulated (*28*) and implemented in ISSM (*25*, *28*). This formulation can model RSL at the grounding line of ice sheets with resolutions compatible with ISSM's higher-resolution grounding-line migration, hence enabling a quantitative assessment of all solid-Earth–related feedbacks. We implemented a full two-way coupling between the ice-flow and RSL formulations, in which the entire Antarctic ice sheet was fully represented in terms of mass transport, stress balance, and grounding-line migration, as well as melting rate forcing under every ice shelf [using a calibrated melt-rate parameterization (*11*)], and interacted with a full global-scale RSL simulation in which sea-level and bedrock uplift are computed and refined to high resolutions along Antarctica's grounding lines. The scope of the analysis is not to carry out a fully realistic projection of Antarctica but rather to capture the forcing that we currently understand as being responsible for grounding-line retreat. This is why we relied on a state-of-the-art melt-rate parameterization but did not carry a realistic but uncertain climatology projection. For all other glaciated areas of the world where ice thickness changes are required to source the RSL model, we did not run stress-balance and grounding-line migration models but rather implemented a simple mass-transport scheme in which ice thickness changes were locally constrained to match observed Gravity Recovery and Climate Experiment (GRACE) mass trends from 2003 to 2016 (*29*). This implies that except for Antarctica, all other glaciated areas are contributing a constant amount of melt to the oceans, without feedback on ice-flow dynamics. This assumption is conservative because the contribution of Greenland and other glaciers in the world to RSL is currently understood to significantly increase by the end of the century, but given that our goal is to understand the impact of Antarctica on RSL and vice versa, our control run and experiments needed to experience a modestly realistic RSL increase coming from other glaciated areas while

not resulting in further ice-flow dynamic feedbacks. This also implies that our simulations would capture processes for which the timing might not be fully realistic but compatible with conditions in which elastic feedbacks will manifest, such as during the collapse of TG. We strove to reach conclusions that can be adapted for other timelines and, in particular, for more realistic projections of Antarctica.

Given that we are interested in the impact on short time scales and not on longer time scales, the six models can all be initialized identically by using an instantaneous ice-flow spin-up referenced to year 1999 (supplementary materials, materials and methods) followed by a 1-year relaxation, fully uncoupled from any RSL or solid-Earth process. This can only be done because we do not rely on past history of ice deformation required for a viscous formulation. Starting the model at year 2000, physical processes described in Fig. 2 were activated for EUS, SAL, ELA, ROT, and NSM scenarios. The UNC model run was used as a control run. All runs were carried out for 500 years starting from the exact same configuration at model year 2000.

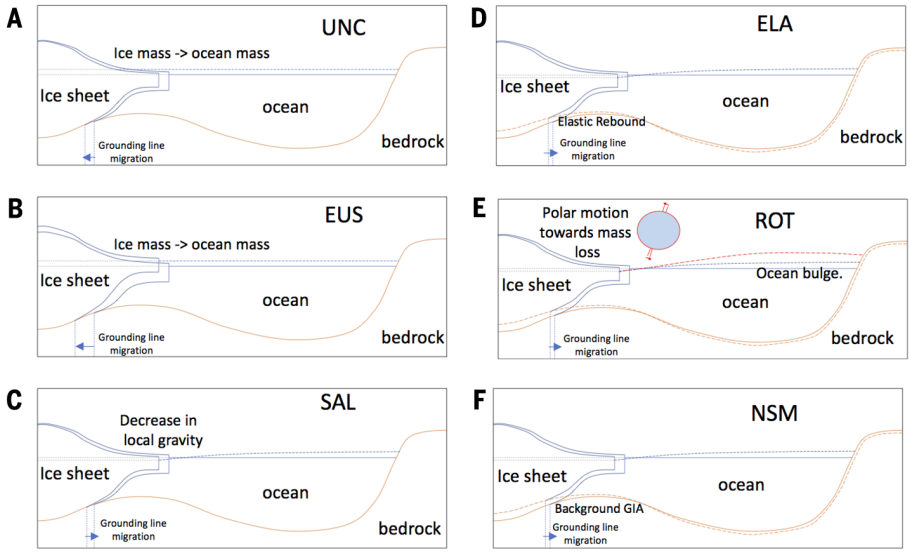


Fig. 2. Processes involved in a dynamically interactive ice sheet/solid-Earth system model. Models are (**A**) UNC, (**B**) EUS, (**C**) SAL, (**D**) ELA, (**E**) ROT, and (**F**) NSM. A description of the different models and how they incrementally introduce feedbacks into the ice evolution is given in Table 1. For each model, we indicate how grounding-line migration is affected, as well as local and far-field RSL. For the ELA, ROT, and NSM models, we also show how sea-level change affects solid-Earth deformation of the bedrock. Solid and dashed lines represent initial and final configurations, respectively. The direction of GL migration is indicated with arrows. Ice-flow dynamics and forcing from melt rates generated by our ice–ocean interaction parameterization will generate a finite GLD, as indicated in (A), the UNC case.

Results

Comparing each model run to the UNC control run, we can demonstrate the critical impact that solid-Earth deformation and SAL effects have on the evolution of Antarctica, both in terms of grounding line retreat as well as resulting contribution to SLR around the world. The global fingerprint of ASL 350 years into the future for the UNC, EUS, ELA, SAL, ROT, and NSM models is shown in Fig. 3 and fig. S18. The dynamic retreat of TG and PIG is clearly visible (as a local collapse in RSL), with associated strong patterns of sea-level fingerprints in the Pacific Ocean. The impact of SAL (Fig. 3A) is substantial, as well as elastic uplift (Fig. 3, A and B). The ROT model exhibits, as expected for a collapsing WAIS (*30*, *31*), strong patterns particularly along the Indian Ocean and North Pacific. Although such effects are expected in terms of global sea-level fingerprint (*24*, *31*), their local expression in terms of grounding-line migration is not well understood. In Fig. 4, we assess the magnitude and scale of such feedbacks on the evolution of the WAIS grounding line. By 2350, the grounding line in the UNC model has propagated on average 240 km upstream of its initial position (Fig. 4, red versus black lines). There is a slight difference

Table 1. Model labels and definitions. For each model, a label is provided along with a corresponding description of the physical processes represented and levels of feedback between the RSL and ice-sheet model. In addition, modeled relative differences (in percent) in GLD against the UNC control run are provided. This difference is measured along the gray flowline (Fig. 4, bottom) for the year 2350. A positive value indicates a positive feedback (where the grounding line migrates further upstream than the control run). A negative value indicates the opposite, with the evolutionary fate of the grounding line drifting downstream of the UNC grounding line position. Brackets indicate a range of values. Similarly, relative difference in TG volume above flotation and TG volume change (in percent of sea-level equivalent) is provided against UNC for three epochs: 2100, 2350, and 2500.

Model	Description	GLD feedback (%)	TG volume above flotation feedback (%) 100/350/500 years	TG volume feedback (%) 100/350/500 years
UNC	Ice-sheet evolution independent of RSL (uncoupled). A posteriori transfer of mass loss to the ocean. Spatially uniform increase in RSL.	0	0/0/0	0/0/0
EUS	RSL update as ice sheets evolve. Eustatic transfer of ice mass loss to the ocean. Spatially uniform increase in RSL.	[0 to 1]	−0.2/1.2/0.69	0.09/1.65/0.51
SAL	EUS model + RSL fingerprint accounting for self attraction and loading from ocean on a self-gravitating, rigid Earth.	−10.6	−0.82/−7.8/−2.1	−0.18/−7.17/−0.6
ELA	SAL model + elastic uplift.	−38	−29/−29.5/−16.7	−1.26/−26.8/−9.2
ROT	ELA model + elastic rotational feedback.	−38	−29/−29.5/−16.9	−1.26/−26.8/−9.2
NSM	ROT model + BGIA adjustment.	−38.5	−43.9/−31.7/−18.5	−1.34/−28.4/−9.9

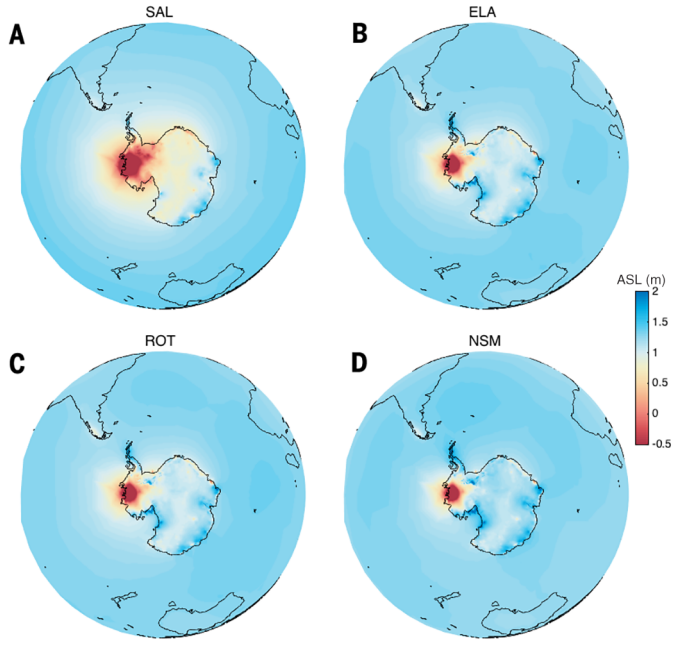


Fig. 3. ASL projection at model time 2350. The projection is determined for the UNC, EUS, SAL, ELA, ROT, and NSM models. All six models are described in Table 1. (**A** to **D**) Nonuniform ASL patterns for the models indicated. For the UNC model, ASL is constant at 1.3076 m, and for the EUS model, ASL is constant at 1.3160 m. Coastlines (*40*) are displayed in black. The other hemisphere is addressed in fig. S18. ASL in the continents should be interpreted as geoid height change plus the EUS value.

between the grounding line position of the UNC model versus the EUS model (Fig. 4, red versus yellow lines), with a positive feedback resulting in a EUS grounding-line position 1 to 2 km further upstream. With the SAL model, the feedback introduced is negative and of a much larger magnitude, with a differential in grounding-line position of 20 to 30 km (Fig. 4, red versus green lines). This is equivalent to 10% less migration in grounding line after 350 years. However, a larger negative feedback is introduced when taking into account elastic land uplift. This feedback delays grounding-line retreat significantly, resulting in a differential position in the grounding line of 100 to 120 km downstream of the UNC position (Fig. 4, red versus purple lines), which is equivalent to a 38% decrease in overall grounding-line migration after 350 years. As the next hierarchical level of complexity is included—ROT—only very minor additional effects are detected (Fig. 4, purple and blue lines, which are completely coincident), demonstrating that rotational feedback has a negligible impact on grounding-line retreat for Antarctica. Additional stabilization occurs (*7*, *8*) through introduction of BGIA (Fig. 4, cyan versus purple lines) responsible for a small grounding-line differential (1 to 2 km), increasing to 10 km in some specific areas in the main trunk of TG (Fig. 4, inset).

Given that our BGIA time series are not interactively computed and are just a representation of past loading history, we carried out a second analysis in which we assessed the impact of three background models derived from a recent GIA statistical study (*26*). The medium model corresponds to the average or expectance rate. The lower- and higher-end models correspond to scenarios with the same probability as that of the average model that either minimize or maximize uplift in this region. For the TG area, the lower-end model sees BGIA signals around 0.6 mm/year, and the higher-end model sees BGIA signals around 2 mm/year. Results are displayed in fig. S3, showing a negligible impact of the lower-end BGIA models and a negative feedback of up to 20 km in specific areas from the higher-end model. This shows that stronger grounding-line stabilization could be expected from higher rates of GIA uplift, which is in line with the expectation of softer rheologies and larger background uplift rates in the area (*1*). Our results in terms of quantifying feedbacks in GLD (along the Fig. 4 gray flowline) and associated volume change (volume in sea-level equivalent) are summarized in Table 1. The relationship is not linear, with, for example, the NSM run (the run that encompasses all five processes above) exhibiting −38.5% grounding-line retreat versus the UNC run at 2350, translating into a −28.4% difference in volume change for TG. The traditional metric of volume above flotation used by modeling efforts—such as the Sea-level Response to Ice Sheet Evolution (SeaRISE) (*32*) or the Ice Sheet Modeling Inter-comparison Project 6 (ISMIP6) (*33*), and provided in Table 1 for reference—cannot be used to quantify sea-level equivalent because the assumption of a rigid surface bedrock is shown here to be invalid, with uplift tending to decrease volume above flotation.

The negative feedbacks from SAL and elastic uplift for WAIS are significant but not specific to the area. Because our model runs are global, the same analysis can be shown for the entire continent in fig. S4, showing negative feedbacks in areas of strong retreat, such as the tributary ice streams of the Ronne and Ross ice shelves (figs. S5 and S6). However, the impact in WAIS is particularly relevant because of the existing retrograde slope of the bedrock and the presence of a prominent bedrock trough upstream of TG, which triggers marine ice-sheet instability (*23*) and results in large ice thickness change rates upon ungrounding. In addition, strong ice–ocean interactions are captured for this area in our melt rate parameterization under the TG ice shelf (*11*). The melt rates computed for this area are much larger (reaching highest values of 60 to 80 m at the grounding line) than for other areas in Antarctica (*34*). The rate at which TG loses mass to the oceans starting year 2250 is strong enough as to generate changes in surface velocity of 3 km/year inland (figs. S11 and S12), resulting in dynamic changes in surface elevation of up to 45 m/year by 2500 (figs. S13 and S14). The changes in ice load are responsible for generating elastic uplift on the order of 3 to 5 cm/year by year 2100–2300, increasing to more than 20 cm/year at the onset of TG's dynamic retreat, culminating at 45 cm/year around year 2500 (figs. S15 and S16). This uplift rate generates large differences in the vertical position of the bedrock along TG flowlines (Fig. 4, flowline profile) on the order of tens of meters. The uplift rates have been independently validated (fig. S17) with a benchmark experiment (*35*).

When we monitored projected SLR generated by the retreat of TG and all glaciated areas around the world, a kink in the rise around year 2350 for four different cities was revealed (fig. S2). Before 2350, most of the SLR trend is due to the linearly extrapolated contribution of all glaciated areas around the world. The evolving contribution from TG after the time of the kink (the time at which the most dynamic retreat is initiated) is also delayed by elastic uplift. Shown in Fig. 5 is the corresponding change in ice volume (in meters-equivalent SLR) generated by the retreat of TG as relative mass change evolves in time from 0% in 2000 to 100% at 2500, when most of the collapse has occurred. The delay between UNC and NSM is 12% in terms of normalized mass change [corresponding to roughly 23 years at 2350 (fig. S1)]. This causes a negative feedback for the TG contribution to SLR of 0.12 m. This represents a 28.4% reduction in its SLR contribution. The differential in grounding-line migration evolves through time (figs. S7 and S9). By year 2300, the differential stands at ~50 to 80 km, and by year 2350, it has reached 100 to 120 km and holds above 80 km throughout year 2450. For corresponding TG ice volume change (Table 1), by year 2100 the negative feedback reaches −1.34%; by year 2350, −28.4%; and by year 2500, −9.9%. This implies that if we apply

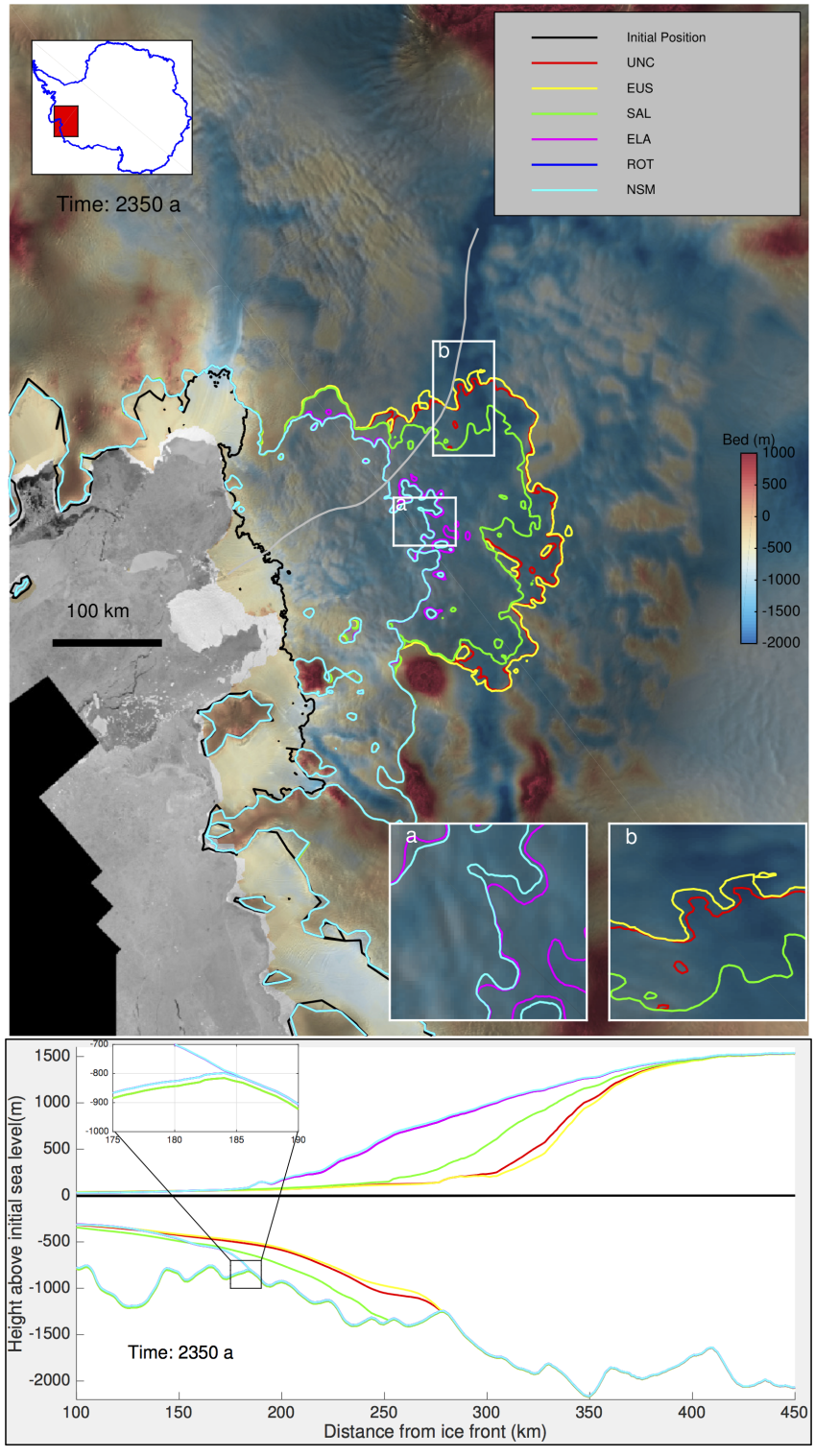


Fig. 4. Grounding-line projection for TG and PIG at model year 2350. (**Top**) The projection is carried out for the UNC, EUS, SAL, ELA, ROT, and NSM models. Initial grounding-line position at 2000 is displayed in black. Zooms on the grounding line in the deep interior of TG (a and b) are also displayed in the corresponding insets. Grounding-line positions are overlaid on a local bedrock topography map (supplementary materials, materials and methods). General location of the area in Antarctica is given in the top left inset. (**Bottom**) A section profile along the gray flowline at top is shown for the same six models, with surface, bedrock, and ice-shelf draft elevations plotted. (Inset) A zoom on the grounding line for the NSM, ROT, and ELA models, showing the uplifted versus initial bedrock at year 2350.

our sensitivity study to more realistic SLR projections that incorporate realistic climatologies, we would need to potentially take into account such dynamic effects in GLD and resulting sea-level contribution within two to three centuries. Projections toward 2100 CE should not be substantially affected by such negative feedback. In addition, a 1-km resolution is required, at least (figs. S7 and S8). Any coarsening past this resolution results in considerable delays in GLD, with a 1- to 8-km coarsened mesh for TG resulting in a delay of 160 years (fig. S8). Below 1-km resolution, our model is currently computationally too expensive. We therefore cannot infer whether convergence in uplift rates and grounding-line migration rates has been achieved. However, constraints in the bedrock topography are such that resolutions below 1 km have currently not been achieved by NASA's Operation IceBridge or any other measurement campaign. It would therefore be difficult to achieve realistic simulations below the 1-km threshold.

Discussion

For 21st-century projections (*36*, *37*), the effects we have modeled are negligible. However, for the period starting 2250 and after, RSL projections that would not account for such dynamic geodetic effects run the risk of consistently overestimating (by 20 to 40%) RSL values (Table 1 and fig. S2B). Again, the impact of realistic climatologies in running such projections is difficult to assess, but we believe that our sensitivity study is robust enough to provide a better road map for making future projections. In general, our analysis suggests that any significant dynamic mass loss of an ice sheet, once triggered, cannot be realistically modeled if dynamic feedbacks (SAL, elastic uplift, and BGIA) are ignored. Inferences from current geodetic (uplift) measurements (*1*) that near-term stabilization is realized have to be treated with some caution. The main caveat is that the full high-resolution geometry of the outlet glacier and drainage basin must be considered. Our approach shows that significant stabilization in grounding-line migration occurs when uplift rates start approaching 10 cm/year for TG. In addition the offset between NSM (the most comprehensive run considered in our analysis) and UNC runs keeps increasing as time progresses after 2350 (fig. S2A). This means that the grounding-line migration differential is not compensated for as time passes by but rather keeps increasing between both models. This has strong implications for late Quaternary reconstructions of SLR, in which all the feedbacks associated with the NSM model need to be actively accounted for. For example, the inclusion of these solid-Earth processes will allow climate change modelers to improve their understanding of the time scales involved in reaching maximum coastal inundation levels during the extended warm periods of the late Quaternary that are now fairly well recorded in ocean sediment and ice core data sets (*38*).

The implications of a strong negative feedback, particularly from elastic uplift, are important

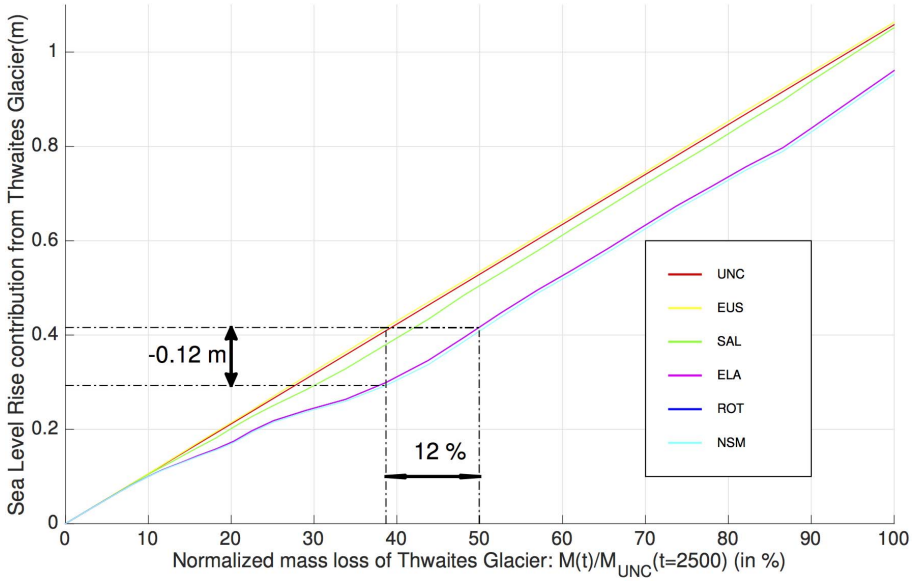


Fig. 5. 500-year contribution of TG to SLR (in meters SLR equivalent). The *x* axis represents the normalized mass loss (in percent) defined here as the ratio of mass loss M(t) from TG at time t to final mass loss MUNC(t = 2500) of TG for the UNC control run at time t = 2500. This results in a UNC SLR contribution that scales linearly with normalized mass loss. This linearity breaks down for the other runs. Normalized mass loss of the UNC run is acting here as our absolute time reference. A plot with the corresponding timeline (in years) is provided in fig. S1. Approximately 0.42 m SLR is achieved for 38% of TG normalized mass loss in the UNC run, whereas including all solid-Earth processes, the same amount of SLR is achieved only after an additional 12% mass loss occurs [or after a 23-year delay (fig. S1)], which corresponds to an offset of 0.12 m in SLR.

in that it will lead to a revision of current SLR projections past 2250. Our results over the whole Antarctic show that this feedback manifests mainly for the WAIS area, where ice–ocean interactions and marine ice sheet instability combine to generate substantial uplift. There is an increasing body of evidence suggesting that the upper mantle under WAIS is softer than the rest of Antarctica (*21*, *39*), which has not been considered here. This means that AIS could experience GLD negative feedbacks even stronger than 38.5% and delays in the corresponding SLR spike of more than half a century. Preliminary estimates from (*21*) suggest that a doubling of the elastic contribution should be considered as an estimate for the total viscoelastic feedback experienced by WAIS glaciers on time scales of 300 years. This also means that current models systematically overestimate SLR projections past 2250 and that the timing of paleo reconstructions currently used to validate and constrain such projections (*36*) might be substantially affected.

REFERENCES AND NOTES

1. V. R. Barletta *et al*., Observed rapid bedrock uplift in Amundsen Sea Embayment promotes ice-sheet stability. *Science* **360**, 1335–1339 (2018). doi: 10.1126/science.aao1447; pmid: 29930133
2. J. Kingslake *et al*., Extensive retreat and re-advance of the West Antarctic Ice Sheet during the Holocene. *Nature* **558**, 430–434 (2018). doi: 10.1038/s41586-018-0208-x; pmid: 29899456
3. W. E. Farrell, J. A. Clark, On postglacial sea level. *Geophys. J. Int.* **46**, 647–667 (1976). doi: 10.1111/j.1365-246X.1976.tb01252.x
4. K. Lambeck, *The Earth's Variable Rotation, Geophysical Causes and Consequences* (Cambridge Univ. Press, 2009).
5. W. R. Peltier, The impulse response of a Maxwell Earth. *Rev. Geophys.* **12**, 649 (1974). doi: 10.1029/RG012i004p00649
6. N. Gomez, J. X. Mitrovica, M. E. Tamisiea, P. U. Clark, A new projection of sea level change in response to collapse of marine sectors of the Antarctic Ice Sheet. *Geophys. J. Int.* **180**, 623–634 (2010). doi: 10.1111/j.1365-246X.2009.04419.x
7. N. Gomez, J. X. Mitrovica, P. Huybers, P. U. Clark, Sea level as a stabilizing factor for marine-ice-sheet grounding lines. *Nat. Geosci.* **3**, 850–853 (2010). doi: 10.1038/ngeo1012
8. S. Adhikari *et al*., Future Antarctic bed topography and its implications for ice sheet dynamics. *Solid Earth* **5**, 569–584 (2014). doi: 10.5194/se-5-569-2014
9. H. Konrad, I. Sasgen, D. Pollard, V. Klemann, Potential of the solid-Earth response for limiting long-term West Antarctic Ice Sheet retreat in a warming climate. *Earth Planet. Sci. Lett.* **432**, 254–264 (2015). doi: 10.1016/j.epsl.2015.10.008
10. E. Rignot, J. Mouginot, M. Morlighem, H. Seroussi, B. Scheuchl, Widespread, rapid grounding line retreat of Pine Island, Thwaites, Smith, and Kohler glaciers, West Antarctica, from 1992 to 2011. *Geophys. Res. Lett.* **41**, 3502–3509 (2014). doi: 10.1002/2014GL060140
11. H. Seroussi *et al*., Continued retreat of Thwaites Glacier, West Antarctica, controlled by bed topography and ocean circulation. *Geophys. Res. Lett.* **44**, 6191–6199 (2017). doi: 10.1002/2017GL072910
12. E. Rignot, J. Mouginot, B. Scheuchl, Ice flow of the Antarctic ice sheet. *Science* **333**, 1427–1430 (2011). doi: 10.1126/science.1208336; pmid: 21852457
13. L. Favier *et al*., Retreat of Pine Island Glacier controlled by marine ice-sheet instability. *Nat. Clim. Chang.* **4**, 117–121 (2014). doi: 10.1038/nclimate2094
14. K. Matsuoka *et al*., Antarctic ice rises and rumples: Their properties and significance for ice-sheet dynamics and evolution. *Earth Sci. Rev.* **150**, 724–745 (2015). doi: 10.1016/j.earscirev.2015.09.004
15. G. H. Gudmundsson, J. Krug, G. Durand, L. Favier, O. Gagliardini, The stability of grounding lines on retrograde slopes. *Cryosphere* **6**, 1497–1505 (2012). doi: 10.5194/tc-6-1497-2012
16. S. Anandakrishnan, D. D. Blankenship, R. B. Alley, P. L. Stoffa, Influence of subglacial geology on the position of a West Antarctic ice stream from seismic observations. *Nature* **394**, 62–65 (1998). doi: 10.1038/27889
17. E. J. Rignot, Fast recession of a West Antarctic glacier. *Science* **281**, 549–551 (1998). doi: 10.1126/science.281.5376.549; pmid: 9677195
18. I. Joughin, B. E. Smith, B. Medley, Marine ice sheet collapse potentially under way for the Thwaites Glacier Basin, West Antarctica. *Science* **344**, 735–738 (2014). doi: 10.1126/science.1249055; pmid: 24821948
19. F. Pattyn *et al*., Grounding-line migration in plan-view marine ice-sheet models: Results of the ice2sea MISMIP3d intercomparison. *J. Glaciol.* **59**, 410–422 (2013). doi: 10.3189/2013JoG12J129
20. B. de Boer, P. Stocchi, P. L. Whitehouse, R. S. W. van deWal, Current state and future perspectives on coupled ice-sheet – sea-level modelling. *Quat. Sci. Rev.* **169**, 13–28 (2017). doi: 10.1016/j.quascirev.2017.05.013
21. C. C. Hay *et al*., Sea level fingerprints in a region of complex Earth structure: The case of WAIS. *J. Clim.* **30**, 1881–1892 (2017). doi: 10.1175/JCLI-D-16-0388.1
22. R. Bindschadler *et al*., Ice-sheet model sensitivities to environmental forcing and their use in projecting future sea level (the SeaRISE project). *J. Glaciol.* **59**, 195–224 (2013). doi: 10.3189/2013JoG12J125
23. J. Weertman, Stability of the junction of an ice sheet and an ice shelf. *J. Glaciol.* **13**, 3 (1974). doi: 10.1017/S0022143000023327
24. G. A. Milne, J. X. Mitrovica, Postglacial sea-level change on a rotating Earth. *Geophys. J. Int.* **133**, 1–19 (1998). doi: 10.1046/j.1365-246X.1998.1331455.x
25. E. Larour, E. R. Ivins, S. Adhikari, Should coastal planners have concern over where land ice is melting? *Sci. Adv.* **3**, e1700537 (2017). doi: 10.1126/sciadv.1700537; pmid: 29152565
26. L. Caron *et al*., GIA model statistics for GRACE hydrology, cryosphere, and ocean science. *Geophys. Res. Lett.* **45**, 2203–2212 (2018). doi: 10.1002/2017GL076644
27. E. Larour, H. Seroussi, M. Morlighem, E. Rignot, Continental scale, high order, high spatial resolution, ice sheet modeling using the Ice Sheet System Model (ISSM). *J. Geophys. Res.* **117**, F01022 (2012).
28. S. Adhikari, E. R. Ivins, E. Larour, ISSM-SESAW v1.0: Mesh-based computation of gravitationally consistent sea-level and geodetic signatures caused by cryosphere and climate driven mass change. *Geosci. Model Dev.* **9**, 1087–1109 (2016). doi: 10.5194/gmd-9-1087-2016
29. S. Adhikari, E. R. Ivins, Climate-driven polar motion: 2003–2015. *Sci. Adv.* **2**, e1501693 (2016). doi: 10.1126/sciadv.1501693; pmid: 27152348
30. J. L. Bamber, R. E. M. Riva, B. L. A. Vermeersen, A. M. LeBrocq, Reassessment of the potential sea-level rise from a collapse of the West Antarctic Ice Sheet. *Science* **324**, 901–903 (2009). doi: 10.1126/science.1169335; pmid: 19443778
31. J. X. Mitrovica, N. Gomez, P. U. Clark, The sea-level fingerprint of West Antarctic collapse. *Science* **323**, 753 (2009). doi: 10.1126/science.1166510; pmid: 19197056
32. S. Nowicki *et al*., Insights into spatial sensitivities of ice mass response to environmental change from the SeaRISE ice sheet modeling project I: Antarctica. *J. Geophys. Res.* **118**, 1002–1024 (2013).
33. S. M. J. Nowicki *et al*., Ice Sheet Model Intercomparison Project (ISMIP6) contribution to CMIP6. *Geosci. Model Dev.* **9**, 4521–4545 (2016). doi: 10.5194/gmd-9-4521-2016; pmid: 29697697
34. M. P. Schodlok, D. Menemenlis, E. J. Rignot, Ice shelf basal melt rates around Antarctica from simulations and observations. *J. Geophys. Res. Oceans* **121**, 1085–1109 (2016). doi: 10.1002/2015JC011117
35. G. Spada *et al*., A benchmark study for glacial isostatic adjustment codes. *Geophys. J. Int.* **185**, 106–132 (2011). doi: 10.1111/j.1365-246X.2011.04952.x
36. R. M. DeConto, D. Pollard, Contribution of Antarctica to past and future sea-level rise. *Nature* **531**, 591–597 (2016). doi: 10.1038/nature17145; pmid: 27029274
37. C. Ritz *et al*., Potential sea-level rise from Antarctic ice-sheet instability constrained by observations. *Nature* **528**, 115–118 (2015). pmid: 26580020
38. Past Interglacials Working Group of PAGES, Interglacials of the last 800,000 years. *Rev. Geophys.* **54**, 162–219 (2016). doi: 10.1002/2015RG000482
39. W. van der Wal, P. L. Whitehouse, E. J. Schrama, Effect of GIA models with 3D composite mantle viscosity on GRACE mass balance estimates for Antarctica. *Earth Planet. Sci. Lett.* **414**, 134–143 (2015). doi: 10.1016/j.epsl.2015.01.001

40. P. Wessel, W. H. F. Smith, A global, self-consistent, hierarchical, high-resolution shoreline database. *J. Geophys. Res. Oceans* **101** (B4), 8741–8743 (1996). doi: 10.1029/96JB00104

ACKNOWLEDGMENTS

The research was carried out at the Jet Propulsion Laboratory (JPL), California Institute of Technology, under a contract with the National Aeronautics and Space Administration (NASA). Resources supporting this work were provided by the NASA High-End Computing (HEC) Program through the NASA Advanced Supercomputing (NAS) Division at Ames Research Center. During the time elapsed between electronic and printed versions, G. Milne read the manuscript and found two serious typographical errors, and we are indebted to him for communicating these to us promptly. **Funding:** This work was funded by JPL Research, Technology and Development Program grant #01STCR R.17.235.118 (S.A.). It was also funded by the following programs at NASA: Cryospheric sciences under grants 105393 509496.02.08.08.53 and 105393 444491.02.04.01.80 (E.L. and N.S.) and grant 105393 281945.02.53.04.07 (H.S.), Modeling Analysis and Prediction under grants 105479 509496.02.08.10.07 (E.L. and N.S.) and 105479 509496.02.08.08.49 (H.S.), GRACE Science Team under grant E.8.1.1 (E.L.), Sea-Level Science Team under grants 105393 509496.02.08.10.65 (E.I., E.L., L.C., N.S., and S.A.) and 105393 281945.02.53.03.97 (E.I.), and Earth System and Interior under grant 105526-281945.02.47.03.86. It was also funded by NFS grant 1739031 (M.M.). **Author contributions:** E.L., S.A., E.I., L.C., and H.S. contributed to the theory. E.L. led the calculations. E.I., L.C., and S.A. assisted with interpretation of the results. M.M. assisted with modeling of the bedrock. H.S. assisted with modeling of ice/ocean interactions. N.S. assisted with model setup. All authors contributed to the writing of the paper. **Competing interests:** The authors declare that they have no competing interests. **Data and materials availability:** All data are available in the manuscript or the supplementary materials. All simulations were carried out using the Ice Sheet System Model, which is freely and publicly available at http://issm.jpl.nasa.gov.

SUPPLEMENTARY MATERIALS

science.sciencemag.org/content/364/6444/eaav7908/suppl/DC1
Materials and Methods
Figs. S1 to S19
References (*41–47*)

22 October 2018; accepted 12 April 2019
Published online 25 April 2019
10.1126/science.aav7908

RESEARCH ARTICLE SUMMARY

HUMAN GENETICS

RNA sequence analysis reveals macroscopic somatic clonal expansion across normal tissues

Keren Yizhak, François Aguet, Jaegil Kim, Julian M. Hess, Kirsten Kübler, Jonna Grimsby, Ruslana Frazer, Hailei Zhang, Nicholas J. Haradhvala, Daniel Rosebrock, Dimitri Livitz, Xiao Li, Eila Arich-Landkof, Noam Shoresh, Chip Stewart, Ayellet V. Segrè, Philip A. Branton, Paz Polak, Kristin G. Ardlie, Gad Getz*

INTRODUCTION: Cancer genome studies have contributed to the analysis and discovery of somatic mutations that drive cancer growth. However, studying the genetic makeup of a tumor when it is already fully developed limits our ability to uncover how and which somatic mutations accumulate in normal tissues in the stages preceding cancer initiation. To address this challenge, recent studies performed deep sequencing in a limited number of tissue types and a small number of individuals, identifying a large number of microscopic clones carrying somatic mutations, some in known cancer genes. These findings emphasize the need to uncover the genomic events that occur in all normal tissues. Although efforts have begun to collect and analyze DNA from normal tissues, we still lack a comprehensive catalog of genetic events and clonal properties across a large number of tissues and individuals. By analyzing the information-rich content in RNA now available from recent advances in RNA sequencing methods, we may be able to substantially expand the scope and scale of these studies.

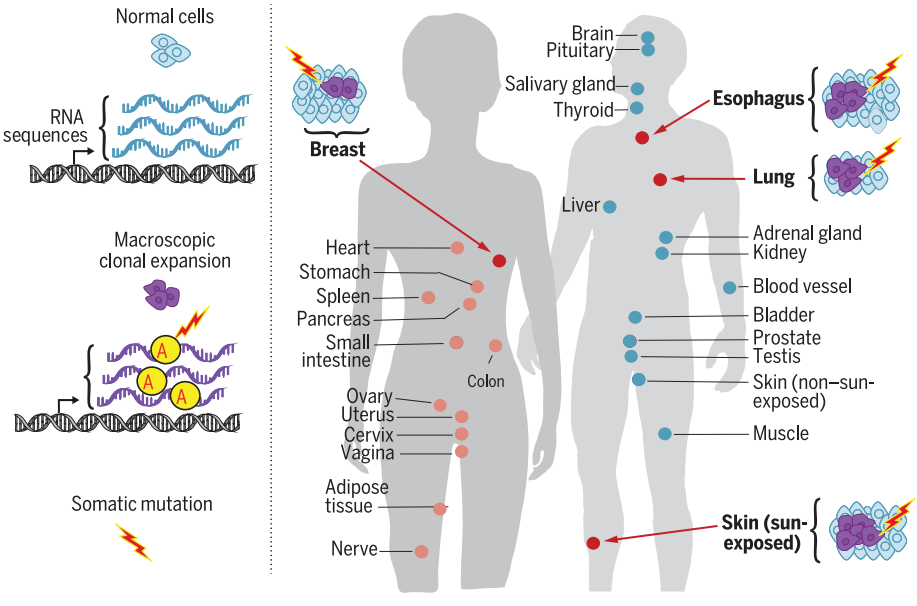
RATIONALE: Some mutations found in the DNA can be detected in the corresponding RNA, depending on the mutation allele fraction and sequence coverage. We therefore hypothesized that a careful analysis of RNA sequences from normal bulk tissues could uncover somatic mutations reflecting macroscopic clones within the samples. In this work, we used the large collection of RNA sequences from the Genotype–Tissue Expression (GTEx) project, representing more than 6700 samples from ~500 individuals, spanning across 29 different normal tissues.

ON OUR WEBSITE

Read the full article at http://dx.doi.org/10.1126/science.aaw0726

RESULTS: We developed a new method, called RNA-MuTect, to identify somatic mutations using a tissue-derived RNA sample and its matched-normal DNA. We validated RNA-MuTect on both tumor-adjacent and cancer samples from The Cancer Genome Atlas (TCGA), wherein DNA and RNA were coextracted from the same samples. Focusing on mutations contained within sufficiently covered sequences, RNA-MuTect achieved high sensitivity and precision, enabling the discovery of most driver events and mutational processes from TCGA tumor RNA data. When applied to the GTEx dataset of normal tissues, multiple somatic mutations were detected in almost all individuals and tissues studied here, including in known cancer genes. The three tissues with the largest number of somatic mutations were sun-exposed skin, esophagus mucosa, and lung; this finding suggests that environmental exposure can promote somatic mosaicism. Both the individuals' age and tissue-specific proliferation rate were found to be associated with the number of detected mutations. A dN/dS (ratio of nonsynonymous to synonymous substitutions) analysis suggested that some of the mutations identified in cancer genes may confer a selective advantage. In addition, allelic imbalance events at the chromosome arm level were detected in normal tissues.

CONCLUSION: Genetic clones carrying somatic mutations are detected across normal tissues to different extents, and these differences depend on factors such as the tissue's exposure to environmental mutagens, natural architecture, proliferation rate, and the microenvironment. Some of these clones may be the result of genetic drift. Others, however, may develop as a result of positive selection driven by certain somatic events, thus potentially representing the earliest stages of tumorigenesis. Higher-resolution studies of normal tissues and precancerous lesions are required if we are to advance our understanding of both aging and early cancer development. ■



Somatic clonal expansions in normal human tissues. RNA sequences from 29 normal human tissues collected as part of the Genotype–Tissue Expression (GTEx) project are analyzed using RNA-MuTect, a method developed for detecting somatic mutations in RNA-seq data. Macroscopic clonal expansions, characterized by shared somatic mutations, are detected in all tissues; skin, esophagus, and lung have the largest number of somatic mutations.

The list of author affiliations is available in the full article online.
*Corresponding author. Email: gadgetz@broadinstitute.org
Cite this article as K. Yizhak *et al.*, *Science* **364**, eaaw0726 (2019). DOI: 10.1126/science.aaw0726

RESEARCH ARTICLE

HUMAN GENETICS

RNA sequence analysis reveals macroscopic somatic clonal expansion across normal tissues

Keren Yizhak[1], François Aguet[1], Jaegil Kim[1], Julian M. Hess[1], Kirsten Kübler[1,2,3], Jonna Grimsby[1], Ruslana Frazer[1], Hailei Zhang[1], Nicholas J. Haradhvala[1,2], Daniel Rosebrock[1], Dimitri Livitz[1], Xiao Li[1], Eila Arich-Landkof[1,2], Noam Shoresh[1], Chip Stewart[1], Ayellet V. Segrè[1,3,4], Philip A. Branton[5], Paz Polak[6], Kristin G. Ardlie[1], Gad Getz[1,2,3,7]*

How somatic mutations accumulate in normal cells is poorly understood. A comprehensive analysis of RNA sequencing data from ~6700 samples across 29 normal tissues revealed multiple somatic variants, demonstrating that macroscopic clones can be found in many normal tissues. We found that sun-exposed skin, esophagus, and lung have a higher mutation burden than other tested tissues, which suggests that environmental factors can promote somatic mosaicism. Mutation burden was associated with both age and tissue-specific cell proliferation rate, highlighting that mutations accumulate over both time and number of cell divisions. Finally, normal tissues were found to harbor mutations in known cancer genes and hotspots. This study provides a broad view of macroscopic clonal expansion in human tissues, thus serving as a foundation for associating clonal expansion with environmental factors, aging, and risk of disease.

As cells divide during life, they accumulate somatic mutations. Although most of these mutations are thought to be either neutral or slightly deleterious (*1*), a few may increase cellular fitness and contribute to clonal expansion. This process is associated with aging as well as with diseases such as coronary heart disease (*2*, *3*), neurological disorders (*4*), and cancer (*5*). In cancer, the accumulation of several mutations (known as "cancer drivers") eventually may transform the cells and promote uncontrolled cellular growth. Despite work contributing to our understanding of the molecular and cellular aspects of cancer (*6*–*14*), we still only partially understand the initiation and progression of this disease. Acknowledging this gap, studies have focused on studying somatic mutations in normal human tissues and precancerous lesions, aiming to identify early clonal expansions (*3*, *15*–*18*). Clonal expansions detected in normal blood are enriched with mutations in several genes implicated in hematologic cancers (*3*, *19*). Ultradeep sequencing studies by Martincorena *et al.* (*17*, *18*) in normal skin and esophagus tissues focused on 74 cancer genes and detected a high burden of low-allele frequency mutations associated with skin and esophagus squamous cell carcinoma. Despite these associations, it remains unclear which specific clones will eventually develop into cancer. Collectively, these findings emphasize the need to comprehensively map and study the prevalence and size of clonal expansion across human tissues.

[1]Broad Institute of MIT and Harvard, Cambridge, MA, USA. [2]Center for Cancer Research, Massachusetts General Hospital, Boston, MA, USA. [3]Harvard Medical School, Boston, MA, USA. [4]Ocular Genomics Institute, Department of Ophthalmology, Massachusetts Eye and Ear, Boston, MA, USA. [5]Biorepositories and Biospecimen Research Branch, Cancer Diagnosis Program, National Cancer Institute, Bethesda, MD, USA. [6]Oncological Sciences, Icahn School of Medicine at Mount Sinai Hospital, New York, NY, USA. [7]Department of Pathology, Massachusetts General Hospital, Boston, MA, USA.
***Corresponding author. Email: gadgetz@broadinstitute.org**

A pipeline for detecting somatic mutations using RNA-seq data

For genomic data derived from normal tissues, we leveraged the Genotype–Tissue Expression (GTEx) project (*20*), a collection of data generated from more than 30 normal primary tissues from hundreds of healthy individuals. These data include RNA sequencing (RNA-seq) data of the tissues as well as whole-genome and whole-exome sequencing data of DNA extracted from matched blood samples (release V7), providing an opportunity to explore all genes and tissues for the existence of macroscopic clones that have expanded to a detectable level in bulk RNA-seq.

To detect somatic mutations from bulk RNA-seq data, we needed to first develop a pipeline, called RNA-MuTect, to analyze this type of data. To develop our approach for detecting somatic mutations from RNA-seq data, we initially focused on a training set of 243 tumor samples (representing six tumor types) from The Cancer Genome Atlas (TCGA) for which both DNA and RNA were co-isolated from the same cells (table S1). Applying our standard somatic mutation calling pipeline (that was developed for DNA) to both DNA and RNA from the tumor samples, and using the matched-normal DNA as a germline control (*21*), we found that the number of mutations in RNA exceeded the number in the corresponding DNA by a factor of 5 (Fig. 1A and fig. S1A) (*21*). Moreover, 65% of the DNA-based mutations were not detected in the RNA, and 92% of the RNA-based mutations were not found in the DNA (*21*). One obvious reason for not detecting DNA-based mutations in the RNA is the insufficient sequence coverage in genes with low expression levels; indeed, in a typical RNA sample, only 55% of the transcriptome had sufficient coverage (≥95% sensitivity) to detect mutations at the median DNA allele fraction (fig. S1B). When accounting for the actual allele fractions of the DNA mutations and coverage of RNA transcripts, RNA-MuTect detected 82% of the sufficiently covered mutations (fig. S2, A to D) (*21*).

Next, to address the excessive mutations detected only in the RNA, we developed RNA-MuTect, which is based on several key filtering steps (fig. S3), including (i) removal of alignment errors by using two different RNA aligners; (ii) removal of sequencing errors by a site-specific error model built upon thousands of normal RNA-seq data; and (iii) removal of RNA editing sites using known databases (*21*). The vast majority (93%) of RNA mutations were filtered out (fig. S2, E to G), reaching a median precision of 0.91 across samples (Fig. 1B), and only a median of three detected mutations per sample remained in the RNA-only set. RNA-MuTect retained a high overall median sensitivity of 0.7 after filtering (Fig. 1B and fig. S2E) (*21*), removing as few as 10% of mutations that were detected in the DNA. Of note, RNA-MuTect outperformed previous methods (*22*, *23*) in terms of both sensitivity and precision for detecting mutations in RNA-seq (*21*). To evaluate the robustness of RNA-MuTect on an independent dataset, we collected a validation set of 303 TCGA samples representing six tumor types (five differed from the training set; table S1). RNA-MuTect achieved high sensitivity and precision on the validation set, in agreement with the training set results (sensitivity of 0.72 and precision of 0.87; Fig. 1B).

The high overall performance of RNA-MuTect enabled us to apply our standard tools for finding drivers and mutational signatures to RNA-based mutations (*21*, *24*, *25*), which yielded results very similar to what was found in the DNA (Fig. 1, C and D, and figs. S4 and S5) (*21*). Our analysis did, however, identify a yet-unreported mutational signature in the RNA dominated by C>T mutations; this signature represented only 7% of the mutations, with the majority originating from a single colon cancer sample (Fig. 1D). Of these mutations, 75% were sufficiently covered but not detected in the DNA, which suggests that this signature may reflect a C>U RNA-editing process.

Notably, to obtain a conservative (i.e., higher) estimate of the false positive rate, we considered

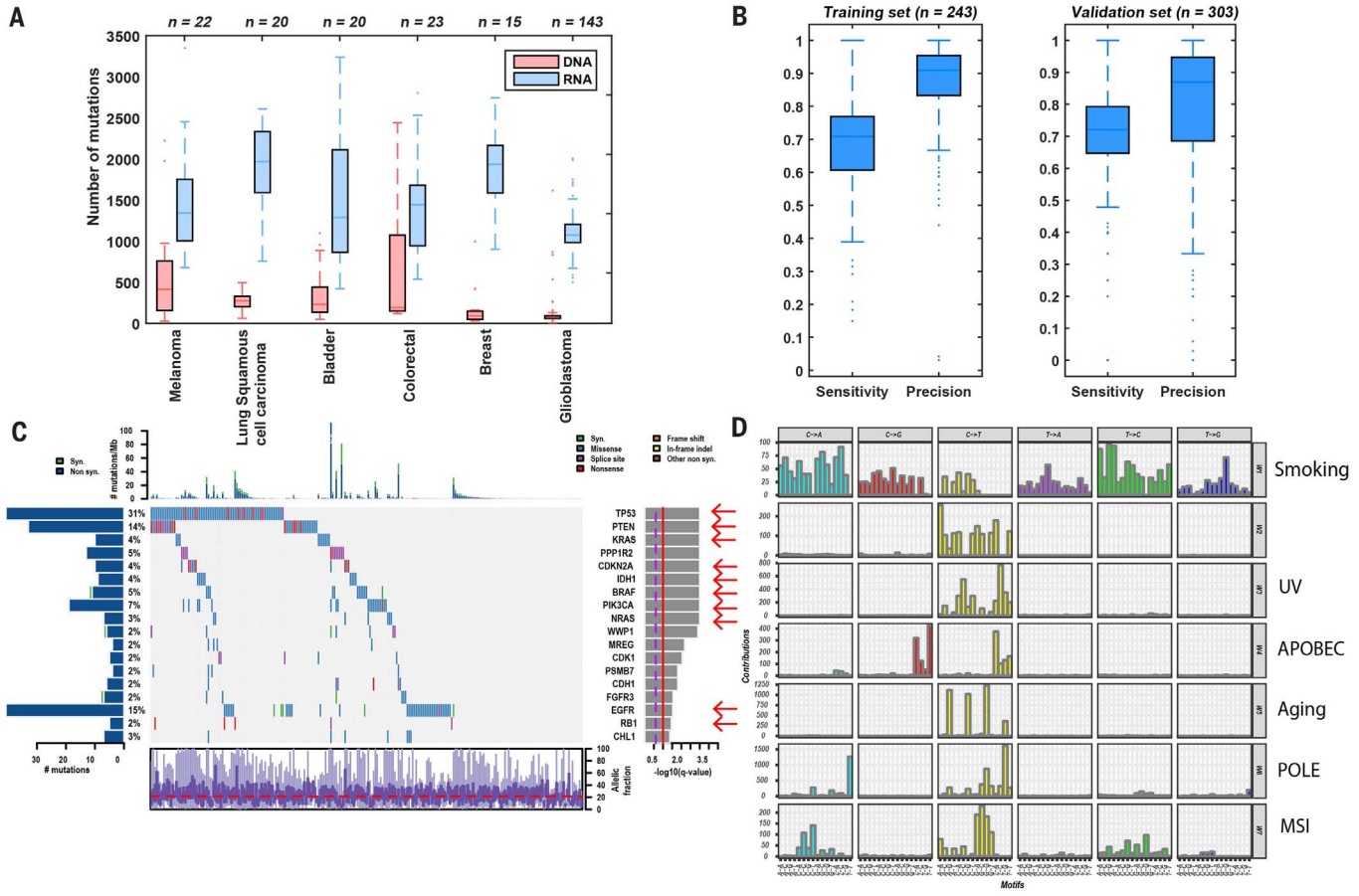


Fig. 1. Validation of RNA-MuTect in TCGA samples. (**A**) Total number of mutations detected before filtering in DNA (red) and RNA (blue) across samples in each TCGA cohort. (**B**) Sensitivity and precision of sufficiently covered sites across training and validation samples. Box plots show median, 25th, and 75th percentiles. The whiskers extend to the most extreme data points not considered outliers, and the outliers are represented as dots. (**C**) Co-mutation plot with mutations across the 243 TCGA samples, overall frequencies, allele fractions, and significance levels of candidate cancer genes ($Q < 0.05$) identified by applying MutSig2CV (*24*) on the mutations detected in the RNA. Genes marked with a red arrow were also identified as significantly mutated in the DNA. (**D**) Mutational signatures identified by SignatureAnalyzer (*25*) on the basis of mutations detected in the RNA. The mutational signatures identified are (i) a mixture of smoking and nucleotide-excision repair signatures (W1, combination of COSMIC signatures 4 and 5, cosine similarities of 0.7 and 0.75, respectively); (ii) UV (W3, COSMIC signature 7, cosine similarity = 0.95); (iii) APOBEC (W4, COSMIC signature 13, cosine similarity = 0.9); (iv) aging (W5, COSMIC signature 1, cosine similarity = 0.9); (v) POLE (W6, COSMIC signature 10, cosine similarity = 0.88); (vi) MSI (W7, COSMIC signature 15, cosine similarity = 0.8); and (vii) W2, a signature found only in the RNA.

mutations as false positives if they were detected in the RNA but not in the DNA while having sufficient coverage in the DNA. Although these mutations could in theory be true RNA-only mutations generated via RNA-specific processes (but not in the RNA-editing databases), it is more likely that they are in fact present in the DNA but at allele fractions too low to be detected, as our detection sensitivity calculations assume that the underlying allele fractions of a mutation are the same in the DNA and RNA. Although these two allele fractions are often close, they can vary as a result of variable gene- and allele-specific expression in different cell types within the sample. One way to test this is by examining the correlation between the number of RNA-only mutations and the number of true positive mutations detected in both RNA and DNA. We observed a high correlation (Spearman $R = 0.6$, $P = 4.2 \times 10^{-30}$). This indicates that many of the RNA-only mutations are likely also in the DNA, because we would not expect any correlation to exist between false positive (generated by either noise or RNA processes) and true positive mutations. Nonetheless, we continued with our conservative approach throughout this study and considered all RNA-only mutations detected in sufficiently covered corresponding DNA loci to be false positive mutations. Overall, we conclude that high-precision analysis of somatic mutations based on RNA is achievable despite the apparent limitations in calling mutations de novo from RNA-seq data, allowing for most cancer-associated genes as well as mutational processes to be revealed from RNA-seq data.

Finally, to evaluate the performance of RNA-MuTect on normal tissues, we applied it to a set of 35 tumor-adjacent normal samples collected in TCGA, wherein DNA and RNA were co-isolated from the same sample (table S1). After ensuring that the samples were not contaminated with tumor cells (*26*), we detected 114 DNA-based mutations, with a median allele fraction of 0.06. These mutations and their low allele fractions reflect the existence of small, yet macroscopic, clones in these samples, as expected in normal tissues. Of only eight mutations detected in the DNA that had sufficient sequencing coverage in the RNA to enable detection (*21*), three were indeed detected, one had evidence in two reads (just below our detection level), and the remaining four had no supporting reads in the RNA (table S2). Similarly, the 175 RNA-based mutations had an average allele fraction of 0.07; of the 86 that were sufficiently covered in the DNA, 13 mutations were detected. Overall, the number of RNA-only mutations per sample was very low (median of 1, average of 2; table S2). Because only half of the RNA-based mutations had sufficient coverage in the DNA, we conservatively estimated

the total number of false positive RNA-based mutations per sample to be between 2 and 4.

Overall, when applying RNA-MuTect to normal samples with coextracted DNA and RNA data, we found that DNA mutations with allele fractions of >0.07 could be detected in the RNA in cases where the gene was sufficiently highly expressed. As a specific example, a mutation with an allele fraction of 0.05 requires coverage by at least 124 reads in order to have >95% chance of being detected, and ~17% of a typical transcriptome from a TCGA RNA-seq sample is covered to that depth (fig. S1B). More important, RNA-MuTect detected a low number of potential false positive calls per sample in normal tissues, consistent with what we found in our cancer samples.

Detecting somatic clonal expansions in normal tissues

After establishing RNA-MuTect's performance on both cancer and normal samples, we sought to study somatic mutations across a comprehensive collection of normal tissues by analyzing RNA-seq data from the GTEx project (*20*). For a mutation to be detected in bulk RNA extracted from a normal tissue, a macroscopic clone that harbors and expresses the somatic mutation needs to contribute a sufficient amount of RNA such that the signal can be observed over the background RNA from other cells in the sample (e.g., muscle and fat cells typically do not proliferate, thus diluting the signal from the expanding clone) (Fig. 2A). Thus, the ability to detect a somatic mutation depends on (i) the clonal diversity of the sample, (ii) the depth of sequencing, and (iii) the expression level of the mutated gene. In the GTEx dataset, RNA was extracted from a relatively large amount of tissue material [~20 mg of tissue, estimated to represent 30,000 to 730,000 cells depending on tissue type (*21*)], limiting our ability to identify mutations present in microscopic clonal populations. We did, however,

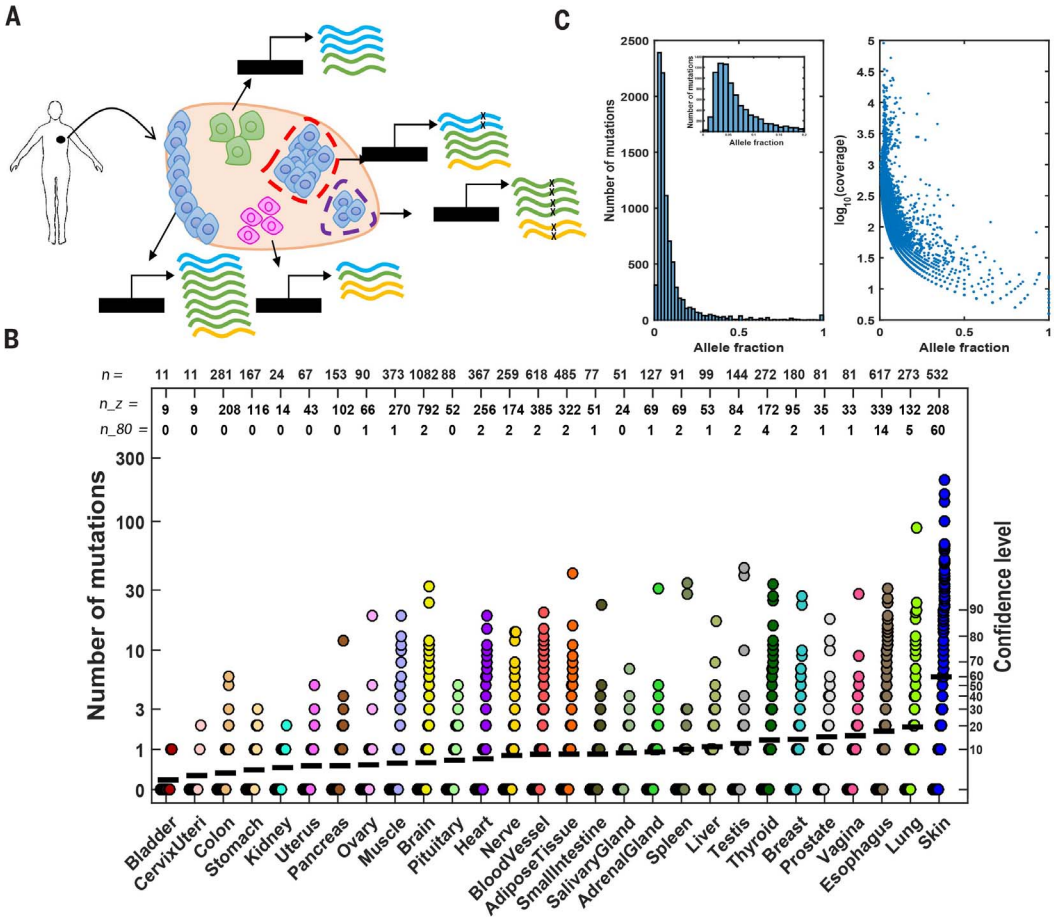


Fig. 2. Somatic clonal expansion in normal tissues. (**A**) An illustration of the composition of bulk RNA extracted from a normal human tissue. The biopsy consists of three different cell types that express different transcripts (marked in blue, green, and yellow) at different levels. Blue cells represent cells with a higher probability to form clones. Two clones, small and large, are denoted by purple- and red-dashed outlines, respectively. Mutated reads are marked with an X. The allele fractions of the mutations in the blue and green genes are the same (0.25; 2/8 and 4/16 reads, respectively), despite the different clone sizes. Additionally, the allele fraction of the mutation in the yellow gene is higher than the allele fractions of the mutations in the blue and green genes (0.33; 2/6 reads), even though the yellow mutation is supported by the same (or smaller) number of reads. These scenarios illustrate the challenge of identifying somatic mutations in bulk normal tissue due to a mixture of cell types and the relatively small clones. Moreover, inferences about clone size are limited because different cell types exist in different proportions and express transcripts at different levels. (**B**) Numbers of mutations detected in RNA-seq of 28 of the 29 studied tissues (we did not detect mutations in six fallopian tube samples). Each sample is represented by a circle. Black horizontal bars represent mean numbers of mutations in each tissue type. A confidence level from our estimation of false positives in the validation data is indicated in the right *y* axis. Specifically, this confidence level is computed as the *x*th percentile on the number of false positive calls (RNA-only mutations in DNA-powered sites) found in the validation set. "*n*" values represent the total number of samples analyzed in each tissue; "*n_z*" values represent the number of samples in which no mutations were detected; and "*n_80*" values represent the number of samples in which more than 13 mutations were found (equivalent to a confidence level of 80%). (**C**) Left: Distribution of allele fraction across all samples in which somatic mutations were detected. Inset: Mutations with allele fraction ≤ 0.2. Right: Allele fraction as a function of $\log_{10}$(coverage) for all detected mutations.

expect to detect macroscopic clones harboring mutations found in ~10% of the cells.

Applying RNA-MuTect to 6707 RNA-seq samples against their matched-blood DNA, which spanned 29 human tissues and 488 individuals (*21*), we detected 8870 somatic mutations in 37% (2519) of the samples, representing nearly all individuals (95%, 467/488; Fig. 2B and table S3). Applying our conservative estimate based on the TCGA data of two to four false positives per sample, 374 samples across 24 tissues had more than four mutations (within these, 106 samples across 13 tissues had more than 13 mutations, which is the conservative estimate at the 80th percentile of false calls). Note that mutations detected in samples with four or fewer mutations are not necessarily false positives; for example, some of these samples harbored known cancer driver mutations that likely increased cell fitness. The analyses described below provide evidence indicating that many of the detected mutations are somatic mutations that reflect clonal expansions in normal tissue.

Similar to what we observed from analyzing the tumor-adjacent normal samples from TCGA, the median allele fraction of the mutations in the GTEx normal tissue samples was 0.05 (Fig. 2C). Although our ability to detect low-allele fraction mutations in both DNA and RNA in GTEx samples was limited because they were extracted from adjacent but different samples, we were able to experimentally validate 5 of 28 mutations by deep sequencing (table S4) (*21*). Consistent with the majority of mutations being passengers, like we observe in cancer, ~59% of the GTEx mutations were missense mutations (fig. S6). However, we also found that a few mutations in normal tissue types matched mutations observed in their corresponding cancer types (table S5). Overall, these results support the idea that macroscopic clonal expansion occurs across many normal tissues throughout the body.

As expected, we found a negative correlation between RNA-seq coverage and allele fraction (Spearman $R = -0.8$, $P < 10^{-200}$; Fig. 2C) due to a higher probability of identifying low-allele fraction mutations in highly covered sites. However, after correcting for detection sensitivity [given the mutation allele fraction and the effective gene coverage (*21*)], we also observed a negative correlation between expression level and expected number of mutations (fig. S7). Similar findings in cancer are attributed to transcription-coupled repair, which is more active in highly expressed genes (*27*–*29*).

The tissues that typically harbor the greatest number of mutations are skin, lung, and esophagus. Associations between cancer incidence in these tissues and environmental factors such as ultraviolet (UV) radiation, air pollution, smoking, and nutritional habits were previously shown (*30*–*36*). Of note, sorting the normal tissues by mutation frequency rather than by the average number of mutations yielded essentially the same order (fig. S8). Looking at tissue subregions, we found that non–sun-exposed skin had more mutations than nonexposed skin and contained the highest number of mutations overall. Similarly, esophagus mucosa, from which esophageal squamous cell carcinomas derive (rather than from either the gastroesophageal junction or esophagus muscularis), had the second-highest mutational burden (fig. S9). Interestingly, the only tissue with a significant difference in the number of mutations between males and females was breast ($P = 2.1 \times 10^{-5}$, two-sided Wilcoxon test; fig. S10), reflecting the observation that breast tissue samples from males in the GTEx dataset are mainly composed of fat cells, whereas female breast tissue also includes epithelial cells.

Finally, we examined whether somatic mutations could be detected in the blood (*21*). Focusing on a previously defined set of 332 single-nucleotide variants detected in the blood of healthy individuals (*3*), we identified 87 mutations in the DNA across 83 individuals (17% of the studied individuals). For each of these 83 individuals, we next tested whether the exact variant was present in other solid tissues from the same individual. Only seven mutations were found in at least one RNA sequencing read in other tissues (each in a different individual) across different tissue types (five in brain, one each in thyroid and heart; table S6). This result most likely suggests that blood had been captured in the tissue samples. Previous results found an increase in the number of detected mutations above the age of 70 (*3*). Although the oldest person in our dataset was 70 years old, we did observe a trend (with borderline significance: $P = 0.049$, one-sided Wilcoxon test) in which these 83 individuals were older than the rest of the cohort.

Clonal expansion increases with age and tissue-specific cell proliferation rate

Several factors can affect the number of mutations accumulated in normal tissues: (i) age, (ii) accumulated DNA damage, and (iii) a tissue's propensity for forming macroscopic clones. All are expected to be more prominent in tissues with a higher cell proliferation rate (*37*, *38*). To test for these associations, we examined whether the age of the individual correlated with the average number of accumulated mutations across tissues. After the age of 45 (the cohort median age), both the number of CpG>T mutations (aging signature) and the total number of mutations significantly increased ($P = 0.001$ and $P = 2.2 \times 10^{-4}$, respectively, one-sided Wilcoxon test; Fig. 3A, top row). This significant association remained after (i) controlling for the number of tissues sequenced in each individual (table S7) and (ii) splitting all individuals into three age groups (fig. S11, A, B, and E). As expected, when considering the top 10 tissues with the highest level of cell proliferation (as determined by *MKI67* expression, a marker of proliferation) (table S8), this relationship became more significant for the total number of mutations ($P = 2.3 \times 10^{-5}$, one-sided Wilcoxon test) and remained similar for the aging mutations ($P = 0.004$, one-sided Wilcoxon test). In the 10 tissues with the lowest cell proliferation, no significant association with age was observed.

Next, we tested whether there was a tissue-specific association with age. A significant association was detected in skin and esophagus tissues ($P = 2.1 \times 10^{-6}$ and $P = 1.5 \times 10^{-5}$, respectively, one-sided Wilcoxon test; Fig. 3A, bottom row). When considering sun-exposed and non–sun-exposed skin separately, we found that although the number of observed mutations increased with age in both skin types, the increase was significantly greater in sun-exposed versus non–sun-exposed skin [odds ratio = 3.29 and 1.26, $P = 1.7 \times 10^{-8}$ and 0.68, respectively (Fisher's exact test), using the number of mutations below or above the tissue's median mutation number (= 2); fig. S11C]. Because these samples derive from the same tissue type, and hence are expected to have a similar cell proliferation rate, this result suggests that either (i) increased exposure to UV light and other environmental factors contributes to DNA damage as an individual ages, or (ii) the size of clones increases in both skin types with increasing age, but the clones in sun-exposed skin enable us to detect the mutations that were acquired earlier in life. Differences were also observed when testing esophagus-derived mucosa, gastroesophageal junction, and muscularis tissues [odds ratio = 4.3, 0.87, and 4.7; Fisher's $P = 2.6 \times 10^{-7}$, 1, and 0.17, respectively (median = 2); fig. S11D]. The lack of association in other tissues could be due to either low cell proliferation rates or the presence of clones below our detection threshold.

We next directly examined whether cell proliferation was associated with the number of accumulated mutations across tissues. Indeed, *MKI67* expression was significantly higher in tissues with a higher number of mutations ($P = 8.2 \times 10^{-4}$ and $P = 1.2 \times 10^{-4}$ for all primary and subregion tissues, respectively, one-sided Wilcoxon test; overall Spearman correlation of $R = 0.44$ and $P = 0.01$; Fig. 3B and fig. S11F) (*21*). Overall, these data suggest that both aging and exposure to mutagenic factors contribute to the number of accumulated mutations, especially in tissues with high cell proliferation rates (*37*, *39*).

Mutational signatures in normal tissues

In addition to the identified aging mutations (CpG>T), we examined whether and which other mutational processes were active in normal samples by applying SignatureAnalyzer (*21*, *25*). Because most samples had a small number of mutations (fig. S12) (*21*), we analyzed only the 169 samples with ≥10 mutations. SignatureAnalyzer identified a UV signature in skin samples. This UV signature is common in melanoma and has been reported in skin fibroblasts and normal skin samples (*17*, *36*). When examining sun-exposed and non–sun-exposed skin separately, the UV signature was active in 62/67 sun-exposed samples and only 1/5 non–sun-exposed samples (Fig. 3C; $P = 5.7 \times 10^{-4}$, Fisher's exact test). Interestingly, all the skin samples with ≥10 mutations analyzed here were from the 447 individuals of European ancestry. In contrast, none of the samples from the 74 individuals of African ancestry had more than six mutations (Fig. 3C), regardless of sun

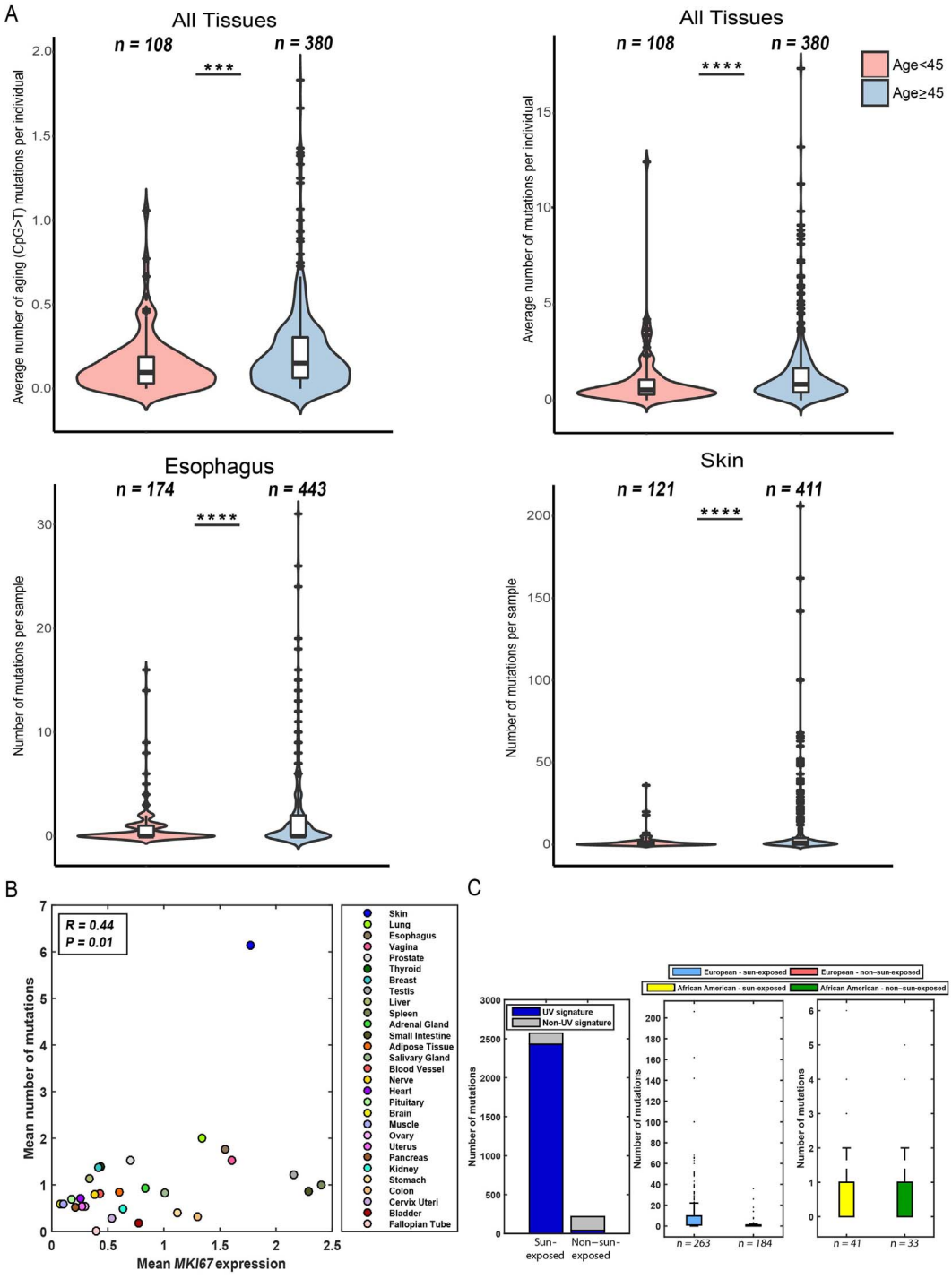


Fig. 3. Mutation load is associated with age and tissue-specific proliferation rate. (**A**) Top: Differences in the average number of aging-related mutations and total number of mutations before and after the age of 45 (left and right, respectively). Bottom: Differences in mutation number in esophagus and skin samples before and after the age of 45 (left and right, respectively). Box plots show median, 25th, and 75th percentiles in each group. Black crosses represent the outliers; asterisks represent significance levels. (**B**) Mean expression of the proliferation marker *MKI67* versus the average number of mutations found in each tissue. (**C**) Left: Number of mutations associated with the UV signature in sun-exposed and non–sun-exposed skin samples. Center: Number of mutations found in sun-exposed and non–sun-exposed skin samples taken from individuals of European ancestry. Right: Number of mutations found in sun-exposed and non–sun-exposed skin samples taken from individuals of African American ancestry. Boxes and whiskers are box plots with dots reflecting outliers.

exposure. Indeed, no difference in mutations was found between sun-exposed and non–sun-exposed skin among African American individuals (an average of 0.87 and 0.81 mutations, respectively; $P = 0.58$, one-sided Wilcoxon test). Overall, skin was the only tissue that showed a significant difference between the total number of mutations detected in European-ancestry versus African-ancestry samples ($P = 1.9 \times 10^{-5}$, one-sided Wilcoxon test; fig. S13).

Mutations in cancer genes in normal tissues

To determine whether somatic mutations in normal tissues occur in known cancer genes, we tested the frequency of nonsynonymous mutations within Cancer Gene Census (CGC) genes (*40*). This CGC set represents genes in which mutations have been causally implicated in cancer. We found that 3% of the samples and 33% of the individuals carried at least one nonsynonymous mutation in a CGC gene. Examining the tissues enriched with nonsynonymous mutations (*21*), we found that skin, esophagus, adipose, adrenal gland, and uterus tissues were significantly enriched with mutations in CGC genes (empirical $Q < 0.1$) after controlling for both gene length and coverage (fig. S14A).

Consistent with previous findings (*17*, *18*), the most frequently mutated cancer genes in our data were *TP53* and *NOTCH1* (Fig. 4A). Examining

whether the number of mutations differed between samples carrying *TP53* mutations and those that did not, we found that the *TP53*-associated samples had significantly more mutations ($P = 9.2 \times 10^{-9}$, two-sided Wilcoxon test). To test whether these *TP53* mutations conferred a growth advantage to the cell, we analyzed their allele fraction level relative to all other detected mutations in the same sample (*21*). Indeed, the allele fractions of *TP53* mutations were significantly higher than other mutations in the corresponding sample (empirical $P < 0.02$; fig. S14B). Similarly, we also found that the *NOTCH1*-mutated cases had a significant increase in the overall number of mutations ($P = 1 \times 10^{-7}$, two-sided Wilcoxon test) as well as a significantly higher allele fraction of the *NOTCH1* mutation (empirical $P < 9.9 \times 10^{-4}$; fig. S14C). These findings were independent of *TP53* and *NOTCH1* expression levels (fig. S14, B and C). This higher allele fraction of the *TP53* and *NOTCH1* mutations relative to other mutations in the same samples suggests that these mutations appear early in the history (i.e., the trunk) of these clones and potentially affected by loss of heterozygosity. However, because early appearance in the trunk does not guarantee that these mutations conferred a growth advantage, we cannot rule out the possibility that these early events are the result of genetic drift; we do consider this possibility unlikely, however, because both *TP53* and *NOTCH1* are known cancer genes. Overall, samples carrying *TP53* or *NOTCH1* mutations were found only in skin and esophagus tissues (with equal proportions in each tissue; table S3), but no samples harbored mutations in both of these genes.

We next examined whether any of the ~1760 recurrently mutated sites (hotspots) in known cancer genes were observed in normal tissues (table S9). We found 30 such mutations in eight tissues that overall included 27 hotspots in 12 genes (Fig. 4A and table S10). The gene with the greatest number of detected hotspot mutations was *TP53* with 16 known hotspot mutations in both skin and esophagus samples, 14 of which were observed once in our dataset (Fig. 4A). In total, 10 of these mutations were previously reported in either (i) normal human skin or peritoneal or uterine lavage fluids taken from healthy women, or (ii) human pluripotent stem cells (*16*, *17*, *41*, *42*). Reviewing the International Agency for Research on Cancer (IARC) TP53 database (*43*), we found that all of these mutations were annotated as deleterious by the SIFT algorithm (*44*). Interestingly, although all of the mutations were annotated as loss-of-function in yeast, three (R248Q, R248W, R282W) were reported to have gain-of-function activities (*45*). R248Q knock-in mice showed an earlier onset of tumor formation and reduced lifespan, as well as an expansion of

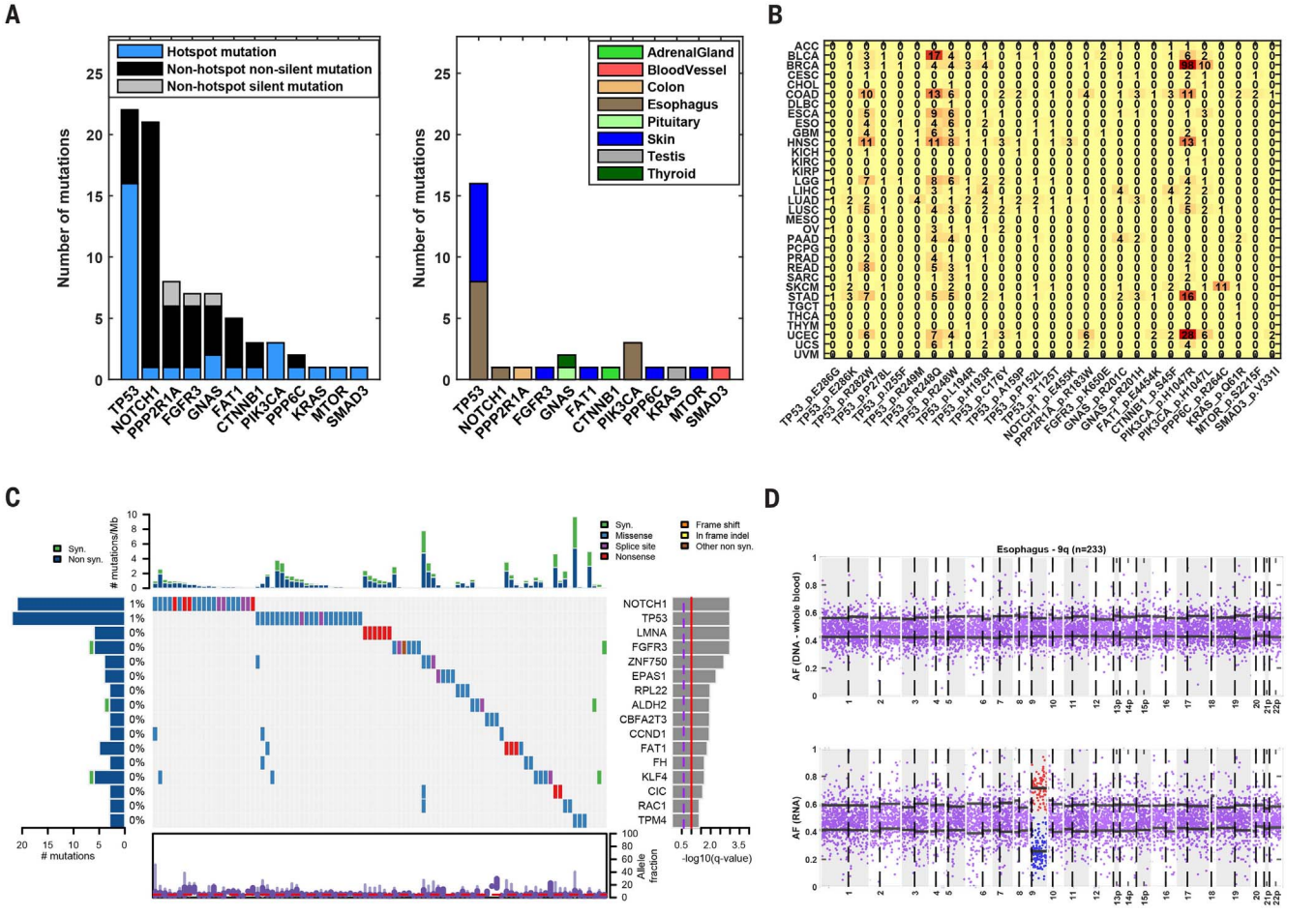


Fig. 4. Mutations in cancer genes across normal tissues. (**A**) Genes in which hotspot mutations were detected. Left: Number of hotspot mutations detected in each gene, and numbers of silent and nonsilent mutations that are not in hotspots. Right: Normal tissues in which the hotspot mutations were detected. All hotspot mutations except two (*FAT1* p.E4454K; *FGFR3* p.K650E) were annotated as pathogenic. (**B**) Occurrences of each hotspot mutation found in different TCGA cohorts. (**C**) Co-mutation plot for genes significantly mutated in a pan-normal analysis, ordered by their significance level (by MutSig2CV); data show 93 of 6707 samples with at least one mutation in these genes and the overall frequency among samples with at least one mutation. The distribution of allele fraction of mutations appears at the bottom. (**D**) Allelic imbalance in chromosome 9q of a normal esophagus sample. Top: Allele fraction of 233 heterozygous sites based on DNA from a matched-blood sample. Bottom: Allele fraction of heterozygous sites based on RNA from the esophagus sample. The black horizonal lines indicate the mean allele fraction per chromosomal arm of sites with allele fraction smaller or greater than 0.5.

hematopoietic and mesenchymal stem cell progenitors (*46*). The R248W variant was involved in multiple gain-of-function activities, including promotion of cell invasion (*47*) and increased cell proliferation (*48*) among others (*45*). The R282W variant increased colony formation (*49*). We found that these 14 hotspot sites shared some tissue specificity with the corresponding primary cancerous tissue, wherein four skin mutations and five esophagus mutations were also observed in melanoma and esophagus TCGA samples, respectively (Fig. 4B).

Among the other 14 non-*TP53* hotspot mutations, all but two were annotated as pathogenic by FATHMM (*50*), and seven were also observed in their corresponding cancer type (Fig. 4B). Three *PIK3CA* mutations in the p.H1047L and p.H1047R hotspots, which are common in multiple cancers (including esophageal cancer), were observed in normal esophagus mucosa samples. The well-known p.Q61R *KRAS* hotspot mutation found in a normal testis sample of a 58-year-old male was also reported in testicular germ cell cancer (*51*). The p.R183W hotspot mutation in the cell growth regulator *PPP2R1A* detected in a normal colon sample here was also detected in colorectal cancer. Although the β isoform (*PPP2R1B*) was discovered as a tumor suppressor in colon cancer cell lines and primary tumors (*52*), the α isoform had also been observed in a cohort of primary colon tumors (*53*). The hotspot mutation p.S45F in *CTNNB1* (β-catenin) found in the normal adrenal gland sample of a 58-year-old female had previously been detected in adrenocortical adenomas; *CTNNB1* is also significantly mutated in adrenocortical tumors (*10*, *54*, *55*) and when mutated deregulates the Wnt/β-catenin pathway. The hotspot mutation p.R264C in the *PPP6C* gene that we detected in normal skin was also observed in melanoma, wherein this gene was found to be significantly mutated (*56*).

To further explore whether clonal expansion observed in normal tissues was in part due to positive selection, we computed the dN/dS (ratio of nonsynonymous to synonymous substitutions) per gene (*57*), taking into account the trinucleotide context and the mutational spectrum (*21*). We found that both CGC genes and cancer genes listed in Lawrence *et al*. (*24*) were enriched with genes exhibiting a higher rate of nonsynonymous mutations (one-sided Wilcoxon $P = 3.4 \times 10^{-4}$ and $P = 9.3 \times 10^{-4}$, respectively). These data suggest that some of these mutations may confer a selective advantage. Of note, these results become insignificant when removing genes identified in skin and esophagus tissues. This finding could be due to the overall low number of mutations detected in the other tissues; alternatively, it may suggest that clones in skin and esophagus tissues undergo positive selection, whereas clones in the other tissues reflect genetic drift.

To more specifically identify which of these cancer genes are significantly mutated, we performed a pan-normal analysis by applying MutSig2CV (*24*) to all 2519 samples in which we detected at least one mutation, restricting the test to 718 known cancer genes (table S11). This analysis yielded 16 significantly mutated genes, with 99 nonsilent mutations spanning 17 tissues, 93 samples, and 82 individuals (Fig. 4C and fig. S14D). In addition to *TP53*, *NOTCH1*, and *FAT1* previously reported as significantly mutated in normal skin (*17*), we also identified other genes such as *RAC1* and *ZNF750*, which are significantly mutated in melanoma and esophagus squamous cell carcinoma, respectively (*9*, *24*). Overall, our results show that cancer genes and hotspots are present in normal tissues, especially in skin and esophagus tissues.

Allelic imbalance in normal tissues

To study other somatic alterations in normal samples, we developed a method for identifying allelic imbalance across chromosome arms using RNA-seq data (*21*), which is similar to previous approaches used for detecting allelic imbalance (*58*, *59*). To test our approach, we applied it to four TCGA samples for which DNA and RNA were coextracted and showed that the vast majority of allelic imbalance events at the chromosomal arm level detected in the RNA were also found in the DNA, and vice versa (fig. S15). In addition, we found a high correlation between the allele fraction of heterozygous sites in the RNA and in the DNA (R range = 0.45 to 0.7, $P < 8 \times 10^{-225}$; fig. S16), which suggests that approaches developed for detecting allelic imbalance in DNA can also work for RNA.

Similar to a recent concurrent study of normal esophagus DNA (*18*), we identified eight esophagus mucosa samples that had an allelic imbalance in 9q (Fig. 4D and fig. S17). Two of the eight samples also had a nonsense or missense mutation in *NOTCH1* (hypergeometric $P = 0.02$), a gene also located on 9q. The allele fraction of these mutations was relatively high (0.22 and 0.12, respectively) and at the top quintile of their corresponding samples. This might suggest that either the wild-type copy of these chromosome arms was lost, or that the mutated copy was gained. Interestingly, 9q loss was more common in esophageal dysplasia than in esophageal squamous cell carcinoma (*60*). Its detection here in nondysplastic lesions suggests that this may be an early event in the development of dysplasia. One additional sample with 9q imbalance was found to carry mutations in both *TP53* and *FAT1*. An allelic imbalance in 22p and a mutation in *NOTCH1* were also identified in an additional esophagus sample (fig. S17). Finally, we identified a testis sample with a strong allelic imbalance in 17p, with no point mutation detected (fig. S17).

Discussion

This study presents a comprehensive overview of somatic clonal expansion in human tissues. Although the use of RNA to detect somatic mutations is limited to expressed genes, we found that RNA analysis can reveal true somatic variations after accounting for both sequencing and alignment noise; moreover, RNA-based analysis can identify both underlying mutational processes and significantly mutated genes. Our approach enabled us to detect thousands of somatic mutations across all human tissues and in almost all tested individuals, including mutations at cancer hotspots and other cancer genes.

Macroscopic clonal expansion was detected in all tissues. However, greater numbers of accumulated mutations were observed in sun-exposed skin, esophagus mucosa, and lung than in other tissues. All three of these tissues are exposed to carcinogenic environmental factors, emphasizing the contribution of extrinsic factors to the mutagenesis process. Indeed, these tissues are also among those carrying the greatest number of somatic mutations in cancer patients (*28*), consistent with the notion that a non-negligible proportion of the mutations observed in cancer accumulate well before disease (*37*). In both skin and esophagus, we observed an association between the number of mutations in normal tissue and age, suggesting a contribution of somatic mosaicism to the aging phenotype (*61*). The lack of association with age in normal lung tissue may be masked as a result of the effects of other factors that are missing in our data, such as smoking or exposure to air pollution.

Beyond these intrinsic and extrinsic factors, the cellular microenvironment and tissue architecture are likely to influence the differences observed among tissues. Studies of different tumor types have shown differences in both the composition of the microenvironment and the transcriptional program active in each tissue (*62*–*69*). In addition, it was previously argued that tissue compartmentalization can affect the rate at which cancer mutations accumulate (*70*). For instance, the arrangement of the intestinal epithelium into crypts and villi is believed to limit the expansion of fitter cells (*71*). Overall, the complex nature of transformation from a normal to a cancer cell within different tissues is a result of the interplay among genetic and epigenetic events, tissue structure, exposure, and the tissue microenvironment. More comprehensive and dedicated data and metadata from various tissues should be collected to further study these relationships.

Relative to studies focusing on microscopic clones (*17*, *18*), we found a significantly lower number of clonal expansions, even though our scale was much larger and not restricted to a specific set of genes. Although this result can be partially explained by our missing mutations in genes with low expression levels, it also suggests that the majority of clones remain microscopic and do not expand to a size that can currently be detected by bulk RNA-seq. In addition, *TP53* and *NOTCH1* were the most mutated genes in our data with a relatively high allele fraction, but their overall frequency was lower than previously observed in microscopic clones. This suggests that mutations in these gene might not be able to drive clonal growth beyond a certain size without additional genetic, epigenetic, or environmental contributions. Furthermore, it should be noted that we identified known driver genes in some clones but not in many others. This observation may suggest that these clones

do not have greater fitness and are the result of genetic drift. In this study, we decided not to draw any conclusions from the distribution of allele fractions on selection beyond our findings for *TP53* and *NOTCH1* because of the nontrivial relation between variant allele fraction in RNA-seq and clone size. Large-scale studies analyzing DNA sequencing data are needed to better distinguish selection versus drift in macroscopic clones in normal tissues.

The overall low rate of cancer-related events in our data (<10%) most likely reflects both our detection sensitivity and the fact that we have analyzed only a single biopsy from each tissue type in each individual. Given previous results from deep sequencing on much smaller tissue biopsies (*17*, *18*), it is reasonable to assume that we would have detected a larger number of somatic mutations across all normal tissues if we analyzed more biopsies from any given tissue type, and if those biopsies were more enriched with epithelial cells. This implies that although these macroscopic clones have expanded to the point of detection, they would remain harmless and may not develop into cancer until—and only if—additional transforming events occur. Also, the detection of hotspots and other mutations in cancer genes across various normal human tissues emphasizes the need for identifying drivers of the disease while considering the nonpathogenic landscape of mutations. Such findings may have an impact on the selection of therapeutic and vaccination targets.

Understanding the earliest genetic events that occur in human tissues may advance our understanding of aging and cancer. Therefore, initiatives such as the Pre-Cancer Genome Atlas (*72*) will substantially aid our ability to detect and treat the disease in its early stages. Because all individuals in this study are deceased, we cannot determine whether the detected clones would have eventually developed into cancer upon acquisition of additional genetic or epigenetic abnormalities. Studying clonal expansion of normal samples longitudinally as they progress from normal tissue to microscopic clones and finally to macroscopic clones will shed light on which of these premalignant lesions has the capacity to transform into cancer; moreover, such a longitudinal study can reveal the required combinations of genetic and/or epigenetic events needed for transformation.

Methods summary

We developed a method, called RNA-MuTect, for identifying somatic mutations from a tissue RNA sample and its matched-normal DNA. RNA-MuTect includes several filtering steps designed for RNA sequences. RNA-MuTect was validated on both cancer and normal samples from TCGA, wherein DNA and RNA were coextracted from the same samples. A power analysis was performed to evaluate the statistical power of observing a mutation, given the mutation allele fraction and sequence coverage at the site. MutSig2CV and SignatureAnalyzer (*24*, *25*) were applied for identifying significantly mutated genes and mutational signatures, respectively. A context-dependent dN/dS analysis was performed for identifying genes with an excessive number of protein-altering mutations. We applied HaplotypeCaller and fitted a beta distribution in order to detect events of allelic imbalance at the chromosome arm level.

REFERENCES AND NOTES

1. C. D. McFarland, K. S. Korolev, G. V. Kryukov, S. R. Sunyaev, L. A. Mirny, Impact of deleterious passenger mutations on cancer progression. *Proc. Natl. Acad. Sci. U.S.A.* **110**, 2910–2915 (2013). doi: 10.1073/pnas.1213968110; pmid: 23388632
2. M. Vermulst *et al.*, DNA deletions and clonal mutations drive premature aging in mitochondrial mutator mice. *Nat. Genet.* **40**, 392–394 (2008). doi: 10.1038/ng.95; pmid: 18311139
3. S. Jaiswal *et al.*, Age-related clonal hematopoiesis associated with adverse outcomes. *N. Engl. J. Med.* **371**, 2488–2498 (2014). doi: 10.1056/NEJMoa1408617; pmid: 25426837
4. A. Poduri, G. D. Evrony, X. Cai, C. A. Walsh, Somatic mutation, genomic variation, and neurological disease. *Science* **341**, 1237758 (2013). doi: 10.1126/science.1237758; pmid: 23828942
5. M. Greaves, C. C. Maley, Clonal evolution in cancer. *Nature* **481**, 306–313 (2012). doi: 10.1038/nature10762; pmid: 22258609
6. Cancer Genome Atlas Research Network, The Molecular Taxonomy of Primary Prostate Cancer. *Cell* **163**, 1011–1025 (2015). doi: 10.1016/j.cell.2015.10.025; pmid: 26544944
7. C. W. Brennan *et al.*, The somatic genomic landscape of glioblastoma. *Cell* **155**, 462–477 (2013). doi: 10.1016/j.cell.2013.09.034; pmid: 24120142
8. Cancer Genome Atlas Research Network, Integrated genomic characterization of oesophageal carcinoma. *Nature* **541**, 169–175 (2017). doi: 10.1038/nature20805; pmid: 28052061
9. D.-C. Lin *et al.*, Genomic and molecular characterization of esophageal squamous cell carcinoma. *Nat. Genet.* **46**, 467–473 (2014). doi: 10.1038/ng.2935; pmid: 24686850
10. S. Zheng *et al.*, Comprehensive Pan-Genomic Characterization of Adrenocortical Carcinoma. *Cancer Cell* **29**, 723–736 (2016). doi: 10.1016/j.ccell.2016.04.002; pmid: 27165744
11. Cancer Genome Atlas Research Network, Integrated genomic and molecular characterization of cervical cancer. *Nature* **543**, 378–384 (2017). doi: 10.1038/nature21386; pmid: 28112728
12. K. A. Hoadley *et al.*, Cell-of-Origin Patterns Dominate the Molecular Classification of 10,000 Tumors from 33 Types of Cancer. *Cell* **173**, 291–304.e6 (2018). doi: 10.1016/j.cell.2018.03.022; pmid: 29625048
13. G. Genovese *et al.*, Synthetic vulnerabilities of mesenchymal subpopulations in pancreatic cancer. *Nature* **542**, 362–366 (2017). doi: 10.1038/nature21064; pmid: 28178232
14. T. A. Knijnenburg *et al.*, Genomic and Molecular Landscape of DNA Damage Repair Deficiency across The Cancer Genome Atlas. *Cell Rep.* **23**, 239–254.e6 (2018). doi: 10.1016/j.celrep.2018.03.076; pmid: 29617664
15. X. Cai *et al.*, Single-cell, genome-wide sequencing identifies clonal somatic copy-number variation in the human brain. *Cell Rep.* **8**, 1280–1289 (2014). doi: 10.1016/j.celrep.2014.07.043; pmid: 25159146
16. J. D. Krimmel *et al.*, Ultra-deep sequencing detects ovarian cancer cells in peritoneal fluid and reveals somatic TP53 mutations in noncancerous tissues. *Proc. Natl. Acad. Sci. U.S.A.* **113**, 6005–6010 (2016). doi: 10.1073/pnas.1601311113; pmid: 27152024
17. I. Martincorena *et al.*, High burden and pervasive positive selection of somatic mutations in normal human skin. *Science* **348**, 880–886 (2015). doi: 10.1126/science.aaa6806; pmid: 25999502
18. I. Martincorena *et al.*, Somatic mutant clones colonize the human esophagus with age. *Science* **362**, 911–917 (2018). doi: 10.1126/science.aau3879; pmid: 30337457
19. G. Genovese *et al.*, Clonal hematopoiesis and blood-cancer risk inferred from blood DNA sequence. *N. Engl. J. Med.* **371**, 2477–2487 (2014). doi: 10.1056/NEJMoa1409405; pmid: 25426838
20. J. Lonsdale *et al.*, The Genotype-Tissue Expression (GTEx) project. *Nat. Genet.* **45**, 580–585 (2013). doi: 10.1038/ng.2653; pmid: 23715323
21. See supplementary materials.
22. X. Tang *et al.*, The eSNV-detect: A computational system to identify expressed single nucleotide variants from transcriptome sequencing data. *Nucleic Acids Res.* **42**, e172 (2014). doi: 10.1093/nar/gku1005; pmid: 25352556
23. Q. Sheng, S. Zhao, C.-I. Li, Y. Shyr, Y. Guo, Practicability of detecting somatic point mutation from RNA high throughput sequencing data. *Genomics* **107**, 163–169 (2016). doi: 10.1016/j.ygeno.2016.03.006; pmid: 27046520
24. M. S. Lawrence *et al.*, Discovery and saturation analysis of cancer genes across 21 tumour types. *Nature* **505**, 495–501 (2014). doi: 10.1038/nature12912; pmid: 24390350
25. J. Kim *et al.*, Somatic ERCC2 mutations are associated with a distinct genomic signature in urothelial tumors. *Nat. Genet.* **48**, 600–606 (2016). doi: 10.1038/ng.3557; pmid: 27111033
26. A. Taylor-Weiner *et al.*, DeTiN: Overcoming tumor-in-normal contamination. *Nat. Methods* **15**, 531–534 (2018). doi: 10.1038/s41592-018-0036-9; pmid: 29941871
27. M. A. Chapman *et al.*, Initial genome sequencing and analysis of multiple myeloma. *Nature* **471**, 467–472 (2011). doi: 10.1038/nature09837; pmid: 21430775
28. M. S. Lawrence *et al.*, Mutational heterogeneity in cancer and the search for new cancer-associated genes. *Nature* **499**, 214–218 (2013). doi: 10.1038/nature12213; pmid: 23770567
29. E. D. Pleasance *et al.*, A comprehensive catalogue of somatic mutations from a human cancer genome. *Nature* **463**, 191–196 (2010). doi: 10.1038/nature08658; pmid: 20016485
30. B. A. Gilchrest, M. S. Eller, A. C. Geller, M. Yaar, The pathogenesis of melanoma induced by ultraviolet radiation. *N. Engl. J. Med.* **340**, 1341–1348 (1999). doi: 10.1056/NEJM199904293401707; pmid: 10219070
31. B. Pesch *et al.*, Cigarette smoking and lung cancer—Relative risk estimates for the major histological types from a pooled analysis of case-control studies. *Int. J. Cancer* **131**, 1210–1219 (2012). pmid: 22052329
32. F. Kamangar, W.-H. Chow, C. C. Abnet, S. M. Dawsey, Environmental causes of esophageal cancer. *Gastroenterol. Clin. North Am.* **38**, 27–57 (2009). doi: 10.1016/j.gtc.2009.01.004; pmid: 19327566
33. O. Raaschou-Nielsen *et al.*, Air pollution and lung cancer incidence in 17 European cohorts: Prospective analyses from the European Study of Cohorts for Air Pollution Effects (ESCAPE). *Lancet Oncol.* **14**, 813–822 (2013). doi: 10.1016/S1470-2045(13)70279-1; pmid: 23849838
34. F. Islami *et al.*, High-temperature beverages and foods and esophageal cancer risk—A systematic review. *Int. J. Cancer* **125**, 491–524 (2009). doi: 10.1002/ijc.24445; pmid: 19415743
35. Y. Chen *et al.*, Consumption of hot beverages and foods and the risk of esophageal cancer: A meta-analysis of observational studies. *BMC Cancer* **15**, 449 (2015). doi: 10.1186/s12885-015-1185-1; pmid: 26031666
36. N. Saini *et al.*, The Impact of Environmental and Endogenous Damage on Somatic Mutation Load in Human Skin Fibroblasts. *PLOS Genet.* **12**, e1006385 (2016). doi: 10.1371/journal.pgen.1006385; pmid: 27788131
37. C. Tomasetti, B. Vogelstein, G. Parmigiani, Half or more of the somatic mutations in cancers of self-renewing tissues originate prior to tumor initiation. *Proc. Natl. Acad. Sci. U.S.A.* **110**, 1999–2004 (2013). doi: 10.1073/pnas.1221068110 pmid: 23345422
38. C. Tomasetti, B. Vogelstein, Variation in cancer risk among tissues can be explained by the number of stem cell divisions. *Science* **347**, 78–81 (2015). doi: 10.1126/science.1260825; pmid: 25554788
39. L. B. Alexandrov *et al.*, Clock-like mutational processes in human somatic cells. *Nat. Genet.* **47**, 1402–1407 (2015). doi: 10.1038/ng.3441; pmid: 26551669
40. S. A. Forbes *et al.*, COSMIC: Exploring the world's knowledge of somatic mutations in human cancer. *Nucleic Acids Res.* **43**, D805–D811 (2015). doi: 10.1093/nar/gku1075; pmid: 25355519
41. N. Nair *et al.*, Genomic Analysis of Uterine Lavage Fluid Detects Early Endometrial Cancers and Reveals a Prevalent Landscape of Driver Mutations in Women without Histopathologic Evidence of Cancer: A Prospective Cross-Sectional Study. *PLOS Med.* **13**, e1002206 (2016). doi: 10.1371/journal.pmed.1002206; pmid: 28027320
42. F. T. Merkle *et al.*, Human pluripotent stem cells recurrently acquire and expand dominant negative P53 mutations. *Nature* **545**, 229–233 (2017). pmid: 28445466
43. A. Petitjean *et al.*, Impact of mutant p53 functional properties on TP53 mutation patterns and tumor phenotype: Lessons from recent developments in the IARC TP53 database. *Hum. Mutat.* **28**, 622–629 (2007). doi: 10.1002/humu.20495; pmid: 17311302
44. P. Kumar, S. Henikoff, P. C. Ng, Predicting the effects of coding non-synonymous variants on protein function using

the SIFT algorithm. *Nat. Protoc.* **4**, 1073–1081 (2009). doi: 10.1038/nprot.2009.86; pmid: 19561590
45. P. A. J. Muller, K. H. Vousden, Mutant p53 in cancer: New functions and therapeutic opportunities. *Cancer Cell* **25**, 304–317 (2014). doi: 10.1016/j.ccr.2014.01.021; pmid: 24651012
46. W. Hanel *et al*., Two hot spot mutant p53 mouse models display differential gain of function in tumorigenesis. *Cell Death Differ.* **20**, 898–909 (2013). doi: 10.1038/cdd.2013.17; pmid: 23538418
47. P. A. J. Muller *et al*., Mutant p53 drives invasion by promoting integrin recycling. *Cell* **139**, 1327–1341 (2009). doi: 10.1016/j.cell.2009.11.026; pmid: 20064378
48. W. Yan, X. Chen, Identification of GRO1 as a critical determinant for mutant p53 gain of function. *J. Biol. Chem.* **284**, 12178–12187 (2009). doi: 10.1074/jbc.M900994200; pmid: 19258312
49. M. J. Scian *et al*., Tumor-derived p53 mutants induce oncogenesis by transactivating growth-promoting genes. *Oncogene* **23**, 4430–4443 (2004). doi: 10.1038/sj.onc.1207553; pmid: 15077194
50. H. A. Shihab *et al*., Predicting the functional, molecular, and phenotypic consequences of amino acid substitutions using hidden Markov models. *Hum. Mutat.* **34**, 57–65 (2013). doi: 10.1002/humu.22225; pmid: 23033316
51. H. Shen *et al*., Integrated Molecular Characterization of Testicular Germ Cell Tumors. *Cell Rep.* **23**, 3392–3406 (2018). doi: 10.1016/j.celrep.2018.05.039; pmid: 29898407
52. S. S. Wang *et al*., Alterations of the PPP2R1B gene in human lung and colon cancer. *Science* **282**, 284–287 (1998). doi: 10.1126/science.282.5387.284; pmid: 9765152
53. Cancer Genome Atlas Network, Comprehensive molecular characterization of human colon and rectal cancer. *Nature* **487**, 330–337 (2012). doi: 10.1038/nature11252; pmid: 22810696
54. S. Bonnet *et al*., Wnt/β-catenin pathway activation in adrenocortical adenomas is frequently due to somatic CTNNB1-activating mutations, which are associated with larger and nonsecreting tumors: A study in cortisol-secreting and -nonsecreting tumors. *J. Clin. Endocrinol. Metab.* **96**, E419–E426 (2011). doi: 10.1210/jc.2010-1885; pmid: 21084400
55. L. F. Leal *et al*., Wnt/β-catenin pathway deregulation in childhood adrenocortical tumors. *J. Clin. Endocrinol. Metab.* **96**, 3106–3114 (2011). doi: 10.1210/jc.2011-0363; pmid: 21849527
56. E. Hodis *et al*., A landscape of driver mutations in melanoma. *Cell* **150**, 251–263 (2012). doi: 10.1016/j.cell.2012.06.024; pmid: 22817889
57. M. Kimura, Preponderance of synonymous changes as evidence for the neutral theory of molecular evolution. *Nature* **267**, 275–276 (1977). doi: 10.1038/267275a0; pmid: 865622
58. J. R. González *et al*., A fast and accurate method to detect allelic genomic imbalances underlying mosaic rearrangements using SNP array data. *BMC Bioinformatics* **12**, 166 (2011). doi: 10.1186/1471-2105-12-166; pmid: 21586113
59. U. Weissbein, M. Schachter, D. Egli, N. Benvenisty, Analysis of chromosomal aberrations and recombination by allelic bias in RNA-Seq. *Nat. Commun.* **7**, 12144 (2016). doi: 10.1038/ncomms12144; pmid: 27385103
60. Z. Z. Shi *et al*., Consistent and differential genetic aberrations between esophageal dysplasia and squamous cell carcinoma detected by array comparative genomic hybridization. *Clin. Cancer Res.* **19**, 5867–5878 (2013). doi: 10.1158/1078-0432.CCR-12-3753; pmid: 24009147
61. R. A. Risques, S. R. Kennedy, Aging and the rise of somatic cancer-associated mutations in normal tissues. *PLOS Genet.* **14**, e1007108 (2018). doi: 10.1371/journal.pgen.1007108; pmid: 29300727
62. E. W. Lin, T. A. Karakasheva, P. D. Hicks, A. J. Bass, A. K. Rustgi, The tumor microenvironment in esophageal cancer. *Oncogene* **35**, 5337–5349 (2016). doi: 10.1038/onc.2016.34; pmid: 26923327
63. X. Sui, L. Lei, L. Chen, T. Xie, X. Li, Inflammatory microenvironment in the initiation and progression of bladder cancer. *Oncotarget* **8**, 93279–93294 (2017). doi: 10.18632/oncotarget.21565; pmid: 29190997
64. J. Villanueva, M. Herlyn, Melanoma and the tumor microenvironment. *Curr. Oncol. Rep.* **10**, 439–446 (2008). doi: 10.1007/s11912-008-0067-y; pmid: 18706274
65. D. F. Quail, J. A. Joyce, The Microenvironmental Landscape of Brain Tumors. *Cancer Cell* **31**, 326–341 (2017). doi: 10.1016/j.ccell.2017.02.009; pmid: 28292436
66. A. E. Place, S. Jin Huh, K. Polyak, The microenvironment in breast cancer progression: Biology and implications for treatment. *Breast Cancer Res.* **13**, 227 (2011). doi: 10.1186/bcr2912; pmid: 22078026
67. I. Soncin *et al*., The tumour microenvironment creates a niche for the self-renewal of tumour-promoting macrophages in colon adenoma. *Nat. Commun.* **9**, 582 (2018). doi: 10.1038/s41467-018-02834-8; pmid: 29422500
68. A. Ghoneum, H. Afify, Z. Salih, M. Kelly, N. Said, Role of tumor microenvironment in ovarian cancer pathobiology. *Oncotarget* **9**, 22832–22849 (2018). doi: 10.18632/oncotarget.25126; pmid: 29854318
69. V. Mittal *et al*., The Microenvironment of Lung Cancer and Therapeutic Implications. *Adv. Exp. Med. Biol.* **890**, 75–110 (2016). doi: 10.1007/978-3-319-24932-2_5; pmid: 26703800
70. J. Cairns, Mutation selection and the natural history of cancer. *Nature* **255**, 197–200 (1975). doi: 10.1038/255197a0
71. H. Quastler, F. G. Sherman, Cell population kinetics in the intestinal epithelium of the mouse. *Exp. Cell Res.* **17**, 420–438 (1959). doi: 10.1016/0014-4827(59)90063-1; pmid: 13672199
72. J. D. Campbell *et al*., The Case for a Pre-Cancer Genome Atlas (PCGA). *Cancer Prev. Res.* **9**, 119–124 (2016). doi: 10.1158/1940-6207.CAPR-16-0024; pmid: 26839336

ACKNOWLEDGMENTS

We thank B. Ebert, A. Bass, and T. R. Golub for helpful comments on the manuscript; J. Gastier-Foste and E. Zmuda for helpful information regarding TCGA samples; and M. Miller for help in editing the manuscript. **Funding:** Supported by the Broad-ISF postdoctoral fellowship and the Weizmann award for Women in Science (K.Y.) and by the GTEx LDACC (HHSN268201000029C) and the Paul C. Zamecnick, MD, Chair in Oncology at MGH (G.G.). **Author contributions:** K.Y., P.P., and G.G. conceived the idea; K.Y. and G.G. designed the study; J.H. helped with the MutSig analysis; F.A., J.K., C.S., H.Z., D.L., and D.R. contributed code for the analysis; K.K. and P.A.B. reviewed the pathological samples; J.G. performed the Fluidigm experiments; R.F. generated the docker with the RNA-MuTect pipeline; N.J.H., X.L., E.A.-L., N.S., A.V.S., and K.A. helped with the interpretation of the data; and K.Y. and G.G. wrote the manuscript. **Competing interests:** G.G. receives research funds from IBM and Pharmacyclics. G.G. is an inventor on patent applications related to MuTect, MutSig, and ABSOLUTE. **Data and materials availability:** All data are available in the manuscript or the supplementary materials. The code of RNA-MuTect is available on Zenodo (https://zenodo.org/record/2620062) and in the FireCloud workspace RNA_MuTect (https://portal.firecloud.org). RNA-MuTect is a pipeline that uses multiple tools subject to their own licenses and copyrights. All of these tools are free for academic use. Some tools may require a license from for-profit entities. The details (exact versions) of the different tools that are used in RNA-MuTect are listed in the README.txt in the Zenodo repository of the software.

SUPPLEMENTARY MATERIALS

science.sciencemag.org/content/364/6444/eaaw0726/suppl/DC1
Materials and Methods
Figs. S1 to S18
Tables S1 to S15
References (*73*–*88*)

15 November 2018; accepted 2 May 2019
10.1126/science.aaw0726

RESEARCH ARTICLE SUMMARY

NEURODEVELOPMENT

Spatiotemporal structure of cell fate decisions in murine neural crest

Ruslan Soldatov*, Marketa Kaucka*, Maria Eleni Kastriti*, Julian Petersen, Tatiana Chontorotzea, Lukas Englmaier, Natalia Akkuratova, Yunshi Yang, Martin Häring, Viacheslav Dyachuk, Christoph Bock, Matthias Farlik, Michael L. Piacentino, Franck Boismoreau, Markus M. Hilscher, Chika Yokota, Xiaoyan Qian, Mats Nilsson, Marianne E. Bronner, Laura Croci, Wen-Yu Hsiao, David A. Guertin, Jean-Francois Brunet, Gian Giacomo Consalez, Patrik Ernfors, Kaj Fried, Peter V. Kharchenko†, Igor Adameyko†

INTRODUCTION: Multipotent progenitors must choose among multiple downstream fates. In developing embryos, progenitor cells exhibit transcriptional or epigenetic heterogeneity that is related to early biases in cell fate choices, and can be externally induced or stochastic in nature. Molecular assessment of the transient states assumed by cells during these developmental progressions has the potential to illuminate how such fate-specific biases emerge and unfold to ensure fate commitment. With this aim, we examine multipotent neural crest cells—transient embryonic progenitors unique to vertebrates that build the head, teeth, neuroendocrine tissue, and autonomic and sensory nervous systems. Cranial neural crest preferentially gives rise to a multitude of mesenchymal types of facial cartilage and bones, in addition to neuronal, glial, and pigment cell–type progeny. By contrast, trunk neural crest does not form bone or cartilage derivatives in vivo. The logic and molecular mechanisms that allow neural crest to resolve multiple potential cell fates at each axial level remain poorly understood.

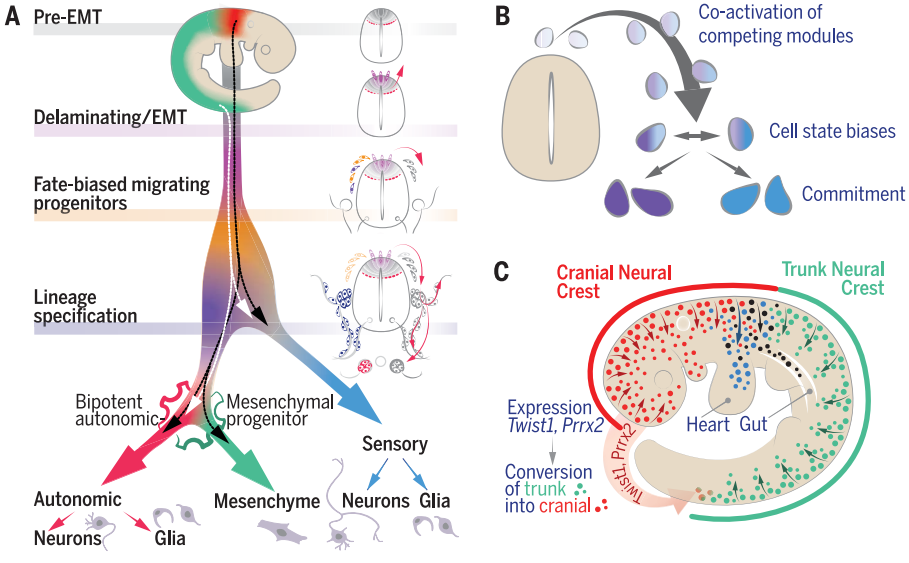
RATIONALE: Here we used single-cell and spatial transcriptomics with statistical analysis of branching trajectories to investigate lineage relationships in mouse neural crest. Combined with lineage tracing and functional perturbations, we addressed spatiotemporal dynamics associated with early cell fate decisions in mouse trunk and cranial neural crest cells with different fate potential.

RESULTS: We find that up to early migration, neural crest cells progress through a sequence of common transcriptional states, followed by fate bifurcations during migration that can be formalized as a series of sequential binary decisions. The first decision separates sensory neuro-glial fate from all other fates, whereas the second decision occurs between autonomic and mesenchymal lineages and reveals a bipotent *Phox2b*$^{+}$/*Prrx1*$^{+}$ subpopulation. Decision points uncover distinct roles of neural crest regulators: *Neurog2* is involved in early repression of melanocytes and activation of sensory fate at later steps. Each decision consists of initial coactivation, gradual biasing, and commitment phases. Early genes of competing cell fate programs coactivate in the same cells, starting from premigratory stage. As cells approach cell fate bifurcation points, increased synchronization of fate-specific programs and repulsion of competing fate programs lead to gradual appearance of cell fate bias, which becomes pronounced upon neural crest migration. Cell fate commitment culminates with activation of mutually exclusive, fate-specific gene expression programs. Early transcriptional patterns reveal that fate biasing of neural crest is already detectable when neural crest cells delaminate from the neural tube. In particular, the neuronal bias of trunk and mesenchymal bias of cranial neural crest emerge during delamination, indicating that this might be the time when the mesenchymal potential, distinct between cranial and trunk neural crest, is installed. In support to this hypothesis, we find that sustained overexpression of a single gene, *Twist1*, normally activated upon delamination only in the cranial compartment, is sufficient to reverse the trunk crest developmental program to a mesenchymal route.

ON OUR WEBSITE

Read the full article at http://dx.doi.org/10.1126/science.aas9536

CONCLUSION: Our analysis resolved a branching transcriptional trajectory of the differentiating neural crest, illustrating transcriptional implementation of major cell fate decisions and pinpointing the key differences defining cranial versus trunk neural crest potential. Our results show that neural crest cells differentiate through a series of stereotypical lineage-restriction events that involve coexpression and competition of genes driving alternative fate programs. ■



Cell fate acquisition in neural crest. (**A**) Stepwise model of neural crest developmental dynamics. EMT, epithelial-to-mesenchymal transition. (**B**) Key phases of fate decision in neural crest cells. (**C**) Different fate potential of cranial versus trunk neural crest is encoded by the mesenchymogenic genes *Twist1* and *Prrx2*. A single factor, *Twist1*, confers mesenchymal potential to trunk neural crest.

The list of author affiliations is available in the full article online.
*These authors contributed equally to this work.
†Corresponding author. Email: igor.adameyko@ki.se (I.A.); peter.kharchenko@post.harvard.edu (P.V.K.)
Cite this article as R. Soldatov *et al.*, *Science* **364**, eaas9536 (2019). DOI: 10.1126/science.aas9536

RESEARCH ARTICLE

NEURODEVELOPMENT

Spatiotemporal structure of cell fate decisions in murine neural crest

Ruslan Soldatov[1]*, Marketa Kaucka[2,3]*, Maria Eleni Kastriti[2,3]*, Julian Petersen[2,3], Tatiana Chontorotzea[3], Lukas Englmaier[2], Natalia Akkuratova[3,4], Yunshi Yang[3], Martin Häring[5], Viacheslav Dyachuk[6,7], Christoph Bock[8,9,10], Matthias Farlik[8], Michael L. Piacentino[11], Franck Boismoreau[12], Markus M. Hilscher[5,13], Chika Yokota[13], Xiaoyan Qian[13,14], Mats Nilsson[13], Marianne E. Bronner[11], Laura Croci[15], Wen-Yu Hsiao[16], David A. Guertin[16], Jean-Francois Brunet[12], Gian Giacomo Consalez[15], Patrik Ernfors[5], Kaj Fried[6], Peter V. Kharchenko[1,17]†, Igor Adameyko[2,3]†

Neural crest cells are embryonic progenitors that generate numerous cell types in vertebrates. With single-cell analysis, we show that mouse trunk neural crest cells become biased toward neuronal lineages when they delaminate from the neural tube, whereas cranial neural crest cells acquire ectomesenchyme potential dependent on activation of the transcription factor *Twist1*. The choices that neural crest cells make to become sensory, glial, autonomic, or mesenchymal cells can be formalized as a series of sequential binary decisions. Each branch of the decision tree involves initial coactivation of bipotential properties followed by gradual shifts toward commitment. Competing fate programs are coactivated before cells acquire fate-specific phenotypic traits. Determination of a specific fate is achieved by increased synchronization of relevant programs and concurrent repression of competing fate programs.

Multipotent progenitors acquire one of the multiple downstream fates. In developmental systems, progenitor cells exhibit transcriptional or epigenetic heterogeneity related to early biases in cell fate choices and can be oscillatory or stochastic (*1*–*3*). Understanding how fate-specific biases emerge and unfold to ensure fate commitment requires deeper understanding of cell profiles during progenitor, transient, and derivative states. Toward that goal, we examined a continuum of states in the neural crest (NC) lineage at different points along the murine rostrocaudal body axis during embryogenesis. As neural crest cell fate decisions are traceable, irreversible, and produce well-known differentiated cell types, we were able to investigate the interplay of multiple fate-specific genetic programs.

Multipotent neural crest cells are a migratory embryonic cell population found only in vertebrates that confers traits such as complex head, teeth, elaborate endocrine regulation, and autonomic and sensory nervous systems. Neural crest cells have distinct developmental potential along the anterior-posterior axis. Cranial neural crest cells give rise to mesenchymal cell types of the head, including facial cartilage and bone, glia, and some neurons of cranial ganglia and pigment cells (*4*). By contrast, trunk neural crest cells do not form bone or cartilage derivatives in vivo, even after being grafted to the head (*5*). However, despite knowledge about genes and signals that regulate neural crest development (*6*), the mechanisms that enable neural crest cells to commit to a multitude of possible cell fates at each axial level remain unclear.

Here we combine single-cell RNA sequencing (scRNA-seq) with spatial transcriptomics and lineage tracing to examine the spatiotemporal transcriptional landscape and cell fate decisions involved in cranial and trunk neural crest differentiation in the mouse embryo at the embryonic day 8.5 (E8.5) to E10.5 stages.

[1]Department of Biomedical Informatics, Harvard Medical School, Boston, MA 02115, USA. [2]Department of Molecular Neurosciences, Center for Brain Research, Medical University Vienna, 1090 Vienna, Austria. [3]Department of Physiology and Pharmacology, Karolinska Institutet, 17177 Stockholm, Sweden. [4]Institute of Translational Biomedicine, St Petersburg University, 199034 St Petersburg, Russia. [5]Department of Medical Biochemistry and Biophysics, Division of Molecular Neurobiology, Karolinska Institutet, 17177 Stockholm, Sweden. [6]Department of Neuroscience, Karolinska Institutet, 17177 Stockholm, Sweden. [7]National Scientific Center of Marine Biology, Far Eastern Branch, Russian Academy of Sciences, Vladivostok 690041, Russia. [8]CeMM Research Center for Molecular Medicine of the Austrian Academy of Sciences, Vienna, Austria. [9]Department of Laboratory Medicine, Medical University of Vienna, Vienna, Austria. [10]Max Planck Institute for Informatics, Saarbrücken, Germany. [11]Division of Biology and Biological Engineering, California Institute of Technology, Pasadena, CA 91125, USA. [12]Institut de Biologie de l'ENS (IBENS), INSERM, CNRS, École Normale Supérieure, PSL Research University, 75005 Paris, France. [13]Science for Life Laboratory, Department of Biophysics and biochemistry, Stockholm University, 17165 Solna, Sweden. [14]Cartana AB, 17165 Solna, Sweden. [15]San Raffaele Scientific Institute and Università Vita-Salute San Raffaele, 20132, Milan, Italy. [16]Program in Molecular Medicine, University of Massachusetts Medical School, Worcester, MA 01605, USA. [17]Harvard Stem Cell Institute, Cambridge, MA 02138, USA.
*These authors contributed equally to this work.
†Corresponding author. Email: igor.adameyko@ki.se (I.A.); peter.kharchenko@post.harvard.edu (P.V.K.)

scRNA-seq reveals the transcriptional changes in neural crest during delamination

Wnt1^{Cre} recombines in the dorsal neural tube where the premigratory neural crest resides. Focusing first on trunk neural crest, we dissected, then dissociated, the cervical region and trunk areas posterior to the otic vesicle from E9.5 *Wnt1*^{Cre}/*R26R*^{Tomato} mouse embryos (Fig. 1A), and measured mRNAs of single TOMATO^{+} cells with high coverage using Smart-seq2 protocol (median of 7025 genes detected per cell) (fig. S1A). Our design takes advantage of the developmental asynchrony of neural crest formation along the anteroposterior axis of the embryo to sample cellular states along neural crest maturation trajectories.

Analysis of transcriptional heterogeneity (*7*) separates neural tube and neural crest populations into two compartments (*6*) (Fig. 1, B, C, and E, and fig. S1, F and G). These are connected by two "bridges," corresponding to neural crest delamination [marked by activation of epithelial-to-mesenchymal transition (EMT) drivers such as *Snai1*] (*6*) (Fig. 1, G to I, and fig. S1C) and neurogenesis processes [marked by proneurogenic transcription factors (TFs)] (fig. S2, B to E). Estimates of RNA velocity, which predict the direction in which cells are moving in transcriptional space (*8*), show a convergent velocity pattern in the neurogenesis bridge, reflecting convergence of neural crest and neural tube neurogenesis programs (Fig. 1D). By contrast, the delaminating bridge shows pronounced movement from the neural tube toward differentiating neural crest cells. Although delamination of neural crest has been viewed as an abrupt transition of pre-EMT to migrating neural crest (*9*), our data reveal an extensive sequence of transcriptional events that unfold during delamination and early migration (Fig. 1, B, H, and I; fig. S1C; and table S2).

This enabled us to separate the premigratory neural crest into two distinct subpopulations. The earliest, pre-EMT population, is composed of cells that have not yet started delaminating from the neural tube. It is marked by peak expression of neural plate border specifiers previously tied to NC, such as *Zic1/3/5*, *Msx1* (*9*, *10*), *Mafb* (*11*), and *Gdf7* (*12*) (Fig. 1, E and G, and fig. S1C). The pre-EMT population, however, still expresses neural tube markers such as *Olig3* and *FoxB1* and is localized to the neural tube (Fig. 1H and fig. S1, C and F). The second, delaminating subpopulation is marked by activation of the key EMT gene *Snai1* (*6*) and absence of *Atoh1*, and is accompanied by sequential transient upregulation of a battery of genes, including *Dlx5*, *Pak3*, *Pdgfra*, and *Hapln* (Fig. 1H,I). Up-regulation of classical neural crest specifiers (*Sox9*, *Foxd3*, and *Ets1*) and down-regulation of many neural plate border specifiers (*Zic3*, *Mafb*, *Gdf7*) show variable timing across this progression, with some neuroectodermal border specifiers, such as *Msx1*, *Msx2*, *Wnt3a*, and *Lmx1a* (*9*, *13*, *14*), retaining expression in the delamination cluster. On the side opposite the neural tube, the delamination bridge connects with a subpopulation of *Sox9*$^{+}$

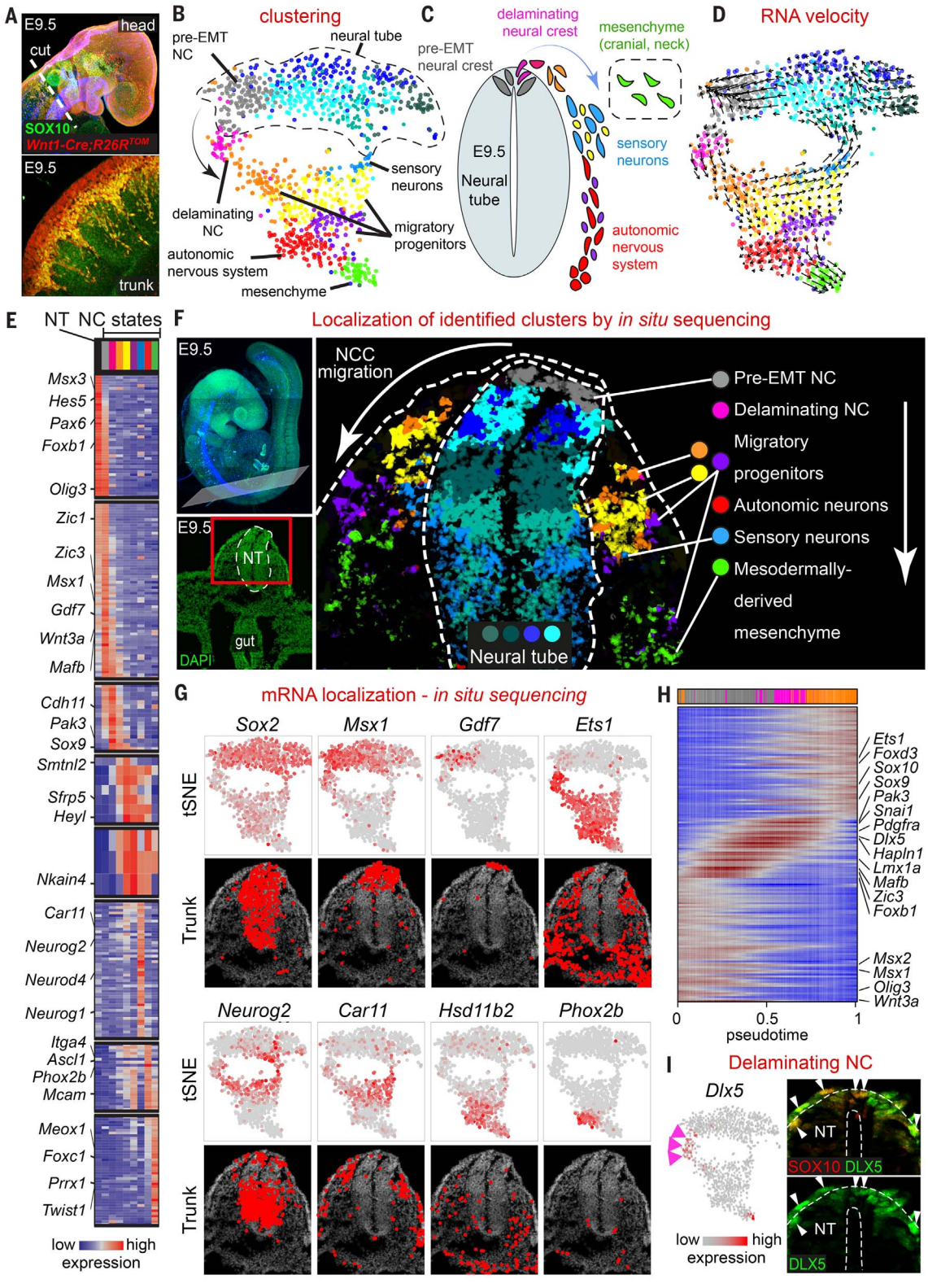


Fig. 1. Major aspects of trunk neural crest heterogeneity. (**A**) Immunohistochemistry of E9.5 *Wnt1*^{Cre};*R26R*$^{TOM+}$ embryo, showing SOX10^{+}/*Wnt1*$^{TOM+}$ neural crest cells (NCCs) migrating in the head and trunk. Note post-otic vesicle incision (dashed lines), showing separation between cranial and trunk portions. (**B** and **C**) t-SNE embedding shows 1107 cells (points) from mouse E9.5 *Wnt1*^{Cre}/*R26R*^{Tomato} trunk. The embedding reflects spatio-temporal aspects of neural crest (NC) development. Twelve major clusters of transcriptionally similar cells (colors) correspond to different stages of NC and ventral neural tube (vNT) development. (**D**) Analysis of RNA velocity shows major directions of cell progression in transcriptional space. The arrow start and end points indicate observed-current and predicted-future cell states, respectively. (**E**) Gene markers (cluster-specific) link NC clusters to developmental states. (**F**) Anatomical localization of NC clusters inferred from in situ sequencing of 32 cluster-specific genes in E9.5 sections (representative trunk section). Cell identity of vNT, which was not captured in the single-cell dataset, is imputed using the observed NC and NT clusters. (**G**) Characteristic gene expression patterns as detected by scRNA-seq (upper) and in situ sequencing (bottom) of a representative trunk section (see data S11 for others). (**H**) Transcriptional dynamics around delamination illustrate relationships between previously unknown and known markers. Cells of pre-EMT, delaminatory, and early migratory clusters were ordered by their delamination pseudotime, estimated using a principal curve. (**I**) scRNA-seq data predicts specific *Dlx5* expression around delamination (left), validated through immunochemistry (right).

cells that express *Cdh11* or *Itga4,* genes involved in neural crest migration (*15*, *16*), but do not yet express known markers of downstream neural crest fates (Fig. 1E). We will refer to these populations as migrating progenitors. Overall, single-cell data identify substages within the pre- and postmigratory neural crest stages (*6*, *9*) and yield sets of marker genes for various stages (table S1).

In situ sequencing shows spatial segregation of distinct neural crest states

Transcriptional profiles reveal a cascade of states from neural crest formation to fate commitment (Fig. 1, A to E). The early pre-EMT and delaminating crest gives rise to a pool of migrating progenitors, whose heterogeneity is linked to transcriptional properties of the downstream fates (fig. S1D), as they begin to express fate-specific genes. RNA velocity (Fig. 1D) shows a general flow of neural crest cells along the sequence of these developmental stages, followed by divergent flows of migrating progenitors toward more mature neural crest derivatives, including autonomic and sensory neuronal lineage and mesenchyme (Fig. 1, H and I, and data S1). All subpopulations demonstrated robust and uniform cell cycle signatures, except for a small number of cells committed to neuronal lineages (fig. S4, A to D). Immunohistochemistry-validated markers of major subpopulations (fig. S1, F to I) and RNAscope confirm migratory spatial patterns of classical lineage markers and new genes predicted to be implicated in fate specification (fig. S2 and data S12) (*17*, *18*).

To establish the relative anatomical distribution of the identified subpopulations, we used in situ sequencing (*19*) to simultaneously detect 32 subpopulation-specific transcripts in a spatially resolved manner in 15 serial sections of the E9.5 embryo (Fig. 1G and data S1 and S11). These two-dimensional measurements confirmed the expected anatomical separation of the neural crest and neural tube populations, and a dorsal neural tube localization of pre-EMT cluster, as well as spatial segregation of mature fates along the dorsoventral axis (Fig. 1, F and G, and fig. S1E). The subpopulations of migratory progenitors showed dorsoventral spatial segregation, with progenitors transcriptionally adjacent to the sensory fate (yellow, Fig. 1B) biased toward dorsal regions, and the progenitors transcriptionally adjacent to autonomic and mesenchymal fates (violet, Fig. 1B) biased toward ventral regions (Fig. 1F and fig. S1E).

Differentiating neural crest undergoes sequential binary fate restrictions

To disentangle the transcriptional logic of neural crest differentiation in the trunk, we used a branching process to computationally model the progression of emigrating neural crest cells through the heterogeneous pool of progenitors toward committed fates. Specifically, we adapted a principal graph approach (*20*) to derive a statistical ensemble of contiguous tree trajectories that best explain the observed cell distribution in a high-dimensional transcriptional space (Fig. 2A and fig. S3, A to D; see methods). The resulting trees capture transcriptional changes associated with transitions between pre-EMT, delaminating, and migratory states, followed by multiple cell fate decision branches (figs. S3, A to C, and S4, H to J, and table S3). The developmental potential of neural crest cells has been the subject of previous investigations, showing that pre-EMT and early migrating neural crest cells are multipotent (*21*, *22*). However, it remains unclear how neural crest cells lose multipotency and whether the choice of multiple fates occurs in a stochastic manner or follows a structured pattern of lineage restrictions (*23*, *24*). Our results demonstrate a well-defined transcriptional structure of cell-fate splits, which appear as a sequence of binary bifurcations separated by additional robust transcriptional changes (Fig. 2A and figs. S3, A to C, and S4, H to J). The first stable bifurcation separates sensory lineage from common progenitors of autonomic and mesenchymal branches. The second stable fate split, separating autonomic neuronal fate from mesenchymal differentiation, captures a spatially restricted process that takes place within the cervical region. Additional branches can be attributed to glial differentiation as they show expression of early glial markers (*Mpz*, *Fabp7*, *Zfp488*, *Plp1*, *Sox10*) and transcriptional signatures of E10.5 Schwann cell precursors (SCPs) (fig. S4, E to G). Furthermore, removal of the top 50 cells associated with SCP development leads to disappearance of these glia-specific branches (fig. S4, H and I). Although the topology relating sensory, autonomic, and mesenchymal branches is stable, the anchoring of the glial branch is uncertain, with some of the trees in the ensemble placing it within the sensory branch, and others positioning it within the autonomic-mesenchyme branch (fig. S4J). This likely reflects both technical uncertainties arising from limited number of such glial precursors, as well as the fact that glial precursors arise in both sensory and autonomic lineages.

Because it has been previously noted that $Wnt1^{Cre}$ line can activate the *Wnt1* signaling pathway and induce a developmental phenotype (*25*), we generated another single-cell snapshot of the E9.5 trunk neural crest, using a different neural crest-specific *Cre* line ($Sox10^{CreERT2}/R26R^{Tomato}$). Transcriptional dynamics, structure of bifurcations, and patterns of markers expression were similar between $Wnt1^{Cre}$ and $Sox10^{CreERT2}$ snapshots, indicating that the effect of *Wnt1* activation in early neural crest is relatively minor (fig. S5, A to I), consistent with observations by others (*26*). To evaluate the extent of spatiotemporal conservation of transcriptional program in posterior neural crest, we also generated a single-cell snapshot of hindlimb and tail crest at E10.5 using $Wnt1^{Cre}/R26R^{Tomato}$ line. The results recapitulate transcriptional dynamics at E9.5 in trunk, revealing more advanced stages of sensory neurogenesis (fig. S5, H and I). These combined results show that upon maturation, trunk NC proceeds through a stereotypical sequence of binary lineage-restriction decisions.

Distinct functions of early and late *Neurog2* expression

Many genes exhibit statistically significant and robust changes along the reconstructed trunk neural crest developmental tree [1048 genes at a false discovery rate (FDR) of 0.05; Fig. 2, B and C, and table S4], which we grouped into 21 major clusters based on the similarity of their expression patterns (Fig. 2C and data S2). Although expression of many clusters recapitulated the canonical stages of neural crest (*6*), others captured more complex regulatory patterns, such as down-regulation after delamination followed by reactivation upon mesenchymal specification (cluster 20, data S2). Among the tree-associated genes, we identified 137 TFs, many of which were not previously described in the context of neural crest development (e.g., *Maf*, *Ikzf2*, *Rfx4*, *Ldb2*, *Plagl1*, *Nhlh2*) (data S2). Differential expression of a TF, however, does not establish its regulatory role, as TF activity may be modulated by cofactors or other regulatory machinery. We therefore looked for coordinated up-regulation or down-regulation of the predicted TF targets as an indicator of TF regulatory activity (Fig. 2D). We used regularized linear models (*27*) to analyze 50 of out 137 trajectory-associated TFs that had known nonredundant sequence binding sequence motifs, and identified TFs whose transcriptional changes show statistically significant regulatory impact on their corresponding target genes (FDR < 0.25) (Fig. 2D and fig. S6). A pattern of TF activity matching TF expression was observed for transcriptional activators, and a complementary pattern for repressors (e.g., *Foxd3*). A repressive effect of *Foxd3* in non-ectomesenchymal developmental stages is in agreement with the results of *FoxD3* loss-of-function experiments (*28*), including a biasing role of *FoxD3* against the mesenchymal program (*29*). Several TFs showed expression in parts of the neural crest development tree without exhibiting a detectable regulatory impact on their target genes, suggesting modulation by other processes. For example, *Insm1* is expressed in both autonomic and sensory branches, but shows detectable regulatory impact only in the autonomic branch. Indeed, activity of *Insm1* is modulated by autonomic-specific factor *Ascl1* in specification of autonomic lineage (*30*).

Proneurogenic *Neurog2* exhibits two peaks of expression (Fig. 2B): early after the delamination stage that appears to lack direct regulatory impact (Fig. 2E), and late at the onset of sensory neurogenesis that can be linked to corresponding regulatory activity (*31*). Expression of *Neurog2* around the dorsal neural tube has been previously assumed to mark sensory progenitors (*32*), and in that regard, the early expression of *Neurog2* that precedes any bifurcation points is surprising. It suggests that instead of being limited to sensory lineage, all neural crest derivatives may exhibit transient expression of *Neurog2* during differentiation (Fig. 2E). Indeed, lineage tracing in $Neurog2^{CreERT2/+};R26R^{YFP}$ mouse line starting from E9.5 confirms that cells expressing *Neurog2* at this early stage end up being widely

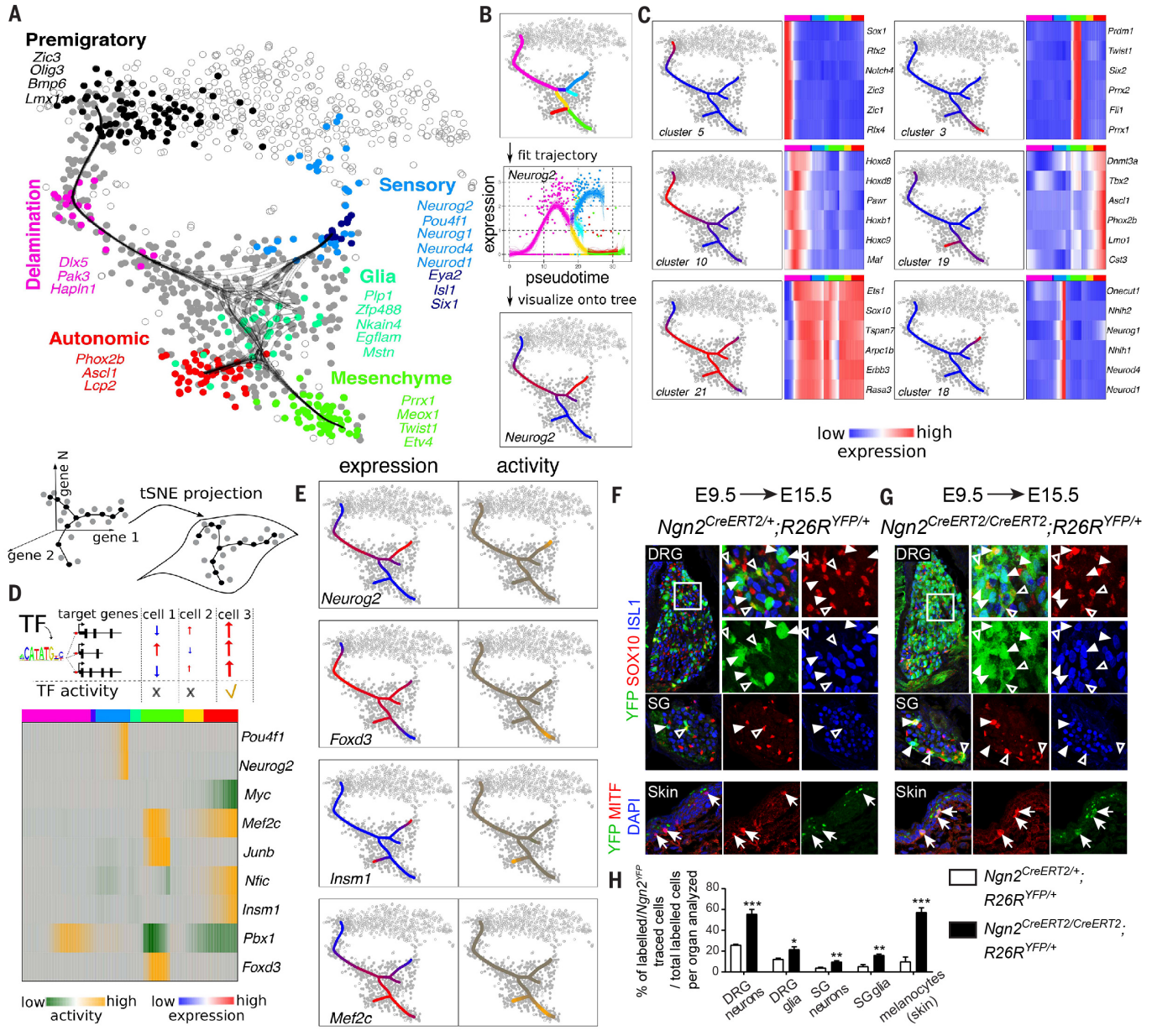


Fig. 2. Developmental portrait of trunk neural crest cells. (**A**) Developmental progression of trunk NCCs modeled using principal trees. Non-NCCs (empty circles) were excluded from the analysis. Cells with high average expression of fate-specific markers are shown by distinct vibrant colors; a heterogeneous pool of migrating progenitors is shown in gray. (**B**) Projections of cells onto the principal tree yield smoothed pseudotime-associated gene expression profiles. Top: Color-coded segments of the principal tree; segment colors match the colors of corresponding unbiased clusters in Fig. 1A, where possible. (**C**) Clustering of genes based on similarity of NCC expression profiles (see data S1 for extended set of clusters). (**D**) Transcription factor (TF) regulatory activity along the NCC developmental progression. Lower: A pseudotime activity pattern is shown for a set of TFs predicted to be active during NCC differentiation (FDR < 0.25). (**E**) Patterns of expression (left) and activity (right) shown for representative TFs. (**F** and **G**) Immunohistochemistry of control $Neurog2^{CreERT2/+}$;$R26R^{YFP/+}$ (carrying one copy of *CreERT2*) and mutant $Neurog2^{CreERT2/CreERT2}$;$R26R^{YFP/+}$ (carrying two copies of *CreERT2*, see methods for details) tamoxifen-injected at E9.5 and analyzed at E15.5 shows fate partitioning of traced cells between sensory neurons ($ISL1^+$) (white solid arrowheads), glia ($SOX10^+$) (empty arrowheads), and melanocytes ($MITF^+$) (white solid arrows). Note that no melanocytes are traced in control embryos. (**H**) Quantification of the percentage of traced sensory neurons, glia, and melanocytes between control and mutant embryos per organ shows doubling of tracing in neurons and glia, but significantly higher proportion in melanocytes (*$p < 0.05$, **$p < 0.01$, ***$p < 0.001$). DRG, dorsal root ganglion; SG, sympathetic ganglion.

distributed across all types of the neural crest progeny in the trunk and are not limited to the canonical sensory fate (Fig. 2F). Earlier studies have shown that *Neurog2* knockout results in transient delay of sensory lineage differentiation, which is subsequently compensated by its homolog *Neurog1* (*31*) that also has detectable regulatory impact in the sensory branch (fig. S6A). To assess broader functional impact of early *Neurog2* expression on fates distribution, we analyzed knockin $Neurog2^{CreERT2/CreERT2}$;$R26R^{YFP}$ embryos (*33*). In the absence of *Neurog2*, the efficiency of genetic tracing appeared proportionally higher in all neural crest derivatives except melanocytes, indicating that early

Neurog2 expression is not primarily associated with committed or biased sensory progenitors. Rather, it suggests a nonneurogenic role of *Neurog2* in active repression of the melanocyte fate during early neural crest migration (Fig. 2, G and H).

Coactivation of alternative programs and biasing precede fate commitment

To investigate the process of cell fate commitment, we examined how transcriptional modules associated with alternative cell fates assemble and compete around decision points, focusing initially on the first bifurcation separating sensory and autonomic branches (Fig. 3A). We approximated fate-specific modules by sets of genes selectively up-regulated in one branch compared to another (Fig. 3, B and C). Whereas some fate-specific genes are up-regulated after the bifurcation point (late genes, 45 sensory, 36 autonomic), others show earlier up-regulation in the progenitor branch, before the actual bifurcation point (early genes, 53 sensory, 86 autonomic) (Fig. 3B and data files S3 and S4). For example, *Neurod1*, thought to be a master regulator of sensory fate, is induced late in the sensory branch, whereas another sensory TF, *Pou4f1*, is up-regulated earlier during delamination, in a manner similar to that of *Neurog2* (Fig. 3B). This is expected, as bifurcation points capture trajectory positions where the extent of the transcriptional differences between the alternative cell fates becomes sufficiently large. The expression onset differences were also confirmed by the RNAscope measurements of select genes in both sensory and autonomic branches (fig. S2). We observed that early modules of competing cellular fates are coexpressed in progenitor cells and exhibit gradual coactivation as the cells progress toward the bifurcation point, followed by selective up-regulation of one module and down-regulation of another after the bifurcation point (Fig. 3C). By contrast, late-competing modules show mutually exclusive activation in their corresponding branches, without coexpression in individual cells, consistent with commitment to a particular fate (Fig. 3D). Many known critical master regulators do not show detectable expression around the bifurcation point (including autonomic *Phox2b*, *Ascl1*, and sensory *Neurog1*, *Neurod4*, and *Neurod1*), indicating contribution of other genes or mechanisms to the early steps of the decision process. These likely include exposure to extracellular signals such as *Wnt* signaling, BMP signaling, or Delta-Notch interactions (*34*).

We next examined whether despite general coactivation of competing-fate modules, the progenitor cells exhibit an early transcriptional bias toward a particular fate beyond the effects of expression noise. In doing so, we controlled for apparent biases due to developmental asynchrony of the subpopulations being analyzed, which can limit interpretation of similar analysis based on targeted or bulk measurements (fig. S7I) (*2*). For the cells positioned around the actual bifurcation point, the transcriptional bias toward one of the possible fates manifests itself as a pronounced negative correlation between the competing gene modules (Fig. 3E). We find that as cells move toward the first bifurcation point following the initial coactivation stage, the degree of transcriptional coordination within each module increases, and antagonistic expression of the competing modules becomes more apparent (Fig. 3, E and F). Simulated controls, with expression profiles randomized across cells with similar pseudotime to preserve the overall gene activation profiles, fail to show such local coordination of gene modules (fig. S7, A and B). This indicates that as cells progress toward the bifurcation point, they undergo gradual transcriptional biasing toward one of the competing fates. The biasing phase does not appear to be driven by up-regulation of a single gene. Rather, we observe broad expression shifts between genes of the competing fate-specific modules (Fig. 3F). These results indicate the presence of lineage priming early in neural crest migration, prior to the predicted sensory-autonomic bifurcation point. The transcriptional correlations within the competing modules are reduced following the bifurcation point. This reduction illustrates that most of the observed intramodule correlation can be attributed to compositional heterogeneity of cells around the bifurcation point (*35*). When considering more homogeneous cell populations within the branches following the bifurcation point, correlation of genes within the module becomes relatively low, indicating that regulatory interactions between genes, such as correlations induced by stochastic covariation of a TF and its target genes, are not apparent in such data (*36*) (Fig. 3F).

To determine the initial transcriptional events in the assembly of the fate-specific modules, we monitored coordinated expression of gene subsets, tracking backward along the progenitor branch. In doing so, we controlled for the overall pattern of module activation, as such general trends can overshadow correlations within a subset (fig. S8). The results show that early correlated subsets of modules specific to either sensory or autonomic fate can be statistically distinguished at the delamination stage, but not in the pre-EMT neural crest (Fig. 3G and data files S5 and S6). We detect earlier formation of the sensory module, compared to the autonomic module. Overall, we observe three primary phases of cell fate decision, formalized as a sequence of initial coactivation, gradual biasing, and commitment phases (Fig. 3H). The initial coactivation stage is characterized by coexpression of competing modules within individual cells that gradually shifts in favor of one of the modules during the biasing phase, culminating in up-regulation of mutually exclusive fate-specific gene expression patterns during commitment. The three-phase scheme of cell fate decision also holds for the autonomic-mesenchyme bifurcation discussed below (fig. S7, C to H). This model elaborates on earlier observations of co-expression of key regulatory factors (*37*–*40*) or programs (*41*–*43*) from alternative fates prior to cell fate commitment noted in other tissues.

Autonomic-mesenchymal bifurcation reveals bipotent progenitors

Studies of neuroblastoma, a tumor of sympathetic nervous system that originates from neural crest cells, revealed that tumor cells can transit between adrenergic and mesenchymal phenotypes, creating inter- and intra-tumoral heterogeneity that poses a therapeutic challenge (*44*, *45*). Our data uncovered the developmental bifurcation that separates autonomic and mesenchymal fates (Fig. 4A). After the initial stage of co-activation of both programs (Fig. S7C-E), commitment to fates is marked by expression of two fate-specific late genes: *Phox2b*, a key driver of autonomic neuronal lineage (*46*); and *Prrx1*, a marker of specified mesenchyme (*47*). However, some transient cells co-express both genes at high levels (Fig. 4A). Consistent with this, corresponding *Prrx1* and *Phox2b* mRNA molecules colocalize and proteins are coexpressed in the same few cells in the ventral neural crest pathway of migration (Fig. 4, C and D). Nearly all late genes of the autonomic module are coexpressed with late genes of the mesenchymal module in at least a few cells, illustrating ubiquitous stochastic coactivation of the alternative fate modules (Fig. 4B).

To test whether the cells expressing *Phox2b* can end up in the mesenchymal domain, we performed lineage tracing with a $Phox2b^{Cre}/R26R^{TOMATO}$ mouse line (Fig. 4, F and G). As expected, the autonomic neurons and numerous glial cells proximal to autonomic components were traced. However, we also observed tracing of multiple cells of the mesenchymal phenotype in the cervical region, as well as in the heart, in the proximity of autonomic components (parasympathetic neurons of the heart) (Fig. 4H). Detailed analysis at the region of the heart and the proximal autonomic ganglia showed that 21.6 ± 3.1% of traced cells contributed to glia, 9.9 ± 1.6% to autonomic neurons, and 68.4 ± 4.7% to mesenchyme (Fig. 4H). These results confirm that some of the cells expressing late-autonomic signatures subsequently deviate toward mesenchymal specification in the cervical region. The opposite experiment with lineage tracing in $Prrx1\text{-}Cre;R26R^{mTmG}$ showed no traced autonomic neurons or glial cells in the entire embryo, including the cervical region where the large superior cervical ganglion is positioned (Fig. 4, E and H). Thus, cells expressing *Prrx1* always differentiate into mesenchymal fates. As a result, when both *Prrx1* and *Phox2b* master regulators are coactivated in the same cells, cell fate is resolved in the direction of mesenchymal derivates in vivo (Fig. 4B). No sensory neurons were traced from progenitors expressing *Phox2b*, demonstrating that $Phox2b^{+}$ cells at the second bifurcation point are bipotent. The possibility of transdifferentiation of more committed $Ascl1^{+}/Phox2b^{+}$ autonomic progenitors into mesenchymal population is not supported by RNA velocity analysis (Fig. 1D) and lineage tracing from E10.5 with $Ascl1^{CreERT2};R26R^{TOM}$ (fig. S9).

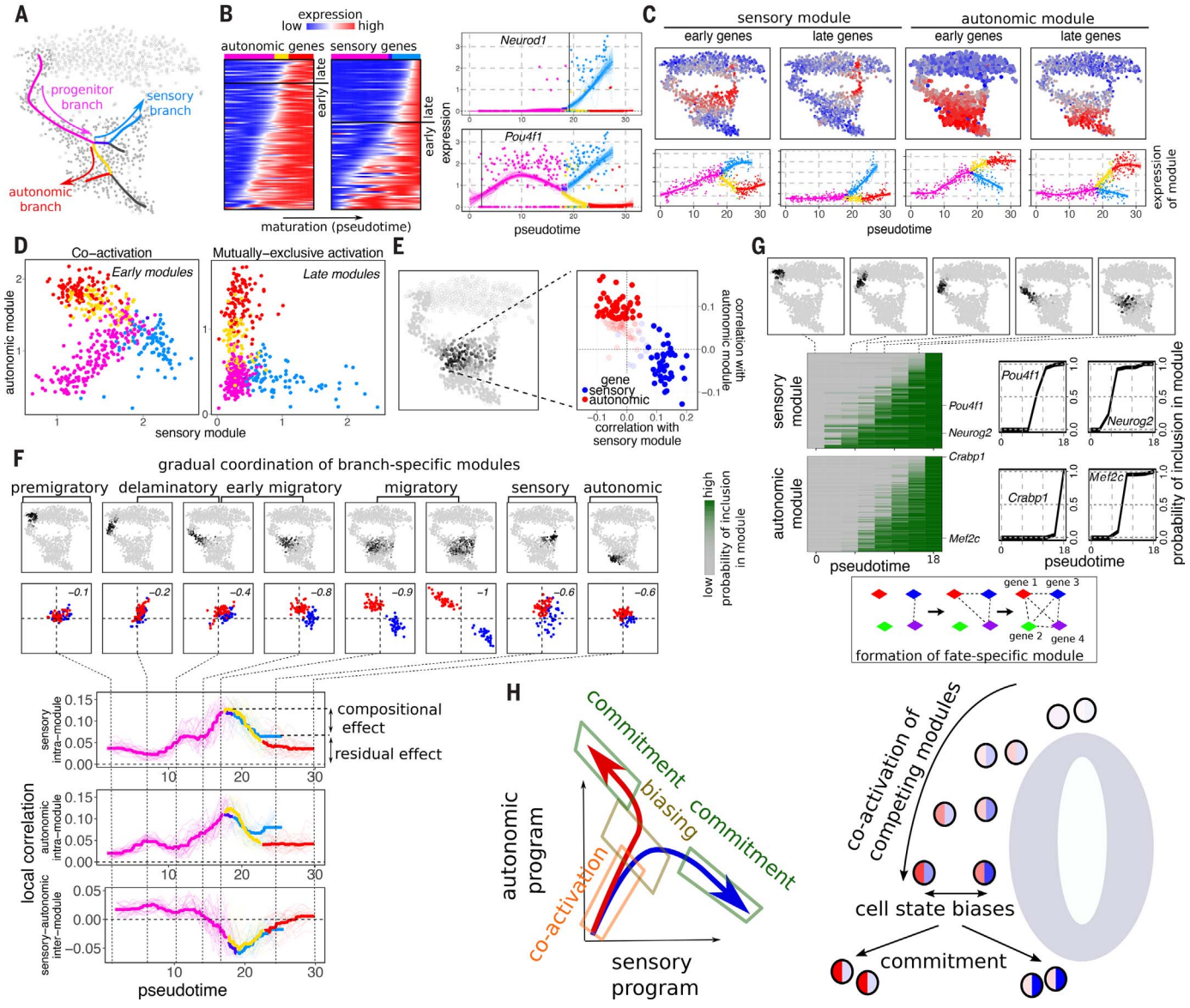


Fig. 3. Logic of cell fate selection for sensory-autonomic bifurcation. (**A**) Schematic overview of the sensory-autonomic split in NC differentiation. (**B**) Branch-specific (sensory versus autonomic) genes classified as activated early (before split) and late (after split). Right: Example of an early (*Pou4f1*) and a late (*Neurod1*) sensory-specific gene. Vertical line marks predicted time of up-regulation. Time of up-regulation of all genes can be found in data S3 and S4. Colors encode branches [as in (A)]. (**C**) Average expression pattern of early and late branch-specific modules. Early and late modules are set of genes activated before or after the bifurcation. (**D**) Scatter plots show average expression of sensory and autonomic modules in each cell. Left: Early competing modules show gradual coactivation, followed by selective up-regulation of one fate-specific module and down-regulation of another. Right: Late modules show almost mutually exclusive up-regulation. Colors encode tree branches. (**E**) Bifurcation point is characterized by correlated expression of genes within modules, and repulsion of competing modules. Left: Probability of a cell proximity to the sensory-autonomic bifurcation point shown (darker colors corresponding to higher probability). Right: Average correlation of each early sensory- or autonomic-specific gene (points) with the genes from the sensory- (*x* axis) and autonomic-specific (*y* axis) modules among cells around the bifurcation point. Genes that have low average correlation with their own module (<0.07) are shown with faded colors and are excluded from analysis in (F) for clarity. (**F**) Early modules show gradual intramodule coordination and intermodule repulsion. Upper: The plots show average local correlations of module genes with autonomic and sensory modules in a set of cells with similar developmental time (marked by black points). Bottom: Average local correlations of genes within and between branch-specific modules show gradual increase in coordination within each module and increasing antagonistic expression between the branch-specific modules. The difference between intra- and intermodule correlations, which characterize the extent of the antagonistic expression between the alternate modules, is shown in the upper right corner of tSNEs. (**G**) Time of gene inclusion in coordinated branch-specific module shows early signatures of fate-biased expression programs. Bottom: Schematic illustrating of formation of a branch-specific module, with connecting lines indicating onset of expression correlation between genes. Heatmap: Probabilities of gene inclusion in the branch-specific module during early stages of differentiation (see data S5 and S6 for gene names). Right: Examples of inclusion probability estimates for individual genes in the two modules. (**H**) Cell fate decisions formalized as a three-phase process: Initially, cells coactivate competing cell fate–specific programs, gradually switch to preferential expression of one module, and culminate by activating mutually exclusive fate-specific expression.

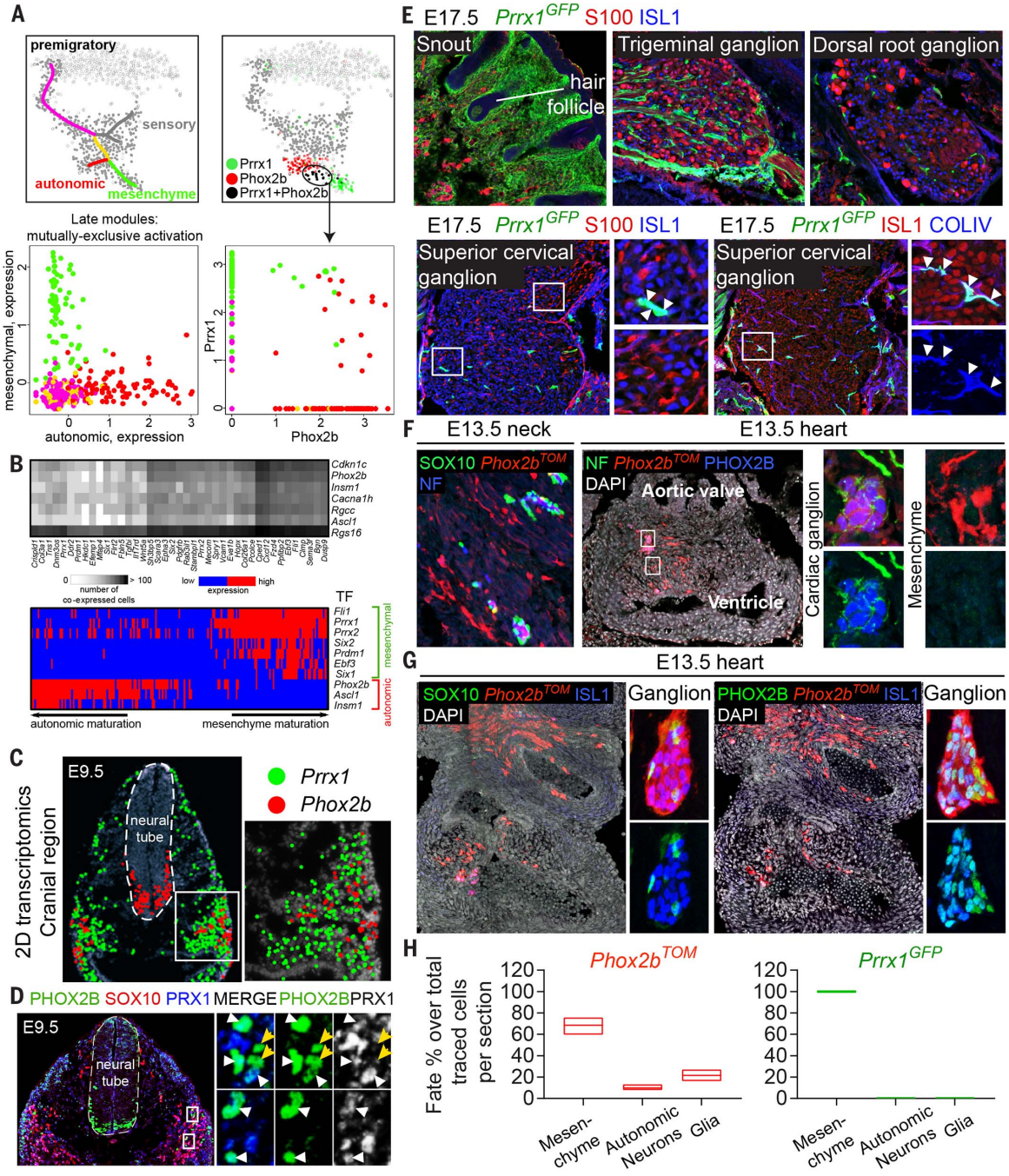


Fig. 4. *Phox2b* and *Prrx1* coexpression reveals bipotent progenitors. (**A**) Infrequent coexpression of *Phox2b* and *Prrx1* is observed despite mutually exclusive expression of modules. Bottom left: Late modules of the autonomic-mesenchyme bifurcation show mutually exclusive expression. Bottom right: *Prrx1* and *Phox2b* show largely branch-specific expression pattern, but are coexpressed in some cells. (**B**) The majority of antagonistic pairs of branch-specifying genes are coexpressed at high levels in a few cells. Upper: Heatmap with color indicating numbers of cells with coexpression of two genes from competing late modules (rows, autonomic; columns, mesenchymal). Lower: Heatmap showing expression of branch-specific TFs in cells assigned to either branch. (**C**) Pattern of *Prrx1* and *Phox2b* expression (by in situ sequencing) at E9.5. Coexpression of the two genes is observed at the prospective cranial ganglia. (**D**) Immunofluorescence for PHOX2B, PRX1, and SOX10 in E9.5 trunk ($PHOX2B^+/PRX1^+$ cells shown by white arrowheads, $PHOX2B^+/PRX1^-$ by yellow arrows). (**E**) Immunohistochemistry on E17.5 embryo for $Prrx1^{GFP}$, S100, and ISL1 shows absence of overlap between the mesenchyme ($Prrx1^{GFP+}$), glia, and sensory neurons. Note that $Prrx1^{GFP+}$ shows colocalization with COLIV, indicating that the vascular mesenchyme was traced. (**F**) Immunohistochemistry on E13.5 embryo for SOX10, $Phox2b^{TOM+}$, neurofilaments, and PHOX2B (in heart-related panels). Note the presence of numerous $Phox2b^{TOM+}/$ $PHOX2B^-$ mesenchymal cells in the cervical region and surrounding $Phox2b^{TOM+}/$ $PHOX2B^+$ autonomic neurons in the heart. (**G**) Immunohistochemistry on E13.5 embryo for SOX10 or PHOX2B, $Phox2b^{TOM+}$, and ISL1. Note the presence of numerous $Phox2b^{TOM+}/$ mesenchymal cells in aortic areas, negative for ISL1, PHOX2B, or SOX10. (**H**) Analysis of the percentage contribution of $Phox2b^{TOM+}$ and $Prrx1^{GFP+}$ cells to mesenchyme, autonomic neurons, and glia over the total number of traced cells in the area of the heart (N = 3 embryos per strain).

Transcriptional specificity of cranial neural crest emerges during delamination

Migration and differentiation of cranial neural crest are spatiotemporally separated from events occurring in the trunk. The cranial crest primarily gives rise to mesenchymal populations responsible for building the head, which are not produced by the trunk crest (*48*). We analyzed single-cell snapshots of anterior cranial, pre-otic, and post-otic *Wnt1*-traced populations at E8.5 (Fig. 5A). Early neural crest was composed of three spatially distinct populations: *Hox*$^-$ population that corresponds to the anterior cranial neural crest, *Hoxb2*$^+$ that contributes primarily to the mandibular level, and *HoxD3*$^+$ population that includes post-otic (including cardiac and vagal) streams of the neural crest (Fig. 5A, fig. S10A, table S5, and data S7) (*49*). The developmental portrait of *Hox*$^-$ anterior cranial neural crest at E8.5 represented a single differentiation trajectory that encompasses diverse transcriptional events: down-regulation of a neural tube–associated program, including *Zic3* and *Pax8*; transient expression of a battery of genes such as *Pak3* and *Bmper*; coherent, but not simultaneous, up-regulation of neural crest markers, including *Foxd3*, *Sox9* and *Sox10*, and mesenchymal fate–specifying genes, including the TFs *Twist1* and *Prrx2* (Fig. 5, B and C, table S6, and data S8). Consistent with this, analysis of *Hox*$^-$ neural crest variability shows trajectory-associated and cell cycle processes (fig. S10G). Although we did not observe fate bifurcations in the cranial crest at the E8.5 stage, an anticorrelation of the mesenchymal and neuronal genetic programs emerged, coinciding with the down-regulation of the early neural crest genes *Foxd3* and *Sox9* and activation of the mesenchymal factors (Fig. 5D and fig. S10B). Thus, cranial neural crest, similar to trunk cells, progresses through a biasing stage before commitment to a specific fate. This indicates that signs of ongoing cell fate bifurcations often can be detected in advance, similar to early detection of transitions noted in other fields (*50*). As in the case of the anterior cranial neural crest, the snapshot of *Hoxb2*$^+$ neural crest cells underwent a differentiation progression through an intermediate step toward migrating cells expressing mesenchymal markers (fig. S10, C and D; Table S7; and data S9). *Hoxb2*$^-$/*Hoxd3*$^+$ neural crest population was represented as an isolated cluster.

Cranial neural crest at all spatial levels expresses a shared core program (including classical markers *Sox10*, *Sox9*, *Foxd3*, and *Ets1*). As a result, *Hox*$^-$ and *Hoxb2*$^+$ neural crest subpopulations are more similar to each other than to the corresponding neural tube regions from which they originate (Fig. 5E). Nevertheless, *Hox*$^-$ and *Hoxb2*$^+$ neural crest shows expression differences (fig. S10, E and F), which may be a consequence of divergent differentiation trajectories, or simply reflect residual differences of their distinct starting states prior to delamination from the neural tube. We find evidence for the former, with the difference between *Hox*$^-$ and *Hoxb2*$^+$ neural crest correlating well with the differences in the neural crest developmental programs induced at the corresponding spatial levels (r = 0.49), but not correlated with the difference of their starting *Hox*$^-$ and *Hoxb2*$^+$ neural tube states (Fig. 5E). This indicates that the transcriptional divergence of the neural crest from different spatial levels arises primarily during downstream delamination and migration stages through the activation of new gene expression programs.

Cranial and trunk crest follow different paths through a shared differentiation landscape

To compare more-differentiated populations arising from different neural crest levels, we further sampled crest-derived cells of cranial region at E9.5, post-otic (vagal and cardiac) at E10.5, and lumbar and tail regions at E10.5. Joint alignment of all crest datasets (see methods) revealed that neural crest cells at various positional levels and time points navigate a stereotypic space of transcriptional states, with some notable biases (Fig. 5F; fig. S10, H and I; and tables S9 and S10). The distribution of mature cells of the cranial compartment is biased toward mesenchymal fate, whereas cells of the trunk compartments gravitate toward sensory and autonomic fates (Fig. 5G and fig. S10M). In line with this, the fraction of mesenchymal committed cells was high in the anterior population, whereas the fraction of sensory committed cells was high in the posterior population as inferred from *Hox* gene expression (fig. S10J). The cranial neural crest progressed to a more mature mesenchymal state at E9.5 as compared to the earlier E8.5 time point, as evident from activation of *Prrx1* and *Twist2*. By contrast, trunk neural crest showed active maturation of sensory progenitors from E9.5 to E10.5, including activation of *Dcx*, *Stmn2*, and down-regulation of *Neurog2* (fig. S10I). Post-otic neural crest occupied an intermediate position between anterior cranial and trunk neural crest, and shared some features with each of those populations (*51*). Snapshot of post-otic neural crest populations at E10.5 represented mostly *Hoxd3*$^+$ cells, indicating a dominant contribution from the vagal neural crest (Fig. 5G). The population contains cells of autonomic and cardiac-mesenchyme fates with a small admixture of sensory-committed cells. Cardiac mesenchyme is necessary for development of cardiac valves and the outflow tract (*52*). Heterogeneity of this subpopulation revealed three initial steps of ectomesenchyme differentiation that are marked by sequential acquisition and down-regulation of *Six2* followed by transient up-regulation of *Dlx6* and activation of *Msx2* and heart-specific *Hand2*, and then activation of downstream cardiac markers *Hand1*, *Dkk1*, and *Gata6* (Fig. 5H, table S8, and data S10). Screening of the neural crest snapshot at E8.5, E9.5, and E10.5 stages did not reveal coexpression of the melanoblast markers (*Mitf*, *Pmel*, *Dct*) or a broader transcriptional signature of prospective melanoblasts at any of the spatiotemporal levels, indicating late consolidation of melanocytic fate (fig. S10, K and L).

During delamination and early migration stages, both cranial and trunk neural crest progress through a similar sequence of transcriptional steps, as illustrated by intermixing in joint expression space (Fig. 5G and fig. S11A). Nevertheless, in addition to such common maturation signatures, cranial and trunk neural crest also activate their own distinct modules (Fig. 6A and fig. S11, A and D). For cranial cells, this includes activation of a broad mesenchymal program, including regulatory factors such as *Twist1*, *Prrx2*, and *Dlx2* (Fig. 6B), whereas activation of the sensory program that includes *Neurog2*, *Pou4f1*, and *Nkx2.1* is specific to trunk cells. Therefore, we hypothesized that early activation of fate-specific programs after delamination can predispose cells toward specific fates and account for the distinct downstream fate biases of trunk and cranial neural crest cells.

Twist1 activation is sufficient to reroute trunk neural crest into a mesenchymal fate

To test if activation of mesenchymal regulators can bias trunk neural crest toward mesenchymal differentiation, we electroporated *Twist1*-expression constructs into the developing chick neural crest. Such targeted and sustained overexpression of *Twist1* in the trunk neural crest starting from pre-EMT stage resulted in down-regulation of traditional trunk fates such as neuronal sensory, autonomic, and glial and alteration of the neural crest migration patterns (Fig. 6C). Instead of the expected migration toward the dorsal aorta, *Twist1*$^+$ cells in the trunk predominantly followed a path to dermal regions, where they activated expression of a dermal mesenchymal marker *Prrx1*, not observed in wild-type trunk neural crest (Fig. 6C). Some *Twist1*$^+$ cells migrated to sensory ganglia and the dorsal aorta, where they did not take neuronal or glial fates (fig. S12, A and B). Conversely, CRISPR-Cas9–based knockdown of *Twist1* in chick cranial neural crest resulted in a reduction of mesenchymal populations and an increase in glial and neuronal derivatives (fig. S12, C to F), consistent with previous studies (*53*, *54*).

Overexpression of the downstream mesenchymal factor *Prrx2* in the trunk resulted in massive apoptosis of neural crest cells (fig. S11B). The rare surviving cells were not able to pick traditional trunk fates, as compared to controls [green fluorescent protein (GFP)–only DNA or neuro-glia–related genes, such as *Crabp1*; fig. S11B]. By contrast, regulator of sensory fate *Pou4f1* is strongly activated upon delamination in the trunk, but is poorly expressed in cranial crest: Overexpression of the dominant-negative version of *Brn3c*, a homolog of *Pou4f1* in chick, in cranial and trunk chick neural crest resulted in no obvious phenotype in the trunk, as expected, whereas it caused a decrease of *Sox9*$^+$/*Pax7*$^+$ cranial neural crest cells (fig. S11C). This suggests that *Pou4f1* might be another factor differentially regulating fates in different NC populations along the anteroposterior axis.

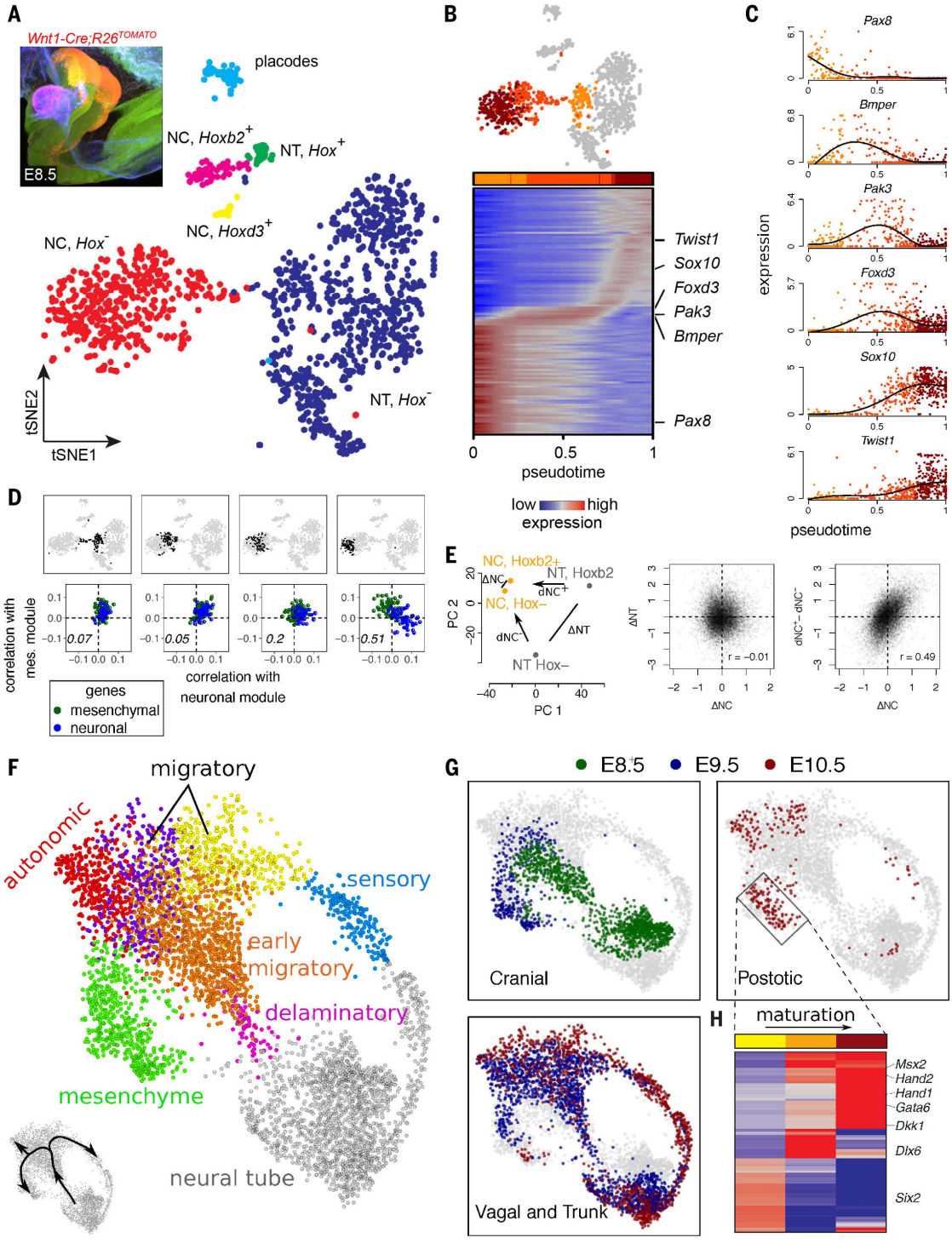


Fig. 5. Spatiotemporal analysis of cranial neural crest. (**A**) t-SNE embedding shows subpopulations observed in 1345 cells collected from the cranial part of E8.5 *Wnt1-Cre;R26*$^{TOM+}$ embryos (left: representative embryo shown). (**B**) Analysis of the developmental progression identifies timing of transcriptional events of early *Hox*$^{-}$ cranial NCCs. (**C**) Pseudotime expression trends of representative genes [from (B)] are shown for early *Hox*$^{-}$ cranial NCCs. (**D**) Correlation of fate-specific gene modules reveals emergence of mesenchymal versus neuronal biases in migration. Similar to Fig. 3F, the cells were arranged by pseudotime and binned in groups of 50 cells (upper panels) to estimate intra- and intermodule correlations between the mesenchymal and neuronal (sensory, autonomic) gene modules from E9.5 trunk NCC analysis (lower panels). (**E**) Transcriptional differences of migratory *Hoxb2*$^{+}$ and *Hox*$^{-}$ cranial NCCs emerge during delamination. Left: NCCs from *Hox*- and *Hoxb2*$^{+}$ populations show more similar profiles in the migratory stage, compared to NT, whereas transcriptional differences between *Hox*- and *Hoxb2*$^{+}$ in NT (ΔNT) and migratory stage (ΔNC) are not correlated. Right: The difference in transcriptional shifts accompanying delamination in *Hoxb2*$^{+}$ (dNC^{+}) and *Hox*- (dNC^{-}) NCCs correlates with the resulting expression difference between *Hox*$^{-}$ and *Hoxb2*$^{+}$ populations at the migratory stage (ΔNC), indicating that most migratory differences between levels emerge during delamination, instead of reflecting initial differences at the NT stage. (**F**) A joint embedding of NCCs from different stages (E8.5, E9.5, E10.5) and locations (cranial, trunk, cardiac, hindlimb, and tail) shows stereotypic landscape of NC development. Inset shows schematic tree of differentiation. (**G**) Distribution of transcriptional states of spatiotemporally distinct datasets (colored according to developmental time). (**H**) Three early ectomesenchyme developmental states of progressive maturation in cardiac NC population.

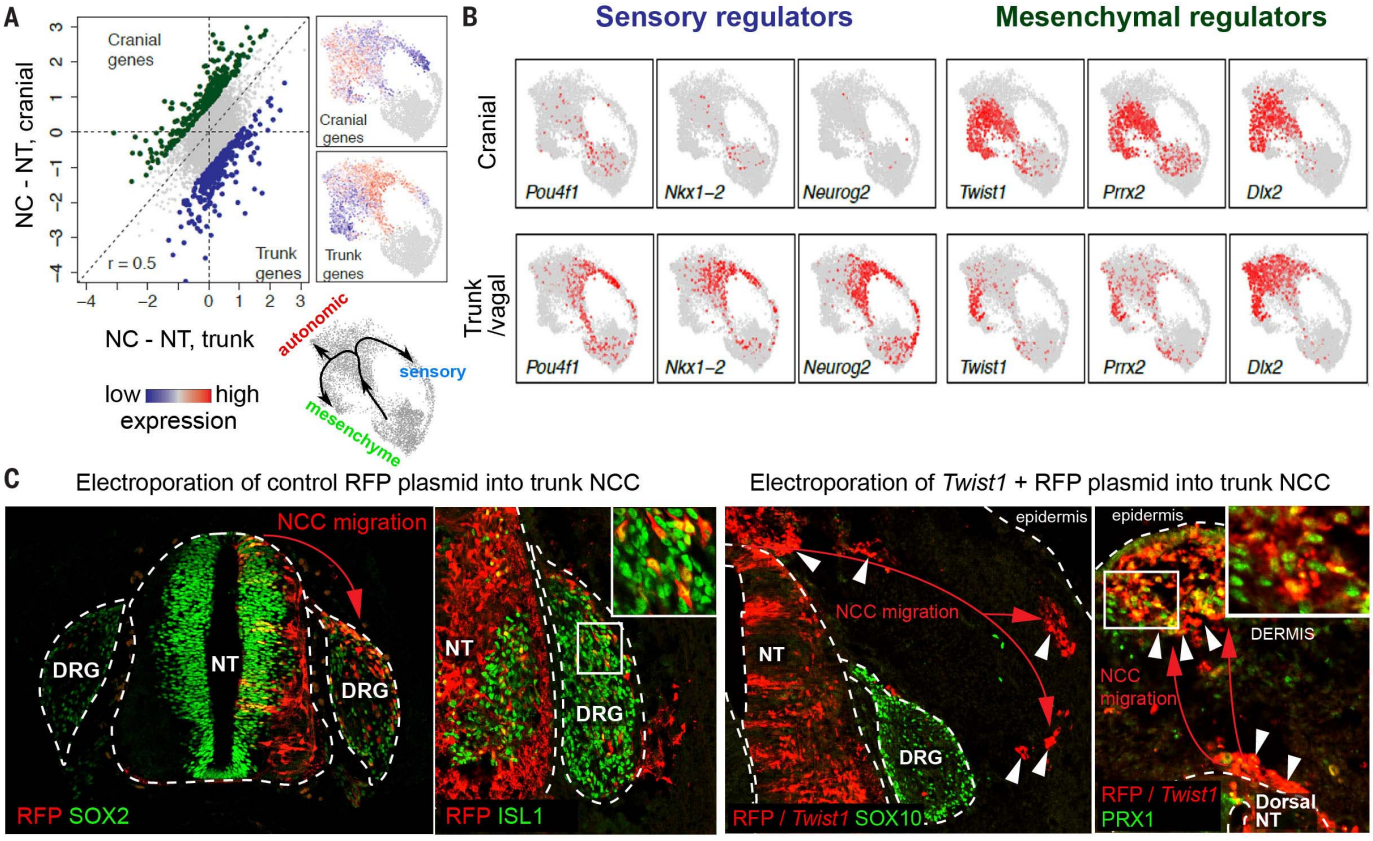


Fig. 6. Activation of early mesenchymal and sensory transcriptional programs. (**A**) Scatter plot contrasts expression changes accompanying NC transition from pre-EMT to migrating stages in cranial and trunk NC shows overall correlation (r = 0.5). However, more up-regulated genes upon transition in trunk or in cranial compartments end up preferentially expressed in sensory and mesenchymal-autonomic fates, respectively. (**B**) Mesenchymal regulators are activated early in cranial cells (top, only cranial expression shown), whereas sensory regulators are activated early in trunk cells (bottom, only trunk expression shown). (**C**) Immunofluorescence for SOX2, ISL1, and RFP (red fluorescent protein) after electroporation of control RFP-containing plasmid (left) versus after *Twist1* electroporation (right) in the developing chicken embryo trunk shows ectopic mesenchymal induction upon *Twist1* overexpression. NC, neural crest; NT, neural tube; NCC, neural crest cell; DRG, dorsal root ganglion.

Discussion

We used single-cell profiling to characterize spatiotemporal transcriptional dynamics of neural crest, showing progressive restrictions of cell fates, each realized through sequential phases of coactivation, biasing, and resolution of competing fates (Fig. 7A). Computational reconstruction of such differentiation trajectories from transcriptional similarity merely predicts likely lineage relationships, requiring additional validation (*55*). Here we relied on targeted lineage tracings of *Neurog2*, *Phox2b*, and *Prrx1* to validate gradual restriction of the developmental potential predicted by the derived transcriptional tree (Fig. 7B). However, clonal tracing techniques that are being developed to progressively record clonal histories of individual cells (*56*) would be ideally suited for validation of a complex differentiation process such as the one that takes place in neural crest.

The process of delamination largely erases the transcriptional signatures that distinguish different anteroposterior neural crest levels within the neural tube and activates fate-specifying gene programs. Such dissipation of pre-EMT signatures is consistent with the transient phenotype observed by Simoes-Costa *et al.*, who identified a cranial-specific pre-EMT gene regulatory network capable of transient activation of the mesenchymal properties in trunk, but unable to overcome the environmental signals and generate trunk mesenchyme (*57*). It indicates that acquisition of a fate likely requires appropriate cell-intrinsic state and extrinsic signaling during delamination. Consistently, we find that mesenchymal transcriptional bias emerges during delamination, indicating that this might be the point where mesenchymal potential is imbued to the neural crest. In support of this hypothesis, we noted that sustained overexpression of *Twist1*, normally activated upon delamination only in the cranial compartment, is sufficient to reverse trunk crest developmental program to a mesenchymal route. This parallels previous observations in chordates, where misexpression of a tunicate *Twist* resulted in conversion of a cephalic melanocyte lineage into migrating ectomesenchyme (*58*). *Twist1* might therefore be the ancient and sufficient factor defining the mesenchymal potential of migrating neural crest—a key step in the evolutionary development of the head in vertebrates.

The spatiotemporal data presented here may provide a resource for studies of neural crest biology and regulation, as well as investigations of neural crest–derived cancers and neurocristopathy-associated diseases. Although cell fate decisions in other systems may be based on different organizational principles, the molecular logic of cell fate decision characterized here for murine neural crest may also be shared by other organisms or tissues. Additional data, arising from analogous single-cell transcriptional studies or the new generalized lineage-tracing techniques, might soon allow such interorganismal comparisons to be performed.

Materials and methods summary

Neural crest cells were traced using the *Wnt1*^{TOMATO} and *Sox10*^{CreERT2};*R26R*^{TOMATO} strains from E8.5 to E10.5 mouse embryos. Embryos were collected and the TOMATO^{+} parts of the tissue were selected after stereoscopical observation using ultraviolet illumination. The tissue was dissociated and TOMATO^{+} cells were sorted by fluorescence-activated cell sorting on a 384-well plate in single-cell mode. The sorted cells were lysed and their

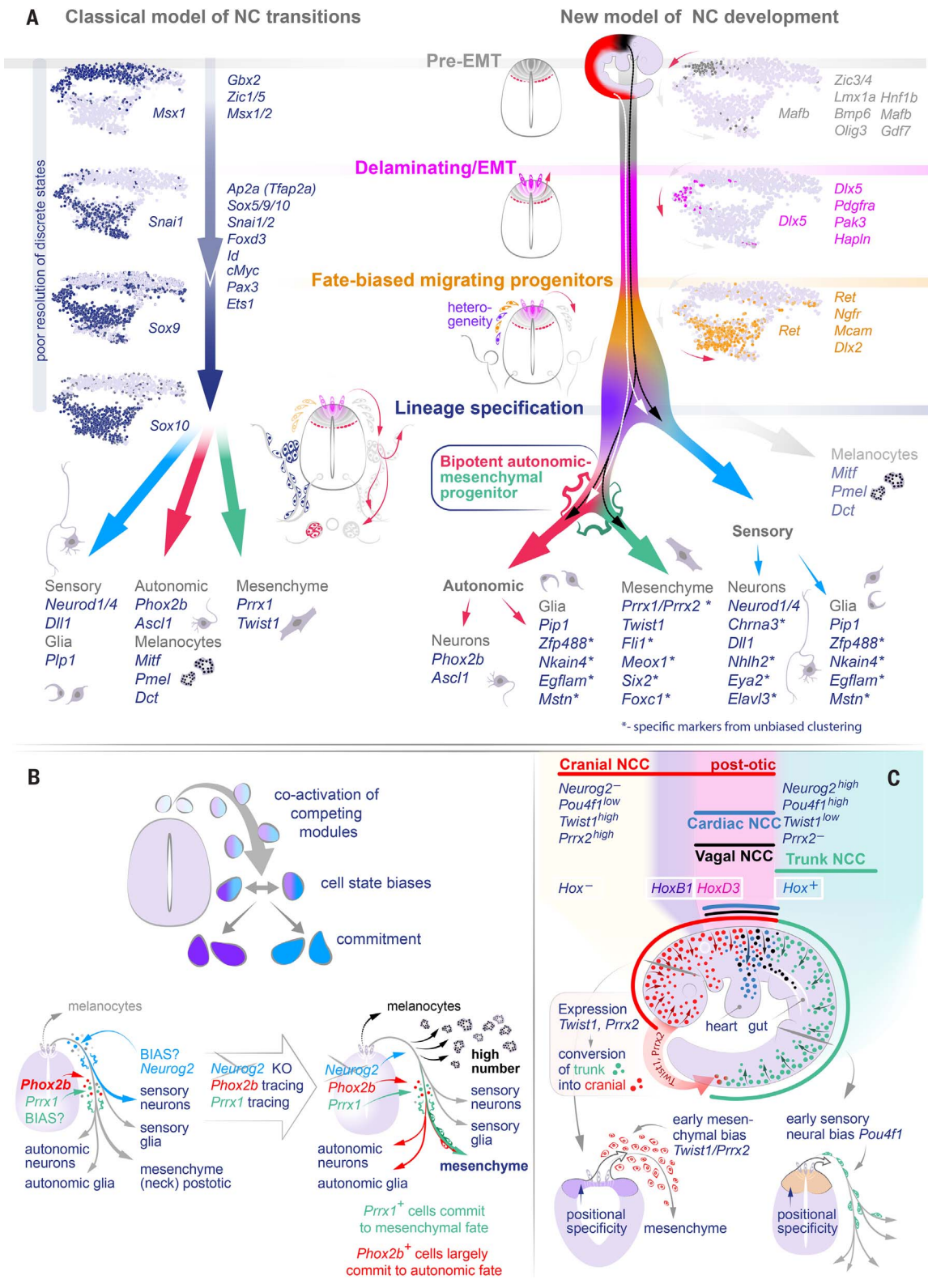


Fig. 7. Schematic representation of neural crest fate decisions. (**A**) Compared to a classical model (left), the model of NC development proposed here resolves a sequence of stages around delamination, heterogeneity of migratory progenitors, and sequential structure of lineage restrictions. (**B**) Upper: Individual binary decisions are resolved via a three-phase mechanism involving coactivation, biasing, and commitment. Lower: Lineage tracing shows that early activation of *Neurog2* is linked to repression of melanocytes in multipotent progenitors, whereas *Prrx1* and *Phox2b*, involved in coactivation and biasing phases, mark downstream mesenchymal and autonomic fates with sporadic coexpression in bipotent population around fate bifurcation. (**C**) Distinct gene modules, activated upon delamination along the cranial to post-otic axis of the embryo, establish bias toward either mesenchymal (e.g., *Twist1*) or sensory neuronal fate.

transcriptomes sequenced using the Smart-seq2 protocol. Individual single-cell datasets were preprocessed using PAGODA1 and PAGODA2 packages, which includes normalization, clustering of cells, and t-distributed stochastic neighbor embedding (t-SNE) for visualization (7). Joint analysis of multiple datasets was performed using the CONOS package (59).

Individual populations of clustered cells were validated using a variety of approaches. Major subpopulations (pre-EMT, delaminating and migrating neural crest, sensory neurons, autonomic neurons, and mesenchyme) were validated on E9.5 embryos using immunofluorescence and comparison with public in situ databases

(Allen Brain Atlas and Eurexpress) (*17*, *18*). Anatomical localization of the subpopulations was established using multiplexed in situ sequencing of 32 genes (*19*), followed by computational alignment of the single-cell transcriptional profiles with the spatially resolved in situ measurements. Expression patterns of specific markers of the sensory lineages were validated on E9.5 and E11.5 stages using RNAscope.

RNA velocity was used to assess transcriptional dynamics of cells (*8*). To quantify segregation of lineages, we adapted a computational method to reconstruct transcriptional trajectory tree from single-cell profiles using principal graph approach (*20*). Expression of transcription factors and their potential targets, predicted on the basis of DNA binding motifs, was analyzed to assess regulatory activity along the tree. We developed a computational method to analyze patterns of cell fate decisions, which tracks formation of fate-specific gene modules prior to fate bifurcations. Dynamics around major branches of neural crest fate acquisition (mesenchyme, sensory and autonomic neurogenesis) were further analyzed using lineage tracing with the *Prrx1-Cre;R26R*^{mTmG}, *Phox2b-Cre;R26R*^{TOMATO} and *Ascl1*^{CreERT2}*;R26R*^{TOMATO} mouse strains.

Additional validation included the analysis of knockin *Neurog2*^{CreERT2}*;R26R*^{YFP} mice (where *Neurog2* is replaced by *CreERT2*, constituting homozygous embryos Neurog2 knockouts). Overexpression of *Twist1*, as well as CRISPR-Cas9–mediated knockdown, performed as described in (*60*), in developing chicken embryos using in ovo electroporation, was used to validate *Twist1* involvement in mesenchymal fate acquisition. Similarly, in ovo chicken electroporation was used to overexpress *Prrx2* (mesenchymal driver) and *Crabp1* (driver of neuron-glia fate acquisition) and a dominant-negative version of *Brn3c* (avian homolog of *Pou4f1*).

REFERENCES AND NOTES

1. I. Imayoshi *et al*., Oscillatory control of factors determining multipotency and fate in mouse neural progenitors. *Science* **342**, 1203–1208 (2013). doi: 10.1126/science.1242366; pmid: 24179156
2. C. Pina *et al*., Inferring rules of lineage commitment in haematopoiesis. *Nat. Cell Biol.* **14**, 287–294 (2012). doi: 10.1038/ncb2442; pmid: 22344032
3. V. W. C. Yu *et al*., Epigenetic Memory Underlies Cell-Autonomous Heterogeneous Behavior of Hematopoietic Stem Cells. *Cell* **168**, 944–945 (2017). doi: 10.1016/j.cell.2017.02.010; pmid: 28235203
4. D. R. Cordero *et al*., Cranial neural crest cells on the move: Their roles in craniofacial development. *Am. J. Med. Genet. A.* **155**, 270–279 (2011). doi: 10.1002/ajmg.a.33702; pmid: 21271641
5. N. M. Le Douarin, *The Neural Crest* (Cambridge Univ. Press, 1982).
6. M. Simões-Costa, M. E. Bronner, Establishing neural crest identity: A gene regulatory recipe. *Development* **142**, 242–257 (2015). doi: 10.1242/dev.105445; pmid: 25564621
7. J. Fan *et al*., Characterizing transcriptional heterogeneity through pathway and gene set overdispersion analysis. *Nat. Methods* **13**, 241–244 (2016). doi: 10.1038/nmeth.3734; pmid: 26780092
8. G. La Manno *et al*., RNA velocity of single cells. *Nature* **560**, 494–498 (2018). doi: 10.1038/s41586-018-0414-6; pmid: 30089906
9. M. E. Bronner, M. Simões-Costa, The Neural Crest Migrating into the Twenty-First Century. *Curr. Top. Dev. Biol.* **116**, 115–134 (2016). doi: 10.1016/bs.ctdb.2015.12.003; pmid: 26970616
10. K. Nakata, T. Nagai, J. Aruga, K. Mikoshiba, Xenopus Zic3, a primary regulator both in neural and neural crest development. *Proc. Natl. Acad. Sci. U.S.A.* **94**, 11980–11985 (1997). doi: 10.1073/pnas.94.22.11980; pmid: 9342348
11. K. F. Liem Jr., G. Tremml, T. M. Jessell, A role for the roof plate and its resident TGFbeta-related proteins in neuronal patterning in the dorsal spinal cord. *Cell* **91**, 127–138 (1997). doi: 10.1016/S0092-8674(01)80015-5; pmid: 9335341
12. L. Lo, E. L. Dormand, D. J. Anderson, Late-emigrating neural crest cells in the roof plate are restricted to a sensory fate by GDF7. *Proc. Natl. Acad. Sci. U.S.A.* **102**, 7192–7197 (2005). doi: 10.1073/pnas.0502581102; pmid: 15883363
13. K. J. Millen, J. H. Millonig, M. E. Hatten, Roof plate and dorsal spinal cord dI1 interneuron development in the dreher mutant mouse. *Dev. Biol.* **270**, 382–392 (2004). doi: 10.1016/j.ydbio.2004.03.008; pmid: 15183721
14. W. Yanfeng, J. P. Saint-Jeannet, P. S. Klein, Wnt-frizzled signaling in the induction and differentiation of the neural crest. *BioEssays* **25**, 317–325 (2003). doi: 10.1002/bies.10255; pmid: 12655639
15. S. H. Kil, C. E. Krull, G. Cann, D. Clegg, M. Bronner-Fraser, The alpha4 subunit of integrin is important for neural crest cell migration. *Dev. Biol.* **202**, 29–42 (1998). doi: 10.1006/dbio.1998.8985; pmid: 9758701
16. S. Nakagawa, M. Takeichi, Neural crest emigration from the neural tube depends on regulated cadherin expression. *Development* **125**, 2963–2971 (1998). pmid: 9655818
17. G. Diez-Roux *et al*., A high-resolution anatomical atlas of the transcriptome in the mouse embryo. *PLOS Biol.* **9**, e1000582 (2011). doi: 10.1371/journal.pbio.1000582; pmid: 21267068
18. E. S. Lein *et al*., Genome-wide atlas of gene expression in the adult mouse brain. *Nature* **445**, 168–176 (2007). doi: 10.1038/nature05453; pmid: 17151600
19. R. Ke *et al*., In situ sequencing for RNA analysis in preserved tissue and cells. *Nat. Methods* **10**, 857–860 (2013). doi: 10.1038/nmeth.2563; pmid: 23852452
20. Q. Mao, L. Wang, I. W. Tsang, Y. Sun, Principal Graph and Structure Learning Based on Reversed Graph Embedding. *IEEE Trans. Pattern Anal. Mach. Intell.* **39**, 2227–2241 (2017). doi: 10.1109/TPAMI.2016.2635657; pmid: 28114001
21. A. Baggiolini *et al*., Premigratory and migratory neural crest cells are multipotent in vivo. *Cell Stem Cell* **16**, 314–322 (2015). doi: 10.1016/j.stem.2015.02.017; pmid: 25748934
22. M. Bronner-Fraser, S. Fraser, Developmental potential of avian trunk neural crest cells in situ. *Neuron* **3**, 755–766 (1989). doi: 10.1016/0896-6273(89)90244-4; pmid: 2484346
23. N. M. Le Douarin, G. W. Calloni, E. Dupin, The stem cells of the neural crest. *Cell Cycle* **7**, 1013–1019 (2008). doi: 10.4161/cc.7.8.5641; pmid: 18414040
24. L. Zurkirchen, L. Sommer, Quo vadis: Tracing the fate of neural crest cells. *Curr. Opin. Neurobiol.* **47**, 16–23 (2017). doi: 10.1016/j.conb.2017.07.001; pmid: 28753439
25. A. E. Lewis, H. N. Vasudevan, A. K. O'Neill, P. Soriano, J. O. Bush, The widely used Wnt1-Cre transgene causes developmental phenotypes by ectopic activation of Wnt signaling. *Dev. Biol.* **379**, 229–234 (2013). doi: 10.1016/j.ydbio.2013.04.026; pmid: 23648512
26. M. Minoux *et al*., Gene bivalency at Polycomb domains regulates cranial neural crest positional identity. *Science* **355**, eaal2913 (2017). doi: 10.1126/science.aal2913; pmid: 28360266
27. H. Suzuki *et al*., The transcriptional network that controls growth arrest and differentiation in a human myeloid leukemia cell line. *Nat. Genet.* **41**, 553–562 (2009). doi: 10.1038/ng.375; pmid: 19377474
28. R. A. Stewart *et al*., Zebrafish foxd3 is selectively required for neural crest specification, migration and survival. *Dev. Biol.* **292**, 174–188 (2006). doi: 10.1016/j.ydbio.2005.12.035; pmid: 16499899
29. N. A. Mundell, P. A. Labosky, Neural crest stem cell multipotency requires Foxd3 to maintain neural potential and repress mesenchymal fates. *Development* **138**, 641–652 (2011). doi: 10.1242/dev.054718; pmid: 21228004
30. J. Jacob *et al*., Insm1 (IA-1) is an essential component of the regulatory network that specifies monoaminergic neuronal phenotypes in the vertebrate hindbrain. *Development* **136**, 2477–2485 (2009). doi: 10.1242/dev.034546; pmid: 19542360
31. Q. Ma, C. Fode, F. Guillemot, D. J. Anderson, Neurogenin1 and neurogenin2 control two distinct waves of neurogenesis in developing dorsal root ganglia. *Genes Dev.* **13**, 1717–1728 (1999). doi: 10.1101/gad.13.13.1717; pmid: 10398684
32. M. Zirlinger, L. Lo, J. McMahon, A. P. McMahon, D. J. Anderson, Transient expression of the bHLH factor neurogenin-2 marks a subpopulation of neural crest cells biased for a sensory but not a neuronal fate. *Proc. Natl. Acad. Sci. U.S.A.* **99**, 8084–8089 (2002). doi: 10.1073/pnas.122231199; pmid: 12060754
33. M. Florio *et al*., Neurogenin 2 regulates progenitor cell-cycle progression and Purkinje cell dendritogenesis in cerebellar development. *Development* **139**, 2308–2320 (2012). doi: 10.1242/dev.075861; pmid: 22669821
34. T. J. Stuhlmiller, M. I. García-Castro, Current perspectives of the signaling pathways directing neural crest induction. *Cell. Mol. Life Sci.* **69**, 3715–3737 (2012). doi: 10.1007/s00018-012-0991-8; pmid: 22547091
35. M. Crow, A. Paul, S. Ballouz, Z. J. Huang, J. Gillis, Exploiting single-cell expression to characterize co-expression replicability. *Genome Biol.* **17**, 101 (2016). doi: 10.1186/s13059-016-0964-6; pmid: 27165153
36. C. Trapnell, Defining cell types and states with single-cell genomics. *Genome Res.* **25**, 1491–1498 (2015). doi: 10.1101/gr.190595.115; pmid: 26430159
37. E. Abranches *et al*., Stochastic NANOG fluctuations allow mouse embryonic stem cells to explore pluripotency. *Development* **141**, 2770–2779 (2014). doi: 10.1242/dev.108910; pmid: 25005472
38. M. Hu *et al*., Multilineage gene expression precedes commitment in the hemopoietic system. *Genes Dev.* **11**, 774–785 (1997). doi: 10.1101/gad.11.6.774; pmid: 9087431
39. S. Huang, Y. P. Guo, G. May, T. Enver, Bifurcation dynamics in lineage-commitment in bipotent progenitor cells. *Dev. Biol.* **305**, 695–713 (2007). doi: 10.1016/j.ydbio.2007.02.036; pmid: 17412320
40. M. Thomson *et al*., Pluripotency factors in embryonic stem cells regulate differentiation into germ layers. *Cell* **145**, 875–889 (2011). doi: 10.1016/j.cell.2011.05.017; pmid: 21663792
41. J. A. Briggs *et al*., The dynamics of gene expression in vertebrate embryogenesis at single-cell resolution. *Science* **360**, eaar5780 (2018). doi: 10.1126/science.aar5780; pmid: 29700227
42. J. A. Farrell *et al*., Single-cell reconstruction of developmental trajectories during zebrafish embryogenesis. *Science* **360**, eaar3131 (2018). doi: 10.1126/science.aar3131; pmid: 29700225
43. S. Semrau *et al*., Dynamics of lineage commitment revealed by single-cell transcriptomics of differentiating embryonic stem cells. *Nat. Commun.* **8**, 1096 (2017). doi: 10.1038/s41467-017-01076-4; pmid: 29061959
44. V. Boeva *et al*., Heterogeneity of neuroblastoma cell identity defined by transcriptional circuitries. *Nat. Genet.* **49**, 1408–1413 (2017). doi: 10.1038/ng.3921; pmid: 28740262
45. T. van Groningen *et al*., Neuroblastoma is composed of two super-enhancer-associated differentiation states. *Nat. Genet.* **49**, 1261–1266 (2017). doi: 10.1038/ng.3899; pmid: 28650485
46. A. Pattyn, X. Morin, H. Cremer, C. Goridis, J. F. Brunet, Expression and interactions of the two closely related homeobox genes Phox2a and Phox2b during neurogenesis. *Development* **124**, 4065–4075 (1997). pmid: 9374403
47. A. E. Doufexi, M. Mina, Signaling pathways regulating the expression of Prx1 and Prx2 in the chick mandibular mesenchyme. *Dev. Dyn.* **237**, 3115–3127 (2008). doi: 10.1002/dvdy.21762; pmid: 18942149
48. C. Gans, R. G. Northcutt, Neural crest and the origin of vertebrates: A new head. *Science* **220**, 268–273 (1983). doi: 10.1126/science.220.4594.268; pmid: 17732898
49. I. Espinosa-Medina *et al*., Dual origin of enteric neurons in vagal Schwann cell precursors and the sympathetic neural crest. *Proc. Natl. Acad. Sci. U.S.A.* **114**, 11980–11985 (2017). doi: 10.1073/pnas.1710308114; pmid: 29078343
50. M. Scheffer *et al*., Anticipating critical transitions. *Science* **338**, 344–348 (2012). doi: 10.1126/science.1225244; pmid: 23087241
51. E. J. Hutchins *et al*., Migration and diversification of the vagal neural crest. *Dev. Biol.* **444** (suppl. 1), S98–S109 (2018). doi: 10.1016/j.ydbio.2018.07.004; pmid: 29981692
52. F. J. de Lange *et al*., Lineage and morphogenetic analysis of the cardiac valves. *Circ. Res.* **95**, 645–654 (2004). doi: 10.1161/01.RES.0000141429.13560.cb; pmid: 15297379
53. H. Bildsoe *et al*., Requirement for Twist1 in frontonasal and skull vault development in the mouse embryo. *Dev. Biol.* **331**, 176–188 (2009). doi: 10.1016/j.ydbio.2009.04.034; pmid: 19414008
54. J. W. Vincentz *et al*., Twist1 controls a cell-specification switch governing cell fate decisions within the cardiac neural crest. *PLOS Genet.* **9**, e1003405 (2013). doi: 10.1371/journal.pgen.1003405; pmid: 23555309

55. C. Weinreb, S. Wolock, B. K. Tusi, M. Socolovsky, A. M. Klein, Fundamental limits on dynamic inference from single-cell snapshots. *Proc. Natl. Acad. Sci. U.S.A.* **115**, E2467–E2476 (2018). doi: 10.1073/pnas.1714723115; pmid: 29463712
56. L. Kester, A. van Oudenaarden, Single-Cell Transcriptomics Meets Lineage Tracing. *Cell Stem Cell* **23**, 166–179 (2018). doi: 10.1016/j.stem.2018.04.014; pmid: 29754780
57. M. Simoes-Costa, M. E. Bronner, Reprogramming of avian neural crest axial identity and cell fate. *Science* **352**, 1570–1573 (2016). doi: 10.1126/science.aaf2729; pmid: 27339986
58. P. B. Abitua, E. Wagner, I. A. Navarrete, M. Levine, Identification of a rudimentary neural crest in a non-vertebrate chordate. *Nature* **492**, 104–107 (2012). doi: 10.1038/nature11589; pmid: 23135395
59. N. Barkas *et al*., Wiring together large single-cell RNA-seq sample collections. *bioRxiv* (2018). doi: 10.1101/460246
60. S. Gandhi, M. L. Piacentino, F. M. Vieceli, M. E. Bronner, Optimization of CRISPR/Cas9 genome editing for loss-of-function in the early chick embryo. *Dev. Biol.* **432**, 86–97 (2017). doi: 10.1016/j.ydbio.2017.08.036; pmid: 29150011

ACKNOWLEDGMENTS

We thank the Eukaryotic Single Cell Genomics Facility for the single-cell RNA-seq and the in situ sequencing pilot facility at the Science for Life Laboratory, Sweden (for technical assistance with the in situ sequencing experiments). We also thank O. Kharchenko for help with illustrations and V. Petukhov for assistance with computational analysis of in situ sequencing data. **Funding:** I.A. was funded by a Swedish Research Council (Vetenskapsradet, VR) grant, ERC Consolidator grant "STEMMING-FROM-NERVE" N647844, the Paradifference Foundation, and the Bertil Hallsten Research Foundation. P.V.K. was supported by NSF-14-532 CAREER award and NIH R01HL131768. M.N. was funded by a Swedish Research Council (Vetenskapsradet) grant 2016-03645, the Knut and Alice Wallenberg Foundation, and Familjen Erling Perssons stiftelse. V.D. was supported by a Russian Science Foundation grant (18-75-10005, immunochemistry) and the Swedish Research Council (2015-03387). M.E.K. was supported by Stiftelsen Riksbankens Jubileumsfond (Erik Rönnbergs fond stipend). N.A. was supported by RSF grant 16-15-10237. **Author contributions:** M.K., M.E.K., J.P., L.E., N.A., Y.Y., M.H., V.D., M.F., M.L.P., F.B., C.Y., X.Q., W.-Y.H., and L.C. acquired all biological data and performed the relevant analysis. R.S., P.V.K., and T.C. performed computational analysis of single-cell data. R.S. and P.V.K. developed computational methods. R.S. and M.M.H. performed computational analysis of in situ sequencing data. C.B., M.N., M.E.B., D.A.G., J.-F.B., G.G.C., P.E., K.F., P.V.K., and I.A. gave feedback on experimental aspects, supervised experimental approaches, and implemented the data interpretation. R.S., M.K., M.E.K., and J.P. made all figures containing data and resulting analysis (except Fig. 7). R.S., M.K., M.E.K., P.V.K., and I.A. designed the study, organized experimental work, and wrote the manuscript. All authors provided feedback on figures, manuscript composition, and structure. **Competing interests:** M.N. holds shares in Cartana AB, a company commercializing in situ sequencing reagents. Other authors declare no conflicts of interest. **Data and materials availability:** All single-cell RNA-seq datasets have been deposited in the GEO under accession code GSE129114. Processed data, code, supplementary materials, and interactive views of datasets can be accessed on the authors' website: http://pklab.med.harvard.edu/ruslan/neural.crest.html. These URLs will be maintained exactly as they are for at least 5 years with no changes. The *Sox10*^{CreERT2} strain is available from the laboratory of Vassilis Pachnis (The Francis Crick Institute, UK) under a material transfer agreement with the institution. All other data needed to evaluate the conclusions in the paper are present in the paper or the supplementary materials.

SUPPLEMENTARY MATERIALS

science.sciencemag.org/content/364/6444/eaas9536/suppl/DC1
Materials and Methods
Supplementary Text
Figs. S1 to S12
Data S1 to S12
Data Tables S1 to S11
References (*61*–*75*)

9 January 2018; resubmitted 12 December 2018
Accepted 10 April 2019
10.1126/science.aas9536

RESEARCH ARTICLE SUMMARY

PALEOBOTANY

Eocene Fagaceae from Patagonia and Gondwanan legacy in Asian rainforests

Peter Wilf*, Kevin C. Nixon, Maria A. Gandolfo, N. Rubén Cúneo

INTRODUCTION: The flowering plant family Fagaceae includes all oaks, beeches, chestnuts, stone oaks, and allies across 10 genera and >900 species. The family stands out for its very high biomass and its domination of forests from the northern temperate zone to the tropics, especially the Southeast (SE) Asian tropics. Numerous Fagaceae are keystone species that define forest structure, supply substantial food reserves through their famously nutritious fruits, and hold considerable economic and cultural importance. Until now, no living or fossil member of Fagaceae had been found south of the Malay Archipelago, and, accordingly, the Southern Hemisphere has not been seriously considered in the family's history (the southern beech, *Nothofagus*, belongs to a separate family).

RATIONALE: We discovered two fossil infructescences of Fagaceae, one mature and one immature with >110 fruits preserved, along with abundant fagaceous leaves in the early Eocene (52-million-year-old) Laguna del Hunco flora of Chubut, southern Argentina. The highly diverse fossil assemblage represents rainforest vegetation from the terminal phase of Gondwana; South America, Antarctica, and Australia had not yet separated, and global warmth allowed floral and faunal interchange among those landmasses. Subsequently, Australia moved northward and eventually collided with SE Asia, initiating new biotic exchanges. The Laguna del Hunco flora reflects these Earth processes in preserving numerous taxa that survive in Australasia and SE Asia, among which several characteristically associate with tropical Fagaceae today and provide rich biogeographic context for the discovery. Examples include *Eucalyptus* (gum), *Gymnostoma* (rhu), engelhardioid Juglandaceae (walnut family), *Ceratopetalum* (coachwood), Lauraceae (laurels), *Ripogonum* (supplejack), *Agathis* (kauri), diverse podocarps (yellowwoods), *Papuacedrus* (a New Guinean cypress), and *Todea* (king fern).



Discovering Argentina's lost *Castanopsis* rainforest. (Top) Early Eocene fossil lake beds at Laguna del Hunco. (Bottom) Left to right: Field-discovery photos of the *Castanopsis* mature (large nut length, 17 mm) and immature (length, ~15 cm) infructescence segments, a fagaceous leaf (length, 18.5 cm), a *Eucalyptus caldericola* infructescence (length, 8.2 cm), and a *Papuacedrus prechilensis* leafy branch (length, 10.2 cm).

RESULTS: We place the new fossil infructescences in Fagaceae and the living Asian genus *Castanopsis*, a close relative of the chestnuts, because of their preservation of cupule-fruit complexes with lateral, solitary placement on their spikelike infructescence axes; complete enclosure of the (single) nut; (two) asymmetrical valves; scaly ornamentation; lobed perianth; and three linear styles with unexpanded stigmas. The fossil leaves are also consistent with *Castanopsis* and in all likelihood represent the same source plant as the infructescences; both occur in the same strata with the just-listed taxa that are local associates of living *Castanopsis*, especially in New Guinea's montane rainforests. The new fossils represent a major southern extension of the historical range of Fagaceae, as well as the oldest record, by ~8 million years, of the genus *Castanopsis*, which has ~120 living species and is dominant at lower montane elevations from New Guinea to the Himalaya and Japan.

ON OUR WEBSITE

Read the full article at http://dx.doi.org/10.1126/science.aaw5139

CONCLUSION: The fossils' diagnostic characters, early Eocene age, and occurrence in floral associations markedly similar to today's all suggest that *Castanopsis* evolved in the Southern Hemisphere, most likely from an ancestor that had dispersed earlier from North America, and followed the southern route to Asia along with the associated survivor taxa. This discovery substantially increases the known Gondwanan legacy in Asia and Malesia and shows the persistence of the survivor lineages, which tracked their preferred cool-wet rainforest environments through time and space from Gondwana to Asia. The modern analog forests, often located in biodiverse watershed areas, are now threatened by anthropogenic change that is occurring orders of magnitude more rapidly than in the geologic past. The abundant fossil leaves with feeding marks from diverse insects, the large nuts, and the associated flora all indicate that the ancient trees were keystone species in early Eocene "oak-laurel" forests of Patagonia, much like *Castanopsis* is today in Asia. Subsequently, *Castanopsis* and many other rainforest taxa appear to have gone extinct in Patagonia with the earliest phases of Antarctic separation and drying regional climates. ■

The list of author affiliations is available in the full article online.
*Corresponding author. Email: pwilf@psu.edu
Cite this article as P. Wilf *et al.*, *Science* **364**, eaaw5139 (2019). DOI: 10.1126/science.aaw5139

RESEARCH ARTICLE

PALEOBOTANY

Eocene Fagaceae from Patagonia and Gondwanan legacy in Asian rainforests

Peter Wilf[1]*, Kevin C. Nixon[2], Maria A. Gandolfo[2], N. Rubén Cúneo[3]

The beech-oak family Fagaceae dominates forests from the northern temperate zone to tropical Asia and Malesia, where it reaches its southern limit. We report early Eocene infructescences of *Castanopsis*, a diverse and abundant fagaceous genus of Southeast Asia, and co-occurring leaves from the 52-million-year-old Laguna del Hunco flora of southern Argentina. The fossil assemblage notably includes many plant taxa that associate with *Castanopsis* today. The discovery reveals novel Gondwanan history in Fagaceae and the characteristic tree communities of Southeast Asian lower-montane rainforests. The living diaspora associations persisted through Cenozoic climate change and plate movements as the constituent lineages tracked post-Gondwanan mesic biomes over thousands of kilometers, underscoring their current vulnerability to rapid climate change and habitat loss.

Fagaceae sensu stricto (s.s.) (i.e., excluding *Nothofagus*) is one of the highest-biomass and most economically important plant families; it is the only angiosperm group that consistently dominates forests from the northern temperate zone to the tropics, especially the Southeast (SE) Asian and Malesian tropics, where it ranges into low southern latitudes (*1*–*5*). Among its 10 genera and >900 species, numerous Fagaceae are keystone species that define forest structure in biodiverse areas and produce abundant protein-rich, animal-dispersed fruits (*6*, *7*). The family's fossil record is extensive but entirely restricted to the Northern Hemisphere (*8*–*15*); likewise, biogeographic hypotheses for the living genera do not consider the Southern Hemisphere (*16*–*22*). The southernmost occurrences of Fagaceae are in New Guinea, where a few species of the castaneoid genera *Castanopsis* and *Lithocarpus* are abundant (*1*, *23*, *24*).

In 1925, E. W. Berry (*25*) assigned two fossil leaves of interest from the "Mirhoja" site in Argentine Patagonia to Dilleniaceae and the species "*Tetracera*" *patagonica*. Mirhoja, now Laguna del Hunco, has produced one of the most diverse Eocene floras [at 52.2 million years (Ma) old] worldwide (*26*, *27*). The site captures a distinctive, high-resolution snapshot of the last ecosystems of Gondwanan South America, coinciding with the early Eocene climatic optimum (*28*). At that time, frost-free climates and diverse biotas prevailed, and substantial dispersal took place across middle and high latitudes of both the Northern and Southern hemispheres; deep-water separation of South America, Antarctica, and Australia had not yet occurred (*28*–*30*).

Laguna del Hunco preserves fossils of numerous paleo-Antarctic rainforest lineages (PARLs) (*31*) whose living relatives characteristically associate with tropical Fagaceae in perhumid, lower-montane rainforests of Malesia (*1*, *2*, *23*, *24*, *32*–*37*). These taxa include two members of Fagales, *Gymnostoma* (Casuarinaceae) and *Alatonucula* (extinct engelhardioid Juglandaceae); the additional angiosperms *Eucalyptus* (Myrtaceae), *Ceratopetalum* (Cunoniaceae), and *Ripogonum* (Ripogonaceae); conifers in Cupressaceae (*Papuacedrus*), Araucariaceae (*Agathis* and *Araucaria* Section *Eutacta*), and Podocarpaceae (*Dacrycarpus*, *Podocarpus*, and a species similar to those of *Phyllocladus*); and the fern *Todea* (Osmundaceae) (*27*, *38*–*45*). New Guinea, in particular, has all the listed lineages in its living flora in associations with *Castanopsis* and *Lithocarpus* (*23*, *24*, *36*, *37*, *46*–*48*). Leaves of Lauraceae, which also co-occur today with Fagaceae throughout SE Asia's lower-montane "oak-laurel" or "montane oak" forests (*5*, *49*) (the term includes non-oak Fagaceae such as *Castanopsis*), are abundant at Laguna del Hunco but not identifiable to the genus level (*27*).

Most of the Laguna del Hunco PARLs are also known as fossils in Australia and elsewhere in Gondwana; nearly all went extinct in South America but survived in the Old World, especially on post-Gondwanan, northward-moving Australia (Sahul) (*29*, *31*, *50*, *51*). Their dispersal to Asia (Sunda) began with the late Oligocene (*52*) onset of Sahul-Sunda collision. The notable persistence of PARL associations over time and space is considered to result from a convergence of individualistic responses to climatic and tectonic change mediated by niche conservatism and physiological drought intolerance (*31*, *53*, *54*). Because of the presumed Northern Hemisphere origins of all Fagaceae, the modern-day co-occurrences of Fagaceae and PARLs in Malesia have been considered a mix of Laurasian and Gondwanan influences, respectively (*5*, *55*–*57*).

The rich biogeographic context of the Laguna del Hunco flora and the widespread associations of its diverse living relatives with tropical Fagaceae have foreshadowed the potential discovery of fossil Fagaceae at the site. Here, we report two infructescences and abundant "*Tetracera*" leaves as the first reliable evidence of Fagaceae from Gondwana or the extratropical Southern Hemisphere. We refer the infructescences to *Castanopsis*, which today has ~120 species from the Himalaya to New Guinea and Japan (*2*, *58*, *59*), and the leaves to a fagaceous organ genus. These fossils reveal a new southern component of Fagaceae biogeography and substantially increase the known Gondwanan legacy in Asian tropical rainforests. We propose and critically discuss a biogeographic hypothesis to explain our observations.

Systematic paleontology

Family Fagaceae Dumortier, 1829. Genus Castanopsis *(D. Don) Spach, 1841*

Castanopsis rothwellii Wilf, Nixon, Gandolfo et Cúneo sp. nov.

Holotype here designated MPEF-Pb 6433a and MPEF-Pb 6433b (part and counterpart) (Fig. 1). Paratype: MPEF-Pb 8198a and MPEF-Pb 8198b (Fig. 2). Museo Paleontológico Egidio Feruglio (MEF), Trelew, Argentina (repository acronym MPEF-Pb).

Type locality: Laguna del Hunco, Tufolitas Laguna del Hunco, La Huitrera Formation, early Eocene (~52.2 Ma). Holotype from quarry LH13, paratype from quarry LH27 of (*26*, *39*), collected 7 December 2002 and 8 December 2016, respectively.

Etymology: Honoring G. W. Rothwell, paleobotanist, for his eminence in research, teaching, and mentoring.

Diagnosis

Cupules numerous on the infructescence axis; two asymmetrical valves per cupule, abaxial valve larger than the adaxial, apices of open valves recurved; cupule ornamentation of imbricate, helically arranged, flattened, triangular scales; cupule fully enclosing a single nut.

Description

The holotype (Fig. 1) is a bent infructescence segment bearing four maturing fruits and several fruit scars, and the paratype (Fig. 2) is a bent, ~15-cm-long, unbranched, spikelike infructescence segment with >110 immature fruits. Fruits are solitary, lateral, and alternate on the infructescence axis, most of them strongly directed toward the axis apex but some nearly perpendicular, leaving ellipsoid scars of ~1.6 mm major axis length (Fig. 1H); fruits consist of solitary nuts

[1]Department of Geosciences, Pennsylvania State University, University Park, PA 16802, USA. [2]Liberty Hyde Bailey Hortorium, Plant Biology Section, School of Integrative Plant Science, Cornell University, Ithaca, NY 14853, USA. [3]CONICET, Museo Paleontológico Egidio Feruglio, 9100 Trelew, Chubut, Argentina.
*Corresponding author. Email: pwilf@psu.edu

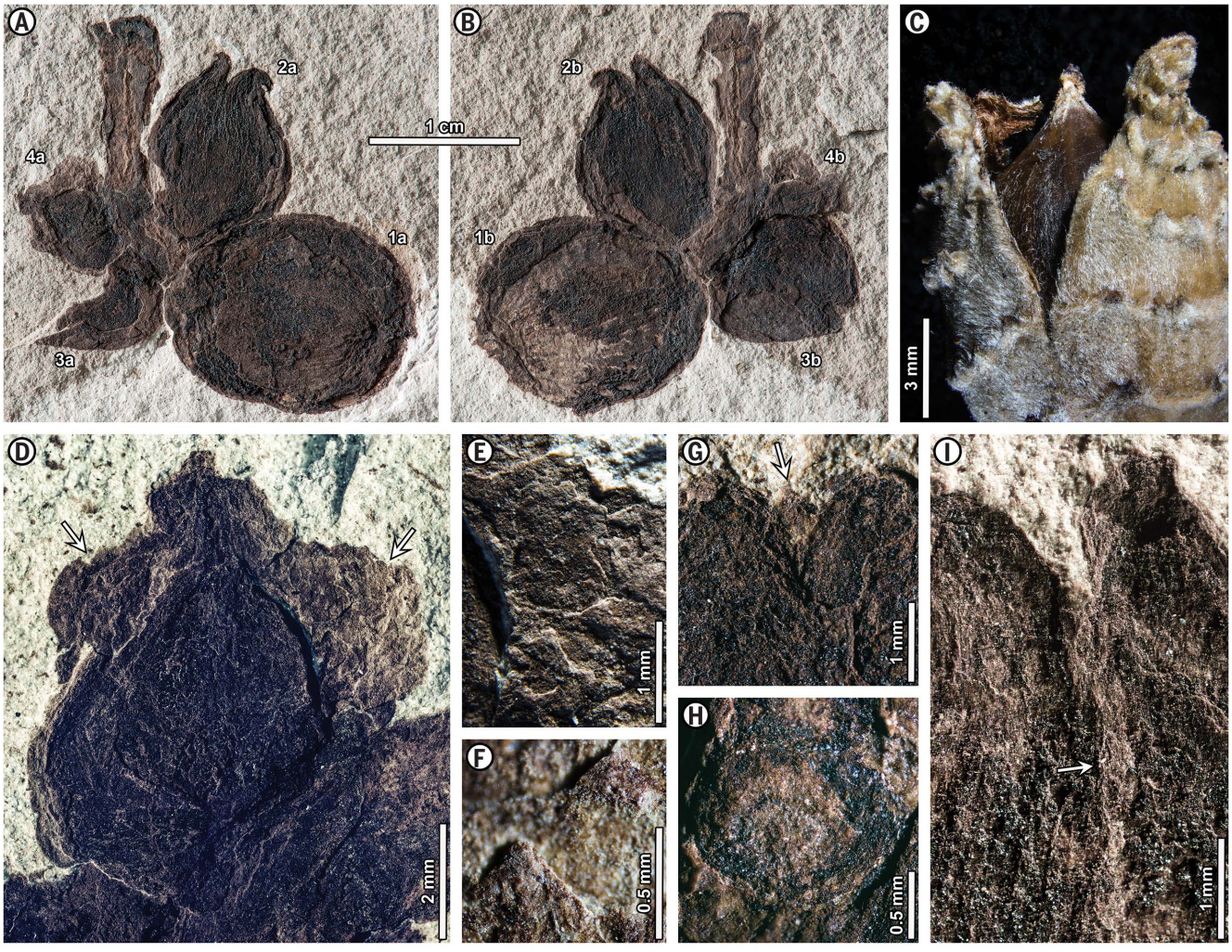


Fig. 1. *Castanopsis rothwellii* sp. nov. holotype. (**A** and **B**) *C. rothwellii* holotype, MPEF-Pb 6433, showing the infructescence segment (A) part and (B) counterpart with four fruits labeled 1 to 4. Fruit 1 preserves a longitudinally striated nut seated in abraded cupule remnants. Fruits 2 and 3 are cupules splitting into two unequal valves [also shown in (G) and (I)]. Recurved valve apices are well developed in fruit 2; fruit 3b preserves the nut apex exposed between the valve tips [also shown in (G)]. Fruit 4a has an ovate nut exposed and seated in cupule remnants with imbricate scaly ornamentation [see also (D) to (F)]. (**C**) *C. cuspidata* litter specimen, Kyoto, Japan, similar to fossil fruit 2 [see (A), (B), and (I)], with the cupule splitting into two unequal valves with recurved apices; a single nut; and banded, scaly ornamentation. (**D**) Detail of fossil fruit 4a (A), showing a coalified, ovate nut with scaly cupule remnants (arrows) [also shown in (E) and (F)]. (**E** and **F**) Cupule scale details from (D). (**G**) The apex of cupule 3b [also shown in (B)] splitting into two valves, exposing the nut apex (arrow). (**H**) Fruit scar from the infructescence axis, located immediately distal to fruit 2b (B). (**I**) Detail of opening valves and extensive suture zone (arrow) of fruit 2b [also shown in (B)].

(Fig. 1D) fully enclosed by sessile to shortly pedicellate, two-valved, ovate to ellipsoid, asymmetrical cupules. Cupules are ornamented with imbricate, flattened, triangular, symmetrical, helically arranged scales with straight to acuminate apices (Figs. 1, D to F, and 2, B and J); cupules lack spines or tubercles. Maturing fruits (Fig. 1) are asymmetrical and two-valved, the inferred abaxial valve larger and more convex than the adaxial. Cupules are ovate or ellipsoid, the largest 17 mm long and 13.4 mm wide, splitting into two valves along a distinct suture zone (Fig. 1I), the freed valve apices recurved (Fig. 1, A, B, and I). Nuts are ovate (Fig. 1D), not visibly angled, with longitudinal striations; the scale length (visible portion) is ~0.75 mm. Immature fruits (Fig. 2) have ellipsoid cupules on smaller (younger) fruits (Fig. 2H) and ovate-acuminate cupules with a thickened wall on more developed fruits (Fig. 2F). The perianth is lobed, the lobes apparently numbering six according to symmetry (Fig. 2E). The three styles are slender and undivided, with unexpanded stigmas (Fig. 2, B and E to I).

Remarks

Castanopsis rothwellii sp. nov. has cupule-fruit complexes, a synapomorphy of Fagaceae (*17*, *60*–*62*). The maturing fruits have asymmetrical, valved and sutured, solitary cupules that fully enclose a single nut; this configuration is specific to *Castanopsis* among living Fagaceae (*2*, *58*, *59*, *63*–*65*). The immature fruits preserve the distinctive lobed perianth of Fagaceae and three linear styles with unexpanded stigmas, as seen only in the castaneoids *Castanopsis* and *Lithocarpus* among extant Fagaceae; however, the low insertion angle of most fruits to the axis is more typical of *Castanopsis* (*2*, *58*, *59*, *61*, *63*, *66*). The spikelike, unbranched infructescence with laterally inserted fruits is also distinctive for *Castanopsis* and other Castaneoideae, although the total number of fruits per infructescence (as seen in the paratype) (Fig. 2, A and D) is much higher than in living *Castanopsis*; this may be a plesiomorphic condition relative to modern *Castanopsis*. Thus, both specimens of *C. rothwellii* have diagnostic characters of extant *Castanopsis*, and the two fossils



Fig. 2. *Castanopsis rothwellii* sp. nov. paratype. (**A**, **B**, and **D** to **J**) MPEF-Pb 8198; [(A), (B), and (D) to (G) part; [(I) and (J)] counterpart. (A) Spikelike infructescence segment with >110 immature cupules preserved [also shown in (D)]. (B) Single cupule ornamented with triangular, imbricate, helical scales, preserving three slender styles. (**C**) *C. acuminatissima*, US 3256853 (Papua New Guinea), young fruit similar to the fossil fruits, with comparable scale ornamentation, rounded perianth lobes, and three styles. (D) Detail from (A), across the hairline rock fracture, showing densely packed cupules at variable orientations to the axis. (E) Fruit apex with two perianth lobes preserved, indicating an original configuration of six lobes by symmetry, and with two of three original styles (as indicated by symmetry). (F) Ovate cupule, nearly perpendicular to the axis, with three styles [see (G)]. (G) Detail of the cupule apex from (F), with a partially preserved perianth lobe and three styles. (H) Small cupule at an acute angle to the axis, with three styles. (I) Fruit apex with three styles. (J) Cupule with well-preserved ornamentation of triangular, imbricate, helical scales. Arrows, styles; PL, perianth lobe.

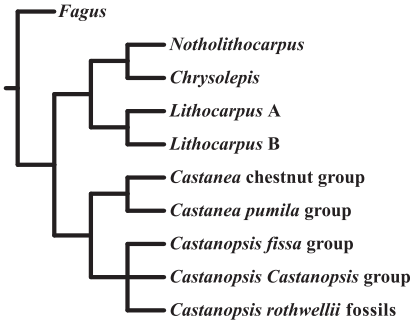


Fig. 3. Phylogenetic analysis. Consensus of the two most parsimonious trees, based on a matrix of seven morphological characters (Table 1), with the fossil infructescence, *C. rothwellii*, allowed to float on a scaffold according to the results of Manos *et al*. (*98*). See the text and Table 1 for additional details.

Table 1. Character scores for phylogenetic analysis. Scores were assigned for characters, shown left to right in the following order. Style number: three = 0; six = 1. Cupule appendages: scaly = 0; spinose = 1. Cupule dehiscence: valvate = 0; hemispheric indehiscent = 1. Female flowers per node: solitary = 0; clustered = 1. Flowers per cupule: one = 0; three = 1; more than three = 2; nonadditive. Valve dehiscence: complete = 0; partial = 1; none = 2; nonadditive. Inflorescence sexuality: unisexual = 0; unisexual and mixed = 1. Brackets indicate polymorphisms. Cupule appendages were scored according to the predominant state in mature cupules. Female flowers per node is inapplicable in *Fagus* because there is only a single node (this is indicated in the score by a dash). Figure 3 shows the consensus tree from the phylogenetic analysis.

Taxon	Score
Castanopsis rothwellii fossils	0000010
Fagus	000-000
Castanea chestnut group	110[01]101
Castanea pumila group	1101001
Castanopsis fissa group	00[01]00[12]0
Castanopsis Castanopsis group	01[01]0[01][012]0
Chrysolepis	0101201
Lithocarpus A	001[01]020
Lithocarpus B	0011020
Notholithocarpus	0011021

share several features, especially their deployment on a single infructescence axis of solitary, single-fruited, lateral cupules that entirely enclose the nut with ornamentation of helically arranged, imbricate scales. On the basis of the available information, we consider the two *C. rothwellii* specimens as an ontogenetic series of the same species.

Several extant *Castanopsis* species are similar to the fossils, although none is identical. Most living *Castanopsis* species have spiny or tubercular cupules; however, scaly ornamentation, often deployed in bands but sometimes imbricate, also occurs in various growth stages of several species (*1*, *2*, *58*, *59*, *65*). Young cupules of *Castanopsis acuminatissima* (New Guinea) (Fig. 2C) are very similar to the fossils; they are two-valved and one-fruited, with imbricate, triangular, helical scales. However, they are unlike the fossils in that their valve apices are not recurved, and their scales become more irregular and exserted with maturity. Cupules of *Castanopsis cuspidata* (Japan and Korea) (Fig. 1C) have a single nut and two or more valves with apices that are recurved and liplike when the valves are opened, closely resembling one of the mature fossil fruits (Fig. 1, A, B, and I); they also have flattened, helically arranged, triangular scales, like those of the fossils but separated into bands instead of helical. Because of the biogeographic interest of *Nothofagus* (*67*), we briefly note critical differences in this genus (*1*), including its single-fruited infructescences, symmetrical cupules, and expanded, strap-shaped stigmas.

In summary, the *C. rothwellii* infructescences have numerous distinctive features of extant *Castanopsis* and differ substantially from the living genus only in having large numbers of fruits per infructescence, which we consider insufficient cause to erect a new genus. We find the available evidence compelling to assign the new infructescences to *Castanopsis*. Phylogenetic analysis strongly supports our taxonomic assignment, placing the fossils either as sister to living *Castanopsis* or within the *Castanopsis* crown group (Fig. 3 and Table 1). The new fossils imply a minimum age of 52.2 Ma for the *Castanea-Castanopsis* divergence, older than recent molecular-dating estimates (*68*), which are usually constrained by *Castanopsis crepetii* from the middle Eocene (~43.8 Ma) of Oregon (*11*). The oldest known *Castanea* fossil is from the middle Eocene of Tennessee (*69*, *70*).

Family Fagaceae Dumortier, 1829. Genus Castaneophyllum *Jones et Dilcher, 1988*

Castaneophyllum patagonicum (Berry) Wilf, Nixon, Gandolfo et Cúneo comb. nov.

Basionym: *Tetracera patagonica* Berry, *Johns Hopkins University Studies in Geology*, vol. 6, p. 219 (1925) (*25*). Lectotype here designated USNM 201951 (Fig. 4, A to C), drawn in fig. 4 of plate I of (*25*), Paleobotanical Division, National Museum of Natural History, Smithsonian Institution, Washington, DC (USNM). Syntype: USNM 201952 (Fig. 4, D and E), drawn in figs. 5 and 6 of plate I of (*25*).

Type locality: Laguna del Hunco, Tufolitas Laguna del Hunco, La Huitrera Formation, early Eocene (~52.2 Ma). The precise location is unknown, but the matrix and secondary mineral staining in the paratype (Fig. 4D) are specific to the bed containing quarry LH04 of (*26*). Additional material: MPEF-Pb 8200 to 8202, 8204, and 8205, from Laguna del Hunco quarry LH02 of (*26*, *39*); 8209, 8222, 8224, 8227, 8228 (Fig. 4J), 8230, 8235, 8236, 8238, 8242 to 8245, 8248, 8249, and 8252 (LH04); 8255 (Fig. 4G), 8257 (Fig. 4H), 8259, 8262, and 8263 (LH13); 8266 (Fig. 4, F and I) (LH15); 8268 and 8269 (LH16); 8271 (LH18); 8272 (LH20); 8274 (LH23); 8275 (Fig. 4K) (LH26); 8278 (LH27); and 1453 and 1454 (precise location unknown).

Emended species description

Leaf organization inferred simple. Petiole insertion marginal, petiole length to >55 mm, petiole width to 4 mm. Lamina unlobed and margin prominently serrate, the teeth present over most of the blade and nearly to the leaf base. Laminar size microphyll to mesophyll, reconstructed leaf area to ~8150 mm^2, length to 185 mm, width to 70 mm, length:width ratio 2.2 to 3.6:1. Laminar shape elliptical to ovate, with medial symmetry and asymmetrical basal insertion. Base and apex angle acute; base shape variably subrounded, convex, concavo-convex, or cuneate; apex shape straight to acuminate. Venation well organized, rank 4. Primary venation pinnate. Secondary veins craspedodromous, robust, subopposite to alternate and excurrent on midvein, up to 17 pairs observed on the largest leaves, spacing and angle regular to slightly irregular, rarely forking well inside the margin. Secondary course nearly straight, gently then increasingly curving apically on approach to and within the tooth, entering the tooth in the basal longitudinal half as the tooth's principal vein. Fimbrial vein present throughout blade, intermittently weakened or irregularly expressed as loops of exterior tertiaries. Intersecondary veins absent. Intercostal tertiary veins thin and closely spaced, course mixed percurrent but deflected by strong quaternaries, appearing ladderlike at a distance but less distinct when viewed closely because of deflections, angle obtuse to midvein and nearly perpendicular to the secondaries at departure. Epimedial tertiaries mixed percurrent and deflected as for intercostals, proximal course perpendicular to midvein, distal course basiflexed and parallel to intercostal tertiaries. Exterior tertiary course looped or terminating at the fimbrial vein. Quaternary and quinternary vein fabric regular reticulate, areoles at fifth order, freely ending veinlets zero-, one-, or two-branched. Teeth in one order (simple); tooth spacing regular, ~2 teeth/cm, with one tooth per secondary. Tooth apical flank concave, straight, or flexuous; basal flank the same

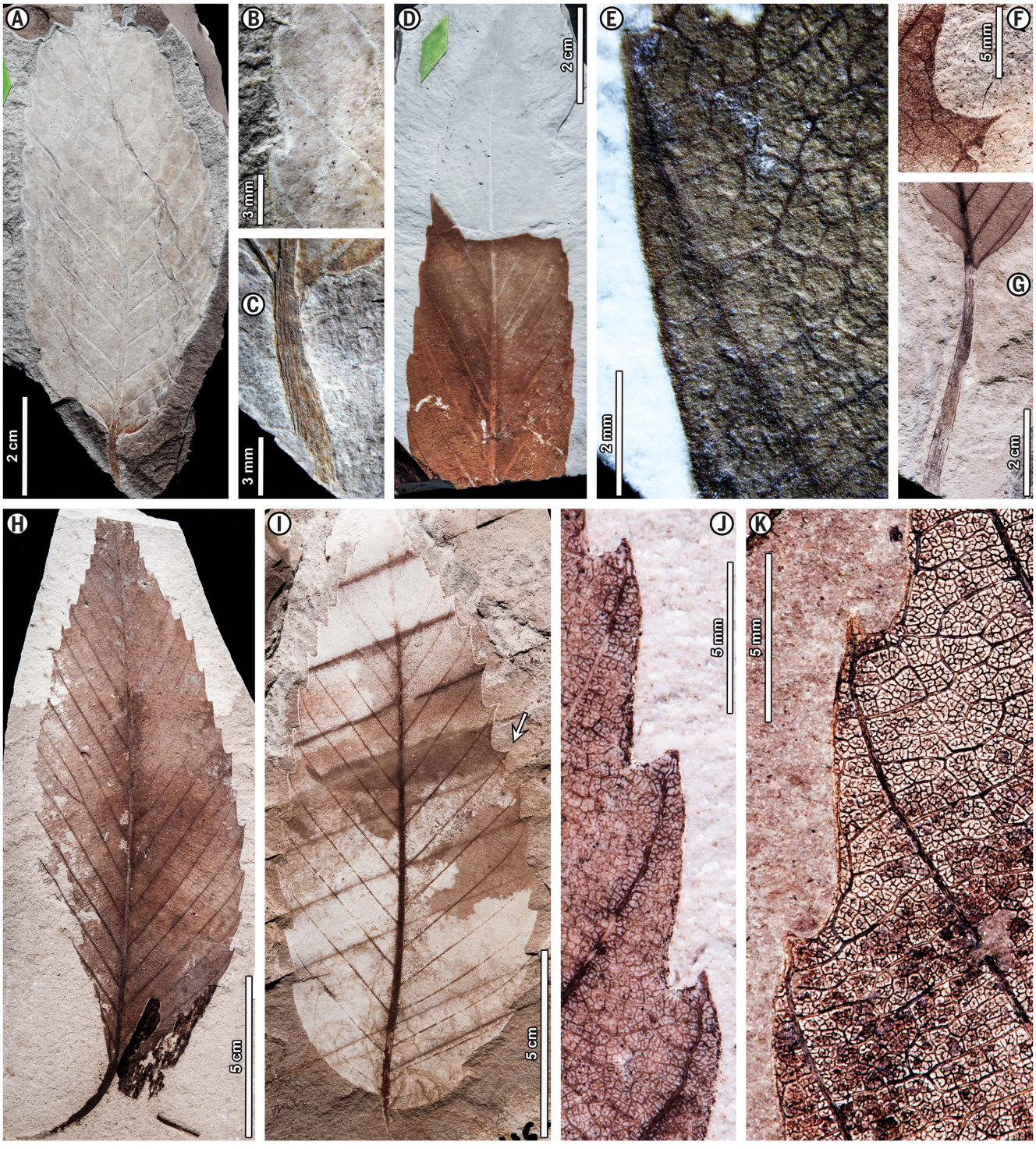


Fig. 4. *Castaneophyllum patagonicum* (Berry) comb. nov. (**A** to **C**) Lectotype, USNM 201951, with details of (B) the margin and (C) base, showing a long petiole and asymmetrical lamina insertion. (**D** and **E**) Syntype, USNM 201952 (with secondary iron staining); the base of (D), at left, expands to (E) detail of vein preservation. (**F**) MPEF-Pb 8266, margin detail with bristle-tipped tooth at lower right [also shown in (I)]. (**G**) MPEF-Pb 8255a, with a long petiole segment. (**H** and **I**) MPEF-Pb 8257 (H) and MPEF-Pb 8266 (I), large leaves with representative architecture including asymmetrical lamina insertion (I); robust, regular secondary veins each terminating in a conspicuous tooth; ladderlike tertiary veins; a fimbrial vein; and teeth with long-arcuate sinuses and pointed to bristled apices. Deeply bifurcating secondary veins occur at center left and center right of (H). Parallel lineations in (H) are rock fractures. Arrow for (I), bristle shown in (F). (**J** and **K**) MPEF-Pb 8228 (J) and MPEF-Pb 8275 (K), marginal venation of leaves with strongly (J) and weakly (K) expressed teeth, showing characteristic fimbrial vein, deflected-percurrent tertiary veins, freely ending veinlets, deflected principal veins, and nonglandular apices.

plus convex; sinus usually long and arcuate. Principal vein deflected within the tooth at junctions with tertiary veins, terminating at the nonglandular tooth apex or extending beyond it in a bristle. Stipules, cuticles, and trichomes not preserved. Insect-feeding damage is diverse; a previous report (*71*) included damage types (DTs) (*72*) on "*Tetracera*" leaves from hole and surface feeding (DTs 1 to 5, 7, 8, 29, and 57), margin feeding (DTs 12 to 15), skeletonization (DTs 16, 19, and 22), galling (DT32), and mining (DT90).

Remarks

Jones and Dilcher's (*10*) diagnosis of *Castaneophyllum* ("isolated leaves resembling, in general form, those of modern *Castanea*"), their generic description (even in the absence here of fossil cuticle), and their intent that *Castaneophyllum* "serve as a repository for isolated *Castanea*-like fossil leaves" make this genus ideal for taxonomic placement of the Patagonian leaf fossils. The only difference, deemed negligible, is that the original description of *Castaneophyllum* (*10*) included no more than one branching of the freely ending veinlets. Berry's type specimens (*25*) (Fig. 4, A to E) preserve sufficient details to establish that they represent the same entity as the new leaf material, including a long petiole, basal insertion asymmetry, tooth configuration, and total venation pattern.

The leaf architecture of the fossils is definitely fagaceous, seen in the characteristic combination of robust, regular, craspedodromous secondary veins that each terminate at the apex of a single tooth and only rarely branch, far from the margin (Fig. 4H); thin, closely spaced, percurrent, ladderlike tertiary veins; and simple teeth with long-arcuate sinuses and nonglandular, pointed to bristle-tipped apices. These features are widespread among Fagaceae, especially in species of *Castanea*, *Castanopsis*, and *Quercus* (*8*–*10*, *58*, *73*), and the fossils would undoubtedly be assigned to Fagaceae if found in Northern Hemisphere deposits. The only angiosperm family with closely comparable leaves is Dilleniaceae, as historically identified (*25*). However, the toothed Dilleniaceae (e.g., some *Dillenia*, *Tetracera*, and *Davilla* species) feature prominent, expanded glands at the tooth apices (*74*) that do not occur in the fossil specimens. The toothed *Nothofagus* species, though variable, have a suite of features that do not conform to the fossils (*75*), including the prevalence of markedly asymmetrical leaves, plications, compound teeth, zig-zagging or curved primary veins, and irregular secondary veins that fork near the margin or include agrophic veins. In *Castanopsis*, leaves very similar to the fossils occur in several serrate-margined species of the Asian mainland, especially *Castanopsis indica*, from which the fossils differ only in their much longer petioles and their more deflected tertiaries and tooth principal veins (Fig. 4). Long petioles like those of the fossils are unusual in living *Castanopsis* but occur in some species (e.g., *Castanopsis ouonbiensis*, China).

The isolated *Castaneophyllum* leaves occur at the same localities as the *Castanopsis rothwellii* infructescences and are likely to represent the same source plant, given the lack of evidence for other fossils of fagaceous fruit or leaf species. However, the leaves' nomenclatural priority and lack of clear generic affinities within extant Fagaceae, when taken alone, require their maintenance under a separate name in the absence of organic attachment.

Berry (*76*) also included "*T.*" *patagonica* in his 1938 monograph on the ~47.8-Ma-old (*27*, *40*) Río Pichileufú flora from Río Negro province; however, he did not illustrate material or cite specimens. Nevertheless, Berry determined "*T. patagonica*" on handwritten tags for three specimens (USNM 219128 to 219130), which we found markedly dissimilar to the types and more likely to represent sapindalean leaflets. We have not seen any fossils resembling Fagaceae from Río Pichileufú in either the historical (*76*) or our ongoing (*27*) collections. Jones and Dilcher (*10*) considered some of Berry's 1938 (*76*) fossils from Río Pichileufú to be "somewhat similar to *Castaneophyllum*" but did not indicate which fossils these were.

Gondwanan "oak-laurel" forest

Castaneophyllum patagonicum leaves frequently occur at Laguna del Hunco, where they are the third most common leaf species, with a census count of 9.8% of total leaves (*27*). Moreover, most of the leaf specimens (84%) came from the same two quarries (LH02 and LH04) where leaves of Lauraceae are most abundant (*27*). This notable pattern indicates a Gondwanan iteration of the "oak-laurel" associations that now dominate lower-montane rainforests from the eastern Himalaya to New Guinea (*5*) and include many other PARLs known as fossils from Laguna del Hunco. Like living *Castanopsis*, which is abundant and insect pollinated (*6*), the Eocene trees presumably were keystone species that provided forest structure, nutritious nuts, and substantial pollinator rewards.

Southern Route to Asia hypothesis

The discovery of Gondwanan fossil Fagaceae raises important biogeographic questions. We outline and critically discuss a "Southern Route to Asia" hypothesis that arises from our findings, as follows: An ancestral castaneoid lineage dispersed from North America into Gondwanan South America and joined the widespread paleo-Antarctic rainforest biome (*31*). *Castanopsis* evolved in the Southern Hemisphere by the Eocene, followed the Sahul pathway along with the associated PARLs to the Asian collision, and diversified through the Neogene in Sahul and eventually in Sundaland.

There is ample precedent for Late Cretaceous or early Paleogene dispersal from North to South America. At Laguna del Hunco itself, other Fagales with northern connections co-occur with the new fossils, such as engelhardioid Juglandaceae (*47*) and members of the family Casuarinaceae (*Gymnostoma* spp.) (*46*), a close relative of the Laurasian family Betulaceae (*68*). The faunal record is rich with Late Cretaceous dispersals from North America to Patagonia and on to Antarctica, including hadrosaurs and diverse mammal groups (*77*–*79*). A postulated latest Cretaceous, ephemeral land connection or island chain along the Antillean Arc (*80*) would have been comparatively accessible to higher-latitude organisms because of Maastrichtian cooling (*81*), and the dispersing mammals themselves could have taken part in bringing castaneoids to South America. The alternative to dispersal, in situ evolution in South America, is unlikely because of the robust North American record of Late Cretaceous Fagaceae (*12*, *82*) and the lack of any Mesozoic or other South American fossils of the family.

The idea of southern origins and biogeographic history for *Castanopsis* can be tested in at least three ways. First, the oldest Asian *Castanopsis* fossils should not predate the late Oligocene (*52*) onset of the Sahul-Sunda collision, and this condition is met so far (*20*). The earliest reliable Asian fossils of the genus are diagnostic fruits from late Miocene sediments of SE China (*83*). If North America and Europe were instead the sources of Asian *Castanopsis*, the genus apparently did not take advantage of numerous opportunities to reach Asia earlier (*84*).

Second, early *Castanopsis* fossil associations should be similar to living *Castanopsis* assemblages with substantial Gondwanic history, and this is overwhelmingly the case for the new fossils, which are the oldest known of the genus despite much more extensive collection of Northern Hemisphere than of Patagonian Paleogene floras. Local *Castanopsis* associations with the same paleo-Antarctic lineages seen at Laguna del Hunco (as listed earlier), and usually with several of them at a time, are extensively documented in Malesia (*1*, *2*, *23*, *24*, *32*–*37*). Northern Hemisphere fossils assigned to *Castanopsis* are younger and never co-occur with PARLs (*11*, *15*, *85*). We find the marked spatial and temporal stability of the old southern associations, requiring a high degree of biome conservatism over time (*31*, *53*, *54*), to be especially compelling evidence of a direct connection from Laguna del Hunco to SE Asia for *Castanopsis*. Although some Northern Hemisphere *Castanopsis* fossils co-occur with a different set of extant Malesian taxa, as seen in the Eocene of Oregon (*11*), comparatively few examples are known of those genera associating locally, collectively, and repeatedly with living *Castanopsis* (*86*).

Third, the hypothesis requires that the North American and European fossils assigned to *Castanopsis* be more distant relatives of the extant genus than are the new Argentine fossils. This issue is challenging, but the close affinity of the new Patagonian fossils to living *Castanopsis* is well supported by our morphological analysis (Fig. 3). Among Laurasian fossils, *Castanopsis kaulii*, a spectacular pistillate inflorescence from late Eocene Baltic amber, is clearly consistent with the living genus (*15*); however, fruits that would confirm its relationships with extant lineages are not yet known. European fruit fossils referred to *Castanopsis* are nuts that are never found in cupules, making their systematic placement

uncertain (85). *C. crepetii* fruits from the middle Eocene of Oregon include cupules and several anatomical characters consistent with living *Castanopsis* (11), although they do not preserve infructescence structure, perianth, or styles. Otherwise, the diverse North American reproductive fossils that are similar to *Castanopsis* belong to extinct genera (17, 87, 88).

We favor a southern origin for *Castanopsis* on the basis of the preservation of diagnostic infructescence and fruit characters in the new fossils from Argentina, their early Eocene age, and the marked similarities of fossil Patagonian and living Malesian plant associations. If *Castanopsis* is instead older than the postulated north-south dispersal and has both northern and southern history, older Laurasian *Castanopsis* fossils and a corresponding deep split in the genus' phylogeny, both so far unknown, would supply the necessary evidence. Notably, *C. acuminatissima* is a dominant living species in New Guinea (1, 24), where it associates with more Laguna del Hunco "survivor" taxa (e.g., *Eucalyptus* and *Araucaria*) than any other *Castanopsis* species; *C. acuminatissima* might be a true relict of Sahul rather than an immigrant from Asia as conventionally assumed. Genetic data from across that species' range, which extends to India (2), could be used to test this idea.

Concluding remarks

The discovery of *Castanopsis* in Eocene Patagonia adds a novel element to our understanding of late-Gondwanan rainforest vegetation, for which Malesian lower-montane rainforests provide a more robust analog than previously thought. New Guinea offers especially compelling similarities to Eocene Patagonia because of a large number of shared living-fossil genera. *Castanopsis* history now shows unexpected alignment with the austral genus *Nothofagus*, whose co-occurrence with *Castanopsis* and *Lithocarpus* in New Guinea historically puzzled biogeographers before the separation of Nothofagaceae from Fagaceae s.s. (57, 67, 89). However, despite their biogeographic parallels, we note that *Castanopsis* and *Nothofagus* are distant relatives within Fagales (82, 90). Adding further complexity, indisputably Laurasian Fagaceae, such as *Quercus* (14), also inhabit Malesia (but not New Guinea) (2). Thus, we propose that the classical idea of the region's montane rainforests as a meeting ground of Laurasian and Gondwanan lineages (55, 57) now applies within Fagaceae s.s.

Living *Castanopsis* is diverse, with high standing biomass and an extensive range reaching to Japan and the Himalaya. Thus, the fossils reported here substantially increase the recognized Gondwanan footprint in Asian forests. The marked conservatism of paleo-Antarctic lineages (31, 54), which have tracked their preferred biomes over time and space instead of adapting to climate change in situ, highlights their vulnerability to rapid anthropogenic disturbance (91, 92). In Patagonia, the lack of Fagaceae in the 47.8-Ma-old Río Pichileufú flora adds to a growing list of dissimilarities between the two iconic assemblages (29). The loss in such a geologically short time (52.2 to 47.8 Ma) of abundant angiosperms such as *Castanopsis*, *Eucalyptus*, and *Gymnostoma* suggests that the earliest phases of Antarctic separation and concurrent cooling and drying had substantial effects in southern South America.

Materials and methods

The Tufolitas Laguna del Hunco are fossiliferous caldera-lake deposits of La Huitrera Formation in northwest Chubut, Argentina, paleolatitude ~47°S (27, 93). Berry (25) first reported the fossil flora in 1925 from a small collection. The flora is now known to be highly diverse (26) and to hold the only South American (or global) records of a variety of extant Australasian, Asian, and neotropical plant genera (29, 44, 94). The stratigraphy of the 170-m-thick lake-bed sequence and its fossil quarries (LH01 to LH28) is reported elsewhere (26, 27, 40). In summary, three ^{40}Ar-^{40}Ar ages and two paleomagnetic reversals, especially a 52.22 ± 0.22 Ma ^{40}Ar-^{40}Ar age on sanidine from the middle of the sequence, constrain all the fossil beds to a ~52.2-Ma age.

We studied the fossils at MEF and the Penn State Paleobotany Laboratory by using the same procedures for specimen preparation and imaging detailed in several previous papers (40, 43), with the addition of a Nikon DSFi3 camera and L4 control unit on the MEF Nikon Eclipse 50i microscope. Herbarium material of a majority of the *Castanopsis* species was examined at Herbarium Bogoriense (BO, Java, Indonesia), the L. H. Bailey Hortorium Herbarium (BH, Cornell University), the Singapore Herbarium (SING), and the U.S. National Herbarium (US, Smithsonian Institution). Several hundred images were downloaded from online herbaria, including the consortium sites JStor Global Plants (95) and the Chinese Virtual Herbarium (96). Fruit litter of living *C. cuspidata* (Fig. 1C) was collected in Kyoto and kindly provided by Y. Onoda. Leaf descriptive terminology is from Ellis *et al.* (97).

Phylogenetic analyses of the *C. rothwellii* infructescences used a scaffold tree for living Fagaceae subfamily Castaneoideae on the basis of the published molecular results of Manos *et al.* (98), which remain among the most comprehensive for the family. That phylogeny (98) was rooted on *Fagus* as a sister to all other Fagaceae, which divided into two clades, *Trigonobalanus* sensu lato and all remaining genera. Among these, *Quercus* was a sister to the Castaneoideae, wherein *Castanopsis* and *Castanea* formed a sister clade to the other genera (*Lithocarpus*, *Chrysolepis*, and *Notholithocarpus*). We note that many topologies have been published for Fagaceae, and Castaneoideae often resolve as paraphyletic (68, 90, 99). A matrix of seven morphological characters was developed on the basis of relevancy in the fossils (Table 1). The genus *Fagus* was used as the outgroup. *Castanea* and *Castanopsis* were split into subgroups according to results from (98), and *Lithocarpus* was split into artificial subgroups based on the consistency of cupule morphology characters. This approach allows testing of whether the fossil would fall within a crown group of the genera but does not imply that all the subgroups are monophyletic. Parsimony analyses were performed using TNT version 1.2 (100) [see (101) for updates]. Thorough tree searches of the molecular [internal transcribed spacer (ITS)] scaffold tree, allowing the fossil to float, were done by using the parsimony ratchet with 500 replications, followed by tree fusion and tree drift (102, 103). Two most parsimonious trees resulted, one with the fossil species as a sister to the entire genus *Castanopsis* and a second with the fossil species as a sister to the *Castanopsis* subgroup within *Castanopsis* (the consensus tree is shown in Fig. 3). Additional analyses using more recent molecular data (99) similarly placed the fossils as a sister to extant *Castanopsis*. Further phylogenetic resolution within *Castanopsis* is not methodologically possible because sufficient diagnostic characters of the *Castanopsis* subgroups are not available in the fossils; moreover, no comprehensive phylogeny of the diverse castaneoid Fagaceae has been done that would justify the development of a large-scale morphological character matrix. Although refinement of the phylogenetic position of the fossils may become possible with additional studies of the living species, the placement within subfamily Castaneoideae is unequivocal with the currently available data.

REFERENCES AND NOTES

1. E. Soepadmo, Fagaceae. *Flora Males. Ser. 1* **7**, 265–403 (1972).
2. E. Soepadmo, S. Julia, R. Go, "Fagaceae," in *Tree Flora of Sabah and Sarawak*, E. Soepadmo, L. G. Saw, Eds. (Sabah Forestry Department, Kuala Lumpur, Malaysia, 2000), vol. 3, pp. 1–117.
3. R. B. Kaul, E. C. Abbe, Inflorescence architecture and evolution in the Fagaceae. *J. Arnold Arbor.* **65**, 375–401 (1984).
4. A. Kremer *et al.*, Genomics of Fagaceae. *Tree Genet. Genomes* **8**, 583–610 (2012). doi: 10.1007/s11295-012-0498-3
5. P. S. Ashton, *On the Forests of Tropical Asia: Lest the Memory Fade* (Royal Botanic Gardens, Kew, 2014).
6. R. B. Kaul, E. C. Abbe, L. B. Abbe, Reproductive phenology of the oak family (Fagaceae) in the lowland rain forests of Borneo. *Biotropica* **18**, 51–55 (1986). doi: 10.2307/2388362
7. S. B. Vander Wall, The evolutionary ecology of nut dispersal. *Bot. Rev.* **67**, 74–117 (2001). doi: 10.1007/BF02857850
8. S. R. Manchester, P. R. Crane, Attached leaves, inflorescences, and fruits of *Fagopsis*, an extinct genus of fagaceous affinity from the Oligocene Florissant Flora of Colorado, U.S.A. *Am. J. Bot.* **70**, 1147–1164 (1983). doi: 10.1002/j.1537-2197.1983.tb12464.x
9. J. H. Jones, Evolution of the Fagaceae: The implications of foliar features. *Ann. Mo. Bot. Gard.* **73**, 228–275 (1986). doi: 10.2307/2399112
10. J. H. Jones, D. L. Dilcher, A study of the "*Dryophyllum*" leaf forms from the Paleogene of southeastern North America. *Palaeontographica Abt. B* **208**, 53–80 (1988).
11. S. R. Manchester, Fruits and seeds of the middle Eocene Nut Beds flora, Clarno Formation, Oregon. *Palaeontogr. Am.* **58**, 1–205 (1994).
12. P. S. Herendeen, P. R. Crane, A. N. Drinnan, Fagaceous flowers, fruits, and cupules from the Campanian (Late Cretaceous) of central Georgia, USA. *Int. J. Plant Sci.* **156**, 93–116 (1995). doi: 10.1086/297231
13. F. Grímsson, G. W. Grimm, R. Zetter, T. Denk, Cretaceous and Paleogene Fagaceae from North America and Greenland: Evidence for a Late Cretaceous split between *Fagus* and the

remaining Fagaceae. *Acta Palaeobot.* **56**, 247–305 (2016). doi: 10.1515/acpa-2016-0016

14. E. Barrón, A. Averyanova, Z. Kvaček, A. Momohara, K. B. Pigg, S. Popova, J. M. Postigo-Mijarra, B. H. Tiffney, T. Utescher, Z. K. Zhou, "The fossil history of *Quercus*," in *Oaks Physiological Ecology: Exploring the Functional Diversity of Genus* Quercus *L.*, E. Gil-Pelegrín, J. J. Peguero-Pina, D. Sancho-Knapik, Eds. (Springer, 2017), pp. 39–105.
15. E.-M. Sadowski, J. U. Hammel, T. Denk, Synchrotron X-ray imaging of a dichasium cupule of *Castanopsis* from Eocene Baltic amber. *Am. J. Bot.* **105**, 2025–2036 (2018). pmid: 30548995
16. R. A. Couper, Southern Hemisphere Mesozoic and Tertiary Podocarpaceae and Fagaceae and their palaeogeographic significance. *Proc. R. Soc. London Ser. B* **152**, 491–500 (1960). doi: 10.1098/rspb.1960.0056
17. W. L. Crepet, K. C. Nixon, Earliest megafossil evidence of Fagaceae: Phylogenetic and biogeographic implications. *Am. J. Bot.* **76**, 842–855 (1989). doi: 10.1002/j.1537-2197.1989.tb15062.x
18. P. S. Manos, A. M. Stanford, The historical biogeography of Fagaceae: Tracking the Tertiary history of temperate and subtropical forests of the Northern Hemisphere. *Int. J. Plant Sci.* **162** (S6), 77–93 (2001). doi: 10.1086/323280
19. C. H. Cannon, P. S. Manos, Phylogeography of the Southeast Asian stone oaks (*Lithocarpus*). *J. Biogeogr.* **30**, 211–226 (2003). doi: 10.1046/j.1365-2699.2003.00829.x
20. J.-Y. Wu *et al.*, A new species of *Castanopsis* (Fagaceae) from the upper Pliocene of West Yunnan, China and its biogeographical implications. *Palaeoworld* **23**, 370–382 (2014). doi: 10.1016/j.palwor.2014.10.005
21. T. Denk, F. Grímsson, R. Zetter, Fagaceae from the early Oligocene of Central Europe: Persisting new world and emerging old world biogeographic links. *Rev. Palaeobot. Palynol.* **169**, 7–20 (2012). doi: 10.1016/j.revpalbo.2011.09.010
22. J. Cavender-Bares *et al.*, The role of diversification in community assembly of the oaks (*Quercus* L.) across the continental U.S. *Am. J. Bot.* **105**, 565–586 (2018). doi: 10.1002/ajb2.1049; pmid: 29689630
23. R. J. Johns, G. A. Shea, W. Vink, P. Puradyatmika, "Montane vegetation of Papua," in *The Ecology of Papua, Part Two*, A. Marshall, B. Beehler, Eds. (Periplus, 2007), pp. 977–1024.
24. L. Brass, The 1938-1939 expedition to the Snow Mountains, Netherlands New Guinea. *J. Arnold Arbor.* **22**, 271–342 (1941).
25. E. W. Berry, A Miocene flora from Patagonia. *Johns Hopkins Univ. Stud. Geol.* **6**, 183–251 (1925).
26. P. Wilf *et al.*, High plant diversity in Eocene South America: Evidence from Patagonia. *Science* **300**, 122–125 (2003). doi: 10.1126/science.1080475; pmid: 12677065
27. P. Wilf *et al.*, Eocene plant diversity at Laguna del Hunco and Río Pichileufú, Patagonia, Argentina. *Am. Nat.* **165**, 634–650 (2005). doi: 10.1086/430055; pmid: 15937744
28. J. Zachos, M. Pagani, L. Sloan, E. Thomas, K. Billups, Trends, rhythms, and aberrations in global climate 65 Ma to present. *Science* **292**, 686–693 (2001). doi: 10.1126/science.1059412; pmid: 11326091
29. P. Wilf, N. R. Cúneo, I. H. Escapa, D. Pol, M. O. Woodburne, Splendid and seldom isolated: The paleobiogeography of Patagonia. *Annu. Rev. Earth Planet. Sci.* **41**, 561–603 (2013). doi: 10.1146/annurev-earth-050212-124217
30. P. E. Morse *et al.*, New fossils, systematics, and biogeography of the oldest known crown primate *Teilhardina* from the earliest Eocene of Asia, Europe, and North America. *J. Hum. Evol.* **128**, 103–131 (2019). doi: 10.1016/j.jhevol.2018.08.005; pmid: 30497682
31. R. M. Kooyman *et al.*, Paleo-Antarctic rainforest into the modern Old World tropics: The rich past and threatened future of the "southern wet forest survivors." *Am. J. Bot.* **101**, 2121–2135 (2014). doi: 10.3732/ajb.1400340; pmid: 25480709
32. I. Yamada, Forest ecological studies of the montane forest of Mt. Pangrango, West Java: IV. Floristic composition along the altitude. *South East Asian Stud.* **15**, 226–254 (1977).
33. P. V. Gonzales-Salcedo, Floral diversity and vegetation zones of the northern slope of Mt. Amuyao, Mountain Province, Luzon, Philippines. *Asia Life Sci.* **10**, 119–157 (2001).
34. J. H. Beaman, R. S. Beaman, *The Plants of Mount Kinabalu 3: Gymnosperms and Non-Orchid Monocotyledons* (Natural History Publications Borneo, 1998).
35. S. Aiba, K. Kitayama, R. Repin, Species composition and species-area relationships of trees in nine permanent plots in altitudinal sequences on different geological substrates of Mount Kinabalu. *Sabah Parks Nat. J.* **5**, 7–69 (2002).
36. R. J. Johns, A provisional classification of the montane vegetation of New Guinea. *Sci. New Guinea* **4**, 105–117 (1976).
37. R. J. Johns, Altitudinal zonation of pteridophytes in Papuasia. *Proc. R. Soc. Edinburgh B* **86**, 381–389 (2011).
38. P. Wilf *et al.*, *Papuacedrus* (Cupressaceae) in Eocene Patagonia: A new fossil link to Australasian rainforests. *Am. J. Bot.* **96**, 2031–2047 (2009). doi: 10.3732/ajb.0900085; pmid: 21622323
39. M. A. Gandolfo *et al.*, Oldest known *Eucalyptus* macrofossils are from South America. *PLOS ONE* **6**, e21084 (2011). doi: 10.1371/journal.pone.0021084; pmid: 21738605
40. P. Wilf, Rainforest conifers of Eocene Patagonia: Attached cones and foliage of the extant Southeast Asian and Australasian genus *Dacrycarpus* (Podocarpaceae). *Am. J. Bot.* **99**, 562–584 (2012). doi: 10.3732/ajb.1100367; pmid: 22334450
41. M. R. Carvalho *et al.*, First record of *Todea* (Osmundaceae) in South America, from the early Eocene paleorainforests of Laguna del Hunco (Patagonia, Argentina). *Am. J. Bot.* **100**, 1831–1848 (2013). doi: 10.3732/ajb.1200637; pmid: 24018858
42. R. J. Carpenter, P. Wilf, J. G. Conran, N. R. Cúneo, A Paleogene trans-Antarctic distribution for *Ripogonum* (Ripogonaceae: Liliales)? *Palaeontol. Electron.* **17**, 17.13.39A (2014).
43. P. Wilf *et al.*, First South American *Agathis* (Araucariaceae), Eocene of Patagonia. *Am. J. Bot.* **101**, 156–179 (2014). doi: 10.3732/ajb.1300327; pmid: 24418576
44. P. Wilf, M. P. Donovan, N. R. Cúneo, M. A. Gandolfo, The fossil flip-leaves (*Retrophyllum*, Podocarpaceae) of southern South America. *Am. J. Bot.* **104**, 1344–1369 (2017). doi: 10.3732/ajb.1700158; pmid: 29885237
45. M. A. Gandolfo, E. J. Hermsen, *Ceratopetalum* (Cunoniaceae) fruits of Australasian affinity from the early Eocene Laguna del Hunco flora, Patagonia, Argentina. *Ann. Bot.* **119**, 507–516 (2017). pmid: 28110267
46. M. C. Zamaloa *et al.*, Casuarinaceae from the Eocene of Patagonia, Argentina. *Int. J. Plant Sci.* **167**, 1279–1289 (2006). doi: 10.1086/507873
47. E. J. Hermsen, M. A. Gandolfo, Fruits of Juglandaceae from the Eocene of South America. *Syst. Bot.* **41**, 316–328 (2016). doi: 10.1600/036364416X691830
48. D. J. Boland, J. Davidson, N. Howcroft, *Eucalyptus deglupta* Blume and *Araucaria cunninghamii* Lambert provenance seed collections in Irian Jaya, Indonesia, 3–17 June 1975. *For. Genet. Resour. Inf.* **6**, 3–15 (1977).
49. C. F. Symington, Foresters' manual of dipterocarps. *Malay. For. Rec.* **16**, 1–244 (1943).
50. R. S. Hill, "The history of selected Australian taxa," in *History of the Australian Vegetation: Cretaceous to Recent*, R. S. Hill, Ed. (Cambridge Univ. Press, 1994), pp. 390–419.
51. T. J. Brodribb, R. S. Hill, Southern conifers in time and space. *Aust. J. Bot.* **47**, 639–696 (1999). doi: 10.1071/BT98093
52. R. Hall, Australia-SE Asia collision: Plate tectonics and crustal flow. *Geol. Soc. Lond. Spec. Publ.* **355**, 75–109 (2011). doi: 10.1144/SP355.5
53. T. J. Brodribb, A functional analysis of podocarp ecology. *Smithson. Contrib. Bot.* **95**, 165–173 (2011). doi: 10.5479/si.0081024X.95.165
54. T. Brodribb, R. S. Hill, "The rise and fall of the Podocarpaceae in Australia—a physiological explanation," in *The Evolution of Plant Physiology: From Whole Plants to Ecosystems*, A. R. Hemsley, I. Poole, Eds. (Academic Press, 2004), pp. 381–399.
55. O. Stapf, On the flora of Mount Kinabalu, in North Borneo. *Trans. Linn. Soc. London 2nd Ser. Bot.* **4**, 69–263 (1894).
56. C. G. G. J. Van Steenis, Plant geography of the mountain flora of Mt Kinabalu. *Proc. R. Soc. London Ser. B* **161**, 7–38 (1964). doi: 10.1098/rspb.1964.0072
57. C. G. G. J. Van Steenis, Plant-geography of east Malesia. *Bot. J. Linn. Soc.* **79**, 97–178 (1979). doi: 10.1111/j.1095-8339.1979.tb01511.x
58. A. Camus, *Les Châtaigniers: Monographie des Genres* Castanea *et* Castanopsis (Lechevalier, 1929), p. 604.
59. C. Huang, Y. Zhang, B. Bartholomew, Fagaceae. *Flora China* **4**, 314–400 (1999).
60. A. de Candolle, Cupuliferae. *Prodromus Systematis Naturalis Regni Vegetabilis* **16**, 1–123 (1864).
61. E. C. Abbe, Flowers and inflorescences of the "Amentiferae." *Bot. Rev.* **40**, 159–261 (1974). doi: 10.1007/BF02859135
62. B. S. Fey, P. K. Endress, Development and morphological interpretation of the cupule in Fagaceae. *Flora* **173**, 451–468 (1983). doi: 10.1016/S0367-2530(17)32023-6
63. H. Hjelmqvist, Studies on the floral morphology and phylogeny of the Amentiferae. *Bot. Not.* **2** (suppl.), 1–171 (1948).
64. L. L. Forman, Generic delimitation in the Castaneoideae (Fagaceae). *Kew Bull.* **18**, 421–426 (1966). doi: 10.2307/4115795
65. R. B. Kaul, Cupular structure in paleotropical *Castanopsis* (Fagaceae). *Ann. Mo. Bot. Gard.* **75**, 1480–1498 (1988). doi: 10.2307/2399297
66. R. B. Kaul, Reproductive structure of *Lithocarpus* sensu lato (Fagaceae): Cymules and fruits. *J. Arnold Arbor.* **68**, 73–104 (1987).
67. C. G. G. J. Van Steenis, *Nothofagus*, key genus of plant geography, in time and space, living and fossil, ecology and phylogeny. *Blumea* **19**, 65–98 (1971).
68. X.-G. Xiang *et al.*, Large-scale phylogenetic analyses reveal fagalean diversification promoted by the interplay of diaspores and environments in the Paleogene. *Perspect. Plant Ecol. Evol. Syst.* **16**, 101–110 (2014). doi: 10.1016/j.ppees.2014.03.001
69. W. L. Crepet, C. P. Daghlian, Castaneoid inflorescences from the middle Eocene of Tennessee and the diagnostic value of pollen (at the subfamily level) in the Fagaceae. *Am. J. Bot.* **67**, 739–757 (1980). doi: 10.1002/j.1537-2197.1980.tb07704.x
70. S. R. Manchester, R. M. Dillhoff, *Fagus* (Fagaceae) fruits, foliage, and pollen from the Middle Eocene of Pacific Northwestern North America. *Can. J. Bot.* **82**, 1509–1517 (2004). doi: 10.1139/b04-112
71. P. Wilf, C. C. Labandeira, K. R. Johnson, N. R. Cúneo, Richness of plant-insect associations in Eocene Patagonia: A legacy for South American biodiversity. *Proc. Natl. Acad. Sci. U.S.A.* **102**, 8944–8948 (2005). doi: 10.1073/pnas.0500516102; pmid: 15956213
72. C. C. Labandeira, P. Wilf, K. R. Johnson, F. Marsh, *Guide to Insect (and Other) Damage Types on Compressed Plant Fossils, Version 3.0* (Smithsonian Institution, 2007).
73. G. King, The Indo-Malayan species of *Quercus* and *Castanopsis*. *Ann. R. Bot. Gard. Calcutta* **2**, 17–107 (1889).
74. L. J. Hickey, J. A. Wolfe, The bases of angiosperm phylogeny: Vegetative morphology. *Ann. Mo. Bot. Gard.* **62**, 538–589 (1975). doi: 10.2307/2395267
75. M. A. Gandolfo, E. J. Romero, Leaf morphology and a key to species of *Nothofagus* Bl. *Bull. Torrey Bot. Club* **119**, 152–166 (1992). doi: 10.2307/2997028
76. E. W. Berry, Tertiary flora from the Río Pichileufú, Argentina. *Spec. Pap. Geol. Soc. Am.* **12**, 1–149 (1938).
77. J. A. Case *et al.*, The first duck-billed dinosaur (Family Hadrosauridae) from Antarctica. *J. Vertebr. Paleontol.* **20**, 612–614 (2000). doi: 10.1671/0272-4634(2000)020[0612:TFDBDF]2.0.CO;2
78. J. A. Case, F. J. Goin, M. O. Woodburne, "South American" marsupials from the Late Cretaceous of North America and the origin of marsupial cohorts. *J. Mamm. Evol.* **12**, 461–494 (2005). doi: 10.1007/s10914-005-7329-3
79. F. J. Goin *et al.*, The earliest Tertiary therian mammal from South America. *J. Vertebr. Paleontol.* **26**, 505–510 (2006). doi: 10.1671/0272-4634(2006)26[505:TETTMF]2.0.CO;2
80. M. A. Iturralde-Vinent, Meso-Cenozoic Caribbean paleogeography: Implications for the historical biogeography of the region. *Int. Geol. Rev.* **48**, 791–827 (2006). doi: 10.2747/0020-6814.48.9.791
81. B. T. Huber, K. G. MacLeod, D. K. Watkins, M. F. Coffin, The rise and fall of the Cretaceous hot greenhouse climate. *Global Planet. Change* **167**, 1–23 (2018). doi: 10.1016/j.gloplacha.2018.04.004
82. M. A. Gandolfo, K. C. Nixon, W. L. Crepet, D. A. Grimaldi, A late Cretaceous fagalean inflorescence preserved in amber from New Jersey. *Am. J. Bot.* **105**, 1424–1435 (2018). doi: 10.1002/ajb2.1103; pmid: 29901855
83. R. Li *et al.*, Two new *Castanopsis* (Fagaceae) species based on cupule and foliage from the upper Miocene of eastern Zhejiang, China. *Plant Syst. Evol.* **301**, 25–39 (2015). doi: 10.1007/s00606-014-1051-7
84. S. R. Manchester, Biogeographical relationships of North American Tertiary floras. *Ann. Mo. Bot. Gard.* **86**, 472–522 (1999). doi: 10.2307/2666183
85. D. H. Mai, Fossile Funde von *Castanopsis* (D. Don) Spach (*Fagaceae*) und ihre Bedeutung für die europäischen Lorbeerwälder. *Flora* **182**, 269–286 (1989). doi: 10.1016/S0367-2530(17)30416-4

86. T. Masunaga, D. Kubota, M. Hotta, T. Wakatsuki, Nutritional characteristics of mineral elements in leaves of tree species in tropical rain forest, west Sumatra, Indonesia. *Soil Sci. Plant Nutr.* **44**, 315–329 (1998). doi: 10.1080/00380768.1998.10414454
87. R. A. Mindell, R. A. Stockey, G. Beard, *Cascadiacarpa spinosa* gen. et sp. nov. (Fagaceae): Castaneoid fruits from the Eocene of Vancouver Island, Canada. *Am. J. Bot.* **94**, 351–361 (2007). doi: 10.3732/ajb.94.3.351 pmid: 21636406
88. M. L. DeVore, K. B. Pigg, D. L. Dilcher, D. Freile, "*Catahoulea grahamii*, a new genus and species of fagaceous involucres from the Oligocene Catahoula Formation, central Texas, and the middle Eocene Claiborne Formation of Kentucky and Tennessee, U.S.A.," in *Paleobotany and Biogeography*, W. D. Stevens, O. M. Montiel, P. H. Raven, Eds. (Missouri Botanical Garden Press, 2014), pp. 39–50.
89. T. C. Whitmore, *Wallace's Line and Plate Tectonics* (Clarendon Press, 1981).
90. K. Larson-Johnson, Phylogenetic investigation of the complex evolutionary history of dispersal mode and diversification rates across living and fossil Fagales. *New Phytol.* **209**, 418–435 (2016). doi: 10.1111/nph.13570; pmid: 26204796
91. C. D. Allen *et al*., A global overview of drought and heat-induced tree mortality reveals emerging climate change risks for forests. *For. Ecol. Manage.* **259**, 660–684 (2010). doi: 10.1016/j.foreco.2009.09.001
92. M. D. Crisp *et al*., Phylogenetic biome conservatism on a global scale. *Nature* **458**, 754–756 (2009). doi: 10.1038/nature07764; pmid: 19219025
93. E. Aragón, M. M. Mazzoni, Geología y estratigrafía del complejo volcánico piroclástico del Río Chubut medio (Eoceno), Chubut, Argentina. *Rev. Asoc. Geol. Argent.* **52**, 243–256 (1997).
94. P. Wilf, M. R. Carvalho, M. A. Gandolfo, N. R. Cúneo, Eocene lantern fruits from Gondwanan Patagonia and the early origins of Solanaceae. *Science* **355**, 71–75 (2017). doi: 10.1126/science.aag2737; pmid: 28059765
95. JStor Global Plants; https://plants.jstor.org.
96. Chinese Virtual Herbarium; www.cvh.ac.cn.
97. B. Ellis, D. C. Daly, L. J. Hickey, J. V. Mitchell, K. R. Johnson, P. Wilf, S. L. Wing, *Manual of Leaf Architecture* (Cornell Univ. Press, 2009).
98. P. S. Manos, Z. K. Zhou, C. H. Cannon, Systematics of Fagaceae: Phylogenetic tests of reproductive trait evolution. *Int. J. Plant Sci.* **162**, 1361–1379 (2001). doi: 10.1086/322949
99. P. S. Manos, C. H. Cannon, S.-H. Oh, Phylogenetic relationships and taxonomic status of the paleoendemic Fagaceae of western North America: Recognition of a new genus, *Notholithocarpus*. *Madroño* **55**, 181–190 (2008). doi: 10.3120/0024-9637-55.3.181
100. P. A. Goloboff, J. S. Farris, K. C. Nixon, TNT, a free program for phylogenetic analysis. *Cladistics* **24**, 774–786 (2008). doi: 10.1111/j.1096-0031.2008.00217.x
101. TNT: Tree analysis using New Technology; www.lillo.org.ar/phylogeny/tnt/.
102. K. C. Nixon, The parsimony ratchet, a new method for rapid parsimony analysis. *Cladistics* **15**, 407–414 (1999). doi: 10.1111/j.1096-0031.1999.tb00277.x
103. P. A. Goloboff, Analyzing large data sets in reasonable times: Solutions for composite optima. *Cladistics* **15**, 415–428 (1999). doi: 10.1111/j.1096-0031.1999.tb00278.x
104. P. Wilf, K. C. Nixon, M. A. Gandolfo, N. R. Cunéo, Image Archive for: Eocene Fagaceae from Patagonia and Gondwanan legacy in Asian rainforests, Figshare (2019); doi: 10.6084/m9.figshare.7480007

ACKNOWLEDGMENTS

We thank M. Caffa, L. Canessa, I. Escapa, A. Iglesias, K. Johnson, N. Jud, L. Merkhofer, N. Pfeiffer, P. Puerta, L. Reiner, E. Ruigomez, T. Su, E. and R. Wilf, Z. Zhou, and many others for assistance and comments; R. Kooyman and S. Manchester for extensive discussions; three anonymous reviewers for thoughtful insights; Y. Onoda for litter samples; and the staff of BH, BO, PAC, SING, US, and USNM for collections assistance. **Funding:** This research was supported by NSF grants DEB-1556666, DEB-1556136, DEB-0919071, DEB-0918932, and DEB-0345750; the National Geographic Society; and the David and Lucile Packard Foundation. **Author contributions:** Conceptualization, principal draft writing, fossil imaging, and visualization: P.W. Phylogenetic analysis and visualization: K.C.N. and M.A.G. Investigation, text contributions, draft editing, resources, and validation: all authors. Funding acquisition and project administration: P.W., M.A.G., and N.R.C. **Competing interests:** The authors declare no competing interests. **Data and materials availability:** All fossils studied are permanently curated at MPEF and USNM as cited in the main text. A high-resolution image archive of the fossils is available open access at Figshare (*104*).

30 December 2018; accepted 23 April 2019
10.1126/science.aaw5139

REPORT

MAGNETISM

Probing magnetism in 2D materials at the nanoscale with single-spin microscopy

L. Thiel[1], Z. Wang[2,3], M. A. Tschudin[1], D. Rohner[1], I. Gutiérrez-Lezama[2,3], N. Ubrig[2,3], M. Gibertini[2,4], E. Giannini[2], A. F. Morpurgo[2,3], P. Maletinsky[1]*

The discovery of ferromagnetism in two-dimensional (2D) van der Waals (vdW) crystals has generated widespread interest. Making further progress in this area requires quantitative knowledge of the magnetic properties of vdW magnets at the nanoscale. We used scanning single-spin magnetometry based on diamond nitrogen-vacancy centers to image the magnetization, localized defects, and magnetic domains of atomically thin crystals of the vdW magnet chromium(III) iodide (CrI_3). We determined the magnetization of CrI_3 monolayers to be ≈16 Bohr magnetons per square nanometer, with comparable values in samples with odd numbers of layers; however, the magnetization vanishes when the number of layers is even. We also found that structural modifications can induce switching between ferromagnetic and antiferromagnetic interlayer ordering. These results demonstrate the benefit of using single-spin scanning magnetometry to study the magnetism of 2D vdW magnets.

Magnetism in individual monolayers of van der Waals (vdW) crystals has recently been observed in a range of materials, including semiconducting (*1*, *2*) and metallic (*3*–*5*) compounds. The discovery of such two-dimensional (2D) magnetic order is nontrivial (*6*) and has garnered considerable attention owing to emerging exotic phenomena such as magnetoelectric effects (*7*–*10*) or potential, 2D Kitaev spin liquids (*11*, *12*). Two-dimensional magnets have been used as functional elements in spintronics; examples include spin filters (*13*, *14*), spin transistors (*15*), tunneling magnetoresistance devices (*16*, *17*), and magnetoelectric switches (*8*–*10*). Quantitative study of the magnetic response of these atomically thin crystals at the nanoscale is highly desirable, but the required experimental methods are still lacking. Indeed, transport experiments (*8*, *9*, *13*–*16*) probe magnetic properties only indirectly. Spatially resolved studies rely on optical techniques, such as fluorescence (*18*, *19*) or the magneto-optical Kerr effect (MOKE) (*1*, *2*, *4*), and are therefore limited to the micrometer scale. Even more critically, these techniques do not provide quantitative information about magnetization [MOKE, for instance, may yield nonzero signals even for antiferromagnets (*20*)] and are susceptible to interference effects that may obscure magnetic signals in thin samples (*1*).

We overcame these limitations and employed a scanning nitrogen-vacancy (NV) center spin in diamond as a sensitive, atomic-scale magnetometer (*21*) to quantitatively determine key magnetic properties of CrI_3 and to directly image magnetic domains with spatial resolutions of a few tens of nanometers. For magnetometry, we exploited the Zeeman effect, which led to a shift of the NV spin's energy levels as a function of magnetic field. In the regime relevant for this work, the NV spin shows a linear Zeeman response for magnetic fields B_{NV} along its spin-quantization axis $\vec{e}_{NV}$ (Fig. 1A), whereas it is largely insensitive to fields orthogonal to $\vec{e}_{NV}$ (*21*). The NV spin therefore offers a direct and quantitative measurement of the vectorial component B_{NV} of stray magnetic fields emerging from a sample.

The Zeeman shifts of the involved NV spin-levels can be conveniently read out by optically detected magnetic resonance (ODMR) with 532-nm laser excitation, microwave spin driving, and NV fluorescence detection for spin readout (*22*, *23*). For nanoscale imaging, we employed a single NV spin held in the tip of an atomic force microscope and placed the NV down to a distance z_{NV} ~ 60 nm from the sample, which resulted in a magnetic imaging resolution on the order of z_{NV} (*21*). The scanning probe containing the NV (*24*, *25*) was integrated into a confocal optical microscope for optical spin readout and the whole apparatus immersed in a liquid ^{4}He cryostat. Superconducting magnets were used to enable vectorial magnetic field control up to 0.5 T. The measurement temperature of ~7 K was determined by a resistive thermometer placed near the sample.

We studied CrI_3 samples of various thicknesses, which were encapsulated in either hexagonal

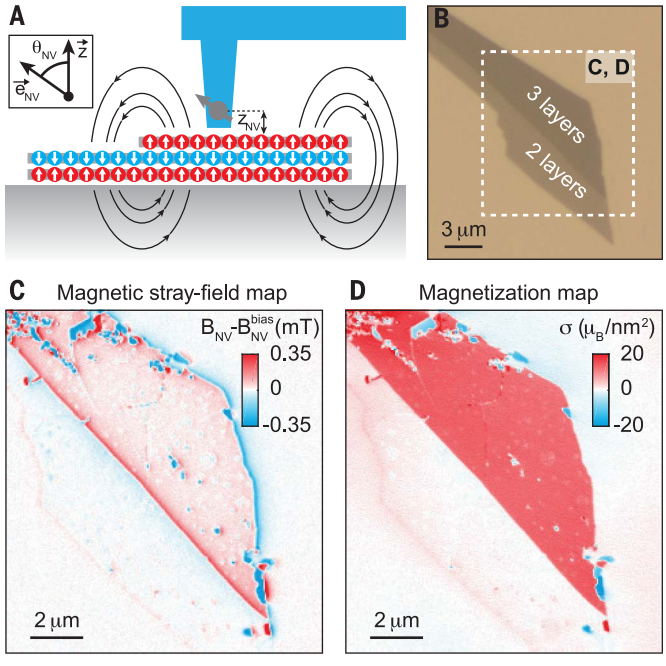


Fig. 1. Nanoscale imaging of magnetism in two-dimensional van der Waals magnets. (**A**) Schematic of the scanning single-spin magnetometry technique employed in this work. A single NV electronic spin is scanned across few-layer flakes of encapsulated CrI_3 (encapsulation not shown). Stray magnetic fields from the sample are sensed by optically detected Zeeman shifts of the NV spin states and imaged with nanoscale resolution (set by the sensor–sample separation z_{NV}) by lateral scanning of the NV. The method detects magnetic fields along the NV spin quantization axis $\vec{e}_{NV}$ at an angle θ_{NV}~54° from the sample normal. (**B**) Optical micrograph of the CrI_3 bi- and trilayer flake of sample D1. (**C**) Magnetic field map of B_{NV} across sample D1 recorded in a bias field B_{NV}^{bias} = 172.5 mT and at a typical green laser power P_{laser} ≈ 40 μW. Strong (or weak) stray fields emerge from the edges of the trilayer (or bilayer) flake. (**D**) Map of magnetization distribution in sample D1, determined by reverse propagation of the magnetic field map in (C) [see text and (*23*)].

[1]Department of Physics, University of Basel, Klingelbergstrasse 82, Basel CH-4056, Switzerland. [2]Department of Quantum Matter Physics, University of Geneva, 24 Quai Ernest Ansermet, CH-1211 Geneva, Switzerland. [3]Group of Applied Physics, University of Geneva, 24 Quai Ernest Ansermet, CH-1211 Geneva, Switzerland. [4]National Centre for Computational Design and Discovery of Novel Materials (MARVEL), École Polytechnique Fédérale de Lausanne, CH-1015 Lausanne, Switzerland.
*Corresponding author. Email: patrick.maletinsky@unibas.ch

boron nitride or graphene to assure the stability of CrI_3 under oxygen atmosphere [for details, see (*23*)]. The samples (Fig. 1B) were fabricated by mechanical exfoliation of CrI_3 and subsequently encapsulated using an established pick-and-place technique (*16*). Samples of various CrI_3 thicknesses in the range of a few (<10) layers were produced to study the effect of thickness on magnetic ordering. For each CrI_3 sample, the number of atomic layers was determined by a combination of atomic force microscopy and optical microscopy (*23*). For preparation and analysis of the magnetic state of CrI_3, the samples were mounted in the NV magnetometer and cooled in zero magnetic field to the final measurement temperature.

Figure 1C shows a typical magnetic field map acquired on an area containing bilayer and trilayer CrI_3 (sample D1). The presented data were acquired in a bias field $B_{NV}^{bias} = 172.5$ mT, where magnetometer performance was optimal, but similar images and results were found at lower fields as well (fig. S7). We obtained such maps from NV ODMR spectra acquired at each pixel (acquisition time ≈2 s per pixel), from which we determined B_{NV} through a fit (*23*). We confirmed experimentally that for typical parameters used in our study, our approach induced no appreciable back-action onto the sample (e.g., through heating by laser illumination or microwave irradiation) (*23*). The resulting data show stray magnetic fields emerging predominantly from the edges of the trilayer flake, as expected for a largely uniform magnetization (*26*), and thereby provide evidence for the magnetization of few-layer CrI_3.

To reveal further details of the underlying magnetization pattern in CrI_3, we used well-established reverse-propagation protocols (*27*) to map the magnetic field image of B_{NV} to its source [see (*23*) for details]. For a 2D, out-of-plane magnetization, as in the present case, such reverse propagation yields a unique determination of the underlying magnetization pattern (Fig. 1D), provided that the distance z_{NV} between sensor and sample is known. In our refined reverse-propagation protocol, we determine z_{NV} through an iterative procedure described in the supplementary materials and a recent study by Appel *et al.* (*23*, *28*). The reverse propagation thereby additionally yields the spatial resolution of our magnetic field and magnetization images, which is directly given by z_{NV} (for the data in Fig. 1, z_{NV} = 62 nm). In the following paragraphs, we focus our discussion on magnetization maps obtained through such reverse propagation; the raw magnetic field images are presented in the supplementary materials (*23*).

The magnetization pattern in Fig. 1D clearly shows a largely homogeneous magnetization for this trilayer CrI_3 flake, which is typical for most samples that we investigated. In addition, sparsely scattered, localized defects, mostly with vanishing magnetization, were visible across the flake, and several irregularities occurred at the flake edges, which were likely caused by curling and rippling induced on the edges during sample preparation. On the flake, we found an average magnetization $\sigma_z \approx (13.0 \pm 2.4)\mu_B/nm^2$ (with μ_B the Bohr magneton), consistent with a single layer of fully polarized Cr^{+3} spins, for which $\sigma_z^{mono} = 14.7\mu_B/nm^2$ would be expected (*29*). The data thus support the notion of antiferromagnetic interlayer exchange coupling in few-layer CrI_3 (*1*), which results in a net magnetization σ_z^{mono} for a magnetically ordered trilayer sample.

Sample D1 additionally contained a region of bilayer CrI_3 for which we observed zero bulk moment, again consistent with antiferromagnetic interlayer coupling. However, the bilayer also showed weak magnetization located within less than our spatial resolution from the edge (Fig. 1D). The origin of this magnetization is currently unknown but may be related to magnetoelectric effects (*7*, *9*), a narrow region of monolayer CrI_3 protruding from the bilayer, or spin canting (*30*) near the edge of the flake.

We applied our measurement procedure to a variety of samples, including a monolayer and the five- and nine-layer flakes shown in Fig. 2, A, B, and C, respectively. Notably, all of these flakes exhibit near-uniform magnetization at a magnitude comparable to σ_z^{mono}. We additionally determined σ_z in an independent manner by measuring B_{NV} along lines crossing the edges of each flake (Fig. 2, lower panels). Assuming a purely out-of-plane magnetization, analytical fits (*23*) to these data allow for the quantitative determination of both σ_z and z_{NV}. Potential tilting of the magnetization away from z in the vicinity of the edge caused by, for instance, the Dzyaloshinskii-Moriya interaction would lead to negligible deviations from our findings (*31*). For the monolayer, five-, and nine-layer flakes, we find $\sigma_z = (16.1 \pm 0.6)\mu_B/nm^2$, $(16.4 \pm 0.2)\mu_B/nm^2$, and $(14.1 \pm 0.2)\mu_B/nm^2$, respectively, where uncertainties denote statistical errors of the fit [$z_{NV} \approx 60$ nm in all cases, see (*23*)]. The general agreement of these fits with the values of σ_z found in Fig. 2, A to C, further confirms the validity of our reverse-propagation method.

Our observations thus far corroborate previous results of studies of few-layer CrI_3 (*10*, *13*, *19*), which all found CrI_3 flakes with odd (or even) numbers of layers to exhibit nonzero (or near-zero) magnetization as a result of antiferromagnetic interlayer exchange coupling. These observations, however, are in conflict with the established fact that CrI_3 is a bulk ferromagnet (*32*). We shed light on this dichotomy in a subsequent experiment on sample D2, where our diamond scanning probe induced an unintentional local puncture through the encapsulation layer of the CrI_3 flake (Fig. 3A) (*23*). After this incident, the entire sample, up to several micrometers away from the puncture, exhibited a substantially enhanced magnetization, as evidenced by a representative magnetization map (Fig. 3B) and B_{NV} linescan (Fig. 3C) across the flake. The data show a ≈9.7-fold increase of magnetization from initially $(14.1 \pm 0.2)\mu_B/nm^2$ to $(136.9 \pm 0.4)\mu_B/nm^2$. For the nine-layer flake, this enhancement suggests that the puncture induced a transition from antiferromagnetic to ferromagnetic interlayer coupling.

To investigate the possibility of a structural transition in our punctured sample, we compared its low-temperature Raman spectrum with that of a pristine flake, in a spectral region where characteristic Raman modes for CrI_3 exist (Fig. 3D) (*33*). Although the data do not allow for an unambiguous determination of the crystalline structure of our samples, the markedly different spectra clearly point to a change in structure occurring simultaneously with the change in magnetic order discussed above. This observation is consistent with recent results of density

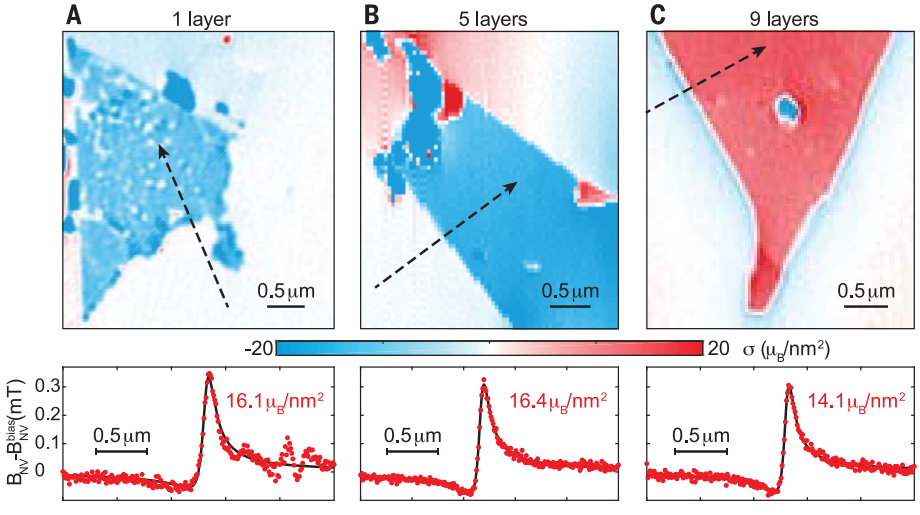


Fig. 2. Magnetization maps of few-layer CrI_3 flakes. Data were acquired after zero-field cooling and spontaneous magnetic ordering under the experimental conditions described in the Fig. 1 legend. Magnetization maps were obtained for (**A**) a monolayer, (**B**) a five-layer-thick sample, and (**C**) a nine-layer-thick sample [see text and (*23*)]. The colorbar applies to all panels. (Bottom) Independently acquired data of magnetic field B_{NV} measured across the borders of each flake, along the lines indicated in the maps. These data allow for an independent determination of magnetization σ_z and sensor–sample separation z_{NV} using analytic fits (black) (*23*).

functional calculations (*16*, *34*–*37*), predicting an interplay between stacking order and interlayer exchange coupling in CrI_3. Further study is needed to elucidate the nature of the structural transition induced by the puncture and the crystalline structure before the puncture.

The connection between crystal structure and magnetism also offers an explanation for the occurrence of magnetic domains in some of our CrI_3 samples. Figure 4A shows a representative image of such domains on sample D2 (nine-layer flake). Notably, the measured domain magnetizations only assume values close to integer multiples of σ_z^{mono}; i.e., $\sigma_z = n\sigma_z^{mono}$, with $n \in \mathbb{Z}$. This observation can be explained by spatial variations (either in-plane or out-of-plane) in the interlayer exchange coupling due to, for instance, local changes in stacking order. Such variations would result in regions with varying numbers of (anti) ferromagnetically coupled CrI_3 layers, consistent with the observed domains. This domain formation mechanism would preserve the parity of n, and we observe well-separated regions on the sample where n is either even or odd (see outlines in Fig. 4A and histogram in Fig. 4B). The removal or addition of a monolayer of CrI_3 between these areas can explain this observation and could have occurred during material exfoliation or sample preparation.

In this study, we used scanning NV magnetometry to observe a direct connection between structural and nanoscale magnetic ordering in CrI_3 and thereby address the question of why few-layer CrI_3 shows antiferromagnetic interlayer exchange coupling despite the bulk being ferromagnetic. Our work establishes scanning NV magnetometry as a powerful tool for addressing nanoscale magnetism in vdW crystals, down to the limit of a single atomic layer. Such direct, quantitative imaging and sensing is vital to advance our understanding of these materials and their development toward applications in future spintronics devices (*3*, *5*). Our approach is general and may even be applied under ambient conditions (*3*, *21*) or to materials that have thus far not been suitable for the application of optical methods (*38*). Finally, the ability to perform NV magnetometry on vdW magnets offers perspectives for high-frequency sensing (*39*) of their magnonic excitations (*14*, *38*), which may enable vdW-based atomic-scale platforms in magnonics applications.

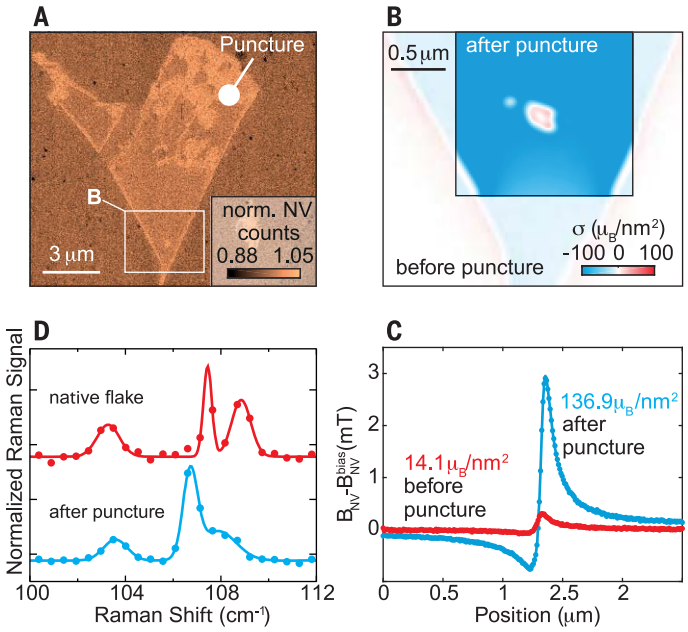


Fig. 3. Interplay of structural and magnetic order in few-layer CrI_3. (**A**) Overview image of sample D2 (*23*), indicating the location of the puncture and the representative region sampled subsequently. The data show normalized NV counts acquired while a fixed-frequency microwave tone was applied (*23*). (**B**) Enhanced magnetization observed in the nine-layer flake of sample D2 after puncture of the CrI_3 encapsulation. The puncture is located a few micrometers from the imaged region [see (A)]. The faint background shows the (inverted) data from Fig. 2C for comparison. The colorbar applies to all data. (**C**) Linecut of B_{NV} across a representative edge of the punctured flake (blue), indicating a magnetization $\sigma_z \approx (136.9 \pm 0.4)\mu_B/nm^2$, which is close to the expected value for a fully polarized nine-layer sample. For reference, the red trace shows the corresponding data from before the puncture. (**D**) Raman spectra from the punctured flake and an unpunctured reference, suggesting the concurrence of a structural transition with the magnetic transition.

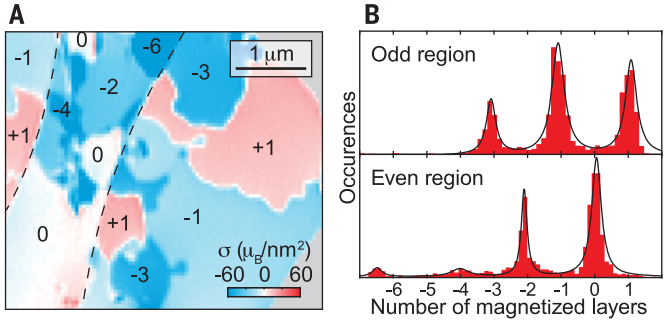


Fig. 4. Magnetic domains in CrI_3. (**A**) Spontaneously occurring magnetic domains observed in the nine-layer flake of sample D2. The magnetization σ_z was found to be discretized in integer multiples of the monolayer magnetization σ_z^{mono}. Numbers indicate σ_z in multiples of σ_z^{mono}, where positive (or negative) values denote magnetizations along the $+z$ (or $-z$) direction. A clear separation of the flake into regions of even and odd multiples of σ_z^{mono} is observed. Even-numbered regions are assigned to a missing or added monolayer (see text). Areas where no flake was present were false-colored in gray. Dashed lines indicate the boundary between regions of even and odd multiples of σ_z^{mono}. (**B**) Histograms of magnetization pixel values obtained in the odd- and even-numbered regions of the data in (A).

REFERENCES AND NOTES

1. B. Huang *et al.*, *Nature* **546**, 270–273 (2017).
2. C. Gong *et al.*, *Nature* **546**, 265–269 (2017).
3. M. Bonilla *et al.*, *Nat. Nanotechnol.* **13**, 289–293 (2018).
4. Z. Fei *et al.*, *Nat. Mater.* **17**, 778–782 (2018).
5. Y. Deng *et al.*, *Nature* **563**, 94–99 (2018).
6. N. D. Mermin, H. Wagner, *Phys. Rev. Lett.* **17**, 1133–1136 (1966).
7. Z. Wang *et al.*, *Nat. Nanotechnol.* **13**, 554–559 (2018).
8. S. Jiang, J. Shan, K. F. Mak, *Nat. Mater.* **17**, 406–410 (2018).
9. S. Jiang, L. Li, Z. Wang, K. F. Mak, J. Shan, *Nat. Nanotechnol.* **13**, 549–553 (2018).
10. B. Huang *et al.*, *Nat. Nanotechnol.* **13**, 544–548 (2018).
11. A. Banerjee *et al.*, *Nat. Mater.* **15**, 733–740 (2016).
12. A. Banerjee *et al.*, *Science* **356**, 1055–1059 (2017).
13. T. Song *et al.*, *Science* **360**, 1214–1218 (2018).
14. D. R. Klein *et al.*, *Science* **360**, 1218–1222 (2018).
15. S. Jiang, L. Li, Z. Wang, J. Shan, K. F. Mak, arXiv:1807.04898 [cond-mat.mes-hall] (13 July 2018).
16. Z. Wang *et al.*, *Nat. Commun.* **9**, 2516 (2018).
17. H. H. Kim *et al.*, *Nano Lett.* **18**, 4885–4890 (2018).
18. D. Zhong *et al.*, *Sci. Adv.* **3**, e1603113 (2017).
19. K. L. Seyler *et al.*, *Nat. Phys.* **14**, 277–281 (2018).
20. N. Sivadas, S. Okamoto, D. Xiao, *Phys. Rev. Lett.* **117**, 267203 (2016).
21. L. Rondin *et al.*, *Rep. Prog. Phys.* **77**, 056503 (2014).
22. A. Gruber *et al.*, *Science* **276**, 2012–2014 (1997).
23. See supplementary materials for additional information.
24. P. Maletinsky *et al.*, *Nat. Nanotechnol.* **7**, 320–324 (2012).
25. P. Appel *et al.*, *Rev. Sci. Instrum.* **87**, 063703 (2016).
26. T. Hingant *et al.*, *Phys. Rev. Appl.* **4**, 014003 (2015).
27. B. J. Roth, N. G. Sepulveda, J. P. Wikswo Jr., *J. Appl. Phys.* **65**, 361–372 (1989).
28. P. Appel *et al.*, *Nano Lett.* **19**, 1682–1687 (2019).
29. M. A. McGuire, H. Dixit, V. R. Cooper, B. C. Sales, *Chem. Mater.* **27**, 612–620 (2015).

30. F. Garcia-Sanchez, P. Borys, A. Vansteenkiste, J.-V. Kim, R. L. Stamps, *Phys. Rev. B* **89**, 224408 (2014).
31. J. P. Tetienne *et al*., *Nat. Commun.* **6**, 6733 (2015).
32. J. F. Dillon Jr., C. E. Olson, *J. Appl. Phys.* **36**, 1259–1260 (1965).
33. S. Djurdjić-Mijin *et al*., *Phys. Rev. B* **98**, 104307 (2018).
34. P. Jiang *et al*., *Phys. Rev. B* **99**, 144401 (2019).
35. D. Soriano, C. Cardoso, J. Fernández-Rossier, arXiv:1807.00357 [cond-mat.mes-hall] (1 July 2018).
36. N. Sivadas, S. Okamoto, X. Xu, C. J. Fennie, D. Xiao, *Nano Lett.* **18**, 7658–7664 (2018).
37. S. W. Jang, M. Y. Jeong, H. Yoon, S. Ryee, M. J. Han, *Phys. Rev. Mater.* **3**, 031001(R) (2019).
38. D. Ghazaryan *et al*., *Nat. Electron.* **1**, 344–349 (2018).
39. C. Du *et al*., *Science* **357**, 195–198 (2017).
40. L. Thiel *et al*., Replication Data for: Probing magnetism in 2D materials at the nanoscale with single spin microscopy, Version 1.0, Zenodo (2019); https://dx.doi.org/10.5281/zenodo.2574907.

ACKNOWLEDGMENTS

We thank A. Högele, V. Jacques, M. Munsch, and J.-V. Kim for discussions and feedback on the manuscript and A. Ferreira for technical help. **Funding:** We acknowledge financial support from the SNI; NCCR QSIT; SNF grants 155845, 169016, and 178891; the EU Graphene Flagship project; and the EU Quantum Flagship project ASTERIQS (820394). N.U. and M.G. acknowledge support through an Ambizione fellowship of the SNF (Swiss National Science Foundation). **Author contributions:** All authors contributed to all aspects of this work. **Competing interests:** The authors declare no competing interests. **Data and materials availability:** All data shown in this paper are available at Zenodo (*40*).

SUPPLEMENTARY MATERIALS

science.sciencemag.org/content/364/6444/973/suppl/DC1
Materials and Methods
Supplementary Text
Figs. S1 to S9
Reference (*41*)

10 October 2018; accepted 8 April 2019
Published online 25 April 2019
10.1126/science.aav6926

SUPERCONDUCTIVITY

Magnetic field–induced pair density wave state in the cuprate vortex halo

S. D. Edkins[1,2,3], A. Kostin[1], K. Fujita[1,4], A. P. Mackenzie[3,5], H. Eisaki[6], S. Uchida[7], Subir Sachdev[8], Michael J. Lawler[1,9], E.-A. Kim[1], J. C. Séamus Davis[1,4,10,11]*, M. H. Hamidian[1,8]*

High magnetic fields suppress cuprate superconductivity to reveal an unusual density wave (DW) state coexisting with unexplained quantum oscillations. Although routinely labeled a charge density wave (CDW), this DW state could actually be an electron-pair density wave (PDW). To search for evidence of a field-induced PDW, we visualized modulations in the density of electronic states $N(r)$ within the halo surrounding $Bi_2Sr_2CaCu_2O_8$ vortex cores. We detected numerous phenomena predicted for a field-induced PDW, including two sets of particle-hole symmetric $N(r)$ modulations with wave vectors Q_P and $2Q_P$, with the latter decaying twice as rapidly from the core as the former. These data imply that the primary field-induced state in underdoped superconducting cuprates is a PDW, with approximately eight CuO_2 unit-cell periodicity and coexisting with its secondary CDWs.

Theory predicts that Cooper pairs with finite center-of-mass momentum $\boldsymbol{p} = \hbar\boldsymbol{Q_P}$ (where $\hbar$ is Planck's constant h divided by 2π) should form a state in which the density of pairs modulates spatially at wave vector $\boldsymbol{Q_P}$ (*1*, *2*). In the phase diagram of underdoped cuprates, such a "pair density wave" (PDW) state (*3*–*5*), generated by strong local electron-electron interactions (*6*–*11*), is anticipated to be another principal state, along with uniform superconductivity. Numerous experimental observations may be understood in that context. For example, although intraplanar superconductivity appears in $La_{2-x}Ba_xCuO_4$ at relatively high temperatures, interplanar superconductivity is strongly frustrated (*12*), which is consistent with the existence of orthogonal unidirectional PDW states in each sequential CuO_2 plane (*3*, *13*, *14*). Moreover, the measured momentum-space electronic structure of the cuprate pseudogap phase is consistent with predictions that are based on a biaxial PDW (*4*). Reported breaking of time-reversal symmetry could be caused by a PDW with inversion breaking (*15*–*18*). The field-induced momentum-space reconstruction and quantum oscillation phenomenology are potentially the consequences of a PDW state (*19*–*21*), although this view is not universal (*22*). At the highest fields, strong diamagnetism in torque magnetometry (*23*) and supercurrents in dc transport might also be understood as being due to a field-induced PDW state. Most recently, scanned Josephson tunneling microscopy allows direct visualization of cuprate pair density modulations (*24*). Taken together, these studies indicate that a fundamental PDW state may exist in underdoped cuprates, with the most common model invoked being an eight unit-cell ($8a_0$) periodic modulation of the electron-pair condensate.

Such a PDW state clearly does not predominate at low temperature in zero magnetic field, where global d-wave superconductivity is robust. However, suppression of the superconductivity by high magnetic fields generates a peculiar DW state (*25*–*32*) along with exotic quantum oscillation phenomenology (*33*, *34*). For type II superconductors in general, application of a magnetic field generates quantized vortices. At the vortices of a conventional d-wave superconductor, the four zeros in the energy gap should generate a slowly decaying, star-shaped, zero-energy resonance oriented along the nodal (±1, ±1) directions. For cuprates, however, strong $N(\boldsymbol{r}, E)$ modulations oriented along (1, 0); (0, 1) directions have long been observed in the "halo" region that surrounds the cuprate vortex core (*35*–*38*). Many theories hypothesize that this phenomenon is a field-induced DW (*5*, *39*–*43*), and some hypothesize that it is not a conventional CDW but a PDW (*4*, *5*, *22*, *43*). This is a fundamental distinction because the PDW and CDW are extremely different states in terms of their broken symmetries and many-body wave functions. Thus, to determine whether the primary DW state induced by magnetic field in superconducting cuprates is a PDW has recently become an urgent research challenge.

To search for evidence of such a state, we studied the field-induced modulations of the density of electronic states $N(\boldsymbol{r}, E)$ within the halo surrounding quantized vortex cores (*35*–*38*). Any periodic modulations of electronic structure can be described by $A(\boldsymbol{r}) = AF(\theta)\cos(\boldsymbol{Q}\cdot\boldsymbol{r} + \phi_0)$, where $A(\boldsymbol{r})$ represents the modulating electronic degree of freedom with amplitude A, $\boldsymbol{Q}$ is the wave vector, and $F(\theta)$ is the modulation form factor defined in terms of the angle θ from the (1, 0) axis. An s-symmetry form factor $F_S(\theta)$ is even under 90° rotations, whereas a d-wave form factor is $F_d(\theta)$ is odd. Following (*5*), the order parameters we considered are those of homogenous d-wave superconductivity $\Delta(\boldsymbol{r}) = F_{SC}\Delta_{SC}$, with $F_{SC} = F_d$, and that of a PDW $\Delta_{PD}(r) = F_P\Delta_P^Q(e^{i\boldsymbol{Q_P}\cdot\boldsymbol{r}} + e^{-i\boldsymbol{Q_P}\cdot\boldsymbol{r}})$, with wave vector $\boldsymbol{Q_P}$ and either an F_s or F_d type of form factor [(*44*), section 1]. A field-induced PDW may be identified from Ginzburg-Landau (GL) analysis (*5*, *22*, *43*) of the interactions between these two order parameters within vortex halos—regions of suppressed but nonzero superconductivity that surround vortex cores (Fig. 1A). Given a generic GL free-energy density of the form

$$\mathcal{F}_{A-SC} = \mathcal{F}(\Delta_{SC}) + \mathcal{F}(\Delta_A) + u_1|\Delta_A|^2|\Delta_{SC}|^2 \quad (1)$$

where $\mathcal{F}(\Delta_{SC})$ and $\mathcal{F}(\Delta_A)$ are the free-energy densities of a superconductor and of an alternative repulsively coupled ($u_1 > 0$) state Δ_A, the observation of coexistence of Δ_A with Δ_{SC} within the vortex halo [(*44*), section 2] means that the two ordered states are almost energetically degenerate (*39*). Such a near degeneracy occurs naturally between a superconductor Δ_{SC} and a PDW Δ_P^Q that are made up of the same electron pairs. In this case, allowed $N(\boldsymbol{r})$ modulations generated by interactions between Δ_{SC} and Δ_A can be found from products of these order parameters that transform as density-like quantities. For example, the product of PDW and uniform SC order parameters

$$A_{\boldsymbol{Q_P}} \propto \Delta_P^Q\,\Delta_{SC}^* \Rightarrow N(\boldsymbol{r}) \propto \cos(\boldsymbol{Q_P}\cdot\boldsymbol{r}) \quad (2)$$

results in $N(\boldsymbol{r})$ modulations at the PDW wave vector $\boldsymbol{Q_P}$. The product of a robust PDW with itself

$$A_{\boldsymbol{2Q_P}} \propto \Delta_P^Q\Delta_P^{-Q*} \Rightarrow N(\boldsymbol{r}) \propto \cos(2\boldsymbol{Q_P}\cdot\boldsymbol{r}) \quad (3)$$

produces $N(\boldsymbol{r})$ modulations occurring at $2\boldsymbol{Q_P}$. Thus, a key signature of a field-induced PDW with wave vector $\boldsymbol{Q_P}$ in cuprate vortex halos (Fig. 1A) would be coexistence of two sets of $N(\boldsymbol{r})$ modulations at $N(\boldsymbol{r})$ and at $2\boldsymbol{Q_P}$ within each halo (Fig. 1B) (*5*, *22*, *43*).

Within GL theory, substantial further information can be extracted from measured rates of decay of the induced $N(\boldsymbol{r})$ modulations away from the vortex center and from the form factors of these modulations within the vortex halo. For a field-induced PDW, the $N(\boldsymbol{r}, E)$ modulations at $2\boldsymbol{Q_P}$ should decay with distance from the core at twice the rate as those at $\boldsymbol{Q_P}$. This is because if $\Delta_P^Q = \Delta_P^Q(|\boldsymbol{r}| = 0)e^{-|r|/\xi}$, then $\Delta_P^Q\Delta_P^{-Q*}$ decays with $|r|$ at twice the rate of $\Delta_P^Q\Delta_{SC}^*$ (Fig. 1B). Current theory (*22*, *43*) indicates that if the $N(\boldsymbol{r}, E)$ modulations at $\boldsymbol{Q_P}$ caused by $\Delta_P^Q\Delta_{SC}^*$

[1]Laboratory of Atomic and Solid State Physics, Department of Physics, Cornell University, Ithaca, NY 14853, USA. [2]Department of Applied Physics, Stanford University, Stanford, CA 94305, USA. [3]School of Physics and Astronomy, University of St. Andrews, Fife KY16 9SS, Scotland. [4]Condensed Matter Physics Department, Brookhaven National Laboratory, Upton, NY, USA. [5]Max-Planck Institute for Chemical Physics of Solids, D-01187 Dresden, Germany. [6]Institute of Advanced Industrial Science and Technology, Tsukuba, Ibaraki 305-8568, Japan. [7]Department of Physics, University of Tokyo, Bunkyo-ku, Tokyo 113-0033, Japan. [8]Department of Physics, Harvard University, Cambridge, MA 02138, USA. [9]Department of Physics and Astronomy, Binghamton University, Binghamton, NY 13902, USA. [10]Department of Physics, University College Cork, Cork T12R5C, Ireland. [11]Clarendon Laboratory, Oxford University, Oxford, OX1 3PU, UK.
*Corresponding author. Email: jcdavis@ccmr.cornell.edu (J.C.S.D.); mhh32@cornell.edu (M.H.H.)

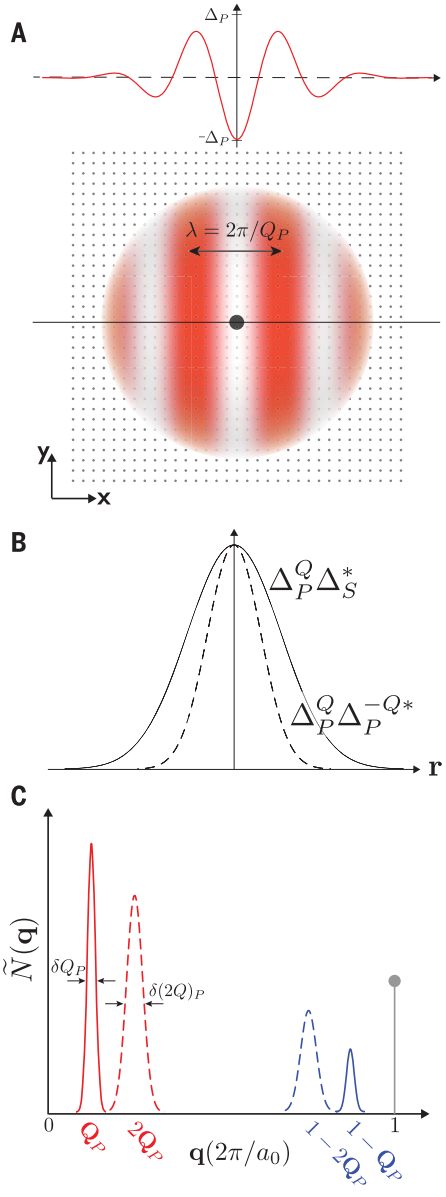


Fig. 1. Schematic of field-induced unidirectional $8a_0$ PDW. (**A**) Diagram of the halo region (gray) surrounding the vortex core (black) of a cuprate superconductor (SC). The CuO_2 plane orientation and Cu–Cu periodicity are indicated by using a dot for each Cu site. Within the halo, a unidirectional PDW modulation along the *x* axis with periodicity $8a_0$, characterized by an order parameter $\Delta_P^Q(\boldsymbol{r})$ shown as red curve in the top graph, is indicated schematically with red shading. (**B**) Solid curve indicates envelope containing nonzero amplitude $\Delta_P^Q \Delta_{SC}^*$ of the $N(\boldsymbol{r})$ modulations caused by the interaction between the SC and PDW order parameters, plotted along the fine horizontal line in (A) through the vortex core. Dashed curve indicates the envelope containing nonzero amplitude $\Delta_P^Q \Delta_P^{-Q*}$ of the $N(\boldsymbol{r})$ modulations caused by PDW itself, plotted along the same fine line. For clarity, we ignore the small region (less than 1 nm) at the core where $\Delta_P^Q \Delta_{SC}^*$ must rise from zero as Δ_{SC} does. (**C**) Within a GL model, if the field-induced PDW has a pure *d*-symmetry form factor, $F_P = F_d$, then two sets of $N(\boldsymbol{r})$ modulations should appear together. The first is $N(\boldsymbol{r}) \propto \cos(\boldsymbol{Q_P} \cdot \boldsymbol{r})$ caused by $\Delta_P^Q \Delta_S^*$ and indicated in $\tilde{N}(\boldsymbol{q})$ [the Fourier transform of $N(\boldsymbol{r})$] with a solid red curve. The second $N(\boldsymbol{r}) \propto \cos(2\boldsymbol{Q_P} \cdot \boldsymbol{r})$ caused by $\Delta_P^Q \Delta_P^{-Q*}$ is indicated in $\tilde{N}(\boldsymbol{q})$ with a dashed red curve. The decay length for the $2\boldsymbol{Q_P}$ modulation should be half that of the $\boldsymbol{Q_P}$ modulation, meaning that the linewidth $\delta(2Q)_P$ of the $2\boldsymbol{Q_P}$ modulation (dashed red) should be twice that of the $\boldsymbol{Q_P}$ modulation, δQ_P (solid red). If the PDW has a pure *s*-symmetry form factor, $F_P = F_S$, then a different pair of $N(\boldsymbol{r})$ modulations should appear together. First is $N(\boldsymbol{r}) \propto \cos[(\boldsymbol{Q_B} - \boldsymbol{Q_P}) \cdot \boldsymbol{r}]$, caused by $\Delta_P^Q \Delta_S^*$ (solid blue line), and second $N(\boldsymbol{r}) \propto \cos(2\boldsymbol{Q_P} \cdot \boldsymbol{r})$, caused by $\Delta_P^Q \Delta_P^{-Q*}$ (dashed blue line). Here, $\boldsymbol{Q_B}$ is the Bragg wave vector of the CuO_2 unit cell.

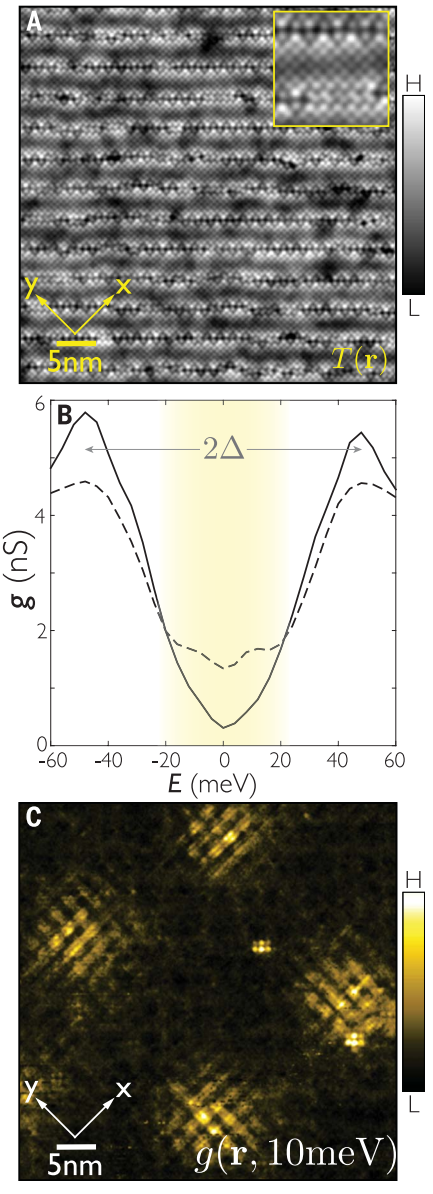


Fig. 2. Four-unit-cell quasiparticle modulations at vortex halos in $Bi_2Sr_2CaCu_2O_8$. (**A**) Topographic image $T(\boldsymbol{r})$ of BiO termination layer of our $Bi_2Sr_2CaCu_2O_8$ sample. The displacement of every specific atomic site in this field of view between zero field and B = 8.25 T was constrained by post processing of all low- and high-field data sets to be less than 10 pm [(*45*), section 3]. (**B**) Measured differential tunnel conductance spectrum $g(\boldsymbol{r}, E = \text{eV}) \equiv dI/dV(\boldsymbol{r}, V)$ showing how to identify the symmetry point of a vortex core (dashed line). The full line shows measured $g(\boldsymbol{r}, E = \text{eV})$ at the identical location in zero field. Yellow-shaded region indicates low-energy Bogoliubov quasiparticle states generated by the vortex. (**C**) Measured $\delta g(\boldsymbol{r}, 12\text{ meV}) = g(\boldsymbol{r}, 12\text{ meV}, B = 8.25\ T) - g(\boldsymbol{r}, 12\text{ meV}, B = 0)$ showing typical examples of the low-energy Bogoliubov quasiparticle modulations (*35*–*38*) within halo regions surrounding four vortex cores in $Bi_2Sr_2CaCu_2O_8$.

exhibit *s*-symmetry form factor (F_s), this implies that the PDW order parameter Δ_P^Q contains components with *d*-symmetry form factor (F_d), and vice versa [(*44*), section 2]. These studies (*22*, *43*) sustain the original GL approach (*5*) by showing that an $8a_0$ PDW stabilized in the halo of a *d*-wave vortex core does indeed generate both an $8a_0$ and a $4a_0$ periodic charge modulation therein. Overall, because a *d*-symmetry form factor PDW is typically predicted for cuprates (*6*–*11*), its signature within a vortex halo should be two sets of $N(\boldsymbol{r})$ modulations occurring at $\boldsymbol{Q_P}$ and $2\boldsymbol{Q_P}$, both with *s*-symmetry form factor components and with the amplitude of the $2\boldsymbol{Q_P}$ modulation decaying twice as rapidly as that at $\boldsymbol{Q_P}$.

To explore these predictions, we imaged scanning tunneling microscope (STM) tip-sample differential tunneling conductance $dI/dV(\boldsymbol{r}, V) \equiv g(\boldsymbol{r}, E)$ versus bias voltage $V = E/e$ and location $\boldsymbol{r}$ with sub–unit-cell spatial resolution; no scanned Josephson tunneling microscopy (*24*) was involved. We measured slightly underdoped $Bi_2Sr_2CaCu_2O_8$ samples [superconducting transition temperature $T_c \sim 88$K; hole doping $p \sim 17\%$] at temperature T = 2 K. We first measured the $N(\boldsymbol{r}, E)$ at zero field and then at magnetic field B = 8.25 T, in the identical field of view (FOV), using an identical STM tip (*35*). The former was subtracted from the latter to yield the field-induced changes $\delta g(\boldsymbol{r}, E, B) = g(\boldsymbol{r}, E, B) - g(\boldsymbol{r}, E, 0)$, which are related to the field-induced perturbation to the density of states as $\delta N(\boldsymbol{r}, E, B) \propto \delta g(\boldsymbol{r}, E, B)$. This step ensures that the phenomena studied thereafter were only those induced by the magnetic field, with all signatures of the ubiquitous *d*-symmetry form factor DW observed at $B = 0$ (*45*) having been subtracted. Compared with our prior vortex halo studies (*35*), we enhanced the $\boldsymbol{r}$-space resolution using smaller pixels and the $\boldsymbol{q}$-space resolution by using larger FOV (58 by 58 nm), increased the

number of vortices per image, used distortion-corrected sublattice-phase-resolved imaging (*45*), and measured in a far wider energy range $0 < |E| < 80$ meV [(*44*), section 3].

We next identified the location of every vortex halo in $\delta g(\boldsymbol{r}, E, B)$ images using two well-known phenomena: (i) suppression of the superconducting coherence peaks at the vortex symmetry point (Fig. 2B) and (ii) appearance of low-energy periodic conductance modulations (*35*–*38*) surrounding this point. A typical symmetry-point spectrum of the superconducting vortex where maximum suppression of the single-particle coherence peaks occurs is shown in Fig. 2B; these peaks recover very rapidly as a function of radius, so that robust *d*-wave superconductivity signified by full coherence peaks has recovered within a radius of ~1 nm [(*44*), section 4]. At E = 12 meV, the typical halo of conductance modulations we detected surrounding each vortex symmetry point (Fig. 2C) was in excellent agreement with previous studies of modulations of low-energy quasiparticles, with $\boldsymbol{q} \approx (\pm 1/4, 0); (0, \pm 1/4)2\pi/a_0$ within the $Bi_2Sr_2CaCu_2O_{8-x}$ vortex halo (*35*–*38*). We focused on a different energy range $25 < |E| < 50$ meV because analysis of our $\delta g(\boldsymbol{r}, E)$ data revealed major changes in this range. In Fig. 3A, we show measured $\delta g(\boldsymbol{r}, 30\text{ meV})$ containing the modulations detected in the halo of each vortex core. Fourier analysis of this $\delta g(\boldsymbol{r}, 30\text{ meV})$ yields $|\tilde{\delta g}(\boldsymbol{q}, 30\text{ meV})|$ and reveals a set of sharp peaks at $\boldsymbol{q} = (\boldsymbol{Q}_P^x; \boldsymbol{Q}_P^y) \approx [(\pm 1/8, 0)(0, \pm 1/8)]2\pi/a_0$, which we label $\boldsymbol{Q_P}$ for reasons explained below (Fig. 3B). Similarly, there is a second set of weaker modulations in $\tilde{\delta g}(\boldsymbol{q}, 30\text{ meV})$ at $\boldsymbol{q} \approx [(\pm 1/4, 0); (0, \pm 1/4)]2\pi/a_0$, which we label $2\boldsymbol{Q_P}$. The $\boldsymbol{r}$-space amplitude envelopes of the $\boldsymbol{Q_P}$ and $2\boldsymbol{Q_P}$ modulations (Fig. 3, C and D) reveal how these field-induced phenomena are confined to the vortex halo regions only. Averaged over all vortices, the measured amplitude $|\tilde{\delta g}(\boldsymbol{q}, 30\text{ meV})|$ plotted along (1, 0) in Fig. 3E discernibly discriminates the $\boldsymbol{Q_P}$ from the $2\boldsymbol{Q_P}$ modulation peaks. Thus, we discovered strong, field-induced modulations of $N(\boldsymbol{r}, E)$, with period approximately $8a_0$ coexisting with weaker modulations of period approximately $4a_0$, along both the (1, 0); (0, 1) directions within every vortex halo. These particle-hole symmetric phenomena exist within the energy range $25 < |E| < 45$ meV [(*44*), section 5].

To evaluate form factor symmetry for these field-induced modulations [(*44*), section 6], we separated each such $\delta g(\boldsymbol{r}, E)$ image into three sublattice images (*46*): $Cu(\boldsymbol{r}, E)$, containing only the measured values of $\delta g(\boldsymbol{r}, E)$ at copper sites, and $O_x(\boldsymbol{r}, E)$ and $O_y(\boldsymbol{r}, E)$, containing only those at the x/y axis oxygen sites. All of the form factors discussed here refer to modulations in $\delta g(\boldsymbol{r}, E, B)$ and are not necessarily those of the order parameter of the field-induced state that generates them. Complex-valued Fourier transforms of the $O_x(\boldsymbol{r}, E)$ and $O_y(\boldsymbol{r}, E)$ sublattice images yield $\tilde{O}_x(\boldsymbol{q}, E)$; $\tilde{O}_y(\boldsymbol{q}, E)$. Then, modulations at any $\boldsymbol{Q}$ having *d*-symmetry form factor F_d generate a peak in $\tilde{D}^{\delta g}(\boldsymbol{q}, E) \equiv \tilde{O}_x(\boldsymbol{q}, E) - \tilde{O}_y(\boldsymbol{q}, E)$ at $\boldsymbol{Q}$, whereas those with *s*-symmetry form factor F_s generate a peak in $\tilde{S}^{\delta g}(\boldsymbol{q}, E) \equiv [\tilde{O}_x(\boldsymbol{q}, E) + \tilde{O}_y(\boldsymbol{q}, E)] + \tilde{Cu}(\boldsymbol{q}, E)$ at $\boldsymbol{Q}$. When we analyzed the data in Fig. 3, A and B, in this way using measured $\tilde{S}^{\delta g}(\boldsymbol{q}, 30\text{ meV})$, the field-induced $\delta g(\boldsymbol{r}, E)$-modulations occurring at $\boldsymbol{q} \approx (\pm Q_P, 0); (0, \pm Q_P)$ and $\boldsymbol{q} \approx (\pm 2Q_P, 0); (0, \pm 2Q_P)$ all exhibited *s*-symmetry form factors (Fig. 3E).

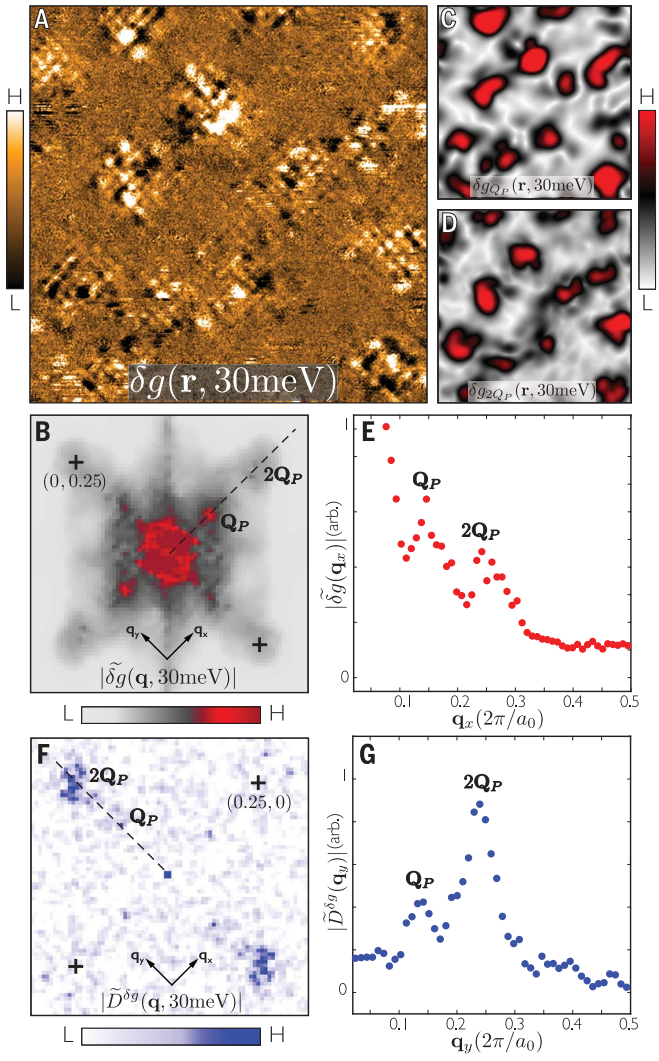


Fig. 3. Field-induced *s*-symmetry form factor modulations within vortex halos. (**A**) Measured field-induced modulations $\delta g(\boldsymbol{r}, 30\text{ meV}) = g(\boldsymbol{r}, 30\text{ meV}, B = 8.25\ T) - g(\boldsymbol{r}, 30\text{ meV}, B = 0)$ in a 58 by 58 nm FOV. The simultaneously measured topographs $T(\boldsymbol{r})$ at B = 8.25 T and 0 T are shown in fig. S2 and (*44*), section 3, and demonstrate by the absence of local maxima at $\boldsymbol{q} \approx [(\pm 1/8, 0); (0, \pm 1/8)]2\pi/a_0$ in their Fourier transforms that the setup effect is not influencing observations of $\delta g(\boldsymbol{r}, E)$ modulations at these wave vectors [(*44*), section 5]. (**B**) Amplitude Fourier transform $|\tilde{\delta g}(\boldsymbol{q}, 30\text{ meV})|$ (square root of power spectral density) of $\delta g(\boldsymbol{r}, 30\text{ meV})$ data in (A). The $\boldsymbol{q} = (\pm 1/4, 0); (0, \pm 1/4)2\pi/a_0$ points are indicated with black crosses. Four sharp maxima, indicated by $\boldsymbol{Q_P}$, occur at $\boldsymbol{q} = (\pm 1/8, 0); (0, \pm 1/8)2\pi/a_0$, whereas four broader maxima, indicated by $2\boldsymbol{Q_P}$, occur at $\boldsymbol{q} = (\pm 1/4, 0); (0, \pm 1/4)2\pi/a_0$. (**C**) Measured amplitude envelope of the modulations in $\delta g(\boldsymbol{r}, 30\text{ meV})$ at $\boldsymbol{Q_P}$ showing that they only occur within the vortex halo regions. (**D**) Measured amplitude envelope of the modulations in $\delta g(\boldsymbol{r}, 30\text{ meV})$ at $2\boldsymbol{Q_P}$, showing that they also only occur within the vortex halo regions. (**E**) Measured $|\tilde{\delta g}(\boldsymbol{q}, 30\text{ meV})|$ along (0,0)-(1/2,0) [(B), dashed line], showing the two maxima in the field-induced $N(\boldsymbol{r})$ modulations, occurring at by $\boldsymbol{Q_P}$ = 0.117 ± 0.01 and $2\boldsymbol{Q_P}$ = 0.231 ± 0.01 (Fig. 4, A to D) (**F**) Amplitude Fourier transform of the *d*-symmetry form factor modulations in $N(\boldsymbol{r})$, $|\tilde{D}^{\delta g}(\boldsymbol{q}, 30\text{ meV})|$, derived from measured $\delta g(\boldsymbol{r}, 30\text{ meV})$ data in (A). Again, $\boldsymbol{q} = (\pm 1/4, 0); (0, \pm 1/4)2\pi/a_0$ points are indicated with black crosses. Two maxima, labeled as $\boldsymbol{Q_P}$, occur at $\boldsymbol{q} = (\pm 1/8, 0); (0, \pm 1/8)2\pi/a_0$, whereas two broader maxima, indicated by $2\boldsymbol{Q_P}$ occur at $\boldsymbol{q} = (\pm 1/4, 0); (0, \pm 1/4)2\pi/a_0$, with both sets oriented along the *y* axis. (**G**) Measured $|\tilde{D}^{\delta g}(\boldsymbol{q}, 30\text{ meV})|$ along (0,0)-(1/2,0) [(F), dashed line], showing the maxima in the field induced $N(\boldsymbol{r})$ modulations occurring at $\boldsymbol{Q_P}$ and $2\boldsymbol{Q_P}$. A unidirectional *d*-symmetry form factor change density modulation, as observed extensively in zero field (*46*), would have such characteristics, as would contributions from an *s*-symmetry form factor PDW. These modulations do not appear in Fig. 3 because, in that unprocessed $\delta g(\boldsymbol{r}, E)$ data, they occur at $\boldsymbol{Q} \approx (0, \pm 7/8)2\pi/a_0$ and $\boldsymbol{Q} \approx (0, \pm 3/4)2\pi/a_0$ owing to their *d*-symmetry form factor (Fig. 4, A to D).

However, the measured $\tilde{D}^{\delta g}(\boldsymbol{q}, 30\text{ meV})$ in Fig. 3, F and G, also revealed that weaker *d*-symmetry $\delta g(\boldsymbol{r}, E)$-modulations occur at $\boldsymbol{q} \approx (0, \pm Q_P)$ and $\boldsymbol{q} \approx (0, \pm 2Q_P)$. They too are confined to the vortex halo because the $\boldsymbol{r}$-space amplitude-envelope of the $2\boldsymbol{Q}_P$-modulations in $\tilde{D}^{\delta g}(\boldsymbol{q}, 30\text{ meV})$ is concentrated there.

The overall measured amplitudes of $|\widetilde{\delta g}(\boldsymbol{q}, 30\text{ meV})|$ derived from $\delta g(\boldsymbol{r}, 30\text{ meV})$ in Fig. 3A are shown in Fig. 4, A and B, plotted along the (1,0) and (0,1) directions of the CuO_2 plane. Equivalent cuts of $|\widetilde{\delta g}(\boldsymbol{q}, -30\text{ meV})|$ derived from $\delta g(\boldsymbol{r}, -30\text{ meV})$ data are shown in Fig. 4, C and D. The four maxima at $|\boldsymbol{q}| \approx 1/8$, $|\boldsymbol{q}| \approx 1/4$, $|\boldsymbol{q}| \approx 3/4$, and $|\boldsymbol{q}| \approx 7/8$ associated with field-induced modulations occur in Fig. 4, A to D. The measured form factor of each set of modulations is identified by color code, red indicating *s*-symmetry and blue indicating *d*-symmetry. Although modulations at $|\boldsymbol{q}| \approx 7/8$ and $|\boldsymbol{q}| \approx 3/4$ (Fig. 4, A to D, blue) appear subdominant, they do merit comment. First,

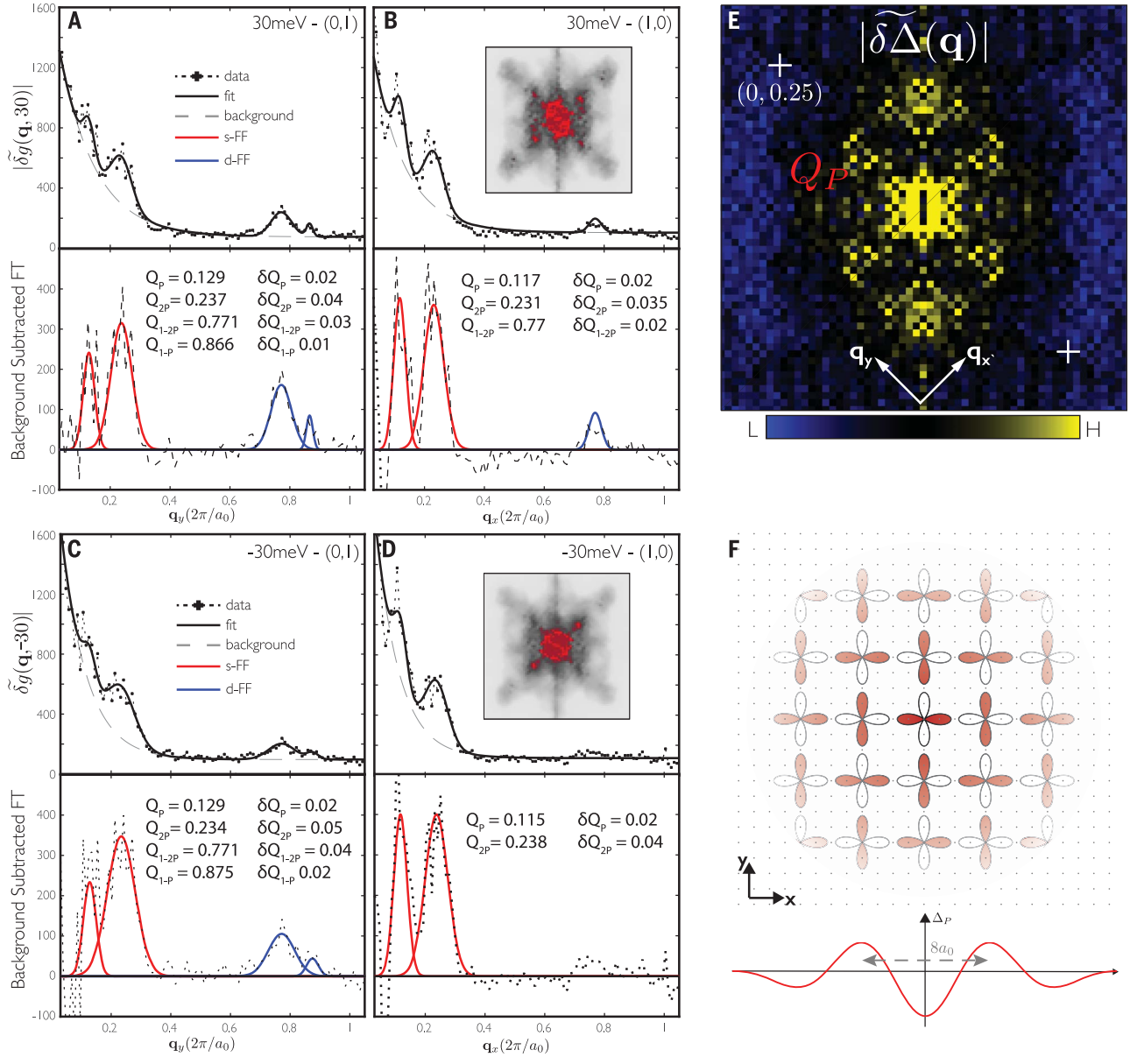


Fig. 4. Field-induced *N*(*r*) modulations indicative of a PDW state in the vortex halo. (**A** and **B**) Amplitude Fourier transform $|\widetilde{\delta g}(\boldsymbol{q}, 30\text{ meV})|$ derived from $\delta g(\boldsymbol{r}, 30\text{ meV})$ data are plotted along two orthogonal axes from (0,0)-(0,1) and (0,0)-(1,0), to reach both Bragg points. All four local maxima, at $\boldsymbol{Q_P}$ and $2\boldsymbol{Q_P}$ from the *s*-symmetry field-induced $N(\boldsymbol{r})$ modulations, plus at $1 - \boldsymbol{Q_P}$ and $1 - 2\boldsymbol{Q_P}$ from the *d*-symmetry field-induced $N(\boldsymbol{r})$ modulations, may be seen. Measurement from these fits of the *q*-magnitude and width δq of the *s*-symmetry peaks at $\boldsymbol{Q_P}$ and $\boldsymbol{2Q_P}$ yields $Q_P^x = 0.117, Q_P^y = 0.129$; $2Q_P^x = 0.231, 2Q_P^y = 0.237$; $\delta Q_P^x = 0.020, \delta Q_P^y = 0.020$; and $\delta 2Q_P^x = 0.034, \delta 2Q_P^y = 0.035$. (Inset) $|\widetilde{\delta g}(\boldsymbol{q}, 30\text{ meV})|$. (**C** and **D**) As in (A) and (B) but at $E = -30$ meV. Measurement yields are $Q_P^x = 0.115, Q_P^y = 0.128$; $2Q_P^x = 0.239, 2Q_P^y = 0.235$; $\delta Q_P^x = 0.020, \delta Q_P^y = 0.020$; and $\delta 2Q_P^x = 0.039, \delta 2Q_P^y = 0.045$. (Inset) $|\widetilde{\delta g}(\boldsymbol{q}, -30\text{ meV})|$. The *s*-symmetry field-induced $N(\boldsymbol{r})$ modulations at $\boldsymbol{Q_P}$ and $2\boldsymbol{Q_P}$ are almost perfectly particle-hole symmetric [(B) and (D), insets] in the sense that $N(\boldsymbol{r}, E > 25\text{ meV}) = N(\boldsymbol{r}, E < -25\text{ meV})$ for these two wave vectors. (**E**) Fourier transform amplitude, $|\widetilde{\delta\Delta}(\boldsymbol{q})|$, of measured $\delta\Delta(\boldsymbol{r}) = \Delta(\boldsymbol{r}, 8.25\text{ T}) - \Delta(\boldsymbol{r}, 0)$ [(*44*), section 7]. The observed peaks revealing field-induced gap modulation occur at points indistinguishable from $\boldsymbol{Q_P}$. The peak along the (1, 1) direction occurs at the wave vector of the crystal supermodulation, where a modulation-induced PDW has long been identified. (**F**) Schematic representation of a bidirectional PDW with a *d*-symmetry form factor induced within a vortex halo that is consonant with the data in this work when considered in the context of vortex halo theory (*5*, *22*, *43*).

they are not inconsistent with an admixture of *s*-symmetry and *d*-symmetry components in the PDW order parameter. However, these modulations may also represent a field-induced version of the unidirectional *d*-symmetry form factor $N(\boldsymbol{r}, E)$ modulation observed in zero field (*45*).

But the predominant phenomena detected are the two sets of *s*-symmetry form factor modulations at $|\boldsymbol{Q_P}| \approx 1/8$ and $|2\boldsymbol{Q_P}| \approx 1/4$ (Fig. 4, A to D, red). Moreover, after subtraction of a smooth background, the widths δq of all $|\boldsymbol{Q_P}| \approx 1/8$ peaks are close to half of the $|2\boldsymbol{Q_P}| \approx 1/4$ peaks, as determined quantitatively by fitting as shown in Fig. 4, A to D. Averaged over the two directions (1, 0) and (0, 1) and energies $E = \pm 30$ meV, we found that $\delta(2\boldsymbol{Q_P}) = (1.8 \pm 0.2)\delta(\boldsymbol{Q_P})$ as expected for a field-induced PDW (Fig. 1) (*5*, *22*, *43*). As additional evidence of a PDW, we searched for energy gap modulations in measured $\Delta(\boldsymbol{r}) = \Delta_{SC} + \Delta_P \cos(\boldsymbol{Q_P} \cdot \boldsymbol{r})$. Generally, in superconductivity studies, the empirical $\Delta(\boldsymbol{r})$ is defined as half the energy separation of the coherence peaks in $N(\boldsymbol{r}, E)$ (Fig. 2B, horizontal arrow), so that field-induced changes to $\Delta(\boldsymbol{r})$ would here be defined as $\delta\Delta(\boldsymbol{r}) = \Delta(\boldsymbol{r}, 8.25\ T) - \Delta(\boldsymbol{r}, 0)$ [(*44*), section 7]. When measured, this $\delta\Delta(\boldsymbol{r})$ yields a Fourier transform $\delta\widetilde{\Delta}(\boldsymbol{q})$, as shown in Fig. 4E. This exhibits evidence for a field-induced energy-gap modulation at $\boldsymbol{Q_P}$ and not at $2\boldsymbol{Q_P}$, as would be expected specifically for a primary field-induced PDW at $\boldsymbol{Q_P}$.

Taken together, the results shown in Figs. 3 and 4 indicate that in $Bi_2Sr_2CaCu_2O_8$, a field-induced PDW state emerges within the halo region surrounding each quantized vortex core. The principal experimental signatures are two sets of $N(\boldsymbol{r})$ modulations occurring at $\boldsymbol{Q_P}$ and $2\boldsymbol{Q_P}$, both being particle-hole symmetric, both exhibiting principal amplitude with *s*-symmetry form factor, with the amplitude of $2\boldsymbol{Q_P}$ modulations decaying twice as rapidly as that of $\boldsymbol{Q_P}$ and with an apparently bidirectional structure, as shown schematically in Fig. 4F [(*44*), section 8]. These phenomena occur in an energy range $25 < |E| < 45$ meV, as might be expected theoretically for an $8a_0$ periodic PDW with energy gap magnitude Δ_P^Q occurring within that range. Several major implications stem from these observations. First and foremost, the primary state induced by high magnetic fields in the superconducting phase of cuprates is inferred to be a PDW with wave vector $\boldsymbol{Q_P}$, accompanied by secondary charge modulations at $\boldsymbol{Q_P}$ and $2\boldsymbol{Q_P}$. Second, the $8a_0$ periodicity points toward a strong correlation-driven microscopic mechanism for the PDW (*6*–*11*), in which case the form factor is generally predicted to have a *d*-symmetry (Fig. 4F). Third, because the PDW is generated by increasing magnetic field, our data imply that the high-field state of cuprates might itself be a PDW state (*4*), and if so, it is likely phase fluctuating and intertwined with additional CDW components. Last, putting all such conjectures aside, we emphasize that the experimental observations reported in Figs. 3 and 4 are in good, detailed, and quantitative agreement with theoretical models (*5*, *22*, *43*, *44*) for a primary PDW with wave vector $\boldsymbol{Q_P}$ induced within the cuprate vortex halo, which generates secondary CDWs at $\boldsymbol{Q_P}$ and $2\boldsymbol{Q_P}$.

REFERENCES AND NOTES

1. P. Fulde, R. A. Ferrell, *Phys. Rev.* **135** (3A), A550–A563 (1964).
2. A. I. Larkin, Y. N. Ovchinnikov, *Sov. Phys. JETP* **20**, 762–769 (1964).
3. E. Berg *et al*., *Phys. Rev. Lett.* **99**, 127003 (2007).
4. P. A. Lee, *Phys. Rev. X* **4**, 031017 (2014).
5. D. F. Agterberg, J. Garaud, *Phys. Rev. B* **91**, 104512 (2015).
6. A. Himeda, T. Kato, M. Ogata, *Phys. Rev. Lett.* **88**, 117001 (2002).
7. M. Raczkowski, M. Capello, D. Poilblanc, R. Fr'esard, A. M. Oleś, *Phys. Rev. B* **76**, 140505 (2007).
8. K.-Y. Yang, W. Q. Chen, T. M. Rice, M. Sigrist, F.-C. Zhang, *New J. Phys.* **11**, 055053 (2009).
9. F. Loder, A. P. Kampf, T. Kopp, *Phys. Rev. B* **81**, 020511 (2010).
10. P. Corboz, T. M. Rice, M. Troyer, *Phys. Rev. Lett.* **113**, 046402 (2014).
11. R.-G. Cai, L. Li, Y.-Q. Wang, J. Zaanen, *Phys. Rev. Lett.* **119**, 181601 (2017).
12. Q. Li, M. Hücker, G. D. Gu, A. M. Tsvelik, J. M. Tranquada, *Phys. Rev. Lett.* **99**, 067001 (2007).
13. E. Berg, E. Fradkin, S. A. Kivelson, *Nat. Phys.* **5**, 830–833 (2009).
14. E. Berg, E. Fradkin, S. A. Kivelson, J. M. Tranquada, *New J. Phys.* **11**, 115004 (2009).
15. C. Pépin, V. S. De Carvalho, T. Kloss, X. Montiel, *Phys. Rev. B* **90**, 195207 (2014).
16. H. Freire, V. S. de Carvalho, C. Pépin, *Phys. Rev. B* **92**, 045132 (2015).
17. Y. Wang, D. F. Agterberg, A. Chubukov, *Phys. Rev. Lett.* **114**, 197001 (2015).
18. D. F. Agterberg, D. S. Melchert, M. K. Kashyap, *Phys. Rev. B* **91**, 054502 (2015).
19. M. Zelli, C. Kallin, A. J. Berlinsky, *Phys. Rev. B* **84**, 174525 (2011).
20. M. Zelli, C. Kallin, A. J. Berlinsky, *Phys. Rev. B* **86**, 104507 (2012).
21. M. R. Norman, J. C. S. Davis, *Proc. Natl. Acad. Sci. U.S.A.* **115**, 5389–5391 (2018).
22. Z. Dai, Y.-H. Zhang, T. Senthil, P. A. Lee, *Phys. Rev. B* **97**, 174511 (2018).
23. F. Yu *et al*., *Proc. Natl. Acad. Sci. U.S.A.* **113**, 12667–12672 (2016).
24. M. H. Hamidian *et al*., *Nature* **532**, 343–347 (2016).
25. T. Wu *et al*., *Nature* **477**, 191–194 (2011).
26. J. Chang *et al*., *Nat. Phys.* **8**, 871–876 (2012).
27. D. LeBoeuf *et al*., *Nat. Phys.* **9**, 79–83 (2012).
28. S. Blanco-Canosa *et al*., *Phys. Rev. Lett.* **110**, 187001 (2013).
29. T. Wu *et al*., *Nat. Commun.* **6**, 6438 (2015).
30. S. Gerber *et al*., *Science* **350**, 949–952 (2015).
31. J. Chang *et al*., *Nat. Commun.* **7**, 11494 (2016).
32. H. Jang *et al*., *Proc. Natl. Acad. Sci. U.S.A.* **113**, 14645–14650 (2016).
33. B. Vignolle, D. Vignolles, M.-H. Julien, C. Proust, *C. R. Phys.* **14**, 39–52 (2013).
34. S. E. Sebastian, C. Proust, *Annu. Rev. Condens. Matter Phys.* **6**, 411–430 (2015).
35. J. E. Hoffman *et al*., *Science* **295**, 466–469 (2002).
36. K. Matsuba *et al*., *J. Phys. Soc. Jpn.* **76**, 063704 (2007).
37. S. Yoshizawa *et al*., *J. Phys. Soc. Jpn.* **82**, 083706 (2013).
38. T. Machida *et al*., *Nat. Commun.* **7**, 11747 (2016).
39. S. A. Kivelson, D. Lee, E. Fradkin, V. Oganesyan, *Phys. Rev. B* **66**, 144516 (2002).
40. D. F. Agterberg, H. Tsunetsugu, *Nat. Phys.* **4**, 639–642 (2009).
41. J. D. Sau, S. Sachdev, *Phys. Rev. B* **89**, 075129 (2014).
42. M. Einenkel, H. Meier, C. P'epin, K. B. Efetov, *Phys. Rev. B* **90**, 054511 (2014).
43. Y. Wang *et al*., *Phys. Rev. B* **97**, 174510 (2018).
44. Materials and methods are available as supplementary materials.
45. M. H. Hamidian *et al*., *Nat. Phys.* **12**, 150–156 (2016).
46. M. J. Lawler *et al*., *Nature* **466**, 347–351 (2010).
47. J. C. Davis, Supporting data for "Magnetic-field Induced Pair Density Wave State in the Cuprate Vortex Halo" by S. D. Edkins *et al*., Harvard Dataverse (2019); doi: 10.7910/DVN/JDSN1W

ACKNOWLEDGMENTS

We acknowledge and thank D. Agterberg, P. Choubey, A. Chubukov, E. Fradkin, P. J. Hirschfeld, P. D. Johnson, D. H. Lee, P. A. Lee, C. Pepin, S. Sebastian, S. Todadri, J. Tranquada, and Y. Wang for helpful discussions, advice, and communications. We are grateful to S. A. Kivelson for crucial proposals on the complete set of PDW phenomena to search for within the vortex halo. **Funding:** S.U. and H.E. acknowledge support from a Grant-in-Aid for Scientific Research from the Ministry of Science and Education (Japan); A.K. and K.F. acknowledge salary support from the U.S. Department of Energy, Office of Basic Energy Sciences, under contract DEAC02-98CH10886. E.-A.K. acknowledges support from the U.S. Department of Energy, Office of Basic Energy Sciences under award DE-SC0018946. S.S. acknowledges support under National Science Foundation under grant DMR- 1664842. J.C.S.D. acknowledges support from Science Foundation Ireland under award SFI 17/RP/5445 and from the European Research Council (ERC) under award DLV-788932. J.C.S.D., S.D.E., and M.H.H. acknowledge support from the Moore Foundation's EPiQS Initiative through grant GBMF4544. **Author contributions:** S.D.E., A.K., and M.H.H. carried out the experiments; K.F., H.E., and S.U. synthesized and characterized the samples; M.H.H., S.D.E., and K.F. developed and carried out analysis; S.S., M.J.L., and E.-A.K. provided theoretical guidance; A.P.M. and J.C.S.D. supervised the project and wrote the paper, with key contributions from S.D.E., K.F., and M.H.H. The manuscript reflects the contributions and ideas of all authors. **Competing interests:** The authors declare no competing financial interests. **Data and materials availability:** The data files for the results presented here are available at (*47*).

SUPPLEMENTARY MATERIALS

science.sciencemag.org/content/364/6444/976/suppl/DC1
Materials and Methods
Supplementary Text
Figs. S1 to S8
References (*48*–*58*)

5 February 2018; accepted 15 May 2019
10.1126/science.aat1773

RADIO ASTRONOMY

A radio ridge connecting two galaxy clusters in a filament of the cosmic web

F. Govoni[1]*, E. Orrù[2], A. Bonafede[3,4,5], M. Iacobelli[2], R. Paladino[3], F. Vazza[3,4,5], M. Murgia[1], V. Vacca[1], G. Giovannini[3,4], L. Feretti[3], F. Loi[1,4], G. Bernardi[3,6,7], C. Ferrari[8], R. F. Pizzo[2], C. Gheller[9], S. Manti[10], M. Brüggen[5], G. Brunetti[3], R. Cassano[3], F. de Gasperin[5,11], T. A. Enßlin[12,13], M. Hoeft[14], C. Horellou[15], H. Junklewitz[16], H. J. A. Röttgering[11], A. M. M. Scaife[17], T. W. Shimwell[2,11], R. J. van Weeren[11], M. Wise[2,18]

Galaxy clusters are the most massive gravitationally bound structures in the Universe. They grow by accreting smaller structures in a merging process that produces shocks and turbulence in the intracluster gas. We observed a ridge of radio emission connecting the merging galaxy clusters Abell 0399 and Abell 0401 with the Low-Frequency Array (LOFAR) telescope network at 140 megahertz. This emission requires a population of relativistic electrons and a magnetic field located in a filament between the two galaxy clusters. We performed simulations to show that a volume-filling distribution of weak shocks may reaccelerate a preexisting population of relativistic particles, producing emission at radio wavelengths that illuminates the magnetic ridge.

The matter distribution of the Universe is not uniform, but rather forms a cosmic web, with a structure of filaments and galaxy clusters surrounding large voids. Galaxy clusters form at the intersections of the cosmic web filaments and grow by accreting substructures in a merging process, which converts most of the infall kinetic energy into thermal gas energy. A residual fraction of nonthermalized energy is expected to manifest itself in the form of turbulent gas motions, magnetic fields, and relativistic particles. Extended radio sources called radio halos and radio relics are found at the center and the periphery of galaxy clusters, respectively, visible through their emission of synchrotron radiation. Magnetic fields and relativistic particles in the large-scale structure of the Universe can be inferred from observations of these sources.

Observations show that magnetic fields are ubiquitous in galaxy clusters (*1*), whereas radio halos and relics are most common in merging clusters, suggesting that cluster mergers provide the acceleration of relativistic particles necessary for synchrotron emission (*2*). Collisions between nearly equal-mass clusters dissipate large amounts of energy within a few billion years. The merging galaxy clusters Abell 0399 and Abell 0401 are separated by a projected distance of 3 megaparsec (Mpc) and host a double radio halo (*3*). The presence of radio halos at the centers of both Abell 0399 and Abell 0401 was unexpected because radio halos are not common sources, and x-ray (*4*–*7*) and optical data (*8*) suggest that the two systems are still in the initial phase of a merger, before the bulk of kinetic energy of the collision has been dissipated. X-ray data show a hot (temperature $T \simeq 6$ to 7 keV) and nearly isothermal filament of plasma in the region between the two clusters (*7*). There may be a weak shock (Mach number $M < 2$) in the outer part of the filament, at ~650 to 810 kiloparsec (kpc) from the collision axis (equivalent to an angular offset of 8 to 10 arc min). Observations with the Planck spacecraft (*9*, *10*) detected a signal due to the Sunyaev–Zeldovich (SZ) effect, revealing a large-scale filament of gas connecting the two systems. The SZ effect is a spectral distortion caused by inverse Compton scattering of the cosmic microwave background radiation by hot electrons (T ~keV), which is sensitive to the total thermal energy of the intervening medium.

We observed the region between Abell 0399 and Abell 0401 at radio wavelengths to investigate whether relativistic particles and magnetic fields exist on cosmic scales larger than those of galaxy clusters. Using the Low Frequency Array (LOFAR) telescope network at a central frequency ν = 140 MHz (corresponding to a wavelength λ = 2.14 m), we detected a filament of diffuse synchrotron emission connecting the two galaxy clusters.

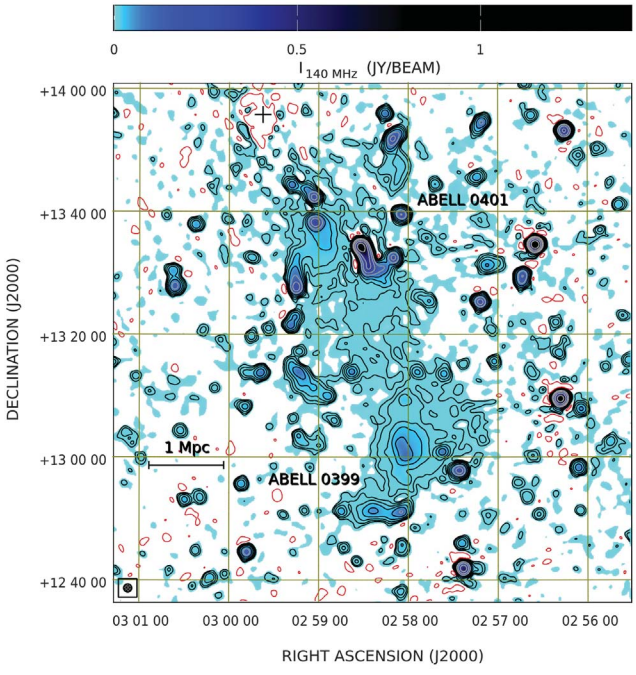


Fig. 1. LOFAR image of the 1.4° × 1.4° region centered on the Abell 0399–Abell 0401 system. Color and contours show the radio emission at 140 MHz with a resolution of 80 arc sec and RMS sensitivity of 1 mJy beam^{-1}. The beam size and shape are indicated by the inset at the bottom left. Contour levels start at 3 mJy beam^{-1} and increase by factors of 2. One negative contour (red) is drawn at −3 mJy beam^{-1}. The black cross (right ascension 02h 59m 38s, declination +13° 54′ 55″, J2000 equinox) indicates the location of a strong radio source that was removed from the image.

[1]Istituto Nazionale di Astrofisica–Osservatorio Astronomico di Cagliari Via della Scienza 5, I09047 Selargius, Italy. [2]ASTRON, the Netherlands Institute for Radio Astronomy, Postbus 2, 7990 AA, Dwingeloo, Netherlands. [3]Istituto Nazionale di Astrofisica–Istituto di Radioastronomia, Bologna Via Gobetti 101, I40129 Bologna, Italy. [4]Dipartimento di Fisica e Astronomia, Università degli Studi di Bologna, Via Gobetti 93/2, I40129 Bologna, Italy. [5]Hamburger Sternwarte, Universität Hamburg, Gojenbergsweg 112, 21029 Hamburg, Germany. [6]Department of Physics and Electronics, Rhodes University, Grahamstown, South Africa. [7]Square Kilometre Array South Africa, 3rd Floor, The Park, Park Road, Pinelands 7405, South Africa. [8]Université Côte d'Azur, Observatoire de la Côte d'Azur, Centre National de la Recherche Scientifique, Laboratoire Lagrange, Blvd. de l'Observatoire, CS 34229, 06304 Nice Cedex 4, France. [9]Swiss Plasma Center, Ecole Polytechnique Fédérale de Lausanne, 1015 Ecublens, Lausanne, Switzerland. [10]Scuola Normale Superiore, Piazza dei Cavalieri 7, I-56126 Pisa, Italy. [11]Leiden University, Rapenburg 70, 2311 EZ Leiden, Netherlands. [12]Max Planck Institut für Astrophysik, Karl-Schwarzschild-Str.1, D-85740 Garching, Germany. [13]Ludwig-Maximilians-Universität München, Geschwister-Scholl-Platz 1, D-80539, München, Germany. [14]Thüringer Landessternwarte, Sternwarte 5, 07778 Tautenburg, Germany. [15]Chalmers University of Technology, Dept. of Space, Earth and Environment, Onsala Space Observatory, SE-439 92 Onsala, Sweden. [16]Argelander Institut für Astronomie, Auf dem Hügel, 71 D-53121 Bonn, Germany. [17]Jodrell Bank Centre for Astrophysics, School of Physics and Astronomy, The University of Manchester, Oxford Road, Manchester M13 9PL, UK. [18]SRON Netherlands Institute for Space Research Sorbonnelaan 2, 3584 CA Utrecht, Netherlands.
*Corresponding author. Email: federica.govoni@inaf.it

Figure 1 shows our LOFAR observation of a diffuse radio ridge encompassing Abell 0399 and Abell 0401 at a resolution of 80 arc sec. Our analysis of LOFAR images at higher resolution (figs. S3 and S4) showed that no extended discrete radio sources are present between the two galaxy clusters (*11*). The ridge encompassing Abell 0399–Abell 0401 is not due to the blending of discrete sources, but rather is associated with the cosmic web filament connecting the two clusters (*11*).

To measure the physical parameters of the ridge encompassing Abell 0399–Abell 0401, we masked the regions occupied by the radio halos and other radio sources not connected to the ridge emission (*11*). Figure 2A shows the radio ridge after the masking. It extends between the two cluster cores with a sky-projected length of 3 Mpc. We extracted the brightness profile of the ridge (Fig. 2B) by computing the average brightness in strips of length 3 Mpc and width 0.108 Mpc (one beam width). We modeled the brightness profile using a Gaussian model characterized by three free parameters: the peak brightness, peak position, and full width at half maximum (FWHM). The ridge emission peaks at ~3.7 milliJansky (mJy) per beam with a FWHM of 1.3 Mpc. The ridge is offset to the northwest by 0.16 Mpc from the line connecting the cores of Abell 0399 and Abell 0401.

The flux density of the ridge was calculated by integrating the surface brightness over an area of 3×1.3 Mpc^2 after excluding the masked regions. The average surface brightness at 140 MHz is $\langle I \rangle_{140\mathrm{MHz}} = 2.75 \pm 0.08$ mJy beam^{-1} (or 0.38 μJy arc sec^{-2}). Taking into account the masked regions, the effective number of instrument beams covering the ridge emission, $N_{\mathrm{eff}} = 160$, is fewer than the 299 beams contained by this area. Assuming that the ridge is present everywhere, even in the masked regions, we extrapolated the total flux density $S_{140\mathrm{MHz}} = \langle I \rangle_{140\mathrm{MHz}} \times 299 = 822 \pm 24$ (±123) mJy. The uncertainties are the 1σ root mean square (RMS) statistical uncertainty and a 15% systematic uncertainty (indicated in parentheses), to account for the uncertain calibration of the LOFAR flux scale (*12*). This flux density corresponds to a radio power $L_{140\mathrm{MHz}} = 1.0 \times 10^{25}$ W Hz^{-1}. By assuming that the ridge occupies a cylindrical volume, we estimate a mean radio emissivity $\langle J \rangle_{140\mathrm{MHz}} = 8.6 \times 10^{-43}$ erg s^{-1} Hz^{-1} cm^{-3}.

It is not possible to reliably determine the spectral index of the ridge emission because the available data at 1.4 GHz (*3*) were obtained on different baselines. However, by adopting the spectral index $\alpha = 1.3$ (where $S_\nu \propto \nu^{-\alpha}$) typically found in radio halos (*13*), the mean radio emissivity extrapolated to 1.4 GHz would be $\langle J \rangle_{1.4\mathrm{GHz}} \simeq 4.3 \times 10^{-44}$ erg s^{-1} Hz^{-1} cm^{-3}. We compared this value with published distributions of emissivities at 1.4 GHz for candidate large-scale filaments (*14*) and with radio halos observed at the center of galaxy clusters (*13*, *15*). The histogram of the emissivity of the candidate filaments and of the radio halos (fig. S2) has two distinct populations with only a partial overlap. The filament in Abell 0399–Abell 0401 is located in the weakest tail of the emissivity distribution of the candidate filaments and is almost two orders of magnitude lower than the typical emissivity of radio halos observed at the center of galaxy clusters.

Figure 3 shows the LOFAR image overlaid on the Planck SZ image, where the SZ effect is quantified with the y parameter ($y \propto \int n_e\, T\, \mathrm{d}l$). The radio ridge is located along the filament of gas connecting Abell 0399 and Abell 0401 detected with Planck (*9*, *10*). There are hints that the radio emission is not homogeneously distributed, e.g., there are some brighter elongated features that align with the filament direction.

The radio ridge encompassing Abell 0399–Abell 0401 has unusual properties. Evidence of large-scale shocks in the accretion flows of intergalactic gas has been found in the merging system ZwCl 2341.1+0000 (*16*), whose diffuse radio emission corresponds with an elongated merging cluster of galaxies. The pair of galaxy clusters Abell 0399–Abell 0401 is at an earlier evolutionary stage, before that of ZwCl 2341.1+0000 (*17*). Radio emission associated with the cosmic web joining Abell 0399 and Abell 0401 indicates that some of the merger energy is converted into nonthermal emission, likely through the acceleration

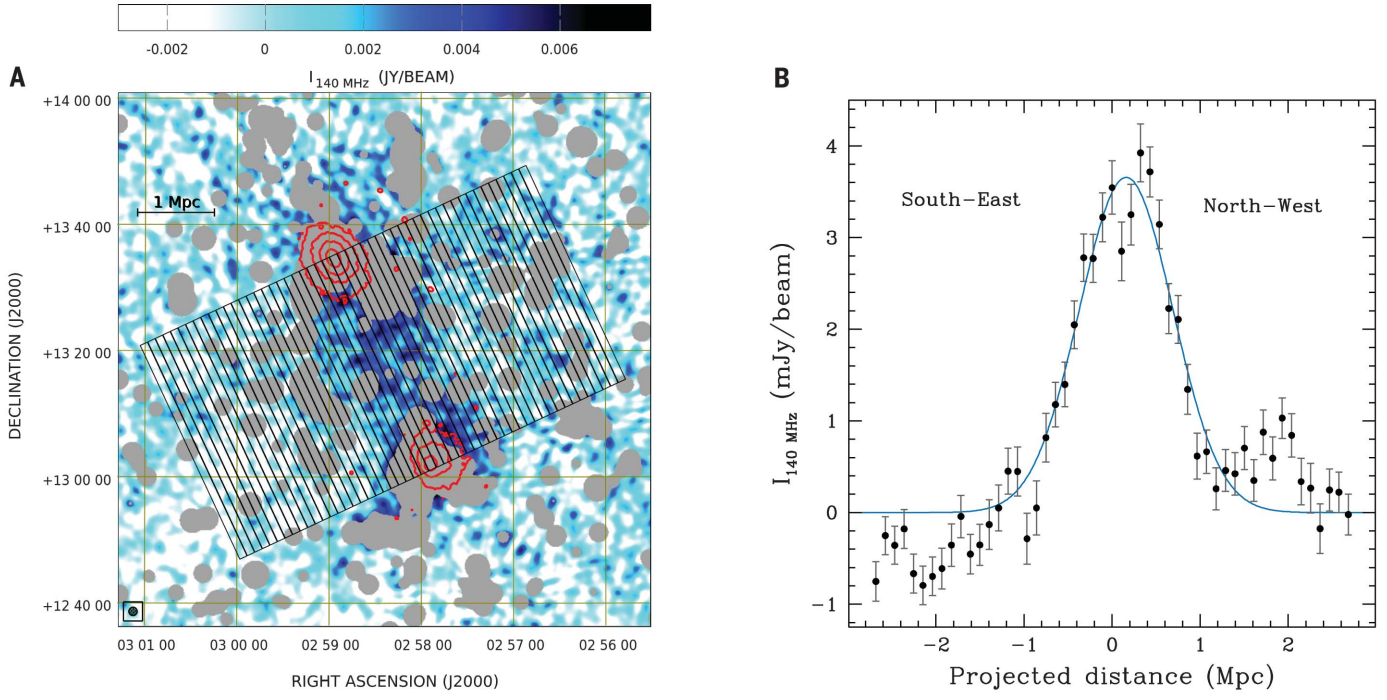


Fig. 2. Brightness profile of the radio ridge. (**A**) Strips used to measure the ridge brightness profile. The x-ray emission (*3*) from Abell 0399 and Abell 0401 is overlaid in red contours. The color bar represents the LOFAR image in Fig. 1 after masking of sources not related to the radio ridge (gray areas). The width of the strips is 0.108 Mpc (one beam width) and their length is 3 Mpc. The strips are inclined 25° east of the vertical axis and a reference point (at right ascension 02h 58m 26s, declination +13° 18′ 17″, J2000 equinox), which is located halfway along the line connecting the x-ray positions of Abell 0399 and Abell 0401. (**B**) Brightness profile of the ridge emission extracted by measuring the average surface brightness in each strip. The error bars indicate $\sigma/\sqrt{N_{\mathrm{eff}}}$, where σ is the image noise rms and N_{eff} is the number of independent beams in each box, excluding the masked areas. The line represents the best-fitting Gaussian model.

of electrons by shock waves and turbulent motions before the collision of the galaxy clusters.

If we assume that the relation between thermal gas density and magnetic field strength found in galaxy clusters (*18*) is also valid in the ridge connecting Abell 0399–Abell 0401, then the thermal gas density of 3×10^{-4} cm^{-3} found in the ridge (*7*) would correspond to a magnetic field strength $B < 1$ μG. Because of energy lost to synchrotron and inverse Compton radiation, the lifetime for relativistic electrons emitting at 140 MHz is ≤230 million years. The maximum distance that these relativistic electrons can travel in their lifetime is ≤0.1 Mpc (*2*), more than an order of magnitude smaller than the size of the ridge. There must be a mechanism that reaccelerates and/or injects the electrons in situ throughout the ridge.

The accretion of matter on large scales along the Abell 0399–Abell 0401 filament likely injects shock waves and turbulent motion on a wide range of spatial scales. As in the case of radio relics, diffusive shock (Fermi-I) acceleration (DSA) or reacceleration may power radio-emitting electrons and explain this large radio ridge. However, it is difficult to account for such strong emission from shocks before the collision between Abell 0399 and Abell 0401. We explored this scenario using magneto-hydrodynamical simulations with the Enzo code (*19*). Our simulations evolved a pair of merging galaxy clusters at a resolution of 3.95 kpc, with final masses and resultant proximity similar to the Abell 0399–Abell 0401 complex (*11*). To quantify the expected radio emission, we combined the electrons freshly accelerated at shock waves in the simulation with a radio-emission model, which has been used previously to model radio relics (*20*–*22*).

Figure 4 shows the projected gas density in the simulation after rotating the system to resemble the observed SZ morphology of the Abell 0399–Abell 0401 complex. Radio emission by freshly accelerated electrons falls ~1000 times below the sensitivity of our LOFAR observation

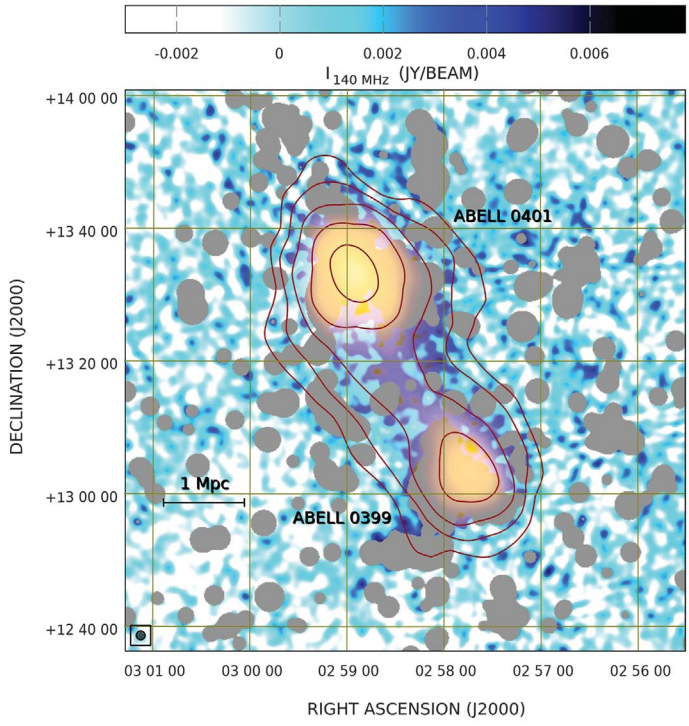


Fig. 3. Composite image showing radio and SZ emission around Abell 0399–Abell 0401 detected by the Planck satellite. The same LOFAR image as in Fig. 2 was overlaid with the Planck *y*-parameter image in yellow tones and brown contours. The Planck data show a bridge of gas between the pair of galaxy clusters Abell 0399–Abell 0401 in the same location as the LOFAR ridge. Contour levels start at 10^{-5} and increase by factors of $\sqrt{2}$.

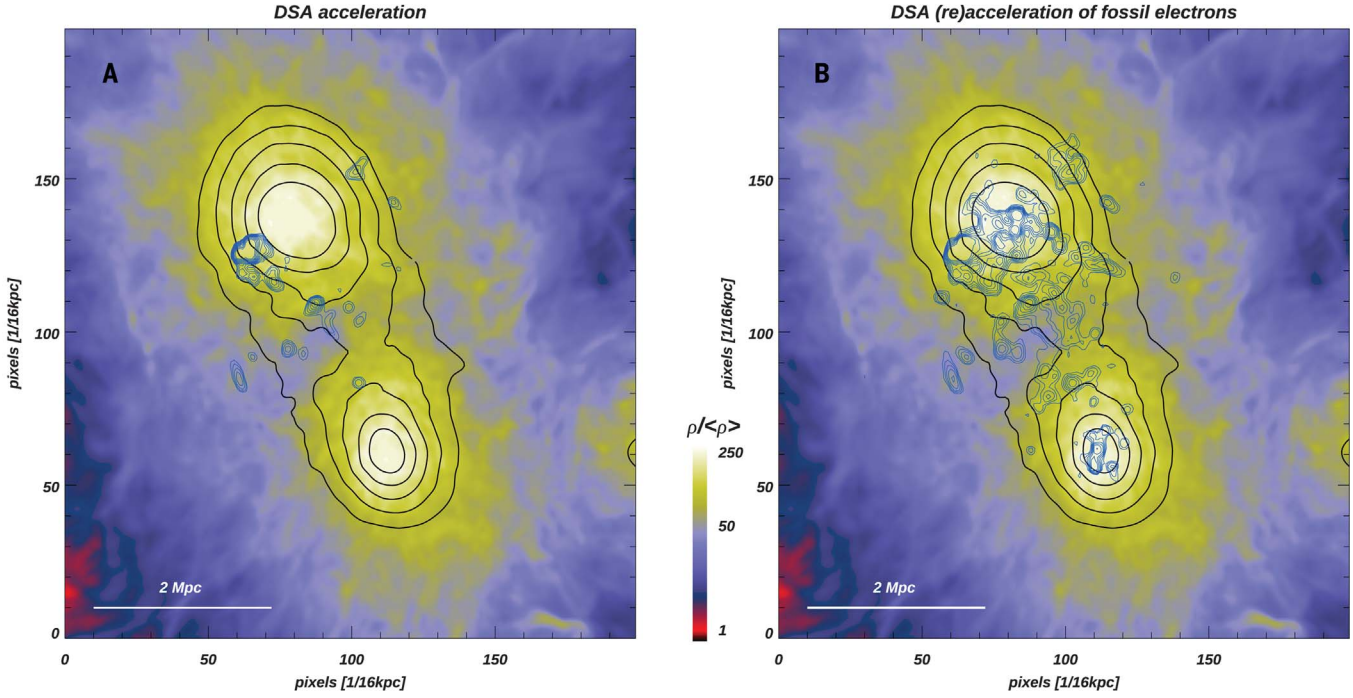


Fig. 4. Volume rendering of the projected gas density (colors), integrated SZ signal (black contours), and radio emission (blue contours) for our simulated pair of interacting clusters (*11*), oriented to resemble the Abell 0399–Abell 0401 pair. Blue contours show the simulated detectable radio emission (≥ 3σ RMS of our LOFAR observation) at 140 MHz, for freshly accelerated electrons (**A**) and with an additional contribution of reaccelerated electrons (**B**). Only the system in (B) resembles the real observation. Movie S1 shows an animated version of this figure.

(Fig. 4A), owing to the scarcity of strong shocks in this region (which is filled by a ~5×10^7 K plasma, heated by gas compression), and to the drop of the assumed electron acceleration efficiency for $M \leq 3$ shocks (*23*). This generates a patchy emission that traces the location of the strongest shocks. In this scenario, the only emission detectable by our LOFAR observation would be associated with a substructure transiting transverse to the line of sight (traced by a weak, M ~3 to 4 shock similar to region "d" in fig. S3). Our LOFAR observation shows emission that is brighter and more broadly distributed across the ridge.

As an alternative model, we tested the additional contribution from a preexisting population of relativistic electrons, reaccelerated by shocks in the region (Fig. 4B). This is a viable mechanism to illuminate the radio ridge only if the preexisting electrons that are reaccelerated by shocks with M ~2 to 3 are accumulated at a Lorentz factor $\gamma \geq 10^3$ and filling most of the ridge volume. This limits the age of these electrons to <1 billion years due to radiative losses. Circumventing this time constraint would require unidentified volume-filling reacceleration mechanisms in such dilute plasmas.

The nonthermal diffuse emission observed in the Abell 0399–Abell 0401 system extends far beyond the boundaries of the two radio halos and fills a region in their outskirts that is still dynamically evolving. We interpret this as evidence of intergalactic magnetic fields connecting two galaxy clusters and of spatially distributed particle reacceleration mechanisms in these regions.

REFERENCES AND NOTES

1. T. E. Clarke, P. P. Kronberg, H. Böhringer, *Astrophys. J.* **547**, L111–L114 (2001).
2. G. Brunetti, T. W. Jones, *Int. J. Mod. Phys. D* **23**, 1430007–1430098 (2014).
3. M. Murgia, F. Govoni, L. Feretti, G. Giovannini, *Astron. Astrophys.* **509**, A86 (2010).
4. I. Sakelliou, T. J. Ponman, *Mon. Not. R. Astron. Soc.* **351**, 1439–1456 (2004).
5. H. Bourdin, P. Mazzotta, *Astron. Astrophys.* **479**, 307–320 (2008).
6. Y. Fujita *et al*., *Publ. Astron. Soc. Jpn.* **60** (sp1), S343–S349 (2008).
7. H. Akamatsu *et al*., *Astron. Astrophys.* **606**, A1 (2017).
8. V. Bonjean, N. Aghanim, P. Salomé, M. Douspis, A. Beelen, *Astron. Astrophys.* **609**, A49 (2018).
9. P. A. R. Ade *et al*., *Astron. Astrophys.* **550**, A134 (2013).
10. N. Aghanim *et al*., *Astron. Astrophys.* **594**, A22 (2016).
11. Materials and methods are available as supplementary materials.
12. T. W. Shimwell *et al*., *Astron. Astrophys.* **598**, A104 (2017).
13. L. Feretti, G. Giovannini, F. Govoni, M. Murgia, *Astron. Astrophys. Rev.* **20**, 54 (2012).
14. V. Vacca *et al*., *Mon. Not. R. Astron. Soc.* **479**, 776–806 (2018).
15. M. Murgia *et al*., *Astron. Astrophys.* **499**, 679–695 (2009).
16. J. Bagchi *et al*., *New Astron.* **7**, 249–277 (2002).
17. G. Giovannini, A. Bonafede, L. Feretti, F. Govoni, M. Murgia, *Astron. Astrophys.* **511**, L5 (2010).
18. F. Govoni *et al*., *Astron. Astrophys.* **603**, A122 (2017).
19. G. L. Bryan *et al*., *Astrophys. J. Suppl. Ser.* **211**, 19 (2014).
20. S. W. Skillman *et al*., *Astrophys. J.* **735**, 96 (2011).
21. D. Wittor, F. Vazza, M. Brüggen, *Mon. Not. R. Astron. Soc.* **464**, 4448–4462 (2017).
22. M. Brüggen, A. Bykov, D. Ryu, H. Röttgering, *Space Sci. Rev.* **166**, 187–213 (2012).
23. M. Hoeft, M. Brüggen, *Mon. Not. R. Astron. Soc.* **375**, 77–91 (2007).

ACKNOWLEDGMENTS

We thank the reviewers for their constructive comments, which helped improve the presentation of the results. LOFAR, the Low-Frequency Array designed and constructed by ASTRON (Netherlands Institute for Radio Astronomy), has facilities in several countries that are owned by various parties (each with their own funding sources) and that are collectively operated by the International LOFAR Telescope (ILT) foundation under a joint scientific policy. Our work is based on observations obtained with Planck (http://www.esa.int/Planck), an ESA science mission with instruments and contributions directly funded by ESA Member States, NASA, and Canada. This research has made use of the NASA-IPAC Extragalactic Database (NED), which is operated by the Jet Propulsion Laboratory, California Institute of Technology, under contract with the National Aeronautics and Space Administration. The Digitized Sky Surveys were produced at the Space Telescope Science Institute under U.S. Government grant NAG W-2166. The images of these surveys are based on photographic data obtained using the Oschin Schmidt Telescope on Palomar Mountain and the U.K. Schmidt Telescope. H.J. acknowledges the European Commission, Joint Research Center, TP262, Via Fermi, 21027 Ispria (VA), Italy. S.M. acknowledges the LIST Spa–Via Pietrasantina 123, 56122 Pisa, Italy. **Funding:** A.B. acknowledges support from European Research Council (ERC) Starting Grant DRANOEL GA 714245. The cosmological simulations were performed on Jureca at Jülich Supercomputing Centre under computing project HHH42 (principal investigator, F.V.). F.V. acknowledges financial support from the European Union's Horizon 2020 program under ERC Starting Grant MAG-COW 714196. F.d.G., R.J.v.W., T.W.S., and H.J.A.R. acknowledge support from the ERC Advanced Investigator program NewClusters 321271. R.J.v.W. acknowledges support from the VIDI research program project no. 639.042.729, which is financed by the Netherlands Organisation for Scientific Research (NWO). A.M.M.S. acknowledges support from the ERC under grant ERC-2012-StG-307215 LODESTONE. **Author contributions:** All authors meet the journal's authorship criteria. F.G. led and coordinated the project. A.B. worked on the LOFAR data reduction and edited the text. E.O., M.I., and R.P. worked on the LOFAR data reduction. F.V. performed the numerical simulations, worked on the comparison between simulations and radio data, and edited the text. M.M. performed the data analysis, edited the text, and provided the data at 1.4 GHz. V.V provided the multifrequency images (optical, x-ray) and interpreted the radio sources detected in the LOFAR observations. G.G., L.F., F.L., C.F., G.B., R.P., and S.M. interpreted the radio sources detected in the LOFAR observations. C.G. assisted with the numerical simulations. This paper is a collaboration between the group of scientists listed above and a group of the LOFAR Survey Key Project. M.B., G.B., R.C., T.A.E., and M.H. provided theoretical expertise on diffuse radio sources in galaxy clusters and are all members of the LOFAR Survey Key Project. E.O., A.B., M.I., C.F., R.P., F.d.G., C.H., H.J., H.J.A.R., A.M.M.S., T.W.S., R.J.v.W., and M.W. provided expertise in low-frequency data reduction and are all members of the LOFAR Survey Key Project. **Competing interests:** The authors declare no competing interests. **Data and materials availability:** The observations are available in the LOFAR Long Term Archive (LTA; https://lta.lofar.eu/) under project LC2 005, observed on 15 to 16 November 2014. Our simulation was produced using the public version of Enzo 2.1 (https://enzo.readthedocs.io/). The simulation input parameters are available at http://doi.org/10.23728/b2share.933d3d24060d4b528c2f6c523ac3844d and the output data used to produce Fig. 4 and fig. S7 are available at http://doi.org/10.23728/b2share.064065cd568343f1a60135cc49a09e78, both at the EUDAT repository.

SUPPLEMENTARY MATERIALS

science.sciencemag.org/content/364/6444/981/suppl/DC1
Materials and Methods
Figs. S1 to S7
Table S1
References (*24*–*54*)
Movies S1 and S2

30 March 2018; accepted 13 May 2019
10.1126/science.aat7500

PHYSICS

Stable Casimir equilibria and quantum trapping

Rongkuo Zhao[1]*, Lin Li[1]*, Sui Yang[1]*, Wei Bao[1]*, Yang Xia[1], Paul Ashby[2], Yuan Wang[1], Xiang Zhang[1,3]†

The Casimir interaction between two parallel metal plates in close proximity is usually thought of as an attractive interaction. By coating one object with a low–refractive index thin film, we show that the Casimir interaction between two objects of the same material can be reversed at short distances and preserved at long distances so that two objects can remain without contact at a specific distance. With such a stable Casimir equilibrium, we experimentally demonstrate passive Casimir trapping of an object in the vicinity of another at the nanometer scale, without requiring any external energy input. This stable Casimir equilibrium and quantum trapping can be used as a platform for a variety of applications such as contact-free nanomachines, ultrasensitive force sensors, and nanoscale manipulations.

In 1948, Hendrik Casimir predicted that an attractive force occurs between two parallel, uncharged, perfectly conducting plates closely separated in a vacuum; this force has come to be known as the Casimir force (*1*). The effect arises from quantum fluctuation–induced temporary electromagnetic fields between the two plates (*2*). Electromagnetic modes between two plates are discretized so that the total intensity of fluctuation-induced electromagnetic fields between the plates is less than that in free space (*3*). Thus, the plates are pushed toward each other as a result of unbalanced electromagnetic pressure in the confined space (*4*).

The Casimir force between two mirror-symmetric objects of the same material has been proven to be always attractive, monotonically increasing as the separation decreases independently of the objects' shape, local dielectric function, and environment (*5*). No stable Casimir equilibria have been found to exist between electrically neutral objects composed of the same materials, regardless of whether their permittivities are higher or lower than that of the environment medium (*6*).

The attractive nature of the Casimir effect is detrimental for micro- and nanomechanical systems, resulting in irreversible adhesion (*7*–*9*) and frictional forces (*10*, *11*) as well as undesired aggregation of nanoparticles (*12*). The possibility of repulsive Casimir interactions has thus prompted researchers to pursue stable Casimir equilibria. The monotonically repulsive Casimir force can be achieved by embedding two objects of different materials in a fluid (*13*–*15*). However, the stable Casimir equilibria remain elusive. In this work, we address the question of whether Casimir equilibrium exists, meaning that Casimir forces can be repulsive at short separation distances and attractive at long distances.

Stable Casimir equilibria were predicted in theory by arranging one of the interacting objects enclosed by another (*16*, *17*) so that the surrounding repulsive Casimir forces could shroud the object at the center. This special topological requirement limits possible applications and also makes experimental verification extremely difficult. Because Casimir forces at large separations are mainly contributed by low electromagnetic frequencies and at small separations by high frequencies, a stable Casimir equilibrium could be realized if small frequencies contribute only attractive forces and large frequencies provide sufficient repulsive forces (*18*, *19*). Owing to difficulties in weak force measurement in liquid environments and the strict combination of materials, no experiment to date has verified this theoretical prediction, although indirect evidence has been found in interfacial premelting of ice (*18*). Other approaches associated with the design of specific geometries (*20*–*22*) were proposed, but these methods can produce Casimir equilibrium only along the axis of symmetry, leaving instability for displacements in other directions. Furthermore, although theoretical studies with exotic materials (*23*–*27*) or excited-state atoms (*28*) also suggest that it is possible to obtain stable Casimir equilibria, no experimental evidence has been demonstrated. In this study, we theoretically propose and experimentally demonstrate that stable Casimir equilibria can be

[1]Nanoscale Science and Engineering Center (NSEC), 3112 Etcheverry Hall, University of California at Berkeley, Berkeley, CA 94720, USA. [2]Molecular Foundry, Lawrence Berkeley National Laboratory, 1 Cyclotron Road, Berkeley, CA 94720, USA. [3]Faculties of Sciences and Engineering, University of Hong Kong, Hong Kong, China.
*These authors contributed equally to this work.
†Corresponding author. Email: xiang@berkeley.edu

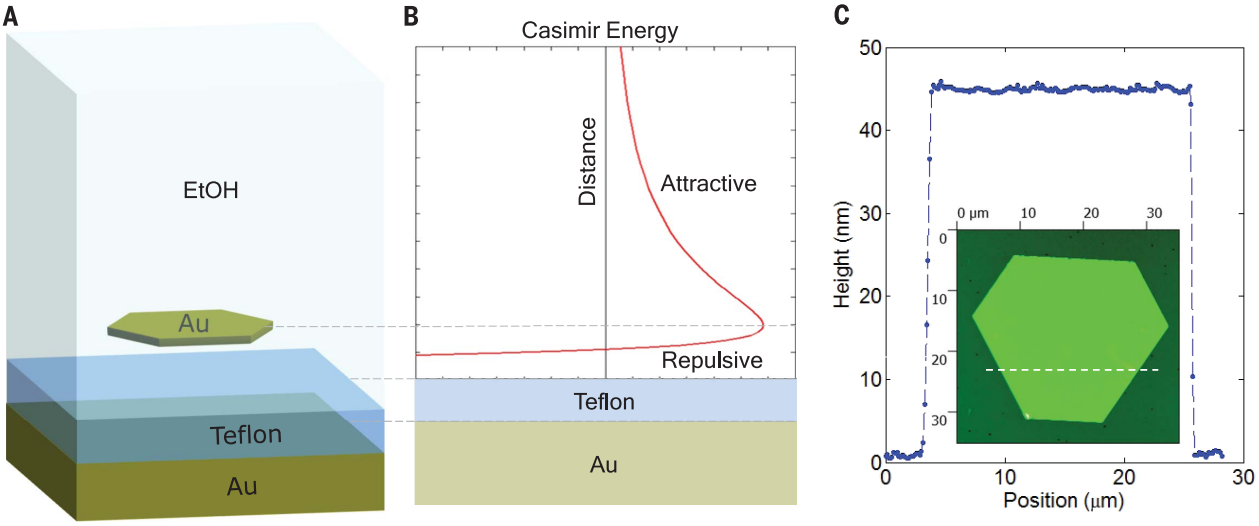


Fig. 1. Stable Casimir equilibrium enabled by a low–refractive index coating layer. (**A**) By coating a thin layer of Teflon on a gold substrate, a stable Casimir equilibrium is formed so that a gold nanoplate can be trapped at an equilibrium position in ethanol. (**B**) Casimir interaction energy between the gold nanoplate and the Teflon-coated gold surface. The Casimir force given by the derivative of the Casimir energy with respect to the distance is repulsive at short distances and attractive at long distances. (**C**) Thickness and surface profile of the gold nanoplate along the dashed line in the inset AFM image of the gold plate.

achieved by coating one high–refractive index object with a thin layer of a low–refractive index dielectric.

We designed an experiment on Casimir trapping in a fluid, between two gold surfaces as high-index media, one of which is coated with a low-index polytetrafluoroethylene (Teflon, DuPont) (Fig. 1A). The three materials were chosen carefully with a designed permittivity relation (fig. S1). Calculations show that the Casimir force between the gold nanoplate and the Teflon-coated gold surface is repulsive when these objects are near each other and attractive at longer distances (Fig. 1B). The gold nanoplates were chemically synthesized with a single-crystal hexagonal shape, a thickness of 45 nm, and a lateral size of ~25 μm (Fig. 1C) (*29*). The atomic force microscopy (AFM) tomography images show that the surface peak-to-valley roughnesses of the gold nanoplate, the gold substrate, and the Teflon film are less than 2 nm (Fig. 1C), 2 nm (fig. S2A), and 6 nm (fig. S2B), respectively. Such a nonmonotonic Casimir interaction between a gold surface and a Teflon-coated gold surface in ethanol solution is confirmed by direct force measurement using AFM (fig. S3). At the equilibrium position, the Casimir interaction energy reaches its minimum, creating a trapping potential. As a result, the gold nanoplate can be trapped near the surface at a certain distance. Moreover, the trapping distance is determined by the thickness of the Teflon coating (fig. S4).

Under an upright microscope, the gold nanoplates were clearly observed undergoing random Brownian motion in a given plane parallel to the surface without adhesion to the Teflon, which suggests that a strong repulsive Casimir interaction exists at a short distance between the gold nanoplate and the Teflon surface. When the devices were flipped upside down and transferred onto an inverted microscope (fig. S5), the gold nanoplates were still able to undergo random Brownian motion (movie S1 and fig. S6), confirming the existence of attractive Casimir interactions at long distances and, therefore, the trapping of gold nanoplates in the vicinity of the Teflon surface.

To quantify this stable Casmir equilibrium, we measured the reflectance spectrum from each gold nanoplate trapped in the vicinity of the Teflon-coated gold substrate (Fig. 2A). The 45-nm-thick gold nanoplate behaves like a low-reflectivity mirror. When the low-reflectivity plate is brought within a certain distance of the high-reflectivity 200-nm-thick gold substrate, the Fabry-Pérot resonance dip is observed in the reflectance spectrum (Fig. 2B). By fitting the measured reflectance spectrum, the trapping distance can be experimentally determined (fig. S7). Variation of the measured trapping distance is very small ($\sigma \sim \pm 3$ nm) (Fig. 2C), which indicates the existence of strong trapping force that provides a steep Casimir trapping potential. This trapping force provided by quantum fluctuation–induced electromagnetic fields is passive without any external energy input and can be much stronger than the optical trapping force where a high-intensity laser is needed.

As the Teflon thickness increased, the measured trapping distance increased proportionally

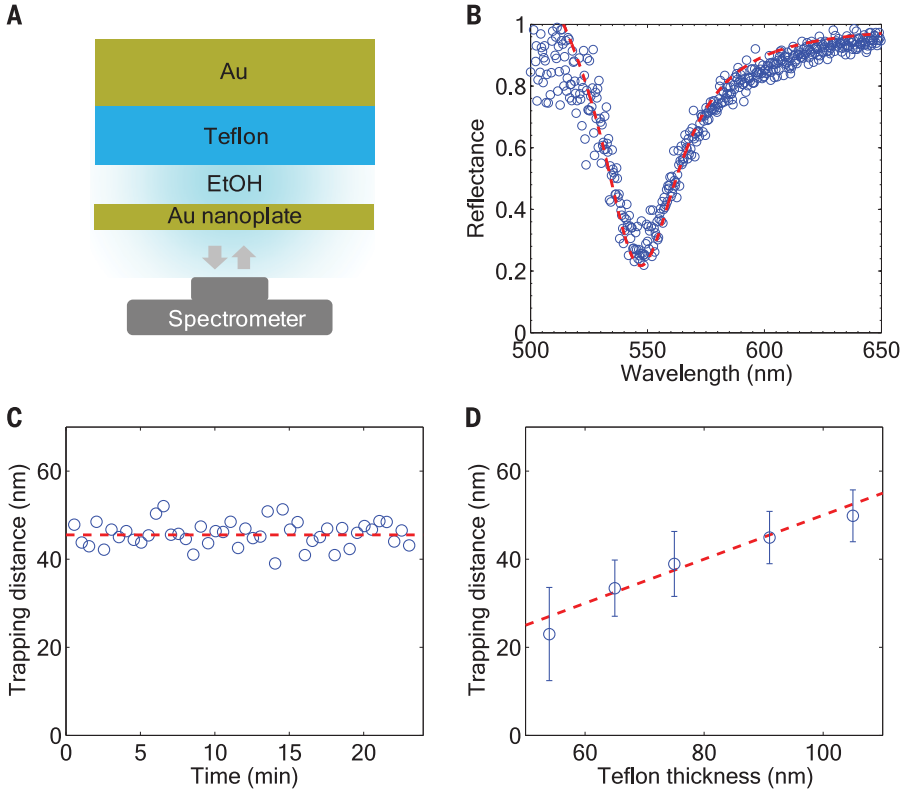


Fig. 2. Trapping distance determined by the thickness of the Teflon film. (**A**) By measuring the reflectance from an area of 5 μm in diameter at the center of the nanoplate (fig. S5), the distance between the gold nanoplate and the Teflon surface can be determined by the Fabry-Pérot resonance in the reflectance spectrum. (**B**) Reflectance spectrum for a sample with a Teflon thickness of 91 nm. The whole spectrum was taken within 0.05 s. The dashed line is the fitting reflectance where the trapping distance is the only fitting parameter. (**C**) Trapping distances of the gold nanoplate over 23 min. The dashed line is the theoretical prediction without considering the thermal variation. (**D**) Trapping distance versus Teflon thickness. The experimental results were averaged over multiple measurements of multiple trapped particles. Error bars show the variation of the average position of multiple trapped particles. Because the Teflon thickness is precisely measured using the ellipsometer and confirmed using AFM, none of the error bars show the Teflon thickness variation. The dashed line is the theoretical prediction calculated by eq. S1.

to nearly half of the Teflon thickness (Fig. 2D). The good agreement between experimental results and theoretical predictions indicates that the trapping potential is solely provided by the balance of Casimir attractive and repulsive interactions. Our further control experiment confirms that the impact of residue charge is negligible (*29*).

Such nonmonotonic Casimir interaction acting on the gold nanoplate results from competition between repulsive forces from the Teflon film and attractive forces from the gold substrate. At small separations, the distance between the gold nanoplate and the Teflon surface is shorter than the distance between the nanoplate and the gold substrate. As a result, the repulsive forces contributed by the Teflon film become predominant, and the Casimir interaction energy thus converges to the repulsive interaction between the gold nanoplate and the Teflon film (green dashed line in Fig. 3A). At large separations, the distances from the gold nanoplate to the Teflon surface and from the gold nanoplate to the gold substrate are comparable. Considering that the gold substrate possesses much higher refractive indices than that of Teflon, the attractive forces from the gold substrate are much stronger than the repulsive forces from the Teflon film, and the Casimir interaction energy thus converges to the attractive interaction between the gold nanoplate and the gold substrate (blue dashed line in Fig. 3A).

The underlying physics can be further understood by investigating Casimir force contributions from different frequencies and different parallel momenta that are two integration variables in Casimir force calculation (eq. S1). The repulsive contributions are mainly from large parallel momenta and high frequencies (Fig. 3B). Here, the fluctuation-induced electromagnetic fields are evanescent surface waves, which decay exponentially away from the surface. The larger parallel momentum and larger frequency indicate that the evanescent field decays faster (*30*). If the decaying field cannot penetrate through the Teflon to interact with the gold substrate underneath, this portion of the fluctuation-induced electromagnetic field will interact only with Teflon, thus

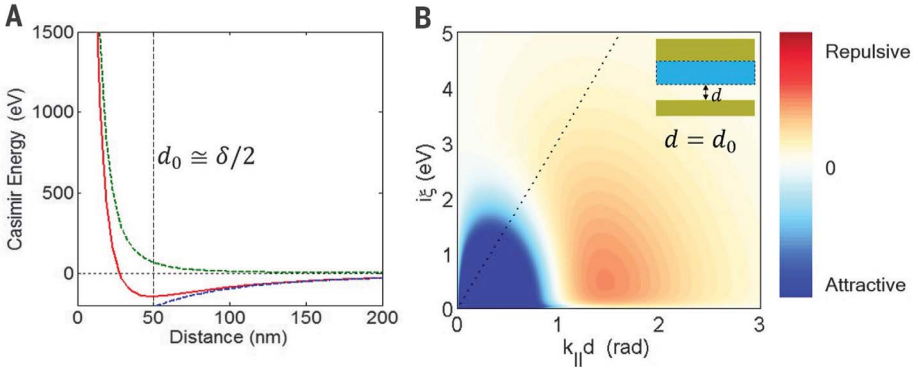


Fig. 3. Theoretical explanation of the Casimir equilibrium. (**A**) Casimir interaction energy between the gold nanoplate and the 91-nm-thick Teflon-coated gold surface (red line), between the gold nanoplate and the Teflon film only (green dashed line), and between the gold nanoplate and the gold substrate (blue dashed line). The vertical dashed line labels the equilibrium distance (d_0), which is roughly equal to half of the Teflon thickness (δ). (**B**) Casimir force contribution from different frequencies and different parallel momenta ($k_{||}$, the parallel component of the wave vector) at the equilibrium distance denoted in (A). The dashed line is the light line of electromagnetic waves in ethanol. $\xi = -i/\omega$, which describes the frequency along the imaginary axis.

contributing repulsive forces to balance the attractive force from the gold substrate (fig. S8).

We have observed that the Casimir interaction between a gold nanoplate and a Teflon-coated gold surface is repulsive at short separations and attractive at long separations. With the demonstrated Casimir equilibrium, two adjacent objects can remain separated at a well-controlled distance. This fundamental quantum trap is passive, which will lead to contact-free nanomechanical systems and controlled self-assembly.

REFERENCES AND NOTES

1. H. B. G. Casimir, *Proc. K. Ned. Akad. Wet.* **51**, 793–795 (1948).
2. L. M. Woods *et al.*, *Rev. Mod. Phys.* **88**, 045003 (2016).
3. M. Bordag, G. L. Klimchitskaya, U. Mohideen, V. M. Mostepanenko, *Advances in the Casimir Effect* (Oxford Univ. Press, 2009).
4. E. M. Lifshitz, *Sov. Phys. JETP* **2**, 73–83 (1956).
5. O. Kenneth, I. Klich, *Phys. Rev. Lett.* **97**, 160401 (2006).
6. S. J. Rahi, M. Kardar, T. Emig, *Phys. Rev. Lett.* **105**, 070404 (2010).
7. F. W. DelRio *et al.*, *Nat. Mater.* **4**, 629–634 (2005).
8. E. Buks, M. L. Roukes, *Phys. Rev. B* **63**, 033402 (2001).
9. F. M. Serry, D. Walliser, G. J. Maclay, *J. Appl. Phys.* **84**, 2501–2506 (1998).
10. Y. Mo, K. T. Turner, I. Szlufarska, *Nature* **457**, 1116–1119 (2009).
11. E. Gnecco, E. Meyer, *Fundamentals of Friction and Wear on the Nanoscale* (Springer, ed. 2, 2015).
12. J. N. Israelachvili, *Intermolecular and Surface Forces* (Elsevier, ed. 3, 2011)
13. J. N. Munday, F. Capasso, V. A. Parsegian, *Nature* **457**, 170–173 (2009).
14. A. Milling, P. Mulvaney, I. Larson, *J. Colloid Interface Sci.* **180**, 460–465 (1996).
15. A. Meurk, P. F. Luckham, L. Bergstrom, *Langmuir* **13**, 3896–3899 (1997).
16. A. W. Rodriguez *et al.*, *Phys. Rev. Lett.* **101**, 190404 (2008).
17. S. J. Rahi, S. Zaheer, *Phys. Rev. Lett.* **104**, 070405 (2010).
18. L. A. Wilen, J. S. Wettlaufer, M. Elbaum, M. Schick, *Phys. Rev. B* **52**, 12426–12433 (1995).
19. A. W. Rodriguez *et al.*, *Phys. Rev. Lett.* **104**, 160402 (2010).
20. M. Levin, A. P. McCauley, A. W. Rodriguez, M. T. H. Reid, S. G. Johnson, *Phys. Rev. Lett.* **105**, 090403 (2010).
21. A. W. Rodriguez, J. D. Joannopoulos, S. G. Johnson, *Phys. Rev. A* **77**, 062107 (2008).
22. L. Tang *et al.*, *Nat. Photonics* **11**, 97–101 (2017).
23. O. Kenneth, I. Klich, A. Mann, M. Revzen, *Phys. Rev. Lett.* **89**, 033001 (2002).
24. F. S. S. Rosa, D. A. R. Dalvit, P. W. Milonni, *Phys. Rev. Lett.* **100**, 183602 (2008).
25. R. Zhao, J. Zhou, Th. Koschny, E. N. Economou, C. M. Soukoulis, *Phys. Rev. Lett.* **103**, 103602 (2009).
26. R. Zhao, Th. Koschny, E. N. Economou, C. M. Soukoulis, *Phys. Rev. B* **83**, 075108 (2011).
27. A. G. Grushin, A. Cortijo, *Phys. Rev. Lett.* **106**, 020403 (2011).
28. D. E. Chang, K. Sinha, J. M. Taylor, H. J. Kimble, *Nat. Commun.* **5**, 4343 (2014).
29. Materials, methods, and additional information are available as supplementary materials.
30. S. A. Maier, *Plasmonics: Fundamentals and Applications* (Springer, 2007).

ACKNOWLEDGMENTS

R.Z. thanks J. Pendry for helpful theoretical discussion at Imperial College London before he joined UC Berkeley. **Funding:** This work was primarily supported by the U.S. Office of Naval Research (ONR) MURI program (grant N00014-17-1-2588), the King Abdullah University of Science and Technology Office of Sponsored Research (OSR) (award OSR-2016-CRG5-2950-03), and the Gordon and Betty Moore Foundation. We also acknowledge the AFM user facility at the Molecular Foundry, supported by the U.S. Department of Energy, Office of Science, Office of Basic Energy Sciences (contract DE-AC02-05CH11231). **Author contributions:** R.Z., S.Y., and X.Z. conceived the project. R.Z. performed theoretical investigations. R.Z., L.L., S.Y., and W.B. designed the trapping experiments. R.Z., L.L., and S.Y. performed the trapping measurements. R.Z., L.L., S.Y., and W.B. fabricated the samples. S.Y. performed the zeta potential measurement. W.B. and Y.X. performed AFM measurements with assistance from P.A. All authors contributed to manuscript preparation and discussion. X.Z. and Y.W. guided the research. **Competing interests:** The authors declare no competing interests. **Data and materials availability:** All data are available in the manuscript or the supplementary materials.

SUPPLEMENTARY MATERIALS

science.sciencemag.org/content/364/6444/984/suppl/DC1
Materials and Methods
Figs. S1 to S10
Table S1
References (*31*–*37*)
Movie S1

20 February 2019; accepted 17 May 2019
10.1126/science.aax0916

NEURODEVELOPMENT

Prenatal activity from thalamic neurons governs the emergence of functional cortical maps in mice

Noelia Antón-Bolaños*, Alejandro Sempere-Ferràndez*, Teresa Guillamón-Vivancos, Francisco J. Martini, Leticia Pérez-Saiz, Henrik Gezelius†, Anton Filipchuk‡, Miguel Valdeolmillos, Guillermina López-Bendito§

The mammalian brain's somatosensory cortex is a topographic map of the body's sensory experience. In mice, cortical barrels reflect whisker input. We asked whether these cortical structures require sensory input to develop or are driven by intrinsic activity. Thalamocortical columns, connecting the thalamus to the cortex, emerge before sensory input and concur with calcium waves in the embryonic thalamus. We show that the columnar organization of the thalamocortical somatotopic map exists in the mouse embryo before sensory input, thus linking spontaneous embryonic thalamic activity to somatosensory map formation. Without thalamic calcium waves, cortical circuits become hyperexcitable, columnar and barrel organization does not emerge, and the somatosensory map lacks anatomical and functional structure. Thus, a self-organized protomap in the embryonic thalamus drives the functional assembly of murine thalamocortical sensory circuits.

The mammalian cerebral cortex is arranged into radial columns that coalesce during development. These columns become functionally organized before adulthood (*1*–*3*). Some evidence suggests that genetic factors regulate initial columnar patterning (*4*); other evidence suggests that functional maps arise postnatally as a result of sensory experience (*5*–*9*). However, spatially organized patterns of spontaneous activity are evident in the embryonic thalamus, before cortical neurons have completed their radial migration (*10*). One well-studied functional map is the somatotopic correspondence between whiskers and their associated clusters of layer 4 neurons (called barrels) in the rodent primary somatosensory cortex (S1) (*11*). Although barrels are apparent anatomically at postnatal day 4 (P4) (*12*), domains of spontaneously co-activated neurons can be identified at birth in S1 in vivo (*13*–*15*). We asked whether the emergence of anatomically discernable structures is preceded by organized activity in the mouse embryo. We discovered that structured patterns of neuronal activity in the embryonic thalamus define functional cortical columns and the concomitant functional somatotopic map in the immature cortex.

The functional properties of embryonic thalamocortical connections were assessed by recording the somatosensory cortical calcium responses elicited by the activation of the ventral posteromedial nucleus (VPM) of the thalamus in slices. By embryonic day 17.5 (E17.5), electrical stimulation of the VPM triggered calcium waves that propagated over a large area of the nucleus, resembling previously reported spontaneous activity (*10*). This thalamic stimulation elicited a cortical calcium response in the S1 (Fig. 1, A and B; fig. S1A; and movie S1). Whereas the activation of thalamocortical axons is confined to the subplate at this stage (fig. S1B), the cortical response spanned the entire thickness of the cortical plate, suggesting that thalamocortical axons activate a radially organized cortical network. From E18.5 onward, VPM stimulation activated a progressively restricted territory within the nucleus (fig. S1C), allowing us to define the functional topography of the nascent thalamocortical projection. Perithreshold stimulation of adjacent regions in the VPM activated distinct columnar territories in the cortex (Fig. 1, C and D), indicating the existence of a functional protomap present in these embryonic thalamocortical circuits. This was evaluated in vivo by transcranial calcium imaging of glutamatergic cortical neurons at E18.5. Mechanical stimulation of juxtaposed areas of the whisker pad activated discrete, segregated, and spatially consistent cortical territories in the contralateral S1 (Fig. 1, E and F, and movie S2), confirming the existence of a cortical somatosensory protomap in the intact embryo.

We then tested whether embryonic thalamic calcium waves influence the emergence of the functional cortical columns that presage the formation of the somatotopic barrel map. To change the normal pattern of spontaneous thalamic activity, we crossed a tamoxifen-dependent *Gbx2Cre^{ERT2}* mouse with a floxed line expressing the inward rectifier potassium channel 2.1 (Kir) fused to the mCherry reporter (fig. S2) (*10*). In this model (referred to hereafter as *Th^{Kir}*), 78% of the VPM neurons express Kir-mCherry protein upon tamoxifen administration at E10.5 (fig. S2). In control slices, more than half of the spontaneous synchronous events in the VPM corresponded to large-amplitude, highly synchronized calcium waves, whereas the remaining activity reflected low-amplitude, poorly synchronized events. The highly synchronized waves were not detected in the *Th^{Kir}* mice, in which only small-amplitude and mostly asynchronous activity persisted, although at a higher frequency than in controls (Fig. 2, A to C, and movies S3 and S4). Collectively, Kir overexpression shifted the pattern of spontaneous activity in the thalamus from synchronized waves to asynchronous activity.

At the cellular level, whereas control neurons were relatively depolarized at E16.5, *Th^{Kir}* cells displayed a bistable pattern of activity with spontaneously alternating periods of hyperpolarized and depolarized membrane potential (Fig. 2D and fig. S3). Action potentials were generated in the depolarized phase in both control and *Th^{Kir}* cells. This change in the electrical properties of the *Th^{Kir}* neurons was sufficient to impede the generation of calcium waves. Barium, an ion that blocks Kir channels (*16*), reversed the electrophysiological profile of *Th^{Kir}* neurons, recovering the wavelike activity in *Th^{Kir}* VPM networks (fig. S4 and movie S5). Thus, although there were no propagating calcium waves in the thalami of *Th^{Kir}* mice, the preservation of thalamic asynchronous activity meant that the thalamus was not silent.

We analyzed how altering the pattern of spontaneous thalamic activity in our *Th^{Kir}* model affected the functional columnar organization in S1. Perithreshold VPM stimulation in E17.5 to E18.5 slices from control mice triggered a columnar-like cortical response (fig. S5A and movie S6). Conversely, this stimulation in *Th^{Kir}* slices consistently elicited a broader (laterally) cortical calcium wave (fig. S5A and movies S7 and S8). Despite these differences, the subplate was the earliest cortical compartment activated in both control and *Th^{Kir}* mice, followed by the upper cortex (fig. S5, B to D). Next, we tested whether the emergence of the functional topographic map was affected in the *Th^{Kir}* mice. Stimulation of adjacent regions in the VPM in the *Th^{Kir}* slices, unlike that in the controls, activated highly overlapping territories in the cortex (Fig. 3A), indicating that the topographical representation of the thalamocortical circuit does not emerge in the absence of embryonic thalamic waves. Postnatally, the cortical response to VPM stimulation narrowed progressively with time in control slices, coinciding at P4 with the dimensions of the cortical barrel, yet this spatial restriction occurred to a lesser extent in the *Th^{Kir}* mice (Fig. 3, B and C, and movies S9 and S10). These differences were observed irrespective of the stimulation strength (fig. S6).

The extended cortical activation in the *Th^{Kir}* mice was not due to more extensive activation of the VPM (fig. S7), yet it was associated with increased levels of intrinsic cortical excitability. This was reflected by the high frequency of spontaneous cortical waves in *Th^{Kir}* slices (fig. S8,

Instituto de Neurociencias de Alicante, Universidad Miguel Hernández-Consejo Superior de Investigaciones Científicas (UMH-CSIC), Sant Joan d'Alacant, Spain.
*These authors contributed equally to this work. †Present address: Science for Life Laboratory, Tomtebodavägen 23A, 17165 Solna, Sweden. ‡Present address: Department of Integrative and Computational Neuroscience (ICN), Paris-Saclay Institute of Neuroscience (NeuroPSI), CNRS/University Paris-Sud, 91198 Gif-sur-Yvette, France.
§Corresponding author. Email: g.lbendito@umh.es

A and B) and the widespread cortical response to intracortical stimulation (fig. S8, C to E). Next, we tested whether this change in cortical network excitability occurred in the Th^{Kir} mice in vivo. Because cortical traveling waves were associated with action potential bursts (fig. S8F), we recorded extracellular cortical activity with multichannel electrodes. We found extensive spontaneous events of synchronous activity spreading horizontally in the Th^{Kir} mice at P2 to P3 (Fig. 3, D to F), consistent with the hyperexcitability observed ex vivo. We then analyzed the possible origin for this excitability and found that the amplitude of the calcium response was the same in the subplate but larger in the upper cortex in the Th^{Kir} mice (fig. S9), suggesting a local alteration in the upper cortical network. As metabotropic glutamate receptors (mGluRs) participate in the propagation of cortical spontaneous activity in newborn rodents (*17*, *18*), we tested whether mGluRs could be involved in the hyperexcitability of cortical networks in Th^{Kir} mice. Bath application of 2-methyl-6-(phenylethynyl)pyridine (MPEP) (100 μM), an mGlu5-specific antagonist, rescued the activation of the thalamocortically induced cortical network into a column-like domain in Th^{Kir} mice. Although MPEP decreased the overall signal intensity in both conditions, it had no effect on the width of the cortical response in controls (fig. S10, A to C). These results are consistent with increased expression of cortical mGlu5 in the Th^{Kir} mice at P0 (fig. S10D). Together, these data reveal that the emergence of functional columns and a somatotopic map in the S1 relies on thalamic control of cortical excitability, implicating mGluRs.

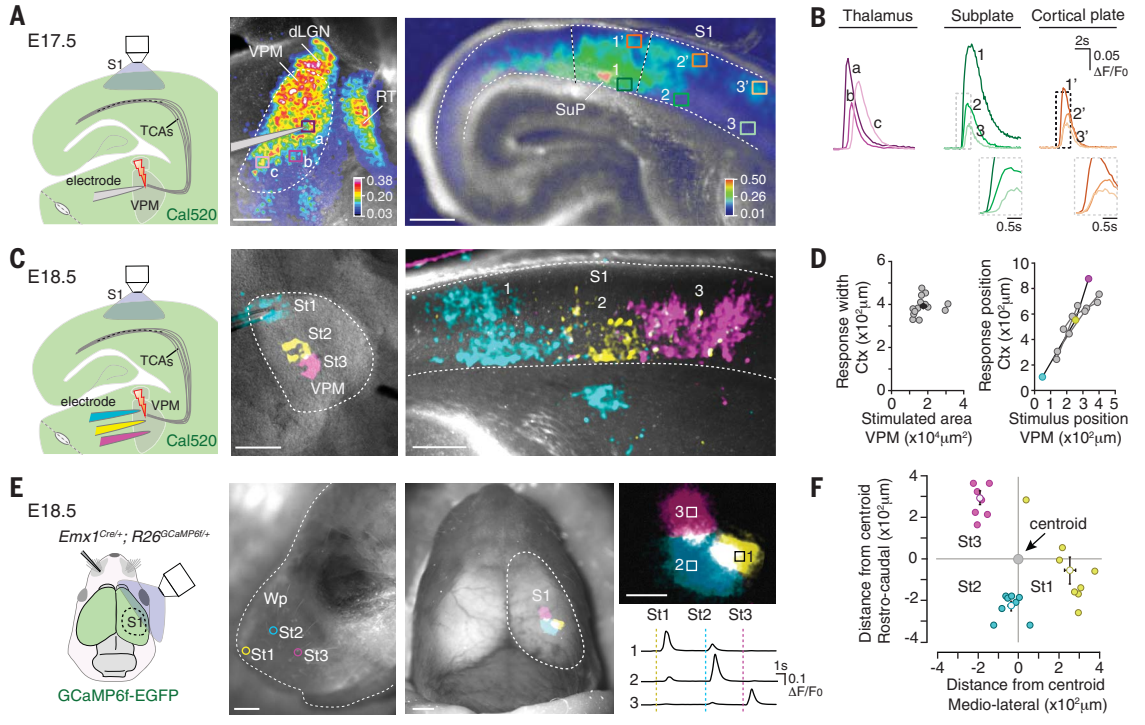


Fig. 1. Embryonic thalamocortical stimulation reveals an organized prenatal cortical map. (**A**) Experimental design. The maximal projection of the calcium responses [measured as the ratio of the change in fluorescence to the baseline fluorescence ($\Delta F/F_0$)] (color coded) in the VPM and cortex after VPM stimulation at E17.5 is shown. (**B**) Calcium transients from boxes in (A). (**C**) Experimental design. The maximal projection of cortical responses after the stimulation of three adjacent VPM regions (St1 to St3) at E18.5 is shown. (**D**) (Left) Plot of the stimulated VPM area versus the cortical response width (the black dot represents the mean value). (Right) Plot of the stimulus position in the VPM versus the cortical response location (n = 16 stimulation sites from 4 slices). Colored circles represent the data in (C). (**E**) Experimental design. Cortical calcium responses were elicited by mechanical stimulation of three contralateral whisker pad (Wp) sites (St1 to St3) at E18.5. (Right) High-magnification images and transients recorded in each region of interest (ROI) (boxes labeled 1 to 3). (**F**) Plot of the position of each cortical response relative to the centroid of the activated area (n = 8 mice). dLGN, dorsolateral geniculate nucleus; RT, reticular thalamus; SuP, subplate; TCAs, thalamocortical axons; Cal520, calcium indicator 520; Ctx, cortex; GCaMP6f-EGFP, calmodulin-based genetically encoded fluorescent calcium indicator 6–fast. Scale bars, 200 μm in (A), 1 mm in (E) (left and middle), and 500 μm in (E) (right).

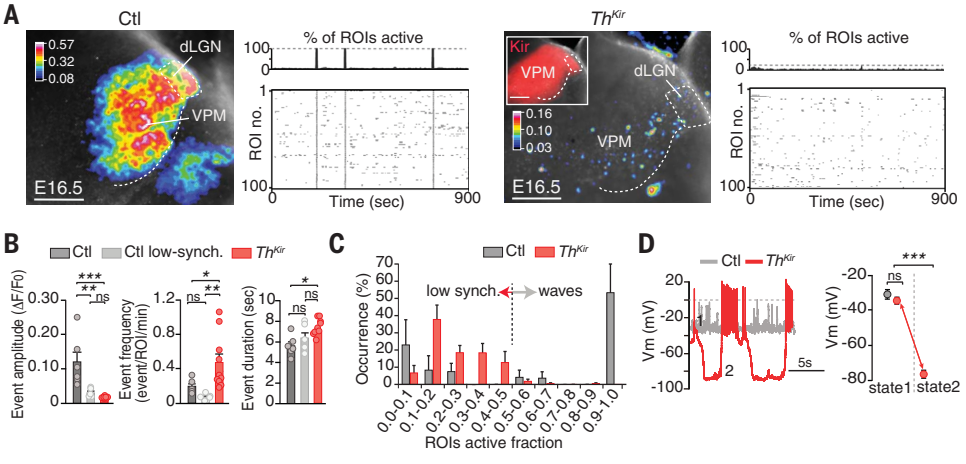


Fig. 2. Desynchronizing the embryonic thalamic pattern of activity. (**A**) Maximal projection of ex vivo spontaneous calcium activity in the VPM and accompanying raster plots for control (Ctl) and Th^{Kir} slices at E16.5. (**B**) Properties of the VPM calcium events (n = 6 control slices, n = 10 Th^{Kir} slices; ns, not significant; *P < 0.05, **P < 0.01, ***P < 0.001). (**C**) Percent distribution of active ROIs. (**D**) Representative traces and quantification of membrane potential (Vm) in control and Th^{Kir} neurons recorded at E16.5 to E18.5 (control, n = 7 slices; Th^{Kir}, n = 7 slices). ***P < 0.001. Scale bars, 200 μm. Data are means ± SEM.

To ascertain whether embryonic thalamic activity and functional columns are prerequisites to establish the postnatal anatomy of the barrel map, we examined thalamocortical axons clustering in the Th^{Kir} mice in which this projection was labeled by green fluorescent protein (GFP) (TCA-GFP mice) (*19*). The barrel map was evident at P4 in control mice (*12*, *20*), but no barrels were detected in tangential or coronal sections of Th^{Kir} mice, where thalamocortical axons targeted layer 4 but did not segregate into discrete clusters (Fig. 4A and fig. S11). Furthermore, there was no arrangement of layer 4 cells into barrel walls in the Th^{Kir} mice. The absence of barrels did not seem to originate from the loss of neurotransmitter

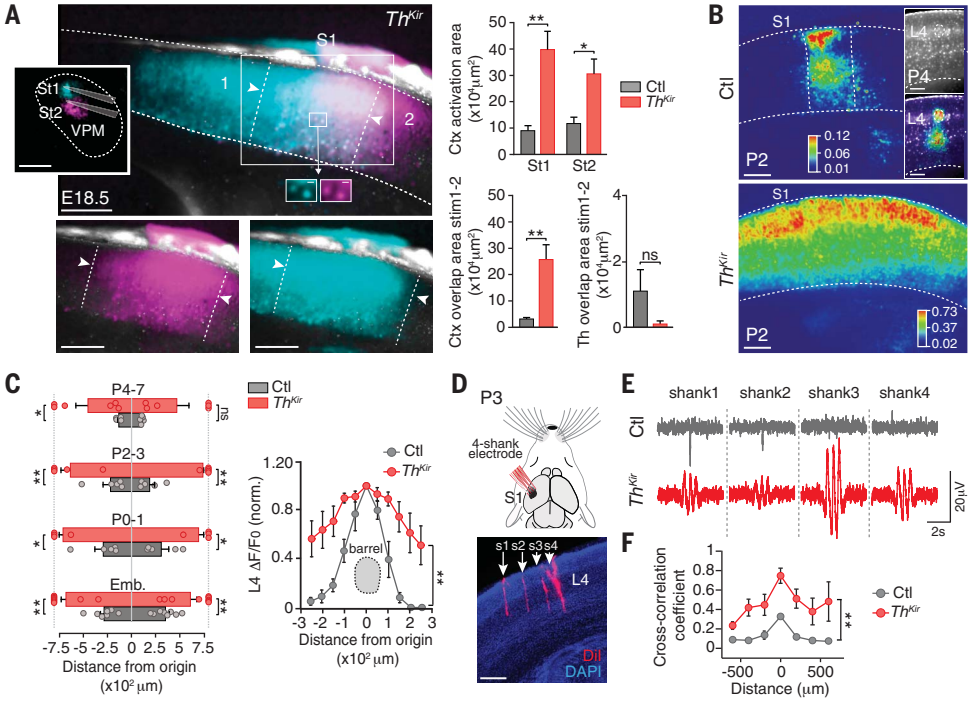


Fig. 3. Loss of functional cortical prebarrel columns in the Th^{Kir} mice. (**A**) Maximal projection of cortical responses after the stimulation (stim) of two adjacent VPM regions in Th^{Kir} slices. (Right) Quantifications of the activated area (n = 6 control slices, n = 6 Th^{Kir} slices; ns, not significant; *P < 0.05, **P < 0.01). Arrowheads indicate the cortical territory with overlapping activation. (**B**) Cortical activation elicited by VPM stimulation at P2 (inset, P4) in control (Ctl) and Th^{Kir} slices. (**C**) Quantification of the horizontal spread of the cortical response [E17 to E18 (emb.), n = 8 control slices, n = 9 Th^{Kir} slices; P0 to P1, n = 5 control, n = 4 Th^{Kir}; P2 to P3, n = 5 control, n = 5 Th^{Kir}; P4 to P7, n = 5 control, n = 6 Th^{Kir}; ns, not significant; *P < 0.05, **P < 0.01]. (Right) Same in layer 4 at P4 to P7 (n = 6 control slices, n = 6 Th^{Kir} slices; **P < 0.01). (**D**) Experimental design and coronal image showing the four-shank (s1 to s4) electrode insertion in S1 (red). (**E**) Representative in vivo recordings of spontaneous cortical network activity. (**F**) Quantification of the cross-correlation coefficient among shanks in control mice (n = 3) and Th^{Kir} mice (n = 6). **P < 0.01. L4, layer 4; norm., normalized; DiI, 1,1′-dioctadecyl 3,3,3′,3′-tetramethylindocarbocyanine perchlorate; DAPI, 4′,6-diamidino-2-phenylindole. Scale bars, 200 µm. Data are means ± SEM.

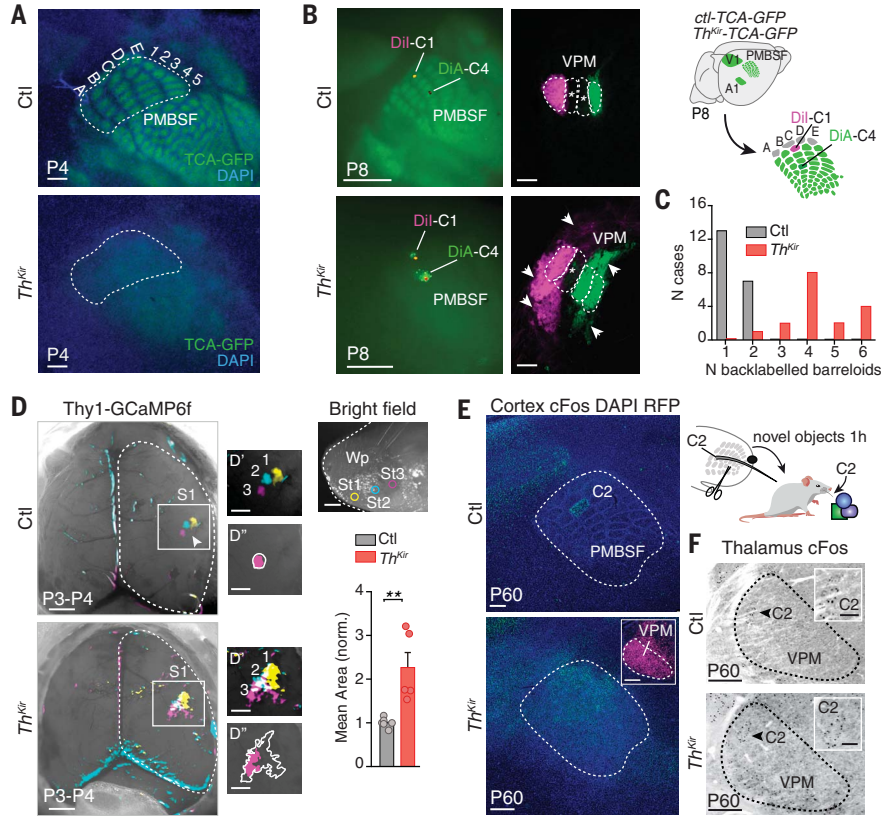


Fig. 4. Long-term anatomical and functional changes in S1 of the Th^{Kir} mice. (**A**) Tangential sections showing the posteromedial barrel subfield (PMBSF) in control (Ctl) and Th^{Kir} TCA-GFP mice at P4. Letters and numbers correspond to the diagram in (B). (**B**) Experimental design and images showing PMBSF injection sites and back-labeled barreloids in the VPM. Arrowheads show back-labeling outside the expected barreloids and asterisks indicate the non-back-labeled barreloids. (**C**) Quantification of data shown in (B) (n = 10 control slices, n = 10 Th^{Kir} slices). (**D**) Maximal projection of the in vivo contralateral cortical responses elicited by mechanical stimulation of three whisker pad (Wp) sites (St1 to St3) at P3 to P4 (top right). (D′) High-power views. (D″) Drawing of initial (pink) and maximal (outline) extension of representative responses. (Bottom right) Quantification of the data (n = 6 control mice, n = 5 Th^{Kir} mice; **P < 0.01). (**E**) Experimental design and cortical cFos immunostaining. (**F**) VPM cFos immunostaining. Scale bars, 300 µm in (A), (B) (right), (E), and (F) (insets, 100 µm); 1 mm in (B) (left) and (D) (insets, 500 µm). DiA, 4-Di-16-ASP (4-(4-(dihexadecylamino)styryl)-*N*-methylpyridinium iodide); A1, primary auditory cortex; V1, primary visual cortex; RFP, red fluorescent protein. Data are means ± SEM.

release (*21*, *22*), as thalamic neurons in the Th^{Kir} mice fire action potentials and activate synaptic currents in cortical cells (figs. S4A, S9D, and S12, A to C) and respond normally to whisker stimulation in vivo (fig. S12, D and E).

The disrupted barrel map in Th^{Kir} mice may reflect altered point-to-point connectivity at several subcortical levels (*8*, *23*, *24*). However, the organization of brainstem barrelettes and thalamic barreloids in the Th^{Kir} mice was normal (fig. S13). As the barrel map ultimately relies on the specific topographic organization of thalamocortical axons (*25*), we explored whether some spatial segregation was conserved in the Th^{Kir} mice. Although dye deposition in barrels C1 and C4 back-labeled cells in the corresponding barreloids of control mice, the back-labeled territories in Th^{Kir} mice were more extensive, including cells located in neighboring barreloids (Fig. 4, B and C). Anterograde tracing from single barreloids also revealed a broader horizontal disposition of thalamocortical axons in layer 4 of the Th^{Kir} mice (fig. S14). Lastly, we determined how this aberrant topographic map generated by the lack of thalamic calcium waves affected the relay of sensory stimuli in early postnatal mice in vivo. Whereas the stimulation of distinct points on the whisker pad at P3 to P4 activated discrete barrel-like patches in the control S1, similar stimulations of Th^{Kir} mice led to enlarged responses in the barrel field (Fig. 4D and movies S11 and S12). Together, these data demonstrate that the postnatal anatomic clustering of thalamocortical axons and the somatotopic functional map are disrupted in the absence of embryonic thalamic waves.

As the critical period of thalamocortical plasticity in the S1 closes between P3 and P7 in rodents (*6*, *20*, *26*), we assessed whether the loss of columnar organization in the Th^{Kir} mice could be overcome by sensory experience. The loss of barrel organization and the lack of a precise functional map persisted in adult Th^{Kir} mice, as indicated by vGlut2 (vesicular glutamate transporter 2) staining and the unrestrained cortical activation of cFos (Fig. 4E and fig. S15). The thalami of Th^{Kir} mice retained a normal functional topography when whiskers were stimulated (Fig. 4F). Hence, the natural period of somatosensory-driven plasticity cannot overcome the altered organization that occurs in the embryo.

Our data reveal that embryonic patterns of thalamic activity organize the architecture of the somatosensory map. We have shown that the development of this map involves the emergence of functional cortical columns in embryos, driven by spontaneous thalamic wavelike activity. These embryonic columns display spatial segregation and somatotopic organization, despite the immature state of the cortical sheet in which they materialize. We propose that patterned activity in precortical relay stations during embryonic stages prepares cortical areas and circuits for upcoming sensory input. As thalamic waves are not exclusive to the somatosensory nucleus but propagate to other sensory nuclei [e.g., visual or auditory (*10*)], the principles of cortical map organization described here may be common to other developing sensory systems.

REFERENCES AND NOTES

1. V. B. Mountcastle, *J. Neurophysiol.* **20**, 408–434 (1957).
2. P. Rakic, *Science* **241**, 170–176 (1988).
3. D. H. Hubel, T. N. Wiesel, *J. Physiol.* **160**, 106–154 (1962).
4. P. Rakic, A. E. Ayoub, J. J. Breunig, M. H. Dominguez, *Trends Neurosci.* **32**, 291–301 (2009).
5. A. Tiriac, B. E. Smith, M. B. Feller, *Neuron* **100**, 1059–1065.e4 (2018).
6. T. K. Hensch, *Annu. Rev. Neurosci.* **27**, 549–579 (2004).
7. P. Gaspar, N. Renier, *Curr. Opin. Neurobiol.* **53**, 43–49 (2018).
8. H. P. Killackey, G. Belford, R. Ryugo, D. K. Ryugo, *Brain Res.* **104**, 309–315 (1976).
9. T. A. Woolsey, J. R. Wann, *J. Comp. Neurol.* **170**, 53–66 (1976).
10. V. Moreno-Juan *et al.*, *Nat. Commun.* **8**, 14172 (2017).
11. T. A. Woolsey, H. Van der Loos, *Brain Res.* **17**, 205–242 (1970).
12. A. Agmon, L. T. Yang, E. G. Jones, D. K. O'Dowd, *J. Neurosci.* **15**, 549–561 (1995).
13. J. W. Yang *et al.*, *Cereb. Cortex* **23**, 1299–1316 (2013).
14. H. Mizuno *et al.*, *Cell Rep.* **22**, 123–135 (2018).
15. O. Mitrukhina, D. Suchkov, R. Khazipov, M. Minlebaev, *Cereb. Cortex* **25**, 3458–3467 (2015).
16. N. Alagem, M. Dvir, E. Reuveny, *J. Physiol.* **534**, 381–393 (2001).
17. J. Wagner, H. J. Luhmann, *Neuropharmacology* **51**, 848–857 (2006).
18. D. P. Calderon, N. Leverkova, A. Peinado, *J. Neurosci.* **25**, 1737–1749 (2005).
19. H. Mizuno *et al.*, *Neuron* **82**, 365–379 (2014).
20. R. S. Erzurumlu, P. Gaspar, *Eur. J. Neurosci.* **35**, 1540–1553 (2012).
21. H. Li *et al.*, *Neuron* **79**, 970–986 (2013).
22. N. Narboux-Nême *et al.*, *J. Neurosci.* **32**, 6183–6196 (2012).
23. H. Van der Loos, T. A. Woolsey, *Science* **179**, 395–398 (1973).
24. W. L. Weller, J. I. Johnson, *Brain Res.* **83**, 504–508 (1975).
25. L. Lokmane, S. Garel, *Semin. Cell Dev. Biol.* **35**, 147–155 (2014).
26. M. C. Crair, R. C. Malenka, *Nature* **375**, 325–328 (1995).

ACKNOWLEDGMENTS

We thank L.M. Rodríguez, R. Susín, and B. Andrés for technical support; T. Iwasato for providing the TCA-GFP mouse; A. Barco for advice on the behavioral experiments; R. Morris, S. Tole, M. Maravall, and D. Jabaudon for critical reading of the manuscript; and the López-Bendito laboratory for stimulating discussions. **Funding:** This work was supported by grants from the European Research Council (ERC-2014-CoG-647012) and the Spanish Ministry of Science, Innovation and Universities (BFU2015-64432-R and Severo Ochoa grant SEV-2017-0723). N.A.-B. held an FPI fellowship from the MINECO. H.G. held postdoctoral fellowships from the Swedish Research Council and the Swedish Brain Foundation. **Author contributions:** N.A.-B., A.S.-F., M.V., and G.L.-B. designed the experiments. N.A.-B., A.S.-F., T.G.-V., F.J.M., and L.P.-S. performed the analysis. N.A.-B. conducted calcium imaging, tracing experiments, and the cFos assays. A.S.-F. conducted calcium imaging and the electrophysiology. T.G.-V. conducted the in vivo calcium imaging. F.J.M. performed the Matlab analysis. L.P.-S. and F.J.M. performed the in vivo multi-electrode recordings. H.G. generated the Kir-mCherry mouse and pioneered Th^{Kir} analysis. A.F. designed, performed, and analyzed initial spontaneous thalamic calcium imaging. G.L.-B. acquired funding. M.V. and G.L.-B. wrote the paper. **Competing interests:** None declared. **Data and materials availability:** All the data in the paper are presented in the main text or supplementary materials.

SUPPLEMENTARY MATERIALS

science.sciencemag.org/content/364/6444/987/suppl/DC1
Materials and Methods
Figs. S1 to S15
References (*27*–*31*)
Movies S1 to S12

12 November 2018; resubmitted 22 March 2019
Accepted 23 April 2019
Published online 2 May 2019
10.1126/science.aav7617

NEUROSCIENCE

Social transmission of food safety depends on synaptic plasticity in the prefrontal cortex

Michaël Loureiro[1], Ridouane Achargui[1], Jérôme Flakowski[1], Ruud Van Zessen[1], Thomas Stefanelli[1], Vincent Pascoli[1], Christian Lüscher[1,2]*

When an animal is facing unfamiliar food, its odor, together with semiochemicals emanating from a conspecific, can constitute a safety message and authorize intake. The piriform cortex (PiC) codes olfactory information, and the inactivation of neurons in the nucleus accumbens (NAc) can acutely trigger consumption. However, the neural circuit and cellular substrate of transition of olfactory perception into value-based actions remain elusive. We detected enhanced activity after social transmission between two mice in neurons of the medial prefrontal cortex (mPFC) that target the NAc and receive projections from the PiC. Exposure to a conspecific potentiated the excitatory postsynaptic currents in NAc projectors, whereas blocking transmission from PiC to mPFC prevented social transmission. Thus, synaptic plasticity in the mPFC is a cellular substrate of social transmission of food safety.

Although metabolic needs ultimately drive food consumption, additional factors determine the moment-to-moment intake. For example, a predator threat may halt eating even when hungry. Conversely, when palatable foods are found, prolonged consumption can occur, leading to accumulation of fat storage (*1*). Moreover, many species use information acquired from peers to decide whether food is safe to eat. Whereas primates rely predominantly on visual cues, rodents use their olfactory system to detect odors, including carbon disulfide (CS_2), a semiochemical component of the rodent breath (*2*, *3*). Such social transmission of food preference (STFP) occurs when an observer mouse exposed to a demonstrator mouse fed with scented food drives a preference for that food over a differently scented alternative (*4*). Recent studies demonstrate the involvement of olfactory sensory neurons and mitral cells in the olfactory bulb for STFP acquisition (*5*), which project to the piriform cortex (PiC). The activity of neurons in the medial prefrontal cortex (mPFC) increases substantially in response to reward-predicting cues (*6*), which may drive decision-making processes (*7*) by cells that project to the nuclear accumbens (NAc projectors). From there, D1R-expressing neurons, a major inhibitory output of the NAc, could control the food intake on a rapid time scale independently of metabolic needs (*8*).

Rodents exposed simultaneously to cumin- and thyme-flavored food exhibit an innate preference for the thyme option (*9*). We first confirmed that observer mice cued by a demonstrator fed with cumin-flavored food increased their time exploring and eating the cumin-scented option, without affecting the total amount of food eaten (fig. s1, A to F). STFP acquisition was efficient only if the food options were unfamiliar to cued observers (fig. s1, G to I), corroborating the transmission of a safety signal, rather than passing a mere preference. We then monitored the activity of neurons projecting to the NAc projectors in the mPFC and the paraventricular nucleus of the thalamus (PVT), involved in decision making (*10*) and the expression of aversive memories (*11*), respectively. To identify NAc projectors, we injected cholera toxin subunit B (CTB) into the NAc of observer mice and quantified cFos expression, a proxy for neuronal activity, after conspecific interaction or the food choice session (Fig. 1, A to C). These manipulations did not affect the interaction between demonstrator and observer mice nor the concomitant cFos expression in NAc projectors (Fig. 1D). However, when quantified immediately after food choice sessions, cFos-positive mPFC NAc projectors (but not the overall number of cFos-positive neurons in the mPFC; fig. s2, C and D) were more abundant in cued mice compared with uncued mice, an effect not observed in PVT NAc projectors (Fig. 1E) despite a similar density of NAc projectors to the two structures (fig. s2, A and B). The amount of food consumed by uncued and cued animals was similar and therefore could not explain the change in mPFC NAc projectors engagement between groups (fig. s2E). We next determined the functional consequences onto medium-sized spiny neurons (MSNs) in the NAc. To record transmission selectively from these synapses, we injected *Fos*$^{creER/T2}$-transgenic mice in the mPFC with a cre-inducible adeno-associated virus (AAV) containing channelrhodopsin (ChR2), along with mCherry for visualization (AAV-DIO-ChR2-mCherry) (Fig. 1, F to H, and fig. s2, F and G). *Fos*$^{creER/T2}$ mice provide a *fos*-dependent labeling of active population when 4-hydroxytamoxifen (4-OHT) is present in the brain (*12*, *13*). Although the density of mPFC cells expressing ChR2-mCherry was similar in cued and uncued mice (Fig. 1H), we observed excitatory postsynaptic currents (EPSCs) in 36% of MSNs (39.4 pA on average) in mice exposed to a demonstrator but in only 19% of MSNs (20.9 pA on average) in uncued controls (Fig. 1I). This difference in connectivity and amplitude was not observed in mice injected with a cre-independent AAV-ChR2-EYFP (enhanced yellow fluorescent protein) virus in the mPFC (fig. s2, H to J). We next tested whether chemogenetic inhibition of mPFC NAc projectors during the food choice session could affect STFP expression. We injected the NAc of observer mice with a retrograde AAV that virally expresses the Cre recombinase (AAV2rg-pkg-Cre), followed by an injection in the mPFC of an AAV that expresses the hM4D(Gi) receptor in a cre-dependent manner (Fig. 1J). Injection of clozapine-n-oxide (CNO) in the absence of hM4D(Gi) receptors did not affect the preference of the observers. However, the inhibition of mPFC NAc projectors in cued animals abolished STFP expression (Fig. 1, K and L).

Because STFP induction requires CS_2, a component of the mouse breath (*2*), we mimicked the switch in food preference by simultaneously exposing mice to CS_2 and cumin-flavored food (fig. s3, A to C). Odors are encoded in the PiC and a single brief exposure to CS_2 increases the number of cFos-positive neurons (fig. s3, D to F), suggesting the involvement of the PiC in STFP acquisition. Given the above results implicating mPFC NAc projectors for STFP expression, we searched for a direct connection between the two brain regions. To test whether mPFC NAc projectors receive monosynaptic inputs from the PiC, we used the retrograde trans-synaptic and rabies-based method TRIO ("tracing the relationship between input and output") (*14*). C57BL6/J mice were injected with retrograde AAV2rg-pkg-Cre in the NAc and helper AAVs in the mPFC, allowing the Cre-dependent expression of the TVA receptor for EnvA fused with mCherry and the rabies glycoprotein (G) (Fig. 2A). One month later, glycoprotein-deleted and green fluorescent protein–expressing rabies viruses (RV*d*G) were injected in the mPFC and efficiently infected NAc projectors (Fig. 2B). Analysis of distal inputs to mPFC NAc projectors revealed major connections from the posterior part of the PiC, as well as from other regions such as the mediodorsal thalamus and the basolateral amygdala (Fig. 2, C and D). We confirmed the synaptic connectivity between PiC neurons and mPFC NAc projectors in acute brain slices. We injected an AAV-ChR2-EYFP in the PiC and optogenetically stimulated its terminals in the mPFC while recording from NAc projectors (CTB-555-positive cells; Fig. 2, E and F). When clamped at −70 mV, we found EPSCs in 76% of NAc projectors, with an average amplitude of 274 ± 23 pA and a membrane capacitance of 116 ± 5 pF, suggesting that most of the recorded cells were

[1]Department of Basic Neurosciences, Medical Faculty, University of Geneva, CH-1211 Geneva, Switzerland. [2]Clinic of Neurology, Department of Clinical Neurosciences, Geneva University Hospital, CH-1211 Geneva, Switzerland.
*Corresponding author. Email: christian.luscher@unige.ch

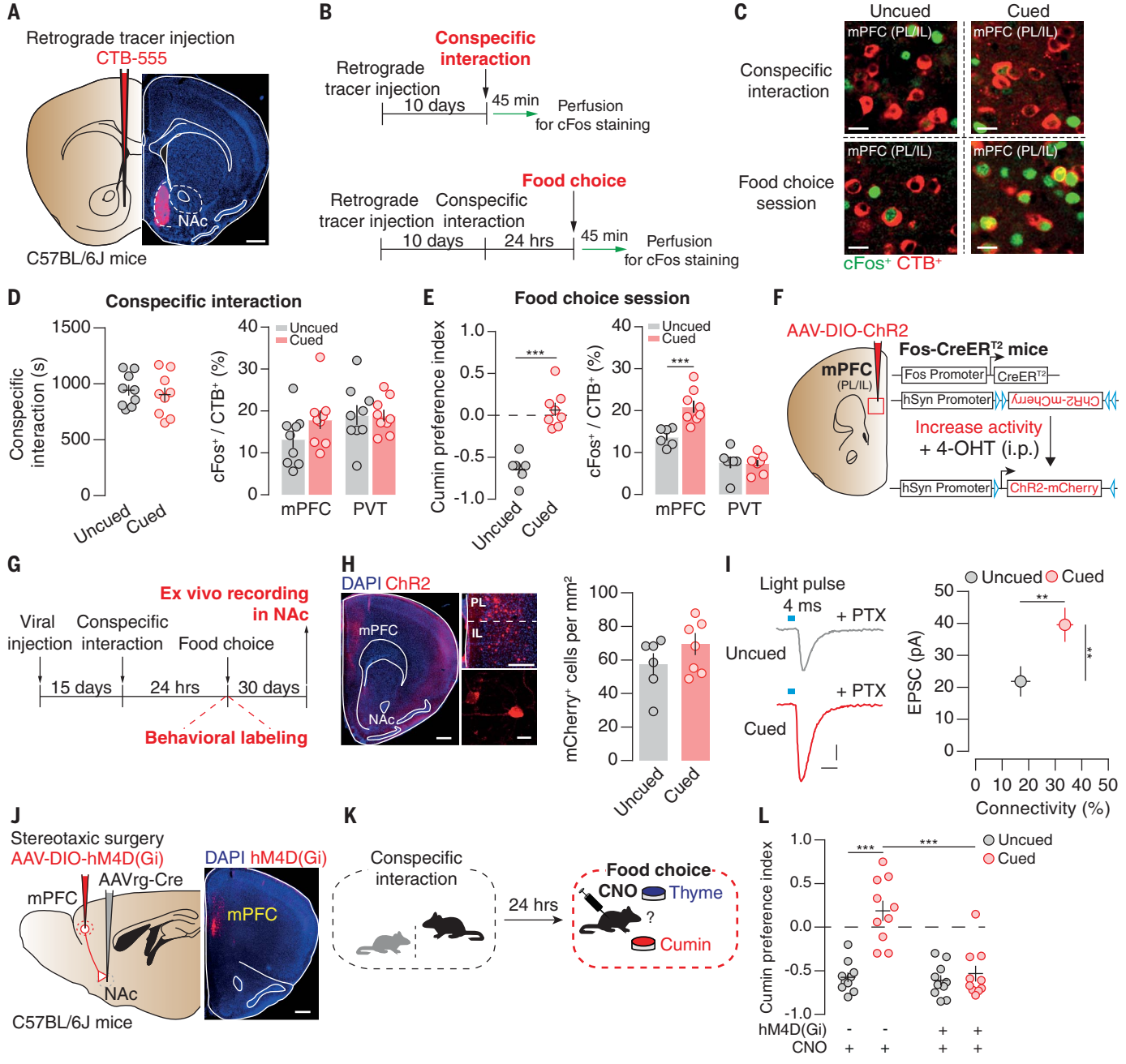


Fig. 1. Implication of mPFC NAc projectors in STFP expression. (**A**) Expression of the retrograde tracer CTB-555 in the NAc. Scale bar, 500 μm. (**B**) Mice were perfused either after conspecific interactions (top) or after the food choice session (bottom). (**C**) Histological example of mPFC NAc projectors (red, CTB-positive) and cFos expression. Yellow cells are mPFC NAc projectors activated during behavior. Scale bars: 20 μm. (**D**) Left: time spent by uncued and cued mice with the demonstrators during the conspecific interaction session before perfusion. Right: cFos quantification in NAc projectors in the mPFC and PVT. (**E**) Left: cumin preference index = (time in cumin food zone − time in thyme food zone)/(time in cumin food zone + time in thyme food zone). Mice cued by a demonstrator fed with cumin showed an increase preference for cumin-flavored food compared with uncued mice (***$p < 0.001$). Right: cFos quantification in the mPFC and PVT NAc projectors after the food choice session. The density of mPFC NAc projectors activated was significantly higher in cued mice compared with uncued animals (***$p < 0.01$). No difference was observed for PVT NAc projectors. (**F**) *Fos*-Cre$^{ER/T2}$ mice were injected with AAV$_{DJ}$-hSyn-DIO-ChR2-mCherry in the mPFC to express ChR2 under the control of the *fos* promotor and the presence of 4-OHT (10 mg/kg). (**G**) Experimental timeline. Mice were injected 4-OHT immediately after the food choice session. (**H**) Left: example of ChR2-mCherry–infected neurons in the mPFC. Scale bars: left, 500 μm; top right, 250 μm; bottom right, 20 μm. Right: The density of mPFC neurons expressing ChR2 was similar between uncued and cued animals. (**I**) Left: example of light-evoked current recorded in uncued (gray) or cued (red) observers. Scale bars: 20 pA, 10 ms. Right: connectivity plot summarizing NAc neurons receiving excitatory inputs from mPFC neurons activated during the food choice session (uncued: $n = 63$ cells from six mice; cued: $n = 80$ cells from seven mice; **$p < 0.01$). (**J**) Viral strategy with histological examples for chemogenetic inhibition of mPFC-to-NAc pathway. Scale bar, 500 μm. (**K**) CNO injections (2 mg/kg, ip) were performed 60 min before the food choice session in uncued and cued observers. (**L**) Impact of mPFC-to-NAc pathway inhibition during the food choice session on the cumin preference score. See tables S1 and S2 for complete statistics and mean ± SEM values, respectively.

pyramidal neurons (Fig. 2, G to J). The sodium channel blocker tetrodotoxin (TTX) reduced but did not abolish EPSC amplitudes, indicating a monosynaptic connection. The AMPA/kainate receptor antagonist 2,3-dihydroxy-6-nitro-7-sulfamoylbenzo[f]quinoxaline (NBQX) blocked the residual EPSCs (Fig. 2K). When NAc projectors were voltage clamped at 0 mV, light stimulation evoked prominent inhibitory postsynaptic currents (IPSCs; average amplitude 732 ± 47 pA), albeit with a longer onset delay than that of EPSCs (Fig. 2, L to N). IPSCs were completely blocked by the γ-aminobutyric acid type A (GABAa) receptor antagonist picrotoxin (PTX) or by TTX (Fig. 2O). In addition, bath application of NBQX also abolished light-evoked IPSCs.

We next investigated whether STFP acquisition would modify the properties of PiC-to-mPFC NAc-projector synapses. Observer mice expressing ChR2-EYFP in PiC neurons and CTB-555 in mPFC NAc projectors were exposed to demonstrator mice fed with cumin-flavored or regular chow. Because feeding could affect synaptic transmission, mPFC slices from observers were prepared for ex vivo recordings of synaptic currents in NAc projectors without being tested for the observers' food preference (Fig. 3A). Although both groups of mice explored the demonstrators for a similar duration (Fig. 3, B and C), optogenetic stimulation of PiC terminals in the mPFC revealed a higher EPSC to IPSC ratio in NAc projectors from cued mice compared with uncued or naïve animals, an effect not observed in unlabeled mPFC cells, likely to project elsewhere (Fig. 3D). The paired-pulse ratio of EPSCs and IPSCs (fig. s4, A to E) and the rectification index of AMPA receptor EPSCs (Fig. 3F), a measure of calcium permeability (*15*), were similar in the three groups. Comparing light-evoked AMPA-EPSCs and *N*-methyl-D-aspartate (NMDA)-EPSCs from uncued and cued mice revealed a significantly higher AMPA/NMDA ratio in cued mice (Fig. 3E).

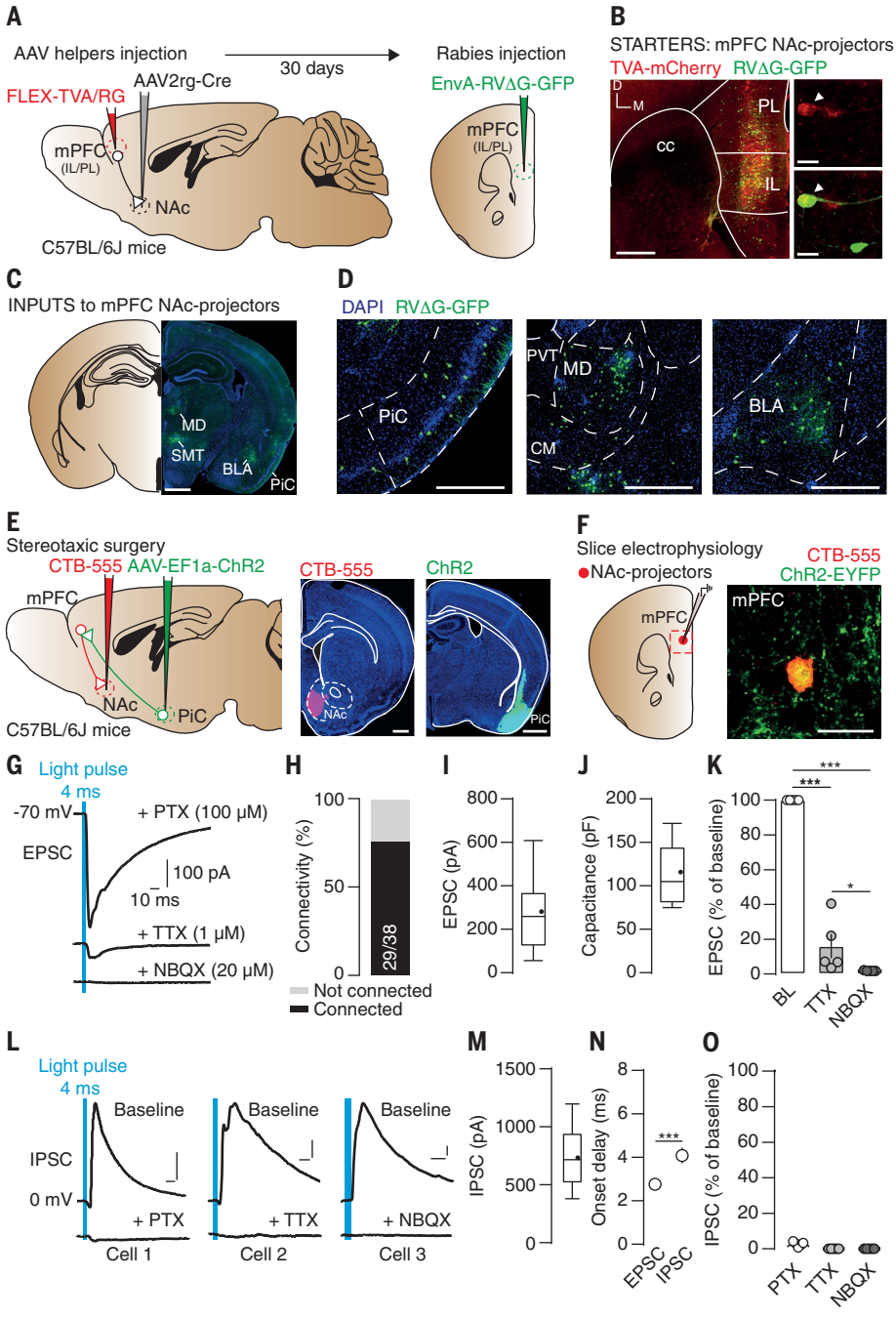


Fig. 2. The connection from the PiC-to-mPFC NAc projectors is monosynaptic and excitatory. (**A**) Schematic of a rabies-based TRIO strategy from NAc projectors in the mPFC. (**B**) Starter cells in the mPFC (PL: prelimbic; IL: infralimbic; cc: corpus callosum). Scale bars: left, 500 μm; right, 25 μm. (**C**) Example of distal inputs to mPFC NAc projectors (MD: mediodorsal thalamus; SMT: submedius thalamus; BLA: basolateral amygdala). Scale bar, 1 mm. (**D**) Higher magnification of the MD, BLA, and PiC. (**E**) Viral injection strategy to record (ex vivo whole-cell voltage-clamp recording) mPFC NAc projectors and to optogenetically stimulate PiC terminals in the mPFC. Scale bars, 500 μm. (**F**) Histological image showing a recorded mPFC NAc projector. Note the surrounding PiC fibers expressing ChR2. Scale bar: 20 μm. (**G**) Example traces of light-induced EPSC. Scale bars: 100 pA, 10 ms. (**H**) Connectivity between PiC and mPFC NAc projectors. (**I**) EPSC amplitudes. (**J**) Capacitance. (**K**) EPSC amplitudes were reduced after bath application of TTX (a voltage-gated NA^+ channel blocker) and completely blocked by bath application of NBQX (an AMPAR blocker). (**L**) IPSC example traces. Scale bars: 100 pA, 10 ms. (**M**) The onset delay was longer for recorded IPSCs compared with EPSCs. (**N**) IPSC amplitudes. (**O**) IPSCs were completely blocked by PTX (a GABAa receptor antagonist) or TTX and NBQX. Box plot represents data as median with 25th to 75th percentile (box) and minimum–maximum (whiskers); black dots represent the mean of the group. Histograms represent mean ± SEM and circles individual cells. *$p < 0.05$; ***$p < 0.001$. See tables S1 and S2 for complete statistics and mean ± SEM values, respectively.

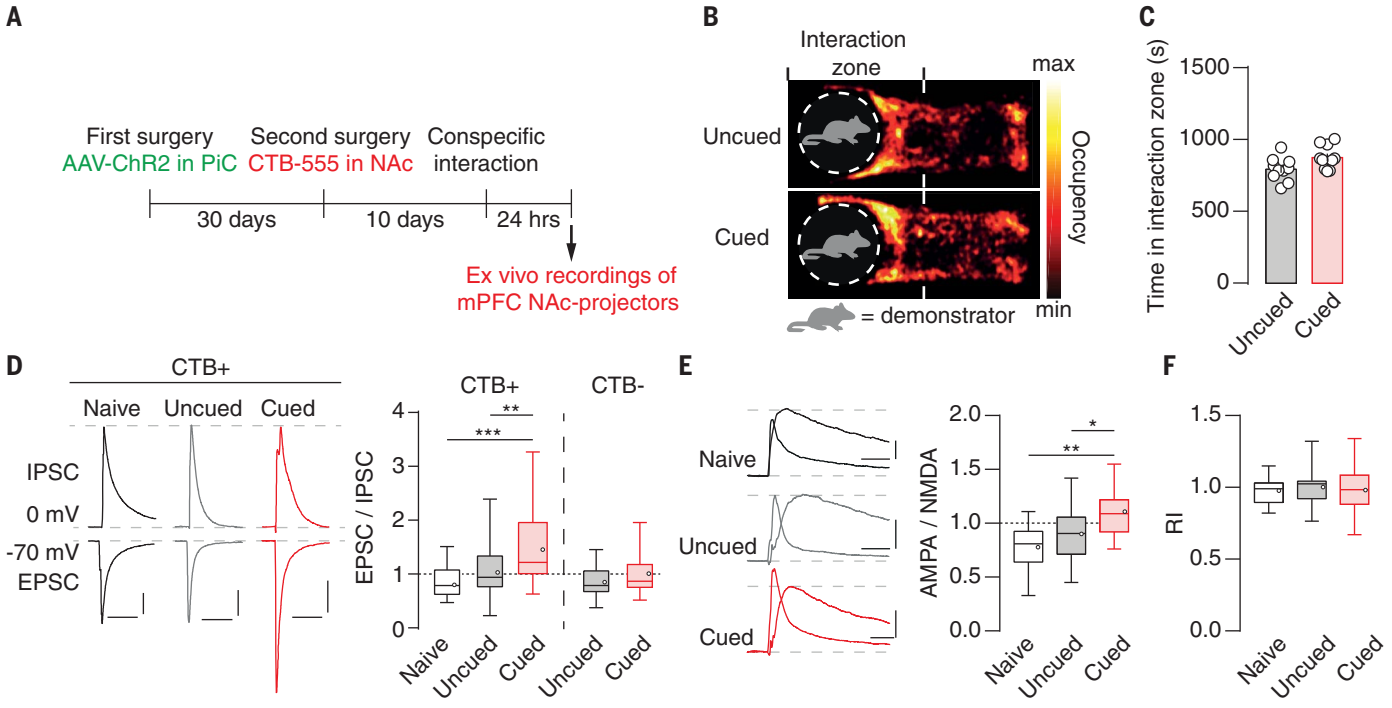


Fig. 3. STFP acquisition increases the excitatory transmission at PiC-to-mPFC NAc projectors. (**A**) Observer mice were perfused 24 hours after conspecific interaction for ex vivo recordings of light-evoked current in mPFC NAc projectors. (**B**) Representative occupancy heat maps of the time spent by an uncued or cued observer during conspecific interaction. (**C**) The time spent by uncued and cued observers in the interaction zone was not different. Black crosses represent mean ± SEM. (**D**) Example traces of IPSC and EPSC amplitude in mPFC NAc projectors (left) and grouped data for EPSC/IPSC ratios (right). *n* = 31 cells per group (five mice per group). Scale bars: 200 pA, 100 ms. (**E**) Example traces of AMPAR and NMDA-EPSCs recorded at +40 mV (left) and grouped data for AMPA/NMDA ratio (right). Scale bars: 100 pA, 50 ms. *n* = 13, 17, and 20 cells recorded in the naïve (*n* = 4 mice), uncued (*n* = 5 mice), and cued (*n* = 5 mice) groups, respectively. (**F**) Grouped data for the rectification index. Box plot represents data as median with 25/75 percentile (box) and minimum–maximum (whiskers); open circles represent the mean of the group. Histograms represent mean ± SEM. $^{**}p < 0.01$; $^{***}p < 0.001$. See tables S1 and S2 for complete statistics and mean ± SEM values, respectively.

To test for causality, we performed a pathway-specific chemogenetic inhibition of the PiC-to-mPFC pathway during the conspecific interaction and recorded NAc projectors 24 hours later. Observer mice were first injected in the mPFC with the retrograde AAV2rg-pgk-Cre virus, followed by an injection in the PiC of an AAV that expresses, in a cre-dependent manner, the hM4D(Gi) receptor (*16*). During the same surgery, the AAV-ChR2-EYFP was injected in the PiC and 30 days later, CTB-*555* was injected in the NAc to label mPFC NAc projectors (Fig. 4, A and B). Application of CNO decreased neuronal excitability and evoked an outward current that was reversed by the potassium channel blocker barium (fig. s4, G to I). Whereas CNO (2 mg/kg, intraperitoneally [ip]) injected in an observer mouse before conspecific interaction did not affect the time spent with the demonstrators (Fig. 4C), ex vivo recordings of light-evoked currents in mPFC NAc projectors revealed that uncued and cued observer mice had similar EPSC/IPSC and AMPA/NMDA ratios (Fig. 4, D and E). Finally, we tested whether chemogenetic inhibition of the PiC-to-mPFC pathway during conspecific interaction could affect STFP expression (Fig. 4F). Injection of CNO in the absence of hM4D(Gi) receptors did not alter the change in preference for cumin-scented food during the food choice session. Conversely, silencing the activity of PiC-to-mPFC pathway in cued observers during conspecific interaction abolished STFP expression (Fig. 4G), without affecting the total amount of food eaten (fig. s5A). Cued mice with the PiC-to-mPFC pathway inhibited during a food choice session showed a similar preference score compared with uncued animals (fig. s5B). If STFP-induced potentiation at PiC-to-mPFC NAc projectors is essential for STFP expression, then depotentiating these synapses in vivo after STFP acquisition should also revert the cumin preference in cued observers. To test this prediction, we induced a long-term depression in vivo of the PiC-to-mPFC pathway by photostimulating ChR2-expressing PiC terminals in the mPFC at 1 Hz, 24 hours after STFP acquisition, a protocol able to robustly reverse potentiated excitatory synapses (*11*, *17*) and validated in mPFC slices (fig. s5C). When tested 4 hours later in a food choice session, a preference index similar to that of control animals was observed (Fig. 4, H and I).

Here, we delineate the circuit that underlies the transmission of a food safety signal emanating from a conspecific that affects the choice of the consumption of an unfamiliar flavor. After the detection of the specific odor and the semiochemical CS_2 in the olfactory bulb (*2*), the message activates a set of PiC neurons. Consistent with a study that identified ensembles coding for specific odorants (*18*, *19*), similar mechanisms may be functioning here to ensure specificity. Activity in the PiC then drives a potentiation of excitatory afferents onto neurons in the mPFC that project to the NAc. As a result, the MSNs may increase the baseline firing frequency, which, when inhibited during decision making, allows for a higher dynamic range of the response. Alternatively, the enhanced excitation and increased activity in the pathway serves to suppress consumption of the preferred option, rather than (or in addition to) promoting selection of a new, nonpreferred choice.

Monitoring the activity of these neurons in vivo will determine the induction mechanism in the mPFC and the synaptic partners of the NAc projectors, which then drive the behavior through temporally precise activity patterns. Microinfusion of pharmacological agents clearly implicates glutamate transmission in a moment-by-moment control of intake (*20*). More generally, the mPFC neurons may also integrate additional conspecific signals in modalities other than olfaction to convey more complex social information and steer choices, such as aggression or mating.

Our results identify the PiC-to-mPFC neurons targeting the NAc as being essential for food preference driven by an olfactory cue in a social

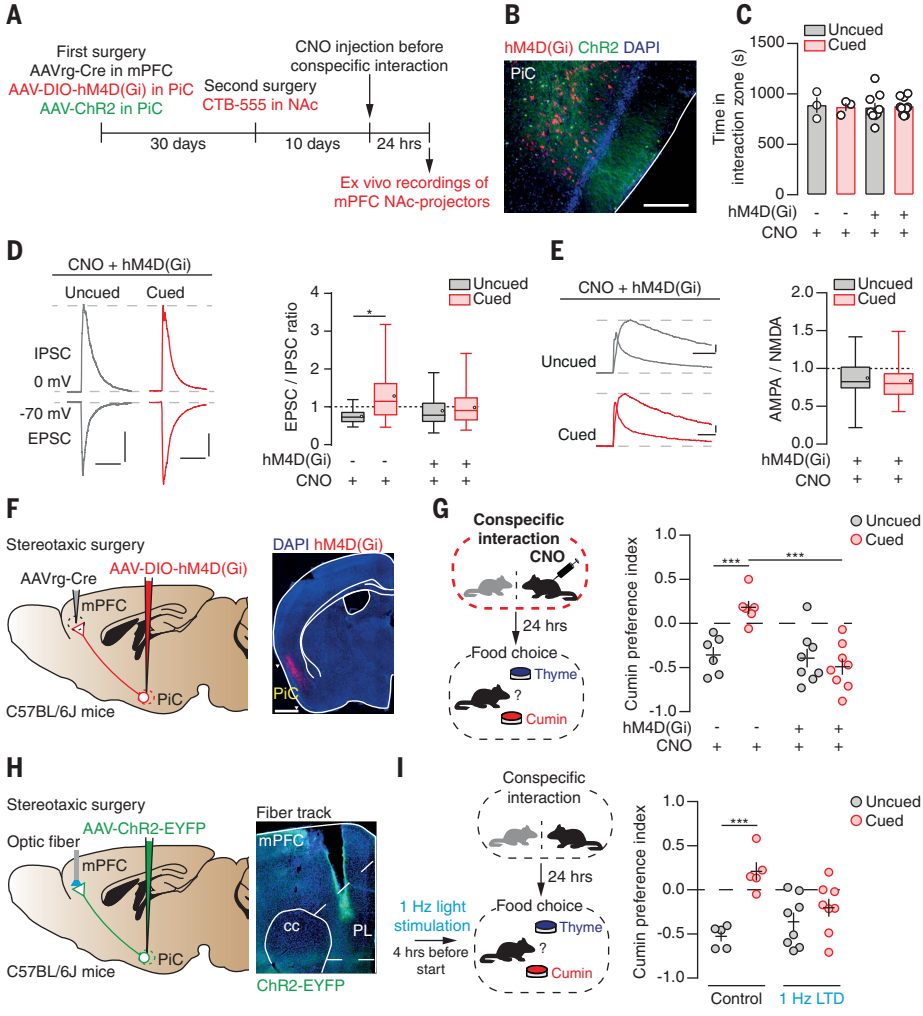


Fig. 4. Inhibition of the PiC-to-mPFC pathway during conspecific interaction prevents STFP expression. (**A**) Virus injection strategy for PiC-to-mPFC chemogenetic inhibition and optogenetic stimulation of PiC terminals in the mPFC. (**B**) Example of PiC-to-mPFC neurons infected with hM4D(Gi) and ChR2. Scale bar, 200 μm. (**C**) Inhibition of the PiC-to-mPFC pathway did not reduce the time spent by uncued and cued mice with the demonstrators. (**D**) Example of EPSC and IPSC after inhibition of PiC-to-mPFC pathway during conspecific interaction (left). Scale bars: 100 pA, 100 ms. When the PiC-to-mPFC pathway was inhibited, EPSC/IPSC ratios were similar between uncued (30 cells from five mice) and cued (30 cells from five mice) groups (right). For the control groups: 15 cells (three mice) and 16 cells (three mice) were recorded from uncued and cued animals, respectively. (**E**) Exampletrace of AMPA-EPSCs recorded at +40 mV after PiC-to-mPFC inhibition and grouped data for AMPA/NMDA ratio (right). Scale bars: 100 pA, 50 ms. 16 and 19 cells were recorded from four uncued and five cued mice, respectively. (**F**) Viral strategy with histological examples for chemogenetic inhibition of PiC-to-mPFC. Scale bar, 500 μm. (**G**) Left: CNO injection (2 mg/kg, ip) was performed 60 min before the conspecific interaction in uncued and cued observers. Right: impact of PiC-to-mPFC pathway inhibition during the conspecific interaction on the cumin preference score. (**H**) Surgery strategy with histological example showing the track of the optic fiber targeting the mPFC. (**I**) Left: in vivo photostimulation of PiC terminals in the mPFC occurred 4 hours before the food choice session. Right: cumin preference index. Black cross represents mean ± SEM. *$p < 0.05$; **$p < 0.01$; ***$p < 0.001$. See tables S1 and S2 for complete statistics and mean ± SEM values, respectively.

context. By combining viral injection strategies and electrophysiological recordings, we demonstrate that STFP acquisition increases the excitatory transmission at PiC-to-NAc projectors in the mPFC, which is the cause of the altered behavior. Our study thus adds a circuit to the complexity of food intake behavior that may override immediate metabolic needs in the interest of survival.

REFERENCES AND NOTES

1. H. Zheng, N. R. Lenard, A. C. Shin, H. R. Berthoud, *Int. J. Obes.* **33** (Suppl 2), S8–S13 (2009).
2. S. D. Munger *et al.*, *Curr. Biol.* **20**, 1438–1444 (2010).
3. J.-F. Gariépy *et al.*, *Front. Neurosci.* **8**, 58 (2014).
4. B. Bessières, O. Nicole, B. Bontempi, *Nat. Protoc.* **12**, 1415–1436 (2017).
5. Z. Liu *et al.*, *Neuron* **95**, 106–122.e5 (2017).
6. J. M. Otis *et al.*, *Nature* **543**, 103–107 (2017).
7. D. R. Euston, A. J. Gruber, B. L. McNaughton, *Neuron* **76**, 1057–1070 (2012).
8. E. C. O'Connor *et al.*, *Neuron* **88**, 553–564 (2015).
9. E. Lesburguères *et al.*, *Science* **331**, 924–928 (2011).
10. A. Friedman *et al.*, *Cell* **161**, 1320–1333 (2015).
11. Y. Zhu, C. F. R. Wienecke, G. Nachtrab, X. Chen, *Nature* **530**, 219–222 (2016).
12. C. J. Guenthner, K. Miyamichi, H. H. Yang, H. C. Heller, L. Luo, *Neuron* **78**, 773–784 (2013).
13. L. Ye *et al.*, *Cell* **165**, 1776–1788 (2016).
14. L. A. Schwarz *et al.*, *Nature* **524**, 88–92 (2015).
15. S. Cull-Candy, L. Kelly, M. Farrant, *Curr. Opin. Neurobiol.* **16**, 288–297 (2006).
16. T. J. Stachniak, A. Ghosh, S. M. Sternson, *Neuron* **82**, 797–808 (2014).
17. V. Pascoli, M. Turiault, C. Lüscher, *Nature* **481**, 71–75 (2011).
18. D. D. Stettler, R. Axel, *Neuron* **63**, 854–864 (2009).
19. B. Roland, T. Deneux, K. M. Franks, B. Bathellier, A. Fleischmann, *eLife* **6**, e26337 (2017).
20. C. S. Maldonado-Irizarry, C. J. Swanson, A. E. Kelley, *J. Neurosci.* **15**, 6779–6788 (1995).

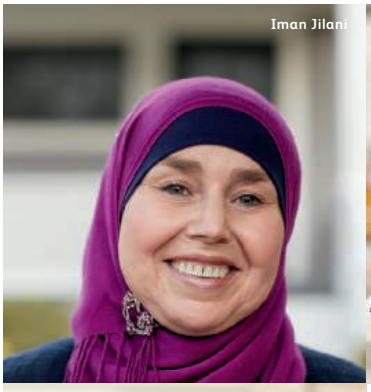
ACKNOWLEDGMENTS

We thank E. C. O'Connor and all the lab members for comments on the manuscript. We also thank Alan Carleton and Ivan Rodriguez for critical comments on the manuscript. **Funding:** This work was supported by the Swiss National Science Foundation (core grant 310030B_170266 to C.L. and Ambizione grant P200P3-154737 to P.V) and by an advanced grant from the European Research Council (MeSSI) (to C.L.). **Author contributions:** M.L. conceived the experiments and performed surgeries for viral infection, behavioral experiments, and eletrophysiological recordings. R.A. and T.S. performed immunohistological staining and histological analysis. J.F. and R.V.Z. performed data analysis. V.P. performed patch recordings. C.L. conceived and supervised the study and wrote the manuscript with M.L. **Competing interests:** C.L. is a member of the scientific advisory boards of Stalicla SA and the Phénix and IRP Foundations. **Data and materials availability:** All data and materials used in the analysis are available in the main text and supplementary materials.

SUPPLEMENTARY MATERIALS

science.sciencemag.org/content/364/6444/991/suppl/DC1
Materials and Methods
Figs. S1 to S5
Tables S1 and S2
Reference (*21*)

7 January 2019; accepted 16 May 2019
10.1126/science.aaw5842











Everything that makes us unique makes us uniquely good at the work we do together.

WE ARE THE MANY DARING, DIFFERENT PEOPLE OF PFIZER

ALL DRIVEN TO DISCOVER THE CURE.

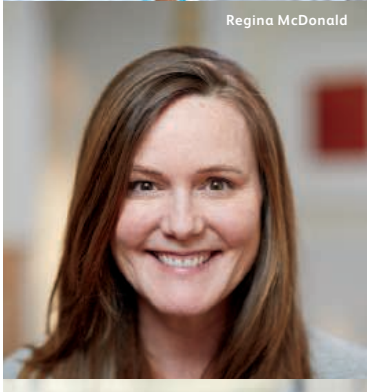
Learn more at

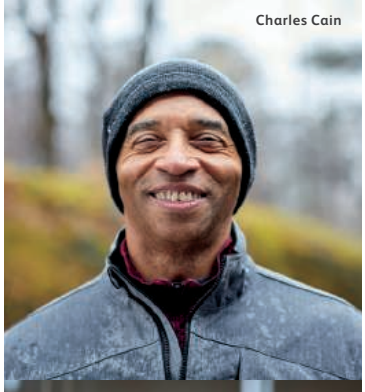
pfizercareers.com

Pfizer

Driven to discover the cure

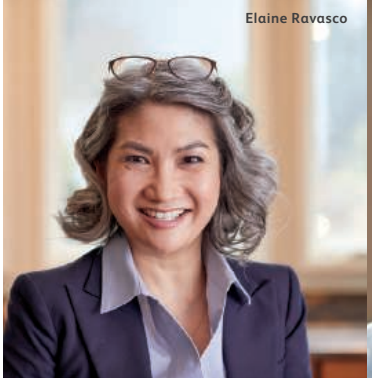




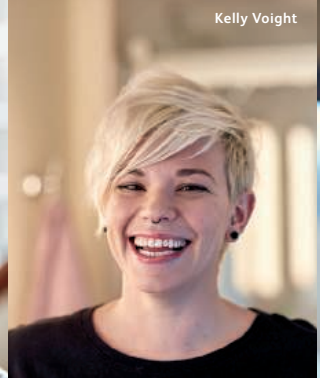


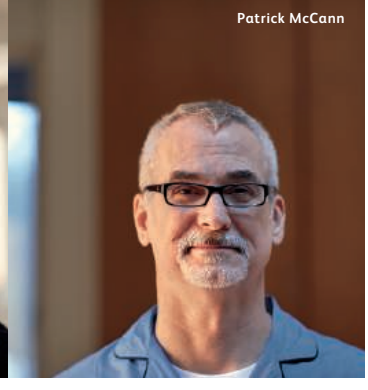












BURROUGHS WELLCOME FUND

President

Mission
The Burroughs Wellcome Fund is an independent private foundation dedicated to advancing the biomedical sciences by supporting research and other scientific and educational activities.

The Burroughs Wellcome provides approximately $40 million in annual funding across the biomedical research landscape and in STEM education in the Fund's home state of North Carolina. BWF believes that a diverse scientific workforce is essential to the process and advancement of research innovation, academic discovery, and public service.

The Opportunity
The Burroughs Wellcome Fund seeks an innovative and creative leader dedicated to advancing biomedical science, promoting career development for biomedical researchers, developing leaders in the research enterprise, and championing STEM education.

The President is responsible for developing, executing, and evaluating BWF competitive award programs and other program-related activities in targeted areas of biomedical research and STEM education. In particular, she or he will provide the visionary leadership for the Fund's grantmaking strategy. The President will also promote the mission of the Fund by engaging with various networks, audiences, and communication channels. Further information on the position can be found in the President's job description.

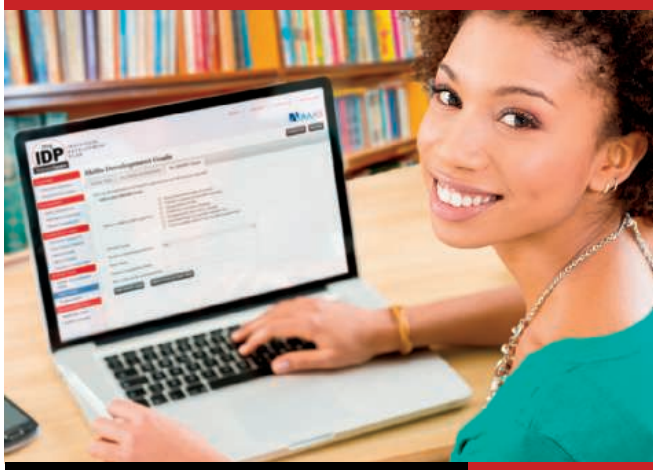
To assure full consideration, applicants must submit by **July 15, 2019,** a curriculum vitae, a statement of interest (maximum of two pages) that includes one's vision for directions for the Fund, and the name and contact information for three references. Interested candidates should submit these materials electronically to **Barbara Evans** at **bevans@bwfund.org**.

Questions regarding the details of this position should be directed to Russ Campbell, Secretary of the Board of Directors of the Burroughs Wellcome Fund, at rcampbell@bwfund.org.

BWF is an Equal Opportunity Employer and encourages women and candidates underrepresented groups to apply.

See www.bwfund.org for full details.

myIDP: A career plan customized for you, by you.



For your career in science, there's only one Science

my IDP ScienceCareers

Recommended by leading professional societies and the NIH

Features in myIDP include:

- Exercises to help you examine your skills, interests, and values.
- A list of 20 scientific career paths with a prediction of which ones best fit your skills and interests.
- A tool for setting strategic goals for the coming year, with optional reminders to keep you on track.
- Articles and resources to guide you through the process.
- Options to save materials online and print them for further review and discussion.
- Ability to select which portion of your IDP you wish to share with advisors, mentors, or others.
- A certificate of completion for users that finish myIDP.

Visit the website and start planning today!
myIDP.sciencecareers.org

ScienceCareers In partnership with:

advancing the life sciences 1912-2012 FASEB Federation of American Societies for Experimental Biology

Medical College of Wisconsin

UCSF University of California San Francisco

Burroughs Wellcome Fund

CityU
香港城市大學
City University of Hong Kong

55th World University
5th World's top 50 Universities under age 50
1st Engineering/Technology/Computer Sciences in Hong Kong
2nd Business School in Asia



Worldwide Search for Talent

City University of Hong Kong is a dynamic, fast-growing university that is pursuing excellence in research and professional education. As a publicly-funded institution, the University is committed to nurturing and developing students' talents and creating applicable knowledge to support social and economic advancement. The University has nine Colleges/Schools. As part of its pursuit of excellence, the University aims to recruit **outstanding scholars** from all over the world in various disciplines, including **business, creative media, data science, energy and environment, engineering, humanities and social sciences, law, science, veterinary medicine and life sciences.**





The University welcomes applications and nominations for all faculty positions of Chair Professor, Professor, Associate Professor and Assistant Professor. The remuneration package will be highly competitive, commensurate with qualifications and experience. Interested parties are invited to submit an online application with current curriculum vitae to apply for current openings at http://go.cityu.hk/hrojobus or by email to "hrojob@cityu.edu.hk".

City University of Hong Kong is an equal opportunity employer and we are committed to the principle of diversity. Personal data provided by applicants will be used for recruitment and other employment-related purposes.

Worldwide recognition ranking 55th, and 5th among top 50 universities under age 50 (QS survey 2019); 1st in Engineering/Technology/Computer Sciences in Hong Kong (ARWU survey 2016); and 2nd Business School in Asia-Pacific region (UT Dallas survey 2017).

SCIENCE PHILANTHROPY ALLIANCE

President

The Science Philanthropy Alliance seeks a president who will lead the organization in its mission to encourage, secure and advise philanthropic support for science and to promote cooperation among the member foundations to achieve greater impact. The accomplished scientist and seasoned leader selected for this half-time position will head a dedicated staff and core group of senior science advisers in an alliance that is currently supported by more than two dozen affiliated philanthropies. Qualifications include a strong record of scientific accomplishment, success as an institutional leader, and experience in gaining philanthropic support for science.

The Alliance is currently headquartered in Palo Alto, though its work takes place in various parts of the United States and occasionally in other countries. Competitive salary and benefits.

Candidates are invited to apply by **30 June 2019**. Inquiries and letters of interest with a current cv should be sent to:

Christine Miller
Office of Human Resources
Gordon and Betty Moore Foundation
1661 Page Mill Rd
Palo Alto CA 94304
(christine.miller@moore.org)

ScienceCareers
FROM THE JOURNAL SCIENCE AAAS

Follow us for jobs, career advice and more!

@ScienceCareers

/ScienceCareers

Science Careers

ScienceCareers.org



FACULTY RECRUITMENT



NUS National University of Singapore

MBI MECHANOBIOLOGY INSTITUTE

Mechanobiology Institute (MBI), jointly with the Department of Biological Sciences (DBS) and the Department of Biomedical Engineering (BME), at the National University of Singapore (NUS) invites applications for multiple tenure-track faculty positions at all levels. We seek candidates committed to collaborative interdisciplinary research in areas of the mechanobiology of aging, degeneration, regeneration, stem cells and organoids, and immune cell functions. Exceptional research programs in other areas, such as mechano-medicine and cancer mechanobiology, or advanced methodology development in imaging, nanotechnology, computing, or diagnostics, will also be considered. Successful applicants will hold a Principal Investigator position at MBI, with a joint tenure-track faculty appointment at either DBS or BME, and can expect internationally competitive salary and benefits, core research infrastructure support, and generous start-up packages.

MBI is a leading multi-disciplinary institute devoted to new paradigms for understanding biological functions in health and disease from the perspective of cell, tissue and organ mechanics/dynamics and mechano-signal transduction. The Institute operates on a fully integrated open-lab platform, with extensive core-facility support dedicated to state-of-the-art technologies in light microscopy, nano- and micro-fabrication, protein expression and cloning, and computing. More details about MBI can be found at **mbi.nus.edu.sg**. Both DBS and BME at NUS hold high global rankings in cutting-edge research and education at both the undergraduate and graduate levels. More details about DBS and BME can be found at **www.dbs.nus.edu.sg** and **www.eng.nus.edu.sg/bme**.

Candidates should hold a Ph.D. degree in relevant fields, with demonstrated excellence in research and experience in teaching. For accelerated consideration, application materials, including a cover letter, Curriculum Vitae with full publication list, 2 to 3-page research interest and plan, a teaching statement, and contact details of 4 referees for Assistant Professor candidates and 6 for Associate and Full Professor candidates, should be submitted to the Faculty Recruitment Committee via email at **mbihr@nus.edu.sg** by July 15, 2019. Late applications will also be considered until the positions are filled.

WARREN ALPERT FOUNDATION

2nd ANNUAL POSTDOCTORAL FELLOWSHIP AWARD

The Warren Alpert Distinguished Scholars is a recently established program, now in its second year, that will support individual scientists of exceptional creativity who have an MD or PhD degree and who have completed a minimum of three years and not more than five years of a post-doctoral fellowship in the field of basic neurosciences at a medical school located in the United States

These awards are given as transitional post-doctoral awards for recipients as they advance to become full time faculty members at the Assistant Professor level or higher. The medical school nominating each scholar will be awarded $200,000 annually for two years to cover their salary, lab costs, and related expenses. Up to fifteen percent of indirect costs is included in the $200,000. All applicants are required to provide a minimum of 75% effort. Deans of medical schools are invited to submit one nomination.

Please see our web page for full details: **www.warrenalpertfoundation.org**

Applications are due by November 1, 2019.

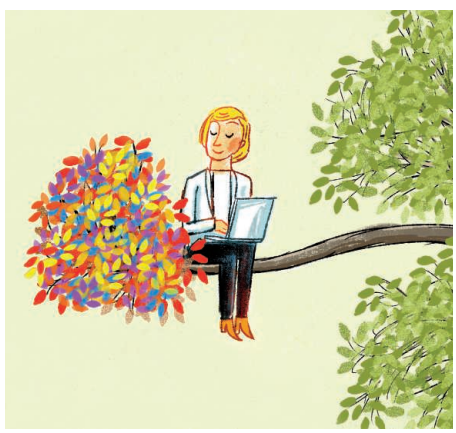
Science Careers online @sciencecareers.org

By **Kara Mosovsky**

Time to branch out

It seemed risky to try something new midway to my tenure review. Since I started my dream job as an assistant professor at a small liberal arts college, the gist of the advice I heard and read was to stick with what I know, and then I could branch out after tenure. I didn't necessarily disagree—it made sense that I could contribute most in my formal area of expertise. But as I chugged along on my research using the same old tried-and-true benchtop assays, my excitement about the work was fading. I needed something new to inspire me again.

I was intrigued by big data projects, long touted as the future of my field of microbiology. But I thought of myself as computer illiterate. Computational biology was intimidating, so I had steered clear of it. But I knew that my field was changing, and I could either get onboard or be left behind. "If I don't try it now, I may never have the courage to try it at all," I thought. Besides, I had an idea for a big data microbiome project that excited me more than any project had for years. If I was this motivated, surely it would turn out OK … right?



"Expertise … can also mean the willingness to move outside of your comfort zone."

"I shouldn't have to be pigeonholed into my 'formal area of expertise' for the rest of my career," I thought to myself. "Doesn't a Ph.D. demonstrate that you have the ability to learn and master something new?" My other research projects were in good shape, and I was feeling comfortable with my status and reputation among my peers. It was time to trust my instincts and give it a shot.

My plan was to ditch the comfort of my benchtop and biosafety cabinet and embark on a 10-week project that would combine field research with bioinformatics. I was almost laughably outside of my comfort zone, and honestly a bit naïve about what was involved, but I was willing to risk a summer to see where it would lead.

And so we began, my talented undergraduate research student and I, with our computers, a huge stack of papers, and a heck of a lot of let's-try-this attitude. We hit our first roadblock earlier than we had expected to: on the very first day. It took us more than 5 hours to download the program we needed to use. Then there was the language barrier—the commands for data analysis might as well have been hieroglyphics. Even the online help forums assumed a level of knowledge we did not have. But, I reminded myself that there was no pressure to succeed. My motto was, "We'll throw everything we have at this, and then see where we stand."

For the first several weeks, progress was slow and steady, with an emphasis on slow. Day after day, we encountered new roadblocks. But we overcame each one and gained confidence. After the 10 weeks we just kept going. Now, more than a year after starting that work, we may not be experts, but we are far from beginners.

Finding success in a new area made me feel proud and pretty wicked smart—a lot smarter and more capable than academia sometimes makes me feel. Accepting my status as a novice also freed me to conduct research for the simplest reason, the one that drew me to the field in the first place: my love of the science. Freed from the pressure of acting the part of an expert, I was able to make it an incredibly productive year. The momentum extended to my other work in sometimes unexpected ways. I resurrected and remastered old techniques and applied them imaginatively. Branching out might have been a bit of a risk, but the reward more than made up for it.

To earn tenure, you must prove to a committee of your peers that you have the skills and capacity for long-term success. But with this particular project, I proved the same thing to myself—which in the long run is just as valuable, if not more. Expertise might be defined by the things you can reliably do and do reliably well, but I've learned that it can also mean the willingness to move outside of your comfort zone; the courage to take a risk, even when failure is a real possibility; and the perseverance and stamina to overcome whatever obstacles you may encounter along the way. ■

Kara Mosovsky is an assistant professor at Moravian College in Bethlehem, Pennsylvania. Send your career story to SciCareerEditor@aaas.org.

ILLUSTRATION: ROBERT NEUBECKER

Published by AAAS